

# THIS WEEK

## EDITORIALS

**CONSERVATION** Why the world should start a great whale sale **p.114**

**WORLD VIEW** Journals must not censor papers on virulent flu **p.115**



**VISION** Life in black and white helps primates to find food **p.116**

## Get tough on nuclear safety

*A refreshingly frank and forward-looking report on the safety of French nuclear power plants in the wake of Fukushima should spur other countries to take a hard look at regulation of their own reactors.*

The Three Mile Island and Chernobyl nuclear accidents each prompted profound rethinks of safety requirements. But as the incidents slipped into history, the nuclear industry, regulators and governments tended to revert to reassuring refrains that atomic energy was once again safe and in expert hands.

So it is probably too early to be confident about the impact of the Fukushima accident in Japan last March. But it is clear that, as the defences at the Fukushima Daiichi power plant crumbled, so too did the fundamental dogma of modern nuclear safety: that a series of back-up and redundant safety systems, combined with physical defences strong enough to resist expert estimates of external threats, was enough to make impossible a catastrophic meltdown and release of radioactivity into the environment.

As the first anniversary of the disaster approaches, and supporters and opponents of nuclear power prepare to use it to underscore their positions, will Fukushima mark a turning point for the nuclear enterprise, or will industry return to business as usual?

André-Claude Lacoste, head of France's Nuclear Safety Authority (ASN) in Paris, suggested at a press conference last week that things have already changed. "There will be a before and an after Fukushima," he promised.

Is he right? Some in industry will always oppose the costs of tougher regulation, and shortsighted or ideological politicians and companies will continue to insist that a repeat of Fukushima is impossible in their own backyards. But many in the nuclear industry were genuinely and deeply shocked to see at Fukushima a sequence of events that they believed impossible. The world's main nuclear operators have an interest in establishing the causes of the disaster and learning the lessons — they know too well that if another major accident were to occur, then in many people's eyes the already-struggling industry would be finished.

The World Association of Nuclear Operators, for example, has stressed the need for its members to respond properly to Fukushima, and has beefed up its own inspection and oversight of plants (see *Nature* 472, 274 and <http://doi.org/hj5>; 2011).

So to France, the world's leading user of nuclear power and arguably the nation with the most to lose from a global rejection of it. Last week, the ASN released a report announcing a sweeping safety upgrade to all the country's reactors (see page 121). The planned multi-billion-euro improvements are part of a programme of tests to assess how well French reactors would stand up to extreme events, and how prepared plants are to deal with a major accident. The ASN's report is written with stunning candour, stating plainly that a loss of coolant or electricity could, in the worst cases, see meltdowns at reactors in hours. It also lists many shortcomings found during 'stress tests', in which some safety aspects of plants were found not to conform to existing standards.

Critics will wonder why the ASN didn't spot these problems earlier, given that it is responsible for regulating the plants. Others will question how the authority can reconcile its statement that France's reactors are

fundamentally safe with its insistence that they must be upgraded on safety grounds. But it would be a mistake to penalize France for listing its nuclear shortcomings, especially when other nations seem less enthusiastic about publicly discussing problems with their own reactors and regulations. The French report makes for a breath of fresh air in a

**"It would be a mistake to penalize France for listing its nuclear shortcomings."**

post-Fukushima climate in which worldwide public reassurance has too often taken priority over transparent debate.

The ASN has also come up with an elegant technical solution to get around the (universal) dilemma of how to protect a plant from external threats, such as natural disasters. The report recommends that all reactors, irrespective of their perceived vulnerability, should add a 'hard core' layer of safety systems, with control rooms, generators and pumps housed in bunkers able to withstand physical threats far beyond those that the plants themselves are designed to resist.

There will, rightly, be scepticism about whether France will ultimately implement the new measures. The bunker concept may prove technically difficult, and Électricité de France — the operator of the reactors — would need to pay for systems that some in the company will probably feel are an expensive luxury.

Whatever happens in the long term, the French plans have an immediate benefit: they raise the post-Fukushima safety bar for other countries. Those governments, regulators and companies that have yet to propose anything close to such far-reaching measures must now explain why not. ■

## A long stretch

*The UK government hopes to squeeze even more out of science — without paying a penny extra.*

David Willetts may not be familiar with the film *Jerry Maguire*, in which Tom Cruise yells: "Show me the money!" But the UK science minister has been on the receiving end of a number of similar quips this week.

By most measures, the United Kingdom has always achieved greater research output than might be expected from the amount of government funding its science base receives. Last week, in a speech to the London-based think-tank Policy Exchange, Willetts said that he wants to stretch this relationship even further.

For starters, he wants the number of British universities rated among the world's top 100 to grow from the current figure of

between 10 and 19, depending on the rankings used. To help make that happen, he announced that his coalition government was “inviting proposals” for “a new type of university” that would focus on science and postgraduates. But there was a catch. “There will,” Willetts stated, “be no additional government funding.” This triggered a storm of protest from experts and several (poor) impressions of Cruise.

During his speech, Willetts was keen to reference plans for a huge university campus in New York being pushed forward by Cornell University (see *Nature* <http://doi.org/hj9>; 2011). And private higher education is clearly on the rise, albeit probably more in teaching than the research arena. But, as critics quickly pointed out, the Cornell project is receiving at least US\$100 million in public funding.

Experts contacted by *Nature* said that the idea that private finance and business sponsorship alone can create a new institution — as Willetts suggested — seems fanciful. “I don’t think this is likely to fly without very, very substantial amounts of new money,” says Paul Nightingale, a science and technology policy expert at the University of Sussex in Brighton, UK. And Roger Geiger, who studies research universities at Pennsylvania State University in University Park, says: “Industry has its own research labs and if they’re going to invest their own money, that’s where they’re going to put it.”

Neither Willetts nor his Department for Business, Innovation and Skills was willing to elaborate on the plans this week, saying only that much depends on the proposals that the department receives. The government insists that there has been “a lot of interest”, but without government incentive, will that interest go any further?

In his speech, given just a stone’s throw from the Houses of

Parliament, Willetts also highlighted the good that his government has done. As the United Kingdom stumbles through one of the worst economic climates in living memory, the fact that the country’s research budget has been largely protected from the severe cuts inflicted on other public sectors (including university teaching) is something to be thankful for.

And it is a shame that Willetts’ high-profile but extremely brief mention of the universities idea distracted from other points in the speech, such as an admission that the government is involved in “picking winners” — investing in technologies under-

pinned by science and research that could bring economic benefit — something that politicians have been reluctant to acknowledge previously.

“The noises are positive. Every time he speaks about science and innovation the thinking seems to get a little more sophisticated,” says Kieron Flanagan, a lecturer in science and technology policy at the University of Manchester, UK. This is a welcome shift

from previous Conservative policies, which tended towards generic initiatives. However, the rhetoric has yet to be matched with much action, Flanagan says, although increased efforts to link businesses and research in key areas are a good start.

Many will be happy to be proved wrong if a number of world-leading finance-free universities do arise in the United Kingdom, as Willetts hopes. Meanwhile, discussion of the idea certainly has one thing in its favour: it’s not costing anything. ■

**“Private higher education is clearly on the rise, albeit probably more in teaching than the research arena.”**

# Whales for sale

*A quota-trading scheme could end conflict between whalers and conservationists.*

**I**n the chilly waters of the Southern Ocean, an annual drama is under way once more. The Japanese whaling fleet has set to sea again. So has a flotilla of vessels crewed by conservationists and activists, determined to keep the hunters from their prey.

Three Australian anti-whaling campaigners boarded the *Shonan Maru No. 2* whaling ship on Sunday. After negotiations, the Japanese government has agreed to release them to an Australian customs ship. The incident came just days after the conservation ship *Brigitte Bardot* was smashed by a giant wave and seriously damaged while pursuing the ship *Nisshin Maru*, some 2,400 kilometres from the Australian coast. Sea Shepherd Conservation Society, a group based in Friday Harbour, Washington, that operates the stricken vessel, is counting the cost of its principles. This isn’t the first time: in January 2010, the group’s powerboat *Ady Gil* sank after a collision with the *Shonan Maru No. 2*. The skirmishes and confrontations continue, with campaigners maintaining their high-risk pursuit and their attempts to foul the propellers of the whaling ships with ropes, and the whalers responding with water cannon. Surely there is a better way?

Perhaps. On page 139 of this issue, three environmental scientists outline a plan to introduce tradable quotas for whale catches. Under the scheme, conservationists could buy (and retire) the quotas from whalers, giving industry a way to profit from the animals without killing them. In return, anti-whaling campaigners could be more certain that their actions were reducing the slaughter. Theoretically, such a scheme would allow both sides to benefit with no loss of face. As the researchers say, it could “open the door to reducing mortality without needing to battle over whether whaling is honourable or shameful”. And both the number of whales killed and the associated costs would go down.

The article’s authors — Christopher Costello and Steven Gaines of the University of California, Santa Barbara, and Leah Gerber of Arizona State University in Tempe — use the per-animal profit of whaling ships to decide that about US\$13,000 would be a fair price to buy the life of a minke whale, and \$85,000 should secure a fin whale. “Whale prices should therefore be within reach of conservation groups and even some individuals,” they suggest.

The idea first surfaced in 1982, to little effect. But perhaps, three decades on, its time has come. Market approaches to environmental problems are now common, with carbon offsets bought by individuals to neutralize their greenhouse-gas emissions. Such systems have even been shown to be effective, reducing sulphur dioxide pollution from US power plants.

To put a price on the head of a whale would be a different matter, of course. Committed anti-whaling campaigners would have to put aside moral objections and accept such a scheme’s tacit legitimization of whaling as an enterprise to be rewarded, as well as the de facto official approval for the heavily disputed notion that whales (and other animals) are a resource to be exploited. Pro-whaling nations would need to be persuaded that the scheme would have more strategic benefit than their continuing political efforts to lift, or find ways to work around, the current commercial whaling moratorium. Then there is the need for scrutiny and verification of the quota market, not to mention getting such a plan through the political quagmire that bogs down annual meetings of the International Whaling Commission, the body that would be best placed to put a market mechanism into action. (And what of the world’s scientists, denied information from some of the 1,000 or so whales slaughtered each year for ‘scientific purposes’? *Nature* suspects that they would manage.)

Still, with political will and goodwill, the idea could work. At the very least, it deserves proper consideration from all involved. As

events in the Southern Ocean show, pro- and anti-whaling groups will both go to extraordinary lengths to pursue their agendas. To those in peril on the sea, the middle ground should seem just as secure as the moral high ground. ■

**➤ NATURE.COM**  
To comment online,  
click on Editorials at:  
[go.nature.com/xhunjv](http://go.nature.com/xhunjv)





## Don't censor life-saving science

Controlling who is allowed access to information about mutations in the H5N1 bird flu virus is unacceptable, says Peter Palese.

The recent arguments over the creation of a transmissible form of the bird flu virus (H5N1) feel very familiar. My colleagues and I were at the centre of a similar controversy in 2005, when we reconstructed the 1918 flu virus, which had killed up to 50 million people worldwide. News stories around the globe debated the merits of our research and television pundits argued opposing viewpoints. Naturally, the US government was concerned — as it is now. Yet our research was published in full. So why are similar concerns being used now to demand unacceptable censorship of the H5N1 scientific papers?

I have spent my career studying potentially dangerous pathogens — 20 years ago, my lab developed the technique that has enabled the H5N1 researchers to insert the mutations that render the virus more easily transmissible. In the 1990s, researchers discovered degraded samples of the 1918 virus in lung tissue from US soldiers who had died from the 'Spanish flu'. Using polymerase chain reaction technology, they amplified and sequenced the virus's RNA. We then took an existing influenza virus and, one by one, swapped its genes with those from the 1918 virus, eventually recreating a live version.

As we prepared our results for publication, the US government convened the National Science Advisory Board for Biosecurity (NSABB), which advises the community about research using agents that pose threats to national security or public health. Our experiments had made some people nervous.

During our discussions with members of the NSABB, we explained the importance of bringing such a deadly pathogen back to life. Although these experiments may seem dangerously foolhardy, they are actually the exact opposite. They gave us the opportunity to make the world safer, allowing us to learn what makes the virus dangerous and how it can be disabled. Thankfully, the discussions were largely constructive — within a week, the NSABB recommended that we continue to study the virus under biocontainment conditions, and publish the results so that other scientists could participate in the research. After we published our full paper in 2005 (T. M. Tumpey *et al. Science* **310**, 77–80; 2005), researchers poured into the field who probably would not otherwise have done, leading to hundreds of papers about the 1918 virus. As a result, we now know that the virus is sensitive to the seasonal flu vaccine, as well as to the common flu drugs amantadine (Symmetrel) and oseltamivir (Tami-flu). Had we not reconstructed the virus and shared our results with the community, we would still be in fear that a nefarious scientist would recreate the Spanish flu and release it on an unprotected world. We now know such a worst-case scenario is no longer possible.

WHO WILL WANT TO  
ENTER A FIELD IN  
WHICH YOU  
CAN'T PUBLISH  
YOUR MOST  
SCIENTIFICALLY  
INTERESTING  
RESULTS?

➔ **NATURE.COM**  
Discuss this article  
online at:  
[go.nature.com/yexx2z](http://go.nature.com/yexx2z)

This experience has made the NSABB's latest recommendation — that the H5N1 researchers not reveal the mutations behind the virus's transmissibility — all the more frustrating. I make the same argument today that we made in 2005 — publishing those experiments without the details is akin to censorship, and counter to science, progress and public health. Why did the (different) members of the committee come to a different conclusion in this case? I can only hope that they take a more sensible stance and change their minds, or that the scientific community at large convinces them to do so. Certainly, the authors of the papers, as well as the journals considering them for publication (including this one), should resist the committee's unworkable compromise that the full information should be released only to approved experts, and insist on full disclosure.

Giving the full details to vetted scientists is neither practical nor sufficient. Once 20–30 laboratories with postdoctoral fellows and students have such information available, it will be impossible to keep the details secret. Even more troublesome, however, is the question of who should decide which scientists are allowed to have the information. We need more people to study this potentially dangerous pathogen, but who will want to enter a field in which you can't publish your most scientifically interesting results?

Knowing which mutations render the virus more dangerous could help on a public-health level — if an outbreak of bird flu occurs in Taiwan, for instance, and researchers sequence the virus and see those mutations, we would know to ramp up the production of appropriate vaccines and antiviral drugs.

Incidentally, I believe that the risk of future outbreaks in humans is low: H5N1 has had the opportunity to cause widespread pandemics for many, many decades, yet it has not done so. Although we know the virus is transmissible between ferrets, little is known about how it will behave in other animals, including humans.

The more danger a pathogen poses, the more important it is to study it (under appropriate containment conditions), and to share the results with the scientific community. Slowing down the scientific enterprise will not 'protect' the public — it only makes us more vulnerable. ■

**Peter Palese** is the Horace W. Goldsmith professor and chair of the Department of Microbiology at the Mount Sinai School of Medicine, New York.

e-mail: [peter.palese@mssm.edu](mailto:peter.palese@mssm.edu)

**Editor's note:** Nature is considering one of the papers and the NSABB's recommendations. It is also involved in consultations about how restricted access to the scientific methods and data might be implemented.

# SEVEN DAYS

The news in brief

## POLICY

### Stem-cell regulation

China has ordered a halt to unapproved stem-cell treatments, and says that it will stop accepting new applications for clinical trials using stem-cell products until July. The 10 January announcement by the government's health ministry was viewed as an effort to crack down on a flourishing trade in unproven stem-cell therapies, which are widely offered and loosely regulated in the country.

### Telescope rivals

The US National Science Foundation (NSF) has launched a competition for a giant ground-based telescope — even though it can't provide funds to build or operate such an instrument until at least 2020 (see *Nature* 479, 18–19; 2011). Two rival US projects, the Thirty Meter Telescope and the Giant Magellan Telescope, hope to earn some backing from the government agency, despite the lack of spare cash. The NSF intends to announce the winning proposal by October 2012.

### Indian overhaul

India needs to transform its scientific landscape if it is to avoid falling further behind other nations, says the country's Prime Minister, Manmohan Singh. His remarks, at the country's largest annual science congress, in Bhubaneswar on 3 January, were triggered by a December 2011 report from his scientific advisory council, which urged him to make structural administration changes, send people abroad for PhD studies and create centres of excellence. India's scientists have heard calls for reform before — but the council's chair, C.N.R. Rao,

thinks that the government will take the panel's advice seriously. See [go.nature.com/cksmj6](http://go.nature.com/cksmj6) for more.

### Beijing smog

Residents of China's capital can expect to get more realistic assessments of the city's air quality. The municipal government said on 5 January that it would publicly report data on levels of particles smaller than 2.5 micrometres across ( $PM_{2.5}$ ), and would report hourly (rather than daily) on other pollutants, such as sulphur dioxide. Without  $PM_{2.5}$  monitoring, public assessments had always underestimated Beijing's air pollution, much to residents'

anger. China is working towards a stricter nationwide air-quality standard that includes measurements on ozone and  $PM_{2.5}$ , but this will not be rolled out until 2016.

### Antibiotic ban

The US Food and Drug Administration is restricting some uses of a major class of antibiotic in farm animals, to slow down the rate at which microbes acquire resistance to the drugs. On 4 January, the agency banned unapproved uses of cephalosporins in cattle, pigs, chickens and turkeys — a ban that it had already ordered in 2008, but revoked after protests from farmers, drug firms and

veterinary surgeons. The new order is less strict than the 2008 rule. See page 125 for more.

### Airline carbon row

Global airlines are protesting a European law that requires them to pay for some of the carbon emissions from their flights using European airports. Last week, China's airlines said they would not pay the charges; US airlines have raised prices for European flights, but the country's government is said to be looking at ways to counter the policy. From 1 January, aviation was included in the European Union's Emissions Trading System, with airlines



PURAVIDA FOTOGRAFIA/DEMOTIX/CORBIS

## Chilean reserve scorched by wildfires

Forest fires in Chile have ravaged almost 15,000 hectares of native forest and steppe in the Torres del Paine National Park in Patagonia — burning more than 8% of one of Chile's most important protected areas. The fires began on 27 December, allegedly caused by a tourist, and by 5 January, five of six pockets of fire in

the park region had been controlled. Chile continues to battle fires in other regions. Fires in 2005 and 1985 caused similar destruction in the park, which the United Nations Educational, Scientific and Cultural Organization has designated as a biosphere reserve. See [go.nature.com/ubvjvq](http://go.nature.com/ubvjvq) for more.

expected to buy permits covering 15% of their carbon dioxide emissions in 2012. First payments will not be collected until next year.

## Safer reactors

France's nuclear regulator is demanding stringent safety upgrades for the country's reactors in response to the disaster at Japan's Fukushima nuclear plant. Its 3 January report was sent to the European Commission, which had asked for 'stress tests' of its member states' reactors. By contrast, a 4 January report from the UK nuclear regulator did not find any fundamental weaknesses in its nation's power stations. See page 121 for more.

### PEOPLE

## MMR lawsuit

Disgraced medical researcher Andrew Wakefield is suing the *British Medical Journal* (BMJ), its editor Fiona Godlee, and journalist Brian Deer over a string of articles that branded him a fraud (F. Godlee *et al.* *Br. Med. J.* 342, c7452; 2011). Wakefield's work posited a now-discredited link between autism and the combined measles, mumps and rubella (MMR) vaccine; in 2010, his 1998 research paper on the subject was retracted and he was struck off the UK medical register for serious professional misconduct.

Wakefield filed the suit on 3 January in a district court in Texas, where he now lives.

## EPA research head

The US Environmental Protection Agency's research head and chief science adviser, Paul Anastas, is leaving the agency after two years in charge. Anastas, a pioneer of green chemistry, spent much of his time reforming the agency's programme for assessing the risks of individual chemicals, while also trying to shift its research focus to a more holistic view of sustainability. He told staff on 5 January that he would be returning in mid-February to his research position at Yale University in New Haven, Connecticut.

### EVENTS



## Drought in China

After a decade-long dry spell, China's largest freshwater lake has shrunk to its smallest size in years, state media said on

5 January. The area of Poyang Lake, in the eastern Jiangxi province, was 183 square kilometres early this year, nearly half the average of 344 square kilometres recorded since 1951. The drought has left thousands of fishing boats stranded on the exposed lake bed (**pictured**).

### BUSINESS

## Cheap genomes

The US\$1,000 genome has arrived — according to US biotech firm Life Technologies of Carlsbad, California, which promised on 10 January that its new bench-top sequencing device could break the symbolic cost barrier. The company said that its \$149,000 Ion Proton sequencer, the latest version of the Ion Personal Genome Machine that it launched late in 2010 (see *Nature* 475, 278; 2011), would be able to sequence a genome in a day for \$1,000.

## Hepatitis C hopefuls

Pharmaceutical giant Bristol-Myers Squibb of New York City has become the latest company to spend billions on the promise of hepatitis C treatments. On 7 January, the firm said that it would pay US\$2.5 billion to acquire Inhibitex, a biopharmaceutical company based in Alpharetta, Georgia. Inhibitex's main asset is a compound against

## COMING UP

### 12 JANUARY

The *British Medical Journal* and Britain's Committee on Publication Ethics host a London meeting on how best to manage research misconduct in the United Kingdom.

### 13 JANUARY

India may have gone a year without reporting a case of polio — a milestone that could see it removed from the list of countries where the disease is still endemic.

### 14–16 JANUARY

Russia's failed Mars mission, Phobos-Grunt, is expected to fall back to Earth.

hepatitis C that is in phase II trials. Last November, Gilead Sciences in Foster City, California, splashed out \$11 billion on biotech firm Pharmasset of Princeton, New Jersey, which has three treatments for hepatitis C in clinical trials. See [go.nature.com/qjoqfn](http://go.nature.com/qjoqfn) for more on hepatitis C drugs.

## Teva rethink

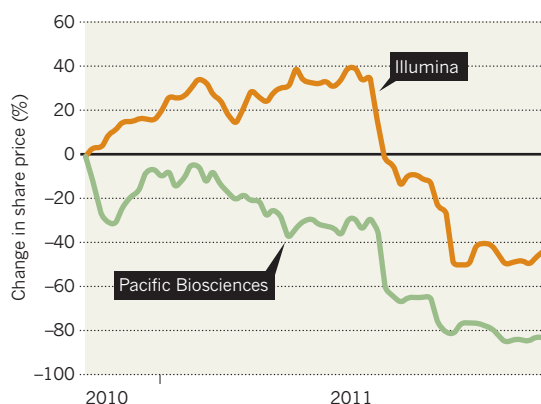
Israeli pharmaceutical firm Teva, the world's largest maker of generic drugs, may shift its focus towards branded medicines after it announced a new chief executive. Jeremy Levin, former head of strategy and alliances at Bristol-Myers Squibb in New York City, has a reputation for making external partnerships and acquisitions and is expected to continue his approach at Teva, which is headquartered near Tel Aviv. "Medicines are medicines," he told investors in a conference call on 3 January. "It doesn't matter if they are branded or generic."

## TREND WATCH

Companies in the gene-sequencing industry — such as Illumina of San Diego, California — are suffering because of slack demand for their machines. But one of the hardest hit is Pacific Biosciences, based in Menlo Park, California, whose share price has fallen more than 82% since its initial public offering in October 2010. The firm has also been hit with a class-action lawsuit alleging that it made misleading statements about its technology in a prospectus shown to potential investors.

## GENE-SEQUENCING STOCK SUFFERS

Pacific Biosciences has fared worse than other sequencing companies since it went public in 2010.



SOURCE: NASDAQ

► [NATURE.COM](http://NATURE.COM)

For daily news updates see:  
[www.nature.com/news](http://www.nature.com/news)



# NEWS IN FOCUS

**GREECE** Europe's financial crisis spurs research shake-up **p.123**

**RADIO ASTRONOMY** Giant array will listen for whispers from the first stars **p.127**

**THERAPEUTICS** NIH launches its translational-medicine institute **p.128**

**CHINA** University president leads the fight against misconduct **p.134**



M. EULER/AP



Nuclear plants such as Tricastin will need to build fail-safe systems that operate even after an accident.

## NUCLEAR POWER

# France 'imagines the unimaginable'

*Regulator demands safety upgrades for nuclear plants to guard against a Fukushima-like disaster.*

BY DECLAN BUTLER

Nowhere did the alarm bells sounded by the Fukushima nuclear disaster ring more loudly than in France, which leads the world in nuclear energy. About three-quarters of its electricity comes from nuclear power stations, and it is one of the main exporters of reactors and related technology.

Now it is leading the way in setting radical

safety standards for the industry, in an effort to ensure that the disaster in Japan on 11 March 2011 could never be replayed on French soil.

Last week, the country's nuclear regulator imposed what are perhaps the toughest safety measures so far in response to the Fukushima accident. In a novel approach, it will require all power plants to build a set of safety systems of last resort, contained in bunkers that will be hardened to withstand more extreme

earthquakes, floods and other threats than plants themselves are designed to cope with.

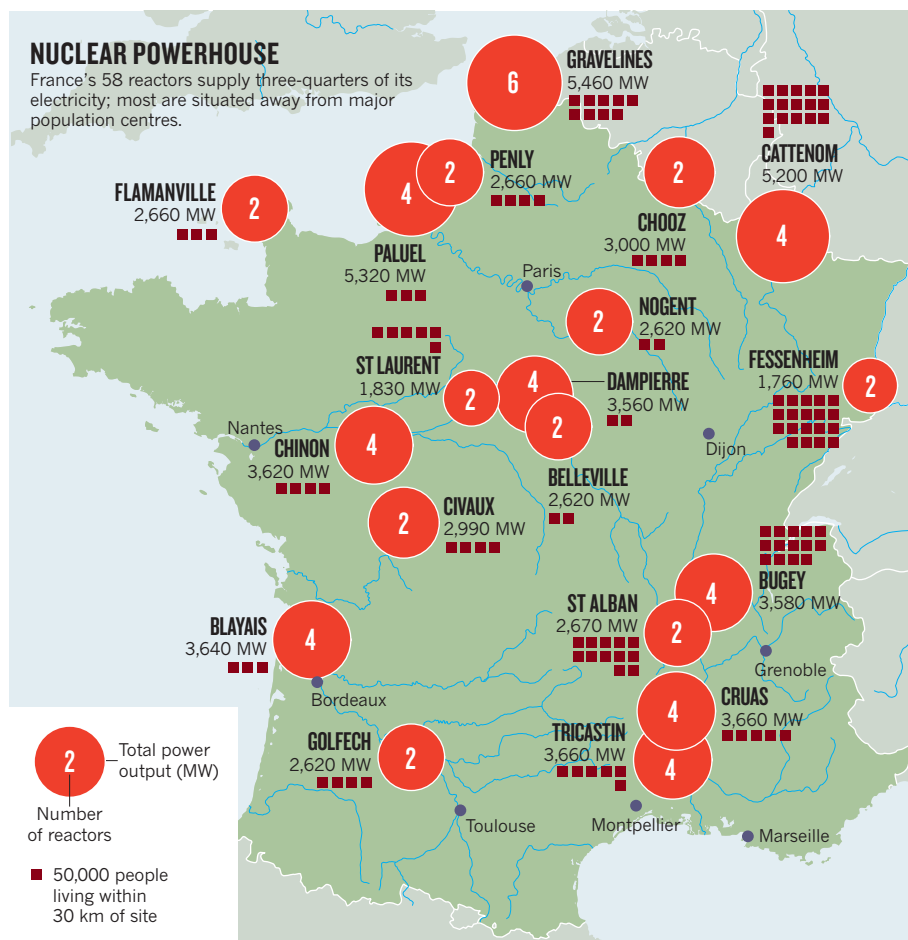
It will also adopt a proposal by Électricité de France (EDF), France's sole nuclear power plant operator, to create an elite force that is specifically trained to tackle nuclear accidents and could be deployed to any site within hours. Both moves respond to the main lessons of Fukushima: that the magnitude of external threats can far exceed those anticipated; that these threats can knock out multiple safety measures; and that to prevent a serious accident degenerating into a catastrophe, it is vital to ensure that key safety capacities — such as a control room, emergency generator and coolant system — remain in working order.

These and a raft of other measures are outlined in a 336-page report published by France's independent Nuclear Safety Authority (ASN), based in Paris, on 3 January (see [go.nature.com/ytkvto](http://go.nature.com/ytkvto)). The report has been submitted to the European Commission as part of ongoing European Union (EU) 'stress tests' of all its member countries' reactors. The ASN report bluntly states that despite existing safety measures, a loss of power or cooling systems at some French plants could result in a "core meltdown within a few hours in the most unfavourable cases".

Keeping systems running in the crucial hours after an accident will be a core doctrine of French nuclear safety in the future. "If you can get the water flowing, you can buy time" and thus avoid the meltdown that made the Fukushima accident so serious, says Martial Jorel, director of reactor safety at the Institute of Radioprotection and Nuclear Safety (IRSN) in Fontenay-aux-Roses near Paris, which gives scientific advice to the ASN. The ASN report incorporates many IRSN recommendations made in November 2011 (see [go.nature.com/b3tjru](http://go.nature.com/b3tjru)). "In France, we're saying, 'imagine the unimaginable'," says Jorel. The current basis of nuclear safety is 'defence-in-depth', in which multiple levels of protection and redundancy are intended to guard against a serious accident, he adds. "But at Fukushima, all of those lines of defence collapsed. The accident has thrown into question all of our safety rules, our ways of thinking."

**NATURE.COM**  
Nature's interactive graphic of the world's nuclear plants:  
[go.nature.com/hgicgt](http://go.nature.com/hgicgt)

Like nuclear regulators in other countries, which are also taking stock of safety, the ASN intends to review and reinforce ►



► conventional measures such as flood-protection barriers. It has also ordered better safety and emergency-response training of plant staff, and a complete review of reactor cooling systems.

The bunker concept is different, however, because it short-circuits the traditional approach to safeguarding against estimated levels of risk. Irrespective of their perceived vulnerability to external threats, plants will need to be equipped with this 'hard core' of protected control rooms, generators and pumps, as well as hardened reservoirs of coolant.

This circumvents the delays and compromises inherent in setting new estimates of seismic, flood or other risks, which requires years of discussions between the regulator, industry and expert advisers, says Jorel. Predicting risk is an imperfect art, and the

bunker concept should protect against any other unforeseen, low-probability event. "It's far easier to design and build a system of last resort than to try to address every potential problem," he says.

The new measures are part of a shift in the emphasis of nuclear safety in the wake of Fukushima, from preventing a nuclear accident to stopping one from spiralling out of control — and mitigating the damage should the worst occur, says nuclear engineer Laurent Stricker, chairman of the World Association of Nuclear Operators (WANO) and a senior adviser to EDF. WANO, which was created as an international forum on nuclear safety in the aftermath of the 1986 Chernobyl accident, announced in November that it would increase its staff from 140 to 415 to address this broader mandate.

France's strategy is also likely to influence the global debate on nuclear safety, with the

bunker safety system and rapid-response team possibly gaining traction internationally, say experts. Stricker endorses both concepts, and adds that WANO will encourage its members to consider creating such specialist response teams in key regions around the world.

Many of the national reports for the EU stress test have been published only in the past few weeks, to meet the commission's deadline of 31 December 2011. But it already seems clear that France's proposals are the most comprehensive. They contrast sharply with those from the United Kingdom, for example, which were released last week and concluded that no major changes were immediately needed at the country's ten plants.

This may reflect differences in the reactors used by each nation, says Andrew Sherry, director of the Dalton Nuclear Institute at the University of Manchester, UK. France uses pressurized water reactors (see 'Nuclear powerhouse'), whereas almost all of Britain's are advanced gas-cooled reactors, which progress to meltdown more slowly in the event of an accident, buying more time to mount an emergency response. "What might be appropriate in France might not be appropriate in the United Kingdom," Sherry says. Experts from EU member states will now peer-review each other's reports and carry out site inspections of nuclear plants, to assess the safety of nuclear reactors across the EU. That exercise is scheduled to be completed in June.

Meanwhile, EDF has said that it fully backs the new rules, but its initial estimate is that adopting them will cost €13 billion (US\$16.6 billion). It must submit initial designs for its new safety features to the ASN by 30 June. The big question, says Jorel, is how fully the planned measures will be implemented.

Yves Marignac, a Paris-based consultant on nuclear and energy issues, says that the French report is a "thorough analysis", particularly in its assessment of the existing safety shortcomings at plants. But he says that the concepts of a protected bunker and rapid-response force will take time to flesh out, and are not likely to be a quick solution. "It's technically wrong to sell politically the idea that billions of euros could fix the problem in the coming months," he says.

Sherry is convinced, however, that the Fukushima accident has been a wake-up call for the nuclear industry. "What's quite clear to me is that they are taking things very seriously." ■



**MORE ONLINE**

#### TOP STORY



Modified mosquitoes set to quash dengue fever  
[go.nature.com/ilakko](http://go.nature.com/ilakko)

#### MORE NEWS

- Return of the super ants [go.nature.com/eisrm3](http://go.nature.com/eisrm3)
- Mathematician claims breakthrough in Sudoku puzzle [go.nature.com/q6tnyj](http://go.nature.com/q6tnyj)
- Thawing permafrost reduces runoff into China's Yangtze River [go.nature.com/ilamsy](http://go.nature.com/ilamsy)

#### PODCAST



Resurrecting ancient proteins, a new hormone and whale markets  
[go.nature.com/sqovzn](http://go.nature.com/sqovzn)



## POLICY

# Greek science on the brink

*Financial woes spur controversial reforms of the country's research system.*

BY ALISON ABBOTT IN ATHENS

**“W**e are trying to survive and go along as if nothing is happening,” says Dimitra Thomaidou, a microscopist at the Hellenic Pasteur Institute in Athens.

Despite Greece's financial crisis, optimism was the prevailing mood at last month's meeting of the Hellenic Society for Biochemistry and Molecular Biology in Athens, where Thomaidou coordinated a session. Meeting attendance was at a record high, and chat was full of references to fancy equipment purchases and Greek success in winning participation in European research-infrastructure programmes.

But as the financial crisis deepens and university and research spending, already among the lowest in Europe, shrink further, staying optimistic is a constant battle. Academic salaries have been cut by 20% and university budgets have halved since the crisis began about two years ago. Still, money from the European Commission and international grants is keeping the best Greek scientists committed to their work. “It may sound irrational, but we just don't think we can live without our research,” said Thomaidou.

Closer conversation, however, reveals anxiety — not about money, but about reforms spurred by the crisis. Just a handful of Greece's universities and research institutions are internationally competitive. A massive restructuring of the system would modernize their governance, giving them more autonomy while introducing greater competition and transparency. Some institutes and universities would be merged to reduce the fragmentation that has arisen in the past 30 years. Expected to take effect this year, the plan also aims to break down barriers that make it difficult for scientists to move between institutions.

Scientists' main concern, says Thomaidou, is that mid-career researchers like herself will survive the upheavals only to find that there is no new generation of researchers to succeed them, because poorly paid and financed research careers are unattractive. “We keep our thoughts firmly on science and hope that things will get better — and that if everything is to be restructured, it will be

**“It may sound irrational, but we just don't think we can live without our research.”**



Despite rallies against austerity in Greece, there is growing acceptance of the need for university reform.

done appropriately,” she says.

Many scientists in Greece accept that their research system needs restructuring. Previous governments failed to win parliamentary support for reform, but the financial crisis has helped to break down resistance, says Achilleas Gravanis, a pharmacologist at the University of Crete in Heraklion and chairman of the biosciences section of the National Council for Research and Technology, which advises the government. A new law for higher education was approved with a huge majority by the Greek parliament on 24 August 2011, and next month a draft law for research should be presented to parliament, where it is expected to have an easy ride.

The academic leadership of the 18 publicly funded research centres in Greece is generally positive about the reforms. “Only good things are likely to happen,” says Dimitris Thanos, a molecular biologist and research director at the Bioacademy in Athens. But scientists in smaller research institutes dread being told to merge with universities, saying that their agility could be crushed by university bureaucracy.

The rectors of Greece's 24 public universities, for their part, seem appalled by the law, which radically changes university governance, depoliticizing it and bringing it into line with European norms. Students will lose their right to vote for department chairs, deans and

rectors. Each university will be responsible for its own budget and must appoint a powerful governing council with 15 members: six from outside the university, and just one student representative. The council will draw up a shortlist for the position of rector, on which faculty members will vote.

## REBELLIOUS RECTORS

Implementation of the law has stalled because rectors are appealing to the Constitutional Court, claiming that the presence of external council members violates their academic independence. Gravanis disagrees with this opposition: “It is shocking that academic leaders would show no respect for a law passed with huge parliamentary majority,” he says. The law was designed with input from a constitutional-court judge, he adds.

Only the University of Crete is complying with the changes. It is to hold elections for internal members of its council on 22 February. “We'll just have to see how we can make the law work well in practice,” says its rector, Euripides Stephanou. But he is nervous. The financial crisis may have encouraged the approval of reform laws, he says, but cash shortages may encourage the incoming governing councils to close faculties that have no revenue-generating potential — such as the University of Crete's prestigious ▶

T. STAVRAKIS/AP



► archaeology and history departments.

The proposed law on research would also need solid financial backing, say scientists. It designs a system in which researchers in different types of institution and in industry would be able to collaborate easily, administration would be efficient and there would be regular calls for competitive research grants. The law would create a mandatory line for research spending in the state budget for the first time. But parliament would have to approve the actual budget each year, and scientists fear that parliament might not be generous.

Greece does not have a dedicated research funding agency, but that absence is offset by the €0.9 billion (US\$1.14 billion) earmarked for research from the country's 2007–13 European Union (EU) Structural Funds, which are effectively subsidies for poorer regions in the union. After years of providing almost no research funding, the Greek government has in the past year put out a handful of calls for infrastructure and competitive-research grant proposals that would use the EU money. Most calls invite applications from academic networks and industry collaborations, but one, made last May, is aimed at individual researchers. Modelled on grants offered by the European Research Council, the calls are worth up to €1 million each. But competition is harsh: of 1,200 applications, fewer than 200 will be funded.

The money will be a life-saver for established researchers, but the future of the system as a whole remains uncertain. Over the next five years, 30% of current faculty members and researchers will retire from Greek universities and research centres, and replacing them may be difficult. Thanks again to EU funding, Greece produces large numbers of PhDs, but most of those who continue on to postdoctoral research do so abroad. In the past, many have returned to seed competitive research groups at home. The proposed law provides schemes to encourage that, but few believe that it will work, given the very low salaries and uncertain funding that researchers can expect.

Vasso Kostourou, a cell biologist at the Alexander Fleming Biomedical Sciences Research Center in Vari, is an exception. She returned to Greece from London in 2008, and recalls colleagues encouraging her because they thought that project funding was about to resume. Instead, she arrived as the crisis hit. At 37 years old, Kostourou thinks that she may be among the last scientists to return to academia in Greece for the foreseeable future. "That's

a shame because the quality of science that can be done here is high," she says. "It's only the funding that's bad." ■

➔ **NATURE.COM**  
Listen to an  
interview about the  
Greek crisis at:  
[go.nature.com/kwsh4c](http://go.nature.com/kwsh4c)

## ECONOMICS

# Disaster toll tallied

*The soaring cost of natural catastrophes is due more to socio-economic than climatic factors.*

BY QUIRIN SCHIERMEIER

Natural disasters around the world last year caused a record US\$380 billion in economic losses. That's more than twice the tally for 2010, and about \$115 billion more than in the previous record year of 2005, according to a report from Munich Re, a reinsurance group in Germany. But other work emphasizes that it is too soon to blame the economic devastation on climate change.

Almost two-thirds of 2011's exceptionally high costs are attributable to two disasters unrelated to climate and weather: the magnitude-9.0 earthquake and tsunami that hit Japan in March, and February's comparatively small but unusually destructive magnitude-6.3 quake in New Zealand.

And the long-term rise in the costs of global disasters is probably due mainly to socio-economic changes, such as population growth and development in vulnerable regions. That conclusion is backed up by a forthcoming study — supported by Munich Re — by economists Fabian Barthel and Eric Neumayer at the London School of Economics. Their analysis of events worldwide between 1990 and 2008 concludes that "the accumulation of wealth in

disaster-prone areas is and will always remain by far the most important driver of future economic disaster damage" (F. Barthel and E. Neumayer *Climatic Change*; in the press). Any major weather event hitting densely populated areas now causes huge losses because the value of the infrastructure has increased tremendously, they note, adding that if the 1926 Great Miami hurricane happened today, for example, it would cause much more damage than it did at the time.

However, weather-related events are generally on the rise. Thanks to a relatively quiet Atlantic hurricane season, damage caused by extreme weather was actually lower in 2011 than in four of the previous five years. But weather accounted for about 90% of the year's 820 recorded natural disasters, which caused at least 27,000 deaths. These disasters include flooding in Thailand, a series of tornadoes that hit the United States Midwest and southern states last spring, and storms and extreme rainfall over parts of the Mediterranean in November.

Since 1980, the report notes, the number of severe floods has almost tripled, and storms have nearly doubled, which insurance experts link, in part, to the impact of climate change (see 'Catastrophe count'). "It would not seem



Heavy rains turned roads into rivers last year as Thailand experienced its worst flooding in 50 years.

P. BROWN/PANOS

► archaeology and history departments.

The proposed law on research would also need solid financial backing, say scientists. It designs a system in which researchers in different types of institution and in industry would be able to collaborate easily, administration would be efficient and there would be regular calls for competitive research grants. The law would create a mandatory line for research spending in the state budget for the first time. But parliament would have to approve the actual budget each year, and scientists fear that parliament might not be generous.

Greece does not have a dedicated research funding agency, but that absence is offset by the €0.9 billion (US\$1.14 billion) earmarked for research from the country's 2007–13 European Union (EU) Structural Funds, which are effectively subsidies for poorer regions in the union. After years of providing almost no research funding, the Greek government has in the past year put out a handful of calls for infrastructure and competitive-research grant proposals that would use the EU money. Most calls invite applications from academic networks and industry collaborations, but one, made last May, is aimed at individual researchers. Modelled on grants offered by the European Research Council, the calls are worth up to €1 million each. But competition is harsh: of 1,200 applications, fewer than 200 will be funded.

The money will be a life-saver for established researchers, but the future of the system as a whole remains uncertain. Over the next five years, 30% of current faculty members and researchers will retire from Greek universities and research centres, and replacing them may be difficult. Thanks again to EU funding, Greece produces large numbers of PhDs, but most of those who continue on to postdoctoral research do so abroad. In the past, many have returned to seed competitive research groups at home. The proposed law provides schemes to encourage that, but few believe that it will work, given the very low salaries and uncertain funding that researchers can expect.

Vasso Kostourou, a cell biologist at the Alexander Fleming Biomedical Sciences Research Center in Vari, is an exception. She returned to Greece from London in 2008, and recalls colleagues encouraging her because they thought that project funding was about to resume. Instead, she arrived as the crisis hit. At 37 years old, Kostourou thinks that she may be among the last scientists to return to academia in Greece for the foreseeable future. "That's

a shame because the quality of science that can be done here is high," she says. "It's only the funding that's bad." ■

➔ **NATURE.COM**  
Listen to an  
interview about the  
Greek crisis at:  
[go.nature.com/kwsh4c](http://go.nature.com/kwsh4c)

## ECONOMICS

# Disaster toll tallied

*The soaring cost of natural catastrophes is due more to socio-economic than climatic factors.*

BY QUIRIN SCHIERMEIER

Natural disasters around the world last year caused a record US\$380 billion in economic losses. That's more than twice the tally for 2010, and about \$115 billion more than in the previous record year of 2005, according to a report from Munich Re, a reinsurance group in Germany. But other work emphasizes that it is too soon to blame the economic devastation on climate change.

Almost two-thirds of 2011's exceptionally high costs are attributable to two disasters unrelated to climate and weather: the magnitude-9.0 earthquake and tsunami that hit Japan in March, and February's comparatively small but unusually destructive magnitude-6.3 quake in New Zealand.

And the long-term rise in the costs of global disasters is probably due mainly to socio-economic changes, such as population growth and development in vulnerable regions. That conclusion is backed up by a forthcoming study — supported by Munich Re — by economists Fabian Barthel and Eric Neumayer at the London School of Economics. Their analysis of events worldwide between 1990 and 2008 concludes that "the accumulation of wealth in

disaster-prone areas is and will always remain by far the most important driver of future economic disaster damage" (F. Barthel and E. Neumayer *Climatic Change*; in the press). Any major weather event hitting densely populated areas now causes huge losses because the value of the infrastructure has increased tremendously, they note, adding that if the 1926 Great Miami hurricane happened today, for example, it would cause much more damage than it did at the time.

However, weather-related events are generally on the rise. Thanks to a relatively quiet Atlantic hurricane season, damage caused by extreme weather was actually lower in 2011 than in four of the previous five years. But weather accounted for about 90% of the year's 820 recorded natural disasters, which caused at least 27,000 deaths. These disasters include flooding in Thailand, a series of tornadoes that hit the United States Midwest and southern states last spring, and storms and extreme rainfall over parts of the Mediterranean in November.

Since 1980, the report notes, the number of severe floods has almost tripled, and storms have nearly doubled, which insurance experts link, in part, to the impact of climate change (see 'Catastrophe count'). "It would not seem



Heavy rains turned roads into rivers last year as Thailand experienced its worst flooding in 50 years.

P. BROWN/PANOS



SOURCE: MUNICH RE

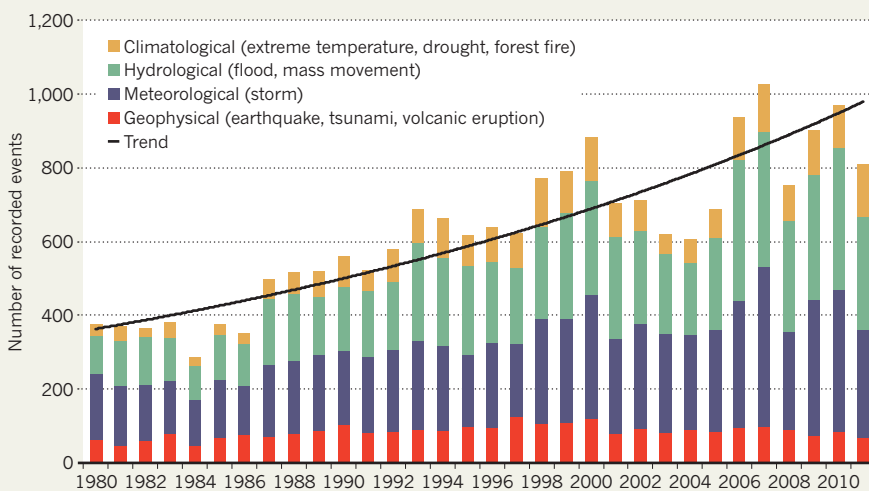
plausible that climate change doesn't play a role in the substantial rise in weather-related disasters," says Ernst Rauch, head of Munich Re's Corporate Climate Centre.

Climate scientists believe that the frequency and severity of extreme-weather events will increase as temperatures continue to rise. The summary of a report published in November by the Intergovernmental Panel on Climate Change supports that view and warns that some areas could even become "increasingly marginal as places to live in".

But attempts to attribute specific events to global warming are in their infancy (see *Nature* 477, 148–149; 2011). "Disasters are a tempting image for advocacy, but the science is just not there to support strong claims," says Roger Pielke Jr, a climate-policy researcher at the University of Colorado in Boulder. "We cannot yet attribute increasing dollar losses to human-caused climate change. Maybe we will one day, but not at present." ■

## CATASTROPHE COUNT

An increase in severe storms is helping to drive up the number of recorded disasters, but this cannot be conclusively attributed to climate change.



## PUBLIC HEALTH

# Rules tighten on use of antibiotics on farms

*Clampdown aims to stop spread of drug-resistant microbes.*

BY NATASHA GILBERT

Alarmed at signs that the overuse of antibiotics in farm animals is blunting these key weapons against human disease, governments are taking action.

In industrial farming, antimicrobials are commonly given to farm animals to treat infections, and prophylactically to prevent disease or spur growth. But there is growing concern that excessive use on farms is helping to breed antibiotic-resistant microbes, from *Salmonella* (see 'Rising resistance') to *Escherichia coli*, which are harder to treat when they infect people.

The US Food and Drug Administration (FDA) is now moving to protect key antibiotics known as cephalosporins, which are used in humans to treat a range of infections, including pneumonia. On 4 January, the agency said that it would prohibit certain uses of cephalosporins in farm animals including cattle, pigs, chickens and turkeys, because overuse of the drugs is "likely to contribute to cephalosporin-resistant strains of certain bacterial pathogens". If cephalosporins become ineffective in treating human diseases, the FDA said, "doctors may have to use drugs that are not as effective, or that have greater side effects".

The new rules, to come into effect on 5 April,

restrict veterinary surgeons to using the two cephalosporin drugs specifically approved for food-producing animals — ceftiofur and cephapirin — and ban prophylactic use. In animals not listed in the FDA order, such as ducks or rabbits, vets will have more discretion to use the drugs.

Most antibiotic classes are used both in animals and in humans, so the FDA is also considering tightening controls on all classes of antimicrobials used on farms. It is reviewing comments on rules that would prohibit the use of any antimicrobial drug to promote animal growth, a move that would be welcomed by many vets. "We would support greater veterinary oversight of antimicrobial drugs," says

Christine Hoang, assistant director of scientific activities at the American Veterinary Medical Association in Schaumburg, Illinois.

The European Union (EU), which already forbids the use of antimicrobials to promote growth, plans to strengthen its own rules. Its new antibiotic-resistance strategy, published in November 2011, calls on EU countries to ensure that antibiotics are only available on prescription, and to strengthen surveillance systems to track and report cases of resistance (see *Nature* <http://doi.org/cshmhv>; 2011).

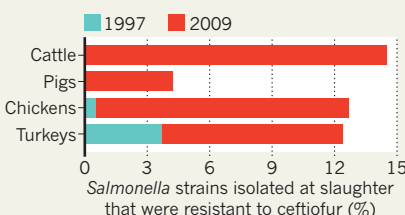
Although it is widely accepted that overusing antibiotics can be a major driver of resistance in microbes, the evidence linking antibiotic use in farm animals with resistance in humans is still controversial (A. E. Mather *et al. Proc. R. Soc. B* <http://doi.org/hj8>; 2011). A research programme coordinated by Europe's Innovative Medicines Initiative could provide some answers: in the next few months it will call for proposals for €350 million (US\$445 million) in grants to understand how resistance arises, and to develop new antimicrobial drugs.

Antimicrobial resistance is also this year's top priority for the intergovernmental World Organisation for Animal Health (OIE), based in Paris. Bernard Vallat, director-general of the OIE, says that it is working with the FDA and the World Health Organization to help developing countries to improve their legislation covering the control, distribution and use of veterinary antimicrobials. The three organizations plan to urge governments to put vets in charge of allocating the drugs and to ban preventative use.

"There are over 100 countries worldwide without legislation. Antibiotics are sold like sweets," Vallat told *Nature*. "There is no control and this is a major risk to animal and human health." ■

## RISING RESISTANCE

Farms in the United States have seen an alarming rise in *Salmonella*'s resistance to ceftiofur.



SOURCE: NATIONAL ANTIMICROBIAL RESISTANCE MONITORING SYSTEM/FDA



SOURCE: MUNICH RE

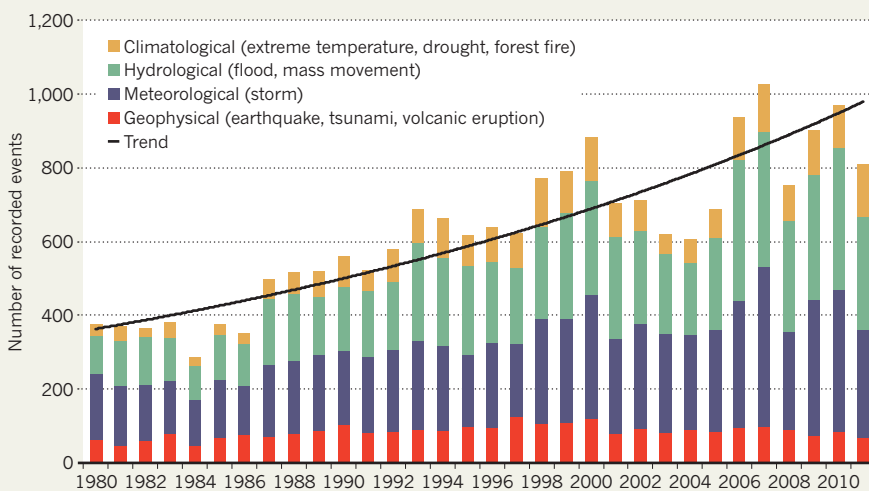
plausible that climate change doesn't play a role in the substantial rise in weather-related disasters," says Ernst Rauch, head of Munich Re's Corporate Climate Centre.

Climate scientists believe that the frequency and severity of extreme-weather events will increase as temperatures continue to rise. The summary of a report published in November by the Intergovernmental Panel on Climate Change supports that view and warns that some areas could even become "increasingly marginal as places to live in".

But attempts to attribute specific events to global warming are in their infancy (see *Nature* 477, 148–149; 2011). "Disasters are a tempting image for advocacy, but the science is just not there to support strong claims," says Roger Pielke Jr, a climate-policy researcher at the University of Colorado in Boulder. "We cannot yet attribute increasing dollar losses to human-caused climate change. Maybe we will one day, but not at present." ■

## CATASTROPHE COUNT

An increase in severe storms is helping to drive up the number of recorded disasters, but this cannot be conclusively attributed to climate change.



## PUBLIC HEALTH

# Rules tighten on use of antibiotics on farms

*Clampdown aims to stop spread of drug-resistant microbes.*

BY NATASHA GILBERT

Alarmed at signs that the overuse of antibiotics in farm animals is blunting these key weapons against human disease, governments are taking action.

In industrial farming, antimicrobials are commonly given to farm animals to treat infections, and prophylactically to prevent disease or spur growth. But there is growing concern that excessive use on farms is helping to breed antibiotic-resistant microbes, from *Salmonella* (see 'Rising resistance') to *Escherichia coli*, which are harder to treat when they infect people.

The US Food and Drug Administration (FDA) is now moving to protect key antibiotics known as cephalosporins, which are used in humans to treat a range of infections, including pneumonia. On 4 January, the agency said that it would prohibit certain uses of cephalosporins in farm animals including cattle, pigs, chickens and turkeys, because overuse of the drugs is "likely to contribute to cephalosporin-resistant strains of certain bacterial pathogens". If cephalosporins become ineffective in treating human diseases, the FDA said, "doctors may have to use drugs that are not as effective, or that have greater side effects".

The new rules, to come into effect on 5 April,

restrict veterinary surgeons to using the two cephalosporin drugs specifically approved for food-producing animals — ceftiofur and cephapirin — and ban prophylactic use. In animals not listed in the FDA order, such as ducks or rabbits, vets will have more discretion to use the drugs.

Most antibiotic classes are used both in animals and in humans, so the FDA is also considering tightening controls on all classes of antimicrobials used on farms. It is reviewing comments on rules that would prohibit the use of any antimicrobial drug to promote animal growth, a move that would be welcomed by many vets. "We would support greater veterinary oversight of antimicrobial drugs," says

Christine Hoang, assistant director of scientific activities at the American Veterinary Medical Association in Schaumburg, Illinois.

The European Union (EU), which already forbids the use of antimicrobials to promote growth, plans to strengthen its own rules. Its new antibiotic-resistance strategy, published in November 2011, calls on EU countries to ensure that antibiotics are only available on prescription, and to strengthen surveillance systems to track and report cases of resistance (see *Nature* <http://doi.org/cshmhv>; 2011).

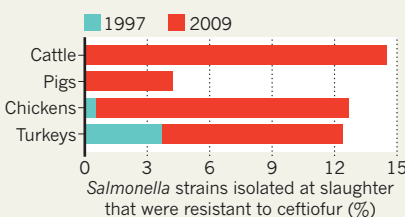
Although it is widely accepted that overusing antibiotics can be a major driver of resistance in microbes, the evidence linking antibiotic use in farm animals with resistance in humans is still controversial (A. E. Mather *et al. Proc. R. Soc. B* <http://doi.org/hj8>; 2011). A research programme coordinated by Europe's Innovative Medicines Initiative could provide some answers: in the next few months it will call for proposals for €350 million (US\$445 million) in grants to understand how resistance arises, and to develop new antimicrobial drugs.

Antimicrobial resistance is also this year's top priority for the intergovernmental World Organisation for Animal Health (OIE), based in Paris. Bernard Vallat, director-general of the OIE, says that it is working with the FDA and the World Health Organization to help developing countries to improve their legislation covering the control, distribution and use of veterinary antimicrobials. The three organizations plan to urge governments to put vets in charge of allocating the drugs and to ban preventative use.

"There are over 100 countries worldwide without legislation. Antibiotics are sold like sweets," Vallat told *Nature*. "There is no control and this is a major risk to animal and human health." ■

## RISING RESISTANCE

Farms in the United States have seen an alarming rise in *Salmonella*'s resistance to ceftiofur.



SOURCE: NATIONAL ANTIMICROBIAL RESISTANCE MONITORING SYSTEM/FDA

## ASTRONOMY

# Radio array starts work

*Giant low-frequency sensor system on track to probe the birth of the first stars.*

BY ERIC HAND

The Netherlands, one of the most densely populated countries in Europe, would seem to be an inauspicious place to detect radio whispers from the distant Universe. Mobile-phone towers, television transmissions, planes overhead and even the odd burst of noise from a windmill create a background din in the radio sky.

But the builders of LOFAR, the Low-Frequency Array of radio receivers centred around the tiny village of Exloo, say that they have found ways to ignore the noise. In doing so, Dutch astronomers at ASTRON, the Netherlands Institute for Radio Astronomy in Dwingeloo, are opening up a region of the electromagnetic spectrum that should hold clues to one of the earliest phases of cosmic history, when the first stars formed — an era beyond the ken of even the biggest optical telescopes.

“Many of the radio astronomers said this couldn’t be done,” says Heino Falcke, an astronomer at Radboud University in Nijmegen and chairman of the International LOFAR Telescope Board, the five-nation foundation that governs the €150-million (US\$192-million) project. Yet Falcke and his colleagues defied the doubters by presenting their first results on 9 January at a meeting of the American Astronomical Society in Austin, Texas. “The message today is: the basic things all work. We can do this,” he said.

Mapping the low-frequency sky requires an expansive telescope as well as the ability to tune out noise. When completed later this year, the array will contain 2,700 slender



LOFAR/ASTRON

At the heart of the LOFAR telescope is a collection of tile-like and dipole antennas.

dipole antennas tuned to 30–80 megahertz, and 43,000 antennas embedded in flat tiles a few metres square that are sensitive to 120–240 megahertz. The antennas will be concentrated in 40 stations across the Netherlands; 8 other stations in the United Kingdom, France, Germany and Sweden give the array extra angular resolution for fine-scale imaging. The fibre-optic data network that links the LOFAR antennas will also support sensor webs for geoscience and agricultural monitoring (see ‘A multi-purpose array’).

LOFAR has already turned up surprises. Its observations of four pulsars — spinning neutron stars that emit regular radio pulses — show that the emissions at a wide range of frequencies are bunched together in time, implying that they emanate from a narrow region near the pulsar. The finding challenges a common picture in which pulsars generate their radio signal in a much wider region, says ASTRON’s Jason Hessels, co-principal investigator of LOFAR’s pulsar working group.

But the real prize would be the detection of a signal from the epoch of re-ionization. That was roughly 400 million to 800 million years after the Big Bang, when radiation from the first stars and galaxies ionized the primordial hydrogen gas that filled the newborn Universe,

creating bubbles of ionized gas like the holes in a Swiss cheese. By mapping the gradual disappearance of the faint 21-centimetre emission line from the primordial hydrogen, LOFAR astronomers hope to distinguish between two re-ionization mechanisms: one driven by the stars’ ultraviolet light and one by X-rays from super-massive black holes in newborn galaxies. That would allow the astronomers to watch the first stars and galaxies being born.

Based on an initial run of ten hours spent staring at several quiet corners of the radio sky, ASTRON’s Ger de Bruyn suspects that the re-ionization signal could be detected with 400 hours of devoted observing time — a campaign he plans to begin by the end of the year.

That schedule would put LOFAR ahead of rival re-ionization projects in remote parts of Australia, South Africa and New Mexico, locations chosen partly for their lack of radio noise. Greg Taylor, an astronomer at the University of New Mexico in Albuquerque and director of the Long Wavelength Array being built in New Mexico, acknowledges that LOFAR is the array to beat in the race to detect re-ionization — but says that would be just the beginning. “If you make the discovery, then it’s a Nobel prize for somebody,” he says. But afterwards, “it has the potential to explode into a field of study”. ■

## A MULTI-PURPOSE ARRAY

The Low Frequency Array was designed for astronomy — but its fibre-optic data links will also be used for seismic monitoring, water management and agricultural sensing.

At the core of the array will be 40 stations centred around the Dutch village of Exloo.

Date stations completed:  
● 2009 ● 2010 ● 2011

## THERAPEUTICS

# US translational-science centre gets under way

*Mission of newly formed NCATS is to dramatically speed up production of drugs and other therapies, but sceptics question agency's ability to deliver.*

BY MEREDITH WADMAN

Scarcely a year after plans to establish it were made public, the National Center for Advancing Translational Sciences (NCATS), the newest branch of the US National Institutes of Health (NIH) in Bethesda, Maryland, is up and running. On 4 January the centre's 230 employees gathered for their first 'all-hands' meeting, at which they heard an exhortation from NIH director Francis Collins and his lieutenants about the importance of the centre's mission: finding ways to radically speed up the development of new drugs, devices and diagnostics.

"Patients suffering from debilitating and life threatening diseases do not have the luxury to wait the 13 years it currently takes to translate new scientific discoveries into treatments," Collins said on 23 December, the day President Barack Obama signed the law creating NCATS. Congress had for months expressed concerns that NCATS could infringe on the private sector, and that the NIH was rushing it into existence. But the critics relented, and Congress approved the US\$576-million centre on 17 December as part of a massive government funding bill.

The law creates NCATS from several existing NIH programmes — most notably, the Clinical and Translational Science Awards (CTSA; see table). In the new law, Congress directs the NIH to spend at least \$488 million on the awards in 2012. At the same time, it dissolves the National Center for Research Resources (NCRR), where the CTSA programme has been housed, and parcels out that centre's programmes to other parts of the NIH. NCATS will also administer a Cures Acceleration Network (CAN), authorized in the 2010 health-reform law and now funded for the first time under the new law. CAN, a competitive grant programme that will allow the agency to circumvent bureaucratic obstacles and push promising drugs forward, received just \$10 million, one-tenth of what Collins had requested. The minimal funding nonetheless means that the programme "can get up and running", says Margaret Anderson, executive director of

**"Getting drugs that work in people is a very hard thing to do."**

## ASSEMBLING THE PUZZLE

NCATS will be created from pre-existing NIH programmes. Their budgets give a sense of their relative scale.

Programme	Original NIH home	Funding in 2011
Clinical and Translational Science Awards	National Center for Research Resources (NCRR)	\$460.5 million (from NCRR); \$22.7 million (from NIH Common Fund*)
Components of the Molecular Libraries Program	National Human Genome Research Institute (NHGRI)	\$21.4 million (from Common Fund)
Therapeutics for Rare and Neglected Diseases	NHGRI	\$24 million (from all NIH institutes and centres)
Bridging Interventional Development Gaps (formerly called RAID)	NHGRI	\$15 million (from Common Fund)
Office of Rare Diseases Research	Office of the director	\$17.8 million
NIH-FDA Regulatory Science Initiative	Office of the director	\$2.7 million (from Common Fund)
Cures Acceleration Network	New	\$0 (\$10 million for 2012)

\*The NIH Common Fund is a discretionary fund for short-term, trans-institute programmes, administered through the office of the director.

FasterCures, a think tank in Washington DC that actively supported the creation of NCATS.

But the new centre has its sceptics — some of whom have voted with their feet. At the NCRR, 26 employees left during 2011 while Congress was debating their centre's future — more than twice the turnover in 2010. The dismantling "was a complete shock and surprise", says Barbara Alving, the former NCRR director, who resigned in September.

Others say that Collins is naive to suggest that the NIH can fix bottlenecks in the drug pipeline when the far-better-funded pharmaceutical industry has failed to do so. Creating NCATS "is sort of like declaring the war on cancer", says one critic. "Now what? Getting drugs that work in people is a very hard thing to do." But Congress wants NCATS to steer clear of industry prerogatives anyway: the legislation establishing it pointedly insists that the centre should "not create duplication, redundancy and competition with industry activities". And Congress explicitly forbids it from sponsoring late-stage clinical trials.

In a separate report, Congress instructs NCATS to protect both the money and the mission of the CTSA programme, which funds recipients at 60 academic medical centres nationwide — even though the recipients' activities do not always overlap with the new centre's mission. The CTSA programme would comprise at least 80% of the NCATS budget. Lawmakers have instructed the agency to

enlist the Institute of Medicine to assess the CTSA's current mission, and to decide within 18 months whether changes are needed. Mark Lively, a biochemist at Wake Forest Baptist Medical Center in Winston-Salem, North Carolina, who served on the NCRR external advisory council, worries that, in the interim, NIH leaders will boost the rest of NCATS's budget by dipping into basic-science funding. NIH officials insist that this will not happen.

Meanwhile, at the top of the new centre's to-do list is finding a director. "We are thrilled with the applicants and are going to start interviews this month," says Kathy Hudson, acting deputy director of NCATS. ■

## CLARIFICATION

The News story 'Last-minute wins for US science' (*Nature* **480**, 423; 2011) implied that the total US contribution to the Global Fund to Fight AIDS, Tuberculosis and Malaria is \$298 million. This is just how much the National Institutes of Health was set to provide in 2012, and which will now be given instead by the Department of State.

## CORRECTION

The News story '2011 in review' (*Nature* **480**, 426–429; 2011) confused its melanoma treatments: 'ipilimumab' should read 'vemurafenib'.



# Never say die

*With a history of public blunders, can Advanced Cell Technology make embryonic stem-cell therapies a reality?*

BY CORIE LOK

“Oh crap, this really puts us in the spotlight!” thought Robert Lanza when he first heard the news. Advanced Cell Technology (ACT), the biotechnology company in Marlborough, Massachusetts, of which Lanza is chief scientific officer, had for more than a year been operating in the shadow of Geron, a rival company in Menlo Park, California. Geron was bigger and better funded than ACT, and it was the first company to be approved by the US Food and Drug Administration (FDA) to test a therapy in humans based on embryonic stem (ES) cells. ACT was second. But in November, Geron announced that it was halting its trial to focus instead on cancer drugs. And with the announcement, Lanza says, he felt the weight of the ES-cell field fall on his shoulders.

Lanza and his company have had plenty of experience in the spotlight, but the attention has not always been flattering. Since the late 1990s, ACT has gained a reputation as a renegade company, accused of overhyping results to raise attention and money. Critics say that the company has damaged the field more than once with its high-profile, controversial announcements, such as one describing the company's attempts to clone a human embryo<sup>1</sup> in 2001. ACT's actions — and the



Robert Lanza has been a public face for Advanced Cell Technology's many ups and downs.

highly politicized nature of stem-cell research — scared off investors, leaving the company teetering on the verge of bankruptcy for most of the past decade.

But the scrappy biotech refused to die, in part because of Lanza's doggedness. ACT is now performing early-phase clinical trials testing the safety of implanting retinal cells derived from human ES cells into the eye to treat certain types of blindness.

Lanza says that this time, he aims to do things right: direct good science focused on treating disease, publish in reputable journals with rigorous peer-review processes and work with high-quality collaborators and clinical centres for its trials. "We're a different company now," says Lanza.

Not everyone is convinced. Even if positive results emerge from these trials, ACT will still face major challenges in getting an ES-cell-based therapy approved for wider use. And some in the field are sceptical about ACT's reformation. "Can you really trust a company that has a spotty record?" says Arthur Caplan, a bioethicist at the University of Pennsylvania in Philadelphia.

It's not just Lanza who has a stake in the answer. With Geron out of the game, ACT's success or failure will be important for a field looking to prove itself worthy of further research funding. "If the trials are positive, that would fundamentally transform the debate," says Christopher Thomas Scott, director of the Program on Stem Cells and Society at Stanford University in California.

## PROBLEM CHILD

ACT began in the mid-1990s as an animal-cloning outfit owned by Avian Farms, a Maine-based poultry genetics company. ACT quickly shifted focus when Michael West — who founded Geron — became its chief executive in 1998. Human ES cells had just been isolated for the first time, and researchers were excited about their potential use in regenerative medicine.

But many were concerned that patients' immune systems would reject cells derived from unrelated embryos. To solve this, West proposed 'therapeutic cloning' — taking the nucleus out of a patient's cell, transferring it into an egg cell to create a cloned embryo, then using that embryo to derive patient-matched stem-cell lines.

In 1999, using money he had made at Geron, West bought ACT. Lanza, a physician who had spent the past 20 years working in academic research and biotech on organ and cell transplantation, was one of West's first recruits. The team moved quickly to try to make therapeutic cloning a reality.

If the American public had not yet heard of human cloning or ACT by the fall of 2001, it could hardly have missed the hype that began on 25 November that year. West appeared on *Meet the Press*, a nationally televised US

political talk show, to discuss a paper, published that day, in which ACT scientists described the first cloning of a human embryo. "We've taken the first halting steps toward what we think is going to be a new area of medicine," West said.

West appeared on several other news shows in the following days. CNN and *US News and World Report* heralded the work as a breakthrough, and West and his team hailed the "dawn of a new age in medicine" in a report for *Scientific American* (now owned by Nature Publishing Group).

In the paper<sup>1</sup>, published in the now-defunct

**"It was our policy not to hide what we were doing and why. We wanted to be honest, accurate and open."**

online journal *e-biomed*, West, Lanza and their colleagues showed that they could pull a nucleus from a human egg cell, replace it with a whole adult ovarian cell and generate an embryo that divided into six cells. It then stopped growing, far short of the 100-cell blastocyst stage from which stem cells can be derived.

The work pressed a political hot button. That summer, President George W. Bush had approved federal funding for human ES-cell research, but only for a small number of cell lines that had already been created. He also voiced staunch opposition to human cloning of any kind, and a bill to ban it had been advancing through the US Congress, much to the chagrin of researchers who saw promise in therapeutic cloning.

ACT's announcement stoked fears that scientists were trying to clone humans for reproductive purposes — and conflated reproductive cloning and human-embryonic-stem-cell research in many people's minds. "It gave critics plenty of ammunition to insist that if stem-cell research was funded, human reproductive cloning would be funded too," says Caplan. "It had a huge deleterious impact for years."

Scientists, meanwhile, dismissed the finding. The ACT team hadn't gained new insight into the human developmental process, says George Daley, a stem-cell researcher at Children's Hospital Boston in Massachusetts. "I was not in a position to defend the cloning that they were doing because it was ineffective in what they were trying to do," he says. "It was more for publicity than for science."

Jose Cibelli, who was first author on the paper and left ACT in 2002 for a faculty position at Michigan State University in East Lansing, says that in an ideal world he would have waited until the team could grow the embryos to the blastocyst stage before publishing the work. But

he had heard rumours that other groups were pursuing the same goal, and he was worried about getting scooped. (A successful derivation of stem cells from a cloned human embryo was not reported until October 2011, and these stem cells had three sets of chromosomes rather than two<sup>2</sup>.)

West says that he pushed ahead with publication in the interest of transparency. "It was our policy not to hide what we were doing and why," he says. "We wanted to be honest, accurate and open."

The announcement ended up hurting the company, however. ACT was trying to raise a needed round of venture-capital financing when the cloning news broke. The negative attention combined with the political uncertainty around stem-cell funding killed the deal, says Greg Bonfiglio, who was with Anthem Venture Partners of Santa Monica, California, at the time, and would have been the lead investor on that round.

## SCRAPING BY

The disappearance of the venture funding sent ACT on a financial downward slide from which it would take nearly ten years to recover, says Bonfiglio, who has dealt with the company on several more occasions. Researchers at Geron, meanwhile, had successfully derived neurons from human embryonic stem cells<sup>3</sup> and were pursuing research that would eventually look to repair the damage caused by spinal-cord injuries, a possible use for embryonic stem cells that was much touted at the time. ACT was largely dismissed as a sideshow.

Lanza is now the longest-serving employee of the company. He says that a "tough childhood" in Stoughton, a town south of Boston, Massachusetts, helped him to develop a thick skin.

Unlike many Boston-area academics, Lanza has the 'R'-dropping accent of the region, most noticeable when he talks about one of his main preoccupations: Stargardt's disease. "Stah-gahdt's" — as he says it — is one of the two types of degenerative blindness his company is targeting in its clinical trials. The other, the 'dry' form of age-related macular degeneration, is the most common cause of age-related blindness. Both diseases result from the death of retinal cells, a process that Lanza suspects can be slowed or even halted using stem-cell-derived replacements.

After the venture funding fell through, West sold ACT's animal-cloning division to generate revenue. By 2004, however, money had again started to run low. But Lanza and West had recently hired Irina Klimanskaya, who, as a researcher at Harvard University in Cambridge, Massachusetts, had helped to derive many of the institution's first human ES-cell lines and who had a knack for working with scant resources. At ACT, she began optimizing a protocol for transforming ES cells (derived from embryos donated through





**1998** ACT scientists and collaborators announce the successful generation of cloned transgenic cattle.



**2001** With a full media blitz, ACT publishes its efforts to clone a human embryo for the purpose of growing stem cells.

ADVANCED CELL TECHNOLOGY/AP

fertility clinics) into retinal pigmented epithelial (RPE) cells. These are lost in both Stargardt's and dry age-related macular degeneration<sup>4</sup>.

Stopping vision loss didn't quite have the dramatic appeal of Geron's goal of reversing paralysis. But focusing on the eye may have been a wise decision, say experts.

"The eye is an ideal place to begin this type of experimental work," says Michael Young, an ophthalmology researcher at the Schepens Eye Research Institute in Boston. Surgeons already have protocols for injecting cells directly into the eye, and they can measure changes in the retina just by peering into it. The eye is relatively sealed off from the immune system compared with other parts of the body, which may reduce the risk of cell rejection.

Moreover, transplanted RPEs do not need to form synapses, or connections, with neurons, unlike other retinal cell types. "If cell-based therapy in the eye is going work, it's got to work with the RPEs," says Thomas Reh, a neurobiologist at the University of Washington in Seattle.

By 2004, Lanza and his team were ready to start testing the RPE cells in animals — but they were paralysed by a lack of money. The cells sat in a freezer for almost a year. Meanwhile, the company's phone service was turned off, purchases of basic lab supplies grew harder to justify and the skeleton crew of remaining scientists wondered week to week whether they would get paid.

Some left, but Klimanskaya opted to stay on. "I believe in the company, in the cells, in the technology and in my own skills," she says. "Why should I quit?"

Out of desperation, West agreed at the end of 2004 to take the company public to gain access to a new source of funding. But the legal, accounting and marketing costs of going public through an initial public offering (IPO)

were far beyond the company's reach. Instead, in early 2005, ACT merged with Two Moons Kachinas, an obscure, Utah-based outfit that sold Native American dolls. Two Moons was essentially a 'shell' company, allowing ACT to take it over and become a publicly traded firm. This 'reverse merger' was much cheaper than an IPO, but the US\$8 million it raised had more strings attached.

As part of the deal, investors required the company to name a new chief executive. "The issue with ACT at that time was never about the quality of the science team," says Bonfiglio, who led the deal. "The business skills were not resident on that team." The new chief executive, William Caldwell, had more than 30 years of experience in banking, transportation and telecommunications, but none in biotech.

#### OUT OF THE ASHES

With the infusion of cash, ACT went on a hiring spree. West, who became the company's president and chief scientific officer, moved to California and recruited several researchers in hope of starting a lab that could tap into funding from the San Francisco-based California Institute for Regenerative Medicine (CIRM), a \$3-billion, state-backed fund for stem-cell research.

Meanwhile, Lanza built up his team in Massachusetts and forged ahead with the RPE transplantation studies in rats. In 2006, positive results began to materialize<sup>5</sup> and ACT opened its new headquarters, a 1,400-square-metre research facility in Alameda, California, which included a lab capable of growing cells according to the strict standards required for human trials.

Just as optimism was running high, the company made another very public stumble. In August 2006, Lanza and his co-authors published a paper<sup>6</sup> in *Nature* showing that a single

cell could be plucked from an 8–10-cell human embryo and grown into stem cells. Lanza wanted to show that it was possible to derive stem cells without destroying the embryo, to sidestep ethical concerns.

In fact, the embryos were destroyed in the experiments, but that had not been made clear in the original version of the paper, the press releases about it or in some of Lanza's press interviews. *Nature* issued two clarifications after its original press release, but many news organizations had already reported that the embryos were unharmed. When the truth became clear, critics pounced.

Opponents of ES-cell research saw the debacle as an attempt to mislead the public, and scientists criticized the method as impractical and still ethically problematic. Biopsying embryos puts them at risk, says Daley, so some will be lost.

Lanza says that the *Nature* paper was only meant to be a proof of principle and that the company soon perfected the technique so that embryos survived. But the episode reinforced perceptions that the company hyped its results, this time to boost its stock value. If that was the intent, the effect was short-lived. The increase in share price on the day of the announcement — from \$0.42 to \$1.83 — would be reversed in the weeks and months that followed.

Unable to raise enough money from conventional sources, Caldwell turned to last-resort financing. ACT borrowed cash from investors and then repaid them in shares on a monthly basis, using the lowest share price of the previous month. As that price dropped, ACT had to issue more and more shares, forcing the price down even further. Caldwell completed several rounds of this 'death-spiral financing' between 2005 and 2010 to keep Lanza's RPE research going, and the company sank further into debt.

E. AMENDOLA/AP



**2006** ACT scientists demonstrate a possible way to derive stem cells from embryos without destroying them.



**2011** ACT begins a clinical trial testing surgical implantation of retinal cells derived from embryonic stem cells as a treatment for blindness.

ADVANCED CELL TECHNOLOGY/AP

By 2007, West says, he was not getting along with Caldwell and left ACT to head another company to develop products for ES-cell research. In 2008, ACT closed its Alameda facility — the CIRM funding never materialized — but Caldwell stayed in Los Angeles. By the time the markets crashed later that year, ACT's stock price had dwindled to pennies. Caldwell lost all of his executives, and the entire RPE development team left.

Still, Lanza was convinced that RPE therapy held the key to the company's survival. He was, moreover, impressed with Caldwell's dedication to the project. "He got all excited [about the science], and that was important," Lanza says. "He was really my partner." The two worked tirelessly throughout 2009 to rebuild the company. Caldwell eked out funding so that Lanza and his team could do the studies needed for FDA approval of the clinical trials. "We knew we had one chance," says Lanza.

In November 2010, when a fax arrived saying that the trial had been approved, a cheer went through the office. "We came out of the ashes," says Lanza. "It was a long time coming."

There was little time for celebration, however. The team still needed approval from the clinical centres conducting the trials before they could start treating patients.

Lanza usually began each morning by answering a slew of e-mails from Caldwell, who often worked later hours in Los Angeles. So he was concerned when, on the morning of 14 December, his inbox was empty. The call came later that afternoon from Caldwell's wife. The man who had kept ACT afloat for the past six years had died unexpectedly, aged 63. Describing the loss now, Lanza becomes quite emotional and almost can't continue. "It was like I lost a father," he says.

The company faced yet another bleak period. But Gary Rabin, an investment banker

who had been on ACT's board since 2007, stepped in as interim leader. Within two weeks, he had secured \$25 million in financing from two firms that Caldwell had been courting. Rabin, who is now ACT's chairman and chief executive, says that the funding is enough to pay for the company's two ongoing trials and should last through 2012.

### THE CHALLENGES AHEAD

Now, the company's future hinges on the outcome of the trials. Final results won't be out until 2013, and they will show mainly whether the cell transplants are safe. The patients enrolled in the trial are in the late stages of vision loss, so the chances of dramatic improvement are remote, experts say.

Still, Rabin and Lanza are optimistic. If the treatment is safe and even moderately effective, they say they would consider partnering with a pharmaceutical company to help take the programme forward — although they are still working out their plan. Scott, with Stanford's Program on Stem Cells and Society, says that positive results could fire up patient advocacy groups, which can be powerful in building support. And a good outcome could encourage investment in other stem-cell therapy companies, says Bonfiglio, who is now managing partner at Proteus Venture Partners in Palo Alto, California.

But even if the trial results are positive, ACT will face enormous challenges in commercializing the technology. The company will have to show the FDA that its RPE cells can slow vision loss in bigger and more expensive clinical trials.

And even if the treatment works, storing and distributing the cells, which often have short shelf-lives, is expensive and logistically difficult, says Chris Mason, head of the Stem Cell and Regenerative Medicine Bioprocess Group at University College London.

These challenges were thrown into stark relief when Geron halted its stem-cell trial in November, having decided that the hurdles to commercializing the therapy were too great. Now, it is up to ACT to face them. "The departure of Geron from the field will ultimately place a greater burden on ACT in terms of educating the FDA and establishing standards for safety and efficacy," Bonfiglio says.

ACT is not entirely alone: other stem-cell-based therapies are moving towards the clinic. For example, a consortium of research groups called the London Project to Cure Blindness aims to test RPE transplants from embryonic stem cells in patients with macular degeneration this year. A group in Japan hopes to test a similar approach in humans using stem cells from reprogrammed adult cells within the next three years.

Still, some who have tracked ACT's trajectory say that the company might have what it takes to succeed. "What has kept ACT going is persistence, tenacity and vision," says Ronald Green, ACT's long-time ethics adviser and a professor of religion and ethics at Dartmouth College in Hanover, New Hampshire.

Lanza says that at times he considered giving up and working on something less controversial. "If I wasn't a stubborn Italian," he says, "I would have thrown up my hands at least 25 times." ■

**Corie Lok** is Nature's Research Highlights Editor.

1. Cibelli, J. B. *et al.* *E-Biomed* **2**, 25–31 (2001).
2. Noggle, S. *et al.* *Nature* **478**, 70–75 (2011).
3. Carpenter, M. K. *et al.* *Exp. Neurol.* **172**, 383–397 (2001).
4. Klimanskaya, I. *et al.* *Cloning Stem Cells* **6**, 217–245 (2004).
5. Lund, R. D. *et al.* *Cloning Stem Cells* **8**, 189–199 (2006).
6. Klimanskaya, I., Chung, Y., Becker, S., Lu, S.-J. & Lanza, R. *Nature* **444**, 481–485 (2006).

R. HUTCHINSON/UCLA



# ZERO TOLERANCE

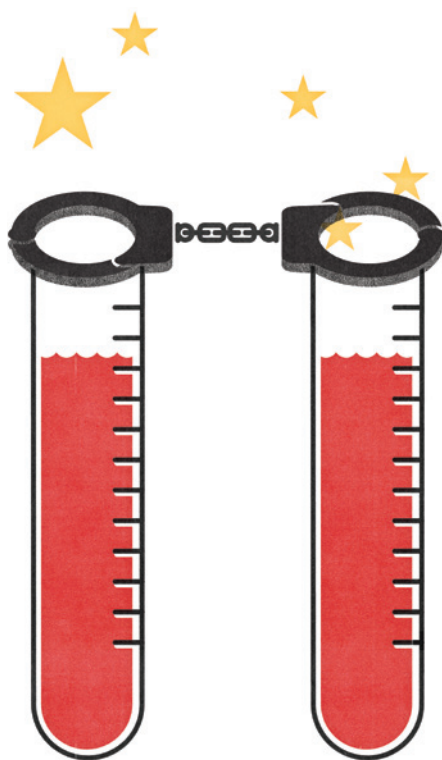
BY DAVID CYRANOSKI

**Y**ang Wei has an easy smile and a care-free, even distracted, air — but he takes such a solemn approach to life that his wife sometimes tells him to relax. “I take everything seriously,” he says.

The former materials scientist certainly took it seriously when, two years after he became president of Zhejiang University (ZJU) in Hangzhou, China, he faced a case of scientific misconduct that became a turning point for his presidency. In early October 2008, the editor of the *International Journal of Cardiology* discovered that figures in a manuscript by He Haibo, a scientist researching traditional Chinese medicine who had been hired by the ZJU only months before, were suspiciously similar to those in an article that He had published elsewhere. Confronted, He quickly owned up, submitting a 12-page confession to Yang on 26 October.

But the case, which eventually led to the retraction of eight papers, spiralled into an international media catastrophe for the ZJU, one of China's oldest and largest universities, as well as one of the most successful in publishing science. Articles attacked the laxity of a system that gave leadership roles to the likes of Li Lianda, dean of the department of pharmaceutical sciences and He's supervisor, who was largely absent from the lab and unfamiliar with the work, but was last author on some of He's papers. “There was plagiarism, fabrication and falsification. It was a showcase of every kind of problem,” says Yang.

Facing one of the best-publicized misconduct



## A UNIVERSITY CRACKS DOWN ON MISCONDUCT IN CHINA.

cases in China's recent history, Yang knew he had to act quickly. He personally wrote to all the editors of the journals involved. They supplied copies of copyright-transfer forms with all the co-authors' signatures, and Yang sent

them to the national calligraphy centre. “Most signatures were identical to He's own,” says Yang. “Even I could tell that.”

In March 2009, the ZJU fired He, terminated the contract of Wu Limao, a co-author on several of He's papers and the laboratory head in Li's absence, and took away Li's dean-ship and graduate students.

Yang didn't stop there: he launched a campaign to make the ZJU more responsive to misconduct. With an energetic companion named Yuehong (Helen) Zhang cracking down on the university's journals (see ‘Policing the plagiarists’), and assistance from a group of university administrators who share his determination and commitment to a zero-tolerance policy for misconduct, Yang hopes to make the ZJU into a role model that can help to clean up China's reputation for rife scientific misconduct. That reputation, exacerbated in the past five years by a string of high-profile cases (see *Nature* 441, 392–393; 2006), has made observers and journal editors increasingly sceptical of the ability of Chinese research institutions to ensure trustworthy science.

Yang, who now tours the country giving lectures on scientific integrity, has established a reputation as the most evangelical of the reformers. His collaborators are impressed. “He is committed to cleaning things up at Zhejiang,” says Mark Frankel, director of the Scientific Freedom, Responsibility and Law Program at the American Association for the Advancement of Science (AAAS) in Washington DC, who is working with Yang to improve

OLIVER MUNDAY

research ethics. Frankel says that efforts such as Yang's are driving change. "What is most impressive is how open and willing the people with whom I work in China are to admit that a serious problem exists, and that they are committed to turning things around for the younger generation of scientists," he says.

### THE SCALE OF THE PROBLEM

There are no comprehensive statistics on the extent of research misconduct in China — and few ministries, agencies or universities make cases public. Surveys and anecdotal evidence, however, reveal a deep-rooted problem, and suggest that students are learning unethical behaviour alongside their science. In an unpublished 2008 survey of 1,641 students at 10 universities, Cao Nanyan, a research-integrity specialist at Tsinghua University in Beijing, found that more than 20% of students admitted to changing data that didn't match their expectations. Some 60% of PhD students said that they sometimes witnessed misconduct, yet only 5% would report it — and Cao found evidence that the students' tolerance of misconduct increased the longer they stayed in education.

"It suggests that the more entangled you are in the system, the less able or motivated you are to pursue good practices," says Daniele Fanelli, a social scientist at the University of Edinburgh, UK, who has studied the frequency of scientific misconduct. Fanelli says that Cao's figures are "clearly worrying, because they would suggest much higher rates of misconduct, and lower rates of reporting, compared to what is usually reported in surveys in Western countries".

Cao and other experts on misconduct point to specific contributing factors. China's research system has developed very rapidly, and universities are scrambling to train the influx of students, scientists and administrators. "As a large, newly developed system of research, China does not have the control of its research programmes that is found in the West," says Nicholas Steneck, who studies research integrity at the University of Michigan in Ann Arbor. Some researchers are simply oblivious to the rules, says Zhong Haining, a neuroscientist who trained at Tsinghua University and is now starting a lab at Oregon Health and Science University in Portland. "The official guideline for scientific misconduct may (or may not) exist, but it's not very well publicized, at least not emphasized so much in training," he says.

Steneck adds that these issues may be rooted in a broader lack of honesty in governance, and that this makes it tough to build a culture of honest research. "It is difficult to have integrity in research if integrity in other aspects of life is questionable," he says.

**➔ NATURE.COM**  
Ten experts give their opinions on how to stop plagiarism:  
[go.nature.com/jiqv8d](http://go.nature.com/jiqv8d)

The government, universities and research institutions have introduced a cornucopia of integrity policies over the past decade. But



Yang Wei wants to reform attitudes towards research ethics at Zhejiang University and across the country.

enforcement is problematic, says Mu-ming Poo, director of the Institute of Neuroscience in Shanghai. Most Chinese funding organizations do not, for example, have permanent offices to deal with misconduct in a systematic and transparent fashion, as the Office of Research Integrity at the US Department of Health and Human Services attempts to do. "Very few people in the funding agency or in the scientific community

do this. I have to do this," he says.

In January 2009, on the basis of lessons learned in the He case, Yang created a research-integrity committee and an investigation task force at the ZJU. That March, at a conference to discuss the He situation, the Chinese minister of education called for a zero-tolerance policy towards misconduct — and Yang signed up. He issued a series of codes to guide behaviour

## "IT IS DIFFICULT TO HAVE INTEGRITY IN RESEARCH IF INTEGRITY IN OTHER ASPECTS OF LIFE IS QUESTIONABLE."

are willing to be the 'bad guy' and enforce the regulations," says Poo. He points to an investigation into what he considered a clear-cut case of misconduct. A researcher was dismissed, but soon found a job elsewhere and continued to get large grants. "There's essentially no punishment for scientific misconduct," says Poo. "The tolerance and appeasement within the community — that really worries me."

### TAKING ACTION

Yang had encountered misconduct before he became president of the ZJU — as a reviewer of manuscripts in fracture mechanics, and in roles such as director-general of the academic degrees committee of the State Council of China, a post that he held from 2004 to 2006. But when the He case came to light, Yang says he felt the weight of responsibility for the ZJU and its students, and this compelled him to act. "It's not that I want to

on authorship, citations and submission procedures, including one that forbids electronic submissions of papers by a non-corresponding author. This addressed one of the key problems in the He case, in which He and some graduate students had submitted papers from an account under the name of the corresponding author, Wu. Yang replaced most of the ZJU's adjunct deans with full-time executive deans in an attempt to avoid the problems created by Li's absentee leadership. And he introduced new investigative procedures and spelled out disciplinary actions.

All this helped Yang to prepare for a second big case, in mid-2010. The editor-in-chief of a journal published by Springer contacted Yang to say that plagiarism and fabrication in an article from a ZJU researcher were so egregious that Springer was considering blocking all submissions from the university to its 2,000 science,



technology and medicine journals. (Yang declines to name the researcher or editor.) “It put pressure on. We had to convince them that we could handle the case,” says Yang.

This time, Yang was ready. He dismissed the main scientist involved, and cut the salary and PhD-student allocation of the corresponding author. “Springer was satisfied,” says Yang.

Over the past two years, Yang says, he has dealt just as briskly with another 40 or so misconduct cases at the ZJU. More than 20 researchers have been found guilty of wrongdoing after discussion by the university administration. For the ten cases involving recent graduates, more than half lost their degrees. One sued the ZJU to overturn the ruling of plagiarism. She lost. If work done during your training is fraudulent, “your degree should be taken away,” says Yang firmly.

In cases involving faculty members, three had their employment terminated, four faced disciplinary action including a pay cut, and the rest were issued with public or internal warnings. Some have been temporarily forbidden from taking on PhD students.

But laws and punishment go only halfway towards tackling the problem — prevention is also essential. At the ZJU, Yang has established a system for mentoring young faculty members on research ethics, and since 2009 the university has held more than ten seminars and lectures on research integrity, with attendance at some surpassing 1,000. Yang also continues his talks at universities around the country. “We have to train them to be honest. It’s not enough to be aware of the ethics code. You need to really understand it,” says Gong Ke, president of Nankai University in Tianjin, who, with Yang and the AAAS, is preparing a book of scientific-misconduct cases that can be used to teach research integrity in China and the United States.

## SLOW PROGRESS

Yang says it is too early to tell whether his efforts are really paying off. Most misconduct cases are several years old by the time they come to light, so the researchers involved haven’t been exposed to the education and enforcement efforts. And there is always the fear that teaching people about misconduct might simply make some determined individuals craftier — as in the case of those who try to outwit plagiarism-detection software with software of their own. “But at least they are more aware that they are doing something wrong,” says Yang.

Yang is not cleaning up Chinese science on his own. Other universities have established ethics courses and strengthened their investigation procedures. And China’s aggressive ‘online police’ have been rooting out frauds — the XYS blog run by Fang Shimin has become famous for its tenacity. Posts on the website discuss problems with data, as well as discrepancies between researchers’

In October 2008, Yuehong (Helen) Zhang became the first journal editor in China to introduce CrossCheck, a tool that compares text against published articles to flag up plagiarism. Two years later, she had found that 31% of the 2,233 submissions over that time to her publication, the *Journal of Zhejiang University* — *Science*, contained unoriginal material. After reporting the number in *Nature* (Y. Zhang *Nature* **467**, 153; 2010), Zhang was harassed on blogs. “Many people criticized me. They say I am unpatriotic. I don’t care. I think I’m doing the right thing. I think it could make science stronger in China.”

Zhang, who is also vice-president of the Society of China University Journals in Beijing, has been working to build a journal that is run to international standards. Unlike many Chinese journals, hers insists on peer review. In December 2010, she became the first Chinese person to win a grant from the International Committee on Publication Ethics, for a project to analyse types of plagiarism. But the biggest reward, she says, has been the improvement: only 15% of submissions in the first half of 2011 contained unoriginal content.

There are 5,000 science and technology journals in China, but only 200 are in English and can use CrossCheck. Zhang says that some 20 do so. A separate effort is under way

CVs and their actual achievements. Fang is not yet convinced that the ZJU is rigorously investigating all the misconduct cases that it should. “I don’t think he takes his own words seriously,” he says of Yang. But Fang notes that he has seen improvements in the 11 years since he started his own “fight” against misconduct. The media are more willing to report misconduct and appeal for reform, he says, “and the government at least admits there are problems”.

Real change will take more time and effort. At a 2007 meeting on research integrity with the China Association for Science and Technology, Frankel recalls, one Chinese speaker after another presented data on how bad the situation was and “openly worried about its effects on how science coming out of China would be perceived”. The professional guidelines that are surfacing now, he says, are “merely a first step. They have adopted investigative practices and procedures similar to the United States but lack experience and manpower needed to be truly effective. This will take time.”

Even the best efforts of administrators such as Yang might not be enough to change deep-rooted behaviours, says Sheila Bonde, an

## POLICING THE PLAGIARISTS

### A software arms race

to police Chinese-language journals. In 2009, the China National Knowledge Infrastructure (CNKI) in Beijing, which shares information about research from the country, launched a system called the Academic Misconduct Literature Check (AMLC). Sun Xiongyong, director of the CNKI Academic Integrity Research Center, says that the organization was pushed by publishers and universities to develop the AMLC, which now includes about 80 million Chinese articles, conference proceedings and doctoral theses. Its subscribers include some 4,500 publishers and 600 universities.

Sun says that a crucial component of the system is the ability to check Chinese articles against the 30 million or so English articles in the database, and vice versa. “It’s the only multi-language check system,” notes Sun.

The systems can be cheated. For example, students who are given access to the AMLC to check their theses before submission might find passages that trigger the plagiarism warning and then tweak them until the text scrapes through. “AMLC is abused,” says Sun. In response, the CNKI has established a monitoring system that can check, for example, whether the AMLC was being used before submission. But the arms race continues: Sun’s latest headache is the use of software available outside China — such as Turnitin — to defeat the check system. **D.C.**

archaeologist and historian at Brown University in Providence, Rhode Island, who is collaborating with the ZJU to create a course in ethics. “Training graduate students about ethics as they enter research laboratories is too little, too late and too specific,” she says. “There is a critical need for broader discussion of ethical choices across the spectrum of Chinese academic, political and economic issues, and this has to begin much earlier in students’ lives.”

Still, the passion for cleaning up China’s science is tangible. Frankel says that reformers such as Yang have a different kind of drive from those in the United States, where “the emphasis is on accountability for spending the public’s money, its impact on research progress, and public trust. My Chinese colleagues view research misconduct as a stain on their country,” says Frankel. “It’s almost personal there.”

The reason, suggests Steneck, is that the stakes for China are so high. “If other countries lose confidence in the integrity of Chinese science, it is the Chinese who will suffer the most,” he says. ■

David Cyranoski is *Nature’s Asia-Pacific correspondent*.

# COMMENT

**CONSERVATION** Buying shares in whales could help to save them **p.139**



**SUSTAINABILITY** A vision of more energy-efficient American cities **p.142**

**MUSIC** Composer of mosquito love songs and firefly symphonies **p.144**

**GENOMICS** A network for linking DNA and geographic location **p.145**



## Deadline 2015

A summit meeting of heads of government is needed to strengthen global ambition on climate change — we should start preparing now, says **Michael Jacobs**.

Climate change has a new target date. The agreement reached last month at the United Nations (UN) conference in Durban, South Africa, specifies that negotiations towards a new, legally binding regime should be concluded by 2015.

At the same time, countries have committed to raising their collective ambition for capping greenhouse-gas emissions, in order to close the gap between their present emissions targets and the pathway likely to achieve the globally agreed goal of limiting global warming to 2°C above pre-industrial temperatures. No timetable has been set for that process, but because almost all present

targets are for 2020, 2015 is the very latest that such a change would have to be agreed.

Bringing these 'legal' and 'ambition' strands of global climate policy together in 2015 will require more than the usual UN conference attended by environment ministers. International decisions of this magnitude can only be made by heads of government. 2015 must be a leaders' summit.

Calls for such a summit will no doubt induce scepticism: the last one, in Copenhagen in 2009, failed spectacularly to yield universal agreement. But Copenhagen was badly undercooked: it became a

leaders' meeting only three months before it happened. For a summit in 2015 there is ample time to prepare.

Indeed, 2015 seems particularly opportune for such an event. The year before will have seen the publication of the fifth assessment report of the Intergovernmental Panel on Climate Change (IPCC). The IPCC's fourth assessment report in 2007 catalysed a wave of public concern about climate change, which in turn forced a build-up of diplomatic pressure on the Copenhagen conference; the 2014 report is likely to dramatize the issue once again. 2015 is also when the UN Framework Convention on Climate Change will ►

ILLUSTRATION BY PHIL DISLEY



► conclude its own review of global climate-change efforts, which will inevitably find present mitigation commitments inadequate to meet the 2°C goal.

Moreover, 2015 is the year in which China will set its next five-year plan, which will determine its emissions targets for 2016–20. Given China's central role both in the future trajectory of global emissions and in international climate politics, its willingness to raise its own emissions-cuts targets for 2020 would do much to encourage higher ambition in the rest of the world. It might even influence the United States: 2015 is the year that a second Obama administration, if it occurs, would have the best chance of finally pushing climate and energy legislation through Congress.

One could argue that to increase ambition for 2020, decisions must be made now. That would of course be desirable, and in the case of the European Union, it could still happen. Europe will this year again consider raising its present emissions-cuts target from 20% by 2020 — which, in the wake of the recession, will be achieved with very little effort — to 30%, which would prop up its now wilting carbon price. But few other countries are likely to tighten their targets so soon after setting them in 2009–10.

### CONFIDENCE BUILDING

Waiting until 2015 to strengthen targets offers some advantages. By then, the worst of the present economic storm should have passed, and countries will have had several years of experience in planning and implementing low-carbon policies — which in most cases should show that cutting carbon is not as difficult or costly as once imagined.

This is particularly true for the big emerging economies such as China and India, which have been understandably nervous about making future commitments without the evidence of actual implementation. If by 2015 countries feel more confident of the potential for emissions reductions, they may be more willing to strengthen their targets.

At the same time, the business community will be clamouring for greater investment certainty. Investors will demand clarity from governments on emissions targets beyond the current 2020 timetable — to 2030 at least.

Making progress towards 2015 will require continued efforts, both 'top-down', through international diplomacy, and 'bottom-up', through national policy.

These are not mutually exclusive, as some have claimed. Since the apparent failure of the climate conference in Copenhagen, it has become fashionable in some circles to discount the possibility of progress under the United Nations, and to argue that the focus should now be entirely on domestic policy in the high-emitting countries. But this is to misunderstand the interdependence of these

processes. International agreement is limited by the feasibility of domestic policy in the major economies, but international pressure helps to determine national ambition.

This was actually demonstrated best at Copenhagen itself. The hyping of diplomatic and media pressure in the run-up to that event has since been widely decried as contributing to its failure. But it was precisely that pressure that led almost every country in the world to adopt radical climate targets in the months before the conference.

Many of those — among them the European Union, China, India, Brazil, Indonesia, Korea, Mexico, South Africa, Japan, Australia and even the United States — would not have announced new targets at all during that period were it not for the elevated expectations for Copenhagen. And they would certainly not have been as ambitious. In this respect, Copenhagen must go down as one of the most successful failures in the history of multilateral diplomacy.

**"Copenhagen must go down as one of the most successful failures in the history of multilateral diplomacy."**

These Copenhagen-induced targets are now the bases for bottom-up domestic climate policies. Implementing these policies successfully must be the top priority for the next few years: the experience of achieving (or not achieving) present targets will determine countries' willingness to raise them next time around.

Perhaps surprisingly, success seems most likely in developing countries. Rapid economic growth is generating considerable resources for investment. Building new low-carbon infrastructure — notably in energy, urban transport and waste management — creates more opportunities than retrofitting existing systems. The costs of low-carbon technologies are falling rapidly — solar power is on its way to reaching parity with coal in India, and wind power has already achieved that in China. Brazil has had remarkable success in cutting deforestation.

In developed countries, by contrast, low growth and high debt make it seem hard to give priority to climate policy. But here there is a growing case for using low-carbon investment as a means of economic recovery. Green infrastructure can stimulate short-term economic demand and employment while boosting productivity and innovation over the longer term. The EU 2050 road maps for climate and energy provide a powerful blueprint for such 'green growth' that need not be confined to Europe.

The key to this is financing. Even the most competitive renewable energy sources, such as solar and wind, are more expensive in the short term. This is partly because of

high upfront capital expenditure and partly because of the policy risks that investors face. There is plenty of finance available in the world at the moment — pension funds, sovereign wealth funds and other investors are sitting on large sums that are earning very little. Mobilizing these resources for low-carbon infrastructure is one of the great challenges facing governments today. To do so, they need to reduce policy risk by guaranteeing their own low-carbon policies. Over the past three years, governments have put up large sums of public funds to bail out banks and guarantee sovereign debt. Doing the same now for low-carbon investment would boost both economic and climate goals.

### MOMENTOUS DECISIONS

It is in this way, through national (and in the case of Europe, multinational) policy, that emissions reduction will occur. But even if present policies are successful, they are insufficient to meet the 2°C goal. And it is implausible that, through solely domestic political and economic processes, every major country will simultaneously increase its targets by enough to close the gap. Only international pressure will do that. And that is why the focal point of such pressure needs to be a leaders' summit.

The decisions required in 2015 will be momentous: to raise collective global ambition for 2020–30 to meet the 2°C pathway; to agree a new, legally binding framework; to identify the sources of finance that can meet the goal of providing US\$100 billion in climate assistance to the poorest countries by 2020; and to agree a new international collaboration on the development, demonstration and deployment of low-carbon technologies.

These decisions are not within the powers of environment ministers, and they will not happen of their own accord. They require the direct engagement of heads of government, under the full glare of a summit spotlight. And that summit requires the kind of pressure that only the coordinated mobilization of global civil society — including the scientific community, businesses, non-governmental organizations and youth movements — can achieve.

So the first task of such a campaign is to persuade governments to hold a summit meeting in 2015. The UN Conference on Sustainable Development (Rio+20) in Brazil this June would be a good place for that to be agreed. ■

*Michael Jacobs is a visiting professor at the Grantham Research Institute on Climate Change and the Environment, London School of Economics and Political Science, London WC2A 2AE, UK. He was special adviser to former British Prime Minister Gordon Brown.  
e-mail: m.u.jacobs@lse.ac.uk*



Introducing tradeable permits for commercial whaling could actually reduce the number of whales that are caught by countries including Japan.

# A market approach to saving the whales

The future of the International Whaling Commission is tenuous. A 'whale conservation market' might rescue it, say **Christopher Costello, Leah R. Gerber and Steven Gaines.**

**D**espite the International Whaling Commission's (IWC) moratorium on commercial whaling beginning in 1986, the number of whales taken has more than doubled since the early 1990s. Almost 2,000 whales are now harvested each year — roughly 1,000 for 'scientific purposes' (by Japan), 600 by countries that object to the ban (Norway and Iceland), and 350 for subsistence (mainly by Denmark, Russia and the United States)<sup>1</sup>. Many populations of large whales have been severely depleted and continue to be threatened by commercial whaling<sup>2</sup>.

The persistence of largely unregulated whaling has sparked heated debate about whether the IWC, long hamstrung by management and ethics issues, should again permit formally sanctioned whaling. In 2010, some anti-whaling nations proposed a compromise: establishing quotas for sanctioned whaling that would still reduce the overall number of whales taken. After much wrangling, the deal fell through — largely because many anti-whaling groups had a

fundamental problem with setting quotas at all, because they felt that these would appear to legitimize commercial whaling. Some people blame Japan for the deal's collapse, because the country refused to sign up to a proposed zero quota on whale catches in the Southern Ocean.

We propose an alternative path forward that could break the deadlock: quotas that can be bought and sold, creating a market that would be economically, ecologically and socially viable for whalers and whales alike. Because conservationists could bid for quotas, whalers could profit from whales even without harvesting the animals. A market would therefore open the door to reducing mortality without needing to battle over whether whaling is honourable or shameful.

## TRIED AND TESTED

Market approaches to environmental protection have expanded substantially over the past 20 years. When carefully designed, they can be remarkably successful. Emissions trading markets for air pollutants such as

sulphur dioxide and nitrogen oxides have reduced emissions more, and at a lower cost, than traditional regulations in the United States. Conservation and wetland mitigation-banking programmes have resulted in more than 200,000 protected acres of habitat and have catalysed investment in conservation by the private sector. And fisheries managed with individual transferable quotas, in which sustainable levels of catch are divided and traded between permit-holding fishermen, in countries such as New Zealand, Iceland and Canada, have simultaneously allowed fisheries to continue and stopped stocks from collapsing.

The concept of auctioning annual whale catch quotas through a 'World Whaling Authority' was suggested in 1982 (ref. 3). It was never implemented, however, perhaps because the concept was ahead of its time (the first such tools — in fisheries, air pollution and biodiversity — were not established until the 1990s), and perhaps because it would have required whalers to purchase a privilege that they were used to receiving for free.



A whale-conservation market would be different. In such a system, 'whale shares' would be allocated in sustainable numbers to all member nations of the IWC, who would have the choice of exercising them, leaving them unused for a year or retiring them in perpetuity. The shares would be tradable in a carefully controlled global market, perhaps with the restriction that members could not trade whale products with non-members. The number of whales hunted would depend on who owned the shares. At one extreme (in which whalers purchase all the shares), whales would be harvested to the agreed sustainable level. At the other extreme (where conservationists purchase all the shares), all whales would be protected from harvest.

There are multiple challenges in getting such a scheme to work, including agreeing on sustainable quotas and on how shares should be allocated. We believe that the IWC is up to the task.

### KILLER QUESTION

Various well-established algorithms could be used to identify sustainable harvest levels for whales<sup>4</sup>. For example, the IWC's 'catch limit algorithm', which sets commercial quotas for baleen whales, could be applied more broadly. The US Marine Mammal Protection Act mandates a more conservative approach, known as 'potential biological removal', to establish sustainable take levels for marine mammals in US waters. Although negotiations to set binding catch quotas, such as the deliberations by IWC members in 2010, have not led to consensus, the major reason has not been objections to the proposed quota numbers per se, but a more philosophical objection to the idea of setting quotas at all. Allowing the quotas to be traded, as we advocate, means that they would not necessarily lead to whale deaths or national caps on takes, appeasing both parties.

The initial allocation of whale shares is a potentially challenging issue. In the realm of climate change, the process of divvying up global emissions targets into national responsibilities has proven intractable, with developing nations arguing that stringent targets will inhibit growth, and others arguing that their circumstances, from particularly cold winters to vast forests acting as carbon sinks, justify higher targets. Allocation has been contentious in fisheries too, where it gives a highly valuable asset to the recipient. In practice, in both the emissions and fisheries markets, the initial allocations almost always coincide with historical use. Research into the global markets for air pollutants<sup>5</sup> and fish<sup>6</sup> offers many potential solutions to the whaling allocation problem. One possibility would be to divide the majority of the quota between whaling and non-whaling nations based on historical whaling patterns, leaving the rest for open auction, the proceeds of

which would go to whale conservation.

Handing out shares within nations has had a greater history of success, and is likely to be less contentious. Initial allocations within non-whaling countries would probably go to conservation trusts that are focused on protecting particular species. Quota rights could be limited in duration, say for ten years with the possibility of renewal, or in perpetuity for subsistence groups.

Policing such a market would not be simple. But a global vessel registry and carefully monitored trading would help to ensure system integrity. Requiring prices and trades to be made public would bring transparency to an industry that has long been accused of back-room deals and vote trading.

The 'whale share' approach stands a good chance of being acceptable both to anti- and to pro-whaling constituents. If quotas are set properly, transactions would reduce the number of whales harvested, quite possibly to zero, unlike existing protocols, which seem to be increasing the catches. Whalers would be suitably compensated. And because trades are voluntary, the market would have the potential to make all parties better off, and simultaneously improve whale conservation.

A fervent anti-whaler will be quick to argue that you cannot and should not put a price on the life of a whale; a species should be protected irrespective of its economic value. But unless all nations can be convinced or forced to adopt this view, whaling will continue. It is precisely because of the lack of a real price tag in the face of different values that anti-whaling operations have had such limited success.

A generous estimate of the total annual profit from all global commercial whaling activity is US\$31 million. Whalers spend millions of dollars to harvest these whales, many of which are then sold on global markets. Recent reports suggest that even some whales hunted for subsistence may end up

for sale elsewhere<sup>7</sup>, suggesting that whale meat is replaceable as a necessary source of protein for some communities.

Simple calculations based on current market prices, whale sizes and whaling costs, suggest that the per-whale profit for whalers is in the ballpark of \$13,000 for a minke whale to \$85,000 for a fin whale. Whale prices should therefore be within reach of conservation groups and even some individuals.

A conservative estimate of the amount spent annually by non-profit organizations on anti-whaling (based on the expenditures of Greenpeace USA, Greenpeace Interna-

**"If quotas are set properly, transactions would reduce the number of whales harvested."**

tional, Sea Shepherd Conservation Society, WWF International and WWF UK) is \$25 million. Rather than supporting anti-whaling protests and movements (and their accompanying carbon

footprint), this money could be used to purchase whales, arguably with the same or better effect. Sea Shepherd, for example, estimates that its multimillion-dollar 2008 campaign saved about 350 minke whales in Antarctic waters. By our calculations, those whales could have been purchased for less than \$4 million.

Properly designed, a whale market could accommodate important concerns such as the by-catch of whales in fisheries or whale ship strikes. It could even be integrated with other market approaches, such as a recent proposal to apply carbon credits to live whales<sup>8</sup>. By placing an appropriate price tag on the life of a whale, a whale conservation market provides an immediate and tangible way to save them. ■

**Christopher Costello and Steven Gaines**

are at the Bren School of Environmental Science and Management, University of California, Santa Barbara, California 93106, USA. **Leah R. Gerber** is in the Ecology, Evolution and Environmental Sciences faculty, School of Life Sciences, Arizona State University, Tempe, Arizona 85281, USA.

e-mail: costello@bren.ucsb.edu



In a market system, charities could 'buy' whales, rather than spending money campaigning.

1. International Whaling Commission Catch Limits & Catches Taken; available at <http://go.nature.com/rcnfq5>
2. Gerber, L. R., DeMaster, D. & Roberts, S. *Am. Sci.* **88**, 316–324 (2000).
3. Clark, C. W. & Lamberson, R. *Mar. Pol.* **6**, 103–120 (1982).
4. Haltuch, M. A., Punt, A. E. & Dorn, M. W. *Fish. Res.* **100**, 42–56 (2009).
5. Goulder, L., Hafstead, M. & Dworsky, M. *J. Environ. Econ. Manage.* **60**, 161–181 (2010).
6. Anderson, T., Arnason, R. & Libecap, G. *Annu. Rev. Res. Econ.* **3**, 159–179 (2011).
7. Black, R. Greenland whale hunt 'commercial' *BBC News* (17 June 2008); available at <http://go.nature.com/vspdy5>
8. Pershing, A. J. et al. *PLoS ONE* **5**, e12444 (2010).

F. BANFI/OCEANS-IMAGE/NHPA/PHOTOSHOT



Scientific studies of humpback and other whales in the 1920s were first to reveal their dwindling numbers.

## CONSERVATION

# Harpoons and heartstrings

A history of cetacean research highlights its precarious place between whaling and politics, finds **Philip Hoare**.

Historian of science D. Graham Burnett is sly in his provocations. In *The Sounding of the Whale*, he has painstakingly gathered evidence for science's conflicted role in providing rigorous data for the preservation — if not always conservation — of whales. He wonders whether the competing interests in this tale have reduced the science, buried under the cumulative weight of that evidence, to an “elaborate form of rhetoric”.

This is a characteristically wry sentiment from Burnett, whose book provides a synopsis of a century of human and natural

history. The fact that it is about whales seems almost accidental; its subject matter has more to do with the human response to whales than the creatures themselves.

Burnett begins with whaling in the early twentieth century, when only the United Kingdom and Norway remained major players. The heyday of US whaling, extolled in Herman Melville's 1851 novel *Moby-Dick*, had long passed. With northern stocks of sperm and right whales reduced, the whalers' attention had swung south to the Falkland Islands and South Georgia, where fast boats and grenade harpoons enabled the hunting

of species such as blue and fin whales.

The scientific response to this multi-million-pound industry (worth even more during the First World War, when whales were a source of glycerine for munitions) was led by zoologist Sidney Harmer, director of the British Museum (Natural History). Harmer was the first ‘statesman-scientist’ to voice concerns over dwindling whale numbers, some species of which seemed about to become extinct before they had been studied.

In the early 1920s, Harmer's deft lobbying of the British government produced generous funds for the Discovery research expeditions, using the ship that had taken explorer Robert Scott to the Antarctic. The scientists' aims were to establish breeding patterns, migratory routes and possible populations of blue, fin and humpback whales. They discovered that, far from being as numerous as whalers claimed, many whale populations were diminished as a result of whaling in both their breeding and feeding grounds.

These scientists moulded themselves in the guise of the great polar explorers, bribing the whaling-station butchers with whisky in exchange for whale fetuses and ovaries to study. Meanwhile, on *Discovery's* sister ship, *William Scoresby*, other scientists were shooting whales with metal darts to track their movements. It was a Faustian pact, Burnett relates, “buying whale science with whale oil”.

The 1920s also saw the first stirrings of the public's conscience over whaling (but not its stomach: 42% of margarine made in Britain contained whale oil at the time), with “Save the Whales” appearing in a 1924 headline in the *Liverpool Daily Courier*. Here Burnett shifts his attention across the Atlantic to US naturalist Remington Kellogg, assistant curator of mammals at the Smithsonian Institution in Washington DC. No longer a whaling nation, the United States could take the moral high ground in the move towards whale conservation. Pelagic fleets run by Russia, Japan and the Netherlands were taking up to 50,000 great whales (including blue, fin, sperm and humpback) each year. Kellogg and his colleagues struggled to assess population sizes in the face of such slaughter.

The League of Nations took up the issue as early as 1930, in a committee chaired by the Argentinian academic José León Suárez, who declared that “the riches of the sea, and especially the immense wealth of the Antarctic region, are the patrimony of the whole human race”. With the founding of



**The Sounding of the Whale: Science and Cetaceans in the Twentieth Century**

D. GRAHAM BURNETT  
University of Chicago  
Press: 2012. 824 pp.  
\$45, £29



the International Whaling Commission (IWC) in 1946 — the machinations of which Burnett lays out using newly uncovered archival material — matters became more complicated as cold-war politics kicked in.

By 1965, a crisis point had been reached. Soviet whaling fleets were exceeding their allotted quota, and seriously under-reporting their catch. The IWC, and the uncertainty of cetacean science, sat uneasily in this sorry story of 'cetapolitics'. Radical conservationists suspected some scientists of perpetuating whaling because it supplied them with the subjects for their studies; other researchers found their work being used as a delaying tactic by the whalers, who could continue their culls under the pretence of aiding science. Thus, the obsessive collection of data, Burnett writes, ended up "obscuring the seriousness of the problem" by becoming an end in itself rather than addressing the pressing issue of population depletion.

Enter the contentious physician John Lilly, whose idea of cetaceans as 'alien species' and wild experiments (culminating in dosing dolphins with the drug LSD) have been seen by some as setting the field back by years. But Burnett shows how Lilly's work was the crucial interface between military bioscience and a new countercultural attitude towards cetaceans. That paved the way for the astonishing effect of a 1971 recording of humpback whale songs by researchers Scott McVay and Roger Payne, which sensitized a generation and galvanized the anti-whaling movement.

The same battle for the fate of the whale is still being fought, three decades after the implementation of the IWC's moratorium on commercial whaling. The scope and weight of Burnett's book symbolizes that continuing inertia.

Perhaps that is why, after his ten years of research, Burnett is left with a Melvillean sense of existential defeat even in his groundbreaking conclusion: "The fundamental lesson I have taken from the research and writing of this book amounts to nothing less than a kind of sweeping epistemological humiliation." Yet by questioning the very nature of our scientific interest in the whale, he has set the tone for a new century of discovery — and, one hopes, recovery. ■

**Philip Hoare** is the Leverhulme artist-in-residence at the Marine Institute at Plymouth University, and a visiting fellow at the University of Southampton, UK. He is the author of *Leviathan* or, *The Whale*.  
e-mail: [phoare@soton.ac.uk](mailto:phoare@soton.ac.uk)

## ENERGY

# Curbing urban greed

An overview of resource-guzzling US cities has lessons for us all, finds **David Orr**.

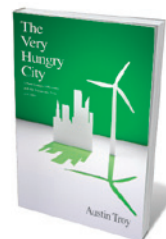
Austin Troy concludes *The Very Hungry City* by writing: "Good cities are good places to live. But they take work." In the United States, that is both the promise and the problem. With few exceptions, such as Washington DC, US cities grew by happenstance, contrivance and often by connivance. The same is increasingly true of megacities worldwide. Growth without planning — as Troy shows in his trek through conurbations from Los Angeles to Copenhagen to Masdar City in Abu Dhabi — has huge implications for energy use and the natural resources that support it.

Troy, an environmental economist, gives us a sure-handed, cogent treatment of urban challenges, focusing on 'urban energy metabolism' — a city's pattern of energy use determined by its location, culture, history and size. Most US cities need massive energy inputs per capita compared with many of their European, Chinese or developing-world counterparts. The price they pay is a vulnerability to scarcity, rising costs and environmental decay. Troy traces energy use through water consumption, transport, construction, the heating and cooling of homes, and the creation of workable communities, and includes sidebars on energy choices from renewables, natural gas and coal to nuclear power, oil and biofuels.

He describes a drearily familiar pattern that has accelerated since the mid-twentieth century. With little planning or foresight, inner cities are forsaken for suburbs, from which people flee to yet more distant 'exurbs' — a pattern of urban greed that consumes land,



Overbuilt Phoenix, Arizona, faces a dry future.



**The Very Hungry City: Urban Energy Efficiency and the Economic Fate of Cities**

AUSTIN TROY  
Yale University Press:  
2012. 384 pp.  
\$28, £25

infrastructure, people and energy. The United States is littered with extreme examples: on the one hand is Detroit, Michigan, a proud industrial city of around 2 million people in 1950 that is now reduced to a beleaguered population of 700,000 circled by affluent suburbs; on the other is glittering, overbuilt Phoenix, Arizona, facing a future of extreme heat and dessication.

Elsewhere, notably in the US Sun Belt, 'zombie' urban subdivisions built far from city centres drive up energy and resource use. Even urban success stories elsewhere, such as Stockholm, face the challenges of energy and resources that come with continued growth.

How did we get to this point? Americans have traditionally regarded cities as places where you make money fast and move on. The combination of greed and devil-take-the-hindmost economic theories led to the abandonment of whole sectors of urban economies when people found their mobile capital could earn them a bit more somewhere else. Racism also played a large part. Banks refused to invest in minority-dominated inner cities, resulting in segregated poverty and crime. And then there is the car, an indiscriminate wrecker of urban fabric, air quality and climate stability.

As a result of all this, the United States still does not have a coherent urban policy. That has cost the country dear — not least in terms of the human cost of wars fought over the oil needed to subsidize inefficient urban growth.

Underpriced and oversubsidized fossil fuels made energy cheap, but that era is stumbling to an end. Accelerating climate destabilization, peak oil extraction, water shortages and rapidly growing urban populations are looming global challenges. More than half the people in the world live in cities, and it is here that humanity's future will be decided — albeit in a global economy with a diminishing margin for waste and policy mistakes.

➔ **NATURE.COM**  
Nature's Science  
and the City special:  
[go.nature.com/9233vu](http://go.nature.com/9233vu)

A. MACLEAN/GETTY

the International Whaling Commission (IWC) in 1946 — the machinations of which Burnett lays out using newly uncovered archival material — matters became more complicated as cold-war politics kicked in.

By 1965, a crisis point had been reached. Soviet whaling fleets were exceeding their allotted quota, and seriously under-reporting their catch. The IWC, and the uncertainty of cetacean science, sat uneasily in this sorry story of 'cetapolitics'. Radical conservationists suspected some scientists of perpetuating whaling because it supplied them with the subjects for their studies; other researchers found their work being used as a delaying tactic by the whalers, who could continue their culls under the pretence of aiding science. Thus, the obsessive collection of data, Burnett writes, ended up "obscuring the seriousness of the problem" by becoming an end in itself rather than addressing the pressing issue of population depletion.

Enter the contentious physician John Lilly, whose idea of cetaceans as 'alien species' and wild experiments (culminating in dosing dolphins with the drug LSD) have been seen by some as setting the field back by years. But Burnett shows how Lilly's work was the crucial interface between military bioscience and a new countercultural attitude towards cetaceans. That paved the way for the astonishing effect of a 1971 recording of humpback whale songs by researchers Scott McVay and Roger Payne, which sensitized a generation and galvanized the anti-whaling movement.

The same battle for the fate of the whale is still being fought, three decades after the implementation of the IWC's moratorium on commercial whaling. The scope and weight of Burnett's book symbolizes that continuing inertia.

Perhaps that is why, after his ten years of research, Burnett is left with a Melvillean sense of existential defeat even in his groundbreaking conclusion: "The fundamental lesson I have taken from the research and writing of this book amounts to nothing less than a kind of sweeping epistemological humiliation." Yet by questioning the very nature of our scientific interest in the whale, he has set the tone for a new century of discovery — and, one hopes, recovery. ■

**Philip Hoare** is the Leverhulme artist-in-residence at the Marine Institute at Plymouth University, and a visiting fellow at the University of Southampton, UK. He is the author of *Leviathan* or, *The Whale*.  
e-mail: [phoare@soton.ac.uk](mailto:phoare@soton.ac.uk)

## ENERGY

# Curbing urban greed

An overview of resource-guzzling US cities has lessons for us all, finds **David Orr**.

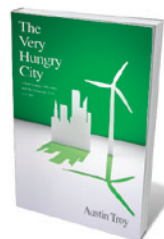
Austin Troy concludes *The Very Hungry City* by writing: "Good cities are good places to live. But they take work." In the United States, that is both the promise and the problem. With few exceptions, such as Washington DC, US cities grew by happenstance, contrivance and often by connivance. The same is increasingly true of megacities worldwide. Growth without planning — as Troy shows in his trek through conurbations from Los Angeles to Copenhagen to Masdar City in Abu Dhabi — has huge implications for energy use and the natural resources that support it.

Troy, an environmental economist, gives us a sure-handed, cogent treatment of urban challenges, focusing on 'urban energy metabolism' — a city's pattern of energy use determined by its location, culture, history and size. Most US cities need massive energy inputs per capita compared with many of their European, Chinese or developing-world counterparts. The price they pay is a vulnerability to scarcity, rising costs and environmental decay. Troy traces energy use through water consumption, transport, construction, the heating and cooling of homes, and the creation of workable communities, and includes sidebars on energy choices from renewables, natural gas and coal to nuclear power, oil and biofuels.

He describes a drearily familiar pattern that has accelerated since the mid-twentieth century. With little planning or foresight, inner cities are forsaken for suburbs, from which people flee to yet more distant 'exurbs' — a pattern of urban greed that consumes land,



Overbuilt Phoenix, Arizona, faces a dry future.



**The Very Hungry City: Urban Energy Efficiency and the Economic Fate of Cities**

AUSTIN TROY  
Yale University Press:  
2012. 384 pp.  
\$28, £25

infrastructure, people and energy. The United States is littered with extreme examples: on the one hand is Detroit, Michigan, a proud industrial city of around 2 million people in 1950 that is now reduced to a beleaguered population of 700,000 circled by affluent suburbs; on the other is glittering, overbuilt Phoenix, Arizona, facing a future of extreme heat and dessication.

Elsewhere, notably in the US Sun Belt, 'zombie' urban subdivisions built far from city centres drive up energy and resource use. Even urban success stories elsewhere, such as Stockholm, face the challenges of energy and resources that come with continued growth.

How did we get to this point? Americans have traditionally regarded cities as places where you make money fast and move on. The combination of greed and devil-take-the-hindmost economic theories led to the abandonment of whole sectors of urban economies when people found their mobile capital could earn them a bit more somewhere else. Racism also played a large part. Banks refused to invest in minority-dominated inner cities, resulting in segregated poverty and crime. And then there is the car, an indiscriminate wrecker of urban fabric, air quality and climate stability.

As a result of all this, the United States still does not have a coherent urban policy. That has cost the country dear — not least in terms of the human cost of wars fought over the oil needed to subsidize inefficient urban growth.

Underpriced and oversubsidized fossil fuels made energy cheap, but that era is stumbling to an end. Accelerating climate destabilization, peak oil extraction, water shortages and rapidly growing urban populations are looming global challenges. More than half the people in the world live in cities, and it is here that humanity's future will be decided — albeit in a global economy with a diminishing margin for waste and policy mistakes.

➔ **NATURE.COM**  
Nature's Science  
and the City special:  
[go.nature.com/9233vu](http://go.nature.com/9233vu)

A. MACLEAN/GETTY



Yet we can curb the urban energy appetite. Troy covers a growing list of successes — stories of improved energy and resource efficiency, better technology, collective solutions and foresight. For example, semiconductor manufacturer Intel is pumping three-quarters of the water it uses in its New Mexico facility back into local aquifers. The city of Los Angeles is belatedly resuscitating its once-extensive urban light-rail system. Vermont has deployed a highly successful statewide energy-efficiency programme.

Policy tools such as location-efficient mortgages — which encourage people to buy houses in areas that have abundant public transport — can help to recalibrate economic incentives with energy and climate realities. Congestion-charge schemes such as that in London are reducing traffic in dense urban areas, and time-of-day charges for electricity cut energy use. Even the Empire State Building in New York has been refurbished to lower its energy use by 38%, hinting at potential changes for older buildings everywhere.

Energy-efficient developments are proving to be popular and economically viable. Denver, Colorado, for instance, has revitalized derelict properties in the lower downtown area. Portland in Oregon set up a growth boundary for the city in 1973, deflecting investment downtown with dramatic results. And creative urban designers such as Peter Calthorpe — a pioneer of community models that integrate principles such as environmental sustainability and mixed-use building — continue to push the boundaries. The keys to making smart development the default setting and not an anomaly are creative, long-term public policies and investment strategies that stress energy efficiency and the deployment of renewable energy.

We may even be seeing the start of a global urban renaissance in places such as Masdar City. Once finished, it will house 50,000 people and get all of its energy from sunlight and other renewable sources. But this does not mean abandoning existing urban settlements. Many older European cities are prosperous, attractive and increasingly sustainable because they have preserved a coherent core and developed a robust urban infrastructure for bikes and light-rail systems. In short, cities in many other countries are doing a great deal better than those in the United States.

There are two models of our urban future. One is a dystopian nightmare of crowded, decaying, violent cities. Troy presents the other: a vision of lean, efficient, human-scaled, sustainable cities fed by efficiency, better design and renewable energy. ■

**David Orr** is the Paul Sears Distinguished Professor of Environmental Studies at Oberlin College, Oberlin, Ohio 44074, USA. e-mail: dorr@oberlin.edu

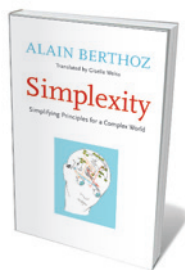
## Books in brief



### That's Disgusting: Unraveling the Mysteries of Repulsion

Rachel Herz W. W. NORTON 288 pp. \$26.95 (2012)

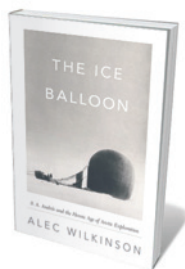
The emotion of disgust has its evolutionary roots in avoiding poisonous food, notes psychologist Rachel Herz. It has penetrated many areas of human life, as shown by lawyers' and politicians' efforts to incite disgust about their opponents. But that doesn't explain why the things that one culture or individual finds repulsive — such as sea-urchin sushi or horror films — are delightful to another. In her lively tour of vileness, Herz argues that disgust is in the mind of the beholder, and explains how studies of Huntington's disease pinpointed the brain areas involved in this emotion.



### Simplicity: Simplifying Principles for a Complex World

Alain Berthoz (translated by Giselle Weiss) YALE UNIVERSITY PRESS 288 pp. \$38 (2012)

Living things navigate their complex worlds superbly, making tasks such as walking — which thwart the most sophisticated machines — look like child's play. Simplicity, says physiologist Alain Berthoz, allows life to achieve such feats. It involves transforming “a rich combination of simple rules” into a model of reality that aids action and decision-making, yet respects complexity. Berthoz uses examples from perception, locomotion and neuroscience, but argues that simplicity is at work on all levels, from cells to societies and even in love.



### The Ice Balloon: S. A. Andrée and the Heroic Age of Arctic Exploration

Alec Wilkinson ALFRED A. KNOPF 256 pp. \$25.95 (2012)

In 1897, the Swedish explorer Salomon August Andrée sought to use a hydrogen balloon to become the first man to reach the North Pole. Alec Wilkinson's tenth book opens in 1930 with the discovery of Andrée's corpse on a remote Arctic island. It recounts the ill-fated journey through the diaries and photographs of Andrée and his two companions. Wilkinson shows how science and exploration went hand in hand, and how Arctic explorers were celebrities, with the balloonists meriting waxworks in Madame Tussauds museum.



### Too Big to Know: Rethinking Knowledge Now That the Facts Aren't the Facts, Experts Are Everywhere, and the Smartest Person in the Room Is the Room

David Weinberger BASIC BOOKS 256 pp. \$25.99 (2012)

Once, says philosopher David Weinberger, experts mastered knowledge and controlled what the rest of us made of it. Now, disciplines such as climate science and molecular biology contain too much data for humans to parse or for theories to explain. Instead, the network is the expert, and anyone can join in. This is creating new forms of communication for science, both educating more people and enabling us to be more emphatically wrong.



### Together: The Rituals, Pleasures and Politics of Co-operation

Richard Sennett ALLEN LANE 336 pp. £25 (2012)

Societies are increasingly complex. Yet we stall at mingling with other ‘tribes’, a trend exacerbated by politicians calling for cultural homogenization. Sociologist Richard Sennett says that the key is learning how to cooperate. In the second of his trio on constructive living, case studies reveal how the upheavals of the early modern era and unethical work practices have broken down cooperation. As a route to remaking it, Sennett advocates ‘everyday diplomacy’, an essential craft that could heal societal rifts from the inside out.

Yet we can curb the urban energy appetite. Troy covers a growing list of successes — stories of improved energy and resource efficiency, better technology, collective solutions and foresight. For example, semiconductor manufacturer Intel is pumping three-quarters of the water it uses in its New Mexico facility back into local aquifers. The city of Los Angeles is belatedly resuscitating its once-extensive urban light-rail system. Vermont has deployed a highly successful statewide energy-efficiency programme.

Policy tools such as location-efficient mortgages — which encourage people to buy houses in areas that have abundant public transport — can help to recalibrate economic incentives with energy and climate realities. Congestion-charge schemes such as that in London are reducing traffic in dense urban areas, and time-of-day charges for electricity cut energy use. Even the Empire State Building in New York has been refurbished to lower its energy use by 38%, hinting at potential changes for older buildings everywhere.

Energy-efficient developments are proving to be popular and economically viable. Denver, Colorado, for instance, has revitalized derelict properties in the lower downtown area. Portland in Oregon set up a growth boundary for the city in 1973, deflecting investment downtown with dramatic results. And creative urban designers such as Peter Calthorpe — a pioneer of community models that integrate principles such as environmental sustainability and mixed-use building — continue to push the boundaries. The keys to making smart development the default setting and not an anomaly are creative, long-term public policies and investment strategies that stress energy efficiency and the deployment of renewable energy.

We may even be seeing the start of a global urban renaissance in places such as Masdar City. Once finished, it will house 50,000 people and get all of its energy from sunlight and other renewable sources. But this does not mean abandoning existing urban settlements. Many older European cities are prosperous, attractive and increasingly sustainable because they have preserved a coherent core and developed a robust urban infrastructure for bikes and light-rail systems. In short, cities in many other countries are doing a great deal better than those in the United States.

There are two models of our urban future. One is a dystopian nightmare of crowded, decaying, violent cities. Troy presents the other: a vision of lean, efficient, human-scaled, sustainable cities fed by efficiency, better design and renewable energy. ■

**David Orr** is the Paul Sears Distinguished Professor of Environmental Studies at Oberlin College, Oberlin, Ohio 44074, USA. e-mail: dorr@oberlin.edu

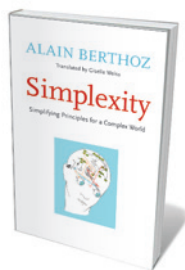
## Books in brief



### That's Disgusting: Unraveling the Mysteries of Repulsion

Rachel Herz W. W. NORTON 288 pp. \$26.95 (2012)

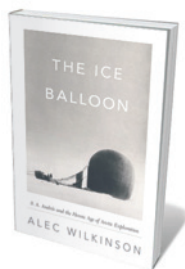
The emotion of disgust has its evolutionary roots in avoiding poisonous food, notes psychologist Rachel Herz. It has penetrated many areas of human life, as shown by lawyers' and politicians' efforts to incite disgust about their opponents. But that doesn't explain why the things that one culture or individual finds repulsive — such as sea-urchin sushi or horror films — are delightful to another. In her lively tour of vileness, Herz argues that disgust is in the mind of the beholder, and explains how studies of Huntington's disease pinpointed the brain areas involved in this emotion.



### Simplicity: Simplifying Principles for a Complex World

Alain Berthoz (translated by Giselle Weiss) YALE UNIVERSITY PRESS 288 pp. \$38 (2012)

Living things navigate their complex worlds superbly, making tasks such as walking — which thwart the most sophisticated machines — look like child's play. Simplicity, says physiologist Alain Berthoz, allows life to achieve such feats. It involves transforming “a rich combination of simple rules” into a model of reality that aids action and decision-making, yet respects complexity. Berthoz uses examples from perception, locomotion and neuroscience, but argues that simplicity is at work on all levels, from cells to societies and even in love.



### The Ice Balloon: S. A. Andrée and the Heroic Age of Arctic Exploration

Alec Wilkinson ALFRED A. KNOPF 256 pp. \$25.95 (2012)

In 1897, the Swedish explorer Salomon August Andrée sought to use a hydrogen balloon to become the first man to reach the North Pole. Alec Wilkinson's tenth book opens in 1930 with the discovery of Andrée's corpse on a remote Arctic island. It recounts the ill-fated journey through the diaries and photographs of Andrée and his two companions. Wilkinson shows how science and exploration went hand in hand, and how Arctic explorers were celebrities, with the balloonists meriting waxworks in Madame Tussauds museum.



### Too Big to Know: Rethinking Knowledge Now That the Facts Aren't the Facts, Experts Are Everywhere, and the Smartest Person in the Room Is the Room

David Weinberger BASIC BOOKS 256 pp. \$25.99 (2012)

Once, says philosopher David Weinberger, experts mastered knowledge and controlled what the rest of us made of it. Now, disciplines such as climate science and molecular biology contain too much data for humans to parse or for theories to explain. Instead, the network is the expert, and anyone can join in. This is creating new forms of communication for science, both educating more people and enabling us to be more emphatically wrong.



### Together: The Rituals, Pleasures and Politics of Co-operation

Richard Sennett ALLEN LANE 336 pp. £25 (2012)

Societies are increasingly complex. Yet we stall at mingling with other ‘tribes’, a trend exacerbated by politicians calling for cultural homogenization. Sociologist Richard Sennett says that the key is learning how to cooperate. In the second of his trio on constructive living, case studies reveal how the upheavals of the early modern era and unethical work practices have broken down cooperation. As a route to remaking it, Sennett advocates ‘everyday diplomacy’, an essential craft that could heal societal rifts from the inside out.





In *The Tragedy of the Commons*, artists Robin Meier and Ali Momeni recorded the sounds of foraging ants.

## Q&A Robin Meier

# Maestro of the swarm

Swiss acoustic artist Robin Meier manipulates the sounds of insects and birds to create ethereal soundscapes. As his mosquito-inspired musical installation *Truce* is aired in the French city of Nantes, he talks about firefly synchrony and setting up feedback loops in nature.

### Why did you choose to work with mosquitoes?

Male mosquitoes serenade potential mates with a 'love song' by vibrating their wings. They synchronize their wingbeats with those of the females to mate in mid-air. I first read about this in a 2006 paper by entomologist Gabriella Gibson and neurobiologist Ian Russell (*Curr. Biol.* 16, 1311–1316; 2006). The constant *glissandi* — gliding from one pitch to another — and 'tuning in' of mosquito wingbeats reminded me of *dhrupad*, an ancient form of Indian classical music often sung by brothers in unison. My collaborator Ali Momeni and I played male mosquitoes some *dhrupad* and, sure enough, they tuned in. We call the piece *Truce: Strategies for Post-Apocalyptic Computation* because we see it as one way that computation could evolve. In the future, the environment could become an extension of our cognitive processes.

### How did you become interested in this area?

I'm a musician but studied cognitive philosophy, and am very interested in artificial intelligence. One of my first installations, with French experimental musician Frédéric Voisin in 2004, involved manipulating



artificial neural networks to make music. The idea of collective intelligence is a theme that is common to all my work. Intelligence isn't just an intrinsic property; it lies in the interaction between organisms and environment. It is all around us, and I want to harness it to make music.

### How did that lead you to work with ants?

With the help of scientists at the Laboratory of Experimental and Comparative Ethology at the University of Paris 13, I conditioned leafcutter ants to associate quinine — which they dislike — with different smells and foods. We built a star-shaped installation called *The Tragedy of the Commons*, which provides a choice of six foods, each in one arm of the star [see [go.nature.com/mvbswm](http://go.nature.com/mvbswm)]. Here we manipulate the ants' foraging decisions through smell. Once they associate quinine with a certain food, we take the quinine away and the smell of that food alone will put them off. They communicate this to other ants, partly through sound signals called stridulation, when they rub body parts together. Using strategically placed microphones and loudspeakers, we have created a soundscape of their foraging decisions on two levels: an amplification of the stridulation, and an amplification of the sounds of ants eating at the positions they choose.

The sound therefore varies spatially across the installation.

### And what about your firefly work?

My virtual firefly project hinges on synchrony. Fireflies synchronize their flashing for courtship purposes. Groups of males of the same species seem to do this so that the passing females can see them better — the flashing pattern is species-specific. When it happens, you see distributed pockets of synchronous flashing appear before they join up and an overall synchrony emerges. Although the behaviour itself is complex, all you need to generate it virtually is a number of identical 'organisms', each equipped with some basic perceptual apparatus and an internal mechanism for adjusting the flashing speed. We have simulated this on a computer.

### How do you turn virtual firefly synchrony into music?

You could think of the fireflies as a sort of amateur orchestra and me as their conductor, only I go further by tinkering with their virtual brains. We manipulate their flashing by altering those underlying parameters — the ones that determine how they perceive and generate flashes — and so change the rhythm or even break up the synchrony completely. My collaborator on this project, Canadian artist Yan Breuleux, is interested in the visual effects that this allows him to create. I transform the flashes into sound and create audio effects using standard music-sampling software.

### What other projects are in the pipeline?

I've long been interested in the neurobiology of songbirds. Starlings are fascinating because they're such good learners. They imitate car alarms, mobile phones, anything. This year, we intend to build birdhouses in the Camargue nature park in the south of France, and we hope that starlings will nest in them. We'll install speakers and play melodies to them. Because starlings are migratory, the fledglings could carry the tunes far and wide.

### Are you 'playing God' with animals?

No: God is top-down, we're bottom-up. I think of what we do as more like hacking. We may end up manipulating a few starlings, for example, and our manipulation may be transmitted, but probably only in a small way before it fades like a ripple on a pond. It's not just us manipulating the organism. The organism reacts to our manipulation, we react to its reaction, and so on. We set up feedback loops. ■

INTERVIEW BY LAURA SPINNEY

NICK HIGGINS

## Leaping lizards and dinosaurs

**Tightrope walkers use poles to keep their balance. A study reveals that agama lizards use their tails much like balancing poles as they leap through the air — and that some dinosaurs may have done the same. [SEE LETTER P.181](#)**

R. MCNEILL ALEXANDER

Agama lizards jump quite well, and have a remarkable ability to land safely. On page 181 of this issue, Libby *et al.*<sup>1</sup> describe a study in which they filmed agamas jumping from a horizontal platform to a vertical wall. The lizards used mid-air tail movements to ensure that their trunk was tilted at an appropriate angle for landing as they approached the wall\*.

The manoeuvre depends on the principle of conservation of angular momentum, which states that the angular momentum of a system remains constant unless external torques act on it. For example, some tightrope walkers carry a balancing pole. By tilting the pole, the performer can make his or her body lean in the opposite direction to that tilt; any change of angular momentum of the pole must be matched by an opposite change of angular momentum of the body, to keep the overall angular momentum constant (Fig. 1a). Small movements of the pole can therefore keep the performer's centre of mass where it needs to be, vertically above the rope. A long, slender pole works better than a short, thick one because it has a larger moment of inertia for the same weight (the angular momentum of a body is its angular velocity multiplied by its moment of inertia). This simple explanation assumes that any transverse movements of the centre of mass are so small that the moment of body weight about the rope is negligible.

In their study, Libby *et al.* found that if a lizard needed to tilt its trunk 'nose-up' during a jump to ensure that it landed correctly on a vertical surface, it bent its long, slender tail upwards (Fig. 1b). This, for example, gave the tail clockwise momentum and the trunk equal anticlockwise momentum, leaving the total angular momentum unchanged, as the conservation principle requires. To find out whether a lizard could adjust its tail movements to compensate for errors at launch, the authors put a slippery surface on the take-off platform for some of the trials. They observed that if a lizard's foot skidded, the angle of the body at take-off was affected, but the animal corrected the error

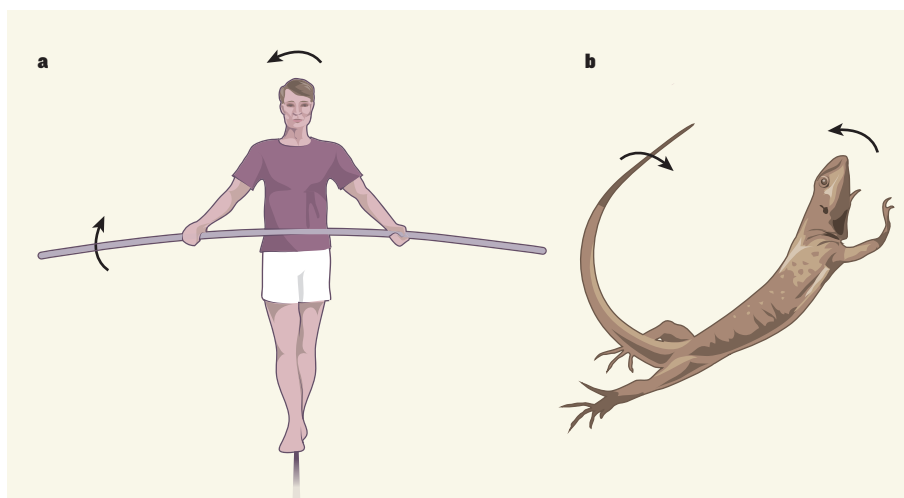


**Figure 1 | Conservation of angular momentum.** a, When a tightrope walker rotates his balancing pole clockwise, his body tilts anticlockwise, in accordance with the principle of conservation of angular momentum. b, Libby *et al.*<sup>1</sup> report that leaping agama lizards similarly bend their tails clockwise in mid-air, to tilt their bodies anticlockwise.

using an appropriate tail movement.

Libby *et al.* used a mathematical model to confirm that their explanation of tail control worked quantitatively. As a further check, they built a delightful toy: a wheeled robot with a tail, which leapt like a ski jumper from a ramp. During each jump, the front wheels of the robot left the ramp first and started falling while the rear ones were still on the ramp, causing the robot to tilt nose-down. But the machine corrected the angle of its body before landing using tail movements that were controlled by feedback from a gyroscope. The robot compensated for its imperfect launch posture brilliantly, even better than did the lizards.

As with all good research, Libby and colleagues' findings raise new questions. The authors considered a lizard's use of its tail as a two-dimensional problem: they considered only the pitch of the body (whether its nose was up or down). But can the tail also be used to adjust the angle of yaw (turning to left or right) and roll? Pitch is paramount when jumping onto a vertical wall, but jumping between irregularly shaped rocks or branches would require adjustments in three dimensions. The same group has previously considered all three dimensions in a paper<sup>2</sup> on body-righting responses of falling geckos, but

there are opportunities for more quantitative work along these lines.

Apart from lizards, Libby *et al.* cite several examples of animals that exploit the moment of inertia of an appendage, including lemurs, kangaroo rats and cats. The authors go on to suggest that some dinosaurs may have jumped, using their tails as agamas do to control the angle of the body. Any dinosaurs that did this, however, must have been relatively small. Very large animals cannot jump far because — assuming that their anatomy is geometrically similar to that of their smaller kin — their weights are proportional to the cube of their lengths, whereas the strengths of their bones and muscles are proportional only to cross-sectional areas, and so to their lengths squared. Horses and elands (a very large species of antelope) are, at around 500 kilograms each, among the largest animals that can jump well. Calculations based on measurements of dinosaur bones<sup>3</sup> and on the estimated dimensions of their muscles<sup>4</sup> show that large dinosaurs cannot have been very agile.

So is there any evidence that smaller dinosaurs jumped? The carnivorous dinosaur *Deinonychus* is estimated to have had a mass of about 70 kilograms — in the size range of leopards, and well within the feasible range

\*This article and the paper<sup>1</sup> under discussion were published online on 4 January 2012.



for jumping. Some fossil evidence has been interpreted<sup>5</sup> as suggesting that *Deinonychus*, hunting in packs, may have preyed on dinosaurs much larger than themselves. Although this suggestion has been challenged<sup>6</sup>, it has been widely assumed that *Deinonychus* leapt onto the backs and flanks of their victims, using enormous claws to get a firm grip<sup>7</sup>. Similarly, lions and other big cats use their sharp claws to grip the hide of their prey, while using their teeth to attack the vulnerable structures of the throat.

There are several drawings on the Internet showing *Deinonychus* in mid-air, jumping onto large prey. Some of the drawings show the animal jumping improbably high, but it is pleasing to see that several of them show the tail swung upwards in the manner used by agamas, as reported by Libby and colleagues<sup>1</sup>. ■

**R. McNeill Alexander** is at the Institute of Integrative and Comparative Biology, University of Leeds, Leeds LS6 4BU, UK. e-mail: r.m.alexander@leeds.ac.uk

1. Libby, T. *et al. Nature* **481**, 181–184 (2012).
2. Jusufi, A., Goldman, D. I., Revzen, S. & Full, R. J. *Proc. Natl Acad. Sci. USA* **105**, 4215–4219 (2008).
3. Alexander, R. M. *Zool. J. Linn. Soc.* **83**, 1–25 (1985).
4. Hutchinson, J. R. & Garcia, M. *Nature* **415**, 1018–1021 (2002).
5. Maxwell, W. D. & Ostrom, J. H. *J. Vert. Paleontol.* **15**, 707–712 (1995).
6. Roach, B. T. & Brinkman, D. L. *Bull. Peabody Mus. Nat. Hist.* **48**, 103–138 (2007).
7. Manning, P. L., Payne, D., Pennicott, J., Barrett, P. M. & Ennos, R. A. *Biol. Lett.* **2**, 110–112 (2006).

## ASTROPHYSICS

# Progenitors of type Ia supernovae

**A study of the remains of a type Ia supernova whose light swept past Earth about 400 years ago finds no sign of a companion star. The result indicates that the supernova's progenitor was a pair of white dwarfs. SEE LETTER P164**

PILAR RUIZ-LAPUENTE

Type Ia supernovae are not just another class of star explosion. They have a pivotal role in cosmology. Measurements of their brightness as a function of their distance from Earth have provided evidence<sup>1,2</sup> that the Universe is expanding at an accelerating rate. However, from the very beginning of the study of these objects, one major worry has been that we do not know exactly what their progenitors are. On page 164 of this issue, Schaefer and Pagnotta<sup>3</sup> describe an analysis that provides insight into the progenitor of a type Ia supernova.

Type Ia supernovae are thought to originate from a white dwarf and a companion star in relatively close proximity to one another. According to this hypothesis, the white dwarf — a dense remnant star, composed of carbon and oxygen, that marks the final evolutionary stage of the vast majority of stars — accretes matter from its companion until it reaches a limit known as the Chandrasekhar mass (about 1.4 times the mass of the Sun). At this point, explosive thermonuclear reactions take place at its centre and the resulting flames propagate all the way to the star's surface, completely disrupting the star and ejecting its material at high speeds.

But the nature of the white dwarf's companion star is unknown. It could be anything: a main-sequence star, which is powered by the fusion of hydrogen into helium; a star in a more advanced evolutionary stage than the main-sequence phase, such as a subgiant, a red giant or a supergiant; or another white dwarf. In the case of a white-dwarf companion, the

two-star system, which is technically known as a double-degenerate progenitor, is destroyed in the runaway accretion process that precedes the explosion. In all other cases, known as single-degenerate progenitors, the companion should survive the explosion. This distinction has led astronomers to search for surviving

companion stars at the sites where type Ia supernovae have occurred.

In their study, Schaefer and Pagnotta set out to look for a companion star to the supernova remnant SNR 0509–67.5 (Fig. 1) in the Large Magellanic Cloud, a satellite galaxy of the Milky Way. SNR 0509–67.5 is the aftermath of a type Ia supernova whose light swept past Earth about 400 years ago. To search for the companion, the authors analysed archive images of the supernova remnant taken with the Hubble Space Telescope. On the basis of their image analysis, they discard the possibility of a companion star with a luminosity greater than 3% of that of the Sun. This means that stars ranging from supergiants (which are at least 8,000 times more luminous than the Sun) and red-giant stars (about 100 or more times the Sun's luminosity) down to main-sequence stars of the cool type K (with luminosities roughly 10% of that of the Sun) can all



**Figure 1 | Supernova remnant SNR 0509–67.5.** Schaefer and Pagnotta's analysis<sup>3</sup> of SNR 0509–67.5 indicates that the progenitor of this system was a pair of white dwarfs. The remnant, which consists of a rapidly expanding bubble of hot gas, is seen here in an image that combines visible-light observations from the Hubble Space Telescope (pink and surrounding star field) with X-ray data from the Chandra X-ray Observatory (blue and green). The bubble is about 7 parsecs (23 light years) across.

NASA, ESA, CXO, HUBBLE HERITAGE TEAM (STSCI/AURA) & J. HUGHES (RUTGERS UNIV.)

for jumping. Some fossil evidence has been interpreted<sup>5</sup> as suggesting that *Deinonychus*, hunting in packs, may have preyed on dinosaurs much larger than themselves. Although this suggestion has been challenged<sup>6</sup>, it has been widely assumed that *Deinonychus* leapt onto the backs and flanks of their victims, using enormous claws to get a firm grip<sup>7</sup>. Similarly, lions and other big cats use their sharp claws to grip the hide of their prey, while using their teeth to attack the vulnerable structures of the throat.

There are several drawings on the Internet showing *Deinonychus* in mid-air, jumping onto large prey. Some of the drawings show the animal jumping improbably high, but it is pleasing to see that several of them show the tail swung upwards in the manner used by agamas, as reported by Libby and colleagues<sup>1</sup>. ■

**R. McNeill Alexander** is at the Institute of Integrative and Comparative Biology, University of Leeds, Leeds LS6 4BU, UK. e-mail: r.m.alexander@leeds.ac.uk

1. Libby, T. *et al. Nature* **481**, 181–184 (2012).
2. Jusufi, A., Goldman, D. I., Revzen, S. & Full, R. J. *Proc. Natl Acad. Sci. USA* **105**, 4215–4219 (2008).
3. Alexander, R. M. *Zool. J. Linn. Soc.* **83**, 1–25 (1985).
4. Hutchinson, J. R. & Garcia, M. *Nature* **415**, 1018–1021 (2002).
5. Maxwell, W. D. & Ostrom, J. H. *J. Vert. Paleontol.* **15**, 707–712 (1995).
6. Roach, B. T. & Brinkman, D. L. *Bull. Peabody Mus. Nat. Hist.* **48**, 103–138 (2007).
7. Manning, P. L., Payne, D., Pennicott, J., Barrett, P. M. & Ennos, R. A. *Biol. Lett.* **2**, 110–112 (2006).

## ASTROPHYSICS

# Progenitors of type Ia supernovae

**A study of the remains of a type Ia supernova whose light swept past Earth about 400 years ago finds no sign of a companion star. The result indicates that the supernova's progenitor was a pair of white dwarfs. SEE LETTER P164**

PILAR RUIZ-LAPUENTE

Type Ia supernovae are not just another class of star explosion. They have a pivotal role in cosmology. Measurements of their brightness as a function of their distance from Earth have provided evidence<sup>1,2</sup> that the Universe is expanding at an accelerating rate. However, from the very beginning of the study of these objects, one major worry has been that we do not know exactly what their progenitors are. On page 164 of this issue, Schaefer and Pagnotta<sup>3</sup> describe an analysis that provides insight into the progenitor of a type Ia supernova.

Type Ia supernovae are thought to originate from a white dwarf and a companion star in relatively close proximity to one another. According to this hypothesis, the white dwarf — a dense remnant star, composed of carbon and oxygen, that marks the final evolutionary stage of the vast majority of stars — accretes matter from its companion until it reaches a limit known as the Chandrasekhar mass (about 1.4 times the mass of the Sun). At this point, explosive thermonuclear reactions take place at its centre and the resulting flames propagate all the way to the star's surface, completely disrupting the star and ejecting its material at high speeds.

But the nature of the white dwarf's companion star is unknown. It could be anything: a main-sequence star, which is powered by the fusion of hydrogen into helium; a star in a more advanced evolutionary stage than the main-sequence phase, such as a subgiant, a red giant or a supergiant; or another white dwarf. In the case of a white-dwarf companion, the

two-star system, which is technically known as a double-degenerate progenitor, is destroyed in the runaway accretion process that precedes the explosion. In all other cases, known as single-degenerate progenitors, the companion should survive the explosion. This distinction has led astronomers to search for surviving

companion stars at the sites where type Ia supernovae have occurred.

In their study, Schaefer and Pagnotta set out to look for a companion star to the supernova remnant SNR 0509–67.5 (Fig. 1) in the Large Magellanic Cloud, a satellite galaxy of the Milky Way. SNR 0509–67.5 is the aftermath of a type Ia supernova whose light swept past Earth about 400 years ago. To search for the companion, the authors analysed archive images of the supernova remnant taken with the Hubble Space Telescope. On the basis of their image analysis, they discard the possibility of a companion star with a luminosity greater than 3% of that of the Sun. This means that stars ranging from supergiants (which are at least 8,000 times more luminous than the Sun) and red-giant stars (about 100 or more times the Sun's luminosity) down to main-sequence stars of the cool type K (with luminosities roughly 10% of that of the Sun) can all



**Figure 1 | Supernova remnant SNR 0509–67.5.** Schaefer and Pagnotta's analysis<sup>3</sup> of SNR 0509–67.5 indicates that the progenitor of this system was a pair of white dwarfs. The remnant, which consists of a rapidly expanding bubble of hot gas, is seen here in an image that combines visible-light observations from the Hubble Space Telescope (pink and surrounding star field) with X-ray data from the Chandra X-ray Observatory (blue and green). The bubble is about 7 parsecs (23 light years) across.

NASA, ESA, CXO, HUBBLE HERITAGE TEAM (STSC/AURA) & J. HUGHES (RUTGERS UNIV.)



be excluded as possible companions.

Stars that are less luminous than main-sequence K-type stars are not massive enough to feed a white dwarf until it reaches the Chandrasekhar mass, so they, too, are not plausible candidates. What's more, because the impact of the supernova ejecta would not make a putative companion less luminous than it was before the explosion, a companion more luminous than a type-K star, if it existed, should have been seen in the images. Because no companion has been detected by their search, Schaefer and Pagnotta conclude that the progenitor of the system that left behind SNR 0509–67.5 was a pair of white dwarfs that merged and exploded as a supernova. This conclusion seems sound.

As a follow-up to the present study, the authors have examined other type Ia supernova remnants in the Large Magellanic Cloud (personal communication). They can exclude, as progenitors for the supernovae that produced these remnants, systems involving companion stars that are at an evolutionary stage beyond the main-sequence phase. An investigation<sup>4</sup> of the remnant of type Ia supernova SN 1572, which was first observed by Tycho Brahe in 1572, ruled out a red-giant companion. It also ruled out the very luminous objects that are predicted by hydrodynamic simulations<sup>5</sup> of the impact of the supernova ejecta on a companion star, and it pointed to a subgiant star as the companion. A later study<sup>6</sup> confirmed that identification, although the issue is still debated<sup>7</sup>.

On the basis of comparisons between hydrodynamic simulations<sup>8</sup> and supernova data, red giants (and supergiants) are unlikely candidates for the companion stars of type Ia supernovae. The impact of the supernova ejecta on a red-giant companion — which could form a system (called symbiotic) in which the white dwarf accretes mass from the stellar wind of its companion, a recurrent nova (a repeatedly bursting star) or some other kind of system with the white dwarf — would produce a bump in the ultraviolet–optical light emission of the supernova at its very early stages. But, so far, this bump has never been seen in any type Ia supernova. Failure to detect this signature would suffice to rule out red-giant companions. However, in a number of type Ia supernovae, such as supernova SN 2006X (ref. 9), the detection of narrow spectral features, associated with sodium moving away from the supernova site at about only 50 kilometres per second, indicates that recurrent novae could be progenitors of at least some type Ia supernovae. This slow-moving sodium would probably come from matter ejected from the system before the white-dwarf explosion. But it could also come from other sources.

A recent theoretical study<sup>10</sup> has shown that the double-degenerate route should produce subluminescent type Ia supernovae, which are

dimmer than their typical counterparts. And the single-degenerate path has been successful<sup>11</sup> in explaining observations of standard type Ia supernovae. All in all, it seems that neither the single-degenerate nor the double-degenerate hypothesis for type Ia supernovae can currently be rejected. What seems clear from Schaefer and Pagnotta's results<sup>3</sup> is that the double-degenerate progenitor path does work in some cases — for SNR 0509–67.5 at least. ■

**Pilar Ruiz-Lapuente** is in the Department of Astronomy and the Institut de Ciències del Cosmos (IEEC–UB), University of Barcelona, Barcelona 08028, Spain.  
e-mail: pilar@am.ub.es

#### ANGELMAN SYNDROME

## Drugs to awaken a paternal gene

**Mutations in the maternal copy of the *UBE3A* gene cause a neurodevelopmental disorder known as Angelman syndrome. Drugs that activate the normally silenced paternal copy of this gene may be of therapeutic value. [SEE LETTER P.185](#)**

ARTHUR L. BEAUDET

Angelman syndrome is characterized by intellectual disability, epilepsy, impaired coordination and a characteristic joyful demeanour. Most commonly, it is caused by a deletion of five to six megabases of DNA from chromosome 15, although 'loss-of-function' mutations, or other abnormalities, in the maternal copy of the *UBE3A* gene also result in Angelman syndrome. In all cases, the outcome is very low expression levels of the enzyme *UBE3A* in neurons.

*UBE3A* is one of a handful of human genes that are subject to genomic imprinting, whereby either the maternal or the paternal copy of a gene is active, with the other copy remaining silent. In the case of *UBE3A*, only the maternal copy is active in neurons. So a child develops Angelman syndrome if they inherit mutant *UBE3A* from their mother. Indeed, in all cases of the disorder, the paternal copy of *UBE3A* is normal. On page 185 of this issue, Huang *et al.*<sup>1</sup> use drug screening to identify compounds that activate the paternal copy of *UBE3A* in a mouse model of Angelman syndrome\*.

Inherited neurological disabilities in children are notoriously resistant to treatment. For some disorders that are characterized by overt abnormalities in the brain (for example, holoprosencephaly, lissencephaly and agenesis

\*This article and the paper<sup>1</sup> under discussion were published online on 21 December 2011.

1. Perlmuter, S. *et al. Astrophys. J.* **517**, 565–586 (1999).
2. Riess, A. G. *et al. Astron. J.* **116**, 1009–1038 (1998).
3. Schaefer, B. E. & Pagnotta, A. *Nature* **481**, 164–166 (2012).
4. Ruiz-Lapuente, P. *et al. Nature* **431**, 1069–1072 (2004).
5. Marietta, E., Burrows, A. & Fryxell, B. *Astrophys. J. Suppl.* **128**, 615–650 (2000).
6. González Hernández, J. I. *et al. Astrophys. J.* **691**, 1–15 (2009).
7. Kerzendorf, W. E. *et al. Astrophys. J.* **701**, 1665–1672 (2009).
8. Kasen, D. *Astrophys. J.* **708**, 1025–1031 (2010).
9. Patat, F. *et al. Astron. Astrophys.* **530**, A63 (2011).
10. Pakmor, R., Hachinger, S., Röpke, F. K. & Hillebrandt, W. *Astron. Astrophys.* **528**, A117 (2011).
11. Hachisu, I., Kato, M. & Nomoto, K. *Astrophys. J.* **679**, 1390–1404 (2008).

of the corpus callosum), the prospects for major interventions after birth remain gloomy. But there may be more room for optimism in conditions in which the brain architecture and function seem quite normal in early infancy — for example, as in fragile X syndrome, Rett syndrome, Angelman syndrome and Prader–Willi syndrome. In these cases, one could hope that the disorder might be cured by restoring normal gene expression.

Other than gene therapy, or perhaps gene correction or recovery of function of a mutant protein, a potential strategy for treating some disorders might be activating the alternative copy of a mutant gene or a gene related to it. For instance, activating the expression of fetal haemoglobin has been a long-term goal for the treatment of sickle-cell anaemia and  $\beta$ -thalassaemia. For many disorders involving genomic imprinting, activating the silenced copy of the gene on the related chromosome may correct the defects associated with the mutant gene.

Mice are useful models for testing whether postnatal restoration of gene expression can overcome the pathological features of a disease. A mouse model of Rett syndrome has, for instance, been tested<sup>2</sup> in this way, with favourable results. Angelman syndrome seems another viable candidate disorder for such treatment, because the brain anatomy in this condition seems normal at birth, and some electrophysiological abnormalities can be reversed in cultured cells<sup>3</sup>.

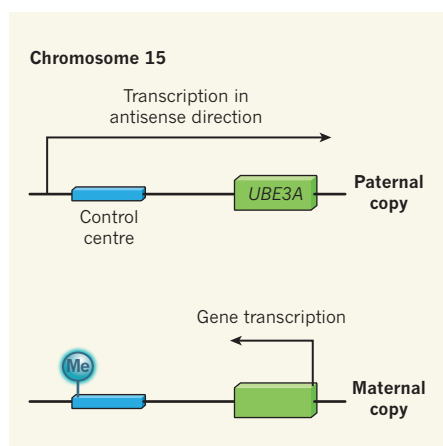


**Figure 1 | Differential regulation of maternal and paternal *UBE3A*.** Of the two copies of the *UBE3A* gene, only the maternal copy is expressed in neurons, with the paternal copy being silenced by genomic imprinting. Specifically, expression of paternal *UBE3A* is inhibited by transcription in the antisense direction of a long sequence that includes not only this gene but also the control centre that regulates its expression. In the equivalent maternal chromosome, the sequence encoding the control centre is methylated (Me) and so is not expressed. This inhibits transcription in the antisense direction and allows expression of *UBE3A*. Huang *et al.*<sup>1</sup> identify drugs that can activate expression of paternal *UBE3A*. Such drugs could be useful for treating Angelman syndrome, a disorder in which maternal *UBE3A* expression is absent or very low.

To search for compounds that could activate the silent paternal copy of *UBE3A*, Huang *et al.*<sup>1</sup> used a mouse model that had an altered copy of *UBE3A*, isolating cortical neurons from the brains of the animals shortly before birth. The mice were engineered so that their neurons expressed a fluorescently tagged version of *UBE3A* in response to drugs that activated the paternal copy of its gene. The screen focused on drugs already approved for human use — so that a future clinical trial might be undertaken more readily — and it identified 16 inhibitors of topoisomerase enzymes that were positive in the assay.

The authors focused on topotecan, the most active of the compounds. When they infused the drug into the lateral-ventricle region of the brains of living mice for two weeks, they found that the paternal copy of *UBE3A* was activated throughout the brain. Remarkably, a brief exposure to the drug also gave persistent *UBE3A* activation in spinal-cord neurons for at least 12 weeks after the termination of treatment.

Silencing of the paternal copy of *UBE3A* is probably mediated by an 'antisense' RNA transcript encompassing *UBE3A* on the paternal chromosome (but transcribed in the opposite direction to the gene sequence). Expression of this transcript is regulated by an imprinting control centre on the maternal chromosome (Fig. 1). The sequence functioning as the control centre, together with its promoter region,

is methylated on the maternal chromosome, suppressing transcription in the antisense direction, which would silence the maternal *UBE3A*. The equivalent control centre on the paternal chromosome is unmethylated, allowing transcription of the antisense sequence and so silencing the paternal *UBE3A*. Huang *et al.* demonstrate that topotecan causes minimal change in methylation of the imprinting control centre on the paternal chromosome, but somehow still reduces expression of the antisense transcript for *UBE3A*, as well as for other paternally expressed genes that are part of the same transcript.

Reduced expression of paternally expressed genes is a potential drawback. If the 5–6-megabase deletion of chromosome 15 is inherited from the father, the child will develop Prader–Willi syndrome, because the deletion includes the genes involved in this disorder. Therefore, treatment with drugs such as topotecan could convert cells that have a molecular status characteristic of Angelman syndrome into cells with a Prader–Willi molecular status. Clearly, it would be preferable to reduce expression of the *UBE3A* antisense transcript while leaving expression of the other paternally expressed genes intact. But it is reasonable to hope that, after treatment with a topoisomerase inhibitor, cells would express a mixture of maternal and paternal transcripts — a situation that might greatly improve the symptoms of Angelman syndrome without causing notable symptoms of Prader–Willi syndrome. Of course, such treatment could also alter the expression of other genes across the genome, with unknown consequences. On all counts, a sequence-specific knock-down of the antisense transcript seems preferable.

An obvious question is how quickly a topoisomerase inhibitor could be prescribed for patients with Angelman syndrome. It is noteworthy that Huang and colleagues did not demonstrate any reversal of the symptoms in their mouse model, and so this is the next step before proceeding further in this direction.

Other issues concern risk–benefit assessments and regulatory processes. In the United States, topotecan has been injected into the cerebrospinal fluid of adults with neoplastic meningitis<sup>4</sup>. So at least in that country, a physician could theoretically inject topotecan into the cerebrospinal fluid of a patient with Angelman syndrome as a compassionate, off-label use of the drug. However, this seems quite risky in the absence of additional safety and dosage information in children. Presumably, the youngest infants would benefit most from the treatment, because normal brain development could then start as early as possible rather than being delayed by some years.

Systematic trials would require a regulatory process for investigating new drugs, and that would take at least a few months. Because the symptoms of Angelman syndrome are quite severe, and as there are no effective treatments



## 50 Years Ago

On December 19 Lord Mills announced in the House of Lords that the Government, after considering the question of decimal coinage ... thought real advantage would follow from adopting a decimal currency. In view of the widespread use of accounting and other monetary machinery, the transitional cost would be substantial, but could be limited by choice of the size of the new units and careful timing of the change-over.

From *Nature* 13 January 1962

## 100 Years Ago

Mr. E. C. Snow, in his paper entitled "The Intensity of Natural Selection in Man" ... has set himself to answer the following question: Has heavy infantile mortality any selective value or tendency to eliminate the more sickly and to spare the hardier children? Of the data available for the investigation of this problem, the most satisfactory are derived from the annual volumes of Prussian statistics ... Thirty rural districts in Prussia were taken, and all the children in them born in the year 1881 were considered. It was ascertained for each district how many of these children died in the first two years of life and how many in the next eight ... If the infantile mortality tends to weed out the weaker children, then in those districts in which the mortality among the children born in 1881 was highest in the years 1881 and 1882 it should tend to be lowest in the years 1883–90, since stronger children less likely to succumb to the ailments of childhood would have survived their first two years ... We are of the opinion that, on the whole, the author is justified in saying: "Natural selection in the form of a selective death-rate is strongly operative in man in the earlier years of life."

From *Nature* 11 January 1912



for the disorder, the risk–benefit ratio may be viewed as quite favourable for giving topotecan to patients on an experimental basis. The infrastructure for a clinical trial is already in place, because clinical trials (albeit unsuccessful ones) using other drugs for treating Angelman syndrome have already been conducted<sup>5</sup>. Moreover, it is feasible to diagnose almost all cases of Angelman syndrome at birth or even *in utero*<sup>6</sup>, so all that is needed is development of

a successful treatment. If topoisomerase inhibitors can indeed reverse disabilities associated with Angelman syndrome, Huang and co-workers' data<sup>1</sup> may lead to clinical trials before too long. ■

**Arthur L. Beaudet** is in the Department of Molecular and Human Genetics, Baylor College of Medicine, Houston, Texas 77030, USA.  
e-mail: [abeaudet@bcm.edu](mailto:abeaudet@bcm.edu)

1. Huang, H.-S. *et al.* *Nature* **481**, 185–189 (2012).
2. Guy, J., Gan, J., Selfridge, J., Cobb, S. & Bird, A. *Science* **315**, 1143–1147 (2007).
3. Weeber, E. J. *et al.* *J. Neurosci.* **23**, 2634–2644 (2003).
4. Gammon, D. C. *et al.* *Am. J. Health-Syst. Pharm.* **63**, 2083–2086 (2006).
5. Bird, L. M. *et al.* *Am. J. Med. Genet. A* **155**, 2956–2963 (2011).
6. Williams, C. A., Driscoll, D. J. & Dagli, A. I. *Genet. Med.* **12**, 385–395 (2010).

## APPLIED PHYSICS

# Nanowire electronics comes of age

**Three-dimensional nanowire-like electronic devices are gaining ground over conventional planar technology. They may be the means to improve the performance of the electronic circuitry of the future.**

TOMÁS PALACIOS

For many years, semiconductor nanowires have offered the prospect of enabling the next generation of electronic devices. But despite this promise, and some exciting preliminary developments<sup>1,2</sup>, nanowire electronics has been hampered by technological limitations. It is extremely challenging to develop a nanowire-based fabrication technology for transistors — the building blocks of electronics — that is compatible with the requirements of future microprocessors. Writing in *Applied Physics Letters*, Dhara and co-workers<sup>3</sup> describe a simple technique that may change the way nanowire-based transistors are made.

Transistors are electric switches. In field-effect transistors, which are ubiquitous in modern electronic circuitry, the flow of current between two metal electrodes (source and drain) is controlled by a voltage applied to a third electrode called the gate. The current typically flows through a two-dimensional planar region called the channel. However, the performance of the device could be greatly improved by the use of a three-dimensional nanowire-based channel, in which the gate electrode is wrapped around the channel.

To make their nanowire wrap-gate transistors, Dhara *et al.*<sup>3</sup> first sandwiched a layer of indium arsenide nanowires between two layers

of a polymer film that changes its structure when exposed to an electron beam. Next, the authors selectively removed some of the polymer film by exposing it to the electron beam of a lithography system. This procedure made the nanowires — which are horizontal and constitute the transistors' channels — free-standing and ready for subsequent fabrication

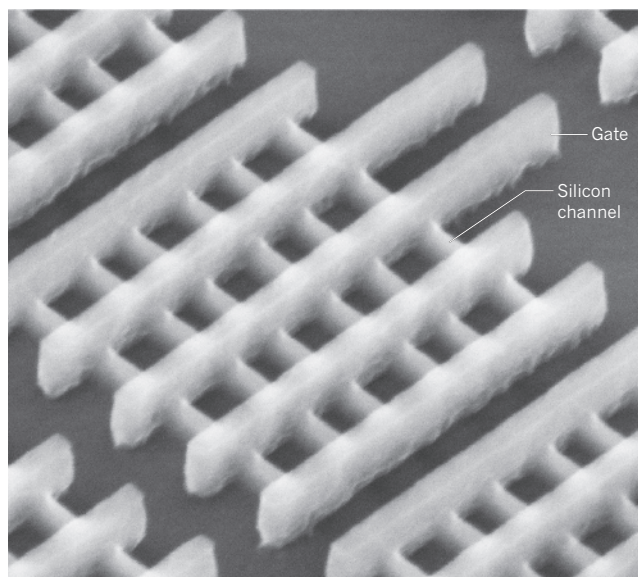


**Figure 1 | Tri-gate transistors.** This scanning electron micrograph shows an intermediate step in the fabrication of Intel's high-performance 22-nm transistors, each of which is made of multiple parallel, nanowire-like silicon channels, or fins. The electrical conductivity of the channels is controlled by a voltage applied to 22-nm-long gate electrodes, which are oriented perpendicularly to the channels. In this technology, only three sides (top, left and right) of the channels are in contact with the gate electrodes. For further improvements in performance, a technology such as the one developed by Dhara *et al.*<sup>3</sup>, which consists of gate electrodes that wrap around the entire channel, is necessary.

of the drain and source electrodes as well as the wrap-gate.

The transistor fabrication technology developed by Dhara and colleagues is much simpler than that traditionally pursued for wrap-gate nanowire transistors, which typically involves several lithography steps as well as chemical-etching procedures. In addition, with the authors' technology, the devices have a tenfold larger electron mobility than that previously reported<sup>4</sup> for horizontal wrap-gate nanowire devices.

In spite of the beautiful simplicity of Dhara and co-workers' technique, their work does not solve the second challenge for nanowire electronics, which is how to integrate the billions of closely packed nanowire devices that will potentially be needed in future microprocessors. But the past year has witnessed several breakthroughs that overcome this problem. In combination with the authors' technology<sup>3</sup>, these advances may take nanowire research in fresh directions and bring nanowire devices closer to the market.

One way to integrate billions of nanowire transistors on the same chip is to relax the nanowire's geometry: instead of free-standing nanowires, one side of the nanowire can be made to touch the surface of an underlying substrate. Last year, Intel announced<sup>5</sup> that its future microprocessors will incorporate transistors in which nanowire-like channels have three sides in contact with 22-nanometre-long gate electrodes, to improve the control of the transistors' current over that of two-dimensional planar devices. These tri-gate devices (Fig. 1) are effectively rectangular nanowires that have one side attached to the substrate. Although their geometry is slightly different from that of prototypical, free-standing nanowire devices, their operating principle is similar. This innovative geometry allows such nanowire-like devices to be made with a technology that is compatible with that used in the microelectronics industry.

INTEL

The good news for nanowire-based devices does not stop with tri-gate transistors and Dhara and colleagues' nanowire fabrication technology. The successful integration of transistors based on indium arsenide nanowires — or, more precisely, nanoribbons — on silicon substrates has recently been demonstrated<sup>6</sup>. Nanoribbon structures a few hundreds of nanometres wide have been patterned, and then etched, on an 18-nm-thick layer of indium arsenide semiconductor. Thanks to these structures' outstanding mechanical properties, they were successfully transferred to a silicon wafer, in which transistors with excellent electrical performance were made. This nanoribbon technology allows transistors made from III–V semiconductors, such as indium arsenide, and transistors made from silicon to be integrated on the same chip. Such an advance may help push the performance of electronic systems to higher levels than those achieved using only silicon.

In addition to these improvements, nanowire and nanoribbon structures have been used to enhance the electronic transport properties of semiconductors<sup>7,8</sup>. For example, use of gallium nitride nanoribbons attached to a substrate increases the charge density in the transistors' channels by more than 50% compared with planar devices of the same total channel width, increasing the device's current and improving the overall performance<sup>7</sup>.

Silicon–germanium nanowires have also allowed the manufacture<sup>8</sup> of transistors with improved performance. The use of a thin germanium layer to wrap the silicon channel in these devices introduces tensile stress into the channel, increasing hole mobility by 40% (where a hole is a charge carrier produced by the absence of an electron). Both gallium nitride- and silicon–germanium-nanostructured transistors, which integrate thousands of parallel nanoribbons or nanowires on the same device, will soon be used in digital as well as analog circuits to improve wireless communications, low-power electronics and high-performance computing.

In summary, nanowire devices are quickly finding their way into high-performance electronics and commercial products. The current trend of nanowire electronics is based on novel fabrication technologies and three-dimensional nanowire or nanoribbon structures in which only three sides of the structure are exposed, with the bottom one being closely coupled to the substrate. These devices will this year be used in microprocessors and memory devices<sup>5</sup>, and should soon improve the performance of mobile phones, radars and other wireless systems. Further improvements will come from technologies such as Dhara and colleagues' technique<sup>3</sup>, which enable truly free-standing devices to be made. Electronics is no longer planar. Three-dimensional nanowire structures are here to stay. ■

**Tomás Palacios** is at the Massachusetts Institute of Technology, Cambridge, Massachusetts 02139, USA.  
e-mail: [tpalacios@mit.edu](mailto:tpalacios@mit.edu)

1. Li, Y., Qian, F., Xiang, J. & Lieber, C. M. *Mater. Today* **9**, 18–27 (2006).
2. Hashemi, P., Teherani, J. T. & Hoyt, J. L. *Proc. IEEE Int. Electron Device Meet.*, San Francisco (IEEE, 2010).

3. Dhara, S. *et al. Appl. Phys. Lett.* **99**, 173101 (2011).
4. Storm, K. *et al. Nano Lett.* **11**, 1127 (2011).
5. Kuhn, K. J. *Proc. Int. Symp. VLSI Technology, Systems Applications* (IEEE, 2011).
6. Ko, H. *et al. Nature* **468**, 286–289 (2010).
7. Aize, M. & Palacios, T. *Appl. Phys. Lett.* **98**, 042103 (2011).
8. Hashemi, P. *et al. Appl. Phys. Lett.* **96**, 063109 (2010).

## EARTH SCIENCE

# Limits of the power law

**Multi-scale modelling of the deformation of magnesium oxide reveals the need for a re-examination of the way in which laboratory data are used to estimate the strength of Earth's lower mantle. [SEE LETTER P.177](#)**

ANDREW M. WALKER

For billions of years, convective currents in Earth's solid mantle have cooled and stirred our planet's deep interior and caused tectonic plates to drift centimetres each year. This process is slow, powerful and, given the presumed physical properties of mantle rocks, inevitable<sup>1</sup>. A fundamental controlling factor in mantle convection is how quickly mantle minerals deform. This parameter is expressed as the relationship between the rate of change of strain of the mantle and the stress imposed on it. Despite progress towards laboratory measurement of this relationship under the conditions of temperature (1,800–4,300 kelvin) and pressure (20–130 gigapascals) found in the lower mantle (660–2,900 kilometres beneath Earth's surface), experiments that reach the low strain rate expected in Earth's mantle have not been possible. The use of experimental data for studies of mantle convection thus requires extrapolation.

On page 177 of this issue, Cordier *et al.*<sup>2</sup> test the reliability of this approach by building a multi-scale model of deformation that works at both the low strain rate found in the mantle and the much higher rate used in experiments. The results suggest that the usual power-law extrapolation is not reliable over the wide range of strain rates that must be considered, potentially changing our view of the way in which the deep mantle deforms.

By focusing on magnesium oxide, with its high melting point and simple rock-salt structure, Cordier and colleagues were able to examine deformation processes in one of the best studied and most clearly understood of all mantle minerals. In magnesium oxide, deformation should be accommodated by the movement of dislocations — imperfections in the crystal structure that allow changes in shape to occur in a similar manner to the way that the smooth surface between playing cards permits

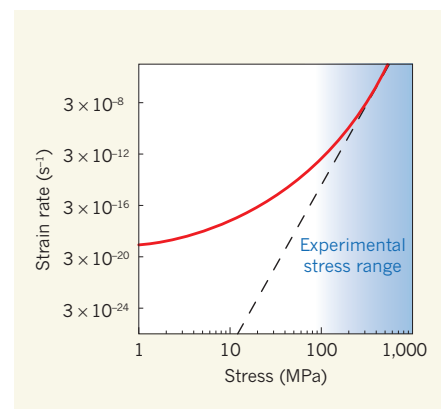


**Figure 1 | Multi-scale model of the deformation of magnesium oxide.** The graph shows the relationship between the stress and strain rate in magnesium oxide that is predicted using Cordier and colleagues' multi-scale model<sup>2</sup> (red line) at a pressure of 60 GPa, a temperature of 1,500 K and a dislocation density of  $10^8 \text{ m}^{-2}$ . The usual power law (dashed line) fits the model adequately over the range of experimentally accessible strain rates. But it deviates significantly from the model and overpredicts the strength of magnesium oxide when extrapolated to the low strain rates expected to exist in Earth's lower mantle. Both axes are logarithmic. (Modified from ref. 2.)

a deck to be easily sheared. By modelling the details of this process at several length scales, the authors created an impressive predictive model of deformation based only on atomic-scale calculations of the interactions between electrons in a faulted crystal<sup>3</sup>.

Cordier *et al.* then used these atomic-scale calculations to parameterize a larger-scale, semi-continuum model of an isolated, straight dislocation, based on a simple description conceived<sup>4</sup> in 1940 and more recently updated<sup>5</sup> to handle potentially complex dislocation structures. Results from this parameterization in turn informed a model of the motion of a single dislocation that is permitted to curve



The good news for nanowire-based devices does not stop with tri-gate transistors and Dhara and colleagues' nanowire fabrication technology. The successful integration of transistors based on indium arsenide nanowires — or, more precisely, nanoribbons — on silicon substrates has recently been demonstrated<sup>6</sup>. Nanoribbon structures a few hundreds of nanometres wide have been patterned, and then etched, on an 18-nm-thick layer of indium arsenide semiconductor. Thanks to these structures' outstanding mechanical properties, they were successfully transferred to a silicon wafer, in which transistors with excellent electrical performance were made. This nanoribbon technology allows transistors made from III–V semiconductors, such as indium arsenide, and transistors made from silicon to be integrated on the same chip. Such an advance may help push the performance of electronic systems to higher levels than those achieved using only silicon.

In addition to these improvements, nanowire and nanoribbon structures have been used to enhance the electronic transport properties of semiconductors<sup>7,8</sup>. For example, use of gallium nitride nanoribbons attached to a substrate increases the charge density in the transistors' channels by more than 50% compared with planar devices of the same total channel width, increasing the device's current and improving the overall performance<sup>7</sup>.

Silicon–germanium nanowires have also allowed the manufacture<sup>8</sup> of transistors with improved performance. The use of a thin germanium layer to wrap the silicon channel in these devices introduces tensile stress into the channel, increasing hole mobility by 40% (where a hole is a charge carrier produced by the absence of an electron). Both gallium nitride- and silicon–germanium-nanostructured transistors, which integrate thousands of parallel nanoribbons or nanowires on the same device, will soon be used in digital as well as analog circuits to improve wireless communications, low-power electronics and high-performance computing.

In summary, nanowire devices are quickly finding their way into high-performance electronics and commercial products. The current trend of nanowire electronics is based on novel fabrication technologies and three-dimensional nanowire or nanoribbon structures in which only three sides of the structure are exposed, with the bottom one being closely coupled to the substrate. These devices will this year be used in microprocessors and memory devices<sup>5</sup>, and should soon improve the performance of mobile phones, radars and other wireless systems. Further improvements will come from technologies such as Dhara and colleagues' technique<sup>3</sup>, which enable truly free-standing devices to be made. Electronics is no longer planar. Three-dimensional nanowire structures are here to stay. ■

**Tomás Palacios** is at the Massachusetts Institute of Technology, Cambridge, Massachusetts 02139, USA.  
e-mail: [tpalacios@mit.edu](mailto:tpalacios@mit.edu)

1. Li, Y., Qian, F., Xiang, J. & Lieber, C. M. *Mater. Today* **9**, 18–27 (2006).
2. Hashemi, P., Teherani, J. T. & Hoyt, J. L. *Proc. IEEE Int. Electron Device Meet.*, San Francisco (IEEE, 2010).

3. Dhara, S. *et al. Appl. Phys. Lett.* **99**, 173101 (2011).
4. Storm, K. *et al. Nano Lett.* **11**, 1127 (2011).
5. Kuhn, K. J. *Proc. Int. Symp. VLSI Technology, Systems Applications* (IEEE, 2011).
6. Ko, H. *et al. Nature* **468**, 286–289 (2010).
7. Aize, M. & Palacios, T. *Appl. Phys. Lett.* **98**, 042103 (2011).
8. Hashemi, P. *et al. Appl. Phys. Lett.* **96**, 063109 (2010).

## EARTH SCIENCE

# Limits of the power law

**Multi-scale modelling of the deformation of magnesium oxide reveals the need for a re-examination of the way in which laboratory data are used to estimate the strength of Earth's lower mantle. [SEE LETTER P.177](#)**

ANDREW M. WALKER

For billions of years, convective currents in Earth's solid mantle have cooled and stirred our planet's deep interior and caused tectonic plates to drift centimetres each year. This process is slow, powerful and, given the presumed physical properties of mantle rocks, inevitable<sup>1</sup>. A fundamental controlling factor in mantle convection is how quickly mantle minerals deform. This parameter is expressed as the relationship between the rate of change of strain of the mantle and the stress imposed on it. Despite progress towards laboratory measurement of this relationship under the conditions of temperature (1,800–4,300 kelvin) and pressure (20–130 gigapascals) found in the lower mantle (660–2,900 kilometres beneath Earth's surface), experiments that reach the low strain rate expected in Earth's mantle have not been possible. The use of experimental data for studies of mantle convection thus requires extrapolation.

On page 177 of this issue, Cordier *et al.*<sup>2</sup> test the reliability of this approach by building a multi-scale model of deformation that works at both the low strain rate found in the mantle and the much higher rate used in experiments. The results suggest that the usual power-law extrapolation is not reliable over the wide range of strain rates that must be considered, potentially changing our view of the way in which the deep mantle deforms.

By focusing on magnesium oxide, with its high melting point and simple rock-salt structure, Cordier and colleagues were able to examine deformation processes in one of the best studied and most clearly understood of all mantle minerals. In magnesium oxide, deformation should be accommodated by the movement of dislocations — imperfections in the crystal structure that allow changes in shape to occur in a similar manner to the way that the smooth surface between playing cards permits

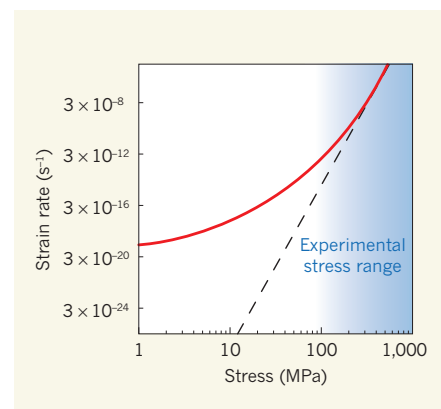


**Figure 1 | Multi-scale model of the deformation of magnesium oxide.** The graph shows the relationship between the stress and strain rate in magnesium oxide that is predicted using Cordier and colleagues' multi-scale model<sup>2</sup> (red line) at a pressure of 60 GPa, a temperature of 1,500 K and a dislocation density of  $10^8 \text{ m}^{-2}$ . The usual power law (dashed line) fits the model adequately over the range of experimentally accessible strain rates. But it deviates significantly from the model and overpredicts the strength of magnesium oxide when extrapolated to the low strain rates expected to exist in Earth's lower mantle. Both axes are logarithmic. (Modified from ref. 2.)

a deck to be easily sheared. By modelling the details of this process at several length scales, the authors created an impressive predictive model of deformation based only on atomic-scale calculations of the interactions between electrons in a faulted crystal<sup>3</sup>.

Cordier *et al.* then used these atomic-scale calculations to parameterize a larger-scale, semi-continuum model of an isolated, straight dislocation, based on a simple description conceived<sup>4</sup> in 1940 and more recently updated<sup>5</sup> to handle potentially complex dislocation structures. Results from this parameterization in turn informed a model of the motion of a single dislocation that is permitted to curve

under the action of an applied stress and that includes the effect of temperature. Finally, the largest length scale involved modelling the elastic interactions between a network of dislocations, a process that becomes important at high temperature. The overall approach thus avoids the use of experimental data and seeks to predict the relationship between stress and strain rate for a single crystal of magnesium oxide at high temperature and pressure without assuming a particular functional form for that relationship.

Because experiments are time limited, accessible measurable strain rates are typically around  $10^{-6}$  per second (where a sample doubles in length in about two weeks). This is much higher than the maximum strain rate expected in the mantle (perhaps  $10^{-12}$  s $^{-1}$ ; at this rate, a sample would take more than 30,000 years to double in length). The usual approach for dealing with such low strain rates is to extrapolate experimental data using a power law — a straight line on a plot of the logarithm of stress against the logarithm of the strain rate. This is assumed to be valid over many orders of magnitude. Cordier and colleagues' multi-scale model<sup>2</sup> makes no such assumption, but, importantly, it reproduces laboratory data at high strain rate over a wide range of temperatures even though these data are not used in the model.

The authors' model can also be used at the low strain rate found in the mantle, allowing the power-law assumption to be tested. Cordier *et al.* found that results from the model differ greatly from the usual power-law extrapolation of laboratory data. The model predicts that magnesium oxide deforming under lower-mantle conditions is significantly weaker than the power-law extrapolation would suggest (Fig. 1).

The most direct implication of this work is that methods used to extrapolate experimental data need to be re-examined. It might be possible to find a way of using experimental data showing the dependence of strain rate on stress, over a wide range of temperatures, to parameterize a non-power-law description of deformation that is consistent with the weakening at very low strain rates predicted by the multi-scale modelling. It remains to be seen whether experiments performed at high enough strain rates for them to be completed in a realistic time-frame can provide enough information to do this.

Magnesium oxide makes up only about 20% of the lower mantle, which is dominated by silicate minerals. A pivotal question is whether Cordier and colleagues' model will be as successful in describing the deformation of these structurally more complex materials as it is for magnesium oxide. One consideration is that the melting point of the silicate phases is lower than that of magnesium oxide, opening up the possibility

that deformation is controlled by the motion of isolated atoms rather than by the movement of dislocations<sup>6</sup>. Which of these two processes controls deformation is crucially dependent on the size of individual crystal grains in lower-mantle rocks, a key geophysical parameter that has stubbornly resisted elucidation.

A second concern is that an increasing list of materials, including some that share the structure adopted by silicates in the lower mantle, show dislocations that have a complex, non-planar structure not found in magnesium oxide<sup>7</sup>. If such dislocations occur in silicates in the lower mantle, the authors' multi-scale model would need modification to properly capture the deformation process.

We now have the tools needed to simulate, from first-principles calculations, the deformation of minerals in the lower mantle by the two most likely underlying mechanisms — the motion of atoms<sup>6</sup> and of dislocations<sup>2</sup>. With careful handling of the interaction between adjacent crystals, it may at last be feasible to simulate mantle convection with full feedback between geodynamics, deformation and thermodynamics. These more realistic

geodynamical simulations would be expected to exhibit history-dependent deformation and strain weakening. If, for example, regions of strong mantle material surrounded by weak shear zones were to develop, the mantle could resist mixing and allow chemical heterogeneity to be retained over geological time. Such effects complicate our view of mantle convection, but detailed determination of the consequences must await the results of such simulations. ■

**Andrew M. Walker** is at the School of Earth Sciences, University of Bristol, Bristol BS8 1RJ, UK.

e-mail: andrew.walker@bristol.ac.uk

1. Tozer, D. C. *Phil. Trans. R. Soc. Lond. A* **258**, 252–271 (1965).
2. Cordier, P., Amodeo, J. & Carrez, P. *Nature* **481**, 177–180 (2012).
3. Christian, J. W. & Vitek, V. *Rep. Prog. Phys.* **33**, 307–411 (1970).
4. Peierls, R. *Proc. Phys. Soc. Lond.* **52**, 34–37 (1940).
5. Denoual, C. *Phys. Rev. B* **70**, 024106 (2004).
6. Ammann, M. W., Brodholt, J. P., Wookey, J. & Dobson, D. P. *Nature* **465**, 462–465 (2010).
7. Vitek, V. & Paidar, V. in *Dislocations in Solids* Vol. 14 (ed. Hirth, J. P.) 439–514 (Elsevier, 2008).

#### COGNITION

## Your face looks familiar

**Paper wasps of the species *Polistes fuscatus* live in strict hierarchical societies in which the ability to identify superiors and subordinates is crucial. Like humans, these insects have a cognitive tool kit for recognizing familiar faces.**

LARS CHITTKA & ADRIAN DYER

The ability to recognize individuals can convey significant benefits to social animals. In humans, the capacity to recognize different faces is crucial for making individual behaviour predictable for other members of a group — for keeping track of who is aggressive, bold or wise — and so for knowing everyone's place in a family or society. Moreover, there is strong evidence<sup>1,2</sup> that primate brains contain specialized modules for face processing and recognition. Writing in *Science*, Sheehan and Tibbetts<sup>3</sup> present evidence that an insect, the paper wasp *Polistes fuscatus*, not only recognizes the faces of individuals of the same species, but is a veritable expert at face discrimination.

Individual queens of many social insects, including *Polistes metricus* — a species closely related to *P. fuscatus* — found colonies in the spring, a perilous and challenging enterprise for a single insect. By contrast, several *P. fuscatus* queens typically join forces to build, defend and provide for a new nest. This boosts the chances of the project's success, but, for many

of the hopeful foundresses, there is a price to pay: a linear hierarchy is established through a series of one-on-one fights. Consequently, the strongest queen dominates egg-laying, whereas subordinates do more menial tasks. After a duel, individuals recognize their opponents by their distinct facial markings, which helps to avoid the repetition of potentially costly battles.

Sheehan and Tibbetts studied face recognition in *P. fuscatus* and *P. metricus*. They trained the insects to choose one of two arms of a maze, each marked by an image (Fig. 1). If the wasp turned to the 'wrong' image, it experienced an electric shock, whereas choosing the 'correct' arm provided safety. The image pairs consisted of normal wasp faces, manipulated wasp faces, simple geometric patterns or caterpillars — the typical prey of these wasps.

The authors report that the face-learning ability of *P. fuscatus* was greater than that of *P. metricus*. Moreover, *P. fuscatus* wasps learned to recognize wasp faces more quickly and more accurately than they did other image types. Intriguingly, this insect had difficulties recognizing faces that lacked antennae or that



under the action of an applied stress and that includes the effect of temperature. Finally, the largest length scale involved modelling the elastic interactions between a network of dislocations, a process that becomes important at high temperature. The overall approach thus avoids the use of experimental data and seeks to predict the relationship between stress and strain rate for a single crystal of magnesium oxide at high temperature and pressure without assuming a particular functional form for that relationship.

Because experiments are time limited, accessible measurable strain rates are typically around  $10^{-6}$  per second (where a sample doubles in length in about two weeks). This is much higher than the maximum strain rate expected in the mantle (perhaps  $10^{-12}$  s $^{-1}$ ; at this rate, a sample would take more than 30,000 years to double in length). The usual approach for dealing with such low strain rates is to extrapolate experimental data using a power law — a straight line on a plot of the logarithm of stress against the logarithm of the strain rate. This is assumed to be valid over many orders of magnitude. Cordier and colleagues' multi-scale model<sup>2</sup> makes no such assumption, but, importantly, it reproduces laboratory data at high strain rate over a wide range of temperatures even though these data are not used in the model.

The authors' model can also be used at the low strain rate found in the mantle, allowing the power-law assumption to be tested. Cordier *et al.* found that results from the model differ greatly from the usual power-law extrapolation of laboratory data. The model predicts that magnesium oxide deforming under lower-mantle conditions is significantly weaker than the power-law extrapolation would suggest (Fig. 1).

The most direct implication of this work is that methods used to extrapolate experimental data need to be re-examined. It might be possible to find a way of using experimental data showing the dependence of strain rate on stress, over a wide range of temperatures, to parameterize a non-power-law description of deformation that is consistent with the weakening at very low strain rates predicted by the multi-scale modelling. It remains to be seen whether experiments performed at high enough strain rates for them to be completed in a realistic time-frame can provide enough information to do this.

Magnesium oxide makes up only about 20% of the lower mantle, which is dominated by silicate minerals. A pivotal question is whether Cordier and colleagues' model will be as successful in describing the deformation of these structurally more complex materials as it is for magnesium oxide. One consideration is that the melting point of the silicate phases is lower than that of magnesium oxide, opening up the possibility

that deformation is controlled by the motion of isolated atoms rather than by the movement of dislocations<sup>6</sup>. Which of these two processes controls deformation is crucially dependent on the size of individual crystal grains in lower-mantle rocks, a key geophysical parameter that has stubbornly resisted elucidation.

A second concern is that an increasing list of materials, including some that share the structure adopted by silicates in the lower mantle, show dislocations that have a complex, non-planar structure not found in magnesium oxide<sup>7</sup>. If such dislocations occur in silicates in the lower mantle, the authors' multi-scale model would need modification to properly capture the deformation process.

We now have the tools needed to simulate, from first-principles calculations, the deformation of minerals in the lower mantle by the two most likely underlying mechanisms — the motion of atoms<sup>6</sup> and of dislocations<sup>2</sup>. With careful handling of the interaction between adjacent crystals, it may at last be feasible to simulate mantle convection with full feedback between geodynamics, deformation and thermodynamics. These more realistic

geodynamical simulations would be expected to exhibit history-dependent deformation and strain weakening. If, for example, regions of strong mantle material surrounded by weak shear zones were to develop, the mantle could resist mixing and allow chemical heterogeneity to be retained over geological time. Such effects complicate our view of mantle convection, but detailed determination of the consequences must await the results of such simulations. ■

**Andrew M. Walker** is at the School of Earth Sciences, University of Bristol, Bristol BS8 1RJ, UK.

e-mail: andrew.walker@bristol.ac.uk

1. Tozer, D. C. *Phil. Trans. R. Soc. Lond. A* **258**, 252–271 (1965).
2. Cordier, P., Amodeo, J. & Carrez, P. *Nature* **481**, 177–180 (2012).
3. Christian, J. W. & Vitek, V. *Rep. Prog. Phys.* **33**, 307–411 (1970).
4. Peierls, R. *Proc. Phys. Soc. Lond.* **52**, 34–37 (1940).
5. Denoual, C. *Phys. Rev. B* **70**, 024106 (2004).
6. Ammann, M. W., Brodholt, J. P., Wookey, J. & Dobson, D. P. *Nature* **465**, 462–465 (2010).
7. Vitek, V. & Paidar, V. in *Dislocations in Solids* Vol. 14 (ed. Hirth, J. P.) 439–514 (Elsevier, 2008).

#### COGNITION

## Your face looks familiar

**Paper wasps of the species *Polistes fuscatus* live in strict hierarchical societies in which the ability to identify superiors and subordinates is crucial. Like humans, these insects have a cognitive tool kit for recognizing familiar faces.**

LARS CHITTKA & ADRIAN DYER

The ability to recognize individuals can convey significant benefits to social animals. In humans, the capacity to recognize different faces is crucial for making individual behaviour predictable for other members of a group — for keeping track of who is aggressive, bold or wise — and so for knowing everyone's place in a family or society. Moreover, there is strong evidence<sup>1,2</sup> that primate brains contain specialized modules for face processing and recognition. Writing in *Science*, Sheehan and Tibbetts<sup>3</sup> present evidence that an insect, the paper wasp *Polistes fuscatus*, not only recognizes the faces of individuals of the same species, but is a veritable expert at face discrimination.

Individual queens of many social insects, including *Polistes metricus* — a species closely related to *P. fuscatus* — found colonies in the spring, a perilous and challenging enterprise for a single insect. By contrast, several *P. fuscatus* queens typically join forces to build, defend and provide for a new nest. This boosts the chances of the project's success, but, for many

of the hopeful foundresses, there is a price to pay: a linear hierarchy is established through a series of one-on-one fights. Consequently, the strongest queen dominates egg-laying, whereas subordinates do more menial tasks. After a duel, individuals recognize their opponents by their distinct facial markings, which helps to avoid the repetition of potentially costly battles.

Sheehan and Tibbetts studied face recognition in *P. fuscatus* and *P. metricus*. They trained the insects to choose one of two arms of a maze, each marked by an image (Fig. 1). If the wasp turned to the 'wrong' image, it experienced an electric shock, whereas choosing the 'correct' arm provided safety. The image pairs consisted of normal wasp faces, manipulated wasp faces, simple geometric patterns or caterpillars — the typical prey of these wasps.

The authors report that the face-learning ability of *P. fuscatus* was greater than that of *P. metricus*. Moreover, *P. fuscatus* wasps learned to recognize wasp faces more quickly and more accurately than they did other image types. Intriguingly, this insect had difficulties recognizing faces that lacked antennae or that

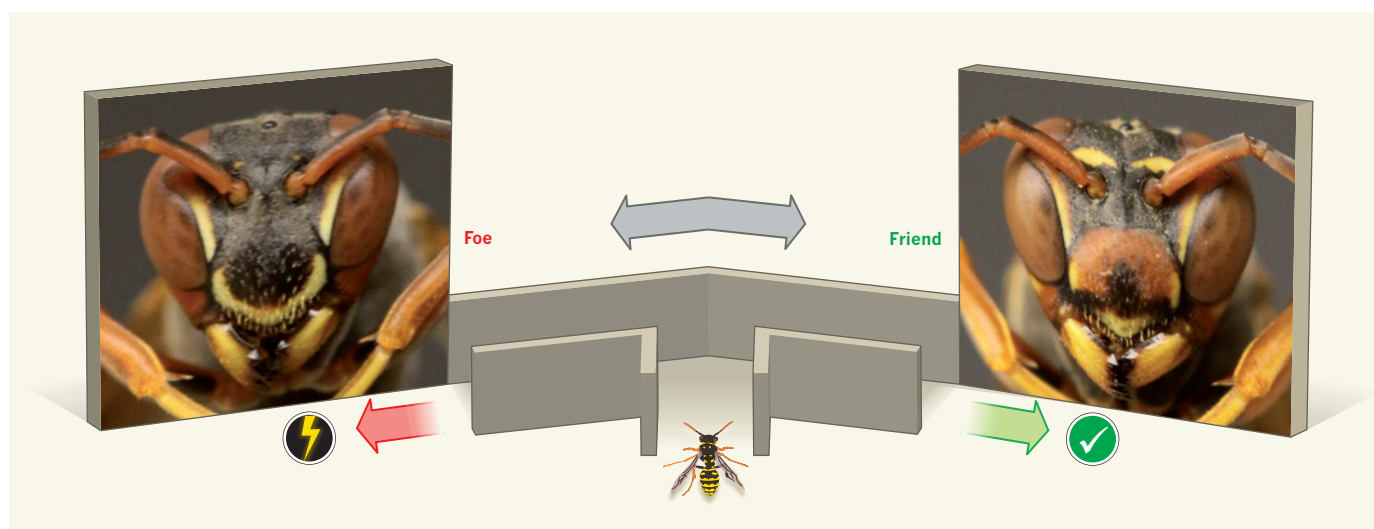


**Figure 1 | Face learning by paper wasps.** Sheehan and Tibbetts<sup>3</sup> tested the learning abilities of two closely related wasp species, *Polistes fuscatus* and *P. metricus*, in a T-shaped maze. When an individual wasp entered the maze, it had two possible routes to take, which were marked by different images. One (Foe) resulted in punishment with an electric shock, whereas the other (Friend) granted entry to a safety zone. The authors found

that *P. fuscatus* is especially skilled at learning to distinguish between correctly configured facial patterns — a unique adaptation to its social environment, in which these wasps use face recognition to establish and enforce dominance hierarchies. In *P. metricus*, individual recognition is not part of social life, and this species failed the face-learning task. (Images, M. J. Sheehan, Univ. Michigan.)

contained scrambled features. This indicates that face learning in *P. fuscatus* is specific to correctly configured faces, and cannot be explained by a general pattern-recognition system.

Because Sheehan and Tibbetts<sup>3</sup> used wasps caught in the wild, it is not clear whether the insects' expertise at face recognition was acquired through evolution, individual experience before capture or an interaction of both. Nonetheless, at the behavioural level, face recognition in *P. fuscatus* shares some features with that in humans. For humans, too, the configuration of facial features is important for reliable recognition<sup>4</sup>. Elemental features such as eyes, nose and mouth are not processed individually but as a whole, and their rearrangement significantly impairs recognition performance.

Several types of processing of facial configurations that have been identified in humans could be explored in wasps. These include detection of a face on the basis of its overall arrangement of features; face processing where certain elemental features are bound together; and sensitivity to second-order relationships, whereby the relative distances between various elemental features enhance recognition<sup>5</sup>.

Neurophysiological investigation of specialized brain areas mediating face processing in humans<sup>1,6</sup> and monkeys<sup>2</sup> confirmed the existence of bespoke neural mechanisms for analysing the arrangement of facial features. Studies in other mammals<sup>7</sup> also indicated that the ability to process configural face information involves specialized neural circuitry and extensive experience. However, work in insects on visual processing of compound patterns (including face images) suggests<sup>8</sup> that species without specialized face-processing abilities

may also be capable of configural processing. In terms of gross neuroanatomy<sup>9</sup>, there are no discernible differences between the visual system of *P. fuscatus* and those of related species that do not use face recognition.

It is therefore likely that neural circuitry similar to that used by insects for prey recognition is co-opted in *P. fuscatus* for face recognition owing to the insect's social lifestyle. This might require only fairly minor adjustments in neural circuitry to embed visual pattern recognition into the appropriate (social) context. Sheehan and Tibbetts's observation<sup>3</sup> that *P. metricus* lacks specialized face recognition lends further support to the view that specialized cognitive capacities can evolve relatively easily in response to pertinent selection pressures.

The finding that a small-brained insect shares the ability to recognize faces with humans and other primates may come as a surprise to adherents of the 'social brain' hypothesis<sup>10</sup> — the idea that group-living and complex social interactions require large brains. However, in asking questions about brain size and cognitive capacity, one must focus on what the computational nature of the task is, and what neural circuitry is actually required to accomplish it. In this view, the specific task that requires a large brain has yet to be discovered.

Analyses of neuronal networks<sup>11</sup> show that reliable face recognition can be achieved with a network of only a few hundred neurons — a circuitry that could be easily accommodated in an insect brain — especially because much of the neural hardware for pattern recognition would also be used for other visual tasks such as recognition of landmarks or prey. Small-brained invertebrates, such as insects, are thus exceptionally useful models for studying how

social and cognitive abilities can be mediated by modest neural circuitry<sup>12</sup>, and of the evolutionary adjustments necessary to generate such abilities. As for bigger brains, many of their advantages might relate to higher memory storage capacity (equivalent to bigger hard drives rather than better processors), more parallel processing, or more precision and detail in sensory information, but not necessarily to more complex cognitive processes<sup>12</sup>. ■

**Lars Chittka** is in the Biological and Experimental Psychology Group, School of Biological and Chemical Sciences, Queen Mary University of London, London E1 4NS, UK. **Adrian Dyer** is in the School of Media and Communication, RMIT University, Melbourne, Victoria 3000, Australia.  
e-mails: l.chittka@qmul.ac.uk; adrian.dyer@rmit.edu.au

1. Kanwisher, N. *Nature Neurosci.* **3**, 759–763 (2000).
2. Tsao, D. Y., Freiwald, W. A., Tootell, R. B. H. & Livingstone, M. S. *Science* **311**, 670–674 (2006).
3. Sheehan, M. J. & Tibbetts, E. A. *Science* **334**, 1272–1275 (2011).
4. Collishaw, S. M. & Hole, G. J. *Perception* **29**, 893–909 (2000).
5. Maurer, D., Le Grand, R. & Mondloch, C. J. *Trends Cogn. Sci.* **6**, 255–260 (2002).
6. Lobmaier, J. S., Klaver, P., Loenneker, T., Martin, E. & Mast, F. W. *NeuroReport* **19**, 287–291 (2008).
7. Peirce, J. W., Leigh, A. E. & Kendrick, K. M. *Neuropsychologia* **38**, 475–483 (2000).
8. Avargués-Weber, A., Portelli, G., Benard, J., Dyer, A. & Giurfa, M. J. *Exp. Biol.* **213**, 593–601 (2010).
9. Gronenberg, W., Ash, L. E. & Tibbetts, E. A. *Brain Behav. Evol.* **71**, 1–14 (2008).
10. Dunbar, R. I. M. *Evol. Anthropol.* **6**, 178–190 (1998).
11. Aitkenhead, M. J. & McDonald, A. J. S. *Eng. Appl. Artif. Intell.* **16**, 167–176 (2003).
12. Chittka, L. & Niven, J. *Curr. Biol.* **19**, R995–R1008 (2009).



# The genetic basis of early T-cell precursor acute lymphoblastic leukaemia

Jinghui Zhang<sup>1\*</sup>, Li Ding<sup>2,3\*</sup>, Linda Holmfeldt<sup>4\*</sup>, Gang Wu<sup>1</sup>, Sue L. Heatley<sup>4†</sup>, Debbie Payne-Turner<sup>4</sup>, John Easton<sup>5</sup>, Xiang Chen<sup>1</sup>, Jianmin Wang<sup>6</sup>, Michael Rusch<sup>1</sup>, Charles Lu<sup>2</sup>, Shann-Ching Chen<sup>4</sup>, Lei Wei<sup>4</sup>, J. Racquel Collins-Underwood<sup>4</sup>, Jing Ma<sup>4</sup>, Kathryn G. Roberts<sup>4</sup>, Stanley B. Pounds<sup>7</sup>, Anatoly Ulyanov<sup>1</sup>, Jared Becksfort<sup>6</sup>, Pankaj Gupta<sup>6</sup>, Robert Huether<sup>1,8</sup>, Richard W. Kriwacki<sup>8</sup>, Matthew Parker<sup>5</sup>, Daniel J. McGoldrick<sup>6</sup>, David Zhao<sup>6</sup>, Daniel Alford<sup>6</sup>, Stephen Espy<sup>6</sup>, Kiran Chand Bobba<sup>6</sup>, Guangchun Song<sup>4</sup>, Deqing Pei<sup>7</sup>, Cheng Cheng<sup>7</sup>, Stefan Roberts<sup>5</sup>, Michael I. Barbato<sup>5†</sup>, Dario Campana<sup>9†</sup>, Elaine Coustan-Smith<sup>9†</sup>, Sheila A. Shurtleff<sup>4</sup>, Susana C. Raimondi<sup>4</sup>, Maria Kleppe<sup>10†</sup>, Jan Cools<sup>10</sup>, Kristin A. Shimano<sup>11</sup>, Michelle L. Hermiston<sup>11</sup>, Sergei Doulatov<sup>12,13</sup>, Kolja Eppert<sup>12,13</sup>, Elisa Laurenti<sup>12,13</sup>, Faiyaz Notta<sup>12,13</sup>, John E. Dick<sup>12,13</sup>, Giuseppe Basso<sup>14</sup>, Stephen P. Hunger<sup>15</sup>, Mignon L. Loh<sup>11</sup>, Meenakshi Devidas<sup>16</sup>, Brent Wood<sup>17</sup>, Stuart Winter<sup>18</sup>, Kimberley P. Dunsmore<sup>19</sup>, Robert S. Fulton<sup>2,3</sup>, Lucinda L. Fulton<sup>2,3</sup>, Xin Hong<sup>2</sup>, Christopher C. Harris<sup>2</sup>, David J. Dooling<sup>2,3</sup>, Kerri Ochoa<sup>2</sup>, Kimberly J. Johnson<sup>2</sup>, John C. Obenauer<sup>6</sup>, William E. Evans<sup>20</sup>, Ching-Hon Pui<sup>3</sup>, Clayton W. Naeve<sup>6</sup>, Timothy J. Ley<sup>2,21,22</sup>, Elaine R. Mardis<sup>2,3,22</sup>, Richard K. Wilson<sup>2,3,22</sup>, James R. Downing<sup>4</sup> & Charles G. Mullighan<sup>4</sup>

**Early T-cell precursor acute lymphoblastic leukaemia (ETP ALL) is an aggressive malignancy of unknown genetic basis. We performed whole-genome sequencing of 12 ETP ALL cases and assessed the frequency of the identified somatic mutations in 94 T-cell acute lymphoblastic leukaemia cases. ETP ALL was characterized by activating mutations in genes regulating cytokine receptor and RAS signalling (67% of cases; *NRAS*, *KRAS*, *FLT3*, *IL7R*, *JAK3*, *JAK1*, *SH2B3* and *BRAF*), inactivating lesions disrupting haematopoietic development (58%; *GATA3*, *ETV6*, *RUNX1*, *IKZF1* and *EP300*) and histone-modifying genes (48%; *EZH2*, *EED*, *SUZ12*, *SETD2* and *EP300*). We also identified new targets of recurrent mutation including *DNM2*, *ECT2L* and *RELN*. The mutational spectrum is similar to myeloid tumours, and moreover, the global transcriptional profile of ETP ALL was similar to that of normal and myeloid leukaemia haematopoietic stem cells. These findings suggest that addition of myeloid-directed therapies might improve the poor outcome of ETP ALL.**

Acute lymphoblastic leukaemia (ALL) is the most common malignancy of childhood, with 85% of cases being of B-cell lineage, and 15% T-cell lineage<sup>1</sup>. Recent studies have identified a subtype of T-cell acute lymphoblastic leukaemia (T-ALL) termed “early T-cell precursor” (ETP) ALL that comprises up to 15% of T-ALL, and is associated with a high risk of treatment failure<sup>2</sup>. ETP ALL is characterized by lack of expression of the T-lineage cell surface markers CD1a and CD8, weak or absent expression of CD5, aberrant expression of myeloid and haematopoietic stem cell markers (for example, CD13, CD33, CD34 and CD117), and a gene expression profile reminiscent of the murine early T-cell precursor<sup>3</sup>. The normal ETP, or double negative 1 (DN1) thymocyte retains the ability to differentiate into cells of both the T-cell and myeloid, but not B-cell, lineages<sup>4</sup>.

## Somatic genetic alterations in ETP ALL

ETP ALL cases commonly exhibit a high burden of DNA copy number alterations, but lack a known unifying genetic alteration<sup>2</sup>.

To define the landscape of genetic alterations in ETP ALL, the St Jude Children's Research Hospital–Washington University Pediatric Cancer Genome Project performed whole-genome sequencing (WGS) for matched leukaemic and normal DNA from 12 children with ETP ALL (Supplementary Tables 1–4 and 7, Supplementary Figs 2–4), and determined the frequency of mutations in a separate cohort of 52 ETP and 42 non-ETP childhood T-ALL cases, 82 of which had matched remission DNA. Transcriptome sequencing was performed for two WGS cases, and whole-exome sequencing for three ETP samples in the recurrence cohort (Supplementary Table 8). Putative somatic sequence mutations, and structural alterations identified using CREST<sup>5</sup>, were validated by PCR and sequencing. We identified an average of 1,140 sequence mutations (range 235–1,929) and 12 structural variations (range 0–25) per case (Supplementary Tables 9, 11 and 12, Supplementary Fig. 5), including 154 non-silent sequence variants. Fifty-four per cent of the missense mutations were predicted to be deleterious (Supplementary

<sup>1</sup>Department of Computational Biology and Bioinformatics, St Jude Children's Research Hospital, Memphis, Tennessee 38105, USA. <sup>2</sup>The Genome Institute at Washington University, St Louis, Missouri 63108, USA. <sup>3</sup>Department of Genetics, Washington University School of Medicine, St Louis, Missouri 63110, USA. <sup>4</sup>Department of Pathology, St Jude Children's Research Hospital, Memphis, Tennessee 38105, USA. <sup>5</sup>Pediatric Cancer Genome Project Laboratory, St Jude Children's Research Hospital, Memphis, Tennessee 38105, USA. <sup>6</sup>Department of Information Sciences, St Jude Children's Research Hospital, Memphis, Tennessee 38105, USA. <sup>7</sup>Department of Biostatistics, St Jude Children's Research Hospital, Memphis, Tennessee 38105, USA. <sup>8</sup>Department of Structural Biology, St Jude Children's Research Hospital, Memphis, Tennessee 38105, USA. <sup>9</sup>Department of Oncology, St Jude Children's Research Hospital, Memphis, Tennessee 38105, USA. <sup>10</sup>Department of Molecular and Developmental Genetics, Center for Human Genetics, VIB, K.U.Leuven, 3000 Leuven, Belgium. <sup>11</sup>Department of Pediatrics, University of California School of Medicine, San Francisco, California 94143, USA. <sup>12</sup>Department of Stem Cell and Developmental Biology, Campbell Family Cancer Research Institute, Ontario Cancer Institute, University Health Network, Toronto, Ontario M5G 2M9, Canada. <sup>13</sup>Department of Molecular Genetics, University of Toronto, Toronto, Ontario M5S 1A8, Canada. <sup>14</sup>Onco-Hematology Laboratory, Department of Pediatrics, University of Padua, 35122 Padua, Italy. <sup>15</sup>Section of Pediatric Hematology/Oncology/Bone Marrow Transplantation and Center for Cancer and Blood Disorders, University of Colorado Denver School of Medicine, Children's Hospital Colorado, Aurora, Colorado 80045, USA. <sup>16</sup>Department of Biostatistics, University of Florida College of Medicine, Gainesville, Florida 32603, USA. <sup>17</sup>Department of Laboratory Medicine, Seattle Children's Hospital, Seattle, Washington 98105, USA. <sup>18</sup>University of New Mexico, Albuquerque, New Mexico 87131, USA. <sup>19</sup>Pediatric Hematology Oncology, University of Virginia, Charlottesville, Virginia 22903, USA. <sup>20</sup>Department of Pharmaceutical Sciences, St Jude Children's Research Hospital, Memphis, Tennessee 38105, USA. <sup>21</sup>Division of Oncology, Washington University, St Louis, Missouri 63110, USA. <sup>22</sup>Siteman Cancer Center, Washington University, St Louis, Missouri 63110, USA. †Present addresses: Human Immunology, Centre for Cancer Biology, SA Pathology, Adelaide, South Australia, 5000 Australia (S.L.H.); Department of Paediatrics, Yong Loo Lin School of Medicine, National University of Singapore, 119077 Singapore (D.C., E.C.-S.); Human Oncology and Pathogenesis Program, Memorial Sloan Kettering Cancer Center, New York, New York 10065, USA (M.K.); Jefferson Medical College, Thomas Jefferson University, Philadelphia, Pennsylvania 19107, USA (M.I.B.).

\*These authors contributed equally to this work.

Table 12), indicating that many of these variants are involved in leukaemogenesis.

Structural rearrangements in ETP ALL

We detected 181 structural variations across the WGS cases (Supplementary Results and Supplementary Tables 13, 14, Fig. 1 and Supplementary Fig. 6). Most abnormalities identified by cytogenetics were also evident on analysis of WGS data (Supplementary Table 15). We also observed evidence of telomere shortening on analysis of WGS data (Supplementary Fig. 7). Three cases (SJTALL001, SJTALL002, SJTALL003) had multiple complex rearrangements with breakpoints suggestive of a single cellular catastrophe (“chromothripsis”<sup>6</sup>; Supplementary Figs 6 and 8). Case SJTALL001 had a nonsense mutation in *MLH3*, a DNA mismatch repair gene with a role in DNA double strand break repair, and SJTALL003 had a missense mutation in *DCLRE1C*, which encodes the non-homologous end-joining factor ARTEMIS, indicating a potential causal relationship between these mutations and the acquisition of structural variations. Case SJTALL007 had a deletion disrupting the mismatch repair gene *MSH5*, and also harboured multiple structural rearrangements.

Remarkably, 51% (77 out of 151) of the validated structural variations had breakpoints in coding genes, including genes with known roles in haematopoiesis and leukaemogenesis, or genes also targeted by sequence mutations (for example, *MLH3*, *SUZ12* and *RUNX1*). A majority of these structural variations (65 out of 77, 84%) are predicted to result in loss-of-function of the involved genes, or occur as part of complex translocations that result in the formation of chimaeric fusion

proteins. Ten chimaeric genes encoding six fusion proteins were detected in five cases (Supplementary Table 16) which resulted in the expression of chimaeric in-frame novel fusion genes disrupting haematopoietic regulators, including *ETV6-INO80D* (case SJTALL002), *NUP214-SQSTM1* (SJTALL009) and *NAP1L1-MLLT10* (SJTALL013) (Supplementary Figs 9–12). Case SJTALL012 harboured a *RUNX1-EVX1* rearrangement arising from transplicing (SJTALL012; Supplementary Figs 10 and 11). No additional cases with these chimaeric fusions were identified upon testing 77 ETP and non-ETP ALL cases with available RNA by PCR with reverse transcription. However, exome sequencing identified *ETV6-INO80D* in case SJTALL208 (Supplementary Fig. 13). *ETV6* encodes a transcription factor required for definitive haematopoiesis that is frequently altered in leukaemia<sup>7–9</sup>. Deletions and mutations of *ETV6* were present in 33% of ETP and 10% of non-ETP T-ALL cases (Supplementary Fig. 14).

Sequence mutations in ETP ALL

In addition to genes known to be mutated in T-ALL, including *NRAS*<sup>10,11</sup> ( $N = 3$  out of 12 WGS cases) *JAK1* (ref. 12,  $N = 2$ ), *NOTCH1* (ref. 13,  $N = 1$ ), *FLT3* (refs. 14–16,  $N = 1$ ), *PHF6* (ref. 17,  $N = 3$ ) and *WT1* (ref. 18,  $N = 1$ ), (Supplementary Fig. 15), we identified multiple novel recurring targets of mutation. These included *DNM2* ( $N = 2$ ), *ECT2L* ( $N = 2$ ), *EP300* ( $N = 2$ ), *GATA3* ( $N = 2$ ), *IL7R* ( $N = 2$ ), *JAK3* ( $N = 3$ ), *RELN* ( $N = 2$ ) and *RUNX1* ( $N = 4$ ) (Table 1, Fig. 2, Supplementary Tables 17 and 18, Supplementary Fig. 15). For the two cases also analysed by transcriptome sequencing (SJTALL002 and SJTALL012), 21 out of 38 mutations were expressed. We did not observe selective expression of mutant alleles, with the exception of those with a concomitant deletion of the wild-type allele (for example, *KRAS* in SJTALL002).

Of 42 genes analysed by Sanger sequencing and single-nucleotide polymorphism microarray analysis in the recurrence cohort, 27 were recurrently mutated (Supplementary Table 19, Figs 2 and 3a, and Supplementary Figs 15 and 16). Of 254 validated non-silent mutations (Supplementary Table 17), 40.7% were indel mutations and 9.4% were nonsense mutations. Eighty-two per cent of missense mutations were predicted to be deleterious, a marked enrichment compared with mutations identified in the WGS samples, consistent with the majority being driver mutations.

We observed a high frequency of mutations known or predicted to result in aberrant cytokine receptor and RAS signalling in ETP ALL. Forty-three out of 64 (67.2%) of ETP cases had mutations in these pathways, compared to 8 out of 42 (19%) non-ETP cases ( $P < 0.0001$ ; Table 1, Fig. 3b and Supplementary Table 20). Known or predicted activating mutations were identified in *BRAF*, *FLT3*, *IGF1R*, *JAK1*, *JAK3*, *KRAS* and *NRAS* (Supplementary Results). Three cases

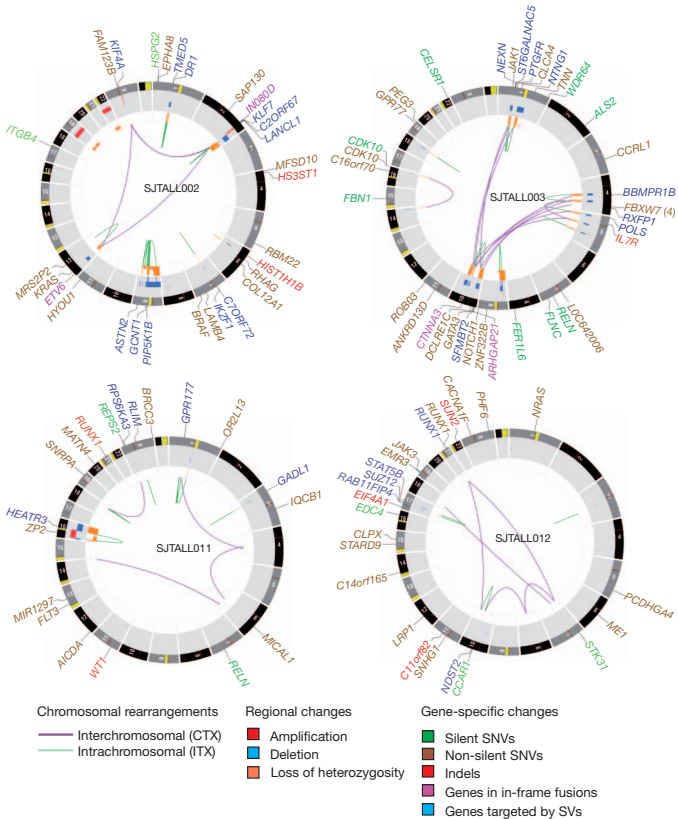


**Figure 1 |** Circos<sup>43</sup> plots of genetic alterations in four representative ETP ALL cases depicting structural genetic variants, including DNA copy number alterations, intra- and inter-chromosomal translocations, and sequence alterations. Loss-of-heterozygosity, orange; amplification, red; deletion, blue. Sequence mutations in RefSeq genes: silent single-nucleotide variants (SNVs), green; non-silent SNVs, brown; indels, red. Genes at structural variant breakpoints: genes involved in in-frame fusions, pink; others, blue. Circos plots for all cases are provided in Supplementary Fig. 6.

**Table 1 |** Recurring mutations in 12 WGS ETP ALL cases

Gene	N	Case (mutation)
JAK1	2	003 (S703I), 005 (I631>RGI)
JAK3	3	012 (M511I), 013 (M511I), 007 (A573V)
NRAS	3	008 (Q61H), 012 (Q61P), 001 (Q61H)
KRAS	1	002 (G60D)
BRAF	1	002 (G466E)
FLT3	1	011 (D835Y)
RUNX1	3	006 (R166*), 011 (V124fs), 012 (V164A, translocation involving chrs 8,7,21,10)
PHF6	3	012 (R274Q) 013 (M125I) 005 (exon 8 splice)
ECT2L	2	009 (V588G), 007 (E384D)
EP300	2	006 (L1639P), 007 (exon 10 splice)
GATA3	2	003 (R276Q), 007 (R276Q)
GATA2	1	011 (R307W)
RELN	2	003 (S1719S) 011 (A2114A)
IL7R	2	007 (GCinsL243) 003 (V253>GFSV)
EED	3	001 and 006 (deletion), 004 (S259F)
EZH2	2	009 (deletion) 013 (R684H)
SUZ12	3	006 and 012 (deletion), 013 (S369fs)
HNRNP1	1	005 (F298fs)
HNRNPR	1	013 (S202fs)



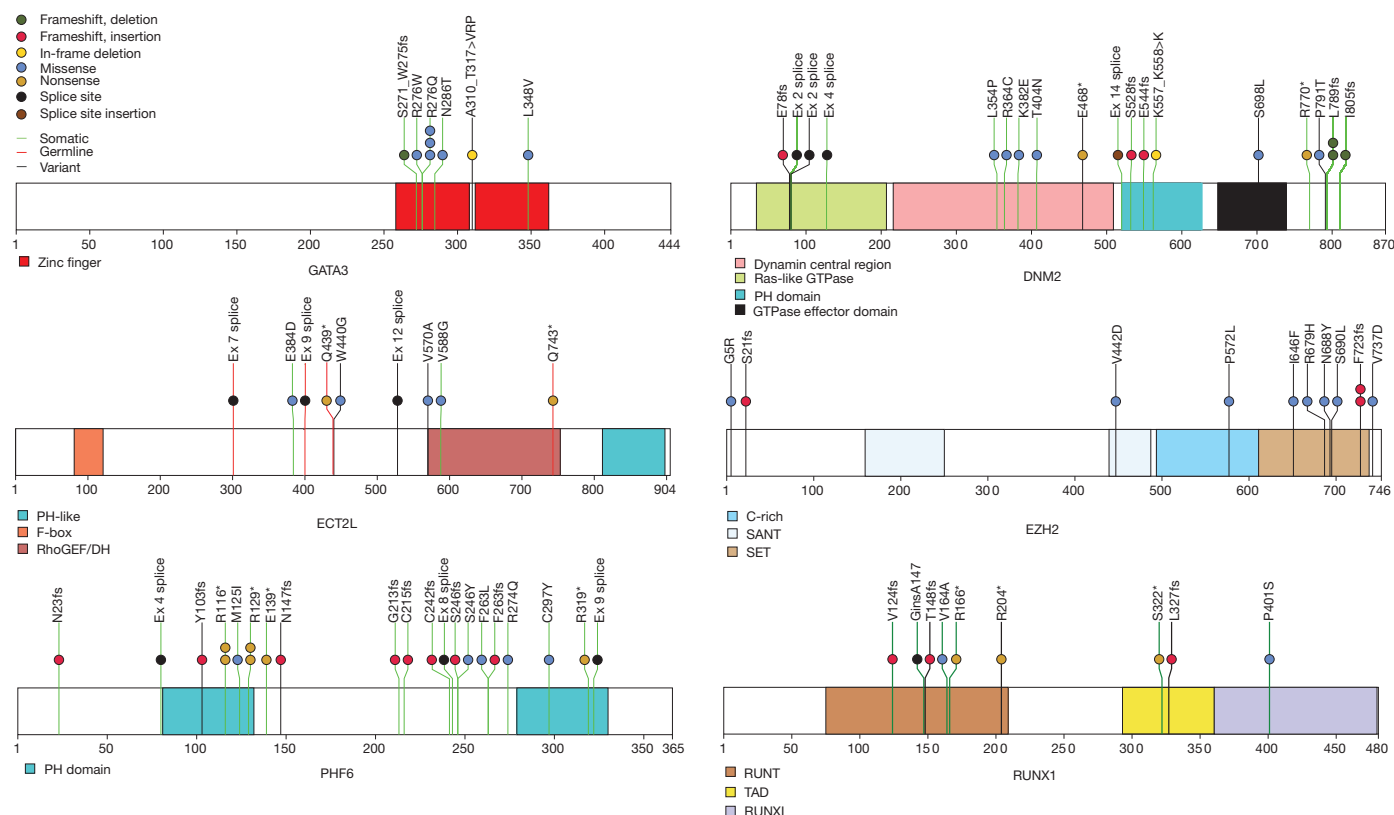


**Figure 2 | Recurring sequence mutations in T-ALL.** Recurring mutations in ETP-ALL. The figures show mutations for the 12 WGS cases, and the recurrence cohort of 94 cases sequenced by Sanger sequencing. The majority of cases had matched remission DNA to distinguish somatic from inherited variants. Where remission DNA was not available, but variants are known or predicted to be deleterious, mutations are shown as 'variants'. The results of

recurrence screening for additional genes sequenced are shown in Supplementary Table 17 and Supplementary Figs 14–17 and 20). The schematics are based on the following NCBI protein reference sequences: GATA3, NP\_001002295; DNM2, NP\_001005360; ECT2L, NP\_001071174; EZH2, NP\_001190176; PHF6, NP\_001015877.1 and RUNX1, NP\_001745.

harboured the JAK3 M511I mutation located adjacent to the pseudokinase domain that has been identified previously in acute myeloid leukaemia and is transforming when introduced into murine haematopoietic progenitor cells<sup>19</sup>. The pseudokinase domain mutation, A573V, has previously been identified in acute megakaryoblastic leukaemia and is transforming<sup>20</sup>. The mutations identified in JAK1 are novel, but are in close proximity to sites of activating mutations previously identified in ALL<sup>12</sup>.

Seven cases (five ETP and two non-ETP) harboured mutations in *IL7R* encoding the IL7RA (interleukin 7 receptor alpha) chain (Fig. 4a). IL7RA forms a heterodimer with IL2RG (common gamma chain) for the cytokine IL7, and with CRLF2 (cytokine receptor like factor 2) forms a receptor for TSLP (thymic stromal lymphopoietin). IL7R and CRLF2 signalling are important in early lymphoid maturation<sup>21</sup>. Rearrangement of *CRLF2* is observed in B-progenitor ALL<sup>22,23</sup>, and *IL7R* mutations have recently been identified in ALL<sup>24</sup>. All seven cases had an in-frame insertion or substitution at residues I241–V253 of the IL7R transmembrane domain. Consistent with prior data, expression of several of the IL7R mutant alleles in the cytokine-dependent murine haematopoietic Ba/F3 and MOHITO<sup>25</sup> cell lines resulted in transformation to cytokine-independent cell growth (Fig. 4b, c). In six cases the mutations introduced a cysteine into the transmembrane domain that induces dimerization of the receptor in the absence of ligand (Fig. 4d). The mutations also induced Stat5 phosphorylation that was attenuated by Jak inhibition (Fig. 4e). Expression of mutant, but not wild type IL7r in primary murine haematopoietic progenitors resulted in enhanced colony replating *in vitro* (Fig. 4f, g), indicating that the IL7R alterations are transforming events in T-ALL.

We also identified a high frequency of alterations of genes with roles in haematopoietic and lymphoid development, including *RUNX1*, *IKZF1*, *ETV6*, *GATA3* and *EP300* (57.8% of ETP cases versus 16.7% of non-ETP T-ALL cases,  $P < 0.0001$ ). Importantly, several of these genes were targeted by multiple mechanisms of alteration across the cohort: sequence mutation, deletion and chromosomal translocations. Six cases (all ETP) had inactivating mutations of *GATA3*, four of which were biallelic due to either biallelic sequence mutations (SJTALL179, R276Q and A310\_T317>VRP; SJTALL010 N286T and S271\_W275fs) (Fig. 2) or due to concomitant deletion of the second allele (Supplementary Table 18). *GATA3* encodes GATA binding protein 3, a member of a family of highly conserved zinc-finger transcription factors that is required for the development of early T-lineage progenitors<sup>26</sup>, and is mutated in the hypoparathyroidism with sensorineural deafness and renal dysplasia syndrome (HDR)<sup>27</sup>. In four cases the mutation was at R276, a residue also mutated in HDR<sup>27</sup>. The R276P mutation results in impaired DNA-binding affinity of *GATA3* for its DNA targets, indicating that the mutations observed in T-ALL are likely to be loss of function. An additional case, SJTALL011, harboured a somatic mutation in *GATA2*, R307W, which is also located in the highly conserved GATA zinc-finger domain and is homologous to the *GATA3* R276W mutation.

Twelve cases (ten ETP, and two non-ETP) harboured alterations of *RUNX1*. Two cases had concomitant deletion of the non-mutated allele, and three had *RUNX1* deletions but no sequence mutation. *RUNX1* is required for definitive haematopoiesis<sup>28</sup> and normal T-lymphoid development, and is commonly rearranged and mutated in myeloid and lymphoid malignancies (Supplementary results)<sup>8,29–32</sup>.

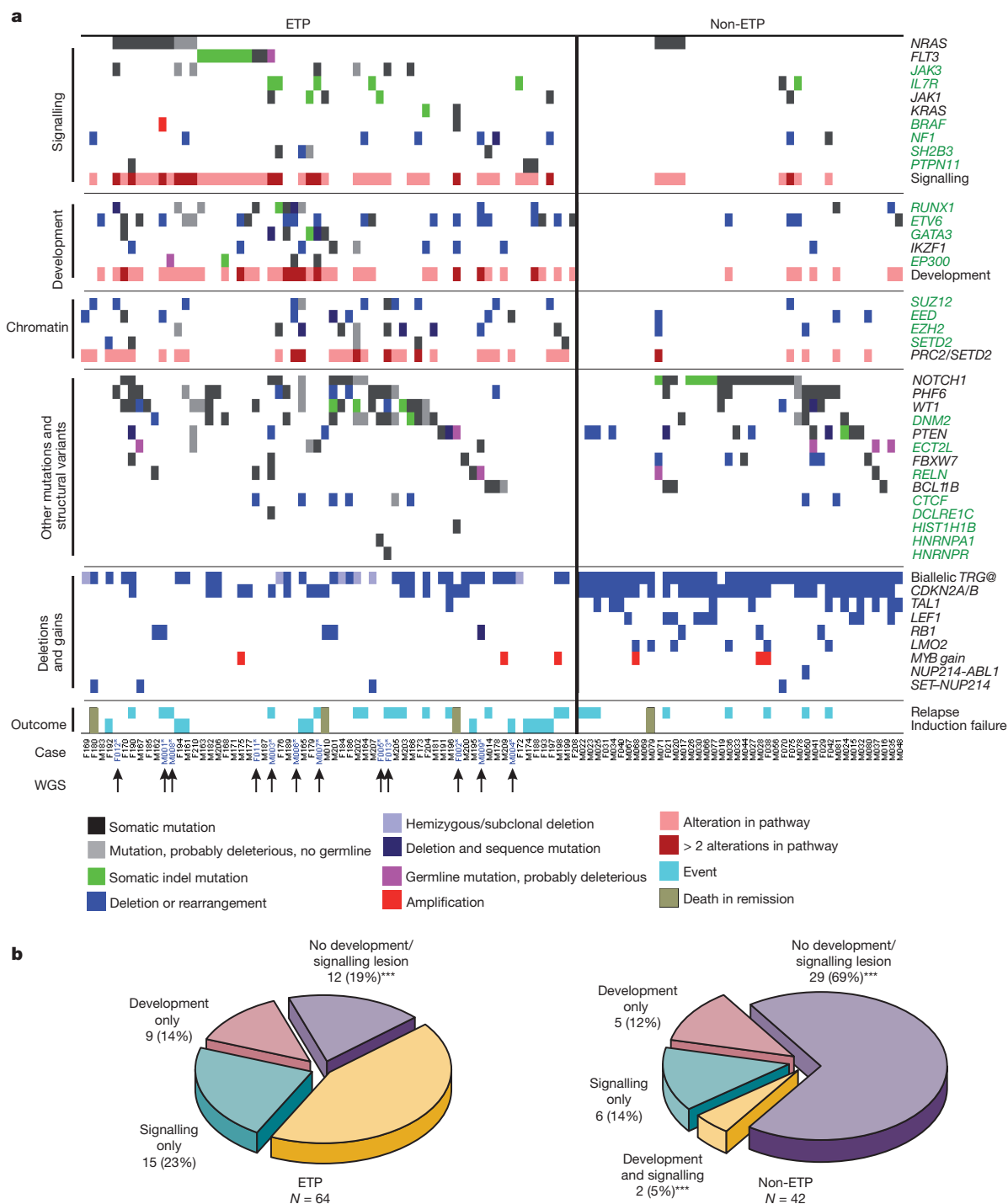


**Figure 3 | Recurring mutations in T-lineage ALL.** **a**, Data are shown for 106 T-ALL cases, including the 12 cases that were subjected to whole-genome sequencing (arrowed), and 94 recurrence cases (52 ETP ALL and 42 non-ETP T-ALL). Cases have been grouped by ETP status, and cases lacking any mutations are shown to the left, followed by cases with *NRAS* and *FLT3*

The mutations observed in T-ALL commonly involve the Runt domain, include frameshift and nonsense mutations, and are predicted to be deleterious. Nine cases (eight ETP) had deletions or sequence mutations of *IKZF1* (IKAROS), which encodes a zinc-finger transcription factor required for the development of all lymphoid lineages that is commonly mutated in high-risk B-progenitor ALL and murine models of T-ALL (Supplementary Fig. 16).

A notable finding was a high frequency of somatic alterations targeting histone modification in ETP ALL. Six WGS cases had

mutations. Genes identified as novel targets of mutation in T-ALL are labelled in green. Four cases died while in remission and are excluded from outcome analysis. **b**, Frequency of somatic alterations targeting haematopoietic and lymphoid development in ETP and non-ETP T-ALL, showing an increased frequency of lesions in these pathways in ETP ALL. \*\*\* $P < 0.0001$ .

alterations in genes encoding components of the polycomb repressor complex 2 (PRC2), including deletions and sequence mutations of *EED*, *EZH2* and *SUZ12* (Table 1, Fig. 2 and Supplementary Fig. 17). *EZH2* catalyses trimethylation of histone 3 lysine 27 (H3K27), resulting in transcriptional repression of genes involved in development, stem cell maintenance and differentiation<sup>33</sup>. Twenty-seven (42.2%) of ETP ALL cases harboured a deletion and/or sequence mutation in these genes, compared to five (11.9%) of non-ETP T-ALL cases ( $P = 0.001$ ). Gain-of-function *EZH2* Y641 mutations are common



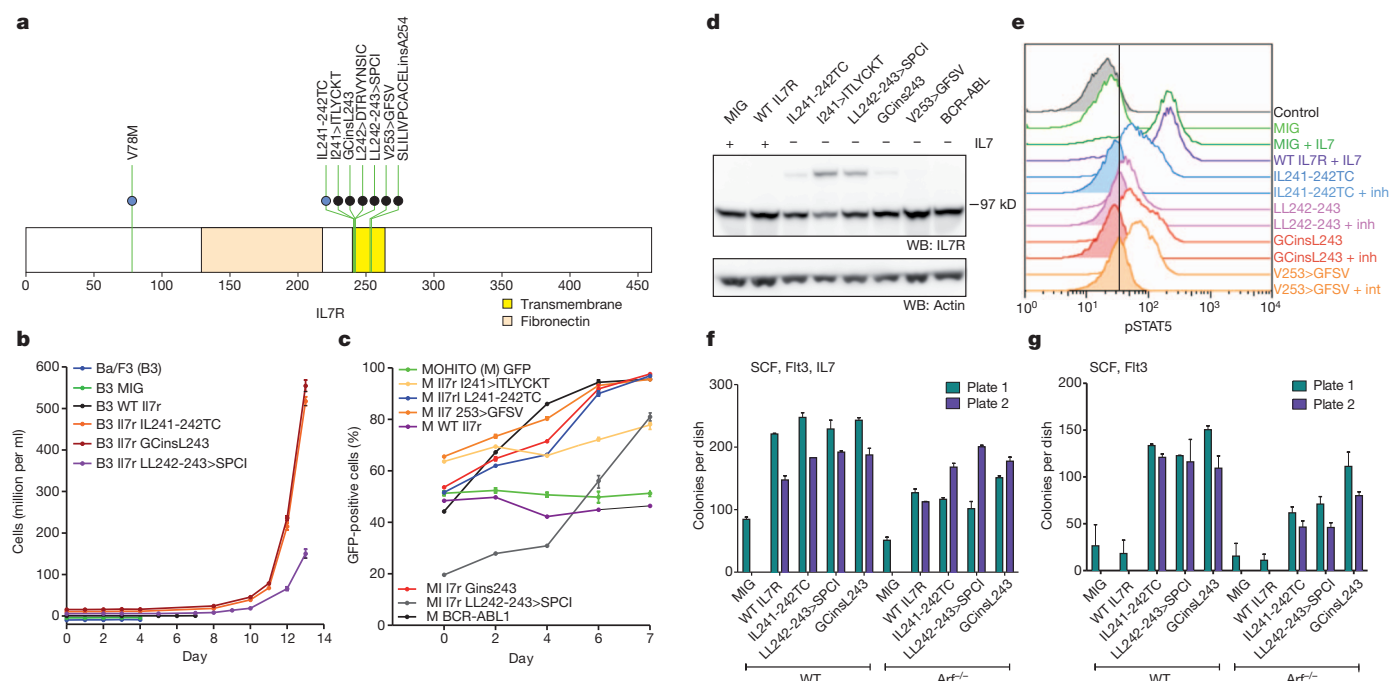


**Figure 4 | IL7R mutations in T-ALL.** **a**, Domain structure of IL7R, showing two hotspots of missense and in-frame insertion-deletion mutations (IL241-242 and VA253-254). The single case with a mutation in the amino-terminal region (V78M) is accompanied by a transmembrane domain mutation. **b**, **c**, Murine IL7r mutant alleles homologous to the human IL7R mutations were expressed in the murine haematopoietic IL-3-dependent Ba/F3 cell lines (**b**) or the murine IL-7-dependent MOHITO T-ALL cell line (**c**). WT, wild type. Expression of these mutant alleles resulted in transformation to cytokine-independent proliferation. MIG, empty MSCV-IRES-GFP vector. In **b**, growth curves have been offset to permit visualization of each allele. Error bars represent mean  $\pm$  s.d. for three replicates. In **c**, transformation to cytokine-independent growth is shown as an increasing proportion of IL7r-mutant-expressing cells (or as a positive control, BCR-ABL1), as measured by the

percentage of GFP-positive cells. **d**, Western blotting for IL7r in MOHITO cells transduced with wild-type or mutant IL7r alleles, showing the formation of IL7r dimers in cells expressing mutant alleles with an unpaired cysteine residue. **e**, Phosphosignalling analysis of MOHITO cells transduced with MIG, WT IL7r or four different IL7r mutant alleles, showing increased Stat5 phosphorylation in cells stimulated with IL7, or cells expressing mutant IL7r alleles in the absence of cytokine. Stat5 phosphorylation was reduced following exposure to Jak inhibitor I (inh) at 3  $\mu$ M for 1 hour. **f**, **g**, Clonogenic assays of lineage-negative WT or Arf<sup>-/-</sup> murine bone marrow cells expressing mutant IL7r alleles show enhanced replating compared to cells transduced with empty vector (**f**), and enhanced replating compared to cells expressing WT IL7r cultured in the absence of IL7 (**g**). Columns show mean of two replicates  $\pm$  s.e.m.

in lymphoma<sup>34</sup>. In contrast, structural modelling predicts that the mutations observed in T-ALL are likely to disrupt the catalytic SET domain and result in loss of function (Supplementary Results and Supplementary Figs 18 and 19). In addition, case SJTALL192 harboured a focal homozygous deletion of *SETD2* which encodes a H3K36 trimethylase, and an additional four cases had loss-of-function mutations of this gene (Supplementary Fig. 20). Three cases had predicted loss-of-function mutations of the histone acetyltransferase gene *EP300* (p300). Together, 31 ETP and 5 non-ETP cases had mutations affecting epigenetic regulation, which were biallelic or involved multiple genes in 10 cases (9 ETP and 1 non-ETP).

### Novel recurrent somatic mutations

Recurring mutations were also identified in genes not previously known to be involved in lymphoid development or oncogenesis. *DNM2* was mutated in 17 cases (13 ETP, 4 non-ETP), including two cases with biallelic mutations (Fig. 2). *DNM2* encodes dynamin 2, a member of a family of large GTPases, and is involved in a wide range of cellular functions, including endocytosis, phagosome formation, intracellular trafficking, interaction with the actin and microtubule networks, and promotion of apoptosis<sup>35</sup>. Inherited *DNM2* mutations result in the degenerative neurologic diseases Charcot-Marie-Tooth peripheral neuropathy and autosomal dominant centronuclear myopathy<sup>35</sup>. As in these diseases, the mutations in T-ALL are located throughout the gene in each functional domain, and include missense, nonsense, splice site and frameshift mutations, and are therefore likely to result in loss of *DNM2* function. The role of *DNM2* in lymphoid development and tumorigenesis is unknown,

although it is expressed in leukaemic lymphoblasts (Supplementary Fig. 22).

Eight cases had missense, nonsense or splice site mutations in *ECT2L* (epithelial cell transforming sequence 2 oncogene gene like). Four cases had non-synonymous mutations in *RELN*, which encodes reelin, a large secreted extracellular matrix protein involved in the regulation of neuronal migration, and which is mutated in the neurodevelopmental disorder autosomal recessive lissencephaly with cerebellar hypoplasia<sup>36</sup>. Notably, several cases had inherited mutations in these two genes that are predicted to be deleterious. Sequence mutations were also found in 12 regulatory RNA genes including one microRNA gene (*MIR1297*).

### Mutations in multiple pathways in ETP ALL

Recurring mutations targeting genes regulating haematopoietic development ('type II lesions', for example, *GATA3*, *RUNX1*, *ETV6*, *IKZF1* and *EP300*) and cytokine receptor and RAS signalling ('type I lesions') were present in 7 out of 12 WGS cases, with an additional three cases having either type I or type II lesions, indicating that these events are central to the pathogenesis of ETP ALL. Consistent with this, pathway analysis incorporating both sequence and structural mutations demonstrated enrichment for lesions in these pathways in the 12 WGS cases (Supplementary Table 23). Across the entire cohort, 52 out of 64 (81.3%) ETP cases harboured mutations in these pathways, compared to 13 out of 42 (31%) non-ETP T-ALL cases ( $P < 0.0001$ ; Fig. 3b and Supplementary Table 20). Forty-eight per cent of ETP cases had mutations in the PRC2 genes sequenced, *SETD2* and *EP300*, compared to 12% of non-ETP ALL ( $P = 0.0001$ ). This is

probably an underestimate of the frequency of mutations perturbing chromatin modification, as not all PRC2 and histone-modifying genes have been sequenced. Pathway analysis of the gene expression profile of ETP ALL (Supplementary Table 24 and Supplementary Figs 23–25) demonstrated significant positive enrichment for genes mediating JAK-STAT signalling, and negative enrichment for T-cell receptor signalling genes in ETP ALL. In addition, flow cytometric intracellular phosphosignalling analysis of primary leukaemic cells demonstrated activation of RAS and JAK-STAT signalling pathways in ETP ALL cases (Supplementary Fig. 26). Furthermore, reconstruction of the transcriptional network of ETP ALL using ARACNE<sup>37</sup> identified 30 gene networks ('regulons') with *RUNX1* and *IKZF1* observed to be hub genes of several of these regulons. Thus, alterations of these haematopoietic transcription factors are key determinants of the transcriptional profile of ETP ALL (Supplementary Table 25).

### ETP ALL is a stem-cell leukaemia

The immunophenotype and gene expression of ETP ALL are similar to the murine early T-cell precursor<sup>3</sup>. However, detailed comparison of the gene expression profiles of ETP ALL and normal human haematopoietic progenitors has not been performed. Comparison of the gene expression profile of ETP ALL with those of purified normal<sup>38,39</sup> and myeloid leukaemic<sup>40</sup> haematopoietic stem cell and progenitor cell populations demonstrated marked negative enrichment of the gene expression profile of normal human early T-cell precursors (Supplementary Fig. 27). In contrast, the ETP ALL signature showed significant positive enrichment of the gene expression profile of normal human haematopoietic stem cells and granulocyte macrophage precursors. In addition, the ETP ALL signature demonstrated enrichment for a leukaemic stem-cell signature associated with poor outcome in acute myeloid leukaemia<sup>40</sup>, and a signature of poor outcome in *IKZF1*-mutated high-risk B-progenitor ALL<sup>41</sup>. Together, these data are compatible with the notion that the genetic alterations identified here result in gross maturational arrest and an aggressive poorly differentiated stem-cell-like leukaemia.

### Discussion

Although the striking uniformity of clinical features, immunophenotype and transcriptional profile suggests a common underlying genetic alteration in ETP ALL, we identified a remarkable diversity of novel recurrent genetic alterations. Despite this diversity, the prevalence of mutations in genes involving cytokine receptor and RAS signalling, haematopoietic development and histone modification suggests a common pathogenesis for the establishment of the ETP leukaemic clone. Mutations known or predicted to result in activated cytokine receptor and RAS signalling are present in two-thirds of ETP cases, but only 19% of non-ETP T-ALL. This includes mutations in genes with known roles in leukaemogenesis as well as novel targets of mutation (*JAK3*, *IL7R*, *IFNRI* and *BRAF*). The ability of the identified *IL7R* activating mutations to induce factor-independent growth of haematopoietic cells coupled with the known function of the other identified signalling mutations strongly supports a direct role for these alterations in leukaemic cell transformation. The high frequency of deleterious mutations in PRC2 genes suggests that disruption of PRC2-mediated gene silencing is a key event in the pathogenesis of this primitive leukaemia, but not more differentiated T-ALL cases. Several of the genes recurrently mutated in ETP are also mutated in inherited disorders (*DNM2*, *EP300*, *GATA3*, *NRAS*, *KRAS*, *PHF6*, *RELN* and *RUNX1*), and the mutational spectrum in several of these genes is similar between the inherited disorders and T-ALL. Thus, sequencing of additional T-ALL cases and other leukaemia genomes will be of great interest to fully examine the relationship of inherited and acquired lesions in leukaemogenesis.

Mutation of genes regulating cytokine receptor and/or RAS signalling pathway and epigenetic modification is a common feature of acute myeloid leukaemia but is less common in T- or B-lineage

ALL (Supplementary Table 28)<sup>42</sup>. Although the gene expression profile of ETP ALL is similar to that of the murine ETP, it shows strong similarity to that of normal and myeloid leukaemic haematopoietic stem cells. This indicates that ETP ALL is distinct from non-ETP T-ALL, and in fact represents a neoplasm of a less mature haematopoietic progenitor or stem cell, with arrest at a very early maturational stage that retains the capacity for myeloid differentiation. This observation raises the possibility that treatment regimens used to treat acute myeloid leukaemia, such as those incorporating high dose cytarabine, and/or targeted therapies that inhibit cytokine receptor and JAK signalling may be beneficial in ETP ALL.

### METHODS SUMMARY

Whole-genome sequencing was performed for tumour and normal DNA from 12 children with ETP ALL treated at St Jude Children's Research Hospital. All cases fulfilled pathologic and immunophenotypic criteria for ETP ALL<sup>2</sup>. Tumour samples were obtained from diagnostic bone marrow aspirates or peripheral blood, and comprised at least 90% tumour cells. Matched non-tumour samples were obtained from remission blood or bone marrow aspirates with less than 1% leukaemic cells. Recurrence testing was performed using a cohort of 94 childhood T-ALL cases, comprising 52 ETP ALL cases from St Jude, the Children's Oncology Group and the Associazione Italiana Ematologia de Oncologia Pediatrica (AIEOP), and 42 non-ETP T-ALL cases from St Jude. Whole-genome DNA sequencing was performed using a paired-end sequencing strategy as described in detail in the Supplementary Information. The frequency of the identified mutations in the recurrence cohort was determined using PCR amplification and Sanger sequencing and analysis of single-nucleotide polymorphism microarray data. The study was approved by the Institutional Review Boards of St Jude Children's Research Hospital and Washington University.

Received 2 May; accepted 18 November 2011.

- Pui, C. H., Robison, L. L. & Look, A. T. Acute lymphoblastic leukaemia. *Lancet* **371**, 1030–1043 (2008).
- Coustan-Smith, E. *et al.* Early T-cell precursor leukaemia: a subtype of very high-risk acute lymphoblastic leukaemia. *Lancet Oncol.* **10**, 147–156 (2009).
- Rothberg, E. V., Moore, J. E. & Yui, M. A. Launching the T-cell-lineage developmental programme. *Nature Rev. Immunol.* **8**, 9–21 (2008).
- Wada, H. *et al.* Adult T-cell progenitors retain myeloid potential. *Nature* **452**, 768–772 (2008).
- Wang, J. *et al.* CREST maps somatic structural variation in cancer genomes with base-pair resolution. *Nature Methods* **8**, 652–654 (2011).
- Stephens, P. J. *et al.* Massive genomic rearrangement acquired in a single catastrophic event during cancer development. *Cell* **144**, 27–40 (2011).
- Bohlander, S. K. ETV6: a versatile player in leukemogenesis. *Semin. Cancer Biol.* **15**, 162–174 (2005).
- Shurtleff, S. A. *et al.* TEL/AML1 fusion resulting from a cryptic t(12;21) is the most common genetic lesion in pediatric ALL and defines a subgroup of patients with an excellent prognosis. *Leukemia* **9**, 1985–1989 (1995).
- Barjesteh van Waalwijk van Doorn-Khosrovani, S. *et al.* Somatic heterozygous mutations in ETV6 (TEL) and frequent absence of ETV6 protein in acute myeloid leukemia. *Oncogene* **24**, 4129–4137 (2005).
- Yokota, S. *et al.* Mutational analysis of the N-ras gene in acute lymphoblastic leukemia: a study of 125 Japanese pediatric cases. *Int. J. Hematol.* **67**, 379–387 (1998).
- Kawamura, M. *et al.* Alterations of the p53, p21, p16, p15 and Ras genes in childhood T-cell acute lymphoblastic leukemia. *Leuk. Res.* **23**, 115–126 (1999).
- Flex, E. *et al.* Somatic acquired JAK1 mutations in adult acute lymphoblastic leukemia. *J. Exp. Med.* **205**, 751–758 (2008).
- Weng, A. P. *et al.* Activating mutations of *NOTCH1* in human T cell acute lymphoblastic leukemia. *Science* **306**, 269–271 (2004).
- Paietta, E. *et al.* Activating *FLT3* mutations in CD117/KIT<sup>+</sup> T-cell acute lymphoblastic leukemias. *Blood* **104**, 558–560 (2004).
- Van Vlierberghe, P. *et al.* Activating *FLT3* mutations in CD4<sup>+</sup>/CD8<sup>+</sup> pediatric T-cell acute lymphoblastic leukemias. *Blood* **106**, 4414–4415 (2005).
- Neumann, M. *et al.* High rate of *FLT3* mutations in adult ETP-ALL. *ASH Annu. Meet. Abstr.* **116**, 1031 (2010).
- Van Vlierberghe, P. *et al.* *PHF6* mutations in T-cell acute lymphoblastic leukemia. *Nature Genet.* **42**, 338–342 (2010).
- Tosello, V. *et al.* *WT1* mutations in T-ALL. *Blood* **114**, 1038–1045 (2009).
- Yamashita, Y. *et al.* Array-based genomic resequencing of human leukemia. *Oncogene* **29**, 3723–3731 (2010).
- Malinge, S. *et al.* Activating mutations in human acute megakaryoblastic leukemia. *Blood* **112**, 4220–4226 (2008).
- Ziegler, S. F. & Liu, Y. J. Thymic stromal lymphopoietin in normal and pathogenic T cell development and function. *Nature Immunol.* **7**, 709–714 (2006).
- Russell, L. J. *et al.* Deregulated expression of cytokine receptor gene, *CRLF2*, is involved in lymphoid transformation in B-cell precursor acute lymphoblastic leukemia. *Blood* **114**, 2688–2698 (2009).



23. Mullighan, C. G. *et al.* Rearrangement of *CRLF2* in B-progenitor- and Down syndrome-associated acute lymphoblastic leukemia. *Nature Genet.* **41**, 1243–1246 (2009).
24. Shochat, C. *et al.* Gain-of-function mutations in *interleukin-7 receptor- $\alpha$*  (*IL7R*) in childhood acute lymphoblastic leukemias. *J. Exp. Med.* **208**, 901–908 (2011).
25. Kleppe, M., Mentens, N., Tousseyn, T., Wlodarska, I. & Cools, J. MOHITO, a novel mouse cytokine-dependent T-cell line, enables studies of oncogenic signaling in the T-cell context. *Haematologica* **96**, 779–783 (2011).
26. Hosoya, T., Maillard, I. & Engel, J. D. From the cradle to the grave: activities of GATA-3 throughout T-cell development and differentiation. *Immunol. Rev.* **238**, 110–125 (2010).
27. Zahirieh, A. *et al.* Functional analysis of a novel GATA3 mutation in a family with the hypoparathyroidism, deafness, and renal dysplasia syndrome. *J. Clin. Endocrinol. Metab.* **90**, 2445–2450 (2005).
28. Okuda, T., van Deursen, J., Hiebert, S. W., Grosveld, G. & Downing, J. R. AML1, the target of multiple chromosomal translocations in human leukemia, is essential for normal fetal liver hematopoiesis. *Cell* **84**, 321–330 (1996).
29. Downing, J. R. *et al.* An *AML1/ETO* fusion transcript is consistently detected by RNA-based polymerase chain reaction in acute myelogenous leukemia containing the (8;21)(q22;q22) translocation. *Blood* **81**, 2860–2865 (1993).
30. Dicker, F. *et al.* Mutation analysis for *RUNX1*, *MLL*-PTD, *FLT3*-ITD, *NPM1* and *NRAS* in 269 patients with MDS or secondary AML. *Leukemia* **24**, 1528–1532 (2010).
31. Gaidzik, V. I. *et al.* *RUNX1* mutations in acute myeloid leukemia: results from a comprehensive genetic and clinical analysis from the AML study group. *J. Clin. Oncol.* **29**, 1364–1372 (2011).
32. Gelsi-Boyer, V. *et al.* Genome profiling of chronic myelomonocytic leukemia: frequent alterations of *RAS* and *RUNX1* genes. *BMC Cancer* **8**, 299 (2008).
33. Margueron, R. & Reinberg, D. The Polycomb complex PRC2 and its mark in life. *Nature* **469**, 343–349 (2011).
34. Morin, R. D. *et al.* Somatic mutations altering *EZH2* (Tyr641) in follicular and diffuse large B-cell lymphomas of germinal-center origin. *Nature Genet.* **42**, 181–185 (2010).
35. Durieux, A. C., Prudhon, B., Guicheney, P. & Bitoun, M. Dynamin 2 and human diseases. *J. Mol. Med.* **88**, 339–350 (2010).
36. Hong, S. E. *et al.* Autosomal recessive lissencephaly with cerebellar hypoplasia is associated with human *RELN* mutations. *Nature Genet.* **26**, 93–96 (2000).
37. Margolin, A. A. *et al.* Reverse engineering cellular networks. *Nature Protocols* **1**, 662–671 (2006).
38. Novershtern, N. *et al.* Densely interconnected transcriptional circuits control cell states in human hematopoiesis. *Cell* **144**, 296–309 (2011).
39. Notta, F. *et al.* Isolation of single human hematopoietic stem cells capable of long-term multilineage engraftment. *Science* **333**, 218–221 (2011).
40. Eppert, K. *et al.* Stem cell gene expression programs influence clinical outcome in human leukemia. *Nature Med.* **17**, 1086–1093 (2011).
41. Mullighan, C. G. *et al.* Deletion of *IKZF1* and prognosis in acute lymphoblastic leukemia. *N. Engl. J. Med.* **360**, 470–480 (2009).
42. Gilliland, D. G. Molecular genetics of human leukemias: new insights into therapy. *Semin. Hematol.* **39**, 6–11 (2002).
43. Krzywinski, M. *et al.* Circos: an information aesthetic for comparative genomics. *Genome Res.* **19**, 1639–1645 (2009).

**Supplementary Information** is linked to the online version of the paper at [www.nature.com/nature](http://www.nature.com/nature).

**Acknowledgements** We thank the many members of St Jude Children's Research Hospital and The Genome Institute and Siteman Cancer Center at Washington University in St Louis for support. We thank H. Mulder for project sample management, M. Stine for assistance with data deposition, B. Pappas and S. Malone for information technology infrastructure, J. Morris, E. Walker, A. Merriman and G. Neale for performing

single-nucleotide polymorphism and gene expression microarrays, W. Yang for assistance with analysis of genomic data, and J. Stokes for artwork. We thank the Tissue Resources Laboratory, the Flow Cytometry and Cell Sorting Core, and the Clinical Applications of Core Technology Laboratories of the Hartwell Center for Bioinformatics and Biotechnology of St Jude Children's Research Hospital. We thank S. Kehoe of Beckman Coulter Genomics for assistance with Sanger sequencing. This work was funded by The St Jude Children's Research Hospital – Washington University Pediatric Cancer Genome Project, ALSAC of St Jude Children's Research Hospital, Cancer Center support grant P30 CA021765, NIH U01 GM 92666—PAAR4Kids, grants to R.K.W. from Washington University in St Louis and the National Human Genome Research Institute (NHGRI U54 HG003079), grants to the Children's Oncology Group (NCI CA98543, CA98413, CA114766), and grants from Alex's Lemonade Stand and St. Baldrick's Foundation (to M.L.H.). S.L.H. was supported by a Haematology Society of Australasia and New Zealand New Investigator Scholarship. S.P.H. is the Ergen Family Chair in Pediatric Cancer. C.G.M. is a Pew Scholar in the Biomedical Sciences and a St. Baldrick's Scholar.

**Author Contributions** C.G.M., J.R.D., T.J.L., E.R.M. and R.K.W. designed the experiments. J.Z., L.D. and C.L. led data analysis. C.G.M., L.H., S.L.H., D.P.-T., J.R.C.-U., prepared patient samples and performed laboratory assays. R.S.F. and L.L.F. supervised whole genome sequencing data generation. K.C.B. managed data transfer. D.J.D. supervised the automated analysis pipeline. C.W.N. supervised computing infrastructure. J.E. performed transcriptome sequencing. J.R.C.-U., M.K. and J.C. performed *IL7R* mutation assays. K.A.S., M.L.H. and K.G.R. performed phosphosignalling analyses. K.G.R. performed colony assays. X.C., M.R., J.W., G.W., J.B., D.M., J.M., D.Z., L.W., X.H., K.J.J. and C.C.H. performed sequence analysis. L.H., C.G.M. and J.M. analysed single-nucleotide polymorphism array data. M.P. performed telomere analysis. S.C.R. reviewed cytogenetic data. P.G. prepared Circos plots. D.A. and S.E. managed data. S.-C.C., J.M. and G.S. analysed gene expression microarray data. S.D., K.E., E.L., F.N. and J.E.D. collected and analysed gene expression data from normal and leukaemic stem and progenitor cells. S.B.P. developed the GRIN model and performed genomic pathway analyses. D.P. and C.C. performed association analyses between clinical and genetic variables and outcome. R.H. and R.W.K. performed *EZH2* structural modelling. S.-C.C. performed pathway analysis. A.U. performed ARACNE analyses. D.C., E.C.-S., G.B., S.P.H., M.L.L., M.D., W.E.E., B.W., S.W., K.P.D., and C.-H.P. provided clinical samples and data. C.G.M., J.R.D. and J.Z. wrote the manuscript. J.Z., L.D., L.H., G.W., S.L.H., D.P.-T., J.E., X.C., J.W., M.R., C.L., S.-C.C., L.W., J.M., K.G.R., S.B.P., A.U., J.B., P.G., R.H., R.W.K., M.P., D.J.M., D.Z., D.A., S.E., K.C.B., G.S., S.R., M.I.B., S.A.S., K.P.D., R.S.F., L.L.F., X.H., C.C.H., D.J.D., K.O., K.I.J., J.C.O., W.E.E., C.-H.P., C.W.N., T.J.L., E.R.M., R.K.W., J.R.D. and C.G.M. are part of the St Jude Children's Research Hospital – Washington University Pediatric Cancer Genome Project.

**Author Information** The sequence data and single nucleotide polymorphism microarray data have been deposited in the dbGaP database (<http://www.ncbi.nlm.nih.gov/gap>) under the accession number phs000340.v1.p1. Affymetrix U133A gene expression data have been deposited in the NCBI gene expression omnibus under GSE33315, and Affymetrix U133 Plus 2.0 PM gene expression data under accession GSE28703. The nucleotide sequence for the full-length *ETV-INO80D* transcript has been deposited in GenBank under accession JF736506. A public data portal for results from the St Jude – Washington University Pediatric Cancer Genome Project is available at <http://explore.pediatriccancergenomeproject.org/>. Reprints and permissions information is available at [www.nature.com/reprints](http://www.nature.com/reprints). This paper is distributed under the terms of the Creative Commons Attribution-Non-Commercial-Share Alike licence, and is freely available to all readers at [www.nature.com/nature](http://www.nature.com/nature). The authors declare no competing financial interests. Readers are welcome to comment on the online version of this article at [www.nature.com/nature](http://www.nature.com/nature). Correspondence and requests for materials should be addressed to J.R.D. ([james.downing@stjude.org](mailto:james.downing@stjude.org)) and C.G.M. ([charles.mullighan@stjude.org](mailto:charles.mullighan@stjude.org)).

# An absence of ex-companion stars in the type Ia supernova remnant SNR 0509–67.5

Bradley E. Schaefer<sup>1</sup> & Ashley Pagnotta<sup>1</sup>

A type Ia supernova is thought to begin with the explosion of a white dwarf star<sup>1</sup>. The explosion could be triggered by the merger of two white dwarfs<sup>2,3</sup> (a ‘double-degenerate’ origin), or by mass transfer from a companion star<sup>4,5</sup> (the ‘single-degenerate’ path). The identity of the progenitor is still controversial; for example, a recent argument against the single-degenerate origin<sup>6</sup> has been widely rejected<sup>7–11</sup>. One way to distinguish between the double- and single-degenerate progenitors is to look at the centre of a known type Ia supernova remnant to see whether any former companion star is present<sup>12,13</sup>. A likely ex-companion star for the progenitor of the supernova observed by Tycho Brahe has been identified<sup>14</sup>, but that claim is still controversial<sup>15–18</sup>. Here we report that the central region of the supernova remnant SNR 0509–67.5 (the site of a type Ia supernova  $400 \pm 50$  years ago, based on its light echo<sup>19,20</sup>) in the Large Magellanic Cloud contains no ex-companion star to a visual magnitude limit of 26.9 (an absolute magnitude of  $M_V = +8.4$ ) within a region of radius 1.43 arcseconds. (This corresponds to the  $3\sigma$  maximum distance to which a companion could have been ‘kicked’ by the explosion.) This lack of any ex-companion star to deep limits rules out all published single-degenerate models for this supernova. The only remaining possibility is that the progenitor of this particular type Ia supernova was a double-degenerate system.

The progenitor of any type Ia supernova has never been identified. Various candidate classes have been proposed (see Table 1 and Supplementary Information section 1), although arguments and counter-arguments have resulted in no decisive solution. It is possible that the observed type Ia supernovae might have two comparable-sized progenitor classes<sup>21</sup>. In double-degenerate systems, the two white dwarfs will both be completely destroyed by the supernova explosion. In single-degenerate systems, the mass-donor star (orbiting the doomed white dwarf) will survive the explosion, and shine at near its pre-explosion brightness from the middle of the expanding supernova remnant. (During the explosion, portions of the outer envelope of the companion star will be stripped off<sup>22,23</sup>, but its location on the colour-magnitude diagram will not change greatly<sup>24</sup>.) An observational programme to distinguish between the progenitor models

by looking for an ex-companion star inside a known type Ia supernova remnant has been attempted only once<sup>14</sup>, for Tycho’s supernova of 1572. A particular G-type subgiant star has been identified as being the ex-companion: if this is correct, it would point to a recurrent nova as the progenitor for Tycho’s supernova<sup>14</sup>. Several concerns have been raised<sup>15,17</sup> about this identification, and these have been answered<sup>18</sup>, although the case remains unresolved.

To break this impasse, we have looked at a supernova remnant in the nearest galaxy to our own, the Large Magellanic Cloud (LMC). We consider the case of SNR 0509–67.5, which was an type Ia supernova (of the SN 1991T class)  $400 \pm 50$  years ago<sup>19,20,25,26</sup>. SNR 0509–67.5 has excellent images in the public domain that were taken by the Hubble Space Telescope (HST). All of the stars in the field have been measured for B, V and I magnitude with standard IRAF aperture photometry and converted to Vega magnitudes with the standard calibration (see Table 2). The faintest visible star (at the  $5\sigma$  detection level) is at  $V = 26.9$  mag.

If any ex-companion still exists after the explosion  $\sim 400$  years ago, then it must be located near the centre of the remnant. We have measured the geometric centre of the shell with three independent methods (see Supplementary Information section 2): using the edge of the H $\alpha$  shell, the edge of the X-ray shell, and the minimum of the H $\alpha$  light in the interior of the remnant. Each of these three derived centres are from different gas masses and regions, so they are independent and provide a measure of the statistical and systematic uncertainties in the centre position. Our combined geometric centre is at right ascension 05 h 09 min 31.208 s, declination  $-67^\circ 31' 17.48''$  (J2000), with  $1\sigma$  uncertainties of  $0.14''$  along the short axis (roughly ENE to WSW) and  $0.20''$  along the long axis (tilted  $18^\circ \pm 3^\circ$  to the west of north).

The position of any ex-companion star will be offset from the estimated geometric centre of the shell, owing to proper motion of the star, asymmetries in the shell, and measurement errors of the centre position. We now consider these factors in order. First, the proper motion of the star will depend on its orbital velocity and the kick onto the star from the supernova explosion. This distribution of the offsets from the centre resulting from the proper motion of the

**Table 1 | Candidate progenitor classes**

Candidate class	$P_{\text{orb}}$ (d)	$V_{\text{ex-comp}}$ (km s <sup>-1</sup> )	Surviving companion	$M_V$ (mag)	$V$ range in LMC (mag)
Double-degenerate	NA	NA	None	NA	NA
Recurrent nova	0.6–520	50–350	Red giant or subgiant	–2.5 to +3.5	16–22
Symbiotic star	245–5,700	50–250	Red giant	–2.5 to +0.5	16–19
Supersoft source	0.14–4.0	170–390	Subgiant or $>1.16 M_\odot$ MS	+0.5 to +4.2	19–22.7
Helium star donor	0.04–160	50–350	Red giant or subgiant core	–0.5 to +2.0	18–20.5
Spin-up/spin-down	245–5,700	50–250	Red giant or subgiant core	–0.5 to +2.0	18–20.5

This table gives the basic classes proposed for progenitors; other possibilities have been exhaustively examined and rejected (Supplementary Information section 1). The orbital periods,  $P_{\text{orb}}$ , in days, give an indication of the size of the companion star, and hence some indication of its brightness in isolation. The velocity of the ex-companion star,  $V_{\text{ex-comp}}$ , in km s<sup>-1</sup>, includes the orbital velocity of the companion with respect to the white dwarf plus the kick velocity, and indicates the maximum proper motion that the companion star can have. The fourth column indicates the type of the ex-companion star for each candidate class, with ‘MS’ indicating a main sequence star. The absolute  $V$ -band magnitude ( $M_V$ ) is that of the ex-companion star after the explosion. The visual magnitude ( $V$ ) range for the ex-companion stars is for a distance modulus of 18.50 mag. A main point of this table is that the various classes of single-degenerate models all predict ex-companion star brightnesses that are 4.2 mag or more above our limit, and this is too large a gap to overcome by fading cores or stripped envelopes. We note that the single-degenerate candidate classes mix together somewhat, with recurrent novae being temporary supersoft sources, some symbiotic systems appearing as supersoft sources, some recurrent novae being also technically symbiotic systems, and models showing that the long term evolution of a supersoft source is to become a recurrent nova before exploding as an type Ia supernova. The ‘supersoft source’ progenitor class is perhaps misnamed, as these nuclear burning white dwarfs can be emitting supersoft X-rays with large or small luminosity either episodically or persistently. NA, not applicable.

<sup>1</sup>Department of Physics and Astronomy, Louisiana State University, Baton Rouge, Louisiana 70803, USA.



**Table 2 | Objects near the centre of SNR 0509–67.5**

Star	RA (h min s), dec. (° ' ")	$\theta$ (")	$V$ (mag)	$I$ (mag)	Comments
A	05 09 30.960, –67 31 16.28	1.7	$26.08 \pm 0.11$	$24.50 \pm 0.08$	Nearest to error circle
B	05 09 30.701, –67 31 18.75	1.7	$24.82 \pm 0.04$	$23.61 \pm 0.04$	...
C	05 09 30.753, –67 31 16.63	1.9	$26.30 \pm 0.13$	$24.77 \pm 0.09$	...
D	05 09 30.916, –67 31 19.91	2.0	$24.02 \pm 0.03$	$22.98 \pm 0.03$	...
E	05 09 30.660, –67 31 19.07	2.1	$23.99 \pm 0.02$	$23.05 \pm 0.03$	...
F	05 09 30.824, –67 31 16.03	2.1	$23.30 \pm 0.02$	$22.53 \pm 0.02$	...
G	05 09 31.212, –67 31 16.30	2.2	$25.36 \pm 0.06$	$23.76 \pm 0.04$	...
H	05 09 30.712, –67 31 16.01	2.5	$22.87 \pm 0.01$	$22.06 \pm 0.02$	...
I	05 09 30.581, –67 31 16.74	2.6	$26.57 \pm 0.15$	$24.72 \pm 0.08$	...
J	05 09 31.454, –67 31 17.21	2.9	$25.84 \pm 0.09$	$24.43 \pm 0.07$	...
K	05 09 30.824, –67 31 15.20	2.9	$22.55 \pm 0.01$	$21.86 \pm 0.01$	Nearest $V < 22.7$
L	05 09 31.299, –67 31 15.72	2.9	$20.56 \pm 0.01$	$20.07 \pm 0.01$	...
M	05 09 31.837, –67 31 19.61	5.2	$24.26 \pm 0.03$	$21.00 \pm 0.01$	Very red star
N	05 09 31.604, –67 31 22.54	5.8	$20.92 \pm 0.01$	$19.87 \pm 0.01$	Nearest subgiant
O	05 09 31.586, –67 31 11.49	7.4	$18.75 \pm 0.01$	$17.68 \pm 0.01$	Nearest red giant

The first column lists a letter name for each star for identification. The stars are labelled in Fig. 1 with the letter placed to the immediate right of the star. The ordering is based on radial distance from the centre of the error circle. The second column gives the position for each star; RA, right ascension; dec., declination (J2000). The third column gives the angular distance,  $\theta$ , from the centre of the error circle to the star. All stars with  $\theta < 3.0''$  are included, for the limiting magnitude of  $V = 26.9$  mag. Importantly, there are no stars within the extreme 99.73% error ellipse ( $\theta < 1.43''$ ). Three additional stars of interest with  $\theta > 3.0''$  are added. The next two columns are the  $V$  and  $I$  magnitudes (with  $1\sigma$  uncertainties), followed by a column for comments.

star does not have a Gaussian profile, so we express the allowed positions as ellipses with a 99.73% probability (that is,  $3\sigma$ ) of containing the position of the ex-companion star. As the proper motion depends on the nature of the companion, we report ellipses for red giants, subgiants and main-sequence stars. Second, for SNR 0509–67.5 in particular, the shell expansion is uniform in all directions except for one quadrant where the interstellar medium is more dense (as shown by the excess 24- $\mu\text{m}$  emission seen in the Spitzer image<sup>27</sup> from pre-existing dust swept up by the shell) and so the expansion has recently slowed down<sup>28</sup>. This slowing in only one quadrant accounts for the small observed ellipticity of the shell, from which we can derive the apparent offset ( $1.39'' \pm 0.14''$  along a line  $18^\circ \pm 3^\circ$  south of west) between the observed geometric centre of the shell and the site of the supernova explosion. Last, our derived best estimate for the site of the explosion is right ascension 05 h 09 min 30.976 s, declination  $-67^\circ 31' 17.90''$  (J2000). The error ellipse is nearly circular, with a conservative radius of  $1.43''$  for a maximal proper motion ( $390 \text{ km s}^{-1}$ ), a maximal age for the remnant (550 years) and for 99.73% ( $3\sigma$ ) containment. (See Supplementary Information section 3 for details.)

The error circle is completely empty of all visible point sources down to the deep limits of HST. Importantly, there are no red giant or subgiant stars in or near the circle. (Red giants and subgiants can be confidently recognized by their position above the main sequence in the colour–magnitude diagram.) The nearest red giant (star O in Fig. 1) is  $7.4''$  from the centre, while the nearest subgiant star (star N) is  $5.8''$  from the centre. The nearest star brighter than  $V = 22.7$  mag (star K), that is, the nearest possible ex-companion of any type, is  $2.9''$  from the centre. The only source in the circle is an extended faint nebula, and the excellent angular resolution of the HST allows us to see that no point source is hidden within the nebula. (This nebula is

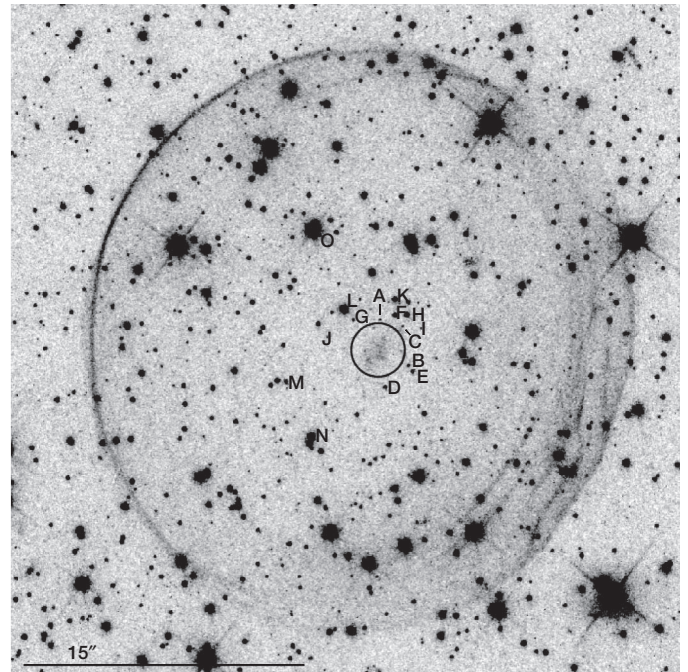


**Figure 1 | SNR 0509–67.5 and the extreme 99.73% error circle.** This is a composite HST image: the  $H\alpha$  image was taken with the WFC2 over three orbits in November 2007 with a total of 5,000 s of exposure; the B, V and I images were taken with the WFC3 over two orbits in November 2010 with 1,010, 696 and 800 s exposure, respectively. North is up and east is to the left. These HST data were processed and combined with standard PYRAF and IRAF procedures. The figure shows a combination of all four filters, with the remarkably smooth  $H\alpha$  shell visible. The error circle (solid line, at centre of image; with  $1.43''$  radius) is the extreme 99.73% region ( $3\sigma$ ), where to be on the edge the ex-companion star must be a main sequence star with the minimum possible mass for any published model ( $1.16$  solar masses), the velocity must be entirely perpendicular to the line of sight, the age of the supernova remnant must be pushed to the  $3\sigma$  highest possible value (550 years), and the measurement error for the remnant's geometric centre must be pushed to the  $3\sigma$  extreme. The only source inside the error circle is a nebulous object that looks like a background galaxy, however the location of this object at the centre suggests it might be related to the supernova event (see Supplementary Information section 4). There are no stars within the extreme error circle to  $V = 26.9$  mag, which corresponds to an absolute magnitude of  $M_V = +8.4$  mag in the LMC. All published models for single-degenerate progenitors have the ex-companion star appearing more luminous than  $M_V = +4.2$  mag ( $V = 22.7$  mag in the LMC). In all, our extreme 99.73% error circle is very conservative, and there is no point source to limits  $4.2$  mag deeper than possible for any published model of single-degenerate systems.

probably an irregular galaxy of moderate redshift, but the coincidence of this nebula with the site of the supernova suggests that its origin might be associated with the explosion, as discussed in Supplementary Information section 4.) The error circle is empty of point sources to a limiting magnitude of  $V = 26.9$  mag (at the  $5\sigma$  level). This requires that any ex-companion be less luminous than  $M_V = +8.4$  mag.

Our new limit can be compared to the expected presence of ex-companion stars for the various single-degenerate models (see Table 1). There is no red giant star in or near the error circle, and this is strongly inconsistent with the symbiotic progenitor model. There is no red giant or sub-giant star in or near the error circle, and this is strongly inconsistent with the recurrent nova, helium star and spin-up/spin-down progenitor models. There is no star brighter than  $V = 22.7$  mag in or near the error circle, and this is strongly inconsistent with the supersoft source progenitor model. The lack of any possible ex-companion star to  $M_V = +8.4$  mag rules out all published single-degenerate progenitor models. With all single-degenerate models eliminated, the only remaining progenitor model for SNR 0509–67.5 is the double-degenerate model.

Received 29 June; accepted 31 October 2011.

1. Branch, D., Livio, M., Yungelson, L. R., Boffi, F. R. & Baron, E. In search of the progenitors of type Ia supernova. *Publ. Astron. Soc. Pacif.* **107**, 1019–1029 (1995).
2. Webbink, R. F. Double white dwarfs as progenitors of R Coronae Borealis stars and type I supernovae. *Astrophys. J.* **277**, 355–360 (1984).
3. van Kerkwijk, M. H., Chang, P. & Justham, S. Sub-Chandrasekhar white dwarf mergers as the progenitors of type Ia supernovae. *Astrophys. J.* **722**, L157–L161 (2010).
4. Iben, I. & Tutukov, A. V. Supernovae of type I as end products of the evolution of binaries with components of moderate initial mass ( $M \leq 9M_{\odot}$ ). *Astrophys. J. Suppl. Ser.* **54**, 335–372 (1984).
5. Whelan, J. & Iben, I. Binaries and supernovae of type I. *Astrophys. J.* **186**, 1007–1014 (1973).
6. Gilfanov, M. & Bogdan, A. An upper limit on the contribution of accreting white dwarfs to the type Ia supernova rate. *Nature* **463**, 924–925 (2010).
7. Meng, X.-C. & Yang, W.-M. Binary population synthesis study of the supersoft X-ray phase of single degenerate type Ia supernova progenitors. *Res. Astron. Astrophys.* **11**, 965–973 (2011).
8. Di Stefano, R. The progenitors of type Ia supernovae. II. Are they double-degenerate binaries? The symbiotic channel. *Astrophys. J.* **719**, 474–482 (2010).
9. Hachisu, I., Kato, M. & Nomoto, K. Supersoft X-ray phase of single degenerate type Ia supernova progenitors in early-type galaxies. *Astrophys. J.* **724**, L212–L216 (2010).
10. Lipunov, V. M., Panchenko, I. E. & Pruzhinskaya, M. V. The mechanism of supernova Ia explosions in elliptical galaxies. *N. Astron.* **16**, 250–252 (2011).
11. Orio, M., Nelson, T., Bianchini, A., Di Mille, F. & Harbeck, D. A census of the supersoft X-ray sources in M31. *Astrophys. J.* **717**, 739–765 (2010).
12. Ruiz-Lapuente, P. The quest for a supernova companion. *Science* **276**, 1813–1814 (1997).
13. Canal, R., Mendez, J. & Ruiz-Lapuente, P. Identification of the companion stars of type Ia supernovae. *Astrophys. J.* **550**, L53–L56 (2001).
14. Ruiz-Lapuente, P. *et al.* The binary progenitor of Tycho Brahe's 1572 supernova. *Nature* **431**, 1069–1072 (2004).
15. Kerzendorf, W. E. *et al.* Subaru high-resolution spectroscopy of star G in the Tycho supernova remnant. *Astrophys. J.* **701**, 1665–1672 (2009).
16. Ozaki, J. & Shigeyama, T. A method to identify the companion stars of type Ia supernovae in young supernova remnants. *Astrophys. J.* **644**, 954–958 (2006).
17. Ihara, Y. *et al.* Searching for a companion star of Tycho's type Ia supernova with optical spectroscopic observations. *Publ. Astron. Soc. Jpn* **59**, 811–826 (2007).
18. Gonzalez Hernandez, J. I. *et al.* The chemical abundances of Tycho G in supernova remnant 1572. *Astrophys. J.* **691**, 1–15 (2009).
19. Rest, A. *et al.* Light echoes from ancient supernovae in the Large Magellanic Cloud. *Nature* **438**, 1132–1134 (2005).
20. Rest, A. *et al.* Spectral identification of an ancient supernova using light echoes in the Large Magellanic Cloud. *Astrophys. J.* **680**, 1137–1148 (2008).
21. Mannucci, F., Della Valle, M. & Panagia, N. Two populations of progenitors for type Ia supernovae? *Mon. Not. R. Astron. Soc.* **370**, 773–783 (2006).
22. Marietta, E., Burrows, A. & Fryxell, B. Type Ia supernova explosions in binary systems: the impact on the secondary star and its consequences. *Astrophys. J. Suppl. Ser.* **128**, 615–650 (2000).
23. Pan, K.-C., Ricker, P. & Taam, R. E. Impact of type Ia supernova ejecta on a helium-star binary companion. *Astrophys. J.* **715**, 78–85 (2010).
24. Podsiadlowski, P. On the evolution and appearance of a surviving companion after a type Ia supernova explosions. Preprint at (<http://arXiv.org/abs/astro-ph/0303660>) (2003).
25. Hughes, J. P. *et al.* ASCA observations of the Large Magellanic Cloud supernova remnant sample: typing supernovae from their remnants. *Astrophys. J.* **444**, L81–L84 (1995).
26. Badenes, C., Harris, J., Zaritsky, D. & Prieto, J. L. The stellar ancestry of supernovae in the Magellanic Clouds – I. The most recent supernovae in the Large Magellanic Cloud. *Astrophys. J.* **700**, 727–740 (2009).
27. Borkowski, K. J. *et al.* Dust destruction in type Ia supernovae remnants in the Large Magellanic Cloud. *Astrophys. J.* **642**, L141–L144 (2006).
28. Helder, E. A., Kosenko, D. & Vink, J. Cosmic-ray acceleration efficiency versus temperature equilibration: the case of SNR 0509–67.5. *Astrophys. J.* **719**, L140–L144 (2010).

**Supplementary Information** is linked to the online version of the paper at [www.nature.com/nature](http://www.nature.com/nature).

**Acknowledgements** The HST images were taken as part of two programmes with Principal Investigators J. P. Hughes and K. Noll. This work was supported by the National Science Foundation.

**Author Contributions** The authors shared the ideas, the data analysis, and the writing of this paper.

**Author Information** HST images comprising Fig. 1 are in the public domain (<http://heritage.stsci.edu/2010/27/index.html>, <http://apod.nasa.gov/apod/ap110125.html>). Reprints and permissions information is available at [www.nature.com/reprints](http://www.nature.com/reprints). The authors declare no competing financial interests. Readers are welcome to comment on the online version of this article at [www.nature.com/nature](http://www.nature.com/nature). Correspondence and requests for materials should be addressed to B.E.S. ([schaefer@lsu.edu](mailto:schaefer@lsu.edu)).



# One or more bound planets per Milky Way star from microlensing observations

A. Cassan<sup>1,2,3</sup>, D. Kubas<sup>1,2,4</sup>, J.-P. Beaulieu<sup>1,2,5</sup>, M. Dominik<sup>1,5</sup>, K. Horne<sup>1,5</sup>, J. Greenhill<sup>1,6</sup>, J. Wambsganss<sup>1,3</sup>, J. Menzies<sup>1,7</sup>, A. Williams<sup>1,8</sup>, U. G. Jørgensen<sup>1,9</sup>, A. Udalski<sup>10,11</sup>, D. P. Bennett<sup>1,12</sup>, M. D. Albrow<sup>1,13</sup>, V. Batista<sup>1,2</sup>, S. Brilant<sup>1,4</sup>, J. A. R. Caldwell<sup>1,14</sup>, A. Cole<sup>1,6</sup>, Ch. Coutures<sup>1,2</sup>, K. H. Cook<sup>1,15</sup>, S. Dieters<sup>1,6</sup>, D. Dominis Prester<sup>1,16</sup>, J. Donatowicz<sup>1,17</sup>, P. Fouqué<sup>1,18</sup>, K. Hill<sup>1,6</sup>, N. Kains<sup>1,19</sup>, S. Kane<sup>1,20</sup>, J.-B. Marquette<sup>1,2</sup>, R. Martin<sup>1,8</sup>, K. R. Pollard<sup>1,13</sup>, K. C. Sahu<sup>1,14</sup>, C. Vinter<sup>1,9</sup>, D. Warren<sup>1,6</sup>, B. Watson<sup>1,6</sup>, M. Zub<sup>1,3</sup>, T. Sumi<sup>21,22</sup>, M. K. Szymański<sup>10,11</sup>, M. Kubiak<sup>10,11</sup>, R. Poleski<sup>10,11</sup>, I. Soszynski<sup>10,11</sup>, K. Ulaczyk<sup>10,11</sup>, G. Pietrzyński<sup>10,11,23</sup> & L. Wyrzykowski<sup>10,11,24</sup>

Most known extrasolar planets (exoplanets) have been discovered using the radial velocity<sup>1,2</sup> or transit<sup>3</sup> methods. Both are biased towards planets that are relatively close to their parent stars, and studies find that around 17–30% (refs 4, 5) of solar-like stars host a planet. Gravitational microlensing<sup>6–9</sup>, on the other hand, probes planets that are further away from their stars. Recently, a population of planets that are unbound or very far from their stars was discovered by microlensing<sup>10</sup>. These planets are at least as numerous as the stars in the Milky Way<sup>10</sup>. Here we report a statistical analysis of microlensing data (gathered in 2002–07) that reveals the fraction of bound planets 0.5–10 AU (Sun–Earth distance) from their stars. We find that  $17_{-9}^{+6}\%$  of stars host Jupiter-mass planets ( $0.3\text{--}10 M_J$ , where  $M_J = 318 M_\oplus$  and  $M_\oplus$  is Earth's mass). Cool Neptunes ( $10\text{--}30 M_\oplus$ ) and super-Earths ( $5\text{--}10 M_\oplus$ ) are even more common: their respective abundances per star are  $52_{-29}^{+22}\%$  and  $62_{-37}^{+35}\%$ . We conclude that stars are orbited by planets as a rule, rather than the exception.

Gravitational microlensing is very rare: fewer than one star per million undergoes a microlensing effect at any time. Until now, the planet-search strategy<sup>7</sup> has been mainly split into two levels. First, wide-field survey campaigns such as the Optical Gravitational Lensing Experiment (OGLE; ref. 11) and Microlensing Observations in Astrophysics (MOA; ref. 12) cover millions of stars every clear night to identify and alert the community to newly discovered stellar microlensing events as early as possible. Then, follow-up collaborations such as the Probing Lensing Anomalies Network (PLANET; ref. 13) and the Microlensing Follow-Up Network ( $\mu$ FUN; refs 14, 15) monitor selected candidates at a very high rate to search for very short-lived light curve anomalies, using global networks of telescopes.

To ease the detection-efficiency calculation, the observing strategy should remain homogeneous for the time span considered in the analysis. As detailed in the Supplementary Information, this condition is fulfilled for microlensing events identified by OGLE and followed up by PLANET in the six-year time span 2002–07. Although a number of microlensing planets were detected by the various collaborations between 2002 and 2007 (Fig. 1), only a subset of them are consistent

with the PLANET 2002–07 strategy. This leaves us with three compatible detections: OGLE 2005-BLG-071Lb (refs 16, 17) a Jupiter-like planet of mass  $M \approx 3.8 M_J$  and semi-major axis  $a \approx 3.6$  AU; OGLE 2007-BLG-349Lb (ref. 18), a Neptune-like planet ( $M \approx 0.2 M_J$ ,  $a \approx 3$  AU); and the

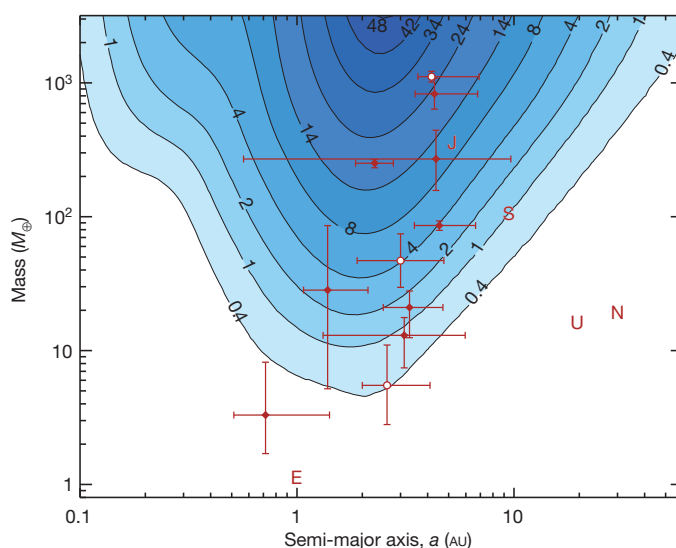


**Figure 1 | Survey-sensitivity diagram.** Blue contours, expected number of detections from our survey if all lens stars have exactly one planet with orbit size  $a$  and mass  $M$ . Red points, all microlensing planet detections in the time span 2002–07, with error bars (s.d.) reported from the literature. White points, planets consistent with PLANET observing strategy. Red letters, planets of our Solar System, marked for comparison: E, Earth; J, Jupiter; S, Saturn; U, Uranus; N, Neptune. This diagram shows that the sensitivity of our survey extends roughly from 0.5 AU to 10 AU for planetary orbits, and from  $5 M_\oplus$  to  $10 M_J$ . The majority of all detected planets have masses below that of Saturn, although the sensitivity of the survey is much lower for such planets than for more massive, Jupiter-like planets. Low-mass planets are thus found to be much more common than giant planets.

<sup>1</sup>Probing Lensing Anomalies Network (PLANET) Collaboration, Institut d'Astrophysique de Paris, Université Pierre & Marie Curie, UMR7095 UPMC-CNRS 98 bis boulevard Arago, 75014 Paris, France.

<sup>2</sup>Institut d'Astrophysique de Paris, Université Pierre & Marie Curie, UMR7095 UPMC-CNRS 98 bis boulevard Arago, 75014 Paris, France. <sup>3</sup>Astronomischen Rechen-Institut (ARI), Zentrum für Astronomie, Heidelberg University, Mönchhofstrasse 12–14, 69120 Heidelberg, Germany. <sup>4</sup>European Southern Observatory, Alonso de Cordoba 3107, Vitacura, Casilla 19001, Santiago, Chile. <sup>5</sup>Scottish Universities Physics Alliance (SUPA), University of St Andrews, School of Physics & Astronomy, North Haugh, St Andrews, KY16 9SS, UK. <sup>6</sup>University of Tasmania, School of Maths and Physics, Private bag 37, GPO Hobart, Tasmania 7001, Australia. <sup>7</sup>South African Astronomical Observatory, PO Box 9 Observatory 7935, South Africa. <sup>8</sup>Perth Observatory, Walnut Road, Bickley, Perth 6076, Australia. <sup>9</sup>Niels Bohr Institute and Centre for Star and Planet Formation, Juliane Mariesvej 30, 2100 Copenhagen, Denmark. <sup>10</sup>Optical Gravitational Lensing Experiment (OGLE) Collaboration, Warsaw University Observatory, Al. Ujazdowskie 4, 00-478 Warszawa, Poland. <sup>11</sup>Warsaw University Observatory, Al. Ujazdowskie 4, 00-478 Warszawa, Poland. <sup>12</sup>University of Notre Dame, Physics Department, 225 Nieuwland Science Hall, Notre Dame, Indiana 46530, USA. <sup>13</sup>University of Canterbury, Department of Physics & Astronomy, Private Bag 4800, Christchurch 8140, New Zealand. <sup>14</sup>Space Telescope Science Institute, 3700 San Martin Drive, Baltimore, Maryland 21218, USA. <sup>15</sup>Institute of Geophysics and Planetary Physics, Lawrence Livermore National Laboratory, PO Box 808, California 94550, USA. <sup>16</sup>Department of Physics, University of Rijeka, Omladinska 14, 51000 Rijeka, Croatia. <sup>17</sup>Technical University of Vienna, Department of Computing, Wiedner Hauptstrasse 10, 1040 Vienna, Austria. <sup>18</sup>Laboratoire Astrophysique de Toulouse (LATT), Université de Toulouse, CNRS, 31400 Toulouse, France. <sup>19</sup>European Southern Observatory Headquarters, Karl-Schwarzschild-Strasse 2, 85748 Garching, Germany. <sup>20</sup>NASA Exoplanet Science Institute, Caltech, MS 100-22, 770 South Wilson Avenue, Pasadena, California 91125, USA. <sup>21</sup>Microlensing Observations in Astrophysics (MOA) Collaboration, Department of Earth and Space Science, Osaka University, Osaka 560-0043, Japan. <sup>22</sup>Department of Earth and Space Science, Osaka University, Osaka 560-0043, Japan. <sup>23</sup>Universidad de Concepción, Departamento de Física, Casilla 160-C, Concepción, Chile. <sup>24</sup>Institute of Astronomy, University of Cambridge, Madingley Road, Cambridge CB3 0HA, UK. <sup>25</sup>Department of Physics and Astronomy, University College London, Gower Street, London WC1E 6BT, UK.

super-Earth planet OGLE 2005-BLG-390Lb (refs 19, 20;  $M \approx 5.5 M_{\oplus}$ ,  $a \approx 2.6$  AU).

To compute the detection efficiency for the 2002–07 PLANET seasons, we selected a catalogue of unperturbed (that is, single-lens-like) microlensing events using a standard procedure<sup>21</sup>, as explained in the Supplementary Information. For each light curve, we defined the planet-detection efficiency  $\varepsilon(\log d, \log q)$  as the probability that a detectable planet signal would arise if the lens star had one companion planet, with mass ratio  $q$  and projected orbital separation  $d$  (in Einstein-ring radius units; ref. 22). The efficiency was then transformed<sup>23</sup> to  $\varepsilon(\log a, \log M)$ . The survey sensitivity  $S(\log a, \log M)$  was obtained by summing the detection efficiencies over all individual microlensing events. It provided the number of planets that our survey would expect to detect if all lens stars had exactly one planet of mass  $M$  and semi-major axis  $a$ .

We used 2004 as a representative season from the PLANET survey. Among the 98 events monitored, 43 met our quality-control criteria and were processed<sup>24</sup>. Most of the efficiency comes from the 26 most densely covered light curves, which provide a representative and reliable sub-sample of events. We then computed the survey sensitivity for the whole time span 2002–07 by weighting each observing season relative to 2004, according to the number of events observed by PLANET for different ranges of peak magnification. This is described in the Supplementary Information, and illustrated in Supplementary Fig. 2. The resulting planet sensitivity is plotted in blue in Fig. 1, where the labelled contours show the corresponding expected number of detections. The figure shows that the core sensitivity covers 0.5–10 AU for masses between those of Uranus/Neptune and ten times the mass of Jupiter, and extends (with limited sensitivity) down to about  $5 M_{\oplus}$ . As inherent to the microlensing technique, our sample of event-host stars probes the natural mass distribution of stars in the Milky Way (K–M dwarfs), in the typical mass range of  $0.14$ – $1.0 M_{\odot}$  (see Supplementary Fig. 3).

To derive the actual abundance of exoplanets from our survey, we proceeded as follows. Let the planetary mass function,  $f(\log a, \log M) \equiv dN/(d\log a \times d\log M)$ , where  $N$  is the average number of planets per star. We then integrate the product  $f(\log a, \log M) S(\log a, \log M)$  over  $\log a$  and  $\log M$ . This gives  $E(f)$ , the number of detections we can expect from our survey. For  $k$  (fractional) detections, the model then predicts a Poisson probability distribution  $P(k|E) = e^{-E} E^k / k!$ . A Bayesian analysis assuming an uninformative uniform prior  $P(\log f) \equiv 1$  finally yields the probability distribution  $P(\log f|k)$  that is used to constrain the planetary mass function.

Although our derived planet-detection sensitivity extends over almost three orders of magnitude of planet masses (roughly  $5 M_{\oplus}$  to  $10 M_J$ ), it covers fewer than 1.5 orders of magnitude in orbit sizes (0.5–10 AU), thus providing little information about the dependence of  $f$  on  $a$ . Within these limits, however, we find that the mass function is approximately consistent with a flat distribution in  $\log a$  (that is,  $f$  does not explicitly depend on  $a$ ). The planet-detection sensitivity integrated over  $\log a$ , or  $S(\log M)$ , is displayed in Fig. 2b. The distribution probabilities of the mass for the three detections (computed according to the mass-error bars reported in the literature) are plotted in Fig. 2c (black curves), as is their sum (red curve).

To study the dependence of  $f$  on mass, we assume that to the first order,  $f$  is well-approximated by a power-law model:  $f = f_0 (M/M_0)^{\alpha}$ , where  $f_0$  (the normalization factor) and  $\alpha$  (the slope of the power-law) are the parameters to be derived and  $M_0$  a fiducial mass (in practice, the pivot point of the mass function). Previous works<sup>18,25–27</sup> on planet frequency have demonstrated that a power law provides a fair description of the global behaviour of  $f$  with planetary mass. Apart from the constraint based on our PLANET data, we also made use in our analysis of the previous constraints obtained by microlensing: an estimate of the normalization<sup>18</sup>  $f_0 (0.36 \pm 0.15)$  and an estimate of the slope<sup>25</sup>  $\alpha (-0.68 \pm 0.2)$ , displayed respectively as the blue point and the blue lines in Fig. 2. The new constraint presented here therefore relies on

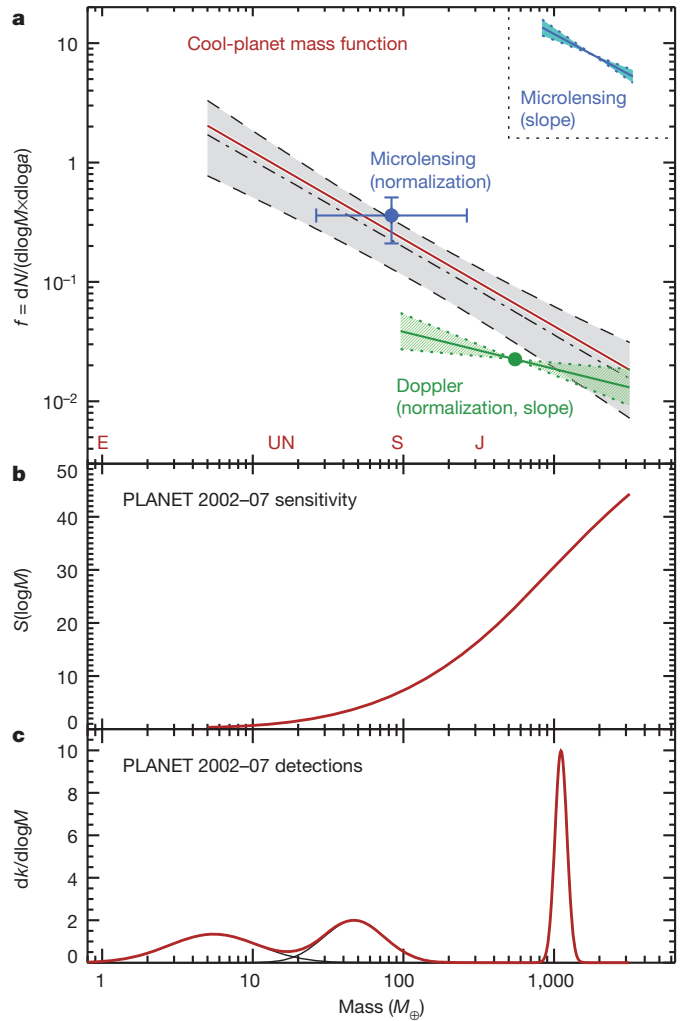


**Figure 2 | Cool-planet mass function.** **a**, The cool-planet mass function,  $f$ , for the orbital range 0.5–10 AU as derived by microlensing. Red solid line, best fit for this study, based on combining the results from PLANET 2002–07 and previous microlensing estimates<sup>18,25</sup> for slope (blue line; error, light-blue shaded area, s.d.) and normalization (blue point; error bars, s.d.). We find  $dN/(d\log a d\log M) = 10^{-0.62 \pm 0.22} (M/M_{\text{Sat}})^{0.73 \pm 0.17}$ , where  $N$  is the average number of planets per star,  $a$  the semi-major axis and  $M$  the planet mass. The pivot point of the power-law mass function is at the mass of Saturn ( $M_{\text{Sat}} = 95 M_{\oplus}$ ). The grey shaded area is the 68% confidence interval around the median (dash-dotted black line). For comparison, the constraint from Doppler measurements<sup>27</sup> (green line and point; error, green shaded area, s.d.) is also displayed. Differences can arise because the Doppler technique focuses mostly on solar-like stars, whereas microlensing a priori probes all types of host stars. Moreover, microlensing planets are located further away from their stars and are cooler than Doppler planets. These two populations of planets may then follow a rather different mass function. **b**, PLANET 2002–07 sensitivity,  $S$ : the expected number of detections if all stars had exactly one planet, regardless of its orbit. **c**, PLANET 2002–07 detections,  $k$ . Thin black curves, distribution probabilities of the mass for the three detections contained in the PLANET sample; red line, the sum of these distributions.

10 planet detections. We obtained  $f = 10^{-0.62 \pm 0.22} (M/M_0)^{-0.73 \pm 0.17}$  (red line in Fig. 2a) with a pivot point at  $M_0 \approx 95 M_{\oplus}$ ; that is, at Saturn's mass. The median of  $f$  and the 68% confidence interval around the median are marked by the dashed lines and the grey area.

Hence, microlensing delivers a determination of the full planetary mass function of cool planets in the separation range 0.5–10 AU. Our measurements confirm that low-mass planets are very common, and that the number of planets increases with decreasing planet mass, in agreement with the predictions of the core-accretion theory of planet formation<sup>28</sup>. The first microlensing study of the abundances of cool gas



giants<sup>21</sup> found that fewer than 33% of M dwarfs have a Jupiter-like planet between 1.5–4 AU, and even lower limits of 18% have been reported<sup>29,30</sup>. These limits are compatible with our measurement of  $5^{+2}_{-2}\%$  for masses ranging from Saturn to 10 times Jupiter, in the same orbit range.

From our derived planetary mass function, we estimate that within 0.5–10 AU (that is, for a wider range of orbital separations than previous studies), on average  $17^{+6}_{-9}\%$  of stars host a 'Jupiter' ( $0.3\text{--}10 M_J$ ) and  $52^{+22}_{-29}\%$  of stars host Neptune-like planets ( $10\text{--}30 M_{\oplus}$ ). Taking the full range of planets that our survey can detect ( $0.5\text{--}10\text{ AU}$ ,  $5 M_{\oplus}$  to  $10 M_J$ ), we find that on average every star has  $1.6^{+0.72}_{-0.89}$  planets. This result is consistent with every star of the Milky Way hosting (on average) one planet or more in an orbital-distance range of 0.5–10 AU. Planets around stars in our Galaxy thus seem to be the rule rather than the exception.

Received 19 January; accepted 28 October 2011.

- Mayor, M. & Queloz, D. A. Jupiter-mass companion to a solar-type star. *Nature* **378**, 355–359 (1995).
- Marcy, G. W. & Butler, R. P. A planetary companion to 70 Virginis. *Astrophys. J.* **464**, L147–L151 (1996).
- Charbonneau, D., Brown, T. M., Latham, D. W. & Mayor, M. Detection of planetary transits across a Sun-like star. *Astrophys. J.* **529**, L45–L48 (2000).
- Howard, A. *et al.* Planet occurrence within 0.25 AU of Solar-type stars from Kepler. *Astrophys. J.* (submitted); preprint at <http://arxiv.org/abs/1103.2541> (2011).
- Mayor, M. *et al.* The HARPS search for southern extra-solar planets XXXIV. Occurrence, mass distribution and orbital properties of super-Earths and Neptune-mass planets. *Astron. Astrophys.* (submitted); preprint at <http://arxiv.org/abs/1109.2497> (2011).
- Mao, S. & Paczynski, B. Gravitational microlensing by double stars and planetary systems. *Astrophys. J.* **374**, L37–L40 (1991).
- Gould, A. & Loeb, A. Discovering planetary systems through gravitational microlenses. *Astrophys. J.* **396**, 104–114 (1992).
- Bennett, D. P. & Rhie, S. H. Detecting Earth-mass planets with gravitational microlensing. *Astrophys. J.* **472**, 660–664 (1996).
- Wambsganss, J. Discovering Galactic planets by gravitational microlensing: magnification patterns and light curves. *Mon. Not. R. Astron. Soc.* **284**, 172–188 (1997).
- Sumi, T. *et al.* Unbound or distant planetary mass population detected by gravitational microlensing. *Nature* **473**, 349–352 (2011).
- Udalski, A. The Optical Gravitational Lensing Experiment. Real time data analysis systems in the OGLE-III survey. *Acta Astronaut.* **53**, 291–305 (2003).
- Bond, I. A. *et al.* Real-time difference imaging analysis of MOA Galactic bulge observations during 2000. *Mon. Not. R. Astron. Soc.* **327**, 868–880 (2001).
- Albrow, M. *et al.* The 1995 pilot campaign of PLANET: searching for microlensing anomalies through precise, rapid, round-the-clock monitoring. *Astrophys. J.* **509**, 687–702 (1998).
- Gould, A. *et al.* Microlens OGLE-2005-BLG-169 implies that cool Neptune-like planets are common. *Astrophys. J.* **644**, L37–L40 (2006).
- Gaudi, B. S. *et al.* Discovery of a Jupiter/Saturn analog with gravitational microlensing. *Science* **319**, 927–930 (2008).
- Udalski, A. *et al.* A Jovian-mass planet in microlensing event OGLE-2005-BLG-071. *Astrophys. J.* **628**, L109–L112 (2005).
- Dong, S. *et al.* OGLE-2005-BLG-071Lb, the most massive M dwarf planetary companion? *Astrophys. J.* **695**, 970–987 (2009).
- Gould, A. *et al.* Frequency of solar-like systems and of ice and gas giants beyond the snow line from high-magnification microlensing events in 2005–2008. *Astrophys. J.* **720**, 1073–1089 (2010).
- Beaulieu, J.-P. *et al.* Discovery of a cool planet of 5.5 Earth masses through gravitational microlensing. *Nature* **439**, 437–440 (2006).
- Kubas, D. *et al.* Limits on additional planetary companions to OGLE 2005-BLG-390L. *Astron. Astrophys.* **483**, 317–324 (2008).
- Gaudi, B. S. *et al.* Microlensing constraints on the frequency of Jupiter-mass companions: analysis of 5 years of PLANET photometry. *Astrophys. J.* **566**, 463–499 (2002).
- Einstein, A. Lens-like action of a star by the deviation of light in the gravitational field. *Science* **84**, 506–507 (1936).
- Dominik, M. Stochastic distributions of lens and source properties for observed galactic microlensing events. *Mon. Not. R. Astron. Soc.* **367**, 669–692 (2006).
- Cassan, A. An alternative parameterisation for binary-lens caustic-crossing events. *Astron. Astrophys.* **491**, 587–595 (2008).
- Sumi, T. *et al.* A cold Neptune-mass planet OGLE-2007-BLG-368Lb: cold Neptunes are common. *Astrophys. J.* **710**, 1641–1653 (2010).
- Howard, A. W. *et al.* The occurrence and mass distribution of close-in super-Earths, Neptunes, and Jupiters. *Science* **330**, 653–655 (2010).
- Cumming, A. *et al.* The Keck Planet Search: Detectability and the minimum mass and orbital period distribution of extrasolar planets. *Publ. Astron. Soc. Pacif.* **120**, 531–554 (2008).
- Pollack, J. B. *et al.* Formation of the giant planets by concurrent accretion of solids and gas. *Icarus* **124**, 62–85 (1996).
- Tsapras, Y. *et al.* Microlensing limits on numbers and orbits of extrasolar planets from the 1998–2000 OGLE events. *Mon. Not. R. Astron. Soc.* **343**, 1131–1144 (2003).
- Snodgrass, C. *et al.* The abundance of Galactic planets from OGLE-III 2002 microlensing data. *Mon. Not. R. Astron. Soc.* **351**, 967–975 (2004).

**Supplementary Information** is linked to the online version of the paper at [www.nature.com/nature](http://www.nature.com/nature).

**Acknowledgements** Support for the PLANET project was provided by the HOLMES grant from the French Agence Nationale de la Recherche (ANR), the French National Centre for Scientific Research (CNRS), NASA, the US National Science Foundation, the Lawrence Livermore National Laboratory/National Nuclear Security Administration/Department of Energy, the French National Programme of Planetology, the Program of International Cooperation in Science France–Australia, D. Warren, the German Research Foundation, the Instrument Center for Danish Astronomy and the Danish Natural Science Research Council. The OGLE collaboration is grateful for funding from the European Research Council Advanced Grants Program. K.Ho. acknowledges support from the Qatar National Research Fund. M.D. is a Royal Society University Research Fellow.

**Author Contributions** A.Ca. led the analysis and conducted the modelling and statistical analyses. A.Ca. and D.K. selected light curves from 2002–07 PLANET/OGLE microlensing seasons, analysed the data and wrote the Letter and Supplement. D.K. computed the magnification maps used for the detection-efficiency calculations. J.-P.B. and Ch.C. wrote the software for online data reduction at the telescopes. J.-P.B. led the PLANET collaboration, with M.D., J.G., J.M. and A.W.; P.F. and M.D.A. contributed to online and offline data reduction. M.D. contributed to the conversion of the detection efficiencies to physical parameter space and developed the PLANET real-time display system with A.W., M.D.A. and Ch.C.; K.Ho. and A.Ca. developed and tested the Bayesian formulation for fitting the two-parameter power-law mass function. J.G. edited the manuscript, conducted the main data cleaning and managed telescope operations at Mount Canopus (1 m) in Hobart. J.W. wrote the original magnification maps software, discussed the main implications and edited the manuscript. J.M., A.W. and U.G.J. respectively managed telescope operations in South Africa (South African Astronomical Observatory 1 m), Australia (Perth 0.61 m) and La Silla (Danish 1.54 m). A.U. led the OGLE campaign and provided the final OGLE photometry. D.P.B., V.B., S.B., J.A.R.C., A.Co., K.H.C., S.D., D.D.P., J.D., P.F., K.Hi., N.K., S.K., J.-B.M., R.M., K.R.P., K.C.S., C.V., D.W., B.W. and M.Z. were involved in the PLANET observing strategy and/or PLANET data acquisition, reduction, real-time analysis and/or commented on the manuscript. T.S. commented on the manuscript. M.K.S., M.K., R.P., I.S., K.U., G.P. and Ł.W. contributed to OGLE data.

**Author Information** Reprints and permissions information is available at [www.nature.com/reprints](http://www.nature.com/reprints). The authors declare no competing financial interests. Readers are welcome to comment on the online version of this article at [www.nature.com/nature](http://www.nature.com/nature). Correspondence and requests for materials should be addressed to A.C. ([cassan@iap.fr](mailto:cassan@iap.fr)).

# Implementation of a Toffoli gate with superconducting circuits

A. Fedorov<sup>1</sup>, L. Steffen<sup>1</sup>, M. Baur<sup>1</sup>, M. P. da Silva<sup>2,3</sup> & A. Wallraff<sup>1</sup>

The Toffoli gate is a three-quantum-bit (three-qubit) operation that inverts the state of a target qubit conditioned on the state of two control qubits. It makes universal reversible classical computation<sup>1</sup> possible and, together with a Hadamard gate<sup>2</sup>, forms a universal set of gates in quantum computation. It is also a key element in quantum error correction schemes<sup>3–7</sup>. The Toffoli gate has been implemented in nuclear magnetic resonance<sup>3</sup>, linear optics<sup>8</sup> and ion trap systems<sup>9</sup>. Experiments with superconducting qubits have also shown significant progress recently: two-qubit algorithms<sup>10</sup> and two-qubit process tomography have been implemented<sup>11</sup>, three-qubit entangled states have been prepared<sup>12,13</sup>, first steps towards quantum teleportation have been taken<sup>14</sup> and work on quantum computing architectures has been done<sup>15</sup>. Implementation of the Toffoli gate with only single- and two-qubit gates requires six controlled-NOT gates and ten single-qubit operations<sup>16</sup>, and has not been realized in any system owing to current limits on coherence. Here we implement a Toffoli gate with three superconducting transmon qubits coupled to a microwave resonator. By exploiting the third energy level of the transmon qubits, we have significantly reduced the number of elementary gates needed for the implementation of the Toffoli gate, relative to that required in theoretical proposals using only two-level systems. Using full process tomography and Monte Carlo process certification, we completely characterize the Toffoli gate acting on three independent qubits, measuring a fidelity of  $68.5 \pm 0.5$  per cent. A similar approach<sup>15</sup> to realizing characteristic features of a Toffoli-class gate has been demonstrated with two qubits and a resonator and achieved a limited characterization considering only the phase fidelity. Our results reinforce the potential of macroscopic superconducting qubits for the implementation of complex quantum operations with the possibility of quantum error correction<sup>17</sup>.

We have implemented a Toffoli gate with three transmon qubits (A, B and C) dispersively coupled to a microwave transmission-line resonator, in a sample that is identical to the one used in ref. 14. The resonator is used for joint three-qubit read-out by measuring its transmission<sup>18</sup>. At the same time, it serves as a coupling bus for the qubits<sup>19</sup>. The qubits have a ladder-type energy level structure with sufficient anharmonicity to allow individual microwave addressing of different transitions. We use the first two energy levels as the computational qubit states,  $|0\rangle$  and  $|1\rangle$ , and use the second excited state,  $|2\rangle$ , to perform two-qubit and qubit-qutrit operations (a qutrit is a quantum ternary digit). From spectroscopy, we deduce a bare resonator frequency  $\nu_r = 8.625$  GHz with a quality factor of 3,300; maximum qubit transition frequencies  $\nu_A^{\max} = 6.714$  GHz,  $\nu_B^{\max} = 6.050$  GHz and  $\nu_C^{\max} = 4.999$  GHz; and respective charging energies  $E_C/h = 0.264$ , 0.296 and 0.307 GHz ( $h$ , Planck's constant) and qubit-resonator coupling strengths  $g/2\pi = 0.36$ , 0.30 and 0.34 GHz for qubits A, B and C. At the maximum transition frequencies, we find respective qubit energy relaxation times of  $T_1 = 0.55$ , 0.70 and 1.10  $\mu$ s and phase coherence times of  $T_2^* = 0.45$ , 0.6 and 0.65  $\mu$ s for qubits A, B and C.

In the conventional realization of the Toffoli gate, a NOT operation is applied to the target qubit (C) if the control qubits (A and B) are in the state  $|11\rangle$ . In our set-up, it is more natural to construct a variation of the Toffoli gate shown in Fig. 1a, in which the state of the target qubit is inverted if the control qubits are in  $|01\rangle$ . This gate can easily be transformed to the conventional Toffoli gate by a redefinition of the computational basis states of qubit A or by applying two  $\pi$ -pulses on qubit A.

The Toffoli gate can be constructed from a 'controlled-controlled-phase' (CCPHASE) gate sandwiched between two Hadamard gates

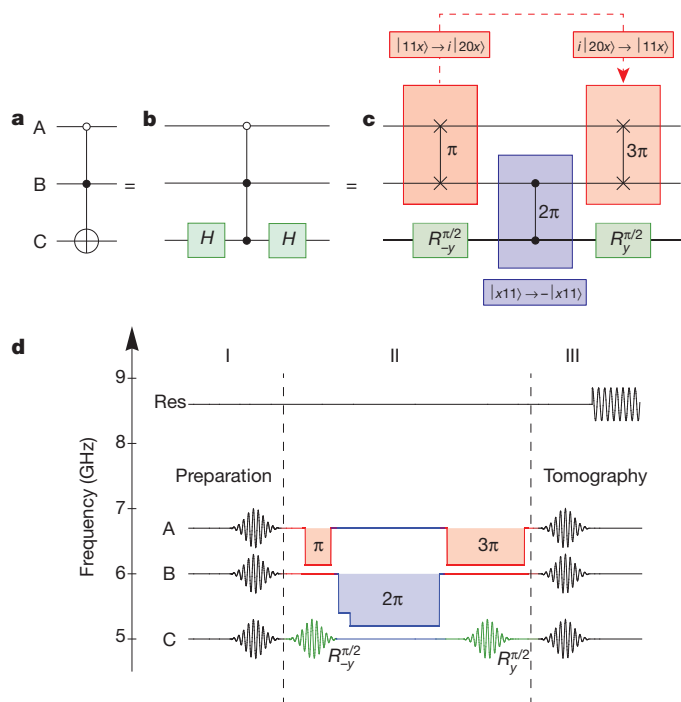


**Figure 1 | Circuit diagram of the Toffoli gate.** **a**, A NOT operation ( $\oplus$ ) is applied to qubit C if the control qubits (A and B) are in the ground ( $\circ$ ) and excited states ( $\bullet$ ), respectively. **b**, The Toffoli gate can be decomposed into a CCPHASE gate sandwiched between Hadamard gates (H) applied to qubit C. **c**, The CCPHASE gate is implemented as a sequence of a qubit-qutrit gate, a two-qubit gate and a second qubit-qutrit gate. Each of these gates is realized by tuning the  $|11\rangle$  state into resonance with  $|20\rangle$  for a  $\{\pi, 2\pi, 3\pi\}$  coherent rotation, respectively. For the Toffoli gate, the Hadamard gates are replaced with  $\pm\pi/2$  rotations about the y axis (represented by  $R_{\pm y}^{\pi/2}$ ). **d**, Pulse sequence used for the implementation of the Toffoli gate. During the preparation (I), resonant microwave pulses are applied to the qubits on the corresponding gate lines. The Toffoli gate (II) is implemented with three flux pulses and resonant microwave pulses (colour coded as in **c**). The measurement (III) consists of microwave pulses that turn the qubit states to the desired measurement axis, and a subsequent microwave pulse applied to the resonator is used to perform a joint dispersive read-out.

<sup>1</sup>Department of Physics, ETH Zurich, CH-8093 Zurich, Switzerland. <sup>2</sup>Disruptive Information Processing Technologies Group, Raytheon BBN Technologies, 10 Moulton Street, Cambridge, Massachusetts 02138, USA. <sup>3</sup>Département de Physique, Université de Sherbrooke, Sherbrooke, Québec J1K 2R1, Canada.



acting on the target qubit as shown in Fig. 1b. A CCPHASE gate leads to a phase shift of  $\pi$  for state  $|1\rangle$  of the target qubit if and only if the control qubits are in state  $|01\rangle$ . In other words, this corresponds to a sign change of only one of the eight computational three-qubit basis states:  $|011\rangle \leftrightarrow -|011\rangle$ .

The basic idea of ‘hiding’ states by transforming them into non-computational states to simplify the implementation of a Toffoli gate was theoretically proposed in refs. 20, 21 and has been experimentally implemented for linear optics and ion trap systems<sup>8,9</sup>. The implementation of the scheme of ref. 20 in our set-up would require three controlled-phase (CPHASE) gates, six single-qubit operations and two single-qutrit operations. Instead, we construct the CCPHASE gate from a single two-qubit CPHASE gate and two qubit–qutrit gates. The latter gates are called  $\pi$ -SWAP and  $3\pi$ -SWAP, respectively (Fig. 1c, red frames). The application of a single CPHASE gate to qubits B and C (Fig. 1c, blue frame) inverts the sign of both  $|111\rangle$  and  $|011\rangle$ . To create the CCPHASE operation, the computational basis state  $|111\rangle$  is transferred to the non-computational state  $i|201\rangle$  by the  $\pi$ -SWAP gate, effectively hiding it from the CPHASE operation acting on qubits B and C. After the CPHASE operation,  $|111\rangle$  is recovered from the non-computational level  $i|201\rangle$  by the  $3\pi$ -SWAP gate. Alternative approaches using optimal control of individual qubits for implementing a Toffoli gate in a single step have been proposed<sup>22</sup> and recently analysed in the context of the circuit quantum electrodynamics architecture<sup>23</sup>.

All three-qubit basis states show three distinct evolution paths through our CCPHASE gate (Table 1). Only input state  $|011\rangle$  is affected by the CPHASE gate acting on qubits B and C, which transfers  $|011\rangle$  to the desired state,  $-|011\rangle$ . The states  $|11x\rangle$  with  $x \in \{0, 1\}$  are transferred by the  $\pi$ -SWAP gate to the states  $i|20x\rangle$ . The subsequent CPHASE gate therefore has no influence on the state. The last gate ( $3\pi$ -SWAP) transfers  $i|20x\rangle$  back to  $|11x\rangle$ . Together the two SWAP gates realize a rotation by  $4\pi$ , such that the state  $|11x\rangle$  does not acquire any extra phase relative to the other states. The states of the last group ( $|010\rangle$  and  $|x0y\rangle$  with  $y \in \{0, 1\}$ ) do not change during the CCPHASE gate sequence.

The actual experimental implementation of the Toffoli gate consists of a sequence of microwave and flux pulses applied to the qubit local control lines (Fig. 1d). The arbitrary rotations about the  $x$  and  $y$  axes<sup>24</sup> are realized with resonant microwave pulses applied to the open transmission line at each qubit. We use 8-ns-long, Gaussian-shaped DRAG-pulses<sup>24,25</sup> to prevent population of the third level and phase errors during the single-qubit operations. Few-nanosecond-long current pulses passing through the transmission lines next to the superconducting loops of the respective qubits control the qubit transition frequency realizing  $z$ -axis rotations. All two-qubit or qubit–qutrit gates are implemented by tuning a qutrit non-adiabatically to the avoided crossing between the states  $|11x\rangle$  and  $|20x\rangle$  or, respectively, that between  $|x11\rangle$  and  $|x20\rangle$  (refs 12, 26, 27). During this time, the system oscillates between these pairs of states with respective frequencies  $2J_{11,20}^{AB}$  and  $2J_{11,20}^{BC}$ . With interaction times  $\pi/2J_{11,20}^{AB} = 7$ ,  $3\pi/2J_{11,20}^{AB} = 21$  and  $\pi/2J_{11,20}^{BC} = 23$  ns, we realize a  $\pi$ -SWAP and a  $3\pi$ -SWAP between qubits A and B and a CPHASE gate between qubits B and C, respectively. Our use of qubit–qutrit instead of single-qutrit operations allows for a more efficient construction of the Toffoli gate. Direct realization of the scheme proposed in ref. 20 in our system would require eight additional microwave pulses (used to implement

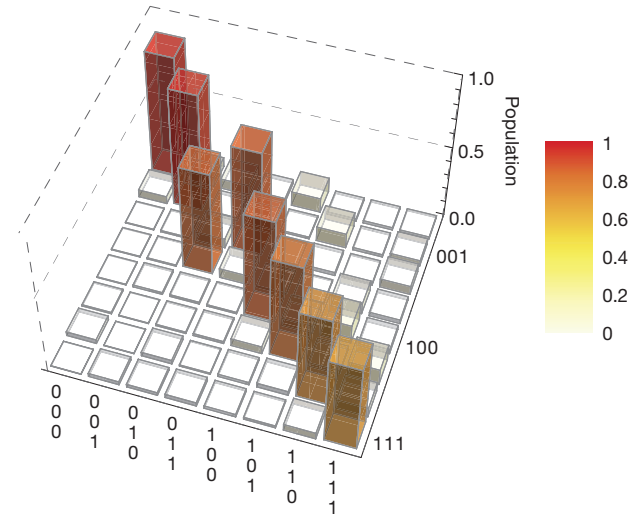


**Figure 2 | Truth table of the Toffoli gate.** The state of qubit C is inverted if qubits A and B are in the state  $|01\rangle$ . The fidelity of the truth table is  $F = (1/8)\text{Tr}(U_{\text{exp}}U_{\text{ideal}}) = 76.0\%$ .

six single-qubit and two single-qutrit gates) with a twofold increase in overall duration of the pulse sequence with respect to our scheme.

We have characterized the performance of this realization of a Toffoli gate by measuring the truth table, by full process tomography<sup>28</sup> and by Monte Carlo process certification<sup>29,30</sup>. The truth table depicted (Fig. 2) shows the population of all computational basis states after applying the Toffoli gate to each of the computational basis states. It reveals the characteristic properties of the Toffoli gate, namely that a NOT operation is applied on the target qubit (C) if the control qubits (A and B) are in the state  $|01\rangle$ . The fidelities of the output states show a significant dependence on qubit lifetime. In particular, input states with qubit A (with the shortest lifetime) in the excited state generally have the lowest fidelity, indicating that the protocol is mainly limited by the qubit lifetime. The fidelity of the measured truth table,  $U_{\text{exp}}$ , with respect to the ideal one,  $U_{\text{ideal}}$ , namely  $F = (1/8)\text{Tr}(U_{\text{exp}}U_{\text{ideal}}) = 76.0\%$ , shows the average performance of our gate when acting on the eight basis states.

As an essential addition to the classical characterization of the gate by the truth table, we have performed full, three-qubit process tomography and reconstructed the process matrix,  $\chi_{\text{exp}}$ , to characterize the quantum features of the Toffoli gate completely, overcoming the limited characterization provided by measurements of the phase fidelity only<sup>15</sup>. For this purpose, we prepared a complete set of 64 distinct input states by applying all combinations of single-qubit operations chosen from the set  $\{\text{id}, \pi/2, \pi, 3\pi/2\}$  for each qubit, and performed state tomography on the respective output states. The process matrix reconstructed directly from the data has a fidelity of  $F = \text{Tr}(\chi_{\text{exp}}\chi_{\text{ideal}}) = 70 \pm 3\%$  (the error represents a 90% confidence interval), where  $\chi_{\text{ideal}}$  is the ideal process matrix. Using a maximum-likelihood procedure<sup>31</sup> to correct for unphysical properties of  $\chi_{\text{exp}}$ , we find that the obtained process matrix,  $\chi_{\text{exp}}^{\text{ML}}$ , has a fidelity of  $F = \text{Tr}(\chi_{\text{exp}}^{\text{ML}}\chi_{\text{ideal}}) = 69\%$  with expected errors at the level of 3%. In Fig. 3a,  $\chi_{\text{exp}}$  shows the same key features as  $\chi_{\text{ideal}}$  (Fig. 3b).

To gain an accurate alternative estimate of the process fidelity without resorting to a maximum-likelihood procedure, we implemented Monte Carlo process certification following the steps described in ref. 29. First we define a Pauli observable as  $\hat{P}_n = \prod_{j=1,\dots,6} \hat{p}_{n,j}$ , a product of six single-qubit operators chosen from the set of the identity and the Pauli operators ( $\hat{p}_{n,j} \in \{1, \sigma_x, \sigma_y, \sigma_z\}$ ). Then we determine the 232 observables with non-vanishing expectation values  $P_n = \text{Tr}(\hat{\rho}_T \hat{P}_n) \neq 0$ , where  $\hat{\rho}_T$  is the Choi matrix of the Toffoli process. For each  $\hat{P}_n$ , we prepare all ( $2^3 = 8$ ) eigenstates of the product of the first three operators comprising  $\hat{P}_n$ , apply the Toffoli operation to this state and measure the expectation value of the product of the last three operators in  $\hat{P}_n$ . Averaging over the results obtained with all eigenstates provides an estimate of  $P_n$ .

**Table 1 | List of states after each step of the CCPHASE gate**

Initial state	After $\pi$ -SWAP	After CPHASE	After $3\pi$ -SWAP
$ 011\rangle$	$ 011\rangle$	$- 011\rangle$	$- 011\rangle$
$ 11x\rangle$	$i 20x\rangle$	$i 20x\rangle$	$ 11x\rangle$
$ x0y\rangle$	$ x0y\rangle$	$ x0y\rangle$	$ x0y\rangle$
$ 010\rangle$	$ 010\rangle$	$ 010\rangle$	$ 010\rangle$

The state  $|011\rangle$  acquires a phase shift of  $\pi$  during the CPHASE pulse; the states  $|11x\rangle$  are transferred to  $i|20x\rangle$ , ‘hiding’ them from the CPHASE gate; and the initial states  $|x0y\rangle$  and  $|010\rangle$  do not change during the sequence.

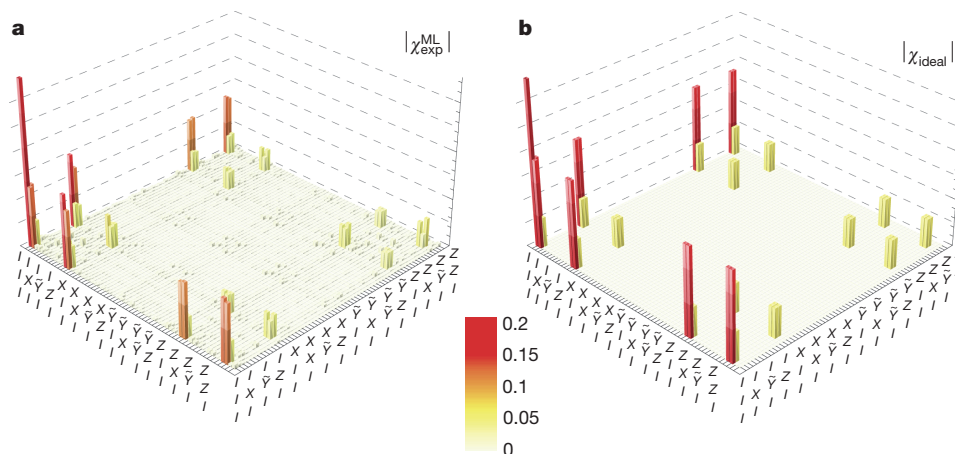


**Figure 3 | Process tomography of the Toffoli gate.** Bar chart of the absolute value of the measured process matrix  $\chi_{\text{exp}}^{\text{ML}}$  (a) and the ideal process matrix  $\chi_{\text{ideal}}$  (b). The elements are displayed in the operator basis  $\{III, IIX, I\tilde{Y}, \dots, ZZZ\}$ ,

Extracting all 232 expectation values in this way allows us to estimate the fidelity of the Toffoli gate as  $68.5 \pm 0.5\%$  using Monte Carlo process certification, which is in good agreement with the fidelity evaluated using process tomography.

The scheme that we use to implement the Toffoli gate is generic and can readily be applied to other systems because the majority of the quantum systems used as qubits have additional energy levels at their disposal. Reduction of the total gate time by use of qubit–qutrit gates together with the recent advances in the extension of the coherence times of the superconducting circuits<sup>32,33</sup> indicates a path towards the realization of practical quantum error correction.

Received 28 August; accepted 15 November 2011.

Published online 14 December 2011.

1. Toffoli, T. *Reversible Computing* (Lect. Notes Computer Sci. 85, Springer, 1980).
2. Shi, Y. Both Toffoli and controlled-NOT need little help to do universal quantum computation. *Quantum Inf. Comput.* **3**, 84–92 (2003).
3. Cory, D. G. *et al.* Experimental quantum error correction. *Phys. Rev. Lett.* **81**, 2152–2155 (1998).
4. Knill, E., Laflamme, R., Martinez, R. & Negrevergne, C. Benchmarking quantum computers: the five-qubit error correcting code. *Phys. Rev. Lett.* **86**, 5811–5814 (2001).
5. Chiaverini, J. *et al.* Realization of quantum error correction. *Nature* **432**, 602–605 (2004).
6. Pittman, T. B., Jacobs, B. C. & Franson, J. D. Demonstration of quantum error correction using linear optics. *Phys. Rev. A* **71**, 052332 (2005).
7. Aoki, T. *et al.* Quantum error correction beyond qubits. *Nature Phys.* **5**, 541–546 (2009).
8. Lanyon, B. P. *et al.* Simplifying quantum logic using higher-dimensional Hilbert spaces. *Nature Phys.* **5**, 134–140 (2009).
9. Monz, T. *et al.* Realization of the quantum Toffoli gate with trapped ions. *Phys. Rev. Lett.* **102**, 040501 (2009).
10. DiCarlo, L. *et al.* Demonstration of two-qubit algorithms with a superconducting quantum processor. *Nature* **460**, 240–244 (2009).
11. Yamamoto, T. *et al.* Quantum process tomography of two-qubit controlled-z and controlled-not gates using superconducting phase qubits. *Phys. Rev. B* **82**, 184515 (2010).
12. DiCarlo, L. *et al.* Preparation and measurement of three-qubit entanglement in a superconducting circuit. *Nature* **467**, 574–578 (2010).
13. Neeley, M. *et al.* Generation of three-qubit entangled states using superconducting phase qubits. *Nature* **467**, 570–573 (2010).
14. Baur, M. *et al.* Benchmarking a teleportation protocol realized in superconducting circuits. Preprint at (<http://arxiv.org/abs/1107.4774>) (2011).
15. Mariani, M. *et al.* Implementing the quantum Von Neumann architecture with superconducting circuits. *Science* **334**, 61–65 (2011).
16. Barenco, A. *et al.* Elementary gates for quantum computation. *Phys. Rev. A* **52**, 3457–3467 (1995).
17. Reed, M. D. *et al.* Realization of three-qubit quantum error correction with superconducting circuits. Preprint at (<http://arxiv.org/abs/1109.4948>) (2011).

where  $I$  is the identity and  $\{X, \tilde{Y}, Z\}$  are the Pauli operators  $\{\sigma_x, -i\sigma_y, \sigma_z\}$ . The fidelity of the process matrix is  $F = \text{Tr}(\chi_{\text{exp}}^{\text{ML}} \chi_{\text{ideal}}) = 69\%$ . The process fidelity estimated using the Monte Carlo certification method is  $68.5 \pm 0.5\%$ .

18. Filipp, S. *et al.* Two-qubit state tomography using a joint dispersive readout. *Phys. Rev. Lett.* **102**, 200402 (2009).
19. Majer, J. *et al.* Coupling superconducting qubits via a cavity bus. *Nature* **449**, 443–447 (2007).
20. Ralph, T. C., Resch, K. J. & Gilchrist, A. Efficient Toffoli gates using qutrits. *Phys. Rev. A* **75**, 022313 (2007).
21. Borrelli, M., Mazzola, L., Paternostro, M. & Maniscalco, S. Simple trapped-ion architecture for high-fidelity Toffoli gates. *Phys. Rev. A* **84**, 012314 (2011).
22. Spörl, A. *et al.* Optimal control of coupled Josephson qubits. *Phys. Rev. A* **75**, 012302 (2007).
23. Stojanovic, V. M., Fedorov, A., Bruder, C. & Wallraff, A. Quantum-control approach to realizing a Toffoli gate in circuit QED. Preprint at (<http://arxiv.org/abs/1108.3442>) (2011).
24. Gambetta, J. M., Motzoi, F., Merkel, S. T. & Wilhelm, F. K. Analytic control methods for high-fidelity unitary operations in a weakly nonlinear oscillator. *Phys. Rev. A* **83**, 012308 (2011).
25. Motzoi, F., Gambetta, J. M., Rebentrost, P. & Wilhelm, F. K. Simple pulses for elimination of leakage in weakly nonlinear qubits. *Phys. Rev. Lett.* **103**, 110501 (2009).
26. Strauch, F. W. *et al.* Quantum logic gates for coupled superconducting phase qubits. *Phys. Rev. Lett.* **91**, 167005 (2003).
27. Haack, G., Helmer, F., Mariani, M., Marquardt, F. & Solano, E. Resonant quantum gates in circuit quantum electrodynamics. *Phys. Rev. B* **82**, 024514 (2010).
28. Chuang, I. L. & Nielsen, M. A. Prescription for experimental determination of the dynamics of a quantum black box. *J. Mod. Opt.* **44**, 2455–2467 (1997).
29. da Silva, M. P., Landon-Cardinal, O. & Poulin, D. Practical characterization of quantum devices without tomography. *Phys. Rev. Lett.* **107**, 210404 (2011).
30. Flammia, S. T. & Liu, Y.-K. Direct fidelity estimation from few Pauli measurements. *Phys. Rev. Lett.* **106**, 230501 (2011).
31. Ježek, M., Fiurášek, J., Hradil, Z. & v. Quantum inference of states and processes. *Phys. Rev. A* **68**, 012305 (2003).
32. Bylander, J. *et al.* Noise spectroscopy through dynamical decoupling with a superconducting flux qubit. *Nature Phys.* **7**, 565–570 (2011).
33. Paik, H. *et al.* How coherent are Josephson junctions? Preprint at (<http://arxiv.org/abs/1105.4652v1>) (2011).

**Acknowledgements** We thank S. Filipp, A. Blais for useful discussions and K. Pakrouski for his contributions in early stages of the experimental work. This work was supported by the Swiss National Science Foundation, the EU IP SOLID and ETH Zurich.

**Author Contributions** A.F. developed the scheme to realize the Toffoli gate. L.S., A.F. and M.B. carried out the experiments and analysed the data. L.S. designed and fabricated the superconducting resonator. A.F. and M.B. designed and fabricated the qubits. M.P.d.S. provided general theoretical support and specific advice on using Monte Carlo process certification. A.F., L.S., M.B. and A.W. contributed to setting up and maintaining the experiment. A.F., A.W. and L.S. wrote the manuscript. All authors commented on the manuscript. A.W. supervised the project.

**Author Information** Reprints and permissions information is available at [www.nature.com/reprints](http://www.nature.com/reprints). The authors declare no competing financial interests. Readers are welcome to comment on the online version of this article at [www.nature.com/nature](http://www.nature.com/nature). Correspondence and requests for materials should be addressed to A.F. ([fedorar@phys.ethz.ch](mailto:fedorar@phys.ethz.ch)) or A.W. ([andreas.wallraff@phys.ethz.ch](mailto:andreas.wallraff@phys.ethz.ch)).



# Charge order and three-site distortions in the Verwey structure of magnetite

Mark S. Senn<sup>1</sup>, Jon P. Wright<sup>2</sup> & J. Paul Attfield<sup>1</sup>

The mineral magnetite ( $\text{Fe}_3\text{O}_4$ ) undergoes a complex structural distortion and becomes electrically insulating at temperatures less than 125 kelvin. Verwey proposed in 1939 that this transition is driven by a charge ordering of  $\text{Fe}^{2+}$  and  $\text{Fe}^{3+}$  ions<sup>1</sup>, but the ground state of the low-temperature phase has remained contentious<sup>2,3</sup> because twinning of crystal domains hampers diffraction studies of the structure<sup>4</sup>. Recent powder diffraction refinements<sup>5–7</sup> and resonant X-ray studies<sup>8–12</sup> have led to proposals of a variety of charge-ordered and bond-dimerized ground-state models<sup>13–19</sup>. Here we report the full low-temperature superstructure of magnetite, determined by high-energy X-ray diffraction from an almost single-domain, 40-micrometre grain, and identify the emergent order. The acentric structure is described by a superposition of 168 atomic displacement waves (frozen phonon modes), all with amplitudes of less than 0.24 ångströms. Distortions of the  $\text{FeO}_6$  octahedra show that Verwey's hypothesis is correct to a first approximation and that the charge and  $\text{Fe}^{2+}$  orbital order are consistent with a recent prediction<sup>17</sup>. However, anomalous shortening of some Fe–Fe distances suggests that the localized electrons are distributed over linear three-Fe-site units, which we call 'trimerons'. The charge order and three-site distortions induce substantial off-centre atomic displacements and couple the resulting large electrical polarization to the magnetization. Trimerons may be important quasiparticles in magnetite above the Verwey transition and in other transition metal oxides.

The cubic spinel type structure of magnetite distorts to a monoclinic superstructure with  $Cc$  space group symmetry below the  $T_V \approx 125$  K Verwey transition<sup>4,20</sup>.  $Cc$  domains<sup>21</sup>  $\sim 1$   $\mu\text{m}$  in size are formed in up to 24 orientations within magnetite crystals, and microtwinning of these domains severely hampers diffraction studies. We have investigated the use of small magnetite grains as potential single-domain crystals for high-energy X-ray structure analysis (Fig. 1). In the smallest and least-twinned grain of many that we investigated, 89% of the scattering was from a single orientation and 11% was from a secondary domain (Fig. 1a). The  $Cc$  crystal structure was determined using 91,433 symmetry-unique Bragg reflections from this 40- $\mu\text{m}$  grain (see Methods Summary and Supplementary Information for details of the structure and derived quantities used below). No further superstructure or lowering of space group symmetry below  $Cc$  was evident in the diffraction data.

The low-temperature  $Cc$  crystal structure of magnetite has 168 variable ( $x, y, z$ ) atomic coordinates, of which 166 are independent and two are constrained to fix the cell origin. The coordinates are equivalently described by the same number of amplitudes of frozen displacement waves (phonons), all with values  $q < 0.24$  Å, as shown graphically in Fig. 2. Only one of these (an O-site  $\Gamma$ -mode) is present in the high-temperature cubic structure and the remainder all freeze at the Verwey transition. The three largest-amplitude modes have  $A_g$  symmetry and are acentric, heralding the large off-centre structural distortions described later, but the smoothly varying distribution of amplitudes shows that many centric and acentric  $A_g$ , X and W modes contribute

significantly. Hence, the superstructure is not approximated well by a few frozen phonons, and even attempts to describe the important features with up to 100 lattice modes were unsuccessful.

Magnetite has an  $\text{AB}_2\text{O}_4$  spinel structure in which  $\text{Fe}^{3+}$  occupies the tetrahedrally coordinated A cation sites, and a 1:1 order of  $\text{Fe}^{2+}$  and  $\text{Fe}^{3+}$  is expected over the 16 inequivalent octahedral B sites of the  $Cc$  superstructure in the Verwey hypothesis. Each B-site  $\text{FeO}_6$  octahedron has an irregular distortion from which the amplitudes of radial expansion (breathing) local modes ( $Q_{\text{Rad}}$ ) and tetragonal Jahn–Teller ( $Q_{\text{JT}}$ ) local modes were extracted because these are sensitive to charge-ordering and associated orbital-ordering displacements. For  $Q_{\text{JT}}$  we find a bimodal Verwey-type distribution (Fig. 3a) in which eight near-zero values are consistent with  $\text{Fe}^{3+}$ , which is Jahn–Teller inactive as the high-spin  $3d^5$  electron configuration is non-degenerate. The other eight  $Q_{\text{JT}}$  values are negative as expected for  $3d^6$   $\text{Fe}^{2+}$ , where tetragonal Jahn–Teller compression removes the degeneracy created by the extra electron occupying one of the three  $t_{2g}$  symmetry  $d$  orbitals ( $d_{xy}$ ,  $d_{xz}$  or  $d_{yz}$ ). In addition, the plot of  $Q_{\text{Rad}}$  (the increase in octahedral average Fe–O bond distance) against  $Q_{\text{JT}}$  shows that the eight Jahn–Teller-distorted B sites are also the eight most expanded, consistent with  $\text{Fe}^{2+}$ , and that the eight undistorted sites are the least expanded, as expected for  $\text{Fe}^{3+}$ . The bimodal distribution of tetragonal distortions and their correlation with the radial amplitudes demonstrate experimentally that Verwey's  $\text{Fe}^{2+}$ – $\text{Fe}^{3+}$  ordering hypothesis is correct to a useful first approximation. However, the distribution of  $Q_{\text{Rad}}$  and

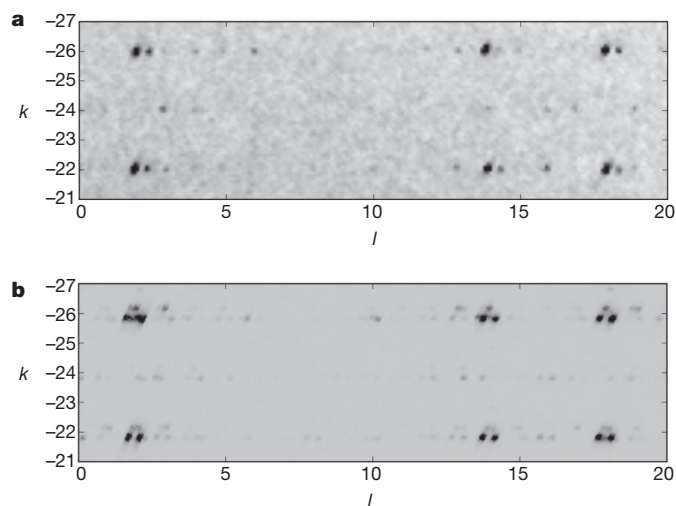


**Figure 1 | Reciprocal lattice synchrotron X-ray diffraction intensities for magnetite microcrystal grains at 90 K.** Sections of  $(hkl)$  intensities in the  $h = 50$  plane are shown. **a**, Intensities for an approximately spherical grain of diameter 40  $\mu\text{m}$ , which was used to determine the crystal structure. The microcrystal is almost single domain; faint spots to the right of the main intensities reveal the secondary twin. **b**, Intensities from an irregular grain of dimension  $\sim 100$   $\mu\text{m}$  showing multiple twin domains.

<sup>1</sup>Centre for Science at Extreme Conditions and School of Chemistry, University of Edinburgh, West Mains Road, Edinburgh EH9 3JZ, UK. <sup>2</sup>European Synchrotron Radiation Facility, 6 rue Jules Horowitz, BP 220, 38043 Grenoble Cedex 9, France.

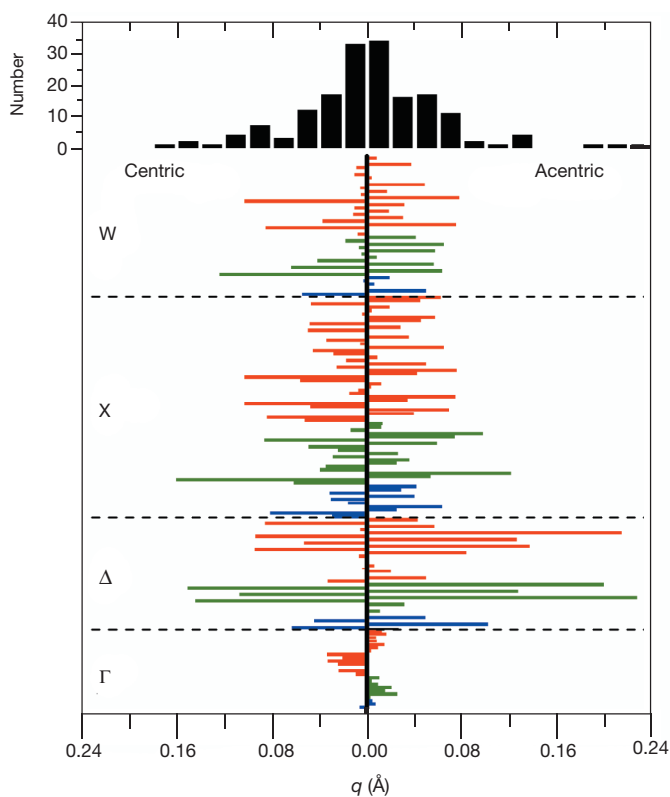


**Figure 2 | The 168 displacement amplitudes of the low-temperature *Cc* magnetite structure.** Main panel: centric and acentric mode amplitudes,  $q$ , which have estimated standard deviations  $<0.003$  Å. Top panel: distribution of amplitudes. A, B and O atom modes of the cubic  $Fd\bar{3}m$   $AB_2O_4$  spinel type structure are coloured blue, green and red, respectively. The displacement waves have periodicities corresponding to the  $\Gamma$  (0, 0, 0),  $\Delta$  (0, 1/2, 0),  $X$  (0, 1, 0) and  $W$  (1/2, 1, 0) points in the Brillouin zone of the cubic structure. Many acentric and centric  $\Delta$ ,  $X$  and  $W$  modes involving the B and O sites contribute significantly to the overall superstructure, but the  $\Gamma$  modes are less important.

equivalent bond valence sum (BVS) estimates of formal Fe charge (Fig. 3a) does not seem bimodal, indicating the more complex electronic order described later.

The average BVS formal oxidation states for the eight  $Fe^{2+}$ - and  $Fe^{3+}$ -like B sites in the *Cc* magnetite structure are 2.47 and 2.75, respectively, consistent with an earlier partial refinement<sup>5,6</sup> and structural results for other charge-ordered transition metal oxides<sup>22</sup>. The  $Fe^{2+}$ - $Fe^{3+}$  arrangement (Fig. 4a) differs from the original prediction of Verwey<sup>23</sup>, but the charge and  $Fe^{2+}$  orbital ordering (Fig. 4b) are in agreement with a recent model based on electronic structure calculations<sup>17</sup>. The arrangement is close to a centric structure in which the  $Fe^{2+}$  states form chains of corner-linked ( $Fe^{2+}$ )<sub>3</sub> triangles, but with a neighbouring  $Fe^{2+}$ - $Fe^{3+}$  pair exchanged at every fourth triangle as shown (Fig. 4a). Anderson's condition<sup>24</sup> that each tetrahedron of four neighbouring B sites should contain two  $Fe^{2+}$  ions is only satisfied in a quarter of the tetrahedra. The complexity of the charge and orbital ordering may be explained in part by the distribution of Jahn–Teller distortions. The octahedral compressions of the 16  $Fe^{2+}$  sites in the basic cell act parallel to the  $a$ ,  $b$ , and  $c$  axes of the high-temperature cubic lattice in a 5:5:6 ratio that minimizes strain in the highly connected spinel lattice. More-symmetric charge and orbital orderings tend to have less equal ratios. The small anisotropy arising from excess distortion in the  $c$  direction may account for the change in magnetic easy-axis from cubic [111] to [001] at temperatures less than  $T_V$ .

Edge sharing of  $FeO_6$  octahedra allows direct B–B electronic interactions within linear chains that extend in six directions. The nearest-neighbour B–B distances,  $D_{BB}$ , are all equivalent in the cubic magnetite structure, but  $D_{BB}(Fe^{2+}-Fe^{3+})$ , the nearest-neighbour  $Fe^{2+}$ - $Fe^{3+}$

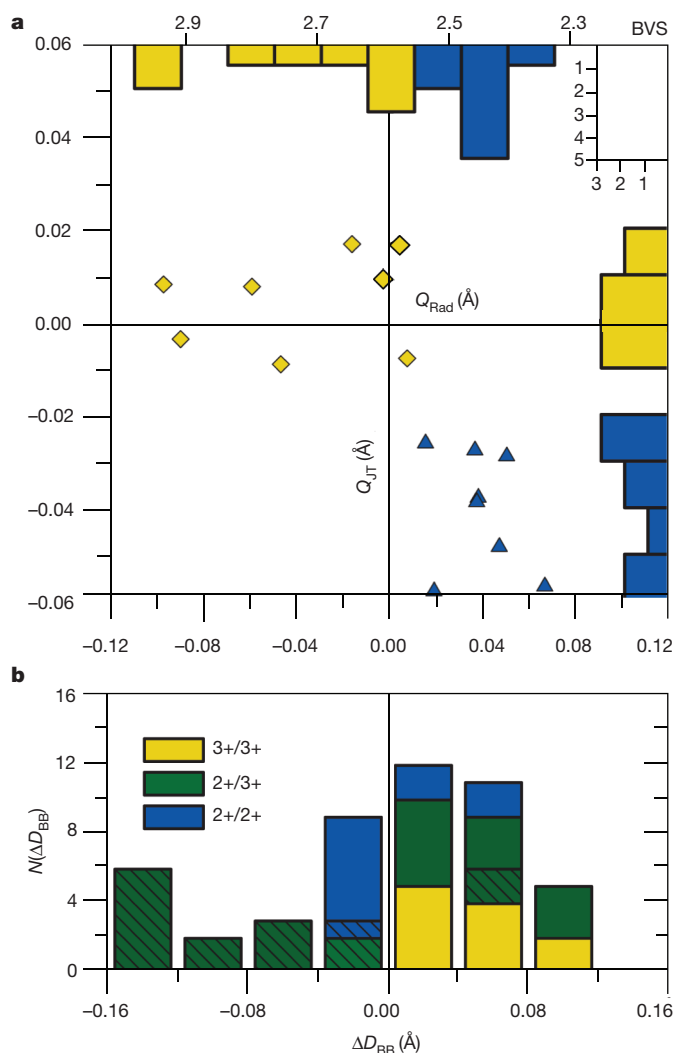


**Figure 3 | Local distortion distributions that reveal electronic order in the low-temperature magnetite structure.** **a**, Plot of local distortions for the 16 distinct  $FeO_6$  octahedra.  $Q_{Rad}$  and  $Q_{JT}$  are the amplitudes of the radial (breathing) and tetragonal Jahn–Teller distortions. Their estimated standard deviations of  $<0.002$  Å are smaller than the symbols shown.  $Q_{Rad}$  is the difference between the average Fe–O bond distance in an  $FeO_6$  octahedron and the average over all octahedra. The points fall into two groups describing characteristic local distortions for  $Fe^{2+}$  and  $Fe^{3+}$  (blue and yellow bars and symbols, respectively). The distributions of the two modes (inside top and right edges of plot, with scales top right) show that there is bimodal segregation of the  $Q_{JT}$  amplitudes but that the  $Q_{Rad}$  dispersion is more continuous. BVS estimates of formal Fe charge are shown above the  $Q_{Rad}$  distribution. **b**, Distribution of the 48 distinct Fe–Fe distances between neighbouring B sites, relative to the average  $D_{BB}$  ( $= 2.967$  Å), coloured according to the Fe charge states. The 16 distances from the eight  $Fe^{2+}$  sites to their two neighbours perpendicular to the local orbital ordering axis ( $Fe^{3+}$  in 15 cases and  $Fe^{2+}$  once) are hatched. The anomalous shortening of most of these distances indicates the linear three-site (trimeron) distortions as shown in Fig. 4c.

distance, in particular shows a wide distribution in the Verwey phase (Fig. 3b). Electrostatic repulsions tend to disperse the distance values such that  $D_{BB}(Fe^{2+}-Fe^{2+}) < D_{BB}(Fe^{2+}-Fe^{3+}) < D_{BB}(Fe^{3+}-Fe^{3+})$ , so the observed tail of anomalously short  $Fe^{2+}$ - $Fe^{3+}$  distances is not expected in a Verwey model and indicates magnetically driven B–B bonding by the additional  $t_{2g}$  electrons. (The five parallel unpaired  $d$ -electron spins at all B sites are ferromagnetically ordered below the Curie temperature (858 K), so only the additional electron from each  $3d^6$   $Fe^{2+}$  state has an opposed, minority, spin and may be delocalized between B sites through bonding.)



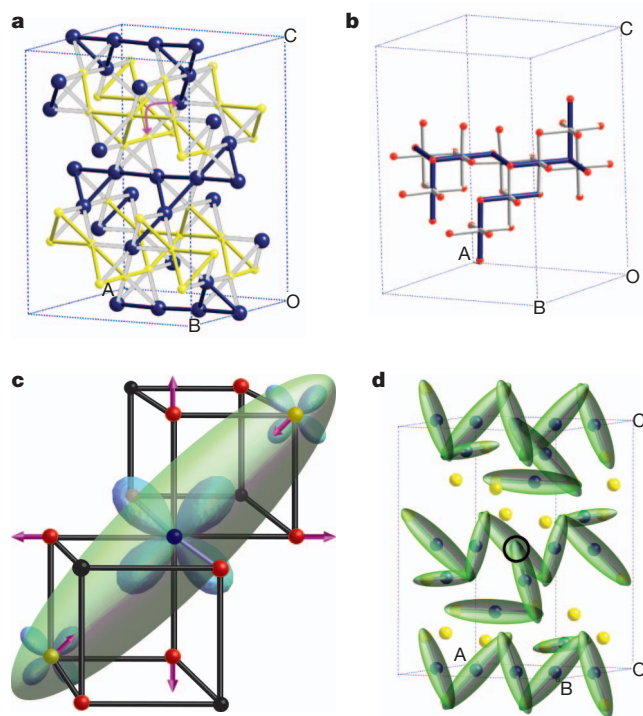


**Figure 4 | Charge, orbital and trimeron order in the low-temperature magnetite structure.** **a**, Distribution of Fe<sup>2+</sup> and Fe<sup>3+</sup> states (blue and yellow spheres, respectively) in the first-approximation Verwey-type model, shown in the  $\sqrt{2}a \times \sqrt{2}a \times 2a$  *Cc* supercell (*a* is the high-temperature cubic-cell parameter). Nearest-neighbour Fe<sup>2+</sup>–Fe<sup>2+</sup> connections (blue lines) describe irregular chains, parallel to the *a* axis, derived from a more symmetric, centric arrangement of corner-linked triangles by exchange of Fe<sup>2+</sup>–Fe<sup>3+</sup> pairs (one pair indicated). **b**, Jahn–Teller distortions arising from orbital order within a single Fe<sup>2+</sup> chain shown as long and short bonds (grey and blue lines, respectively) to oxygen atoms (red spheres). **c**, Coupled distribution of a minority-spin electron (with approximate atomic populations indicated by the sizes of blue *t*<sub>2g</sub> orbitals) and associated atomic displacements (purple arrows) within a linear three-Fe-site (trimeron) unit. Orbital order at the central Fe<sup>2+</sup> site (blue) localizes the minority-spin electron in one of the *t*<sub>2g</sub> orbitals and elongates the four Fe–O bonds perpendicular to the local Jahn–Teller axis. Weak bonding interactions transfer minority-spin density into coplanar *t*<sub>2g</sub> orbitals at two neighbouring B sites (shown as yellow Fe<sup>3+</sup>) and shorten the Fe–Fe distances. The minority-spin electron density is approximated by a scalene ellipsoid encompassing the three Fe sites. Other B-site Fe<sup>2+</sup> or Fe<sup>3+</sup> neighbours (black spheres) do not participate. **d**, Trimeron distribution in the low-temperature magnetite structure, following the experimentally observed distortions, with Fe<sup>2+</sup> and Fe<sup>3+</sup> states shown as blue and yellow spheres, respectively, and trimeron ellipsoids as in **c**. The trimerons are mainly end-linked through Fe<sup>3+</sup> ions, but one trimeron is terminated by an Fe<sup>2+</sup> ion (circled). Some Fe<sup>3+</sup> sites do not participate in any trimerons.

Chains of alternating short and long B–B distances are predicted in bond-dimerized models<sup>13,16,19</sup>, but are not observed in our structure. Instead, the two B–B distances perpendicular to the local orbital-ordering axis at each of the eight Fe<sup>2+</sup> positions both tend to be shortened: this is the case for 14 of these 16 distances (Fig. 3b, hatched). This suggests that minority-spin *t*<sub>2g</sub> electron density is significantly delocalized from an Fe<sup>2+</sup> donor onto two adjacent B-site acceptors, which are usually Fe<sup>3+</sup> sites. This single charge, delocalized over three B sites with associated displacements of the two acceptor B sites and surrounding oxygen atoms (Fig. 4c), corresponds to a highly structured small polaron that may be described as a ‘trimeron’, by analogy with dimeron quasiparticles in La<sub>1–*x*</sub>Ca<sub>*x*</sub>MnO<sub>3</sub> (ref. 25). Fifteen of the 16 trimeron acceptor sites are Fe<sup>3+</sup> ions, but one Fe<sup>2+</sup> (Fig. 4d, circled) accepts into a *t*<sub>2g</sub> orbital that is orthogonal to its own trimeron. Trimeron distortions are intrinsically symmetric (having *D*<sub>BB</sub> = 2.832 and 2.848 Å in the most regular environment of the *Cc* structure, where

*D*<sub>BB</sub> = 2.967 Å on average), but asymmetric connectivity leads to off-centre distortions and long B–B bonds in 2 of 16 cases.

The linear three-site (trimeron) distortions (Fig. 4d) significantly perturb charge order in the *Cc* magnetite structure and couple the magnetism to the complex overall distortion. Only two B ions are available per minority-spin electron, so trimeron units are constrained to share sites. End-sharing connections with angles of 60°, 120° and 180° are possible, but 180° linkages are apparently avoided to maximize charge transfer because two or three different *t*<sub>2g</sub> orbitals are used by an Fe<sup>3+</sup> ion participating in two or three trimerons. This is analogous to the formation of two or three short *cis*-bonds in some *d*<sup>0</sup> transition metal oxides and oxynitrides<sup>26</sup>, and creates off-centre Fe<sup>3+</sup> displacements that contribute strongly to the acentric lattice modes and electric polarization. High connectivity seems favourable because four of the eight Fe<sup>3+</sup> sites participate in the maximum of three trimerons. The orderings of linear three-site, one-electron units along the infinite B chains correspond to charge density waves with wavevector magnitude  $q_c = 1/N$  for a repeat sequence of one trimeron for every *N* B sites. The structural average is  $q_c = 1/6$  but only chains with  $q_c = 0, 1/8$  and  $1/4$  are present, in a 1:6:5 ratio. The unique  $q_c = 0$  chain contains only Fe<sup>2+</sup> ions (Fig. 4a, b) but their three-site distortions are always within other chains.

The linear three-site distortions we attribute to trimerons also account for the non-Verwey distribution of radial amplitudes (*Q*<sub>Rad</sub>) and BVS values for the B-site FeO<sub>6</sub> octahedra (Fig. 3a). Each Fe<sup>2+</sup> ion donates minority-spin *t*<sub>2g</sub> electron density to two B-site acceptors within a trimeron (Fig. 4c), so the eight Fe<sup>2+</sup>-like sites have a narrow *Q*<sub>Rad</sub> distribution and BVS ≈ 2.4. However, Fe<sup>3+</sup> ions are acceptors in varying numbers of trimerons. Two Fe<sup>3+</sup> sites do not participate in any trimerons and so have the two lowest *Q*<sub>Rad</sub> values and the highest B-site BVS values, ~3.0 (Fig. 3a). The other six Fe<sup>3+</sup> sites are acceptors for one to three trimerons and thus have a spread of higher *Q*<sub>Rad</sub> values and lower valences with BVS ≈ 2.6–2.8. Charge transfer within trimerons tends to equalize the electron density across B sites: in the limit of maximum donor-to-acceptor transfers (of 0.2*e*, where *e* is the electron charge), an Fe<sup>3+</sup> ion participating in three trimerons has the same formal charge, +2.4*e*, as the Fe<sup>2+</sup> donor sites. However, the two states are still distinguished by their minority-spin *t*<sub>2g</sub> distributions, as the former site has populations  $d_{xy}^{0.2}d_{xz}^{0.2}d_{yz}^{0.2}$  that preserve the high symmetry of Fe<sup>3+</sup>, whereas the latter has a distribution such as  $d_{xy}^{0.6}d_{xz}^0d_{yz}^0$ , retaining the orbital order of Fe<sup>2+</sup>. This justifies the use of formal valence states to describe charge-ordered structures even when the apparent charge separations are small, as here in magnetite.

The discovery of multiferroism in charge-ordered LuFe<sub>2</sub>O<sub>4</sub> (ref. 27) has led to recent interest in the coupling of magnetism and the ferroelectric polarization expected in the acentric *Cc* magnetite superstructure<sup>16,17</sup>. Measured electric polarization values of  $P \approx 0.05$  C m<sup>–2</sup> for magnetite crystals and thin films agree with estimates from previous structural models<sup>17</sup>, but an Fe<sup>2+</sup>–Fe<sup>3+</sup>–O<sup>2–</sup> point-charge calculation for our structure gives a polarization larger by an order of magnitude ( $P_a = 0.118$  C m<sup>–2</sup>,  $P_c = 0.405$  C m<sup>–2</sup>;  $P = 0.422$  C m<sup>–2</sup>; where  $P_a$  and  $P_c$  are the respective magnitudes of the polarization vector components parallel to the crystallographic *a* and *c* axes and  $P$  is the magnitude of the resultant polarisation vector). The same calculation with average Fe<sup>2.5+</sup> B-site charges gives similar results ( $P_a = 0.080$  C m<sup>–2</sup>,  $P_c = 0.346$  C m<sup>–2</sup>;  $P = 0.355$  C m<sup>–2</sup>), showing that atomic displacements resulting from charge order and three-site distortions are responsible for most of the polarization, with exchange of Fe<sup>2+</sup>–Fe<sup>3+</sup> pairs (Fig. 4a) contributing only 16% of the total. The large  $P_c$  component, parallel to the magnetic easy axis, shows that a substantial magnetoelectric coupling is expected in single magnetite domains.

Lattice effects in the cubic phase of magnetite are indicated by diffuse scattering above the Verwey transition<sup>12,28</sup> and a continuous increase in the electrical conductivity up to a maximum at ~3*T*<sub>V</sub>. Hence, trimeron fluctuations may be important quasiparticles in the

cubic phase. The expected entropy change at the Verwey transition is conventionally assumed to be  $R\ln(4) = 1.4R$  (where  $R$  is the molar gas constant) for full disorder of  $\text{Fe}^{2+}$  and  $\text{Fe}^{3+}$  charges, but our structure shows that this change should be  $R\ln(12) = 2.5R$  for additional randomization of the triply degenerate  $\text{Fe}^{2+}$  orbital states. Hence, the observed entropy change of  $\sim 0.7R$  corresponds to only 30% of the possible disorder at  $T_V$  (ref. 29). Previous estimates have used Anderson's condition or other charge configurations within tetrahedra of four B sites, but trimeron-based models may provide alternative predictions. An approximate calculation based on the above local connectivity of  $\text{Fe}^{3+}$  sites reduces the predicted transition entropy from  $2.5R$  to  $2.1R$  (or from  $1.4R$  to  $1.0R$  if orbital states are neglected), but these estimates are still greater than the observed value and suggest that trimeron or other correlations persist at temperatures greater than  $T_V$ .

This investigation shows that single domains of the Verwey phase may be accessible in  $\sim 10$ – $50$ - $\mu\text{m}$  grains for future low-temperature studies of magnetite. Self-organization of the charge and orbital states couples the spin order of this eponymous magnetic material to the complex Verwey distortion. Trimerons may be important quasiparticles above the Verwey transition and may also be relevant to other transition metal oxides such as superconducting  $\text{LiTi}_2\text{O}_4$  spinel. Finally, we note that a full *ab initio* simulation of the low-temperature magnetite structure starting from calculations on the cubic state presents a future challenge to improve understanding of the Verwey phase, now that the experimental structure has been determined.

## METHODS SUMMARY

Grains from a highly stoichiometric powder used in previous studies<sup>5,6,8</sup> were placed in a  $100$ - $\mu\text{m}$ , focused monochromatic beam (wavelength,  $0.16653(1)$  Å; estimated standard deviation shown in parenthesis) on the ID11 diffractometer at ESRF, Grenoble. Multiple scattering and extinction problems were reduced by using small crystallites and a high X-ray energy ( $74$  keV), which also gave access to an abundance of diffraction peaks at very high momentum transfer and reduced absorption effects. Crystals were aligned and de-twinned using a permanent magnet (producing a field of approximately  $0.1$  T at the sample), and were verified as being cubic single domains at  $130$  K before cooling through the Verwey transition to  $90$  K.

The grain used for structure determination was approximately spherical with diameter  $\sim 40$   $\mu\text{m}$ . We used  $\omega$ -scans with varying exposure times to increase the dynamic range of the data from the charge-coupled-device detector (Frelon2K camera) and these were performed at azimuthal angles  $\phi$  and  $\phi + 180^\circ$  to improve data redundancy and test for multiple scattering. Reciprocal lattice sections (Fig. 1a) were reconstructed using local software. Small-box integrations were used to identify the orientation of the two observed domains, and large-box integration was performed to encompass intensity from both domains and allow structure refinement as a pseudo-merohedral twin.

Two thousand starting models were generated by applying random atomic displacements to the high-temperature structure and were optimized by least-squares refinement. A global minimum at residual  $R[F^2 > 4\sigma] = 4.99\%$  (where  $F$  and  $\sigma$  are the observed magnitude and standard deviation of a structure factor) was observed most frequently (292 times), in addition to local refinement minima ( $R[F^2 > 4\sigma] \geq 5.88\%$ ). The final refinement of the global minimum model used independent anisotropic thermal parameters for all atoms and all data to a resolution of  $d \geq 0.3$  Å, giving  $R$  values  $R[F^2 > 4\sigma] = 3.40\%$ ,  $R[F^2] = 5.18\%$  and weighted residual  $wR_2 = 6.96\%$ . Full crystallographic information and details of the analysis software are given in Supplementary Information.

Received 1 June; accepted 8 November 2011.

Published online 21 December 2011.

1. Verwey, E. J. W. Electronic conduction of magnetite ( $\text{Fe}_3\text{O}_4$ ) and its transition point at low temperatures. *Nature* **144**, 327–328 (1939).

2. Walz, F. The Verwey transition: a topical review. *J. Phys. Condens. Matter* **14**, R285–R340 (2002).
3. Coey, M. Condensed-matter physics: charge-ordering in oxides. *Nature* **430**, 155–157 (2004).
4. Iizumi, M. *et al.* Structure of magnetite ( $\text{Fe}_3\text{O}_4$ ) below the Verwey transition-temperature. *Acta Crystallogr. B* **38**, 2121–2133 (1982).
5. Wright, J. P., Attfield, J. P. & Radaelli, P. G. Long range charge ordering in magnetite below the Verwey transition. *Phys. Rev. Lett.* **87**, 266401 (2001).
6. Wright, J. P., Attfield, J. P. & Radaelli, P. G. Charge ordered structure of magnetite  $\text{Fe}_3\text{O}_4$  below the Verwey transition. *Phys. Rev. B* **66**, 214422 (2002).
7. Blasco, J., Garcia, J. & Subias, G. Structural transformation in magnetite below the Verwey transition. *Phys. Rev. B* **83**, 104105 (2011).
8. Goff, R. J., Wright, J. P., Attfield, J. P. & Radaelli, P. G. Resonant X-ray diffraction study of the charge ordering in magnetite. *J. Phys. Condens. Matter* **17**, 7633–7642 (2005).
9. Nazarenko, E. *et al.* Resonant X-ray diffraction studies on the charge ordering in magnetite. *Phys. Rev. Lett.* **97**, 056403 (2006).
10. Joly, Y. *et al.* Low-temperature structure of magnetite studied using resonant X-ray scattering. *Phys. Rev. B* **78**, 134110 (2008).
11. Bland, S. R. *et al.* Full polarization analysis of resonant superlattice and forbidden X-ray reflections in magnetite. *J. Phys. Condens. Matter* **21**, 485601 (2009).
12. Lorenzo, J. E. *et al.* Charge and orbital correlations at and above the Verwey phase transition in magnetite. *Phys. Rev. Lett.* **101**, 226401 (2008).
13. Seo, H., Ogata, M. & Fukuyama, H. Aspects of the Verwey transition in magnetite. *Phys. Rev. B* **65**, 085107 (2002).
14. Jeng, H. T., Guo, G. Y. & Huang, D. J. Charge-orbital ordering and Verwey transition in magnetite. *Phys. Rev. Lett.* **93**, 156403 (2004).
15. Jeng, H. T., Guo, G. Y. & Huang, D. J. Charge-orbital ordering in low-temperature structures of magnetite: GGA+U investigations. *Phys. Rev. B* **74**, 195115 (2006).
16. van den Brink, J. & Khomskii, D. I. Multiferroicity due to charge ordering. *J. Phys. Condens. Matter* **20**, 434217 (2008).
17. Yamauchi, K., Fukushima, T. & Picozzi, S. Ferroelectricity in multiferroic magnetite  $\text{Fe}_3\text{O}_4$  driven by noncentrosymmetric  $\text{Fe}^{2+}/\text{Fe}^{3+}$  charge-ordering: first-principles study. *Phys. Rev. B* **79**, 212404 (2009).
18. Zhou, F. & Ceder, G. First-principles determination of charge and orbital interactions in  $\text{Fe}_3\text{O}_4$ . *Phys. Rev. B* **81**, 205113 (2010).
19. Fukushima, T., Yamauchi, K. & Picozzi, S. *Ab initio* investigations of  $\text{Fe}^{2+}/\text{Fe}^{3+}$  bond dimerization and ferroelectricity induced by intermediate site/bond-centered charge ordering in magnetite. *J. Phys. Soc. Jpn* **80**, 014709 (2011).
20. Yoshida, J. & Iida, S. X-ray-diffraction study on low-temperature phase of magnetite. *J. Phys. Soc. Jpn* **42**, 230–237 (1977).
21. Kasama, T., Church, N. S., Feinberg, J. M., Dunin-Borkowski, R. E. & Harrison, R. J. Direct observation of ferrimagnetic/ferroelastic domain interactions in magnetite below the Verwey transition. *Earth Planet. Sci. Lett.* **297**, 10–17 (2010).
22. Attfield, J. P. Charge ordering in transition metal oxides. *Solid State Sci.* **8**, 861–867 (2006).
23. Verwey, E. J. W. & Heilmann, E. L. Physical properties and cation arrangement of oxides with spinel structures. 1. Cation arrangement in spinels. *J. Chem. Phys.* **15**, 174–180 (1947).
24. Anderson, P. W. Ordering and antiferromagnetism in ferrites. *Phys. Rev.* **102**, 1008–1013 (1956).
25. Downward, L. *et al.* Universal relationship between magnetization and changes in the local structure of  $\text{La}_{1-x}\text{Ca}_x\text{MnO}_3$ : evidence for magnetic dimers. *Phys. Rev. Lett.* **95**, 106401 (2005).
26. Yang, M. H. *et al.* Anion order in perovskite oxynitrides. *Nat. Chem.* **3**, 47–52 (2011).
27. Ikeda, N. *et al.* Ferroelectricity from iron valence ordering in the charge-frustrated system  $\text{LuFe}_2\text{O}_4$ . *Nature* **436**, 1136–1138 (2005).
28. Yamada, Y., Wakabayashi, N. & Nicklow, R. M. Neutron diffuse-scattering in magnetite due to molecular polarons. *Phys. Rev. B* **21**, 4642–4648 (1980).
29. Shepherd, J. P., Koenitzer, J. W., Aragon, R., Sandberg, C. J. & Honig, J. M. Heat-capacity studies on single-crystal annealed  $\text{Fe}_3\text{O}_4$ . *Phys. Rev. B* **31**, 1107–1113 (1985).

**Supplementary Information** is linked to the online version of the paper at [www.nature.com/nature](http://www.nature.com/nature).

**Acknowledgements** We thank C. Morrison for supplying code for electrical polarization calculations, J. Honig for provision of the magnetite sample, the Leverhulme Trust for financial support, and EPSRC and STFC for financial support and provision of continuing access to ESRF.

**Author Contributions** J.P.A. and J.P.W. designed the study, data were collected and analysed by M.S.S. and J.P.W., and J.P.A. wrote the paper with contributions from M.S.S. and J.P.W.

**Author Information** Reprints and permissions information is available at [www.nature.com/reprints](http://www.nature.com/reprints). The authors declare no competing financial interests. Readers are welcome to comment on the online version of this article at [www.nature.com/nature](http://www.nature.com/nature). Correspondence and requests for materials should be addressed to J.P.A. ([j.p.attfield@ed.ac.uk](mailto:j.p.attfield@ed.ac.uk)) or J.P.W. ([wright@esrf.fr](mailto:wright@esrf.fr)).



# Modelling the rheology of MgO under Earth's mantle pressure, temperature and strain rates

Patrick Cordier<sup>1</sup>, Jonathan Amodeo<sup>1</sup> & Philippe Carrez<sup>1</sup>

Plate tectonics, which shapes the surface of Earth, is the result of solid-state convection in Earth's mantle over billions of years. Simply driven by buoyancy forces, mantle convection is complicated by the nature of the convecting materials, which are not fluids but polycrystalline rocks. Crystalline materials can flow as the result of the motion of defects—point defects, dislocations, grain boundaries and so on. Reproducing in the laboratory the extreme deformation conditions of the mantle is extremely challenging. In particular, experimental strain rates are at least six orders of magnitude larger than in nature<sup>1</sup>. Here we show that the rheology of MgO at the pressure, temperature and strain rates of the mantle is accessible by multiscale numerical modelling starting from first principles and with no adjustable parameters. Our results demonstrate that extremely low strain rates counteract the influence of pressure. In the mantle, MgO deforms in the athermal regime and this leads to a very weak phase. It is only in the lowermost lower mantle that the pressure effect could dominate and that, under the influence of lattice friction, a viscosity of the order of  $10^{21}$ – $10^{22}$  pascal seconds can be defined for MgO.

So far, experimental studies have dominated the contribution of mineral physics to the study of mantle rheology. Experiments are usually designed to describe how a solid deforms under a constant load (creep tests) or how stress evolves with strain at a constant strain rate. The current challenge is to perform such experiments under pressures ( $P$ ) representative of the mantle (that is, up to  $\sim 135$  GPa), and several studies have achieved this<sup>2</sup>. The simultaneous determination of the strain rate ( $\dot{\epsilon}$ ) and of the deviatoric stress ( $\sigma$ ) is necessary to parameterize semi-empirical constitutive flow laws,  $\dot{\epsilon} = f(\sigma, T, P)$  (often of power-law form<sup>3,4</sup>), which are used for extrapolation to

natural conditions (here  $T$  is temperature). A major difficulty is that strain rates available in the laboratory are of the order of  $10^{-6}$ – $10^{-3} \text{ s}^{-1}$ , very different from natural strain rates ( $10^{-12}$ – $10^{-16} \text{ s}^{-1}$ ). Although this issue was recognized early on<sup>1,5</sup>, it has received very little attention, if any, in recent years. Here we propose a physically based model able to describe the rheology of MgO (the magnesium end-member of the second most abundant phase of the lower mantle, ferropericlase (Mg, Fe)O) under very low strain rates representative of mantle convection.

For all crystalline materials, the critical resolved shear stress (CRSS) for plastic yielding follows the same general evolution with temperature (Fig. 1). At 0 K, dislocations move under the influence of stress only. This stress is called the Peierls stress. It measures the intrinsic lattice friction opposed to plastic shear<sup>6</sup>. At finite temperature, dislocation motion is assisted by thermal activation and by stress<sup>7</sup>. A strongly thermally activated regime is observed (Fig. 1) when plastic shear is governed by the intrinsic mobility of dislocations. A microscopic constitutive equation, called the Orowan equation, describes flow in this regime:

$$\dot{\epsilon} = \rho b v \quad (1)$$

Here  $\rho$  is the mobile dislocation density,  $b$  is the Burgers vector modulus and  $v$  is the average dislocation velocity. Above a critical temperature,  $T_a$  (called the athermal temperature), thermal activation is sufficient to overcome lattice friction and plastic shear is essentially athermal, only constrained by the interactions between dislocations. These fundamental features are the basis of our model for the rheology of MgO.

In materials science, multiscale modelling has been developed to link our understanding of a few elementary mechanisms (usually at the

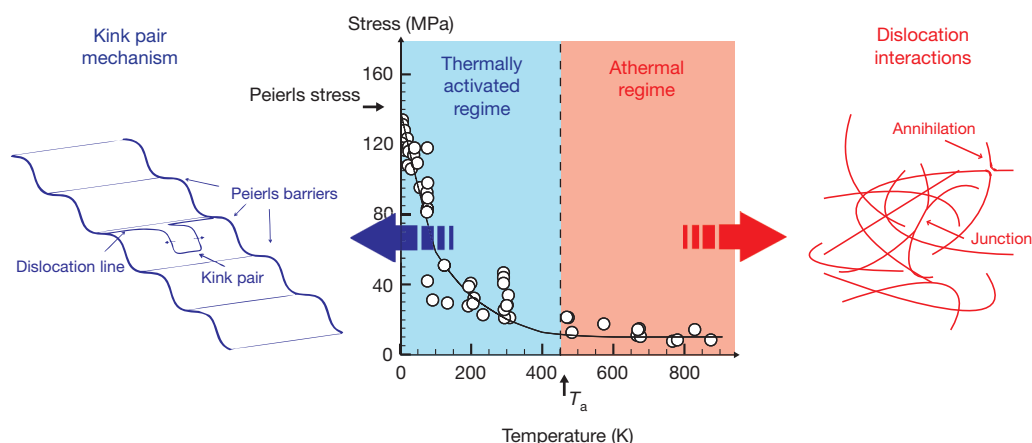


**Figure 1 | Evolution of the critical resolved shear stress (CRSS) with temperature.** Centre panel, CRSS versus temperature for  $\frac{1}{2}\langle 110 \rangle\{110\}$  glide in MgO at ambient pressure; symbols show experimental data (see Supplementary Information for more details), and the line corresponds to our model<sup>12</sup>. As the temperature is increased from 0 K (at which the CRSS is the Peierls stress), the CRSS is strongly temperature dependent until the athermal

temperature,  $T_a$ , is reached. Below  $T_a$ , lattice friction dominates (blue area, 'thermally activated regime') and plastic flow is controlled by the mobility of dislocations governed by the kink-pair mechanism (left panel). Above  $T_a$ , plastic flow is essentially athermal (pink area, 'athermal regime', line reaches a plateau) and dislocation interactions dominate (right panel).

<sup>1</sup>Université Lille 1, Unité Matériaux et Transformations, UMR CNRS 8207, F-59650 Villeneuve d'Ascq, France.

microscopic scale) with behaviour observed at the macroscopic scale, which might be well characterized but which remains poorly understood<sup>8–10</sup>. For plastic deformation, the absence of a global theory results from the range of length scales and timescales spanned. Crystalline plasticity results from the motion of crystal defects: point defects, linear defects (dislocations) or two-dimensional defects (grain boundaries, twin boundaries). The motion of dislocations generally represents the most efficient strain-producing mechanism. Recent calculations<sup>11</sup> have shown that very small grain sizes (100  $\mu\text{m}$ –1 mm) would be required for point defect diffusion to dominate the rheology of the lower mantle. Moreover, mantle temperatures reach only 40–50% of the melting temperature of MgO, which is a very refractory oxide. In the present study, we focus on the contribution of dislocation glide to the rheology of MgO.

We have recently proposed a multiscale model of plasticity that combines three modelling ingredients in a logical chain<sup>12</sup>. As described in Methods, our approach starts with atomistic calculations of dislocation cores, which have a paramount influence on dislocation mobility<sup>13</sup>. This mobility is then modelled in the thermally activated regime using the kink-pairs formalism<sup>14,15</sup> (see below). Finally, above the athermal temperature,  $T_a$ , plastic flow is described within realistic dislocation dynamics (DD) simulations<sup>16</sup>. This multiscale approach has been applied to MgO and has shown its efficiency in reproducing the evolution with temperature of the CRSS observed experimentally (Fig. 1). This model is also able to describe the influence of pressure on the plasticity of MgO (ref. 17). In the range of conditions relevant to Earth's mantle, pressure affects the electronic structure and bonding of MgO and has a strong influence on the core structure and mobility of dislocations. This results in an inversion of slip systems from  $\frac{1}{2}\langle 110 \rangle\{110\}$  to  $\frac{1}{2}\langle 110 \rangle\{100\}$  under the influence of pressure. Another effect of pressure is to shift  $T_a$  towards higher temperatures. At high pressure (and laboratory strain rates), MgO becomes a material characterized by a large lattice friction.

Our physically based description of the mobility of dislocations gives us the capability of modelling the influence of strain rate on the rheology of MgO. Overcoming the Peierls energy barrier requires nucleation of a critical bowing-out (called a kink-pair) of the dislocation line by thermal fluctuations. Rapid lateral motion of the kinks brings the dislocation line into the next low-energy position (Fig. 1). The nucleation rate of kink-pairs is thus generally assumed to limit

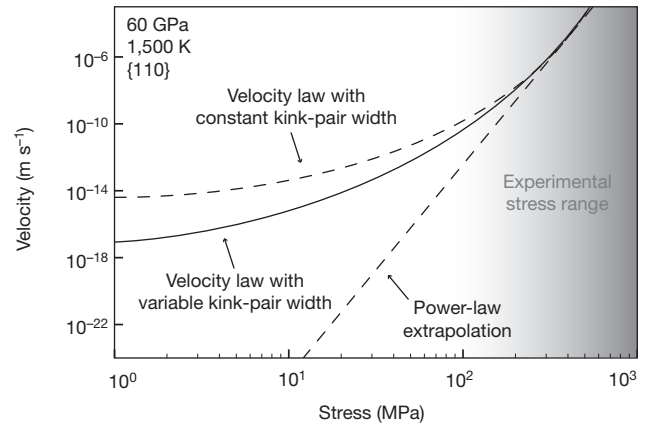


**Figure 2 | Evolution with stress of the velocity of a  $\frac{1}{2}\langle 110 \rangle$  screw dislocation in MgO gliding in  $\{110\}$  at 60 GPa and 1,500 K.** The effect of incorporating variable kink-pair width in equation (2) is shown by the central curve (solid line) which deviates from the case where kink-pair widths are set constant (upper curve, dashed line). As a result, the stress dependence does not obey a power law over a wide stress interval. Extrapolation of laboratory data obtained in the experimental stress range (shaded area) to very low strain rates (corresponding to low stresses) based on a power law fitted to high-stress data (straight dashed line) is thus invalid.

the dislocation velocity<sup>18</sup>. As a result of this mechanism, the average velocity of a moving dislocation (of length  $L$ ) over a Peierls barrier of width  $a'$  can be written as<sup>19</sup>

$$v(\tau, T) = \frac{v_D a' b L}{w^2} \exp\left(\frac{-\Delta H_0}{kT}\right) \sinh\left(\frac{\Delta H_0 - \Delta H(\tau)}{kT}\right) \quad (2)$$

where  $v_D b/w$  is the vibration frequency for a thermal fluctuation of width  $w$  on the dislocation of Burgers vector modulus  $b$  ( $v_D$  is the Debye frequency),  $L/w$  is twice the number of nucleation sites,  $\Delta H(\tau)$  is the activation enthalpy of the kink-pair mechanism under an applied stress  $\tau$  ( $\Delta H_0$  corresponds to the case where  $\tau = 0$ ) and  $k$  is Boltzmann's constant. This formalism satisfactorily reproduces dislocation dynamics in the thermally activated regime<sup>12,20,21</sup>. To extend this formalism to a very low stress (or strain-rate) regime we (1) explicitly incorporate the stress dependence of the kink-pair width,

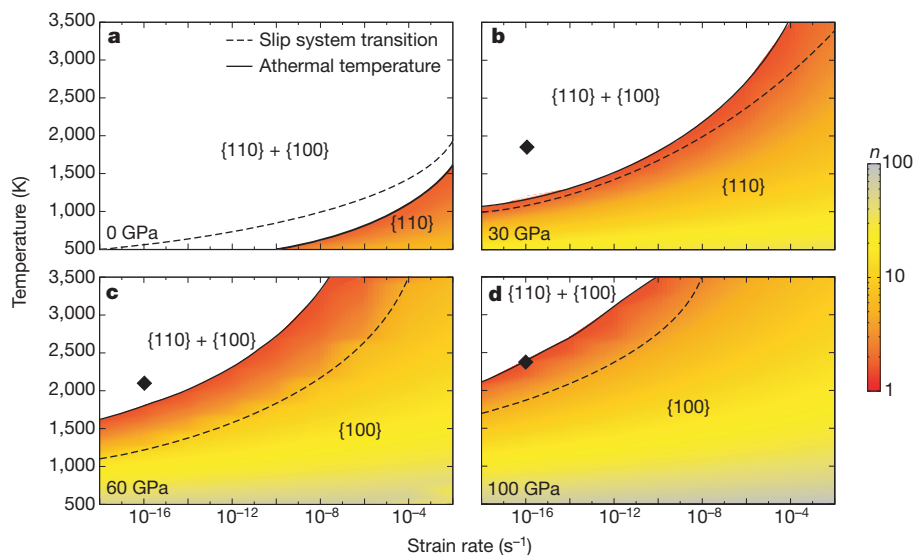


**Figure 3 | Influence of the strain rate and of temperature on the deformation mechanisms of MgO at four pressures.** a, 0 GPa; b, 30 GPa; c, 60 GPa; and d, 100 GPa. The line between the white and coloured regions corresponds to the athermal temperature,  $T_a$ . The domain shown white corresponds to the athermal regime. In the thermally activated domain

(coloured regions), we have calculated and represented an apparent stress exponent,  $n$  (following the colour scale on the right). The dashed line separates domains where different slip systems dominate. The dominant glide planes are given. The filled diamond symbol represents average mantle conditions corresponding to these pressures<sup>22</sup>.



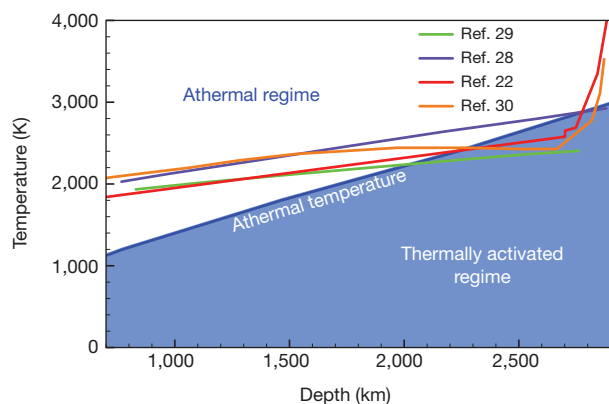


**Figure 4 | Deformation mechanisms of MgO under mantle conditions, and a typical mantle strain rate of  $10^{-16} \text{ s}^{-1}$ .** The athermal temperature is compared to several geotherms<sup>22,28–30</sup>. The exact interval where MgO deforms in the thermally activated regime depends on the thermal state of the mantle and, given lateral thermal heterogeneities<sup>30</sup>, can vary significantly from place to place.

$w(\tau)$ , and of  $\Delta H(\tau)$  as calculated from kink-pair theory (Supplementary Information), and (2) take into account possible backward and forward jumps of the kink-pair through the sinh function. Figure 2 shows that dislocation velocity curves bend significantly with decreasing stress (that is, decreasing strain rates). A power-law-based extrapolation (obtained from a linear approximation on a short stress interval in the high-stress regime) to low strain rates would underestimate the actual velocities.

The rheology of MgO in the thermally activated regime can be inferred from a combination of equations (1) and (2). The evolution with temperature of the CRSS (Supplementary Fig. 4) allows the determination of the athermal temperature,  $T_a$ , at which thermal activation overcomes lattice friction. Figure 3 shows that decreasing pressure, like decreasing strain rate, tends to shift  $T_a$  to lower values. At a given temperature and pressure, laboratory and natural strain rates may induce very different deformation mechanisms. For instance, at 60 GPa and 2,000 K, at laboratory strain rates, MgO deforms on  $\frac{1}{2}\langle 110 \rangle\{100\}$ , under a CRSS of 215 MPa (due to lattice friction) and with a very nonlinear rheology (apparent stress exponent,  $n = 13$ ). Decreasing the strain rate results in a decrease of the stress and of the stress exponent. The second slip system becomes active at  $10^{-8} \text{ s}^{-1}$  under a stress of 100 MPa. When a strain rate of  $\sim 10^{-14} \text{ s}^{-1}$  is reached, the rheology becomes linear. Below this strain rate, MgO deforms in the athermal regime; it becomes very plastic and insensitive to temperature and to strain rate.

The rheology of MgO as a function of temperature and strain rate, at four different pressures<sup>22</sup>, is shown in Fig. 3. It appears that in most cases, the flow corresponds to deformation in the athermal regime, which can only be reached at very high temperatures at laboratory strain rates. All through the lower mantle, both slip systems,  $\frac{1}{2}\langle 110 \rangle\{110\}$  and  $\frac{1}{2}\langle 110 \rangle\{100\}$ , are activated simultaneously. Figure 4 describes the evolution of the rheology of MgO with mantle depth. At depths less than  $\sim 2,000$  km, MgO deforms in the athermal regime. In this regime, the flow stress is governed only by the dislocation microstructure, it is independent of strain rate and a viscosity cannot be defined<sup>23</sup>. In this athermal regime, MgO seems to be very weak (CRSS below 1 MPa for a dislocation density of  $10^8 \text{ m}^{-2}$ ) and should be much weaker than Mg-silicate perovskite in similar conditions. Deeper than  $\sim 2,000$  km, MgO enters a thermally activated regime. Only there can a viscosity be defined from the Orowan law. We find it to be of the order of  $10^{21}$ – $10^{22}$  Pa s, with a depth dependence shown in Fig. 5. In the vicinity of  $T_a$ , the rheology is close to linear and the viscosity is minimum. When the temperature departs from  $T_a$ , the viscosity increases and becomes more dependent on strain rate. Just above the core–mantle boundary, MgO can again enter a very weak,

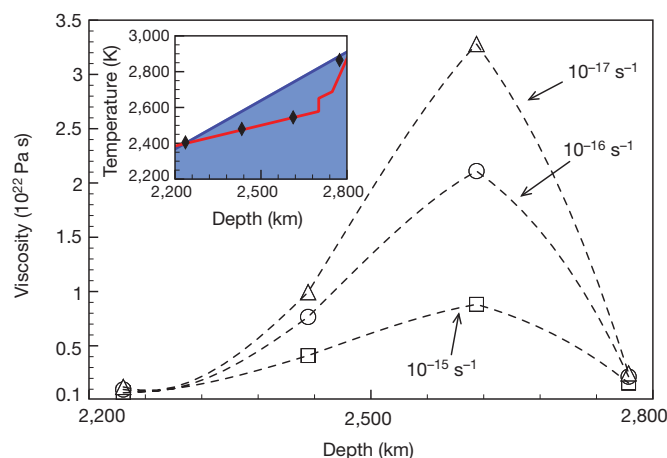


**Figure 5 | MgO viscosity profile in the layer (shown in the inset) governed by the thermally activated deformation regime.** Main panel, viscosity versus depth; dashed lines are a guide for the eye. We note that because decreasing the strain rate by an order of magnitude results in a very small variation of the stress, the viscosity increases when the strain rate decreases. The more the temperature departs from  $T_a$  within the thermally activated regime (blue area in the inset), the more pronounced this nonlinearity becomes. Inset, the depth interval between 2,200 and 2,800 km corresponding to the geotherm of ref. 22 within Fig. 4. The symbols along the geotherm (in red) correspond to the viscosity calculations.

athermal regime. The depth and extent of this layer, characterized by a thermally activated regime, will depend on the thermal state of the lower mantle, as illustrated by Fig. 4, which displays several temperature profiles. The actual situation is probably even more complex, as large thermal heterogeneities (of the order of 1,000 K) are likely to be superimposed on these average temperature profiles<sup>23</sup>.

Changes of the deformation mechanism of MgO could thus account for strong radial and lateral rheology heterogeneities inferred in the lowermost mantle<sup>24</sup>, even in the absence of significant chemical heterogeneities. However, knowledge of the single-crystal rheology of both MgO and Mg-silicate perovskite will not on its own be enough to define the rheology of the mantle. Some form of even larger-scale modelling will be required, which can form a bridge between the scale of a mineral grain and the scale of a convection cell in a general circulation model of lower-mantle dynamics.

## METHODS SUMMARY

In this study, we use the hierarchical multiscale approach developed in ref. 12 to model the plasticity of MgO single crystals. Atomistic dislocation core structures are modelled with a Peierls–Nabarro–Galerkin (PNG) approach<sup>25</sup>. The electronic structure is explicitly taken into account through  $\gamma$ -surfaces calculated *ab initio* using VASP<sup>26</sup>. The dislocation mobility, governed by equation (2), is controlled by kink-pair nucleation. The nucleation enthalpy of kink-pairs,  $\Delta H(\tau)$ , and the kink-pair geometry are evaluated using the elastic interaction method<sup>27</sup>. Low-stress effects are explicitly taken into account in equation (2) by considering the formal geometry of possible backward and forward kink-pairs. Mesoscopic-scale simulations of MgO deformation processes are performed by dislocation dynamics simulations<sup>16</sup> incorporating dislocation mobilities described by equation (2). The accuracy of such a multiscale model has been validated against room-pressure experimental data<sup>12</sup>. An extended description of the techniques is available in the online-only Methods section.

**Full Methods** and any associated references are available in the online version of the paper at [www.nature.com/nature](http://www.nature.com/nature).

**Received 3 June; accepted 25 October 2011.**

- Paterson, M. S. Problems in the extrapolation of laboratory rheological data. *Tectonophysics* **133**, 33–43 (1987).
- Raterron, P. & Merkel, S. *In situ* rheological measurements at extreme pressure and temperature using synchrotron X-ray diffraction and radiography. *J. Synchrotron Radiat.* **16**, 748–756 (2009).
- Poirier, J. P. *Creep of Crystals* (Cambridge Univ. Press, 1985).
- Karato, S. *Deformation of Earth Materials: An Introduction to the Rheology of Solid Earth* (Cambridge Univ. Press, 2008).

5. Heard, H. C. Effect of large changes in strain rate in the experimental deformation of Yule marble. *J. Geol.* **71**, 162–195 (1963).
6. Peierls, R. The size of a dislocation. *Proc. Phys. Soc. Lond.* **52**, 34–37 (1940).
7. Caillard, D. & Martin, J. L. *Thermally Activated Mechanisms in Crystal Plasticity* (Pergamon, 2003).
8. Bulatov, V. V. & Kubin, L. P. Dislocation modelling at atomistic and mesoscopic scales. *Curr. Opin. Solid State Mater. Sci.* **3**, 558–561 (1998).
9. Needleman, A. Computational mechanics at the mesoscale. *Acta Mater.* **48**, 105–124 (2000).
10. de la Rubia, T. D. & Bulatov, V. V. Materials research by means of multiscale computer simulations. *Mater. Res. Soc. Bull.* **26**, 169–175 (2001).
11. Ammann, M. W., Brodholt, J. P., Wookey, J. & Dobson, D. P. First-principles constraints on diffusion in lower-mantle minerals and a weak D'' layer. *Nature* **465**, 462–465 (2010).
12. Amodeo, J., Carrez, P., Devincere, B. & Cordier, P. Multiscale modelling of MgO plasticity. *Acta Mater.* **59**, 2291–2301 (2011).
13. Cai, W., Bulatov, V. V., Chang, J., Li, J. & Yip, S. in *Dislocations in Solids* Vol. 12 (eds Nabarro, F. N. R. & Hirth, J. P.) 1–80 (Elsevier, 2004).
14. Seeger, A. & Schiller, P. Bildung und Diffusion von Kinken als Grundprozess der Versetzungsbewegung bei der Messung der inneren Reibung. *Acta Metall.* **10**, 348–357 (1962).
15. Guyot, P. & Dorn, J. E. A critical review of Peierls mechanism. *Can. J. Phys.* **45**, 983–1016 (1967).
16. Devincere, B., Kubin, L. P., Lemarchand, C. & Madec, R. Mesoscopic simulations of plastic deformation. *Mater. Sci. Eng. A* **309–310**, 211–219 (2001).
17. Amodeo, J., Carrez, P. & Cordier, P. Modelling the effect of pressure on the critical shear stress of MgO single crystals. *Phil. Mag.* (in the press).
18. Frost, H. J. & Ashby, M. F. *Deformation-Mechanism Maps: The Plasticity and Creep of Metals and Ceramics* (Pergamon, 1982).
19. Nabarro, F. N. R. One-dimensional models of thermal activation under shear stress. *Phil. Mag.* **83**, 3047–3054 (2003).
20. Tang, M., Kubin, L. P. & Canova, G. R. Dislocation mobility and the mechanical response of bcc crystals: a mesoscopic approach. *Acta Mater.* **46**, 3221–3235 (1998).
21. Monnet, G., Devincere, B. & Kubin, L. P. Dislocation study of prismatic slip systems and their interactions in hexagonal close packed metals: application to zirconium. *Acta Mater.* **52**, 4317–4328 (2004).
22. Ono, S. Experimental constraints on the temperature profile in the lower mantle. *Phys. Earth Planet. Inter.* **170**, 267–273 (2008).
23. Paterson, M. S. Relating experimental and geological rheology. *Int. J. Earth Sci.* **90**, 157–167 (2001).
24. Forte, A. M. & Mitrovica, J. X. Deep-mantle high-viscosity flow and thermochemical structure inferred from seismic and geodynamic data. *Nature* **410**, 1049–1056 (2001).
25. Denoual, C. Dynamic dislocation modeling by combining Peierls Nabarro and Galerkin methods. *Phys. Rev. B* **70**, 024106 (2004).
26. Kresse, G. & Hafner, J. Ab initio molecular-dynamics for liquid-metals. *Phys. Rev. B* **47**, 558–561 (1993).
27. Koizumi, H., Kirchner, H. O. K. & Suzuki, T. Kink pair nucleation and critical shear stress. *Acta Metall. Mater.* **41**, 3483–3493 (1993).
28. Anderson, O. L. The Earth's core and the phase diagram of iron. *Phil. Trans. R. Soc. Lond. A* **306**, 21–35 (1982).
29. Brown, J. M. & Shankland, T. J. Thermodynamic parameters in the Earth as determined from seismic profiles. *Geophys. J. R. Astron. Soc.* **66**, 579–596 (1981).
30. Schuberth, B. S. A., Bunge, H.-P., Steinle-Neumann, G., Moder, C. & Oeser, J. Thermal versus elastic heterogeneity in high-resolution mantle circulation models with pyrolite composition: high plume excess temperatures in the lowermost mantle. *Geochem. Geophys. Geosyst.* **10**, Q01W01 (2009).

**Supplementary Information** is linked to the online version of the paper at [www.nature.com/nature](http://www.nature.com/nature).

**Acknowledgements** This work was supported by ANR (Diup project).

**Author Contributions** P.C. conceived the project. P.C. and Ph.C. designed the work. J.A. and Ph.C. performed numerical simulations. All authors discussed and interpreted the results. P.C. wrote the paper with feedback and contributions from all co-authors.

**Author Information** Reprints and permissions information is available at [www.nature.com/reprints](http://www.nature.com/reprints). The authors declare no competing financial interests. Readers are welcome to comment on the online version of this article at [www.nature.com/nature](http://www.nature.com/nature). Correspondence and requests for materials should be addressed to P.C. (Patrick.Cordier@univ-lille1.fr).



## METHODS

The hierarchical multiscale model used throughout this study was initially developed in ref. 12 and applied to pure MgO single crystals. It connects modelling at three different scales. The first corresponds to the modelling of dislocation core structures and associated Peierls stresses (the stress required to move a dislocation without the help of thermal activation). The second stage incorporates the temperature effect on intrinsic dislocation mobility. The last stage describes dislocation interactions and yields single crystal mechanical properties.

**Peierls–Nabarro–Galerkin modelling of dislocation cores.** Peierls–Nabarro (PN) methods<sup>6</sup> and their recent developments<sup>25,31,32</sup> based on  $\gamma$ -surfaces are very efficient in modelling dislocation core structures<sup>33</sup>. Here we use the Peierls–Nabarro–Galerkin model<sup>25,34</sup> as implemented in Cod<sup>2</sup>ex software, which offers the possibility of taking multiple glide planes into account and of calculating complex (possibly three-dimensional) dislocation cores. As in the initial PN model, the dislocation core structure is determined from the minimization of an elastic energy (through an approximation of a continuous field representation) and an interplanar potential derived from  $\gamma$ -surface calculations. The present study uses pressure-dependent  $\gamma$ -surfaces calculated from first principles. Indeed, the pressure range of Earth's lower mantle rules out the use of empirical potentials and justifies the use of density functional theory (DFT) calculations, which are believed to be more accurate.

Classical DFT approximations (namely GGA with PAW pseudo-potentials<sup>35–37</sup>, as implemented in the VASP code<sup>26,38</sup>) have been used to calculate the excess energy associated with a rigid-body shear of a supercell along a given plane (corresponding to the strict definition of a  $\gamma$ -surface<sup>39</sup>). Three different  $\gamma$ -surfaces, namely {110}, {100} and {111}, have been considered. As a consequence, three distinct supercells have been built for VASP calculations. Supercells are built on a Cartesian reference frame with the  $z$  axis normal to the shear plane. To reduce the number of atoms in each supercell, the  $x$  and  $y$  directions are chosen according to shortest crystallographic directions, that is,  $\frac{1}{2}\langle 110 \rangle$  and  $\langle 001 \rangle$  for the {110} supercell, two perpendicular  $\frac{1}{2}\langle 110 \rangle$  directions for the {100} supercell and  $\frac{1}{2}\langle 110 \rangle$  and  $\frac{1}{2}\langle 112 \rangle$  for the {111} supercell. Doing so, the supercells contain a minimum of 16 atomic layers with a single stacking fault plane located in the middle of the supercell, isolated from effects created by periodic boundary conditions by a buffer of a vacuum layer with a minimum thickness of 6 Å. A Monkhorst–Pack grid<sup>40</sup> is used to sample the first Brillouin zone with grid point numbers increased to  $6 \times 4 \times 2$  for energy convergence purposes. Calculations have been performed at 0, 30, 60 and 100 GPa.

Both edge and screw dislocation cores have been calculated through the PNG method. In this approach, two distinct fields are used to minimize the energy of a system in which an initial Volterra dislocation has been introduced. One is a three-dimensional displacement field which represents the continuous deformation around the dislocation core, whereas the second is a vector field which represents the displacement jump when crossing discontinuity surfaces characterized by  $\gamma$ -surfaces. Minimization with respect to the vector field is achieved by means of a time-dependent Ginzburg–Landau equation, whereas an element-free Galerkin method is used to compute the evolution of the three-dimensional displacement field.

PNG finite-element cells are defined with a node structure reflecting the crystalline symmetry of the crystal. A classical node density of 12 nodes per Burgers vector is chosen for all the calculations. For calculations of the  $\frac{1}{2}[110]$  screw dislocation, four planes are considered to control the spreading of shear within the core, namely (1 $\bar{1}$ 0), (001), (1 $\bar{1}$ 1) and (11 $\bar{1}$ ). Between those planes (associated with  $\gamma$ -surfaces), the medium has linear elastic behaviour. The method ensures that potentially non-planar core dislocations can be safely reproduced. Once the equilibrium configuration of the dislocation core is reached, the PNG finite-element cells can be strained to determine the Peierls stress, for which a dislocation displacement is irreversible in its glide plane. **Kink-pair model.** In the presence of lattice friction, dislocation motion is thermally activated<sup>13</sup>. Practically, a dislocation line moves from one Peierls valley (corresponding to a minimum-energy position) to the next, through the nucleation and propagation of kink-pairs<sup>7,41</sup>. Several methods<sup>7</sup> exist to model the kink-pair mechanism; among them are the line tension (LT) and elastic interaction (EI) models<sup>14,27</sup>. The EI method has been chosen for this study because it is commonly regarded as a low-stress model<sup>7</sup>. It gives access to the stress dependence of the formation enthalpy for critical configurations of kink-pairs.

The rate of kink-pair nucleation is thermodynamically controlled by the free energy required to displace a critical dislocation segment into the next Peierls valley. When neglecting the associated entropy<sup>42</sup>, this energy can be approximated by the activation enthalpy,  $\Delta H$ . Within the EI assumptions,  $\Delta H$  results from three contributions: the elastic interaction energy,  $\Delta E$ ; the variation of the Peierls energy,  $\Delta P$ , between a straight line and a kinked one; and  $W$ , the work of the applied stress,  $\tau$ . Assuming a rectangular shape for the kink-pair configuration of height  $h$  and width  $w$ , the variation of enthalpy takes the following form:

$$\Delta H(h, w) = \Delta E(h, w) + \Delta P(h, w) - W(h, w) \quad (3)$$

A critical shape ( $h^*$ ,  $w^*$ ) of the bowed-out configuration and the associated critical enthalpy,  $\Delta H^*$ , can thus be calculated in the saddle-point configuration as a function of stress,  $\tau$ .

Considering a rectangular kink-pair, we use the expression of  $\Delta E$  proposed in ref. 41, in which the self-energy of dislocation is controlled by a cut-off length. In this study, this cut-off length is taken to be 5% of the half-width of the dislocation core (accessible from the previous stage of modelling). Half-widths of dislocation cores, core structures and Peierls stresses,  $\tau_p$ , calculated by the PNG method are also used to define the Peierls potential,  $V_p$ , controlling the numerical evaluation of  $\Delta P$  (ref. 27). Therefore, this formalism is closely related and linked to the atomic-scale information previously calculated.

**Dislocation dynamics (DD).** DD simulations have been performed using the open-source simulation package mM<sup>16,21</sup>. This is a discrete three-dimensional DD code accounting for complex boundary conditions. Here, periodic boundary conditions are used in the calculations to model plasticity in bulk conditions<sup>43</sup>. DD simulations with the mM code are also known as discrete DD simulations, as they rely on a discretization of both space and time. For a given slip system geometry, dislocation lines are discretized into a finite set of segments of fixed characters: screw, edge and mixed. Straight, glissile segments are therefore moved on a 3D lattice exhibiting the lattice symmetry of the simulated crystal structure. For MgO, the underlying lattice is thus composed of 96 elementary segments belonging to 12 possible slip planes to describe dislocations from the two possible slip system families,  $\frac{1}{2}\langle 110 \rangle$ –{110} and  $\frac{1}{2}\langle 110 \rangle$ –{100}.

The long-range interactions are treated through Peach–Koehler forces. Apart from the applied stress specific to the loading conditions, stress acting on discretized segments takes into account the stress field associated with the whole set of dislocation lines present in the simulated volume, plus the line tension. During deformation, local rules are prescribed to account for contact reactions, such as annihilations or junction formation<sup>44</sup>. Finally, throughout the thermally activated regime, discrete dislocation segments move with a velocity law described by equation (2). The method assumes that kink-pair nucleation is the controlling stage, and relies on key numerical parameters coming from the two previous steps of the modelling scheme.

A series of compression test simulations at various temperatures are used to determine the CRSS of MgO. To that purpose, one may undertake DD simulations at a constant strain rate in a simulated volume, using a distribution of initially straight dislocations (of either screw or edge character, depending on the pressure–temperature range investigated) of characteristic length  $(1/\sqrt{\rho}) = 100 \mu\text{m}$ . Dislocation lines are initially along a diagonal of the basis plane of the simulated volume which is parallel to {001}, so that identical simulation conditions can be used to promote glide in either {100} or {110} planes simply by varying the compression axis.

- Joós, B., Ren, Q. & Duesbery, M. S. Peierls–Nabarro model of dislocations in silicon with generalized stacking-fault restoring forces. *Phys. Rev. B* **50**, 5890–5898 (1994).
- Bulatov, V. V. & Kaxiras, E. Semidiscrete variational Peierls framework for dislocation core properties. *Phys. Rev. Lett.* **78**, 4221–4224 (1997).
- Schoeck, G. The core structure of dislocations: Peierls model vs. atomic calculations. *Acta Mater.* **54**, 4865–4870 (2006).
- Denoual, C. Modeling dislocation by coupling Peierls–Nabarro and element-free Galerkin methods. *Comput. Methods Appl. Mech. Eng.* **196**, 1915–1923 (2007).
- Perdew, J. P. & Wang, Y. Accurate and simple analytic representation of the electron–gas correlation energy. *Phys. Rev. B* **45**, 13244–13249 (1992).
- Blöchl, P. E. Projector augmented-wave method. *Phys. Rev. B* **50**, 17953–17979 (1994).
- Kresse, G. & Furthmüller, J. Efficiency of ab-initio total energy calculations for metals and semiconductors using a plane-wave basis set. *Comput. Mater. Sci.* **6**, 15–50 (1996).
- Kresse, G. & Hafner, J. Ab initio molecular dynamics simulation of the liquid-metal amorphous-semiconductor transition in germanium. *Phys. Rev. B* **49**, 14251–14269 (1994).
- Vitek, V. Intrinsic stacking faults in body-centered cubic crystals. *Phil. Mag.* **18**, 773–786 (1968).
- Monkhorst, H. J. & Pack, J. D. On special points for Brillouin-zone integrations. *Phys. Rev. B* **13**, 5188–5192 (1976).
- Hirth, J. P. & Lothe, J. *Theory of Dislocations* (Wiley, 1982).
- Schoeck, G. The activation energy of dislocation movement. *Phys. Status Solidi* **8**, 499–507 (1965).
- Madec, R., Devincre, B. & Kubin, L. P. in *IUTAM Symposium on Mesoscopic Dynamics of Fracture Process and Materials Strength* (eds Koizumi, H. & Yip, S.) 35–44 (Kluwer, 2004).
- Kubin, L. P., Madec, R. & Devincre, R. Dislocation intersections and reactions in FCC and BCC crystals. *Mater. Res. Soc. Symp. Proc.* **779**, 25–36 (2003).

# Tail-assisted pitch control in lizards, robots and dinosaurs

Thomas Libby<sup>1</sup>, Talia Y. Moore<sup>2</sup>, Evan Chang-Siu<sup>3</sup>, Deborah Li<sup>2</sup>, Daniel J. Cohen<sup>4</sup>, Ardian Jusufi<sup>2</sup> & Robert J. Full<sup>2</sup>

In 1969, a palaeontologist proposed<sup>1</sup> that theropod dinosaurs used their tails as dynamic stabilizers during rapid or irregular movements, contributing to their depiction as active and agile predators. Since then the inertia of swinging appendages has been implicated in stabilizing human walking<sup>2,3</sup>, aiding acrobatic manoeuvres by primates<sup>4–8</sup> and rodents<sup>9</sup>, and enabling cats to balance on branches<sup>10</sup>. Recent studies on geckos<sup>11–13</sup> suggest that active tail stabilization occurs during climbing, righting and gliding. By contrast, studies on the effect of lizard tail loss show evidence of a decrease, an increase or no change in performance<sup>14,15</sup>. Application of a control-theoretic framework could advance our general understanding of inertial appendage use in locomotion. Here we report that lizards control the swing of their tails in a measured manner to redirect angular momentum from their bodies to their tails, stabilizing body attitude in the sagittal plane. We video-recorded Red-Headed Agama lizards (*Agama agama*) leaping towards a vertical surface by first vaulting onto an obstacle with variable traction to induce a range of perturbations in body angular momentum. To examine a known controlled tail response, we built a lizard-sized robot with an active tail that used sensory feedback to stabilize pitch as it drove off a ramp. Our dynamics model revealed that a body swinging its tail experienced less rotation than a body with a rigid tail, a passively compliant tail or no tail. To compare a range of tails, we calculated tail effectiveness as the amount of tailless body rotation a tail could stabilize. A model *Velociraptor mongoliensis* supported the initial tail stabilization hypothesis<sup>1</sup>, showing as it did a greater tail effectiveness than the Agama lizards. Leaping lizards show that inertial control of body attitude can advance our understanding of appendage evolution and provide biological inspiration for the next generation of manoeuvrable search-and-rescue robots.

Agama lizards (average mass,  $66.96 \pm 2.93$  g) ran within an acrylic track and rapidly transitional to a vertical wall with a shelter on top. To stimulate a leap with a long aerial phase, we directed the animals over a small box that acted as a vault (Fig. 1a, b). To induce perturbations during the transition, we varied the traction available on top of the vault. We proposed that a sandpaper-covered vault would allow the lizard sufficient traction to closely direct its ground reaction force vector through its centre of mass (COM) and thereby minimize body rotation in the aerial phase (Fig. 1a and Supplementary Movie 1). Covering the vault with smooth card stock (Fig. 1b and Supplementary Movie 2) would cause feet to slip, misaligning the ground reaction force vector and imparting a rotational impulse during this critical phase when lizards redirect horizontal momentum upwards. We recorded body and tail motion with a high-speed digital camera.

To quantify the possible effect a tail has on maintaining attitude stability in the pitch axis during the leap, we determined the angle through which a tailless body would rotate after a given perturbation at take-off. We measured the perturbation magnitude at take-off for each trial by estimating the mean total angular momentum ( $H$ ) over the duration of the leap. We computed  $H$  using the lizard's kinematic

data during the aerial phase by fitting a two-link (body and tail), planar dynamic model constructed from morphometric data from five Agama lizard cadavers (Supplementary Table 1). Assuming aerodynamic forces to be negligible<sup>8,12,13</sup>, we took the computed  $H$  to be the perturbation applied during take-off. The variable surface vault produced a broad range in aerial-phase angular momentum,  $\pm 1.5 \times 10^{-3} \text{ kg m}^2 \text{ s}^{-1}$ . To better compare the magnitude of the perturbation among individuals, we normalized  $H$  by body moment of inertia ( $I_b$ ) about its COM and by leap duration ( $t$ ). The normalized perturbation magnitude,  $(H/I_b)t$  (Fig. 2, abscissa), represents the angle through which an individual's body would rotate without its tail, given the observed angular momentum and trial duration. Because the duration of foot slippage was brief, take-off angle was not affected by the perturbation (coefficient of determination,  $r^2 = 0.13$ ). Hence, we proposed that a constant body angle was maintained after the perturbation.

We reasoned that defining inertial appendage control over a range of perturbations could benefit from a physical model with a known control mechanism. We built an Agama-sized, tailed robot that used proportional-derivative (PD) feedback control (Fig. 1c, d) to stabilize body angle<sup>16</sup>. Inertial stabilization of robotic locomotion has been modelled before<sup>17</sup>, and simple air-righting accomplished<sup>18</sup>, but our robot is the first with a specialized tail-like appendage for continuous inertial stabilization. Previous investigations of tails in mobile robots have focused on substrate interaction and passive stability<sup>19,20</sup>. Our wheeled robot swung an aluminium rod tail in the sagittal plane in response to sensing using a microelectromechanical systems gyroscope. A ski-jump-like ramp launched the robot at the same take-off angle that the lizards selected. The unbalanced gravitational moment as the front wheels left the ramp applied a similar rotational perturbation to that induced on the lizards by the low-friction vault. We launched the robot in two situations: with the controller off and the tail rigidly held parallel to the body (Fig. 1c and Supplementary Movie 3) and with the PD feedback controller on and the reference angle set to the take-off angle of the ramp (Fig. 1d and Supplementary Movie 4). Varying the perturbation on the robot by changing the speed with which it left the ramp altered the imparted angular momentum. As the perturbation increased, the robot with PD feedback tail control maintained a nearly constant body angle by swinging its tail upward and incurred 72% less rotation after a perturbation than did the robot without tail control (Fig. 2b).

Lizards swung their tails during leaps in a manner consistent with the control of body pitch observed in the robot. Tail swinging was not an all-or-none behaviour, but was proportional to perturbation magnitude. The change in tail angle relative to the body during the aerial phase correlated with the normalized perturbation magnitude ( $r = 0.79$ ,  $P < 0.001$ ). A larger perturbation at take-off resulted in a correspondingly greater tail swing. Attenuation of body pitch was not unidirectional: lizards swung their tails upwards to compensate for nose-down perturbations and downwards in response to nose-up perturbations (Fig. 2a and Supplementary Movie 5). By rotating their

<sup>1</sup>Center for Interdisciplinary Bio-Inspiration in Education and Research, University of California, Berkeley, California 94720-3140, USA. <sup>2</sup>Department of Integrative Biology, University of California, Berkeley, California 94720-3140, USA. <sup>3</sup>Department of Mechanical Engineering, University of California, Berkeley, California 94720-1740, USA. <sup>4</sup>Department of Bioengineering, University of California, Berkeley, California 94720-1762, USA.

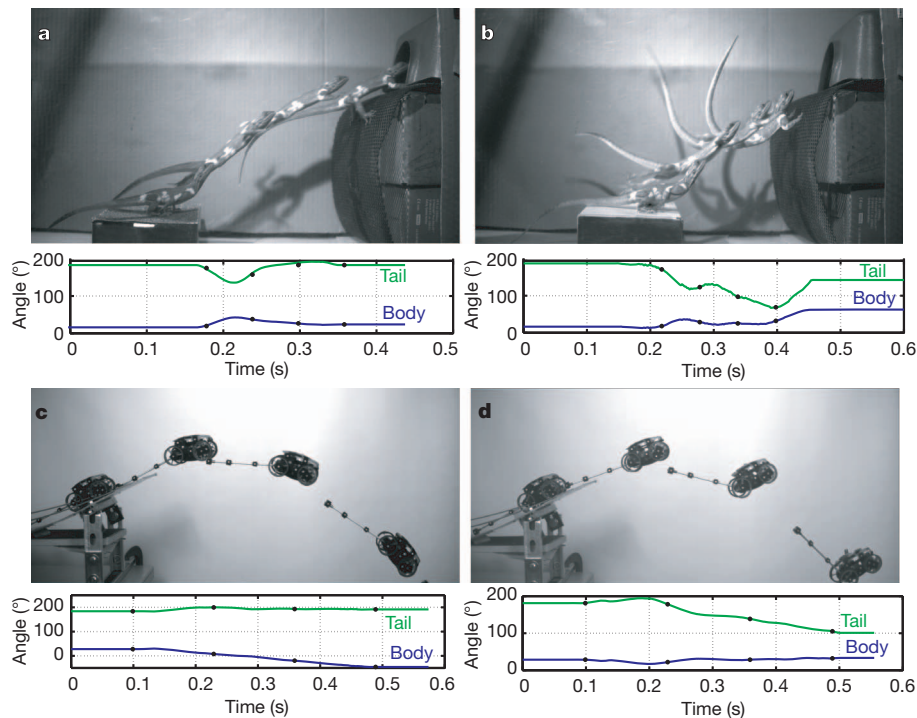


**Figure 1 | Pitch stabilization using a tail in a lizard and robot.** Tail angle (green) relative to body axis and body angle (blue) relative to ground. **a, b,** Agama lizards ran along a track and vaulted off an obstacle to a vertical wall with a shelter on top. Overlain images are separated by 60 ms. **a,** A high-traction vault surface produced small perturbations in body angular momentum, allowing tail and body angles to remain constant (Supplementary Movie 1). **b,** A low-traction vault surface produced slipping that generated an angular momentum perturbation. By swinging their tails upwards, lizards redirected

angular momentum from the body to the tail to maintain body angle (Supplementary Movie 2). **c, d,** A wheeled robot drove off a ramp, producing a nose-down perturbation in body angular momentum. Overlain images are separated by 130 ms. **c,** Without PD feedback control, the robot body and tail rotated as a rigid body (Supplementary Movie 3). **d,** With PD feedback control, the tail swung upwards as the controller applied torque to stabilize the body, keeping the body angle constant (Supplementary Movie 4).

tails with respect to the body in the sagittal plane, the lizards transferred angular momentum from the body to tail, thereby reducing body angular velocity and the effect of perturbation on body rotation (Fig. 2a).

We characterized the sensitivity to pitch perturbations by regressing experimentally observed rotations against the normalized perturbation,

yielding a dimensionless metric ( $S$ , the slope of the lines in Fig. 2a) representing the observed body rotation due to a perturbation relative to the rotation a tailless body would undergo. A sensitivity value, or slope, of one would indicate that the individual stabilized itself no better than would a tailless body. A value less than one signifies that the animal or robot attenuated the effect of the perturbation on its body rotation. A

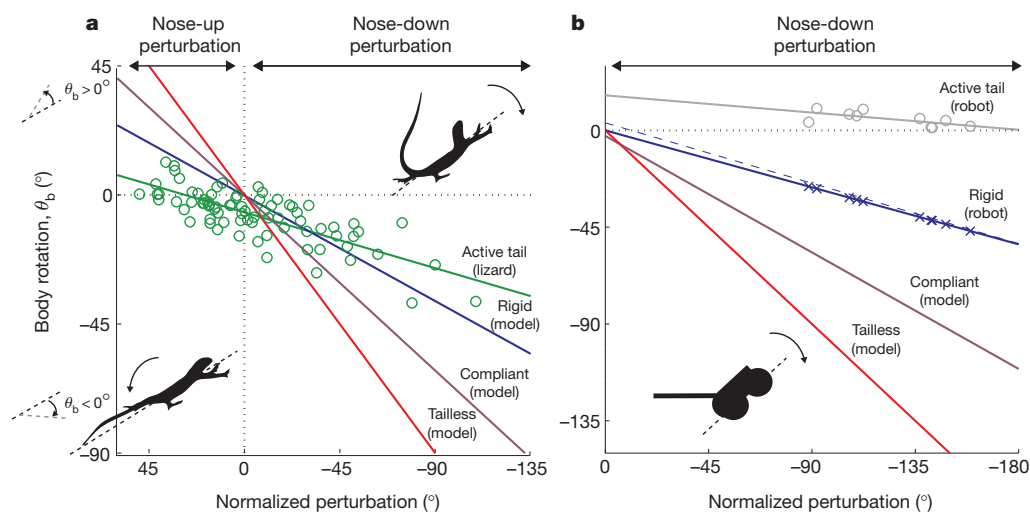


**Figure 2 | Sensitivity of body rotation to a perturbation in a lizard and robot.** Body rotation ( $\theta_b$ ) as a function of perturbation, defined as the angle through which the body would rotate without a tail. The slope of the lines represents sensitivity to perturbations. **a,** Lizards (green circles and line) controlled body rotation by swinging their tails downwards to correct a nose-up pitch (normalized perturbation,  $>0^\circ$ ) and upwards to correct a nose-down pitch (normalized perturbation,  $<0^\circ$ ). Lizards were less sensitive to

perturbations than were tailless (red), compliant-tail (purple) or rigid-tail (blue) Agama models. **b,** Robots (grey circles and line) controlled body rotation by swinging their tails upwards to correct a nose-down pitch (normalized perturbation,  $<0^\circ$ ) more effectively than lizards. Robots were far less sensitive to perturbations than were tailless (red) and compliant-tail (purple) models or robots with rigid tails (blue crosses and line).



value of zero shows perfect compensation (Fig. 2a, b, horizontal dashed line). Supporting the hypothesis of tail-facilitated control, we found the measured sensitivity of Agama lizards to a rotational perturbation to be very low,  $S = 0.22 \pm 0.02$ , relative to the tailless model value,  $S = 1$ , although not as low as that of our PD-feedback-controlled tailed robot ( $S = 0.090 \pm 0.035$ ; Supplementary Table 2).

We compared the lizard's effectiveness in controlling body pitch using an active tail with those of our robot and three mathematical models: a tailless animal (single body link), a rigid-tailed animal (body and tail links with a rigid joint), and a compliant tailed animal (both links with a torque-free pin joint). We used a morphologically averaged Agama model to generate a prediction of perturbation sensitivity for each passive tail condition, and calculated the difference with respect to the experimentally measured value (Supplementary Table 2). Adding a compliant or rigid tail to the tailless model Agama decreased its sensitivity by 36% ( $S = 0.64$ ) or 58% ( $S = 0.42$ ), respectively, indicating that passive tails can improve aerial stability. The actual Agamas actively controlling their tails were significantly less sensitive to perturbations than either passive tail model ( $P < 0.001$ ; Supplementary Table 2). Our model results showed that animals received 48% less rotation after a perturbation than they would if they had held their tails rigid during the aerial phase, 66% less rotation than if they had left the tail compliant and 78% less rotation than if they had no tail at all. By comparing the average proportion of angular momentum in each segment with the expected value for a rigidly linked model, we found that the lizards had  $41.000 \pm 0.043\%$  less angular momentum in their bodies than the rigid model, and a corresponding increase in tail momentum, indicating active momentum transfer.

The PD-feedback-controlled robot incurred 72% less rotation after a perturbation than it would if it had held its tail rigid during the aerial phase, 85% less rotation than if it had left the tail compliant and 91% less rotation than if it had no tail at all (Supplementary Table 2). The experimental control (that is, with PD feedback controller off) was not significantly different from the model case in which the tail was rigidly connected to the body (Fig. 2b, blue line and crosses;  $t = -5.0$ ,  $P < 0.001$ ). We found that the tail contained  $31.00 \pm 0.04\%$  more angular momentum than if it was rotating rigidly with the body, and that the body contained  $40.00 \pm 0.08\%$  less. With the PD feedback controller off, the passive-tail robot's links did not contain significantly different momentum than did the rigid model (analysis of variance,  $F = 0.32$ ,  $P = 0.58$ ). Hence, the effect of the PD feedback controller on regulating body angle was to redirect angular momentum from the body to the tail, supporting our hypotheses for lizards.

Our mathematical model allows us to predict the effectiveness of different tails in preventing body rotation. Assuming that total angular momentum is conserved after a perturbation, the tail must rotate for the body's orientation to remain stable. The amount of rotation required depends on tail morphology<sup>12,13</sup>. We define tail effectiveness as the amount of tailless body rotation a tail could stabilize per degree of tail rotation (that is, the absolute value of the reciprocal slope from Fig. 3 linearized around a tail rotation of  $\phi_t = 0^\circ$ ). For a tail effectiveness of one, a perturbation rotating a tailless animal by  $45^\circ$  could be completely stabilized by rotating the tail through the same angle. Less effective tails would require more tail rotation to stabilize the same perturbation. Because tails are limited in range of motion, effectiveness limits the size of perturbation a tail can completely stabilize. After modelling each lizard in our study, we found their average tail effectiveness to be 0.79: for the typical maximum tail stroke of  $100^\circ$ , the lizards could completely stabilize a perturbation that would rotate a tailless lizard by almost  $80^\circ$  (Fig. 3; range shown by green shaded area). When our robot's body–tail length ratio was similar to those of the Agama lizards, it was over twice as effective (1.84; Fig. 3, dashed line, bottom grey shaded area). This resulted from concentrating mass at the tip (Supplementary Table 1), rather than at the base as in lizards. We modelled a range of possible tail configurations in the robot, from a small tail (5% body mass, 50% body length) to a large tail (10%

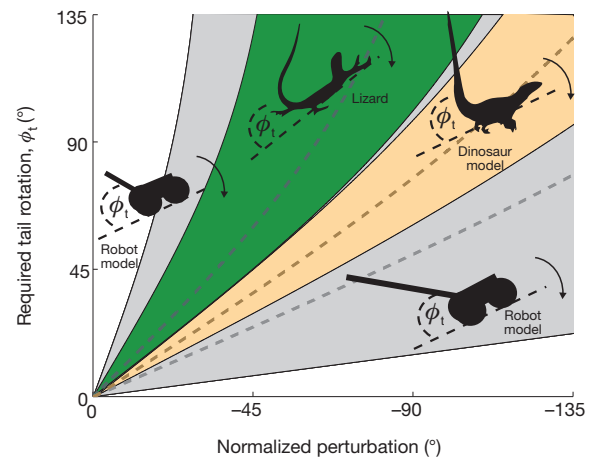


**Figure 3 | Tail effectiveness for *A. agama*, *V. mongoliensis* and a robot with tail.** Tail rotation ( $\phi_t$ ) required to prevent body rotation as a function of perturbation, defined as the angle through which the body would rotate without a tail, normalized by the observed angular momentum and trial duration. The slope of the lines represents the reciprocal of effectiveness (shallower slopes correspond to more effective tails). The average effectiveness for the Agama lizards was 0.79 (dashed line in green shaded area, which represents individual variation). Our robot had a more effective tail (black dashed line in lower grey shaded area), counteracting  $1.84^\circ$  of body rotation for each degree of tail rotation. A robot model with a tail 50% of the body length and 5% of the body mass was least effective (upper bound of grey shaded area), whereas a tail 200% of body length and 10% of the body mass was greater than three times more effective (lower bound of grey shaded area) than our robot. The *Velociraptor* model had a more effective tail than the most effective Agama lizard (slope, 1.23; dashed line in tan area, which represents 15% variation in model body and tail moment of inertia).

body mass, 200% body length). The smallest-tail model was far less effective than in lizards (Fig. 3, upper bound of grey area), whereas the largest-tail model (Fig. 3, lower bound of grey shaded area) was considerably more effective than even our actual robot.

Finally, we tested the original tail stabilization hypothesis<sup>1</sup> with regard to tail use in theropods. By using our model with a conservative morphometric reconstruction<sup>21</sup>, we found that *Velociraptor mongoliensis*<sup>22</sup>, an agile, 20-kg, 1.5-m-tall biped, with a tail effectiveness of 1.23 (Fig. 3, tan shaded area) given sufficient muscular capacity, could have outperformed even the most tail-effective Agama lizard. Although the distal portion of dromosaur tails was bony and possibly stiff<sup>3</sup>, the proximal tail base could bend by up to  $90^\circ$  (ref. 23). Such a range of motion would enable *Velociraptor* to sustain a perturbation that would rotate a tailless animal by  $110^\circ$ , or to adjust its body angle by up to  $45^\circ$  in an unperturbed leap. Despite previously proposed limitations of passive tails<sup>24</sup>, small theropods like *Velociraptor* with active tails might have been capable of aerial acrobatics beyond even those displayed by present-day arboreal lizards<sup>11–13</sup>.

## METHODS SUMMARY

**Dynamic models.** For simple characterization of the underlying dynamics of tail-assisted manoeuvres, we derived a planar, two-link, rigid-body model. By taking the derivative of the total angular momentum of each link and solving for the model's orientation and velocities with respect to actuation torque, we obtained a set of nonlinear, coupled ordinary differential equations realized in state-space form. We initialized the model with links oriented  $180^\circ$  apart. We set angular velocity of the tail link to zero and that of the body link such that the total angular momentum was as desired. We averaged the morphometrics of all animals to create the Agama model used in simulations. Simulations using morphometric models of individual Agama lizards did not yield significantly different perturbation sensitivities from those of the averaged Agama model. We performed numerical simulations in MATLAB.

**Kinematics.** To estimate the angular momentum of the animal or robot from kinematics, we treated the body and tail as rigid bodies with a hinge at the base of the tail (1 cm posterior to the vent in lizards). We used video tracking software (Xcitex PROANALYST) to capture kinematics, and calculated positions and velocities of

COMs in MATLAB. We estimated  $H$  from the two-link, rigid-body model for each video frame and averaged over the leap.

**Statistics.** We used multiple regression analysis in MATLAB to compare sensitivities (linear fits) of the experimental data to model hypotheses ( $t$ -test of slope). Sensitivities of individual animals were not significantly different from one another (analysis of variance,  $F = 2.1$ ,  $P = 0.073$ ).

**Velociraptor model.** To model the tail stabilization performance of an extinct theropod, we estimated mass properties from a two-dimensional reconstruction (Supplementary Table 1). We represented the head, trunk and lung capacity as ellipsoids, the neck as an elliptical cylinder, the limbs as point masses, and the tail as a truncated cone by digitizing points on the dorsal and sagittal views of the reconstruction. Estimates of combined trunk–tail moment of inertia agreed well with ref. 25.

**Full Methods** and any associated references are available in the online version of the paper at [www.nature.com/nature](http://www.nature.com/nature).

**Received 11 August; accepted 10 November 2011.**

**Published online 4 January 2012.**

- Ostrom, J. H. Osteology of *Deinonychus antirrhopus*, an unusual theropod from the Lower Cretaceous of Montana. *Bull. Peabody Mus. Nat. Hist. (Paris)* **30**, 68–80, 144 (1969).
- Pijnappels, M. *et al.* Armed against falls: the contribution of arm movements to balance recovery after tripping. *Exp. Brain Res.* **201**, 689–699 (2010).
- Roos, P. E. *et al.* The role of arm movement in early trip recovery in younger and older adults. *Gait Posture* **27**, 352–356 (2008).
- Dunbar, D. C. Aerial maneuvers of leaping lemurs: the physics of whole-body rotations while airborne. *Am. J. Primatol.* **16**, 291–303 (1988).
- Larson, S. G. & Stern, J. T. Maintenance of above-branch balance during primate arboreal quadrupedalism: coordinated use of forearm rotators and tail motion. *Am. J. Phys. Anthropol.* **129**, 71–81 (2006).
- Günther, M. M., Ishida, H., Kumakura, H. & Nakano, Y. The jump as a fast mode of locomotion in arboreal and terrestrial biotopes. *Z. Morphol. Anthropol.* **78**, 341–372 (1991).
- Demes, B. *et al.* Body size and leaping kinematics in Malagasy vertical clingers and leapers. *J. Hum. Evol.* **31**, 367–388 (1996).
- Peters, A. & Preuschoft, H. in *Biology of Tarsiers* (ed. Niemitz, C.) 227–255 (Fischer, 1984).
- Bartholomew, G. A. & Caswell, H. H. Locomotion in kangaroo rats and its adaptive significance. *J. Mamm.* **32**, 155–169 (1951).
- Walker, C. *et al.* Balance in the cat: role of the tail and effects of sacrocaudal transection. *Behav. Brain Res.* **91**, 41–47 (1998).
- Jusufi, A., Goldman, D. I., Revzen, S. & Full, R. J. Active tails enhance arboreal acrobatics in geckos. *Proc. Natl Acad. Sci. USA* **105**, 4215–4219 (2008).
- Jusufi, A., Kawano, D. T., Libby, T. & Full, R. J. Righting and turning in mid-air using appendage inertia: reptile tails, analytical models and bio-inspired robots. *Bioinspir. Biomim.* **5**, 045001 (2010).
- Jusufi, A., Zeng, Y., Full, R. J. & Dudley, R. Aerial righting reflexes in flightless animals. *Integr. Comp. Biol.* **51**, 937–943 (2011).
- Bateman, P. W. & Fleming, P. A. To cut a long tail short: a review of lizard caudal autotomy studies carried out over the last 20 years. *J. Zool. (Lond.)* **277**, 1–14 (2009).
- Gillis, G. B., Bonvini, L. A. & Irschick, D. J. Losing stability: tail loss and jumping in the arboreal lizard *Anolis carolinensis*. *J. Exp. Biol.* **212**, 604–609 (2009).
- Chang-Siu, E., Libby, T., Tomizuka, M. & Full, R. J. in *IEEE/RSJ Internat. Conf. Intelligent Robots Systems 2011* 1887–1894 (IEEE, 2011).
- Berkemeier, M. D. & Fearing, R. S. Control of a two-link robot to achieve sliding and hopping gaits. *IEEE Trans. Robot. Autom.* **1**, 286–291 (1992).
- Mather, T. W. & Yim, M. in *IEEE/RSJ Internat. Conf. Intelligent Robots Systems 2009* 5905–5910 (IEEE, 2009).
- Hyun Soo, P. *et al.* in *IEEE Internat. Conf. Robotics Automation 2009* 2655–2660 (IEEE, 2009).
- Saunders, A. *et al.* The RiSE climbing robot: body and leg design. *Proc. SPIE* **6230**, 623017 (2006).
- Alexander, R. M. Dinosaur biomechanics. *Proc. R. Soc. B* **273**, 1849–1855 (2006).
- Paul, G. S. *The Princeton Field Guide to Dinosaurs* 137 (Princeton Univ. Press, 2010).
- Paul, G. S. *Dinosaurs of the Air: the Evolution and Loss of Flight in Dinosaurs and Birds* 45 (Johns Hopkins Univ. Press, 2002).
- Carrier, D. R. *et al.* Influence of rotational inertia on turning performance of theropod dinosaurs: clues from humans with increased rotational inertia. *J. Exp. Biol.* **204**, 3917–3926 (2001).
- Sellers, W. I. & Manning, P. L. Estimating dinosaur maximum running speeds using evolutionary robotics. *Proc. R. Soc. B* **274**, 2711–2716 (2007).

**Supplementary Information** is linked to the online version of the paper at [www.nature.com/nature](http://www.nature.com/nature).

**Acknowledgements** We thank P. Jennings for video editing and figure production, T. Full for digitizing the lizard video and K. Padian for his advice on the dinosaur reconstruction and capability. We thank O. O'Reilly, S. Sponberg and N. Sapir for advice on analysis. This work was supported by a US NSF FIBR grant to R.J.F., a MAST CTA grant to R.J.F., an NSF IGERT under award DGE-0903711 and a Swiss NSF Fellowship to A.J.

**Author Contributions** T.L. designed the study and robot, carried out experiments, analysed data and wrote initial drafts of the manuscripts. T.Y.M. designed the study, carried out animal experiments and worked out kinematics. E.C.-S. designed and constructed the robot, carried out experiments and derived the analytical model. D.L. carried out experiments and worked out kinematics. D.J.C. designed experiments and collected and analysed animal kinematic data. A.J. designed and performed experiments and analysed data. R.J.F. directed the project, defined the analysis and wrote the final version of the manuscript.

**Author Information** Reprints and permissions information is available at [www.nature.com/reprints](http://www.nature.com/reprints). The authors declare no competing financial interests. Readers are welcome to comment on the online version of this article at [www.nature.com/nature](http://www.nature.com/nature). Correspondence and requests for materials should be addressed to R.J.F. ([rjfull@berkeley.edu](mailto:rjfull@berkeley.edu)).

## METHODS

**Animals.** Wild-caught Red-Headed Agama lizards were purchased from a commercial vendor (<http://www.reptilesncritters.com>). Six lizards (average mass,  $66.96 \pm 2.93$  g; average snout–vent length,  $12.75 \pm 0.28$  cm) were used for kinematic measurements. Lizards were housed in groups in large opaque tanks, kept in an environmentally controlled room ( $25 \pm 2^\circ\text{C}$ ; relative humidity, 27%) with 12-h light–dark cycles and fed a diet of water and crickets. The Animal Care and Use Committee at the University of California, Berkeley, whose activities are mandated by the US Animal Welfare Act and Public Health Service Policy, approved all experimental procedures.

**Experimental apparatus and protocol.** We ran animals in a specially constructed track made of clear Lexan (acrylic) and steel (track dimensions: 150 cm (length), 30 cm (width), 40 cm (wall height)). The track was designed to allow the animals to reach top speed after an escape response. We placed a 22-cm-high wall at the end of the track; an enclosed plastic shelter at the top of the wall provided the target for the animals to complete the transition. We lined the exterior walls with tinted cellophane to limit the animal's field of view to the track interior.

In each trial, we placed the lizard at the beginning of the track and elicited an escape response by brushing the animal's tail. The animal accelerated rapidly into a run, made an intermediate jump onto the vault (dimensions,  $24 \text{ cm} \times 13 \text{ cm} \times 6 \text{ cm}$ ) and then jumped to the wall. The average horizontal speed during the aerial phase of the transition was  $1.23 \pm 0.33 \text{ m s}^{-1}$  (mean  $\pm$  s.d.). Animals transitioned using one of two general patterns. In 88% of trials, animals pitched up slightly and ran quadrupedally onto the box, where they reared onto their hind legs and jumped bipedally. In cases where their initial speed was high, animals initiated bipedal running before the vault and used the vault as a take-off platform with one or both legs. In all cases, contact with the vault was less than a stride, with contact from either one or both hind feet. Contact with the vault was critical to direct the jump upward to the wall. If animals attempted to jump over the vault they generally landed in the space between the vault and the wall. Hence, we were able to localize a critical transition area where animals must generate large ground reaction forces to initiate a jump. By reducing the traction on the vault, we could apply a perturbation during an important phase of the transition. We used either 60-grit sandpaper or smooth glossy card stock to vary friction on the top of the vault.

We defined a successful trial as one where the individual completed the vault to the wall without a pause. We excluded cases where the lizard struck the vault while climbing on to it, or slipped with one foot and gripped with the other, thereby applying a roll or yaw perturbation. In total, 77 trials from six individuals fitted our criteria for analysis. The selected trials comprised 34 leaps from the sandpaper and 43 leaps from the smooth substrate. Each individual was represented by at least eight trials in the data pool and all spanned a comparable range in perturbation magnitude.

We used typographical correction fluid to place markers on the head, torso, and tail for kinematic analysis. The track was lit with multiple lights and high-speed video was captured at 500 frames per second (X-PRI, AOS Technologies AG). We allowed animals to rest for 10–15 min between running bouts, and to recover for 90 min after every ten trials. The kinematics was extracted from videos with automated tracking software (ProAnalyst, Xcitex) and analysed in MATLAB (Mathworks).

**Morphometrics.** We used cadavers of five animals to construct a morphometric model of the animal. For both body and tail, we measured mass, distance from hip to segment COM, and moment of inertia (MOI) about COM (Supplementary Table 2). We used a pendulum technique to measure MOI, whereby the segment was deep-frozen and then supported by pins near the radius of gyration, following ref. 26. Two of the animals in the kinematic study subsequently died and were included in the morphometric study; the other three were from a previous study, but were in the same size range. We measured total body mass and snout–vent and tail–vent distances for the living animals. We used the average ratio of body mass to tail mass of the cadavers to estimate segment masses of the living animals. We estimated the MOI of the living animals by scaling the average MOI of cadavers by the product of segment mass and the square of segment length.

**Kinematic analysis.** We used a planar, two-link model to estimate the animal's total angular momentum during the aerial phase of the transition. We can write the angular momentum of the two-link model with respect to the system COM as

$$\mathbf{H}_0 = I_b \boldsymbol{\omega}_b + m_b \mathbf{p}_b \times \dot{\mathbf{p}}_b + I_t \boldsymbol{\omega}_t + m_t \mathbf{p}_t \times \dot{\mathbf{p}}_t \quad (1)$$

where  $\mathbf{p}_i$  is the vector from the animal's COM to the COM of the segment,  $\boldsymbol{\omega}_i = \dot{\theta}_i \mathbf{E}_3$  is the angular velocity of the segment,  $\dot{\theta}_i$  is the derivative of the segment angle,  $\mathbf{E}_3$  is the vector orthogonal to the plane,  $I_i$  denotes the segment's MOI about its COM,  $m_i$  is the segment's mass, subscripts  $i = b, t$  denote the body and tail, respectively, and the dot denotes the time derivative. The model did not capture additional angular momentum due to rotation of the limbs or bending of the body and hence represents a conservative estimate of the total perturbation applied.

We defined the position of the segments from the kinematic markers on the animal in each video frame during the aerial phase of the transition. Markers on the head, torso and tail were used to define the location of the body-link end point, the pin joint between the links, and the tail-link end point, respectively. We used our measurement of the segment COM position relative to the hip to calculate the instantaneous position of each segment in the model. The total COM was found by a mass-weighted average of the segment positions. From these vectors and their derivatives, along with measurements of MOI and mass, we calculated angular momentum for each segment at each frame using equation (1). Using the assumption of constant angular momentum, we took the magnitude of perturbation to be the mean measured angular momentum over the duration of the aerial transition.

**Mathematical model.** To test the hypothesis that perturbed animals manipulated angular momentum using their tails, we built a numerical dynamic model. Our task was simplified by the following experimental considerations. First, the critical period for stabilization (that is, maintenance of body pitch before landing) was spent entirely in the air, where only aerodynamic forces acted on the animal. These forces were found to be negligible in a somewhat smaller animal<sup>12,13</sup> and we therefore ignored them here. Second, the perturbation was limited to the brief period directly before take-off. If no external forces acted on the animal, then total angular momentum was conserved. This allowed complete characterization of the perturbation impulse via measurement of the total angular momentum of the animal during the aerial phase. Finally, we restricted our analysis to rotations within the sagittal plane only. Trials that had out-of-plane perturbations were rejected. This allowed use of a relatively simple planar rigid-body model. We chose the simplest model possible: a two-link chain of rigid bodies, with one link representing the body and the other representing the tail.

The model was derived with the absolute body and tail angles referenced to horizontal as shown in Supplementary Fig. 1. We define a Cartesian coordinate system located at the COM of the system, resulting in the constraint  $m_b \mathbf{p}_b + m_t \mathbf{p}_t = \mathbf{0}$ . The two bodies are assumed to be joined by a pin joint, where the relative torque,  $\tau = \tau \mathbf{E}_3$ , represents actuation at the pivot. Assuming that no external forces act on the system during the manoeuvre, the time derivative of equation (1) is zero:  $\dot{\mathbf{H}}_0 = \mathbf{0}$ . Hence, the derivative of the second link's angular momentum,  $\dot{\mathbf{H}}_{t0}$ , is easily written using the derivative of the first link's angular momentum,  $\dot{\mathbf{H}}_{b0} = \tau + (\mathbf{p}_b - \mathbf{p}_t) \times m_b \dot{\mathbf{p}}_b$ , where  $\mathbf{p}_b$  is the vector from the pivot to the link COM. Solving for the states  $\mathbf{x} = [\theta_b \quad \dot{\theta}_b \quad \theta_t \quad \dot{\theta}_t]^T$ , yields a state-space model of the system in the form

$$\dot{\mathbf{x}} = \mathbf{f}(\mathbf{x}) + \mathbf{g}(\mathbf{x})u$$

where the states consist of the angular position and velocity of the links and the control input,  $u = \tau$ , is the relative torque. The details of  $\mathbf{f}(\mathbf{x})$  and  $\mathbf{g}(\mathbf{x})$  are as follows:

$$\mathbf{f}(\mathbf{x}) = \begin{bmatrix} \dot{\theta}_b \\ \frac{a\dot{\theta}_b^2 - b}{d - e} \\ \dot{\theta}_t \\ \frac{-a\dot{\theta}_t^2 + c}{d - e} \end{bmatrix} \quad \mathbf{g}(\mathbf{x}) = \begin{bmatrix} 0 \\ -\frac{f}{d - e} \\ 0 \\ \frac{g}{d - e} \end{bmatrix}$$

where

$$a = \frac{1}{2} I_b^2 I_t^2 m_b^2 m_t^2 \sin(2(\theta_b - \theta_t))$$

$$b = (I_b^2 m_b m_t + I_t(m_b + m_t)) I_b I_t m_b m_t \dot{\theta}_t^2 \sin(\theta_b - \theta_t)$$

$$c = (I_b^2 m_b m_t + I_b(m_b + m_t)) I_b I_t m_b m_t \dot{\theta}_b^2 \sin(\theta_b - \theta_t)$$

$$d = I_b^2 I_t^2 m_b^2 m_t^2 \cos(\theta_b - \theta_t)^2$$

$$e = (I_b^2 m_b m_t + I_b(m_b + m_t))(I_t^2 m_b m_t + I_t(m_b + m_t))$$

$$f = (I_b^2 m_b m_t + I_t(m_b + m_t)) \\ - I_b I_t m_b m_t \cos(\theta_b - \theta_t)(m_b + m_t)$$



$$g = (I_b^2 m_b m_t + I_b (m_b + m_t) - I_b I_t m_b m_t \cos(\theta_b - \theta_t))(m_b + m_t)$$

We used the model to calculate the sensitivity of lizards and robots with a compliant tail, and to estimate tail effectiveness in lizards, robots and *Velociraptor* (numerical solution in MATLAB using 'ode45').

**Physical model (robot).** To complement the mathematical model, we constructed a small bio-inspired robot to test the ability of an inertial appendage to stabilize aerial manoeuvres. We built our model by modifying a small commercial radio-controlled toy (RadioShack Flipz Truck). The design of the toy included two independent d.c. gear motors, which drove the left- and right-hand pairs of wheels. We modified the gear trains such that one gear motor drove the front wheels while the other drove a single pin joint at the rear, onto which we secured an aluminium rod (that is, a tail) approximately twice as long as the body. The tail was completed with the addition of a tunable mass at its distal end. Varying the mass at the tail tip allowed modulation of the tail's MOI. The resulting vehicle could move along a single axis (that is, it had no steering) and rapidly move its tail in the pitch-axis (that is, the sagittal plane of the robot).

We removed the toy's original electronics and installed a microcontroller (Arduino Pro Mini, Sparkfun Electronics), a single-axis microelectromechanical systems gyroscope (Invensense IDG-650) and a motor controller (Polulu TB6612FNG). The package was powered by small lithium-ion batteries (Turnigy 138mAh T1382S-10). This system enabled us to test the ability of simple feedback controllers to use a tail to stabilize body pitch orientation. Orientation of the vehicle was established by integrating the angular rate signal from the gyroscope. Because the accuracy of this scheme degrades with time, we limited the trials to 1–2 s. The controller was activated by a small button on the robot. After a 100-ms delay, the feedback controller ran for 2 s while logging angular velocity. We used a high-speed camera (X-PRI, AOS Technologies AG) to record kinematics at 1,000 frames per second.

We tested two common controllers: a proportional feedback controller and a PD feedback controller. Under the proportional controller, the motor torque was proportional to the difference between the current pitch (the integrated gyroscope measurement) and a desired orientation set at the beginning of the trial. The PD feedback control law added a torque proportional to the vehicle's pitch angular velocity (raw gyroscope signal). The controller had no knowledge of the angle or

velocity of the tail; the servomotors acted directly on the body angle. We tuned the controller gains and tail MOI by dropping the robot from a height of about 2 m from a horizontal attitude and commanding a desired pitch angle of 45°. We chose a tail tip mass that allowed sufficient body rotation within the available range of tail motion ( $\pm 100^\circ$ ). We chose controller gains such that the manoeuvre could be completed in less than 150 ms without body angle oscillation (outside the range of tail motion). Proportional feedback control alone was unable to control overshoot and we thus used only PD feedback control in the final trials.

We drove the robot off an inclined 'ski-jump' ramp. The ramp declined at 20° to the horizontal for 150 cm and inclined at the same angle for the final 25 cm. The robot accelerated to 2.5 m s<sup>-1</sup> before becoming airborne. When the front wheels of the robot left the ramp, the unbalanced gravitational moment imparted an angular momentum perturbation. We repeated trials nine times each for the active and passive cases. The magnitude of the perturbation depended on the duration of unbalanced moment and, hence, on the speed of the vehicle as it left the ramp.

**Velociraptor model.** To model the tail stabilization performance of an extinct theropod dinosaur, we estimated mass properties from a two-dimensional reconstruction. Although some mass and MOI data were available from a previous model<sup>25</sup>, separate trunk and tail estimates were not. We represented the head and trunk as ellipsoids, the neck as an elliptical cylinder and the tail as a truncated cone by digitizing points on the dorsal and sagittal views of the reconstruction. To be conservative in our estimate of tail effectiveness, the cone accounted for the envelope of the vertebrae, without additional external musculature. The density of body tissue was set to 1,000 kg m<sup>-3</sup>, whereas tail density was set higher (1,500 kg m<sup>-3</sup>) to account for the high proportion of bone (the density of which is typically set to 2,000 kg m<sup>-3</sup>). We then scaled limb masses following ref. 25, oriented them as in the reconstruction and calculated their contribution to the body MOI. Our combined trunk–tail MOI agreed well with that of ref. 25. We modelled the animal in two configurations—one in which the limbs were extended and one in which the limbs were held against the body or retracted—and used the average of the two for the effectiveness estimate. We added 15% to the body MOI and subtracted 15% from the tail MOI to generate the lower bound of effectiveness in Fig. 3; the converse procedure generated the upper bound.

26. Dowling, J. J. *et al.* The uncertainty of the pendulum method for the determination of the moment of inertia. *Med. Eng. Phys.* **28**, 837–841 (2006).

# Topoisomerase inhibitors unsilence the dormant allele of *Ube3a* in neurons

Hsien-Sung Huang<sup>1\*</sup>, John A. Allen<sup>2\*</sup>, Angela M. Mabb<sup>1</sup>, Ian F. King<sup>1</sup>, Jayalakshmi Miriyala<sup>1</sup>, Bonnie Taylor-Blake<sup>1</sup>, Noah Sciaky<sup>2</sup>, J. Walter Dutton Jr<sup>1</sup>, Hyeon-Min Lee<sup>2</sup>, Xin Chen<sup>3</sup>, Jian Jin<sup>3</sup>, Arlene S. Bridges<sup>4</sup>, Mark J. Zylka<sup>1,5,6</sup>, Bryan L. Roth<sup>2,5,6,7,8</sup> & Benjamin D. Philpot<sup>1,5,6</sup>

Angelman syndrome is a severe neurodevelopmental disorder caused by deletion or mutation of the maternal allele of the ubiquitin protein ligase E3A (*UBE3A*)<sup>1–3</sup>. In neurons, the paternal allele of *UBE3A* is intact but epigenetically silenced<sup>4–6</sup>, raising the possibility that Angelman syndrome could be treated by activating this silenced allele to restore functional *UBE3A* protein<sup>7,8</sup>. Using an unbiased, high-content screen in primary cortical neurons from mice, we identify twelve topoisomerase I inhibitors and four topoisomerase II inhibitors that unsilence the paternal *Ube3a* allele. These drugs included topotecan, irinotecan, etoposide and dexrazoxane (ICRF-187). At nanomolar concentrations, topotecan upregulated catalytically active *UBE3A* in neurons from maternal *Ube3a*-null mice. Topotecan concomitantly downregulated expression of the *Ube3a* antisense transcript that overlaps the paternal copy of *Ube3a*<sup>9–11</sup>. These results indicate that topotecan unsilences *Ube3a* in cis by reducing transcription of an imprinted antisense RNA. When administered *in vivo*, topotecan unsilenced the paternal *Ube3a* allele in several regions of the nervous system, including neurons in the hippocampus, neocortex, striatum, cerebellum and spinal cord. Paternal expression of *Ube3a* remained elevated in a subset of spinal cord neurons for at least 12 weeks after cessation of topotecan treatment, indicating that transient topoisomerase inhibition can have enduring effects on gene expression. Although potential off-target effects remain to be investigated, our findings suggest a therapeutic strategy for reactivating the functional but dormant allele of *Ube3a* in patients with Angelman syndrome.

No effective therapies exist for Angelman syndrome—an imprinting disorder caused by mutations or deletions in the maternal allele of *UBE3A*<sup>1–3</sup>. *Ube3a* is biallelically expressed in most tissues of the body; however, in rodents and humans, most neurons express *Ube3a* only from the maternally-inherited allele<sup>4,12–14</sup>. This unique epigenetic pattern of regulation suggested that it might be possible to unsilence the dormant paternal *Ube3a* allele in neurons<sup>7,8</sup>.

To test this possibility, we developed a 384-well high-content screen using primary mouse cortical neurons from *Ube3a*-yellow fluorescent protein (*Ube3a*-YFP) knock-in mice<sup>15</sup>, and searched for drug-like molecules that could unsilence the paternal *Ube3a*-YFP allele (Fig. 1a). This screen was based on our observation that the imprinting of *Ube3a*-YFP was maintained *in vitro* in cultured embryonic cortical neurons. Notably, *Ube3a*-YFP expression was undetectable (silenced) in cultured neurons when *Ube3a*-YFP was paternally inherited (*Ube3a*<sup>m+/pYFP</sup>), but was expressed when *Ube3a*-YFP was maternally inherited (*Ube3a*<sup>mYFP/p+</sup>) (Fig. 1b), with expression increasing from 4 to 10 days *in vitro* (DIV) (Fig. 1c). This significant difference between maternal and paternal *UBE3A*-YFP protein levels provided a large

screening window and a Z'-factor score of 0.58 (determined by statistically comparing antibody-enhanced fluorescence intensities and variations between maternal and paternal *UBE3A*-YFP signals at DIV10), making our high-content platform suitable for unbiased screening.

To perform the screen, we cultured *Ube3a*<sup>m+/pYFP</sup> neurons for 7 days and then treated these neurons with compounds (10  $\mu$ M for 72 h) from several small-molecule libraries (Fig. 1d and Supplementary Fig. 1). In total, we screened 2,306 small molecules in quadruplicate, normalizing values to vehicle-treatment (0.2% dimethyl sulphoxide (DMSO)) (for full methods see Supplementary Methods; for list of all compounds tested see Supplementary Table 1). Although methylation and other epigenetic marks are thought to control imprinting of *Ube3a*<sup>9,16–18</sup>, to our surprise, none of the commonly used compounds that target the epigenome, including chromatin-remodelling drugs and DNA methyltransferase inhibitors, unsilenced the paternal *Ube3a*-YFP allele. A number of compounds were identified as false positives (grey compounds in Fig. 1d) due to their intrinsic fluorescence (Supplementary Fig. 2). Our initial screen identified one compound—irinotecan, an FDA-approved topoisomerase type I inhibitor. Irinotecan lacked intrinsic fluorescence and upregulated *UBE3A*-YFP fluorescence (Fig. 1d, e and Supplementary Fig. 3). Irinotecan (10  $\mu$ M) also upregulated paternal *UBE3A*-YFP protein (Fig. 1f) and endogenous *UBE3A* protein (Fig. 1g) in neuronal cultures from *Ube3a*<sup>m+/pYFP</sup> and *Ube3a*<sup>m-/p+</sup> mice (Angelman syndrome model mice<sup>13</sup>), respectively.

Many topoisomerase I inhibitors, including irinotecan and the related FDA-approved drug topotecan, are derived from the natural product camptothecin (CPT)<sup>19</sup>. To explore structure activity relationships, we tested CPT analogues and other topoisomerase inhibitors (Fig. 2a and Supplementary Figs 4–10). The analogues we tested all lack inherent fluorescence (Supplementary Fig. 3). We found that irinotecan and topotecan upregulated paternal *UBE3A*-YFP in a dose- and time-dependent manner in cultured neurons, with topotecan being 20 times more potent than irinotecan (Fig. 2a, b and Supplementary Fig. 11). In contrast, an inactive analogue of CPT (lactam E ring-CPT) that does not inhibit topoisomerases<sup>20</sup> failed to unsilence the paternal *Ube3a*-YFP allele (Fig. 2a and Supplementary Fig. 4). Ten additional topoisomerase I inhibitors unsilenced *Ube3a*-YFP in a dose-dependent manner, including CPT analogues and structurally distinct indenoisoquinolines (Table 1 and Supplementary Figs 4–7). Furthermore, four structurally distinct topoisomerase II inhibitors (etoposide, dexrazoxane, ICRF-193 and amsacrine) also unsilenced the paternal *Ube3a*-YFP allele (Table 1 and Supplementary Figs 8–10). Thus, our data with 16 topoisomerase inhibitors and one inactive analogue strongly suggest that inhibition of topoisomerase I or II can unsilence the paternal *Ube3a* allele.

<sup>1</sup>Department of Cell and Molecular Physiology, University of North Carolina School of Medicine, Chapel Hill, North Carolina 27599, USA. <sup>2</sup>Department of Pharmacology, University of North Carolina School of Medicine, Chapel Hill, North Carolina 27599, USA. <sup>3</sup>Center for Integrative Chemical Biology and Drug Discovery, Division of Chemical Biology and Medicinal Chemistry, University of North Carolina Eshelman School of Pharmacy, Chapel Hill, North Carolina 27599, USA. <sup>4</sup>Department of Pathology and Laboratory Medicine, University of North Carolina School of Medicine, Chapel Hill, North Carolina 27599, USA. <sup>5</sup>Carolina Institute for Developmental Disabilities, University of North Carolina, Chapel Hill, North Carolina 27599, USA. <sup>6</sup>University of North Carolina Neuroscience Center, Chapel Hill, North Carolina 27599, USA. <sup>7</sup>Division of Chemical Biology and Medicinal Chemistry, University of North Carolina Eshelman School of Pharmacy, Chapel Hill, North Carolina 27599, USA. <sup>8</sup>National Institute of Mental Health, Psychoactive Drug Screening Program, Department of Pharmacology, University of North Carolina School of Medicine, Chapel Hill, North Carolina 27599, USA.

\*These authors contributed equally to this work.

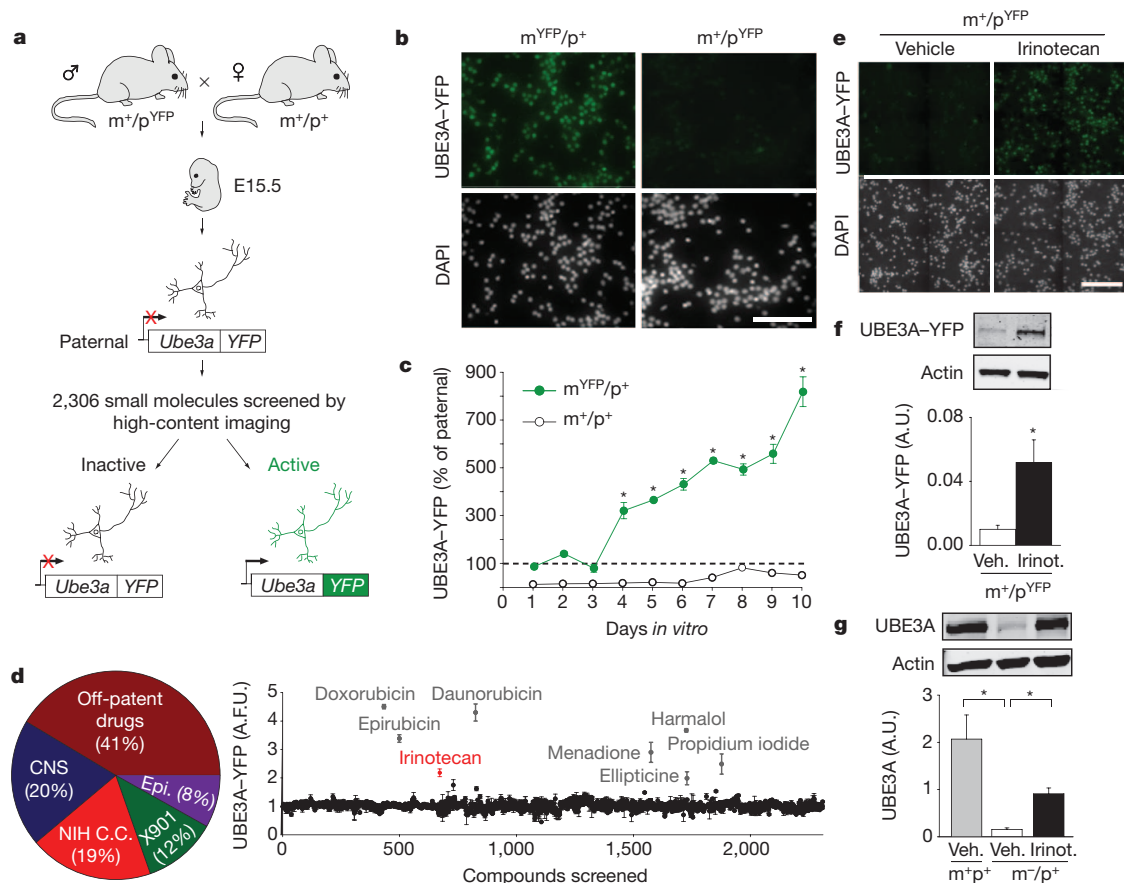


**Figure 1** | A small-molecule screen identifies a topoisomerase inhibitor that unsilences the paternal allele of *Ube3a* in neurons. **a**, High-content screen flowchart. Embryonic day 15.5 (E15.5) cortical neurons with a paternally inherited *Ube3a*-YFP allele were cultured in 384-well plates and treated with small molecules from DIV7–DIV10. Active compounds that unsilence the paternal *Ube3a*-YFP allele were detected with antibody-enhanced fluorescence and high-content imaging. **b**, High-content imaging of DIV7 neurons that inherited *Ube3a*-YFP maternally ( $m^{YFP/p^{+}}$ ) or paternally ( $m^{+/p^{YFP}}$ ). Nuclei were stained with 4',6-diamidino-2-phenylindole (DAPI). Scale bar, 50  $\mu m$ . **c**, Mean  $\pm$  s.e.m. levels of UBE3A-YFP fluorescence in neurons cultured from maternal *Ube3a*-YFP ( $m^{YFP/p^{+}}$ ) or wild-type ( $m^{+/p^{+}}$ ) mice, normalized to levels in age-matched neurons cultured from paternal *Ube3a*-YFP mice ( $m^{+/p^{YFP}}$ ). Two-way analysis of variance (ANOVA) revealed main effects of genotype, duration and a genotype–duration interaction ( $P < 0.001$ ); Bonferroni post hoc test examined comparisons between maternal and paternal *Ube3a*-YFP mice from DIV4 to DIV10,  $*P < 0.001$ ;  $n = 2$ –6 culture wells per

We focused our remaining studies on the topoisomerase I inhibitor topotecan because it is approved for use in humans, it unsilenced *Ube3a* in the low nanomolar range, and topotecan (300 nM, 72 h) restored UBE3A protein to wild-type levels in cultured neurons from *Ube3a*<sup>*m*−/*p*+</sup> mice (Fig. 2c).

Many topoisomerase inhibitors, including topotecan, covalently link topoisomerases to DNA, forming stable DNA–enzyme complexes that are separable from free topoisomerase enzymes<sup>19</sup>. Because topotecan inhibits topoisomerase I (TOP1) and *Top1* is expressed at high levels in the developing and adult brain<sup>19,21</sup>, we focused our subsequent analysis on this enzyme. We found that topotecan (300 nM, 72 h) significantly reduced the amount of free TOP1 (Fig. 2d) in cultured neurons, indicating that topotecan engages its known molecular target at doses that unsilence the paternal *Ube3a* allele.

UBE3A is a HECT (homology to E6 carboxyl terminus) domain E3 ligase that forms a thioester-ubiquitin intermediate in the presence of E1 and E2 enzymes<sup>22</sup>. This thioester-ubiquitin intermediate is required for HECT domain E3 ligases to mono- and polyubiquitinate their substrates<sup>23</sup>. Interestingly, we noticed that topotecan (300 nM, 72 h)

upregulated UBE3A protein in *Ube3a*<sup>*m*−/*p*+</sup> cultures along with a higher molecular weight form (resolved after running gels for longer times; Fig. 2e). This high molecular weight band was also seen in wild-type (*Ube3a*<sup>*m*+/*p*+</sup>) cultures and was lost upon addition of the reducing agent dithiothreitol (DTT) (Fig. 2e). These data indicate that the unsilenced paternal copy of UBE3A is catalytically active and competent to form a thioester-ubiquitin intermediate, just like wild-type, maternal-derived UBE3A.

To demonstrate further that UBE3A was catalytically active, we immunoprecipitated UBE3A from cultured wild-type and *Ube3a*<sup>*m*−/*p*+</sup> neurons (with or without topotecan), then tested these samples using a gel-mobility shift assay in the presence or absence of the ubiquitin E2 UBCH7 (ref. 24). Both wild-type (maternal-derived) and topotecan-unsilenced (paternal-derived) UBE3A underwent mobility shifts in the presence of UBCH7 plus free ubiquitin that were abolished by addition of DTT (Fig. 2f). This observation indicates the mobility shift was due to addition of covalent ubiquitin, and demonstrates that topotecan can upregulate a functional UBE3A enzyme.



**Table 1 | Efficacies and potencies of topoisomerase inhibitors for unsilencing the paternal allele of *Ube3a*-YFP in cultured neurons**

Compound	Potency (half-maximum effective concentration EC <sub>50</sub> , nM)	Efficacy E <sub>max</sub> (fold over vehicle)
Camptothecin derivatives		
7-ethyl-camptothecin (7-ethyl-CPT)	7.2 ± 2.3	1.70 ± 0.04
7-ethyl-10-hydroxy-CPT	11 ± 3.2	1.99 ± 0.06
10-hydroxy-CPT	14 ± 5.7	1.82 ± 0.08
Belotecan (CKD602)	19 ± 4.4	1.88 ± 0.05
Camptothecin (CPT)	21 ± 3.8	2.11 ± 0.05
Topotecan*	54 ± 3.4	2.25 ± 0.05
Rubitecan (9-nitro-CPT)	62 ± 18	2.09 ± 0.09
Irinotecan*	994 ± 13	2.17 ± 0.05
Silatecan (DB67)	2,244 ± 171	1.65 ± 0.05
Lactam E ring-CPT (inactive)	inactive	inactive
Indenoisoquinoline derivatives		
NSC725776	10 ± 1.6	1.76 ± 0.03
NSC706744	11 ± 3.2	1.84 ± 0.07
NSC724998	14 ± 2.2	1.69 ± 0.03
Podophyllotoxin derivative		
Etoposide*	1,600 ± 980	1.68 ± 0.04
Bis-dioxolipiperazine derivatives		
ICRF-193	205 ± 70	2.21 ± 0.09
Dexrazoxane (ICRF-187)*	20,470 ± 1,450	1.82 ± 0.05
Aminoacridine derivative		
Amsacrine	27 ± 5.2	1.74 ± 0.06

\*FDA-approved compounds.

*Ube3a* is repressed in *cis* by a large antisense transcript (*Ube3a*-ATS) that overlaps the paternal allele of *Ube3a* (Fig. 2g)<sup>9–11</sup>. *Ube3a*-ATS is expressed exclusively from the paternal allele as a result of allele-specific methylation of an imprinting centre that overlaps the *Ube3a*-ATS and *Snurf/Snrpn* transcription start site<sup>25</sup>. We next sought to determine if topotecan regulated *Ube3a* expression through changes in *Ube3a*-ATS expression or altered methylation at the imprinting centre. We found that topotecan upregulated expression of *Ube3a* in cultured neurons from *Ube3a*<sup>m-/p+</sup> mice while concomitantly down-regulating expression of *Ube3a*-ATS and *Snurf/Snrpn* (Fig. 2h). However, topotecan did not alter methylation at the imprinting centre (Fig. 2i and Supplementary Fig. 12). Taken together, these data indicate that topotecan unsilences paternal *Ube3a* by reducing transcription of a regulatory antisense RNA without appreciably affecting genomic methylation at the imprinting centre.

We then sought to determine if topotecan could unsilence the paternal *Ube3a* allele *in vivo*. We first identified a dose that was well tolerated, meaning there were no significant decreases in body weight between the beginning and end of the drug treatments (Supplementary Fig. 13). We then administered topotecan (3.74 μg h<sup>-1</sup>) unilaterally into the lateral ventricle of *Ube3a*<sup>m+/pYFP</sup> or *Ube3a*<sup>m-/p+</sup> mice by intracerebroventricular (i.c.v.) infusion for 2 weeks and then killed the mice

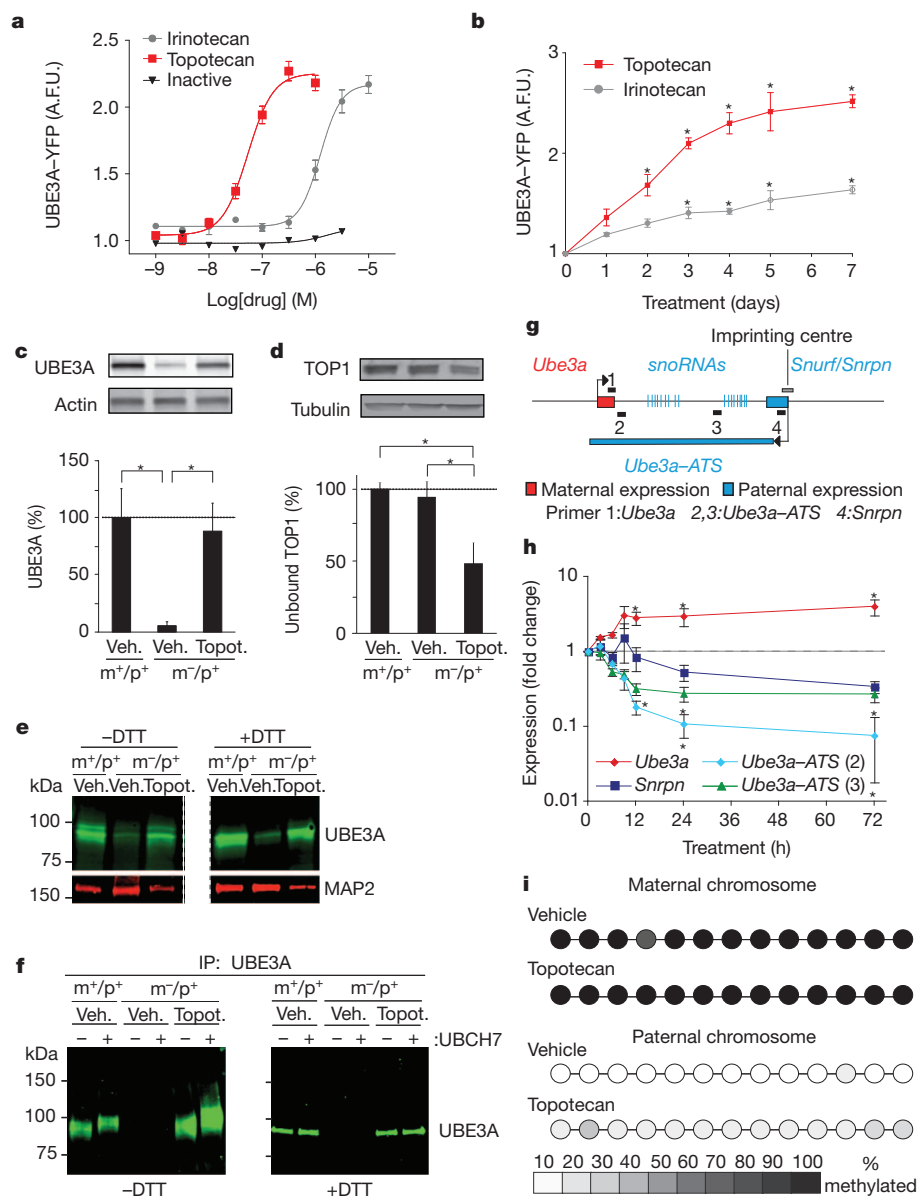


**Figure 2 | Topotecan unsilences the paternal allele of *Ube3a* and the unsilenced protein is catalytically active.** **a**, Dose-response curves for unsilencing paternal *Ube3a*-YFP. Inactive, lactam E ring-camptothecin. **b**, UBE3A-YFP levels in neurons from *Ube3a*<sup>m+/pYFP</sup> mice increase with duration of topotecan (300 nM) or irinotecan (1 μM) treatment. \**P* < 0.05, one-way ANOVA with Bonferroni post hoc tests relative to day zero, *n* = 4–8 per group. A.F.U., arbitrary fluorescence units. **c**, Western blots and quantification of UBE3A and the loading control β-actin. \**P* < 0.05, one-way ANOVA with Bonferroni post hoc tests, *n* = 4 per group. Topot., topotecan. **d**, Quantification of unbound TOP1 and representative western blots. β-tubulin was used as a loading control. One-way ANOVA with Bonferroni post hoc tests, \**P* < 0.05; *n* = 3 per group. **e**, Western blot from vehicle- and topotecan-treated neurons from wild-type (*m*<sup>+/p</sup>) and maternal *Ube3a*-deficient (*m*<sup>-/p</sup>) mice. **f**, Western blots examining UBE3A ubiquitin-thioester formation following immunoprecipitation with an anti-UBE3A antibody and *in vitro* ubiquitination in the presence or absence of the ubiquitin-conjugating enzyme (E2), UBCH7. All data are presented as means ± s.e.m. **g**, Schematic demonstrating location of four primer sets used to probe mRNA expression shown in **h**. **h**, Normalized mRNA levels in cultured *Ube3a*<sup>m-/p+</sup> neurons after vehicle or 300 nM topotecan treatment. Expression is given as a ratio of expression in drug-treated cells to vehicle-treated cells, normalized to the housekeeping gene *RPL22*. \**P* < 0.05 compared to 0 h, Kruskal–Wallis one-way ANOVA followed by post hoc tests, *n* = 4–5 cultures per data point. **i**, Schematic summarizing methylation status of the *Snurf* promoter region on the maternal and paternal chromosome following treatment with vehicle or 300 nM topotecan (see complete data set in Supplementary Fig. 12). Average methylation status is indicated using a greyscale.

either immediately or 5 h after drug cessation. Strikingly, topotecan unsilenced paternal *Ube3a* in the hippocampus, striatum and cerebral cortex of the infused hemisphere, but had only a modest effect on the contralateral (non-infused) hemisphere with no effect in the cerebellum (Fig. 3a–e and Supplementary Figs 14–15). Pharmacokinetic analyses demonstrated that a significant amount of topotecan was detectable in the infused hemisphere immediately after treatment, whereas low levels were present in the contralateral (non-infused) hemisphere and in cerebellum (Fig. 3a and Supplementary Fig. 14). However, a higher dose of topotecan ( $21.6 \mu\text{g h}^{-1}$  for 5 days) did unsilence the paternal allele of *Ube3a* in Purkinje neurons of the cerebellum (Supplementary Fig. 16). No significant difference in topotecan levels was detected in blood between drug- and vehicle-treated mice (data not shown). Topotecan concentrations significantly declined five hours after cessation of i.c.v. drug delivery (Fig. 3a), indicating that topotecan does not persist and is rapidly removed/metabolized in the brain. Taken together, these pharmacokinetic and pharmacodynamic data indicate that the degree to which topotecan unsilences the paternal *Ube3a* allele is directly correlated with drug concentrations in the brain. Moreover, our data indicate topotecan has the potential to unsilence the paternal *Ube3a* allele throughout the nervous system.

Genomic imprinting is thought to be established only during prescribed germline and embryonic periods of development and imprinted

genes typically remain epigenetically regulated throughout life<sup>26</sup>. Thus, we next sought to determine if topotecan had transient or long-lasting effects on paternal *Ube3a* expression. To test this possibility, we turned to an intrathecal (i.t.) delivery protocol (Fig. 3f) because topotecan (Fig. 3g) and irinotecan (not shown) unsilenced paternal *Ube3a* in a sparse population of lumbar spinal neurons, allowing us to quantify all UBE3A–YFP-positive neurons. Moreover, i.t. delivery has been used to deliver topotecan to the brain in humans<sup>27</sup>. We found that topotecan (50 nmol in 5  $\mu\text{l}$ ; i.t. once daily, for 10 out of 14 days) was well tolerated (Supplementary Fig. 13) and significantly increased the number of paternal UBE3A–YFP-positive cells in the lumbar spinal cord of mice (Fig. 3g, h and Supplementary Fig. 17a). The vast majority (>93%) of these UBE3A–YFP-positive cells were NeuN<sup>+</sup> neurons (Supplementary Fig. 17a, b), indicating topotecan primarily unsilences *Ube3a* in neurons *in vivo*. Moreover, the unsilenced paternal UBE3A–YFP protein was expressed at levels comparable to maternal UBE3A–YFP controls (Supplementary Fig. 17c). Remarkably, the number of UBE3A–YFP-positive spinal cord neurons remained elevated 12 weeks after cessation of drug treatment (Fig. 3g, h), much longer than the elimination of topotecan from tissue (Fig. 3a). These results indicate that topotecan can enduringly unsilence paternal *Ube3a* in a subset of spinal neurons and indicate that a single course of drug treatment has the capacity to permanently modify expression of *Ube3a*.

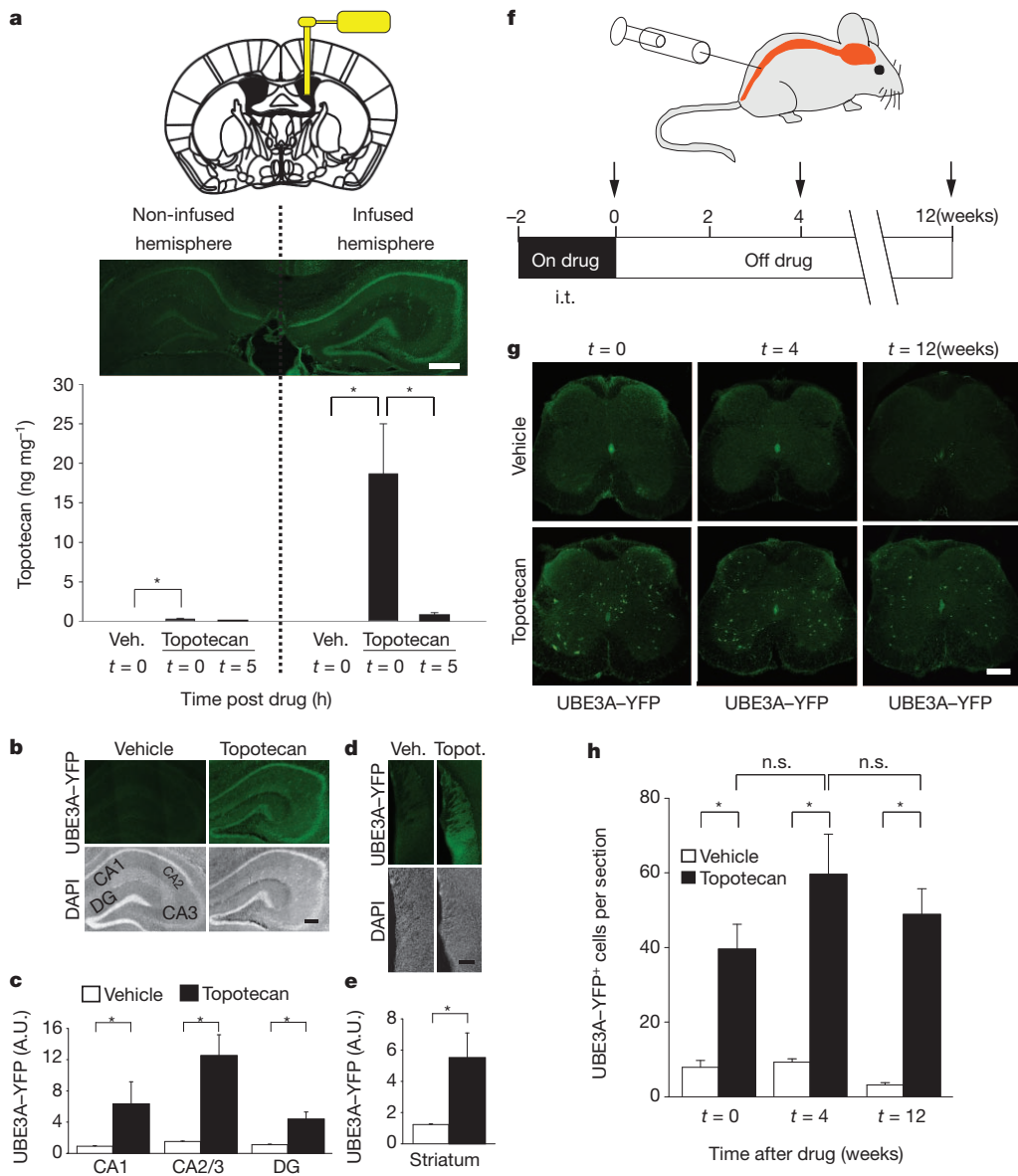


**Figure 3 | Topotecan enduringly unsilences the paternal allele of *Ube3a* in vivo.** **a**, Unilateral delivery of topotecan (i.c.v.) using a mini-osmotic pump into the lateral ventricle of *Ube3a*<sup>m+/pYFP</sup> mice *in vivo*. Two weeks of topotecan infusion ( $3.74 \mu\text{g h}^{-1}$ ) unsilenced the paternal *Ube3a*–YFP allele in the hippocampus of the infused hemisphere near the site of drug delivery, while only modestly unsilencing *Ube3a*–YFP in the contralateral (non-infused) hemisphere. Scale bar, 500  $\mu\text{m}$ . Pharmacokinetic analyses measuring topotecan levels in the infused and non-infused hemisphere immediately ( $t = 0$ ) or 5 hours ( $t = 5$ ) after cessation of drug delivery. \* $P < 0.05$ , one-way ANOVA with Bonferroni post hoc test,  $n = 5$ –9 per group. **b**, Representative sections and quantification of optical intensity of UBE3A–YFP in hippocampal regions (CA1, CA2/3 and dentate gyrus, DG) of the topotecan-infused hemisphere or the hemisphere of vehicle-treated mice. \* $P < 0.05$ , Mann–Whitney rank sum test,  $n = 5$  per group. **c**, Representative sections and quantification of paternal UBE3A–YFP in the striatum following i.c.v. infusion of topotecan. \* $P < 0.05$ , two-tailed  $t$  test,  $n = 4$  per group. **d**, Representative sections and quantification of paternal UBE3A–YFP in the striatum following i.c.v. infusion of topotecan. \* $P < 0.05$ , two-tailed  $t$  test,  $n = 4$  per group. **e**, Representative sections and quantification of paternal UBE3A–YFP in the striatum following i.c.v. infusion of topotecan. \* $P < 0.05$ , two-tailed  $t$  test,  $n = 4$  per group. **f**, Schematic depicting schedule for i.t. delivery of topotecan (50 nmol  $\text{day}^{-1}$  for 10 of 14 days) and endpoints (arrows) immediately, 4 weeks and 12 weeks after cessation of drug. **g**, **h**, Topotecan (i.t.) increased the number of UBE3A–YFP-positive spinal neurons compared to vehicle, and the unsilencing of *Ube3a*–YFP was maintained for at least 12 weeks. \* $P < 0.001$ , one-way ANOVA with Bonferroni post hoc test,  $n = 7$ –8 per group.

In conclusion, we found that topoisomerase inhibitors can unsilence the paternal allele of *Ube3a* and that the paternally-derived protein is functional. These findings suggest that topoisomerase inhibitors have the potential to rescue the molecular, cellular and behavioural deficits associated with loss of *UBE3A*<sup>7,13,28</sup>. *Ube3a* expression is modestly upregulated in the brain of *Top2b* knockout mice<sup>29</sup>, providing genetic support that topoisomerases regulate *Ube3a* expression. We also found that topotecan reduced expression of paternal *Snrpn* and *Ipw*, a genomic region whose deletion is associated with Prader–Willi syndrome<sup>7,17</sup>. To what extent topotecan regulates expression of other genes in the brain, including *Igf2r*-, *Kcnq1*- and *Gnas*-imprinted gene clusters, and whether long-term treatments with topoisomerase inhibitors produce a Prader–Willi-like condition are unknown. However, topotecan and irinotecan are approved for use in patients with cancer, penetrate into the central nervous system, and are well-tolerated when administered chronically to both adult and paediatric patients<sup>27,30</sup>. As well, patients treated with topoisomerase inhibitors do not display symptoms associated with Prader–Willi syndrome. Ultimately, our study indicates that topoisomerase inhibitors regulate gene expression through a transcriptional mechanism and could be used to treat symptoms associated with Angelman syndrome.

## METHODS SUMMARY

All animal procedures were approved by the University of North Carolina at Chapel Hill Animal Care and Use Committee. We used male and female *Ube3a*-YFP knock-in mice<sup>15</sup>, *Ube3a*<sup>m-/p+</sup> mice<sup>13</sup> and their age-matched, wild-type controls. High-content screening was performed on a BD Pathway 855 system. *UBE3A*-YFP was detected for drug screening with an anti-GFP antibody (Novus Biologicals, NB600-308; 1:1,000) because intrinsic YFP fluorescence levels were low in cultured neurons and tissue sections. All data are presented as mean  $\pm$  s.e.m., with sample sizes (*n*) shown in figures or stated in the text. Statistical analyses were performed using SigmaPlot 11 (Systat Software). Normality tests (Shapiro–Wilk) and equal variance tests were run and passed (*P* > 0.05) before parametric statistical analyses were run.

**Full Methods** and any associated references are available in the online version of the paper at [www.nature.com/nature](http://www.nature.com/nature).

Received 28 June; accepted 22 November 2011.

Published online 21 December 2011.

- Kishino, T., Lalande, M. & Wagstaff, J. *UBE3A*/E6-AP mutations cause Angelman syndrome. *Nature Genet.* **15**, 70–73 (1997).
- Matsuura, T. *et al.* De novo truncating mutations in E6-AP ubiquitin-protein ligase gene (*UBE3A*) in Angelman syndrome. *Nature Genet.* **15**, 74–77 (1997).
- Sutcliffe, J. S. *et al.* The E6-AP ubiquitin-protein ligase (*UBE3A*) gene is localized within a narrow Angelman syndrome critical region. *Genome Res.* **7**, 368–377 (1997).
- Albrecht, U. *et al.* Imprinted expression of the murine Angelman syndrome gene, *Ube3a*, in hippocampal and Purkinje neurons. *Nature Genet.* **17**, 75–78 (1997).
- Rougeulle, C., Glatt, H. & Lalande, M. The Angelman syndrome candidate gene, *UBE3A*/E6-AP, is imprinted in brain. *Nature Genet.* **17**, 14–15 (1997).
- Vu, T. H. & Hoffman, A. R. Imprinting of the Angelman syndrome gene, *UBE3A*, is restricted to brain. *Nature Genet.* **17**, 12–13 (1997).
- Mabb, A. M., Judson, M. C., Zylka, M. J. & Philpot, B. D. Angelman syndrome: insights into genomic imprinting and neurodevelopmental phenotypes. *Trends Neurosci.* **34**, 293–303 (2011).
- Peters, S. U. *et al.* Double-blind therapeutic trial in Angelman syndrome using betaine and folic acid. *Am. J. Med. Genet.* **152A**, 1994–2001 (2010).
- Chamberlain, S. J. & Brannan, C. I. The Prader–Willi syndrome imprinting center activates the paternally expressed murine *Ube3a* antisense transcript but represses paternal *Ube3a*. *Genomics* **73**, 316–322 (2001).
- Landers, M. *et al.* Regulation of the large (approximately 1000 kb) imprinted murine *Ube3a* antisense transcript by alternative exons upstream of *Snurf/Snrpn*. *Nucleic Acids Res.* **32**, 3480–3492 (2004).
- Numata, K., Kohama, C., Abe, K. & Kiyosawa, H. Highly parallel SNP genotyping reveals high-resolution landscape of mono-allelic *Ube3a* expression associated with locus-wide antisense transcription. *Nucleic Acids Res.* **39**, 2649–2657 (2011).
- Nakatani, J. *et al.* Abnormal behavior in a chromosome-engineered mouse model for human 15q11–13 duplication seen in autism. *Cell* **137**, 1235–1246 (2009).
- Jiang, Y. H. *et al.* Mutation of the Angelman ubiquitin ligase in mice causes increased cytoplasmic p53 and deficits of contextual learning and long-term potentiation. *Neuron* **21**, 799–811 (1998).
- Miura, K. *et al.* Neurobehavioral and electroencephalographic abnormalities in *Ube3a* maternal-deficient mice. *Neurobiol. Dis.* **9**, 149–159 (2002).
- Dindot, S. V., Antalffy, B. A., Bhattacharjee, M. B. & Beaudet, A. L. The Angelman syndrome ubiquitin ligase localizes to the synapse and nucleus, and maternal deficiency results in abnormal dendritic spine morphology. *Hum. Mol. Genet.* **17**, 111–118 (2008).
- Rougeulle, C., Cardoso, C., Fontes, M., Colleaux, L. & Lalande, M. An imprinted antisense RNA overlaps *UBE3A* and a second maternally expressed transcript. *Nature Genet.* **19**, 15–16 (1998).
- Runte, M. *et al.* The IC-SNURF-SNRPN transcript serves as a host for multiple small nucleolar RNA species and as an antisense RNA for *UBE3A*. *Hum. Mol. Genet.* **10**, 2687–2700 (2001).
- Watanabe, Y. *et al.* Genome-wide analysis of expression modes and DNA methylation status at sense-antisense transcript loci in mouse. *Genomics* **96**, 333–341 (2010).
- Pommier, Y. Topoisomerase I inhibitors: camptothecins and beyond. *Nature Rev. Cancer* **6**, 789–802 (2006).
- Hertzberg, R. P. *et al.* Modification of the hydroxy lactone ring of camptothecin: inhibition of mammalian topoisomerase I and biological activity. *J. Med. Chem.* **32**, 715–720 (1989).
- Plaschkes, I., Silverman, F. W. & Priel, E. DNA topoisomerase I in the mouse central nervous system: age and sex dependence. *J. Comp. Neurol.* **493**, 357–369 (2005).
- Scheffner, M., Nuber, U. & Huibregtse, J. M. Protein ubiquitination involving an E1–E2–E3 enzyme ubiquitin thioester cascade. *Nature* **373**, 81–83 (1995).
- Beaudenon, S., Dastur, A. & Huibregtse, J. M. Expression and assay of HECT domain ligases. *Methods Enzymol.* **398**, 112–125 (2005).
- Kumar, S., Kao, W. H. & Howley, P. M. Physical interaction between specific E2 and Hect E3 enzymes determines functional cooperativity. *J. Biol. Chem.* **272**, 13548–13554 (1997).
- Bressler, J. *et al.* The SNRPN promoter is not required for genomic imprinting of the Prader–Willi/Angelman domain in mice. *Nature Genet.* **28**, 232–240 (2001).
- Reik, W. Stability and flexibility of epigenetic gene regulation in mammalian development. *Nature* **447**, 425–432 (2007).
- Gammon, D. C. *et al.* Intrathecal topotecan in adult patients with neoplastic meningitis. *Am. J. Health Syst. Pharm.* **63**, 2083–2086 (2006).
- Greer, P. L. *et al.* The Angelman syndrome protein *Ube3a* regulates synapse development by ubiquitinating arc. *Cell* **140**, 704–716 (2010).
- Lyu, Y. L. *et al.* Role of topoisomerase II $\beta$  in the expression of developmentally regulated genes. *Mol. Cell. Biol.* **26**, 7929–7941 (2006).
- Bomgaars, L., Berg, S. L. & Blaney, S. M. The development of camptothecin analogs in childhood cancers. *Oncologist* **6**, 506–516 (2001).

**Supplementary Information** is linked to the online version of the paper at [www.nature.com/nature](http://www.nature.com/nature).

**Acknowledgements** We thank A. Beaudet and Y.-h. Jiang for providing *Ube3a*-YFP and *Ube3a*<sup>m-/p+</sup> mice; T. Riday and J. E. Han for assistance in i.c.v. mini-osmotic pump infusion; A. Burns for assistance in maintaining mouse colonies; V. Gukassyan for help with the Surveyor and confocal imaging systems; K. McNaughton for help with tissue sectioning; W. Zamboni for providing belotecan, rubitecan and siletecan; and W. Janzen and the Center of Integrative Chemical Biology and Drug Discovery for providing the epigenetic library. B.D.P., M.J.Z. and B.L.R. were supported by the Simons Foundation Autism Research Initiative (SFARI) and by the Angelman Syndrome Foundation. B.D.P. and M.J.Z. were supported by the National Institute of Mental Health (NIMH) (R01MH093372). B.D.P. was supported by the National Eye Institute (R01EY018323) and NC TrACS (50KR41016). M.J.Z. was supported by the National Institute of Neurological Disorders and Stroke (NINDS) (R01NS060725, R01NS067688). B.L.R. was supported by national Institutes of Health (NIH) HHSN-271-2008-00025-C, the NIMH Psychoactive Drug Screening Program, the Michael Hooker Distinguished Chair of Pharmacology, and grants from NIMH and the National Institute on Drug Abuse (NIDA). H.-S.H. was supported by a NARSAD grant from the Brain and Behavior Research Foundation Young Investigator Award and NC TrACS (10KR20910). J.A.A. was supported by NIH T32HD040127-07, the University of North Carolina–Carolina Institute for Developmental Disabilities, and an Autism Concept Award AR093464 from the US Department of Defense. A.M.M. was supported by a National Research Service Award from NINDS (5F32NS067712). I.F.K. was supported by a Joseph E. Wagstaff Postdoctoral Research Fellowship from the Angelman Syndrome Foundation. Assay development costs were partially supported by NINDS (5P30NS045892). Confocal and montage imaging was performed at the University of North Carolina at Chapel Hill Confocal and Multiphoton Imaging Facility, which is co-funded by grants from NINDS (5P30NS045892) and the National Institute of Child Health and Human Development (NICHD) (P30HD03110).

**Author Contributions** H.-S.H., J.A.A., A.M.M., I.F.K., M.J.Z., B.L.R. and B.D.P. conceived and designed experiments, and wrote the manuscript. All authors reviewed and edited the manuscript. H.-S.H., J.A.A., J.M. and H.-M.L. performed drug screens and validations. H.-S.H., B.T.-B., J.M. and J.W.D. performed *in vivo* studies and immunofluorescence. H.-S.H. and A.S.B. performed pharmacokinetic analyses. A.M.M. performed tests of *UBE3A* functionality. I.F.K. performed quantitative PCR with reverse transcription and methylation analyses. N.S. oversaw high content screening instrumentation and implemented image processing algorithms. X.C. and J.J. synthesized the lactam E ring inactive camptothecin analogue and the three indenoisoquinoline derivatives. The laboratories of M.J.Z., B.L.R. and B.D.P. contributed equally to this work.

**Author Information** Reprints and permissions information is available at [www.nature.com/reprints](http://www.nature.com/reprints). The authors declare no competing financial interests. Readers are welcome to comment on the online version of this article at [www.nature.com/nature](http://www.nature.com/nature). Correspondence and requests for materials should be addressed to M.J.Z. (zylka@med.unc.edu), B.L.R. (bryan\_roth@med.unc.edu) or B.D.P. (bphilpot@med.unc.edu).



## METHODS

**Mice.** *Ube3a*-YFP mice were generated and provided by the laboratory of A. Beaudet<sup>15</sup>. *Ube3a*-deficient mice were generated in the laboratory of A. Beaudet<sup>13</sup> and backcrossed by Y.-h. Jiang onto a C57BL/6J background. C57BL/6 mice (Charles River Laboratories) were used for matings with *Ube3a*-YFP. C57BL/6J mice (Jackson Laboratories) were used for matings with *Ube3a*-deficient mice and CAST/EiJ mice (Jackson Laboratories).

**Primary neuron cultures.** Embryonic day 13.5 (E13.5) to E16.5 mouse cortices were dissected and trypsinized with TrypLE express at 37 °C for 10 min. Dissociated neurons were seeded onto 384-well plates coated with poly-D-lysine (0.1 mg ml<sup>-1</sup>) at a density of  $2 \times 10^4$  cells per well (or at a density of  $1.8 \times 10^6$  cells per well for six-well plates). Neurons were cultured with Neurobasal medium with 5% fetal bovine serum, GlutaMAX (Invitrogen, catalogue no. 35050-061), B27 (Invitrogen, catalogue no. 17504-044) and Antibiotic-Antimycotic (Invitrogen, catalogue no. 15240-062) and changed into Neurobasal medium supplemented with 4.84 µg ml<sup>-1</sup> uridine 5'-triphosphate (Sigma, U6625), 2.46 µg ml<sup>-1</sup> 5-fluoro-2'-deoxyuridine (Sigma, F0503), GlutaMAX (Invitrogen, catalogue no. 35050-061), B27 (Invitrogen, catalogue no. 17504-044), and Antibiotic-Antimycotic (Invitrogen, catalogue no. 15240-062) at DIV1 and DIV5.

**Drug libraries and compounds.** Several drug libraries were used for the screening campaign including the NIMH X-901 Library (source: National Institutes of Health Chemical Synthesis and Drug Supply Program), the NIH Clinical Collection (source: National Institutes of Health), the Prestwick Library (source: Prestwick Chemical), an internal Roth laboratory library comprised mainly of central nervous system active small molecules (source: National Institute of Mental Health Psychoactive Drug Screening Program), a small molecule library of DNA methyltransferase inhibitors, protein lysine methyltransferase inhibitors and other small-molecule modulators of epigenetic targets (source: Center for Integrative Chemical Biology and Drug Discovery, UNC-CH). Suberoylanilide hydroxamic acid (SAHA) was purchased from Cayman Chemical. Irinotecan, zebularine, hydralazine, procainamide, 5-aza-2'-deoxycytidine (decitabine), etoposide, tenoposide, amsacrine and ICRF-193 were all obtained from Sigma-Aldrich. Topotecan, camptothecin (CPT), 10-hydroxy-CPT, 7-ethyl-CPT and 7-ethyl-10-hydroxy-CPT (SN38) were obtained from MOLCAN Corporation. ICRF-187 was provided by the National Cancer Institute's Developmental Therapeutics Program. Belotecan, silatecan and rubitecan were provided by W. Zamboni (University of North Carolina Eshelman School of Pharmacy). The indenoisoquinoline derivatives NSC706744, NSC725776 and NSC724998 were synthesized as described<sup>31,32</sup>. The inactive lactam E ring-CPT analogue was synthesized as described<sup>20</sup>.

**High-content screening microscopy and small-molecule screening.** Primary cortical neurons were isolated from E13.5–16.5 *Ube3a*-YFP mice. Screening was performed in quadruplicate at DIV7 using multiple chemical libraries and a compound concentration of 10 µM in 0.2% DMSO vehicle. After 72 h of drug exposure, neurons were fixed with 4% paraformaldehyde in PBS for 35 min, permeabilized with 0.3% Triton X-100 in PBS on ice for 30 min, and blocked by 5% goat serum with 0.1% Triton X-100 in PBS at room temperature for 1 h. Cells were incubated with a rabbit polyclonal antibody to GFP (1:1,000, Novus Biologicals, NB600-308) at room temperature for 1 h and then incubated with Alexa Fluor 488 goat antibody to rabbit IgG (1:200, Invitrogen, A11008) and DAPI (1:10,000, Invitrogen, D-1306) at room temperature for 30 min. Individual wells of immunofluorescence-processed plates were imaged for DAPI or Alexa 488 fluorescence using the BD Pathway 855 high-content imaging microscope with a 488-nm excitation/515-nm long-pass filter. Antibody-enhanced UBE3A-YFP fluorescence intensities were determined from individual neurons in drug-treated wells and normalized to neurons in wells treated with 0.2% DMSO (vehicle control). Analyses were performed with custom macros and algorithms using NIH Image J and Arrayscan Cell Profiler software programs (Thermo Scientific/Cellomics). These image analyses enabled masking of nuclei in individual neurons and determination of UBE3A-YFP fluorescence intensities in the nuclei of individual neurons (see Supplementary Fig. 1). Drug-induced increases of >50% were initially binned as screening 'hits' if (1) the increases were consistently observed across replicate wells and (2) no apparent toxicities were observed by assessing nuclear structure of neurons co-stained with DAPI. Effective 'hit' compounds were validated in formal dose-response experiments to determine relative compound potencies (EC<sub>50</sub>) and efficacies (E<sub>max</sub>).

After the initial identification of irinotecan as an active, other topoisomerase inhibitors were screened. DIV7 primary neurons from *Ube3a*<sup>+/+</sup>YFP mice were dose-treated for 72 h with topoisomerase I and II inhibitors in ten point dose-responses in full- and half-log molar concentrations (1 nM to 30 µM). Neurons were fixed, processed for immunofluorescence, and UBE3A-YFP fluorescence intensities were again determined by high-content imaging microscopy. The dose-response results were analysed by least squares sigmoidal dose-response

curve-fitting models using Graphpad Prism 5.0 (Graphpad Software). The calculated EC<sub>50</sub> values (potencies) and Y-value top plateau (estimated efficacies or E<sub>max</sub>) enabled comparative analyses of the relative potency and efficacy of the identified compounds. To control for potential false positive 'hit' compounds, cortical neurons from wild-type mice, which lack *Ube3a*-YFP, were also treated to determine if 'hit' compounds exhibit inherent fluorescence.

A Z'-factor score was determined to assess the appropriateness of the screening platform by comparing UBE3A-YFP maternal and paternal fluorescence signals at DIV10. This was done by determining the mean cellular UBE3A-YFP fluorescence of >1,200 neurons in quadruplicate wells for both genotypes, which were normalized to age-matched vehicle-treated control wells. The score was calculated using the following formula: Z' factor =  $1 - ((3 \times (\text{s.d. maternal UBE3A-YFP} + \text{s.d. paternal UBE3A-YFP})) / (\text{mean maternal UBE3A-YFP} - \text{mean paternal UBE3A-YFP}))$ .

**Immunofluorescence staining in central nervous system tissues.** For immunocytochemistry in brain tissues, mice were perfused with 4% paraformaldehyde in 0.1 M PBS, post-fixed overnight, and cryoprotected with 20% sucrose in 0.1 M phosphate buffer, pH 7.4 for two days. Sections (60 µm) were collected and permeabilized with 0.3% Triton X-100 in 0.1 M phosphate buffer for 30 min, and blocked by 5% goat serum for 1 h. Sections were incubated with rabbit polyclonal antibody to GFP (1:1,000, Novus Biologicals, NB600-308) at 4 °C overnight and then incubated with Alexa Fluor 488 goat antibody to rabbit IgG and DAPI for 2 h at room temperature. Images were acquired using a Zeiss LSM 510 and 710 confocal microscopes.

For immunocytochemistry in spinal cord, lumbosacral spinal cord (approximately L1 to S2 and inclusive of the area corresponding to intrathecal injection site) was removed from each mouse and immersion-fixed for 8 h in cold 4% paraformaldehyde and 0.1 M phosphate buffer (pH 7.4). After a period of cryoprotection in 30% sucrose in 0.1 M phosphate buffer, each spinal cord was sectioned on a cryostat at 40 µm. Sections to be stained immediately were collected in PBS, sections to be saved for future study were placed in a PBS/ethylene glycol/glycerol solution and stored at -20 °C. Every fourth section was incubated overnight in a mixture containing a chicken IgY to GFP (1:750; Aves Labs, GFP-1020) and a mouse IgG<sub>1</sub> to NeuN (1:250; Millipore, MAB377) and treated the following day with a cocktail containing goat anti-chicken IgY-Alexa 488 (1:200; Invitrogen, A-11039), goat anti-mouse IgG<sub>1</sub>-Alexa 568 (1:200; Invitrogen, A-21124) and DRAQ5 (1:10,000; Axora, BOS-889-001). Immunostained sections were mounted from PBS onto SuperFrost Plus Slides (Fisher), which were then air-dried briefly, rehydrated with PBS, and coverslipped with FluoroGel (Electron Microscopy Sciences). For quantification studies, sections were imaged using a Nikon Eclipse 80i with Surveyor mosaic imaging software. For qualitative assessment, sections were imaged as maximal projections on a Zeiss LSM 510.

**Optical intensity measurement of UBE3A-YFP in brain tissue and cell counting of UBE3A-YFP-positive neurons in spinal cord.** For optical intensity measurement in selected brain regions, sections were imaged using a Zeiss LSM 510 confocal microscope. With custom macros created using ImageJ software<sup>33</sup>, optical intensity of UBE3A-YFP was measured in different regions of hippocampus and striatum from vehicle- and topotecan-treated mice. Image intensity levels were normalized to background intensities from appropriate regions in vehicle-treated mice. Brain sections between Bregma -1.22 mm and -2.06 mm were chosen for analysis ( $n = 5$  sections per mouse for hippocampus and  $n = 3-5$  sections per mouse for striatum).

For cell counting in spinal cord, we analysed 14 to 18 sections per mouse in segments corresponding to the injection site. Slices were imaged using a Nikon Eclipse 80i microscope equipped with a Qimaging Retiga EXi high-speed CCD camera system and Surveyor mosaic imaging software using a  $\times 10$  objective. For qualitative purposes, we also imaged selected sections on a Zeiss LSM 510 confocal microscope. Cells were counted manually by individuals blind to the experimental groups from raw (unprocessed) images using ImageJ and CellProfiler<sup>34</sup> software.

YFP intensity levels from confocal XYZ image stacks were measured using a semi-automated macro with ImageJ. Individual YFP-positive cells were selected by eye, the criteria being the Z plane having the largest area for each cell. Cell regions were defined by intensity thresholding or manual tracing and the average YFP intensity and percent saturation were calculated for each cell.

**Western blotting.** E13.5–E15.5 primary cortical neurons from *Ube3a*-YFP, *Ube3a*-deficient or wild-type mice were plated in six-well plates. At DIV7, neurons were treated with drug or 0.1% DMSO for 72 h, and then total protein lysates were obtained by lysis buffer (1% Triton X-100, 5 mM EDTA, 0.15 M NaCl, 10 mM Tris-HCl, pH 7.5, phosphatase inhibitor cocktails 1, protease inhibitor cocktail). To assess UBE3A-YFP or UBE3A protein levels, 7.5 µg of total protein lysates from *Ube3a*-YFP or *Ube3a*-deficient neurons were separated by 8% SDS-polyacrylamide gel electrophoresis. Proteins were then transferred to nitrocellulose membranes, and immunoblotting was performed using a rabbit anti-GFP antibody (Novus,

1:500) and Alexa Fluor 680 goat anti-rabbit IgG (Invitrogen, 1:5,000) or rabbit anti-UBE3A antibody (Abcam, 1:500) and Alexa Fluor 680 goat anti-rabbit IgG (Invitrogen, 1:5,000). UBE3A–YFP or native UBE3A protein bands were visualized using an Odyssey system (LI-COR Biosciences). To control for protein loading, UBE3A–YFP or UBE3A protein levels were normalized to actin levels detected in each sample.

**Ubiquitin thioester assay.** DIV10 cortical neurons were collected and lysed in immunoprecipitation buffer (20 mM Tris-HCl, 3 mM EDTA, 3 mM EGTA, 150 mM NaCl, 1% Triton X-100, pH 7.4) containing 10 mM sodium fluoride, 1.0 mM sodium orthovanadate, 1.0  $\mu\text{g ml}^{-1}$  aprotinin, and 0.1 mM DTT. UBE3A protein was immunoprecipitated from cell extracts with 5.0  $\mu\text{g}$  of an anti-UBE3A antibody (Bethyl Laboratories) overnight at 4 °C and then washed twice with immunoprecipitation buffer containing 500 mM NaCl, followed by ubiquitin buffer (50 mM Tris, 5 mM  $\text{MgCl}_2$ , pH 7.6). For *in vitro* ubiquitination of immunoprecipitated UBE3A, UBE3A was mixed with 0.1  $\mu\text{g}$  E1, 0.5  $\mu\text{g}$  UBCH7, 2.5  $\mu\text{g}$  ubiquitin (Boston Biochem) and 10 mM ATP in a total reaction volume of 20  $\mu\text{l}$ . The reaction was incubated at room temperature for 10 min and end products were stopped in 2 $\times$  SDS sample buffer with or without DTT. Samples were boiled, separated by SDS–PAGE gel electrophoresis, transferred to PVDF membrane, and immunoblotted with an anti-UBE3A or anti-ubiquitin (Santa Cruz) antibody.

**Topoisomerase depletion assay.** DIV7 cortical neurons were treated with 300 nM topotecan or vehicle for 72 h. Cells were collected and lysed on ice for 30 min in RIPA buffer (50 mM Tris-HCl, 150 mM NaCl, 1% Triton X-100, 0.5% sodium deoxycholate, 0.1% SDS, pH 7.4) to preserve topoisomerase cleavable complexes. Cell extracts were then centrifuged at 14,000 r.p.m. at 4 °C to pellet insoluble debris. 30  $\mu\text{g}$  of the cell supernatant was diluted in 2 $\times$  SDS sample buffer and separated on a 7.5% SDS–PAGE gel, transferred to nitro cellulose membrane, and immunoblotted with an anti-topoisomerase I antibody (Santa Cruz) to detect free topoisomerase I. An anti- $\beta$ -tubulin (Sigma) antibody was used as a loading control.

**Quantitative PCR.** For quantitative reverse transcriptase polymerase chain reaction (qRT–PCR) analysis, total RNA was extracted from cortical cultures treated with 300 nM topotecan using TRIzol reagent (Invitrogen). First strand cDNA synthesis was performed on 500 ng–2  $\mu\text{g}$  total RNA using Superscript III reverse transcriptase (Invitrogen) primed with random hexamers. qPCR reactions used SYBR green (Invitrogen) and were run on a Rotorgene 3000 (Corbett Research). Standard curves and  $C_t$  values were generated using Rotorgene analysis software version 6.0. Expression of *Ube3a*, *Ube3a*–ATS (2), *Ube3a*–ATS (3) (*Ipw*) and *Snrpn* were determined after normalization of each complementary DNA sample to expression levels of the housekeeping genes *Rpl22* and *Actb*. Primers were as follows: *Ube3a* F (5'–CAAAAGGTGCATCTAACAACATCA–3'), *Ube3a* R (5'–GGGGAATAATCTCCTCTCTC–3'), *Snrpn* 1–3 F (5'–TTGGTTCTGAGGAGTGATTTGC–3')<sup>35</sup>, *Snrpn* 3 R (5'–CCTTGAATTCCACCCTTG–3')<sup>35</sup>, *Ipw* B/C F (5'–TCACCACAACACTGGACAA–3')<sup>10</sup>, *Ube3a*–ATS F (5'–GGCACCTTGTTTGAACCTT–3'), *Ube3a*–ATS R (5'–GCTCATGACCTGTCCTTTC–3'), *Rpl22* F (5'–AAGAAGCAGGTTTGAAG–3'), *Rpl22* R (5'–TGAAGTGACAGTGATCTTG–3'), *Actb* F (5'–CAGCTTCTTGACAGTCCTT–3'), *Actb* R (5'–CAGATGGAGGGGAATACAG–3').

**Bisulphite sequencing.** Genomic DNA was extracted from C57BL/6 (female)  $\times$  CAST/EiJ (male) F1 hybrid cortical cultures treated with 300 nM topotecan using TRIzol reagent. Bisulphite conversion was performed on 200 ng genomic DNA using a MethylCode kit (Invitrogen). Converted DNA (1  $\mu\text{l}$ ) was used as template for PCR. A first round of PCR was performed as described in ref. 36 using the W18 and W19 or W16 and W17 primer sets<sup>36</sup>. A second semi-nested round of PCR was performed using 1  $\mu\text{l}$  of the primary PCR reaction as template. For semi-nested PCR, the W18 primer was used with the nested W19-inside primer (5'–AAATAAAATACACTTTCCTACTAAATC–3'), or the W16 primer was used with the nested W17-inside primer (5'–ACAACAAAACCTCTATCCACAC–3'). Products were separated on an agarose gel and extracted using the QIAquick gel extraction kit (Qiagen). Purified DNA was ligated into the pGem–T Easy vector (Promega). Individual clones were amplified and sequenced to assess methylation status and parent of origin.

**Intrathecal injection.** Topotecan (50 nmol in 5  $\mu\text{l}$ , unless noted) was injected into unanaesthetized mice via a 30-gauge needle attached to a 50  $\mu\text{l}$  Luer–hub Hamilton syringe using the direct lumbar puncture method<sup>37</sup>; injections were made at lower lumbar levels. Following the injection, the syringe is rotated slightly and removed. Topotecan was dissolved with 50 mM tartrate acid buffer in 0.9% saline. Comparable vehicle injections were made in control mice.

**Intracerebroventricular drug infusions.** Mice with paternal *Ube3a*–YFP (*Ube3a*<sup>m+/pYFP</sup>) were anesthetized with ketamine/xylazine (120 mg per kg; 9 mg per kg) and positioned in a stereotaxic apparatus. The scalp was shaved and cut, and the skull exposed. The local anaesthetic (bupivacaine, 2.5 mg  $\text{ml}^{-1}$ ) was applied to the skull, and mineral oil was applied to protect the eyes of the mice. Acetone was

applied on the skull to remove any lipid tissues on the skull as well as to dry the skull surface for optimal adhesion. Next, a cannula (Brain Infusion Kit 1, DURECT Corporation) was positioned into a lateral ventricle at the following coordinates (–0.3 mm A/P, +1.0 mm M/L, –2.5 mm D/V), as described<sup>38</sup>. The free end of the cannula was connected to a mini-osmotic pump (Alzet, Model 2001 or 2002) via a 2.5-cm piece of polyethylene (PE) tubing (DURECT Corporation). The mini-osmotic pump and the connecting PE tubing were filled with, respectively for Alzet models 2002 and 2001, 16.34 mM or 47.17 mM topotecan (CPT06, Molcan Corporation) dissolved in 50 mM tartaric acid with 0.9% saline, unless indicated. The filled pumps were incubated in sterile saline at 37 °C for at least 4 h before being implanted under the dorsal skin of the mouse's back. The cannula base and the attached piece of PE tubing were fixed to the skull with Loctite cyanoacrylic 454. The incision site was closed with prolene suture. During and after surgery, mice were placed on a heating pad to maintain body temperature. 14 days (Alzet model 2002) or five days (Alzet model 2001) following minipump implantation, mice were killed following pentobarbital overdose (150 mg per kg, intraperitoneally) and brains were removed for immunofluorescence staining or pharmacokinetic analysis.

**Pharmacokinetic analysis of topotecan.** Total topotecan concentrations in blood and brain homogenate were determined by liquid chromatography/triple quadrupole mass spectrometry (HPLC/MS–MS). The HPLC–MS/MS system consisted of two Shimadzu Scientific solvent delivery pumps, a Valco switching valve, a thermostated (6 °C) LEAP HTC autosampler, and an Applied Biosystems API3000 triple quadrupole mass spectrometer. Reversed-phase gradient chromatography was used to elute the compounds from an Aquasil (C18 3  $\mu\text{m}$ , 50  $\times$  2.1 mm) analytical column at a flow rate of 0.3  $\text{ml min}^{-1}$ , following a 10  $\mu\text{l}$  injection. Starting conditions for each injection was 85% aqueous (0.1% v/v formic acid in water) and 15% organic (0.1% v/v formic acid in methanol). This was held constant for 0.7 min. After 0.7 min, the organic phase increased linearly to 95% 4.5 min post-injection. The solvent composition was held at 95% organic for 0.5 min to wash the column. The column was re-equilibrated to starting conditions for the final 1 min. Total run time was 6 min. Eluent was diverted to waste for the first 1.5 min. After 1.5 min post-injection, 100% of the eluent was directed to the mass spectrometer. The mass spectrometer was connected to the HPLC system by a TurboIonSpray interface. User-controlled voltages, gas pressures and source temperature were optimized via direct infusion of topotecan, *d6*–topotecan (internal standard) and irinotecan (internal standard). All were analysed in positive ion mode using the following transitions preset in multiple reaction monitoring scans: topotecan 422.0  $\rightarrow$  377.1, *d6*–topotecan (428.0  $\rightarrow$  377.1) and irinotecan 587.2  $\rightarrow$  587.2 (parent to parent transition). To eliminate instrument error due to either in source fragmentation or to cross-talk, care was taken to ensure analytical separation between topotecan and its desmethyl metabolite. Automated sample acquisition and data analysis was performed using the Analyst software (version 1.4.1, Applied Biosystems, Foster City, CA). Calibration curves, prepared from standards prepared in duplicate using appropriate matrix, were generated based on peak area ratios (analyte:internal standard) and followed a linear fit with  $1/x^2$  weighting. The lower limit of topotecan quantification (LLQ) was 0.01  $\mu\text{M}$  in both blood and brain homogenate (0.03 ng per mg of brain). Unknown brain and brain homogenate samples and spiked matrix standards were analysed following addition of internal standard and protein precipitation using 4 $\times$  volume of methanol-containing formic acid (0.1% v/v). Note that brain homogenates were taken from entire hemispheres; because our homogenates included the ventricular cerebrospinal fluid where drug is likely to accumulate, our drug concentrations likely overestimate the concentrations in parenchymal brain tissue.

- Cushman, M. *et al.* Synthesis of new indeno[1,2-*c*]isoquinolines: cytotoxic non-camptothecin topoisomerase I inhibitors. *J. Med. Chem.* **43**, 3688–3698 (2000).
- Nagarajan, M. *et al.* Synthesis and evaluation of indenoisoquinoline topoisomerase I inhibitors substituted with nitrogen heterocycles. *J. Med. Chem.* **49**, 6283–6289 (2006).
- Abramoff, M. D., Magelhaes, P. J. & Ram, S. J. Image processing with ImageJ. *Biophotonics International* **11**, 36–42 (2004).
- Lamprecht, M. R., Sabatini, D. M. & Carpenter, A. E. CellProfiler: free, versatile software for automated biological image analysis. *Biotechniques* **42**, 71–75 (2007).
- Tsai, T. F., Jiang, Y. H., Bressler, J., Armstrong, D. & Beaudet, A. L. Paternal deletion from *Snrpn* to *Ube3a* in the mouse causes hypotonia, growth retardation and partial lethality and provides evidence for a gene contributing to Prader–Willi syndrome. *Hum. Mol. Genet.* **8**, 1357–1364 (1999).
- Peery, E. G., Elmore, M. D., Resnick, J. L., Brannan, C. I. & Johnstone, K. A. A targeted deletion upstream of *Snrpn* does not result in an imprinting defect. *Mamm. Genome* **18**, 255–262 (2007).
- Fairbanks, C. A. Spinal delivery of analgesics in experimental models of pain and analgesia. *Adv. Drug Deliv. Rev.* **55**, 1007–1041 (2003).
- Pierce, A. A. & Xu, A. W. De novo neurogenesis in adult hypothalamus as a compensatory mechanism to regulate energy balance. *J. Neurosci.* **30**, 723–730 (2010).



# A microRNA regulon that mediates endothelial recruitment and metastasis by cancer cells

Kim J. Png<sup>1</sup>\*, Nils Halberg<sup>1</sup>\*, Mitsukuni Yoshida<sup>1</sup> & Sohail F. Tavazoie<sup>1</sup>

Metastatic progression of cancer is a complex and clinically daunting process<sup>1–4</sup>. We previously identified a set of human microRNAs (miRNAs) that robustly suppress breast cancer metastasis to lung and bone<sup>5,6</sup> and which display expression levels that predict human metastasis<sup>7,8</sup>. Although these findings revealed miRNAs as suppressors of cell-autonomous metastatic phenotypes, the roles of non-coding RNAs in non-cell-autonomous cancer progression processes remain unknown. Here we reveal that endogenous miR-126, an miRNA silenced in a variety of common human cancers<sup>7,8</sup>, non-cell-autonomously regulates endothelial cell recruitment to metastatic breast cancer cells, *in vitro* and *in vivo*. It suppresses metastatic endothelial recruitment, metastatic angiogenesis and metastatic colonization through coordinate targeting of *IGFBP2*, *PITPNC1* and *MERTK*—novel pro-angiogenic genes and biomarkers of human metastasis. Insulin-like growth factor binding protein 2 (IGFBP2) secreted by metastatic cells recruits endothelia by modulating IGF1-mediated activation of the IGF type-I receptor on endothelial cells; whereas c-Mer tyrosine kinase (MERTK) receptor cleaved from metastatic cells promotes endothelial recruitment by competitively antagonizing the binding of its ligand GAS6 to endothelial MERTK receptors. Co-injection of endothelial cells with breast cancer cells non-cell-autonomously rescues their miR-126-induced metastatic defect, revealing a novel and important role for endothelial interactions in metastatic initiation. Through loss-of-function and epistasis experiments, we delineate an miRNA regulatory network's individual components as novel and cell-extrinsic regulators of endothelial recruitment, angiogenesis and metastatic colonization. We also identify the IGFBP2/IGF1/IGF1R and GAS6/MERTK signalling pathways as regulators of cancer-mediated endothelial recruitment. Our work further reveals endothelial recruitment and endothelial interactions in the tumour microenvironment to be critical features of metastatic breast cancer.

To determine the role of endogenous miR-126 in metastatic progression, stable miR-126 and control knockdown cells were generated (Supplementary Fig. 1), injected into immunodeficient mice and evaluated for metastatic colonization capacity in tail-vein, intracardiac and portal circulation colonization assays. miR-126 silencing in parental MDA-231 breast cancer cells significantly increased lung metastatic colonization (Fig. 1a and Supplementary Fig. 2), systemic metastatic colonization to multiple organs such as brain and bone (Fig. 1b, c) and hepatic metastatic colonization (Fig. 1d). miR-126 inhibition did not significantly enhance proliferation *in vitro* and resulted in a modest increase in mammary tumour volume (39.4%; Supplementary Fig. 3), which was an order of magnitude smaller than its effect on metastasis enhancement. This indicates that the effect of miR-126 on metastasis was not simply a result of its effect on tumour growth suppression. Histological quantification revealed a significant increase in the total number of metastatic nodules (small and large) in miR-126 knockdown lungs ( $13.6 \pm 3.2$  compared with  $4.9 \pm 1.8$  in controls,  $P < 0.03$ ; Fig. 1e). Importantly, the increase in nodule

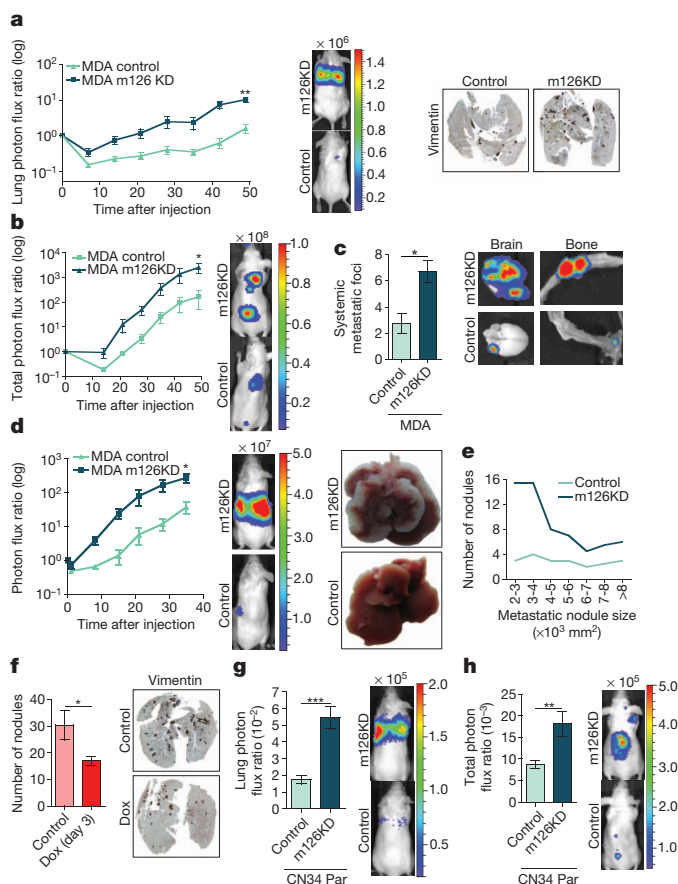


**Figure 1 | Endogenous miR-126 suppresses metastatic colonization.**

**a**, Bioluminescence imaging plot of lung metastasis by  $4 \times 10^4$  MDA-MB-231 breast cancer cells expressing a hairpin (miR-Zip) targeting miR-126 (MDA/miR-126KD (KD, knockdown)) or a control hairpin (MDA/control);  $n = 5$ . Lungs were extracted at D49 and stained for vimentin. **b**, Bioluminescence quantification of systemic metastasis by  $4 \times 10^4$  MDA/miR-126KD or MDA/control cells;  $n = 6$ . **c**, Total number of metastatic foci in mice from **b** were counted. Representative images of brain and bone metastatic nodules shown. **d**, Bioluminescence quantification of liver metastasis by  $5 \times 10^5$  MDA/miR-126KD or MDA/control cells;  $n = 6$ . **e**, Sizes of metastatic nodules in lungs extracted from **a** were measured using ImageJ. **f**,  $4 \times 10^4$  Lm2 cells expressing doxycycline-inducible pre-miR-126 were injected at day 0. At day 3, doxycycline ( $2 \text{ mg ml}^{-1}$ ) was added to the drinking water. At D49, the lungs were removed and stained for vimentin (right). Total number of nodules/lung shown. **g**, Bioluminescence quantification of lung metastasis by  $5 \times 10^5$  poorly metastatic CN34 breast cancer cells expressing a hairpin targeting miR-126 (CN34/miR-126KD) or a control hairpin (CN34/control);  $n = 7$ . **h**, Bioluminescence quantification of systemic metastasis by  $1 \times 10^6$  CN34/miR-126KD and CN34/control cells;  $n = 6$ . Error bars, s.e.m.; all  $P$  values are based on one-sided Student's  $t$ -tests. \* $P < 0.05$ ; \*\* $P < 0.001$ ; \*\*\* $P < 0.0001$ .

<sup>1</sup>Laboratory of Systems Cancer Biology, Rockefeller University, 1230 York Avenue, New York, New York 10065, USA.

\*These authors contributed equally to this work.



number was more pronounced for smaller nodule sizes than larger ones, consistent primarily with an increase in the initiation of metastases rather than an increase in the growth of established metastases. Consistent with a role for miR-126 in metastatic initiation in the niche, conditionally restoring miR-126 expression to metastatic LM2 cells after extravasation in the lung (day 3 (ref. 9)) significantly reduced metastatic colonization (Fig. 1f). Finally, miR-126 knockdown enhanced lung and systemic metastatic colonization by an independent poorly metastatic CN34 line (Fig. 1g, h). These findings reveal endogenous miR-126 to be a suppressor of metastatic initiation and metastatic colonization.

While considering the basis of the selective advantage provided by miR-126 silencing, we noted that miR-126 knockdown metastases displayed higher vessel densities on microscopic visualization of lung tissue sections stained with haematoxylin and eosin. Image analysis and quantification revealed metastases derived from miR-126 knockdown cells to have significantly higher endothelial densities than control cells (Fig. 2a and Supplementary Fig. 4). Lectin injection and cytochemistry revealed miR-126 knockdown metastases to contain increased functional blood vessel densities (Fig. 2b), whereas dextran injection revealed increased perfusion to miR-126 knockdown metastases (Supplementary Fig. 5). Thus, these independent and complementary methods reveal that miR-126 suppresses metastatic endothelial density, functional metastatic angiogenesis and perfusion; consequently, its inhibition provides metastatic cells with a selective advantage in endothelial interactions and angiogenic progression.

We next sought to determine the cellular basis for the miR-126-dependent angiogenesis phenotype observed. miR-126 did not suppress adhesion of metastatic cells to endothelial cells, endothelial proliferation or tube formation as assessed by automated quantification of branch points (Supplementary Fig. 6). We speculated that miR-126 might regulate the recruitment of endothelial cells to metastatic cells. Interestingly, metastatic LM2 cells, which display silencing of miR-126, placed in the bottom of a Boyden chamber strongly recruited human umbilical vein endothelial cells (HUVECs) through a porous trans-well insert and recruited significantly more endothelia than their less metastatic parental line (Fig. 2c). Endothelial recruitment was strongly inhibited by miR-126 overexpression (Fig. 2d). Conversely, miR-126 knockdown through miR-Zip (Fig. 2d and Supplementary Fig. 7) or LNA approaches (Supplementary Fig. 8a) significantly increased endothelial recruitment. The CN34-LM1A metastatic derivative also displayed significantly enhanced endothelial recruitment capacity relative to its poorly metastatic parental line (Supplementary Fig. 8b). miR-126 significantly suppressed endothelial recruitment by the CN34 cell population and the HER2-positive SkBr3 line (Fig. 2e), and suppressed recruitment of HMVEC endothelial cells (Supplementary Fig. 8c). These findings reveal enhanced endothelial recruitment capacity to be a key feature of metastatic breast cancer populations and identify endogenous miR-126 as a major regulator of this process.

We next asked whether endogenous miR-126 can selectively regulate endothelial recruitment to breast cancer cells independent of their location. Endothelial recruitment to metastatic cells injected in the mammary fat-pad was specifically inhibited by miR-126 expression and enhanced by miR-126 suppression (Supplementary Fig. 9a–c), whereas miR-126 silencing did not increase leukocyte (Supplementary Fig. 9d) or macrophage densities (Supplementary Fig. 9e). These findings reveal miR-126 to regulate endothelial recruitment to breast cancer cells selectively, independent of their anatomical location, and they provide a non-cell-autonomous mechanism for the enhanced primary tumour-size phenotype seen with miR-126 silencing.

To identify the targets of miR-126, we used an integrative transcriptomic approach and identified a set of eight genes that were suppressed by endogenous miR-126 (Fig. 2f, Supplementary Fig. 10 and Supplementary Table 1). Interestingly, patients whose primary breast cancers displayed overexpression of these genes were significantly

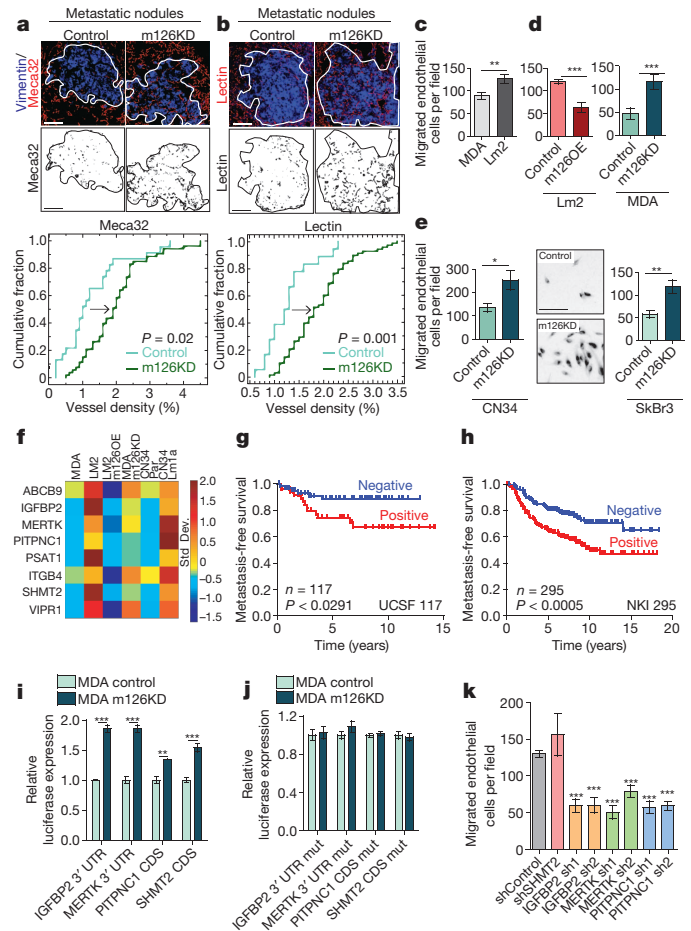


**Figure 2 | Endogenous miR-126 non-cell-autonomously suppresses endothelial recruitment by breast cancer cells.** **a**, Lung sections from Fig. 1a were double-stained for vimentin and MECA-32 or **b**, vimentin and intravenously injected lectin. The border of each nodule was demarcated based on vimentin staining and lectin/MECA-32 staining within a circumscribed region is shown (lower panels). The distribution of percentage vessel density (area positive for lectin/MECA-32 staining per area) is shown in a cumulative fraction plot;  $n = 8$  (18 and 68 nodules in control and miR-126 knockdown groups, respectively).  $P$  value is based on the Kolmogorov–Smirnov test. **c**, Trans-well recruitment of  $5 \times 10^4$  HUVEC cells by  $2.5 \times 10^4$  MDA and LM2 cells was assessed by counting the number of HUVEC cells that migrated to the basal side of the trans-well inserts;  $n = 4$ . **d**, LM2/miR-126OE or LM2/control and MDA/miR-126KD or MDA/control cells were subjected to the HUVEC recruitment assay;  $n = 4$ . **e**, CN34/miR-126KD or CN34/control and SkBr3 breast cancer cells transfected with control or miR-126-targeting LNAs were subjected to the HUVEC recruitment assay;  $n = 5$ . Representative images are shown. Scale bar, 100  $\mu$ m. **f**, The miR-126 metastasis signature comprises eight genes overexpressed in metastatic cells, downregulated by miR-126OE and upregulated by miR-126KD. The heat map represents variance-normalized expression levels based on microarray and quantitative PCR (qPCR) analyses. The colour map corresponds to standard deviation change from the mean. **g**, **h**, Kaplan–Meier curves for the UCSF breast cancer cohort ( $n = 117$ ) and NKI cohort ( $n = 295$ ) depicting metastasis-free-survival of patients as a function of their primary tumours’ miR-126 signature status. An aggregate expression score (sum of the expression values of the eight genes) greater or lower than the mean of the entire population is classified as miR-126 positive or negative, respectively.  $P$  values are based on a Mantel–Cox log-rank test. **i**, Luciferase reporter assays of miR-126 target genes in MDA/miR-126KD or MDA/control cells;  $n = 4$ . UTR, untranslated region; CDS, coding sequence. **j**, The miR-126 complementary regions were mutated and the luciferase reporter assays repeated;  $n = 4$ . **k**, LM2 cells expressing hairpins targeting IGFBP2, MERTK, PTPN1, SHMT2 or a control hairpin were subjected to the HUVEC recruitment assay;  $n = 4$ . Error bars, s.e.m.;  $P$  values were obtained using one-sided Student’s  $t$ -tests (**c–e**, **i–k**).

more likely to develop distal metastases and experienced shorter metastasis-free survival in multiple cohorts than those whose cancers did not (Fig. 2g, h). The prognostic power of this signature was subtype independent and performed robustly in the combined MSK/NKI/UCSF (Memorial Sloan-Kettering Cancer Center/Nederlands Kanker Instituut/University of California, San Francisco) cohorts ( $n = 494$ ;  $P < 0.0004$ ; Supplementary Fig. 11). Thus, miR-126 suppresses the expression of a set of eight genes that are positively and strongly correlated with human metastatic relapse.

Luciferase reporter assays and subsequent mutagenesis of the 3' untranslated regions and coding sequences of this entire set revealed endogenous miR-126 to interact with *IGFBP2* and receptor kinase *MERTK* 3' untranslated regions, and the coding regions of the phosphatidylinositol transfer protein *PITPNC1* and the hydroxymethyltransferase *SHMT2* (Fig. 2i, j and Supplementary Fig. 12). We next asked if any of the miR-126 target genes regulate the recruitment of endothelial cells by cancer cells. Of these four genes, knockdown of *IGFBP2*, *MERTK* or *PITPNC1* significantly suppressed the ability of metastatic LM2 and CN34-LM1A cells to recruit endothelial cells (Fig. 2k and Supplementary Fig. 13h), whereas their overexpression in MDA-231 and CN34-Par cells enhanced endothelial recruitment (Supplementary Fig. 13l). Importantly, knockdown of these genes did not significantly decrease cancer cell proliferation (Supplementary Fig. 14). Given the requirement of each of these genes for endothelial recruitment, we wondered if each of these genes individually correlates with human metastatic relapse. Interestingly, expression levels of *IGFBP2*, *MERTK* and *PITPNC1* were individually and significantly increased in patients with stage III and IV primary tumours relative to those with stage I and II tumours in an additional cohort of 96 patients (Fig. 3a and Supplementary Table 2). We next assessed the requirement of these genes for metastasis and *in vivo* endothelial recruitment. Knockdown of *IGFBP2* using independent short hairpins significantly suppressed metastatic colonization to the lung (sh<sub>1</sub>, tenfold; sh<sub>2</sub>, 6.25-fold; Fig. 3b), whereas knockdown of *PITPNC1* and *MERTK* also strongly inhibited metastatic colonization (*PITPNC1*sh<sub>1</sub>, 7.69-fold; *PITPNC1*sh<sub>2</sub>, 4.55-fold, Fig. 3c; *MERTK*sh<sub>1</sub>, 3.91-fold; *MERTK*sh<sub>2</sub>, 3.08-fold, Fig. 3d). Additionally, shRNA inhibition of *IGFBP2*, *PITPNC1* or *MERTK* using independent hairpins significantly reduced metastatic endothelial density (Fig. 3e) and functional vessel content (Supplementary Fig. 15). Epistasis experiments revealed that knockdown of *IGFBP2*, *MERTK* or *PITPNC1* in miR-126 knockdown cells significantly suppressed endothelial recruitment (Fig. 3f) and metastatic colonization (Fig. 3h and Supplementary Fig. 16) normally seen with miR-126 knockdown. Conversely, *IGFBP2*, *MERTK* or *PITPNC1* overexpression in miR-126-overexpressing cells rescued the ability of cancer cells to recruit endothelia (Fig. 3g). These findings reveal that the miR-126 direct target genes *IGFBP2*, *PITPNC1* and *MERTK* are individually required for endothelial recruitment and metastatic colonization, are downstream of miR-126 and individually correlate in expression with human metastatic progression.

We next sought to determine the mechanisms by which these miR-126 target genes mediate endothelial recruitment and metastasis. Of the miR-126 targets, *IGFBP2* is secreted and thus poised to mediate extracellular effects. Consistent with this, enzyme-linked immunosorbent assay (ELISA) analysis revealed metastatic LM2 cells to secrete 2.1-fold higher levels of this factor than less metastatic parental MDA-231 cells, whereas miR-126 knockdown enhanced *IGFBP2* levels (2.75-fold; Fig. 4a) and had no effect on vascular endothelial growth factor (VEGF) levels (Supplementary Fig. 17). Antibody-mediated inhibition of *IGFBP2* in a trans-well recruitment assay significantly inhibited metastatic-cell endothelial recruitment and prevented miR-126-dependent recruitment in MDA and CN34 Par cells (Fig. 4b and Supplementary Fig. 18a, b). Finally, recombinant *IGFBP2* protein rescued the endothelial recruitment defect of miR-126-overexpressing cells (Fig. 4c). *IGFBP2* is a member of a large family known to bind IGF1 and/or IGF2 in the extracellular space to modulate their signalling

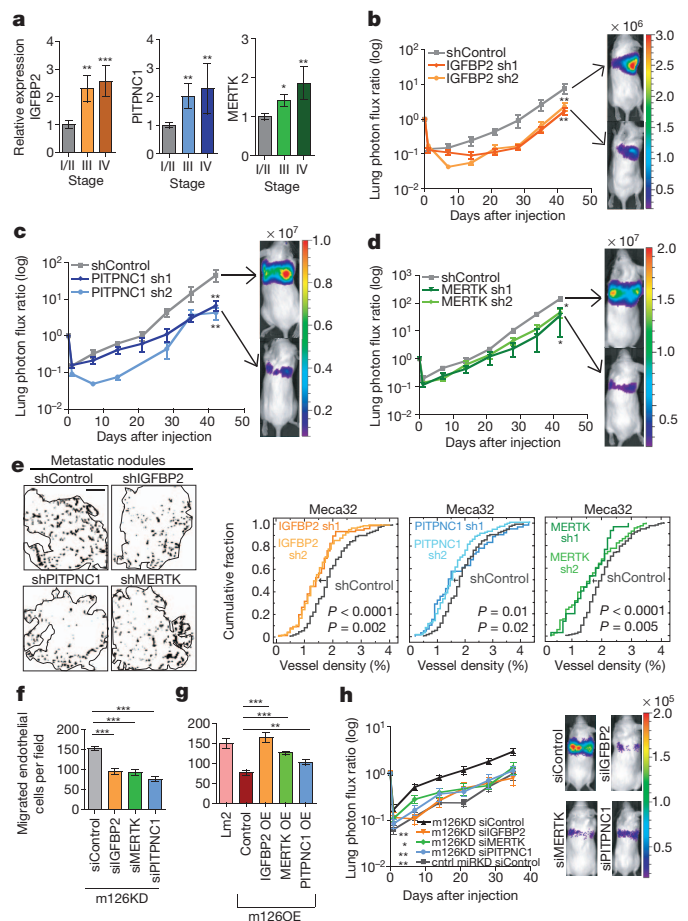


**Figure 3 | *IGFBP2*, *PITPNC1* and *MERTK* promote metastatic colonization and angiogenesis.** **a**, Expression levels of *IGFBP2*, *MERTK* or *PITPNC1* in samples from patients with stage I/II ( $n = 53$ ) compared with stage III ( $n = 29$ ) or stage IV ( $n = 9$ ) breast tumours. **b–d**, Bioluminescence quantification of lung metastasis by LM2 cells expressing the control hairpin or hairpins targeting *IGFBP2* (**b**), *PITPNC1* (**c**) or *MERTK* (**d**);  $n = 5$ . **e**, Lung sections were double stained for vimentin and MECA-32. The metastatic MECA-32 signal is shown in black. Distributions of percentage vessel densities are shown in cumulative fraction plots;  $n = 4$ .  $P$  values are based on the Kolmogorov–Smirnov test. **f**, MDA/miR126 knockdown cells were transfected with short interfering RNAs (siRNAs) targeting *IGFBP2*, *MERTK* and *PITPNC1* or control siRNA and subjected to HUVEC recruitment assays;  $n = 9$ . **g**, Coding regions of *IGFBP2*, *MERTK* and *PITPNC1* were overexpressed in LM2/miR-126-overexpressing cells that were subjected to HUVEC recruitment assays;  $n = 6$ . **h**, Bioluminescence imaging of lung metastasis by MDA/miR-126 knockdown cells transfected with siRNAs targeting *IGFBP2*, *MERTK* and *PITPNC1* or control siRNA;  $n = 5$ . Error bars, s.e.m.,  $P$  values were obtained using a one-sided Student's  $t$ -test (**a–d**, **f**, **h**).

activity<sup>10</sup>. To determine which IGF mediates miR-126-dependent endothelial recruitment, we treated cells with specific blocking antibodies and found that antibody-mediated inhibition of IGF1, which is present in endothelial media, but not IGF2, significantly reduced endothelial recruitment resulting from miR-126 knockdown (Fig. 4d). Next, inhibition of IGF type-1 receptor (IGF1R) with a blocking antibody, but not IGF2R, on endothelial cells significantly reduced endothelial recruitment resulting from miR-126 knockdown (Fig. 4e and Supplementary Fig. 18c, d). Finally, both recombinant *IGFBP2* and conditioned media from miR-126 knockdown cells activated IGF1R on endothelial cells as assessed by western blot (Fig. 4f and Supplementary Fig. 19a), whereas recombinant *IGFBP2* protein was sufficient, in a dose-dependent manner, to promote endothelial chemotaxis (Fig. 4g) and migration (Supplementary Fig. 19b) in an IGF1R-dependent manner. These findings suggest that the miR-126/*IGFBP2*/IGF1 pathway



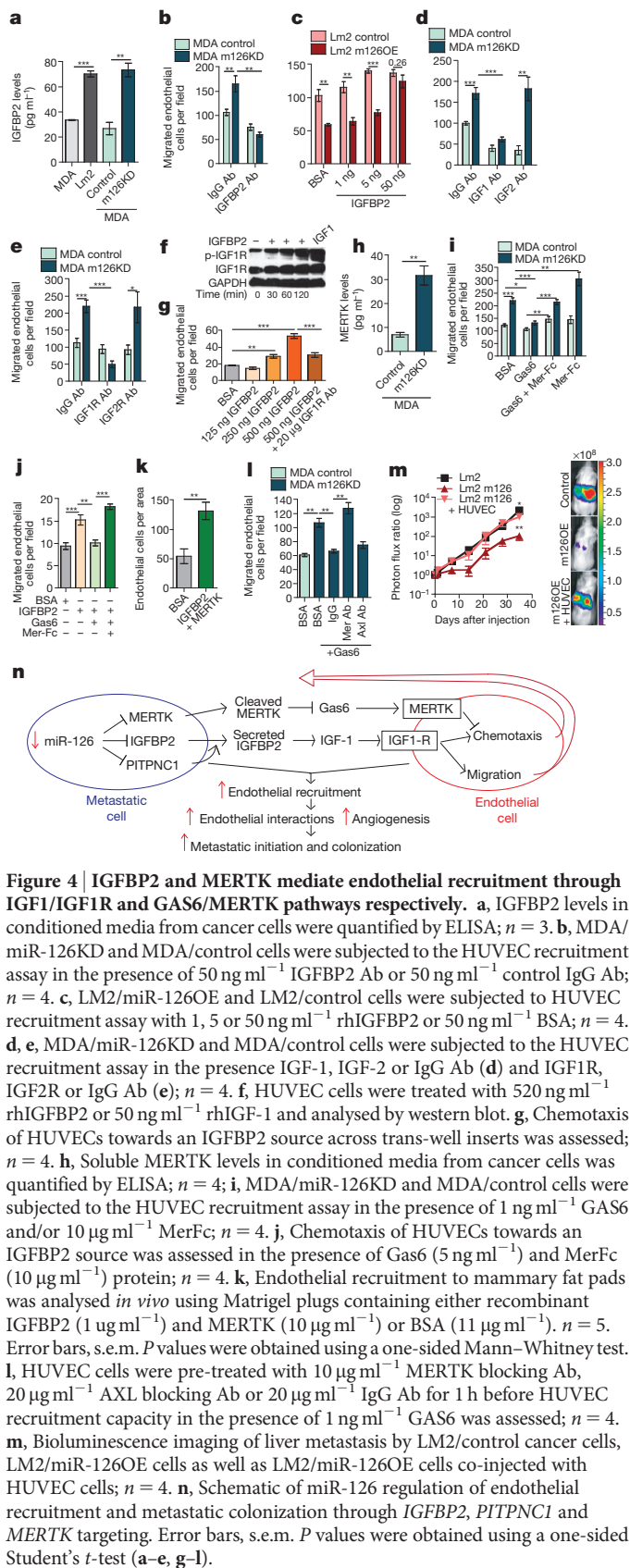


**Figure 4 | IGFBP2 and MERTK mediate endothelial recruitment through IGF1/IGF1R and GAS6/MERTK pathways respectively.** **a**, IGFBP2 levels in conditioned media from cancer cells were quantified by ELISA;  $n = 3$ . **b**, MDA/miR-126KD and MDA/control cells were subjected to the HUVEC recruitment assay in the presence of 50 ng ml<sup>-1</sup> IGFBP2 Ab or 50 ng ml<sup>-1</sup> control IgG Ab;  $n = 4$ . **c**, LM2/miR-126OE and LM2/control cells were subjected to HUVEC recruitment assay with 1, 5 or 50 ng ml<sup>-1</sup> rhIGFBP2 or 50 ng ml<sup>-1</sup> BSA;  $n = 4$ . **d**, **e**, MDA/miR-126KD and MDA/control cells were subjected to the HUVEC recruitment assay in the presence of IGF-1, IGF-2 or IgG Ab (**d**) and IGF1R, IGF2R or IgG Ab (**e**);  $n = 4$ . **f**, HUVEC cells were treated with 520 ng ml<sup>-1</sup> rhIGFBP2 or 50 ng ml<sup>-1</sup> rhIGF-1 and analysed by western blot. **g**, Chemotaxis of HUVECs towards an IGFBP2 source across trans-well inserts was assessed;  $n = 4$ . **h**, Soluble MERTK levels in conditioned media from cancer cells was quantified by ELISA;  $n = 4$ . **i**, MDA/miR-126KD and MDA/control cells were subjected to the HUVEC recruitment assay in the presence of 1 ng ml<sup>-1</sup> GAS6 and/or 10 µg ml<sup>-1</sup> MerFc;  $n = 4$ . **j**, Chemotaxis of HUVECs towards an IGFBP2 source was assessed in the presence of GAS6 (5 ng ml<sup>-1</sup>) and MerFc (10 µg ml<sup>-1</sup>) protein;  $n = 4$ . **k**, Endothelial recruitment to mammary fat pads was analysed *in vivo* using Matrigel plugs containing either recombinant IGFBP2 (1 µg ml<sup>-1</sup>) and MERTK (10 µg ml<sup>-1</sup>) or BSA (11 µg ml<sup>-1</sup>).  $n = 5$ . Error bars, s.e.m.  $P$  values were obtained using a one-sided Mann–Whitney test. **l**, HUVEC cells were pre-treated with 10 µg ml<sup>-1</sup> MERTK blocking Ab, 20 µg ml<sup>-1</sup> AXL blocking Ab or 20 µg ml<sup>-1</sup> IgG Ab for 1 h before HUVEC recruitment capacity in the presence of 1 ng ml<sup>-1</sup> GAS6 was assessed;  $n = 4$ . **m**, Bioluminescence imaging of liver metastasis by LM2/control cancer cells, LM2/miR-126OE cells as well as LM2/miR-126OE cells co-injected with HUVEC cells;  $n = 4$ . **n**, Schematic of miR-126 regulation of endothelial recruitment and metastatic colonization through IGFBP2, PITPNC1 and MERTK targeting. Error bars, s.e.m.  $P$  values were obtained using a one-sided Student's  $t$ -test (**a–e**, **g–l**).

activates IGF1R on endothelial cells, resulting in enhanced endothelial migration towards metastatic cells.

Given our identification of IGFBP2 as a secreted miR-126-dependent factor that mediates endothelial recruitment and metastasis, we asked whether PITPNC1 or MERTK regulate the secretion of this factor from

cancer cells. Indeed, knockdown of the miR-126 target gene *PITPNC1*, whose protein expression is regulated by miR-126, reduced IGFBP2 secretion from breast cancer cells (Supplementary Fig. 20a, b). Overexpression of *PITPNC1* promoted endothelial recruitment, which was inhibited by IGFBP2 antibody neutralization (Supplementary Fig. 20c), placing PITPNC1 upstream of IGFBP2. Knockdown of *MERTK*, however, did not decrease IGFBP2 secretion, suggesting an IGFBP2-independent mechanism of action for MERTK. The addition of recombinant GAS6, a MERTK ligand, at physiological levels<sup>11</sup> potentially reduced miR-126-dependent recruitment (Fig. 4i), suggesting an inhibitory role for GAS6 in endothelial recruitment. MERTK receptor exists in both membrane-bound and soluble forms, where the extracellular domain has been cleaved<sup>12</sup>. Indeed, we detected soluble MERTK in conditioned media of MDA-231 cells (Supplementary Fig. 21a), whereas soluble MERTK levels significantly increased upon miR-126 knockdown (4.59-fold, Fig. 4h). We hypothesized that soluble cleaved MERTK may promote endothelial recruitment through binding and inhibition of GAS6. Consistent with this, recombinant MERTK extracellular domain (MerFc) suppressed serum as well as recombinant GAS6-mediated inhibition of endothelial recruitment (Fig. 4i). Importantly, this effect was miR-126 dependent. These findings suggest that secreted MERTK from metastatic cells acts as a decoy receptor for GAS6, thereby reducing the suppressive effects of GAS6 on endothelial cell recruitment.

We next assessed sufficiency of recombinant forms of IGFBP2, MERTK and GAS6 in trans-well chemotactic assays. Recombinant GAS6 at low, physiological doses inhibited endothelial chemotaxis towards recombinant IGFBP2, whereas recombinant soluble MERTK ectodomain abrogated the GAS6-suppressive effect on endothelial chemotaxis (Fig. 4j). Additionally, injection of recombinant IGFBP2 and MERTK ectodomain into the mammary fat pad was sufficient to enhance endothelial recruitment into mammary fat pad Matrigel plugs (Fig. 4k and Supplementary Fig. 22). These findings reveal that IGFBP2 mediates a positive migratory and chemotactic signal to endothelial cells through the IGF type-1 receptor, whereas soluble MERTK receptor antagonizes an inhibitory chemotactic signal mediated by GAS6.

We then sought to identify the endothelial receptor that mediates the GAS6-suppressive effect on endothelial recruitment. To this end, we inhibited endothelial MERTK and AXL, two GAS6 receptors that are highly expressed by endothelial cells, with neutralizing antibodies as well as RNAi. We found that MERTK inhibition on endothelial cells occluded GAS6-induced suppression of endothelial recruitment. These findings indicate endothelial MERTK receptor as the mediator of the GAS6 phenotype (Fig. 4l and Supplementary Fig. 21b).

Finally, we reasoned that if the suppressive effect of miR-126 on metastasis is indeed secondary to compromised endothelial recruitment and is non-cell autonomous, it should be rescued upon the addition of endothelial cells. To this end, we injected metastatic LM2 cells as well as LM2 cells overexpressing miR-126 into the portal circulation. miR-126 overexpression strongly suppressed hepatic metastatic colonization. Interestingly, co-injection of endothelial cells along with miR-126-overexpressing cells in colonization assays completely rescued their metastatic colonization defect (Fig. 4m and Supplementary Fig. 23). These dramatic findings reveal endothelial recruitment capacity to be the key metastatic phenotype regulated by miR-126 and reveal a major role for cancer–endothelial interactions in metastatic initiation leading to colonization. Metastatic cells displaying silencing of this miRNA and the resulting induction of its targets IGFBP2, MERTK and PITPNC1 are able to establish more readily the endothelial and blood vessel interactions required for metastatic initiation and colonization (Supplementary Discussion). Our findings establish a key required role for cancer–endothelial interactions and cooperation in metastatic initiation leading to colonization. We propose that endothelial cells provide incipient metastases a key signal that promotes metastatic initiation efficiency. This novel non-canonical role for endothelial cells in metastatic initiation results



in enhanced metastatic colonization. Our systematic analysis and focus on metastasis and metastatic angiogenesis has led to the identification of several molecules, including secreted IGFBP2, the transfer protein PTPN1 and the kinase MERTK, as well as their respective pathways IGFBP2/IGF1/IGF1R and cleaved MERTK/GAS6/MERTK as necessary and sufficient for mediating metastatic cell endothelial recruitment (Fig. 4n). The combined modulation of these endothelial-convergent signalling pathways by cancer cells empowers these cells with enhanced endothelial recruitment capacity and metastatic efficiency. It also reveals novel cooperative molecular targets for therapeutic inhibition with the potential for preventing metastatic breast cancer in the adjuvant setting.

## METHODS SUMMARY

See Methods for additional information on cell culture, endothelial assays, luciferase assays, microarray analyses, ELISA, western blotting, histology, survival analyses, statistical methods and animal studies, as well as generation of lentivirus, retrovirus, knockdown and overexpressing cells.

**Full Methods** and any associated references are available in the online version of the paper at [www.nature.com/nature](http://www.nature.com/nature).

**Received 23 January; accepted 21 October 2011.**

**Published online 14 December 2011.**

1. Chiang, A. C. & Massague, J. Molecular basis of metastasis. *N. Engl. J. Med.* **359**, 2814–2823 (2008).
2. Talmadge, J. E. & Fidler, I. J. AACR centennial series: the biology of cancer metastasis: historical perspective. *Cancer Res.* **70**, 5649–5669 (2010).
3. Hanahan, D. & Weinberg, R. A. Hallmarks of cancer: the next generation. *Cell* **144**, 646–674 (2011).
4. Valastyan, S. & Weinberg, R. A. MicroRNAs: crucial multi-tasking components in the complex circuitry of tumor metastasis. *Cell Cycle* **8**, 3506–3512 (2009).
5. Tavazoie, S. F. *et al.* Endogenous human microRNAs that suppress breast cancer metastasis. *Nature* **451**, 147–152 (2008).

6. Png, K. J. *et al.* MicroRNA-335 inhibits tumor reinitiation and is silenced through genetic and epigenetic mechanisms in human breast cancer. *Genes Dev.* **25**, 226–231 (2011).
7. Guo, C. *et al.* The noncoding RNA, miR-126, suppresses the growth of neoplastic cells by targeting phosphatidylinositol 3-kinase signaling and is frequently lost in colon cancers. *Genes Chromosom. Cancer* **47**, 939–946 (2008).
8. Feng, R. *et al.* miR-126 functions as a tumour suppressor in human gastric cancer. *Cancer Lett.* **298**, 50–63 (2010).
9. Gupta, G. P. *et al.* Mediators of vascular remodelling co-opted for sequential steps in lung metastasis. *Nature* **446**, 765–770 (2007).
10. Jones, J. I. & Clemmons, D. R. Insulin-like growth factors and their binding proteins: biological actions. *Endocr. Rev.* **16**, 3–34 (1995).
11. Balogh, I. *et al.* Analysis of Gas6 in human platelets and plasma. *Arterioscler. Thromb. Vasc. Biol.* **25**, 1280–1286 (2005).
12. Sather, S. *et al.* A soluble form of the Mer receptor tyrosine kinase inhibits macrophage clearance of apoptotic cells and platelet aggregation. *Blood* **109**, 1026–1033 (2007).

**Supplementary Information** is linked to the online version of the paper at [www.nature.com/nature](http://www.nature.com/nature).

**Acknowledgements** We thank the members of the Tavazoie laboratory, Saeed Tavazoie, M. Tavazoie, S. Kurdistan, C. Alarcon and E. Mandel for comments on previous versions of this manuscript. We thank V. Gueorguiev and the Memorial Sloan-Kettering Cancer Center's Molecular Cytology Core Facility for help. We thank the Memorial Sloan-Kettering Cancer Center's High-Throughput Screening Core Facility for providing the shRNAs. We thank H. Lee for cloning assistance. K.J.P. is an A\*STAR National Science Scholar. S.F.T. is a Department of Defense Era of Hope Scholar and the Leon Hess Head of the Elizabeth and Vincent Mayer Laboratory at Rockefeller University.

**Author Contributions** S.F.T. conceived the project and supervised all research. K.J.P., N.H. and S.F.T. wrote the manuscript. K.J.P., N.H. and S.F.T. designed the experiments. K.J.P., N.H. and M.Y. performed the experiments.

**Author Information** The data from miR-126-overexpressing and MDA/LM2 microarrays are deposited in Gene Expression Omnibus under accession numbers GSE 23905 and 23904 respectively. Reprints and permissions information is available at [www.nature.com/reprints](http://www.nature.com/reprints). The authors declare no competing financial interests. Readers are welcome to comment on the online version of this article at [www.nature.com/nature](http://www.nature.com/nature). Correspondence and requests for materials should be addressed to S.F.T. ([stavazoie@mail.rockefeller.edu](mailto:stavazoie@mail.rockefeller.edu)).

## METHODS

**Cell culture.** All cancer cell lines were propagated as previously described<sup>5</sup>. HUVEC and HMVEC cells were cultured in EGM-2 and EGM-2 MV media (Lonza) respectively.

**Animal studies.** All animal work was conducted in accordance with protocols approved by the Institutional Animal Care and Use Committee at The Rockefeller University. Six- to eight-week-old age-matched female NOD/SCID mice were used for mammary tumour<sup>13</sup>, lung metastasis<sup>5</sup> and liver metastasis (by intrasplenic injections) assays. Six-week-old age-matched female NOD/SCID gamma mice were used for CN34 lung metastasis assay. Eight-week-old age-matched female athymic mice were used for systemic metastasis assays<sup>14,15</sup>. For cancer cell/HUVEC co-injection liver metastasis colonization assay, 500,000 HUVECs and 500,000 LM2/miR-126 overexpressing cells were mixed in a 1:1 ratio in PBS before injection.

The inducible miR-126 expression construct was generated by cloning pre-miR-126 into the tet-ON containing pTripz vector (Thermo Scientific). At day 3, 2 mg ml<sup>-1</sup> doxycycline (Sigma Aldrich) was added to the drinking water containing 5% sucrose. Control mice were given 5% sucrose water.

**Generation of lentivirus, retrovirus, knockdown and overexpressing cells.** Generation of lentivirus-mediated knockdown and retroviral-overexpressing cells were performed as described previously<sup>5,13</sup>. Primers used to clone overexpression constructs are listed in Supplementary Table 4. shRNA sequences are listed in Supplementary Table 5.

**siRNA-mediated messenger RNA (mRNA) knockdown.** siRNAs (Supplementary Table 6) were transfected into cells using Lipofectamine reagent according to the manufacturer's protocol. Forty-eight hours after transfection, the cells were collected and subjected to either the tail-vein metastasis assay or endothelial recruitment assay. Control siRNAs were obtained from Applied Biosystems and Invitrogen. siRNA targeting IGF1R was purchased from Sigma (siRNA identity: SASI\_Hs01\_00126196 and SASI\_Hs01\_00126194).

**LNA-mediated miRNA knockdown.** miR-126 or control LNA (Exiqon) was transfected into cells using Lipofectamine for 16 h. Cells were used for HUVEC recruitment assays 96 h after transfection.

**Endothelial recruitment.** Twenty-five thousand cancer cells were seeded into 24-well plates approximately 24 h before the start of the recruitment assay. HUVEC cells were serum starved in EGM-2 media supplemented with 0.2% FBS for 24 h. The HUVEC cells were then labelled with CellTracker Red CMTPX dye (Invitrogen) for 45 min and rescued in EGM-2 media supplemented with 2% FBS for 30 min. Meanwhile, cancer cells were washed with PBS and 1 ml 0.2% FBS EGM-2 medium was added to each well. Each well was then fitted with a 3.0 µm HTS Fluoroblock Insert (BD Falcon). For antibody experiments, the appropriate concentration of each antibody was then added to each well: 50 ng ml<sup>-1</sup> anti-IGFBP2 (R&D Systems), 20 µg ml<sup>-1</sup> anti-IGF-1 (R&D Systems), 40 µg ml<sup>-1</sup> anti-IGF-2 (R&D Systems), 20 µg ml<sup>-1</sup> anti-IGF1R (R&D Systems), 5 µg ml<sup>-1</sup> anti-IGF2R (R&D Systems), 10 µg ml<sup>-1</sup> anti-MERTK (R&D Systems), 20 µg ml<sup>-1</sup> anti-Axl (R&D Systems) and anti-IgG (R&D Systems).

For endothelial recruitment assays that required pre-incubation with antibodies, either HUVEC cells or cancer cells were incubated with anti-IGF1R, anti-MERTK, anti-Axl or control IgG antibody for 1 h and washed once with PBS. The HUVEC cells were then serum starved for 1 h before re-suspending 100,000 HUVECs per millilitre of 0.2% FBS EGM-2. Half a millilitre of the re-suspension was then added into each Fluoroblock insert and the recruitment assay was allowed to proceed for 16 h. After completion of the assay, Fluoroblock inserts were fixed with 4% paraformaldehyde for 15 min and mounted onto slides with VectaShield mounting media (Vector Laboratories). Three images of each insert were taken and the images were analysed using ImageJ (NIH).

**Scratch assay.** HUVEC cells were grown to 100% confluency in 60 mm dishes. Twenty-four hours before the start of the scratch assay, HUVEC cells were serum starved in EGM-2 media supplemented with 0.2% FBS whereas cancer cells were seeded on plastic coverslips (Nalgene NUNC International). The HUVEC cells were then labelled with CellTracker Red CMTPX dye (Invitrogen) for 45 min and rescued in EGM-2 media supplemented with 2% FBS for 30 min. Coverslips with cancer cells were washed with PBS and then transferred onto 60 mm dishes containing a HUVEC monolayer. A scratch across the HUVEC monolayer was then made using a 200 µl pipet tip. Three images of each dish were taken after 36 h and analysed using ImageJ (NIH) to quantify the area covered by HUVEC cells.

**Chemotaxis assay.** Matrigel (250 µl) (BD Biosciences) containing bovine serum albumin (Sigma Aldrich), rhIGFBP2 (R&D Systems), rhGas6 (R&D Systems), anti-IGF1R (R&D Systems) and MerFc (R&D Systems) was allowed to solidify in a 24-well plate 30 min before 250 µl HUVEC media containing 0.2% FBS was added to it. A 3.0 µm HTS Fluoroblock Insert (BD Falcon) was then placed in each well. HUVEC cells were labelled with CellTracker Red CMTPX dye (Invitrogen). One hundred and fifty thousand labelled HUVECs in 0.2% FBS EGM-2 were added to each Fluoroblock insert and the assay was allowed to proceed for 20 h. The inserts

were then fixed for 15 min in 4% paraformaldehyde and mounted onto slides. Five fields of the basal side of each insert were imaged and analysed using ImageJ.

**HUVEC migration assay.** HUVEC cells were grown to 90% confluence and treated with stated concentrations of bovine serum albumin (Sigma Aldrich), rhIGFBP2 (R&D Systems) and anti-IGF1R (R&D Systems) in HUVEC media containing 0.2% FBS for 40 min at 37 °C. Fifty thousand cells were then added onto HTS Fluoroblock Inserts (BD Falcon). After 24 h, the membrane was fixed in 4% paraformaldehyde and excised. Migrated HUVEC cells were visualized with DAPI and counted in five fields per membrane using ImageJ.

**Endothelial adhesion.** HUVEC cells were seeded on a 6 cm plate and allowed to grow to confluence. Fifty thousand cancer cells were labelled with CellTracker Green CMFDA dye (Invitrogen) and added to each plate of HUVECs and left at 37 °C for 10 min. The plates were washed with PBS and fixed with 4% paraformaldehyde for 15 min. Six images were taken and the number of cancer cells adherent to the HUVEC cells were then quantified using ImageJ (NIH).

**Endothelial proliferation.** 25,000 HUVEC cells were seeded in triplicate in a six-well plate. The HUVEC cells were then washed with PBS and 3 ml conditioned EGM-2 media from  $1 \times 10^6$  cancer cells was added to each well. After 48 h, the conditioned media were replaced with another 3 ml of conditioned media. After another 48 h, the cells were trypsinized and counted using a haemocytometer.

**Tube formation assay.** Tube formation assay was performed according to the manufacturer's protocol (BD BioCoat Angiogenesis System – Endothelial Cell Tube Formation). Briefly, HUVEC cells were serum starved in EGM-2 media supplemented with 0.2% FBS for 24 h. The HUVEC cells were then labelled with CellTracker Red CMTPX dye (Invitrogen) for 45 min and subsequently treated in EGM-2 media supplemented with 2% FBS for 30 min. Meanwhile, the tube formation assay plate was incubated at 37 °C for 30 min. The cancer cells and HUVEC cells were trypsinized and re-suspended at 400,000 ml<sup>-1</sup> and 800,000 ml<sup>-1</sup> respectively in EGM-2 media supplemented with 2% FBS. The cancer and HUVEC cell suspensions were then mixed at a 1:1 ratio and 50 µl of each mixture was seeded into each well of the tube formation assay plate. The assay plate was incubated at 37 °C for 16 h. Images of each well were taken and processed using MetaMorph analysis software (Molecular Devices) to obtain the number of branch points per image.

**Analysis of miRNA and mRNA expression.** miRNA and mRNA expression quantification was performed as described previously<sup>6</sup>. Primers can be found in Supplementary Table 7. Expression analysis of human breast cancers at various disease stages was performed using the TissueScan qPCR Array Breast Cancer Panels 2 and 3 (Origene).

**miR-126 target prediction.** Potential miR-126 targets were identified by using three sets of microarray profiles: LM2 relative to LM2 cells overexpressing miR-126 (GSE No. 23905, Illumina HT12) and two replicate arrays of MDA and LM2 cells (GSE number 23904, Illumina HT12 and Minn *et al.*<sup>13</sup>, Affymetrix HG-U133A). The following criteria were used to identify possible miR-126 targets genes: (1) genes downregulated more than 1.6-fold upon miR-126 overexpression in LM2 cells and (2) genes upregulated by more than 1.4-fold in one of the two LM2 versus MDA arrays. All potential targets were subsequently verified by qPCR.

**Luciferase reporter assay.** The luciferase reporter assay was performed as described previously<sup>5</sup>. The full-length 3' untranslated regions and coding sequences of *ABCB9*, *IGFBP2*, *ITGB4*, *MERTK*, *PITPNC1*, *PSAT1*, *SHMT2* and *VIPR1* were cloned into the psiCheck2 dual luciferase reporter vector (Promega). Cloning primer sequences are shown in Supplementary Table 8. Potential miR-126 sites in genes were identified by alignment to the complementary miR-126 sequence 5'-TTACTCACGGTACGA-3', and mutagenesis was performed using the QuickChange Multi Site-Directed Mutagenesis Kit (Agilent Technologies). Mutagenesis primers are shown in Supplementary Table 9.

**Cancer cell proliferation.** Twenty-five thousand cells were seeded in triplicate in six-well plates and viable cells were counted at 5 days after seeding.

**Histology.** Lungs were prepared by perfusion fixation with 4% paraformaldehyde infused through the vascular system and the trachea. Five minutes before fixation, 100 mg biotinylated lectin in PBS (Vector Laboratories) was injected through the tail vein. Five-micrometre-thick paraffin sections were stained with primary antibodies against MECA-32 (Developmental Studies Hybridoma Bank), Vimentin (Vector Laboratories) and with fluorescein isothiocyanate (FITC)-labelled Avidin (Vector Laboratories). Primary antibodies were detected using Alexa Fluor dye-conjugated secondary antibodies. Fluorescence was obtained using a Zeiss laser scanning confocal microscope (LSM 510). To determine the vascularization of metastatic nodules, MECA-32 and lectin signals were quantified using ImageJ, whereas co-staining for vimentin identified the metastatic nodules. The collective area covered by vessels was determined by subtracting background (rolling ball radius of one pixel) and by using a predetermined threshold as cut-off using ImageJ. Vessel density is given as the percentage of area covered by the blood vessels compared with the total area of the metastatic nodule. A

Kolmogorov–Smirnov test was used to determine significance (<http://www.physics.csbsju.edu/stats/KS-test.html>). Metastatic nodules were defined as areas greater than 2000  $\mu\text{m}^2$  that were positive for vimentin.

Mammary fat pad tumours were excised and submerged in 4% paraformaldehyde for 24 h. Fixed tissue was embedded in paraffin and sectioned in 5  $\mu\text{m}$  slices. Immunodetection was performed using antibodies against MECA-32 (Developmental Studies Hybridoma Bank), Mac-2 (Cederlane) and CD45 (BD Biosciences).

For co-staining of MECA-32 and CD31, mammary fat pad tumours were excised and fresh frozen in OCT. Ten-micrometre slices were fixed in acetone. Immunodetection, where performed, was with antibodies for MECA-32 (Developmental Studies Hybridoma Bank) and FITC-CD31 (BD Bioscience).

Dextran permeability was determined as described in Arnold *et al.*<sup>16</sup> with slight modifications. Briefly, an intravenous bolus injection of 10 mg ml<sup>-1</sup> rhodamine B labelled with low molecular mass dextran (Invitrogen) was infused. Fifteen minutes later, the mice were anaesthetized and the lungs were perfused with OCT through the trachea, removed and frozen on dry ice. Ten-micrometre sections were cut and the dextran permeability inside metastatic nodules, as determined by vimentin staining, was measured by fluorescence microscopy. Using ImageJ, a preset threshold was used to determine the levels of dextran permeability. The results are presented as the mean percentage of the thresholded area inside the metastatic nodule.

Tracking of HUVEC cells in the liver metastasis assay was performed by labelling 500,000 HUVECs with CellTracker Red CMTPX dye (Invitrogen) and co-injecting them with 500,000 LM2/miR-126 overexpressing cells into the portal circulation. Four days later, the livers were removed, frozen in OCT and cut into 10  $\mu\text{m}$  sections. Cancer cells were stained using antibodies against human vimentin (Vector Laboratories); the mouse endothelial cells were stained using antibodies against mouse CD31 (Biolegend).

**ELISA.** IGF1, IGF2, MERTK and VEGF levels in conditioned media were quantified using the IGF1 ELISA kit (RayBiotech), Total Mer DuoSet (R&D Systems) and the VEGF ELISA kit (R&D Systems).

**In vivo endothelial recruitment (Matrigel plug) assay.** Recombinant IGF1 (1  $\mu\text{g ml}^{-1}$ ) and MerFc (10  $\mu\text{g ml}^{-1}$ ) or BSA (11  $\mu\text{g ml}^{-1}$ ) were mixed with Matrigel (BD Bioscience). One hundred microlitres was injected into the mammary fat pads of NOD-SCID mice and allowed to solidify. Forty-eight hours later, the plugs were removed, fixed in 4% paraformaldehyde overnight and embedded in paraffin. Five-micrometre-thick sections were stained with an antibody targeting MECA32. Mammary fat pads containing large comparable-sized Matrigel plugs that were typically centralized in the fat pad were analysed. Most of the control and experimental plugs were obtained from the same mouse, controlling for inter-animal variability. Six representative images of each plug were obtained at  $\times 20$  magnification and the number of endothelial cells per field was counted.

**Flow cytometry.** Primary mammary fat pad tumours were excised and dissociated into single cells as previously described<sup>13</sup>. To analyse the endothelial cell population of the tumour, FITC-CD45 (eBioscience), PE/Cy7-CD31 (Biolegend) and PerCP/Cy5.5-VEGFR2 (Biolegend) were used. Dead cells were excluded using LIVE/DEAD aqua dead cell stain (Invitrogen). Endothelial cells were analysed using LSRII and FloJo.

**Western blotting.** Cellular lysates from MDA-231 and HUVEC cells were prepared by lysing cells in ice-cold RIPA buffer containing protease and phosphatase inhibitors (Roche). Conditioned media were prepared by incubating MDA-231 cells in serum-free media for 24 h. The media were then concentrated twenty times by spin filtering. Protein (40  $\mu\text{g}$ ) from lysate or conditioned media were separated using SDS–polyacrylamide gel electrophoresis and transferred to a PVDF membrane. The following antibodies were used for protein detection: mouse anti-MERTK (Caveo Therapeutics), goat anti-IGFBP2 (R&D Systems), rabbit anti-human PITPNC1 (custom made against human amino acids 308–325 in the long isoform of human PITPNC1), rabbit anti-phosphoIGF1R $\beta$ -Y1131 (Cell Signaling), rabbit anti-IGF1R $\beta$  (Cell Signaling) and rabbit anti-GAPDH (Sigma-Aldrich).

**Metastasis-free survival analysis.** Published microarray data of series from UCSF<sup>17</sup> (Affymetrix HG-U133A), NKI<sup>18</sup> (Affymetrix HG-U133A) and MSKCC<sup>13</sup> (Affymetrix HG-U133A) were used to obtain probe-level expression values for the eight miR-126-regulated genes. For genes that were represented by multiple probes, probes that displayed sufficient signal intensity as well as the highest coefficient of variation (most informative) in an independent data set were used. Each breast cancer was classified as miR-126 signature positive if the sum of the z-scores for the expression values of the eight genes was greater than the mean of the population. Kaplan–Meier metastasis-free survival curves were generated using Graphpad Prism 5 software (GraphPad Software). Statistical significance for differences between survival curves of patients was determined using the Mantel–Cox log-rank test through use of the Graphpad Prism 5 software.

13. Minn, A. J. *et al.* Genes that mediate breast cancer metastasis to lung. *Nature* **436**, 518–524 (2005).
14. Kang, Y. *et al.* A multigenic program mediating breast cancer metastasis to bone. *Cancer Cell* **3**, 537–549 (2003).
15. Yin, J. J. *et al.* TGF- $\beta$  signaling blockade inhibits PTHrP secretion by breast cancer cells and bone metastases development. *J. Clin. Invest.* **103**, 197–206 (1999).
16. Arnold, S. A. *et al.* Lack of host SPARC enhances vascular function and tumor spread in an orthotopic murine model of pancreatic carcinoma. *Dis Model Mech* **3**, 57–72 (2010).
17. Chin, K. *et al.* Genomic and transcriptional aberrations linked to breast cancer pathophysiology. *Cancer Cell* **10**, 529–541 (2006).
18. Wang, Y. *et al.* Gene-expression profiles to predict distant metastasis of lymph-node-negative primary breast cancer. *Lancet* **365**, 671–679 (2005).



# Ars2 maintains neural stem-cell identity through direct transcriptional activation of Sox2

Celia Andreu-Agullo<sup>1</sup>, Thomas Maurin<sup>1</sup>, Craig B. Thompson<sup>2</sup> & Eric C. Lai<sup>1</sup>

Fundamental questions remain unanswered about the transcriptional networks that control the identity and self-renewal of neural stem cells (NSCs), a specialized subset of astroglial cells that are endowed with stem properties and neurogenic capacity. Here we report that the zinc finger protein Ars2 (arsenite-resistance protein 2; also known as Srrt) is expressed by adult NSCs from the subventricular zone (SVZ) of mice, and that selective knockdown of Ars2 in cells expressing glial fibrillary acidic protein within the adult SVZ depletes the number of NSCs and their neurogenic capacity. These phenotypes are recapitulated in the postnatal SVZ of *hGFAP-cre::Ars2<sup>fl/fl</sup>* conditional knockout mice, but are more severe. *Ex vivo* assays show that Ars2 is necessary and sufficient to promote NSC self-renewal, and that it does so by positively regulating the expression of Sox2. Although plant<sup>1–3</sup> and animal<sup>4,5</sup> orthologues of Ars2 are known for their conserved roles in microRNA biogenesis, we unexpectedly observed that Ars2 retains its capacity to promote self-renewal in *Drosophila* and *Dicer1* knockout NSCs. Instead, chromatin immunoprecipitation revealed that Ars2 binds a specific region within the 6-kilobase NSC enhancer of Sox2. This association is RNA-independent, and the region that is bound is required for Ars2-mediated activation of Sox2. We used gel-shift analysis to refine the Sox2 region bound by Ars2 to a specific conserved DNA sequence. The importance of Sox2 as a critical downstream effector is shown by its ability to restore the self-renewal and multipotency defects of Ars2 knockout NSCs. Our findings reveal Ars2 as a new transcription factor that controls the multipotent progenitor state of NSCs through direct activation of the pluripotency factor Sox2.

Stem cells reside in most mammalian tissues throughout adult life, and contribute to normal homeostasis and repair after injury<sup>6</sup>. They are defined by their capacity to both self-renew and differentiate, thus perpetuating themselves while generating more committed daughter cells. Two major stem-cell niches exist in the adult brain, and these are found within the hippocampus and within the SVZ. Relatively quiescent NSCs give rise to actively proliferating transit-amplifying progenitors, which generate oligodendrocytes that are destined for the corpus callosum<sup>7</sup> and neuroblasts that migrate rostrally and differentiate into local interneurons in the olfactory bulb<sup>8,9</sup>. Much remains to be understood about the mechanisms and factors that control NSC self-renewal and multipotency<sup>10</sup>.

Mammalian Ars2 was reported to be essential for cell proliferation, to be downregulated in quiescent cells, and to be required for the accumulation of several microRNAs (miRNAs) that are implicated in cellular transformation<sup>4</sup>. Unexpectedly, we observed that Ars2 expression in the adult SVZ did not correlate with proliferation, as 95 ± 2% of Ars2<sup>+</sup>-positive (Ars2<sup>+</sup>) cells lacked the proliferative marker Ki67. Moreover, Ars2 was present in only 7 ± 2% of Mash1<sup>+</sup> transit-amplifying progenitors (Supplementary Fig. 1b) and was absent from doublecortin (DCX)-positive (DCX<sup>+</sup>) neuroblasts (Fig. 1a); these comprise the most highly proliferative cells in the SVZ. Ars2 was also absent from GFAP<sup>+</sup>Nestin<sup>+</sup>Sox2<sup>+</sup> astroglial cells and S100β<sup>+</sup> mature astrocytes (Supplementary Fig. 1). Instead, Ars2 was

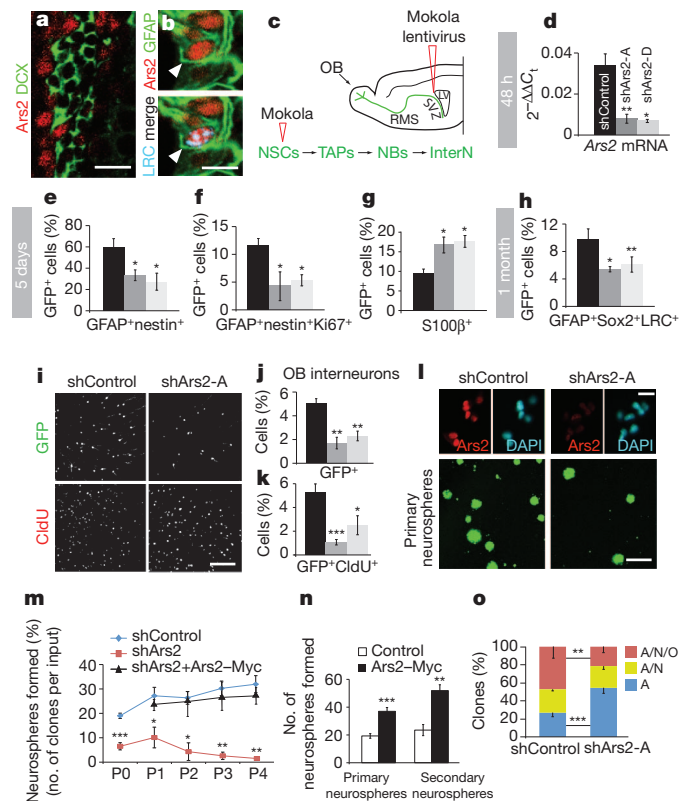


**Figure 1 | Ars2 maintains neural stem cells in the adult SVZ.** a, b, In the adult SVZ, Ars2 (red) is not expressed by DCX<sup>+</sup> (green) neuroblasts (a) but co-localizes with GFAP<sup>+</sup> (green), CldU-retaining (blue) NSCs (b). c, d, Experimental protocol (c) and validation of Ars2 knockdown ( $n = 3$  animals per condition) (d). e–g, Ars2 knockdown in the SVZ exhibited reduced GFAP<sup>+</sup>Nestin<sup>+</sup> NSCs (e), reduced NSC proliferation (f) and increased S100β<sup>+</sup> mature astrocytes (g);  $n = 3$  animals per condition. h, Ars2 knockdown reduced LRCs ( $n = 3–7$  animals per condition). i, Olfactory bulb sections double-stained for green fluorescent protein (GFP) and CldU. j, Percentage of GFP<sup>+</sup> cells per olfactory bulb slice ( $n = 7–11$  animals per condition). k, Reduced newly generated neurons after Ars2 knockdown ( $n = 7–11$  animals per condition). l, Immunocytochemistry for Ars2 (red) and DAPI (4',6-diamidino-2-phenylindole; blue) (top) and GFP<sup>+</sup> transduced primary neurospheres (green; bottom). m, Long-term self-renewal assay ( $n = 4$  cultures per condition). n, In vivo Ars2 overexpression increased neurosphere formation ( $n = 4$  cultures per condition). o, Ars2 deficiency reduced NSC multipotency ( $n = 4$  cultures per condition). A, astrocytes; InterN, interneuron; LV, lateral ventricle; N, neurons; NBs, neuroblasts; O, oligodendrocytes; OB, olfactory bulb; RMS, rostral migratory stream; TAPs, transit-amplifying progenitors. \* $P < 0.05$ ; \*\* $P < 0.01$ ; \*\*\* $P < 0.005$ . Scale bars: a, b, 10 μm; i, 100 μm; l, 200 μm. Errors bars represent s.e.m. Supplementary Table 2 provides details of numbers of scored cells.

<sup>1</sup>Department of Developmental Biology, Sloan-Kettering Institute, 1275 York Avenue, Box 252, New York, New York 10065, USA. <sup>2</sup>Department of Cancer Biology and Genetics, Sloan-Kettering Institute, 1275 York Avenue, Box 252, New York, New York 10065, USA.

expressed by niche astrocytes, ependymal cells and GFAP<sup>+</sup>CD133<sup>+</sup> stem cells<sup>11</sup> (Supplementary Fig. 1). A hallmark of NSCs is their quiescence, which is reflected in their ability to retain S-phase labels such as 5-chlorodeoxyuridine (CldU) for extended periods (that is, label-retaining cells (LRCs))<sup>12,13</sup>. We observed expression of *Ars2* in  $87 \pm 3\%$  of LRCs that were marked 1 month earlier (Fig. 1b), demonstrating the presence of *Ars2* in this slow dividing population *in vivo*.

To assay the roles of *Ars2* in NSCs *in vivo*, we used short hairpin RNAs (shRNAs) that suppressed endogenous *Ars2* (Supplementary Fig. 2c). We packaged these into GFP-expressing Mokola lentivirus, which specifically transduces astroglial cells<sup>14</sup> (Supplementary Fig. 3). We used a defective lentivirus which is pseudotyped with a lyssavirus envelope of the Mokola virus. We injected these viruses into the adult SVZ and killed the mice 48 h, 5 days or 1 month later (Fig. 1c). At 48 h after infection, sh*Ars2*-GFP<sup>+</sup> cells exhibited an 80% reduction in *Ars2* messenger RNA relative to control shRNA cells (Fig. 1d). Apoptosis was unaffected by sh*Ars2*, and the number of GFP<sup>+</sup> Ki67<sup>+</sup> cells and the levels of cyclin D1 or cyclin E transcripts were also unchanged (Supplementary Figs 3, 4b and 5b). However, 5 days after infection, sh*Ars2* SVZs exhibited a 50% reduction in the number and the proliferation rate of the GFAP<sup>+</sup>Nestin<sup>+</sup>NSCs (Fig. 1e, f), but apoptosis was unaffected (Supplementary Fig. 5b). Loss of NSC potential has been linked to an increase in mature astrocytes<sup>15–17</sup>. Consistent with this, we observed a 50% increase in the number of GFP<sup>+</sup>S100b<sup>+</sup> cells (Fig. 1g).

To assess the number of LRCs, shRNA-infected mice were injected with CldU and killed 1 month later. Notably, we observed a decrease of ~50% in transduced LRCs in sh*Ars2* SVZs (Fig. 1h), suggesting that *Ars2* maintains the NSC pool. If this is true, we would expect it to have downstream effects on neurogenesis. Indeed, 5 days after infection, we observed a decrease in DCX<sup>+</sup> neuroblasts (Supplementary Fig. 6). LRCs also label post-mitotic cells that incorporate CldU just before cell cycle exit (such as differentiated cells and newly generated olfactory bulb interneurons). One month after infection, the population of sh*Ars2*-GFP<sup>+</sup>, newly formed CldU<sup>+</sup> olfactory bulb interneurons was strongly reduced (Fig. 1i–k).

We performed additional analysis using neurospheres derived from shRNA-infected SVZ. Long-term self-renewal assays revealed that depletion of *Ars2* rapidly extinguished neurosphere cultures, indicating a defect in self-renewing divisions (Fig. 1l, m). This defect was fully restored by an shRNA-resistant form of *Ars2* (Fig. 1m and Supplementary Fig. 2d). Reciprocally, *in vivo* overexpression of *Ars2* in wild-type mice increased neurosphere formation (Fig. 1n). Multipotency of *Ars2*-deficient neurospheres was also affected, as the frequency of clones that generated  $\beta$ III-tubulin<sup>+</sup> neurons and O4<sup>+</sup> oligodendrocytes was decreased in favour of unipotent GFAP<sup>+</sup> clones (Fig. 1o). We conclude that *Ars2* is required to maintain NSCs in a self-renewing and multipotent state.

We sought to confirm these shRNA results by breeding the conditional knockout allele of *Ars2* (*Ars2*<sup>fl/fl</sup>) with *hGFAP-cre* (ref.<sup>18</sup>). *hGFAP-cre::Ars2*<sup>fl/fl</sup> mice (*Ars2*<sup>Δ/Δ</sup> mice) (Supplementary Fig. 7d) were born at the expected Mendelian ratios relative to wild-type and *hGFAP-cre::Ars2*<sup>fl/fl</sup> littermates (used as controls). However, by postnatal day 15 (P15), *Ars2*<sup>Δ/Δ</sup> mice showed progressive growth retardation, hydrocephalus and ataxia, resulting in death between P20 and P25. Further analysis of P15 *Ars2*<sup>Δ/Δ</sup> mice revealed enlarged ventricles and smaller olfactory bulbs (Fig. 2a, b), suggestive of a requirement of *Ars2* during postnatal neurogenesis. The expression pattern of *Ars2* in P15 wild-type SVZ was analogous to the adult SVZ (Supplementary Fig. 7a,b), and analysis of the conditional knockout confirmed essentially complete absence of *Ars2* in the SVZ (Supplementary Fig. 7c). Notably, the number of NSCs (marked by expression of nestin, Sox2, LeX (also known as Fut4) and GFAP) was reduced by 80% in *Ars2*<sup>Δ/Δ</sup> SVZ, and their proliferation rate decreased twofold (Fig. 2c, d, f). Caspase 3 staining showed that this was not due to cell death (Supplementary Fig. 8a, b). Conversely, assessment by GFAP and S100β staining showed that there was marked astrogliosis in *Ars2*<sup>Δ/Δ</sup> mice (Fig. 2e, f).

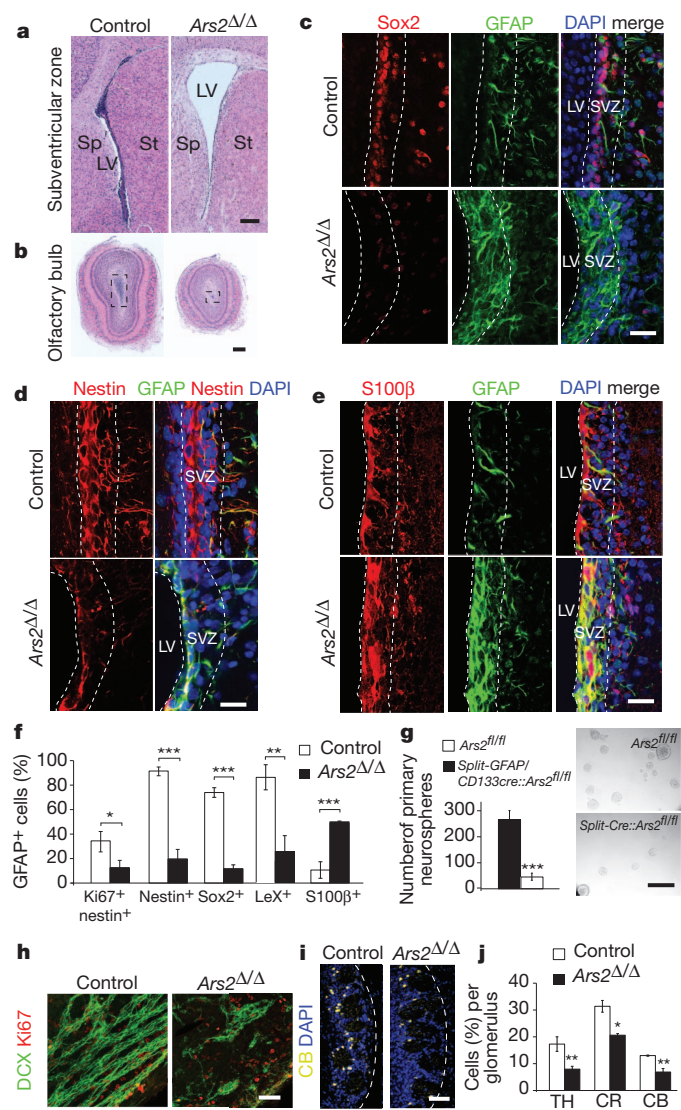


**Figure 2 | *Ars2* regulates postnatal neurogenesis.** **a, b**, Coronal sections from P15 SVZ and olfactory bulb of control and *Ars2*<sup>Δ/Δ</sup> mice, stained with haematoxylin and eosin. **c–e**, SVZ deletion of *Ars2* depleted NSCs and induced astrogliosis, as shown by loss of Sox2<sup>+</sup> (red) and accumulation of GFAP<sup>+</sup> (green) cells (**c**), loss of nestin<sup>+</sup> (red) cells (**d**), and increased S100β<sup>+</sup> (red) cells (**e**); DAPI is in blue. **f, g**, Reduced number and proliferation of NSCs and elevation of mature astrocytes in *Ars2*<sup>Δ/Δ</sup> mice (**f**), and strong reduction of primary neurospheres from GFAP/CD133-cre::*Ars2*<sup>fl/fl</sup> electroporated pups (**g**). **h**, Whole-mount immunostaining for DCX (green) and Ki67 (red). **i**, Olfactory bulb coronal sections immunostained for calbindin (CB; yellow) and DAPI (blue). **j**, Quantification of interneuron reduction in control and *Ars2*<sup>Δ/Δ</sup> mice. CB, calbindin; CR, calretinin; TH, tyrosine hydroxylase. \**P* < 0.05; \*\*\**P* < 0.01; \*\*\*\**P* < 0.005. Scale bars: **a, b**, 100 μm; **c–e**, 30 μm; **g–i**, 50 μm. Error bars represent s.e.m from six animals per genotype or condition.

As *Ars2* is expressed in niche astrocytes and ependymal cells, in addition to NSCs, we wished to demonstrate an autonomous function of *Ars2* in NSCs. We co-injected GFP<sup>+</sup> and Split-Cre plasmids that specifically drive excision in GFAP<sup>+</sup>CD133<sup>+</sup> NSCs<sup>11</sup> into the SVZ of P0–1 *Ars2*<sup>fl/fl</sup> pups, and introduced these plasmids using electroporation. Five days later, we isolated GFP<sup>+</sup> cells and plated for self-renewal assay. GFAP<sup>+</sup>CD133<sup>+</sup> NSCs deleted for *Ars2* were strongly compromised for neurosphere generation, demonstrating a cell-autonomous requirement of *Ars2* in this population (Fig. 2g and Supplementary Fig. 9). Consistent with a decrease in the number of NSCs, *Ars2*<sup>Δ/Δ</sup> mice had approximately 2.5-fold fewer DCX<sup>+</sup> neuroblasts (Fig. 2h) relative to control mice, although their proliferation rate was not affected (data not shown).



In the olfactory bulb, the frequency of tyrosine hydroxylase<sup>+</sup>, calbindin<sup>+</sup> and calretinin<sup>+</sup> interneurons per glomerulus was also deeply reduced in *Ars2*<sup>Δ/Δ</sup> (Fig. 2i, j and Supplementary Fig. 10). In summary, the severe defects of the postnatal SVZ in which *Ars2* has been deleted solidified the requirement of *Ars2* to maintain NSC identity.

As *Ars2* functions in miRNA biogenesis<sup>2–5</sup>, we tested whether the ability of *Ars2* to promote NSC self-renewal was mediated by miRNAs. This was not the case, as overexpression of *Ars2* in *Dicer1*<sup>Δ/Δ</sup> and *Drosha*<sup>Δ/Δ</sup> cells increased neurosphere yield (Fig. 3a,b). We sought to investigate this further by examining transcription factors that are known to have substantial roles in NSC self-renewal, including *Hes1*, *Hes5* and *Sox2* (refs 19–21). *Sox2* mRNA, but not *Hes1* mRNA, was significantly reduced 48 h after *Ars2* knockdown *in vivo* (Fig. 3c). One month after infection, *in vivo* knockdown of *Ars2* decreased *Hes1* and *Hes5* mRNA levels by ~30%, but resulted in a more substantial 70% reduction in *Sox2* (Fig. 3d). Reciprocally, *Sox2* levels increased by ~60% in neurospheres overexpressing *Ars2* (Fig. 3e). These effects seemed to be transcriptional in nature, as *Ars2* activated a 6-kilobase (kb) *Sox2-luc* reporter containing *cis*-regulatory sequences responsible for *Sox2* expression within adult neurogenic zones<sup>22</sup> (Fig. 3f). This was not simply due to the cancelling effects of overexpressing any self-renewal gene, because *in vitro* overexpression of *Sox2* (Fig. 3g), but not *Hes5* (Fig. 3h), rescued the *Ars2*-dependent loss in self-renewal capacity of sh*Ars2* cells. Reciprocally, *in vitro* knockdown of *Sox2* (Supplementary Fig. 11a) caused rapid depletion of self-renewing neurospheres<sup>23</sup> (Fig. 3i) and compromised multipotency (Supplementary Fig. 11b), similar to the effects of *Ars2* knockdown (Fig. 1m, o). Together, these data indicated that *Sox2* is a critical downstream effector of *Ars2* in NSCs.

To evaluate whether the ability of *Ars2* to activate *Sox2* expression might reflect a transcriptional role for this nuclear protein, we performed chromatin immunoprecipitation (ChIP) of *Ars2* in NSCs,

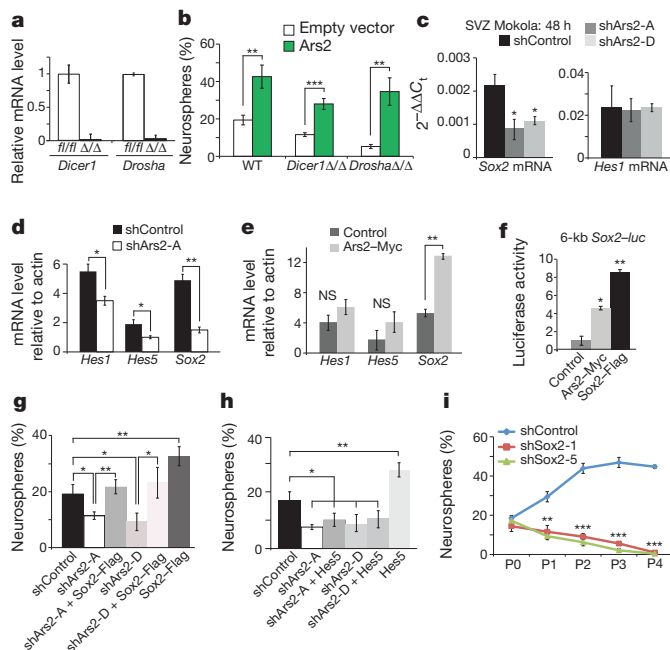


**Figure 3 | *Ars2* acts independently of the miRNA pathway to promote NSC self-renewal through *Sox2*.** **a**, Absence of *Dicer1* and *Drosha* in floxed NSC cultures after Cre treatment ( $n = 2$  experiments per condition). **b**, Ectopic *Ars2* promoted NSC self-renewal in *Dicer1*- and *Drosha*-deleted NSCs ( $n = 3$  experiments per condition). **c**, qPCR measurements from purified GFP<sup>+</sup> cells 48 h after infection ( $n = 3$ ). **d**, qPCR measurements of self-renewal genes from primary infected GFP<sup>+</sup> NSCs ( $n = 3$ ). **e**, Overexpression of *Ars2* increased *Sox2* mRNA ( $n = 3$ ). **f**, Both *Ars2* and *Sox2* activate a *Sox2* transcriptional reporter ( $n = 3$ ). **g**, **h**, Percentage of neurospheres formed from NSCs infected with the indicated constructs ( $n = 3$ ). **i**, Long-term self-renewal assay shows that *Sox2* is required for NSC self-renewing divisions ( $n = 4$ ). \* $P < 0.05$ ; \*\* $P < 0.01$ ; \*\*\* $P < 0.005$ . Error bars represent s.e.m.; NS, not significant; WT, wildtype.

querying across the 6-kb *Sox2* promoter and the *Sox2* transcription unit. Interestingly, *Ars2* associated not only with its 5' untranslated region (UTR) and 3' UTR but was highly enriched in region 8 (−2 to −2.5 kb) of the *Sox2* promoter (Fig. 4a); we validated this binding pattern using an independent antibody (Supplementary Fig. 12a). RNase treatment of chromatin samples eliminated UTR-associated *Ars2* ChIP signals, and this is consistent with CBC-mediated association with capped transcripts<sup>4</sup>. However, binding of *Ars2* to promoter region 8 was maintained, suggesting a more direct association of *Ars2* with chromatin (Fig. 4b). No binding was found to the *Sox2* coding region (Fig. 4a) or to the promoters of *Hes1*, *Hes5* (ref. 24), *K14* and *Myod1* (Supplementary Fig. 12b–e). Chromatin association of *Ars2* was cell-type-dependent, as *Ars2* did not bind the *Sox2* enhancer in NIH3T3 cells (Fig. 4a), which express high levels of *Ars2* (Supplementary Fig. 2a).

Simple binding of *Ars2* to the *Sox2* enhancer might not necessarily be of functional consequence. We prepared two deletions of the 6-kb *Sox2-luc* reporter, removing region 8 that was bound by *Ars2* or region 5 as a

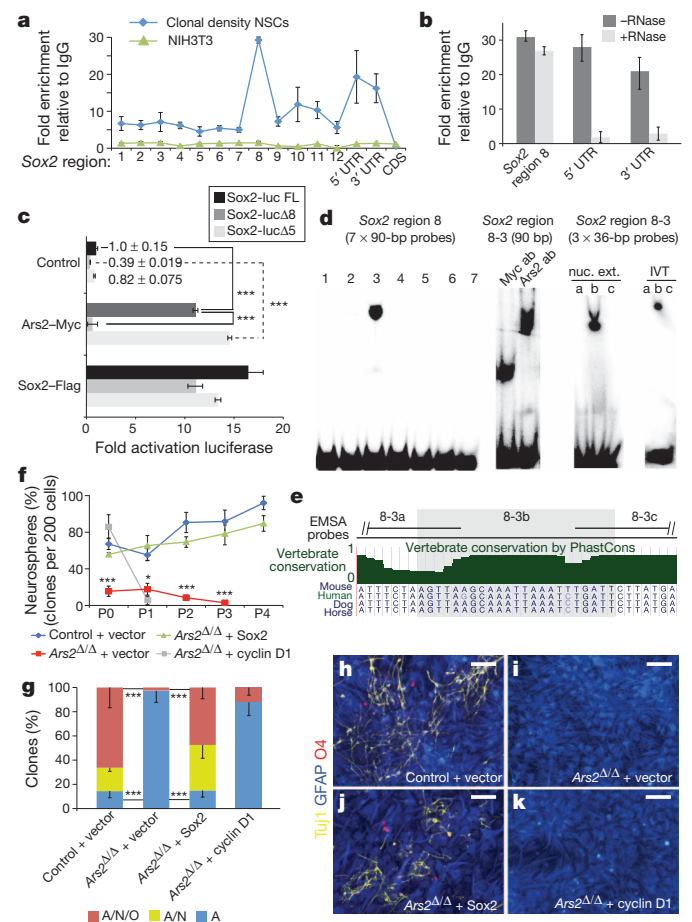


**Figure 4 | *Ars2* directly activates transcription of *Sox2* to mediate NSC self-renewal and multipotency.** **a**, ChIP of *Ars2* to the *Sox2* locus ( $n = 4$  independent experiments). **b**, *Ars2* binding to *Sox2* promoter region 8 is RNA independent ( $n = 2$ ). **c**, *Ars2* requires region 8 to activate *Sox2-luc* ( $n = 4$ ). **d**, Gel shifts of the *Ars2* binding site in the *Sox2* promoter using nuclear extract or *in vitro*-translated *Ars2*. **e**, Conservation of the *Ars2*-binding site in *Sox2*. **f**, Long-term self-renewal assay from NSCs isolated from control and *Ars2*<sup>Δ/Δ</sup> mice electroporated *in vivo* with the indicated constructs ( $n = 6$  animals per condition). **g**, *Ars2*<sup>Δ/Δ</sup> defect in multipotency can be rescued by *in vivo* expression of *Sox2* ( $n = 6$  animals per condition). **h–k**, Differentiated NSC colonies stained for GFAP (blue), mouse anti-β-tubulin (Tuj1, yellow) and O4 (pink). Ab, antibody; bp, base pairs; CDS, coding sequence; EMSA, electrophoretic mobility shift assay; FL, full length; IVT, *in vitro*-translated; Luc, luciferase; Nuc. ext, nuclear extract; UTR, untranslated region; \* $P < 0.05$ ; \*\*\* $P < 0.005$ . Error bars represent s.e.m. Scale bars: **h–k**, 50 μm.



control deletion. Loss of region 8 strongly reduced *Sox2-luc* expression relative to the control deletion, whereas reciprocally, ectopic *Ars2* activated the control deletion but not the version lacking the *Ars2* binding site (Fig. 4c). Therefore, *Ars2* activates *Sox2* through promoter region 8. We then incubated NSC nuclear extract with a series of overlapping 90-bp radiolabelled probes covering the ~500 base pairs (bp) of *Sox2* region 8, and observed a specific gel shift of subregion 8-3 (Fig. 4d). This band was completely super-shifted by inclusion of *Ars2* antibody, but not Myc antibody (Fig. 4d). We defined the *Ars2* binding site more precisely, revealing that *Ars2* bound specifically to the central portion of *Sox2* region 8-3 (Fig. 4d). This reflected direct DNA binding activity of *Ars2*, as *in vitro* translated *Ars2* recapitulated specific binding to *Sox2* probe 8-3b (Fig. 4d). This identified a sequence that is highly constrained across mammalian genomes (Fig. 4e and Supplementary Fig. 13).

To determine whether *Sox2* mediates *Ars2* function *in vivo*, we electroporated *Sox2* expression construct into *Ars2*<sup>Δ/Δ</sup> postnatal SVZ. Notably, *Sox2* rescued the self-renewal and multipotency defects of *Ars2* knockout cells (Fig. 4f–j). By contrast, NSCs derived from *Ars2*<sup>Δ/Δ</sup> SVZ electroporated with cyclin D1 lacked self-renewal capacity (Fig. 4f) and multipotency (Fig. 4g,k). This confirmed that *Ars2* knockout cells cannot be rescued by driving proliferation. Instead, *Ars2* confers NSC identity as a self-renewing cell type by activating *Sox2*.

A central goal of stem-cell biology is to understand the molecular mechanisms that regulate stem-cell self-renewal and multipotency. We show that *Ars2* is specifically expressed by NSCs, and not by transit-amplifying progenitors and neuroblasts, and that it maintains the self-renewal and multipotency capacity of postnatal and adult NSCs. In this setting, *Ars2* is not required for cell viability, but is instead essential for maintaining core NSC properties. *Ars2* depletion or knockout decreased the NSC pool, decreased neurogenesis and strongly increased non-neurogenic astrocytes. We have assigned a new molecular function for the conserved RNA factor *Ars2* as a sequence-specific DNA binding protein, and a critical direct activator of *Sox2* during *in vivo* NSC self-renewal and multipotency. More generally, in light of the interest surrounding the role of *Sox2* as a core pluripotency factor in embryonic stem cells and induced pluripotent stem cells, *Ars2* may regulate stem-cell self-renewal in these settings as well. This possibility is bolstered by the early embryonic arrest of *Ars2* knockout mice<sup>25</sup>, which strongly resembles embryonic arrest in *Sox2* knockout mice<sup>26</sup>.

## METHODS SUMMARY

All procedures using mice were performed in accordance with the Institutional Animal Care and Use Committee (IACUC). For analysis of adult cells, we injected GFP-expressing Moka lentivirus (shControl or sh*Ars2*) into two different locations of the SVZ using stereotaxic control, and processed brain sections for immunohistochemistry. In addition, we dissected infected SVZs, purified GFP<sup>+</sup> cells and assayed them for self-renewal and multipotency capacity, as described<sup>27</sup>. For conditional knockout analysis, we crossed mice carrying the *Ars2* conditional allele<sup>4</sup> with *hGFAP-Cre* mice. For intraventricular electroporation assays using Split-Cre<sup>1</sup>, we used neonatal and P1 *Ars2*<sup>fl/fl</sup> pups and killed them 5 days later for self-renewal and multipotency assays. *Dicer1*<sup>Δ/Δ</sup> and *Drosha*<sup>Δ/Δ</sup> NSC cultures were generated by transfection with 5 μg of pMSCV-GFP-Cre, and resulting GFP<sup>+</sup> cells were isolated and cultured for 2 weeks before analysis. For chromatin immunoprecipitation, three million NSCs were crosslinked in 1% paraformaldehyde (PFA) and incubated with nuclear lysate and *Ars2* antibody. Binding of nuclear extract or *in vitro* translated *Ars2* to radiolabelled *Sox2* probes was assayed in 4% tris-borate-EDTA (TBE) gels. All primers used for cloning, ChIP followed by quantitative PCR (ChIP-qPCR) and gel shifts are listed in Supplementary Tables 1–6.

**Full Methods** and any associated references are available in the online version of the paper at [www.nature.com/nature](http://www.nature.com/nature).

Received 2 March; accepted 14 November 2011.

Published online 25 December 2011.

- Laubinger, S. *et al.* Dual roles of the nuclear cap-binding complex and SERRATE in pre-mRNA splicing and microRNA processing in *Arabidopsis thaliana*. *Proc. Natl Acad. Sci. USA* **105**, 8795–8800 (2008).

- Llobes, D., Rallapalli, G., Schmidt, D. D., Martin, C. & Clarke, J. SERRATE: a new player on the plant microRNA scene. *EMBO Rep.* **7**, 1052–1058 (2006).
- Yang, L., Liu, Z., Lu, F., Dong, A. & Huang, H. SERRATE is a novel nuclear regulator in primary microRNA processing in *Arabidopsis*. *Plant J.* **47**, 841–850 (2006).
- Gruber, J. J. *et al.* *Ars2* links the nuclear cap-binding complex to RNA interference and cell proliferation. *Cell* **138**, 328–339 (2009).
- Sabin, L. R. *et al.* *Ars2* regulates both miRNA- and siRNA-dependent silencing and suppresses RNA virus infection in *Drosophila*. *Cell* **138**, 340–351 (2009).
- Fuchs, E., Tumber, T. & Guasch, G. Socializing with the neighbors: stem cells and their niche. *Cell* **116**, 769–778 (2004).
- Menn, B. *et al.* Origin of oligodendrocytes in the subventricular zone of the adult brain. *J. Neurosci.* **26**, 7907–7918 (2006).
- Kriegstein, A. & Alvarez-Buylla, A. The glial nature of embryonic and adult neural stem cells. *Annu. Rev. Neurosci.* **32**, 149–184 (2009).
- Lledo, P. M., Merkle, F. T. & Alvarez-Buylla, A. Origin and function of olfactory bulb interneuron diversity. *Trends Neurosci.* **31**, 392–400 (2008).
- Shi, Y., Sun, G., Zhao, C. & Stewart, R. Neural stem cell self-renewal. *Crit. Rev. Oncol. Hematol.* **65**, 43–53 (2008).
- Beckervordersandforth, R. *et al.* *In vivo* fate mapping and expression analysis reveals molecular hallmarks of prospectively isolated adult neural stem cells. *Cell Stem Cell* **7**, 744–758 (2010).
- Potten, C. S. Stem cells in gastrointestinal epithelium: numbers, characteristics and death. *Phil. Trans. R. Soc. Lond. B* **353**, 821–830 (1998).
- Cotsarelis, G., Sun, T. T. & Lavker, R. M. Label-retaining cells reside in the bulge area of pilosebaceous unit: implications for follicular stem cells, hair cycle, and skin carcinogenesis. *Cell* **61**, 1329–1337 (1990).
- Alonso, M. *et al.* Turning astrocytes from the rostral migratory stream into neurons: a role for the olfactory sensory organ. *J. Neurosci.* **28**, 11089–11102 (2008).
- Raponi, E. *et al.* S100B expression defines a state in which GFAP-expressing cells lose their neural stem cell potential and acquire a more mature developmental stage. *Glia* **55**, 165–177 (2007).
- Shi, Y. *et al.* Expression and function of orphan nuclear receptor TLX in adult neural stem cells. *Nature* **427**, 78–83 (2004).
- Zencak, D. *et al.* *Bmi1* loss produces an increase in astroglial cells and a decrease in neural stem cell population and proliferation. *J. Neurosci.* **25**, 5774–5783 (2005).
- Zhuo, L. *et al.* hGFAP-cre transgenic mice for manipulation of glial and neuronal function *in vivo*. *Genesis* **31**, 85–94 (2001).
- Ohtsuka, T., Sakamoto, M., Guillemot, F. & Kageyama, R. Roles of the basic helix-loop-helix genes *Hes1* and *Hes5* in expansion of neural stem cells of the developing brain. *J. Biol. Chem.* **276**, 30467–30474 (2001).
- Hitoshi, S. *et al.* Notch pathway molecules are essential for the maintenance, but not the generation, of mammalian neural stem cells. *Genes Dev.* **16**, 846–858 (2002).
- Ferri, A. L. *et al.* *Sox2* deficiency causes neurodegeneration and impaired neurogenesis in the adult mouse brain. *Development* **131**, 3805–3819 (2004).
- Suh, H. *et al.* *In vivo* fate analysis reveals the multipotent and self-renewal capacities of *Sox2*<sup>+</sup> neural stem cells in the adult hippocampus. *Cell Stem Cell* **1**, 515–528 (2007).
- Favaro, R. *et al.* Hippocampal development and neural stem cell maintenance require *Sox2*-dependent regulation of *Shh*. *Nature Neurosci.* **12**, 1248–1256 (2009).
- Ohtsuka, T. *et al.* Visualization of embryonic neural stem cells using *Hes* promoters in transgenic mice. *Mol. Cell. Neurosci.* **31**, 109–122 (2006).
- Wilson, M. D. *et al.* *ARS2* is a conserved eukaryotic gene essential for early mammalian development. *Mol. Cell. Biol.* **28**, 1503–1514 (2008).
- Avilion, A. A. *et al.* Multipotent cell lineages in early mouse development depend on *SOX2* function. *Genes Dev.* **17**, 126–140 (2003).
- Andreu-Agulló, C., Morante-Redolat, J. M., Delgado, A. C. & Farinas, I. Vascular niche factor PEDF modulates Notch-dependent stemness in the adult subependymal zone. *Nature Neurosci.* **12**, 1514–1523 (2009).

**Supplementary Information** is linked to the online version of the paper at [www.nature.com/nature](http://www.nature.com/nature).

**Acknowledgements** We thank X. Lu, M. Götz, A. Rizzino, P. M. Lledo, P. Charneau, M. Segura, P. L. Howard and S. Olejniczak for reagents. We are grateful to K. Hadjantonakis, A. Ferrer-Vaquer, J. Zhang and Y. Ganat for assistance. U. Ruthishauser, V. Tabar and the Molecular Cytology Core Facility at the Memorial Sloan-Kettering Cancer Center shared equipment. S. R. Ferron, H. Mira, A. Joyner, H. Duan, Q. Dai, I. Farinas and S. Shi provided critical comments. Work in E.C.L.'s group was supported by the Burroughs Wellcome Fund, the Starr Cancer Consortium (I3-A139) and the NIH (R01-GM083300). C.A.-A. was funded by a EMBO Long-Term Fellowship (ALTF 718-2008) and a NYSTEM Fellowship.

**Author Contributions** C.A.-A. performed and designed all of the experiments, T.M. performed *in vivo* lentivirus injections and C.B.T. provided reagents. C.A.-A. and E.C.L. conceived the project, interpreted the results and wrote the manuscript.

**Author Information** Reprints and permissions information is available at [www.nature.com/reprints](http://www.nature.com/reprints). The authors declare no competing financial interests. Readers are welcome to comment on the online version of this article at [www.nature.com/nature](http://www.nature.com/nature). Correspondence and requests for materials should be addressed to C.A.-A. ([andreuac@mskcc.org](mailto:andreuac@mskcc.org)) or E.C.L. ([laie@mskcc.org](mailto:laie@mskcc.org)).

## METHODS

**Mice and genotyping.** All mice were housed in the Memorial Sloan-Kettering Cancer Center mouse facility and treated with procedures approved by the Institutional Animal Care and Use Committee (IACUC). For the *Ars2* genotyping, the following primers were used: JG188, 5'-GTTATGCTAGCCCCAGCCC-3'; JG189, 5'-GAAGAGAGCAGCGCACCTCC-3' and JGdel, 5'-CAGCTTACTA TGGCCAGCC-3'. JG188 + JG189 gives a 300-bp band for the wild-type allele and a 400-bp band for the floxed allele. JGdel + JG189 gives a 260-bp band for the deleted allele. Genotyping for *Drosha*<sup>28</sup> and *Dicer1* (ref. 29) was performed as described.

**Lentivirus production.** We cloned *Ars2* and *Sox2* shRNAs into the third generation lentiviral vector pFUGWH1 (ref. 30). The target sequences used are listed in Supplementary Table 1. The shRNA-expressing lentiviral plasmid was co-transfected with psPAX2 and Mokola G envelope plasmids<sup>31</sup> in 293FT cells. Virus-containing media were collected, filtered and concentrated by ultracentrifugation at 45,000g for 2 h, and re-suspended in PBS. Viral titres were measured by serial dilution on NIH3T3 cells followed by flow cytometry analysis after 72 h. The titre of the virus used ranged between  $6-9 \times 10^9$  plaque forming units per ml.

**Lentivirus injection.** Mice were anaesthetized with Ketamine (100 mg per kg, Ketaset) and Xylazine (10 mg per kg, AmTech), and were administered Buprenex (0.05 mg per kg) before being placed on a stereotaxic frame (myNeuroLab, Leica). One microlitre of high titre lentiviral vectors ( $>10^9$  plaque forming units per ml) were injected in the subventricular zone (SVZ) of 2- to 4-month-old ICR mice using a microinjector and a 5- $\mu$ l Hamilton syringe 75RN(32/2"/90 DEG) mounted with a 32 gauge needle. The injection coordinates were optimized according to an injection trial in which mice were injected with a vital dye, the brains were sectioned and the injection site localized. To increase the transduction efficiency of the targeted cell population, we chose to perform two injections at different depths in two different coordinates in the right hemisphere of the brain. The coordinates were (in mm, relative to Bregma and to the surface of the skull, anteroposterior, mediolateral and dorsoventral, respectively) (0.5, 1.1, 2.5–1.7) and (1, 0.9, 3–2.5). After surgery, mice were given an intraperitoneal injection of saline (1 ml) and were closely monitored until fully ambulatory, and were checked again at 24 h and 48 h after surgery. Experiments were conducted in accordance with NIH and IACUC guidelines and the Research Animal Resources Center approved all of the procedures.

**Intraventricular electroporation.** Neonatal to postnatal day 1 (P1) *hGFAP-Cre::Ars2*<sup>fl/fl</sup> pups were used to perform intraventricular electroporation, as previously described<sup>32</sup>. For Split-Cre plasmid electroporations<sup>33</sup> a 1/1.5 CCre/NCre vector ratio was used.

**Histology.** The chlorodeoxyuridine (CldU) administration regime has been described in detail<sup>34</sup>. Mice were anaesthetized with an overdose of Ketamine and Xylazine and transcardially perfused with 4% PFA. Brains were removed and post-fixed in 4% paraformaldehyde (PFA) overnight at 4 °C. A vibratome was used to cut 30- $\mu$ m coronal sections. The following antibodies were used: rabbit anti-Ars2 (1/25,000; gift of X. Lu), sheep anti-tyrosine hydroxylase (1/1,000; Pel-Freez), rabbit anti-calbindin (1/5,000; Swant), rabbit anti-calretinin (1/1,000; Millipore), mouse anti- $\beta$ -tubulin (Tuj1) (1/500; Covance), mouse anti-LeX (1/20; BD Pharmingen), rabbit anti-caspase3 (1/100; Cell Signaling Technologies), mouse anti-Mash1 (1/100; BD Pharmingen), goat anti-Sox2 (1/150; R&D Systems), goat anti-Doublecortin (1/500; Santa Cruz), rat anti-CldU (1/600; Accurate), rabbit anti-Ki67 (1/500; Abcam), rat anti-CD133 (Prominin-1) (1/100; eBioscience), mouse anti-nestin (1/200; Millipore), rabbit anti-GFP (1/500; Molecular Probes), mouse anti-GFP (1/500; Molecular Probes) and chicken anti-GFP (1/500; Molecular Probes).

**In vivo quantification.** A Leica CTR6500 confocal laser-scanning microscope was used for *in vivo* quantification analysis of GFP<sup>+</sup> cells. All images were taken using the same pinhole setting (1  $\mu$ m) and using a  $\times 20$  oil objective or a  $\times 40$  oil objective. Stacks of optical slices (1  $\mu$ m thick) were collected through the z axis of brain sections of the SVZ and olfactory bulb. For SVZ quantifications, the whole extent of the SVZ (from the rostral tip of the crossing of the corpus callosum and extending caudally to the rostral tip of the crossing of the anterior commissure) was cut in coronal sections (30  $\mu$ m thick). For double and triple stain analysis, usually a total of 10–15 slices (one every three slices) from each animal were selected. For quantification, the cells situated within 50–60  $\mu$ m from the lateral wall of the ventricle were counted. For olfactory bulb quantifications, the olfactory bulb (from the rostral tip of the olfactory ventricle to the rostral limit of the accessory olfactory bulb) was sliced in coronal vibratome sections (30  $\mu$ m thick). Usually 10 slices (one every four slices) from each animal were used. In both cases, co-localization was evaluated in single optical planes taken through the entire z axis of each GFP<sup>+</sup> cell. Data are expressed as the percentage of double- or triple-labelled GFP<sup>+</sup> cells normalized to the total GFP<sup>+</sup> cell population. For example, to determine the proliferation rate of GFAP<sup>+</sup>Sox2<sup>+</sup> cells, the number of

GFP<sup>+</sup>GFAP<sup>+</sup>Sox2<sup>+</sup>Ki67<sup>+</sup> cells was scored and divided by the total number of GFP<sup>+</sup>GFAP<sup>+</sup>Sox2<sup>+</sup>-expressing cells. See Supplementary Table 2 for details about the number of GFP<sup>+</sup> cells that were analysed and the total number of animals that were used in each case.

**Plasmid construction.** To generate *Sox2-luc*, the 6-kb mouse *Sox2* promoter was PCR amplified from pBSK plasmid (gift of A. Rizzino) using the restriction enzyme-modified PCR primers Sox2\_XhoI(F) and Sox2\_HindIII(R). To generate Sox2 deletion 5, two fragments were amplified using the following primers: Sox2\_XhoI(F), Sox2\_del5(R), Sox2\_del5(F) and Sox2\_HindIII(R). To generate Sox2 deletion 8, two different fragments were PCR amplified from the full-length construct using the following primers: Sox2\_XhoI(F) and Sox2\_del8(R), Sox2\_del8(F), and Sox2\_HindIII(R). The fragments were cloned into pGL3-basic vector. Cloning was performed using Cold Fusion Kit (SBI, Systems Biosciences) following the manufacturer's instructions. See Supplementary Table 3 for primer sequences.

**Neural stem-cell culture and multipotency assays.** ICR mice were purchased from Taconic and neural stem cells (NSCs) were cultured as previously described<sup>7</sup>. Single neurospheres of similar sizes were collected using a pipette and each one was seeded in a single matrigel-coated P-96 well. They were allowed to differentiate for 7 days *in vitro* (2 days in neurosphere medium containing fibroblast growth factor (FGF) and 5 days in 2% fibroblast bovine serum (FBS)). At least 40 clones were analysed per condition. Retrovirus production and *in vitro* infection of NSCs were performed as described<sup>35</sup>. The following antibodies were used: chicken anti-GFAP (1/1,500; Millipore), mouse anti-O4 (1/2; Developmental Studies Hybridoma Bank) and  $\beta$ -III-tubulin (1/300; Covance).

**NSC transfection and luciferase assays.** NSCs from passages 4 to 8 were grown for 48 h and transfected using Nucleofector (II) (Amaxa Biosystems). A total of 1.5  $\mu$ g DNA was transfected per well. Fifty nanograms (ng) of a *Renilla* luciferase construct was used as an internal control. Twenty-four to thirty-six hours after electroporation, luciferase activity was measured using Dual-Glo (Promega). For each experiment, each value represents the mean luciferase activity in three different wells and each construct was analysed in three independent experiments. Luciferase activity was normalized to empty vector on the full-length *Sox2-luc*.

**Chromatin immunoprecipitation.** Cells were crosslinked with 1% formaldehyde at 23 degrees Celsius for 10 min. Glycine was added to a final concentration of 125 mM to stop crosslinking. Cells were rinsed twice with cold PBS and incubated for 10 min at 4 °C in low salt washing buffer (10 mM Tris (pH 8.0), 1 mM EDTA (pH 8.0), 0.5 mM EGTA (pH 8.0), 0.25% Triton X-100, 1 mM PMSF, 1 $\times$  Complete (Roche)). After centrifugation at 3,500g, the pellet was re-suspended in high salt washing buffer (10 mM Tris (pH 8.0), 1 mM EDTA (pH 8.0), 0.5 mM EGTA (pH 8.0), 0.2 M NaCl, 1 mM PMSF, 1 $\times$  Complete (Roche)) and incubated for 10 min at 4 °C. Nuclei were re-suspended in 1% SDS lysis buffer and chromatin was sonicated to obtain DNA fragments of around 500 bp. One-tenth of total volume was saved for total input DNA control. Lysates were pre-cleared by incubation with 50  $\mu$ l of Protein A-sepharose (50% slurry pre-blocked with salmon sperm DNA, yeast tRNA and BSA) for 1 h. Immunoprecipitation was performed overnight at 4 °C with 4  $\mu$ g rabbit anti-Ars2 antibody, 4  $\mu$ g mouse anti-Ars2 antibody and 4  $\mu$ g mouse or rabbit IgG. After immunoprecipitation, 60  $\mu$ l of pre-blocked Protein A-sepharose (50% slurry) was added and the incubation continued for another 4 h. Precipitates were thoroughly washed and extracted twice in 1% SDS and 0.1 M NaHCO<sub>3</sub> in TE buffer. Elutes were incubated at 65 °C overnight to reverse crosslinking and then incubated for 1 h at 50 °C with 10  $\mu$ M EDTA, 40  $\mu$ M Tris-HCl (pH 6.8) and 20  $\mu$ g proteinase K (Roche). DNA fragments were recovered by Qiaquick PCR purification kit (Qiagen). Primers that were used are listed in Supplementary Table 4.

**Generation of *Dicer1*<sup>ΔA</sup> and *Drosha*<sup>ΔA</sup> NSC cultures.** We generated NSC cultures from the SVZ of 2-month-old wild-type, *Dicer1*<sup>fl/fl</sup> and *Drosha*<sup>fl/fl</sup> mice. At passage 1,  $3 \times 10^6$  NSCs were transfected with 5  $\mu$ g of pMSCV-GFP-Cre (Addgene 20781) using Nucleofector (II) (Amaxa Biosystems). Three days later, we isolated GFP<sup>+</sup> cells using FACS and cultured NSCs for 2 weeks to allow recombination. After this period the cells were collected for genotyping. Five micrograms of pMSCV-Ars2 or empty pMSCV was transfected to each genotype and after 24 h, cells were plated for a self-renewal assay.

**Electrophoretic mobility shift assays.** Nuclear extracts were prepared from NSCs as described<sup>36</sup>. For *in vitro* translation, 20  $\mu$ g of *Ars2* cDNA cloned into pcDNA3.1 (gift of P. Howard) or empty vector pcDNA3.1 were subjected to a transcription reaction for 1 h at 32 °C (Pierce) followed by a translation reaction for 90 min at 30 °C using the Human *In vitro* Protein Expression Kit (Pierce), following the manufacturer's instructions. For the binding reaction of the EMSA assays, 8  $\mu$ g of translated protein was used.

Probes were labelled by incubating 1  $\mu$ l of forward oligonucleotide (100 ng per  $\mu$ l) with 1  $\mu$ l of  $\times 10$  T4 kinase buffer (New England Biolabs), 1  $\mu$ l <sup>32</sup>P  $\gamma$ -dATP, 1  $\mu$ l PNK kinase (New England Biolabs) and 6  $\mu$ l water at 37 °C for 1 h. After adding

90 µl of TE buffer, the forward probe was purified by using Illustra Microspin G-25 columns (GE Healthcare), following the manufacturer's instructions. To anneal oligonucleotides, 5 µl of reverse oligonucleotide (100 ng per µl), 5 µl of 2 M KCl and 90 µl of mQ water were added to the forward labelled probe, and this was boiled for 5 min and cooled down slowly. In each reaction, 1 µl of labelled probe was used. To prepare the unlabelled competitor, 10 µg of forward oligonucleotide and 10 µg of reverse oligonucleotide were incubated with 5 µl of 2 M KCl, and 175 µl of mQ water were added to the forward labelled probe. This was boiled for 5 min and cooled down slowly.

For the binding reaction, 15 µg of nuclear extract, 4 µg of antibody or IgG, 100 ng of labelled probe, 1 µg of poly(dI-dC) and 2 µl of binding buffer (5X) were incubated for 30 min at 23 °C. The binding buffer (5X) contained 375 mM NaCl, 50 mM Tris-HCl pH 7.5, 5 mM EDTA and 30% glycerol. The samples were loaded in a 4% non-denaturing tris-borate-EDTA (TBE) gel that was pre-run for 30 min at 150 V. After 4 h the gel was dried and expose to film using Fujifilm Image Gauge version 4.1. See Supplementary Table 5 for oligonucleotides used in the assay.

**RNA isolation and real-time PCR analysis.** Total RNA was isolated using Trizol (Invitrogen) and 1 µg of total RNA was used to synthesize complementary DNA using random primers and reverse transcriptase (SuperScript II RT; Invitrogen). For quantitative PCR, SYBR PCR Master Mix (Applied Biosystems) was used in a CFX96 Real-Time System thermocycler (Biorad). Primers that were used are listed on Supplementary Table 6.

**Statistical analysis.** Data are always shown as mean values  $\pm$  s.e.m. Analyses of significant differences between means were performed using two-tailed Student's

*t*-tests. The arcsen transformation for normalization was applied to relative values (fold-change and percentage). *n*, number of independent cultures or animals used. In all cases \**P* < 0.05; \*\**P* < 0.01; \*\*\**P* < 0.005.

28. Chong, M. M., Rasmussen, J. P., Rudensky, A. Y. & Littman, D. R. The RNaseIII enzyme Drosha is critical in T cells for preventing lethal inflammatory disease. *J. Exp. Med.* **205**, 2005–2017 (2008).
29. Harfe, B. D., McManus, M. T., Mansfield, J. H., Hornstein, E. & Tabin, C. J. The RNaseIII enzyme *Dicer* is required for morphogenesis but not patterning of the vertebrate limb. *Proc. Natl Acad. Sci. USA* **102**, 10898–10903 (2005).
30. Ivanova, N. *et al.* Dissecting self-renewal in stem cells with RNA interference. *Nature* **442**, 533–538 (2006).
31. Alonso, M. *et al.* Turning astrocytes from the rostral migratory stream into neurons: a role for the olfactory sensory organ. *J. Neurosci.* **28**, 11089–11102 (2008).
32. Boutin, C., Diestel, S., Desoeuvre, A., Tiveron, M. C. & Cremer, H. Efficient in vivo electroporation of the postnatal rodent forebrain. *PLoS ONE* **3**, e1883 (2008).
33. Beckervordersandforth, R. *et al.* In vivo fate mapping and expression analysis reveals molecular hallmarks of prospectively isolated adult neural stem cells. *Cell Stem Cell* **7**, 744–758 (2010).
34. Ferrón, S. R. *et al.* A combined *ex/in vivo* assay to detect effects of exogenously added factors in neural stem cells. *Nature Protocols* **2**, 849–859 (2007).
35. Andreu-Agulló, C., Morante-Redolat, J. M., Delgado, A. C. & Farinas, I. Vascular niche factor PEDF modulates Notch-dependent stemness in the adult subependymal zone. *Nature Neurosci.* **12**, 1514–1523 (2009).
36. Whitman, M. C. & Greer, C. A. Synaptic integration of adult-generated olfactory bulb granule cells: basal axodendritic centrifugal input precedes apical dendrodendritic local circuits. *J. Neurosci.* **27**, 9951–9961 (2007).



# Acquisition of a multifunctional IgA<sup>+</sup> plasma cell phenotype in the gut

Jörg H. Fritz<sup>1†\*</sup>, Olga Lucia Rojas<sup>1\*</sup>, Nathalie Simard<sup>1,2</sup>, Douglas D. McCarthy<sup>1</sup>, Siegfried Hapfelmeier<sup>3†</sup>, Stephen Rubino<sup>4</sup>, Susan J. Robertson<sup>1</sup>, Mani Larijani<sup>1†</sup>, Jean Gosselin<sup>5</sup>, Ivaylo I. Ivanov<sup>6</sup>, Alberto Martin<sup>1</sup>, Rafael Casellas<sup>7</sup>, Dana J. Philpott<sup>1</sup>, Stephen E. Girardin<sup>4</sup>, Kathy D. McCoy<sup>3</sup>, Andrew J. Macpherson<sup>3</sup>, Christopher J. Paige<sup>1,2</sup> & Jennifer L. Gommerman<sup>1</sup>

The largest mucosal surface in the body is in the gastrointestinal tract, a location that is heavily colonized by microbes that are normally harmless. A key mechanism required for maintaining a homeostatic balance between this microbial burden and the lymphocytes that densely populate the gastrointestinal tract is the production and transepithelial transport of poly-reactive IgA (ref. 1). Within the mucosal tissues, B cells respond to cytokines, sometimes in the absence of T-cell help, undergo class switch recombination of their immunoglobulin receptor to IgA, and differentiate to become plasma cells<sup>2</sup>. However, IgA-secreting plasma cells probably have additional attributes that are needed for coping with the tremendous bacterial load in the gastrointestinal tract. Here we report that mouse IgA<sup>+</sup> plasma cells also produce the antimicrobial mediators tumour-necrosis factor- $\alpha$  (TNF- $\alpha$ ) and inducible nitric oxide synthase (iNOS), and express many molecules that are commonly associated with monocyte/granulocytic cell types. The development of iNOS-producing IgA<sup>+</sup> plasma cells can be recapitulated *in vitro* in the presence of gut stroma, and the acquisition of this multifunctional phenotype *in vivo* and *in vitro* relies on microbial co-stimulation. Deletion of TNF- $\alpha$  and iNOS in B-lineage cells resulted in a reduction in IgA production, altered diversification of the gut microbiota and poor clearance of a gut-tropic pathogen. These findings reveal a novel adaptation to maintaining homeostasis in the gut, and extend the repertoire of protective responses exhibited by some B-lineage cells.

Most class switch recombination (CSR) to IgA takes place in the Peyer's patches and requires encounters between B cells and cytokine-secreting T cells within germinal centres. However, IgA CSR can also take place outside of Peyer's patches within isolated lymphoid follicles of the lamina propria<sup>2</sup>. Local production of nitric oxide (NO) via the inducible nitric oxide synthase (NOS2 or iNOS) has been shown to be a critical mediator of CSR to IgA within the small intestinal lamina propria of mice<sup>3,4</sup>. Because lymphotoxin-deficient mice have a significant, unexplained IgA defect<sup>5</sup>, we hypothesized that this could be due to a lack of iNOS in the gut. Indeed, we identified a population of CD11c<sup>lo</sup>iNOS<sup>+</sup> cells by flow cytometric analysis of intestinal lamina propria cell preparations, and these CD11c<sup>lo</sup>iNOS<sup>+</sup> cells were decreased in both lymphotoxin- $\beta$ -deficient and lymphotoxin- $\beta$ -receptor-deficient mice (*Ltb*<sup>-/-</sup> and *Ltbr*<sup>-/-</sup>, respectively; Fig. 1a and Supplementary Table 1), confirming a relationship between iNOS and the generation/maintenance of IgA<sup>+</sup> plasma cells<sup>4</sup>.

The absence of iNOS-expressing cells in lymphotoxin-deficient mice prompted us to ask whether B-lineage cells could influence the expression of iNOS within the gut, as lymphotoxin-deficient mice lack some B-cell subsets in the small intestinal lamina propria<sup>5</sup>. Accordingly, we

examined B-cell-deficient mice for evidence of iNOS expression in the gut and found that CD11c<sup>lo</sup>iNOS<sup>+</sup> cells were absent in *JH*<sup>-/-</sup> mice, *Rag2*<sup>-/-</sup> mice and strongly reduced in  $\mu$ Mt mice (Fig. 1b, Supplementary Table 1 and Supplementary Fig. 1a). Because lymphotoxin-deficient mice also lack IgA<sup>+</sup> plasma cells, and iNOS-expressing cells are strongly reduced in B-cell-deficient and lymphotoxin-deficient mice, we examined the possibility that IgA<sup>+</sup> plasma cells may have the capacity to produce iNOS. Indeed, when we gated on iNOS<sup>+</sup> cells, we found that they expressed IgA (Fig. 1a) and low levels of B220 (not shown), indicating that IgA-producing cells may account for significant iNOS expression within the gut in the steady state. In agreement with this result, we found that purified CD11c<sup>lo</sup>iNOS<sup>+</sup> cells exhibited evidence of a rearranged V-D-JH4 product (Supplementary Fig. 1b).

We next asked what proportion of IgA<sup>+</sup> cells express iNOS. Compared to knockout controls, a subset of IgA<sup>+</sup> plasma cells expresses iNOS and TNF- $\alpha$ , the expression of which has also been described in monocyte-derived cells<sup>6</sup> (see Fig. 1c and Supplementary Table 2 for relative frequencies of each population and Fig. 1e for immunofluorescence microscopy). We further confirmed these observations by performing cytopins on small intestinal lamina-propria-derived cells (Supplementary Figs 2 and 3). Collectively, these data indicate that gut-resident B-lineage cells contribute towards iNOS and TNF- $\alpha$  expression within the small intestinal lamina propria.

To determine better which B-lineage cells were expressing TNF- $\alpha$ /iNOS, we examined whether previous expression of activation induced cytidine deaminase (AID), an enzyme that is required for both CSR and somatic hypermutation in B cells<sup>7</sup>, correlated with iNOS and TNF- $\alpha$  expression. Using AID-Cre  $\times$  YFP mice<sup>8</sup>, we observed three populations of cells in the small intestinal lamina propria: (1) YFP<sup>+</sup> IgA<sup>-</sup> cells, that is, any lamina-propria-derived cells that have not undergone CSR nor somatic hypermutation, such as a dendritic cells or naive B cells; (2) YFP<sup>+</sup> IgA<sup>-</sup> cells, that is, B cells that have undertaken somatic hypermutation or have undergone CSR to a class of immunoglobulin other than IgA; and (3) YFP<sup>+</sup> IgA<sup>+</sup> cells, that is, B cells that have undergone CSR to IgA (Fig. 1d and Supplementary Table 3 for relative frequencies of each population). Confirming that YFP<sup>+</sup> IgA<sup>+</sup> cells probably represent IgA<sup>+</sup> plasma cells, YFP<sup>+</sup> IgA<sup>+</sup> cells also expressed low levels of the plasma cell marker syndecan-1 (CD138) and were CD19<sup>low</sup> (compare YFP<sup>+</sup> IgA<sup>+</sup> (red trace) with YFP<sup>+</sup> IgA<sup>-</sup> B cells (blue trace), which are CD138<sup>-</sup>CD19<sup>hi</sup>; Fig. 1d). Using this approach, we found that some YFP<sup>+</sup> IgA<sup>+</sup> cells (red box) expressed iNOS as well as TNF- $\alpha$  (Fig. 1d and Supplementary Table 4 for the relative expression of TNF- $\alpha$ /iNOS for each population). Furthermore, YFP<sup>+</sup> IgA<sup>+</sup> cells also expressed leukocyte surface markers commonly associated

<sup>1</sup>Department of Immunology, University of Toronto, Toronto M5S 1A8, Canada. <sup>2</sup>Ontario Cancer Institute, Princess Margaret Hospital, University Health Network, Toronto M5G 2M9, Canada. <sup>3</sup>University of Bern, Department Klinische Forschung (Gastroenterologie), Mutenstrasse 35, 3010 Bern, Switzerland. <sup>4</sup>Department of Laboratory Medicine and Pathobiology, University of Toronto, Toronto M5S 1A8, Canada. <sup>5</sup>Department of Molecular Medicine, University of Laval, Quebec G1V 4G2, Canada. <sup>6</sup>Department of Microbiology and Immunology, Columbia University Medical Center, College of Physicians and Surgeons, New York, New York 10032, USA. <sup>7</sup>Genomics and Immunity, National Institute of Arthritis and Musculoskeletal and Skin Diseases, National Institutes of Health, Bethesda, Maryland 20892, USA. <sup>†</sup>Present addresses: Complex Traits Group, Department of Microbiology and Immunology, McGill University, Montreal H3G 0B1, Canada (J.H.F.); University of Bern, Institute of Infectious Disease, Friedbühlstrasse 51, 3010 Bern, Switzerland (S.H.); Division of Biomedical Sciences, Faculty of Medicine, Memorial University of Newfoundland, St John's A1B 3V6, Canada (M.L.).

\*These authors contributed equally to this work.

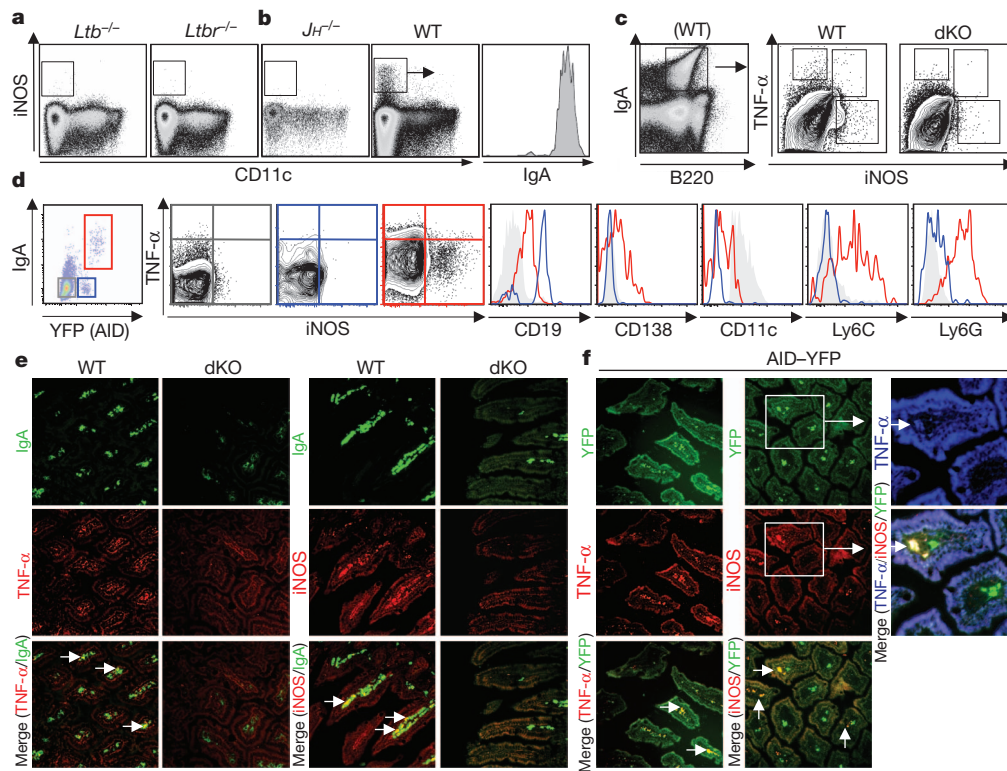


**Figure 1 | IgA<sup>+</sup> plasma cells in the small intestinal lamina propria can produce iNOS and TNF- $\alpha$ .** **a, b**, Small intestinal lamina propria cells from *Ltb*<sup>-/-</sup>, *Ltblr*<sup>-/-</sup>, *JH*<sup>-/-</sup> and wild-type (WT) mice were isolated and viable cells were analysed for CD11c and iNOS expression by flow cytometry. (See also Supplementary Table 1.) iNOS<sup>+</sup> cells were gated and analysed for IgA expression ( $n = 5$  for knockout mice and  $n = 20$  for wild-type mice). **c**, Small intestinal lamina propria cells were isolated from wild-type and *Tnfa*<sup>-/-</sup>iNOS<sup>-/-</sup> double-deficient mice and analysed for IgA, TNF- $\alpha$  and iNOS expression (note a wild-type example here for IgA/B220 staining is shown; although IgA-expressing cells are reduced in double knockout mice (*Tnfa*<sup>-/-</sup>iNOS<sup>-/-</sup> or dKO) mice as per Fig. 3c, it is possible to still gate on IgA-expressing cells within the lamina propria of double knockout mice) ( $n = 10$ –14, see also Supplementary Table 2). **d**, Intestinal lamina propria cells from AID-YFP animals were isolated and viable cells were analysed for their expression of IgA and YFP. YFP<sup>+</sup> IgA<sup>-</sup>, grey rectangle; YFP<sup>+</sup> IgA<sup>+</sup>, blue

rectangle; YFP<sup>+</sup> IgA<sup>+</sup>, red rectangle. (See also Supplementary Table 3.) These gated populations were further analysed for their expression of iNOS and TNF- $\alpha$  (note that cross-hairs were added based on isotype control staining; see also Supplementary Table 4). Expression of other lineage-specific markers for each of the three populations are denoted as histograms (YFP<sup>+</sup> IgA<sup>-</sup>, grey trace; YFP<sup>+</sup> IgA<sup>-</sup>, blue trace; YFP<sup>+</sup> IgA<sup>+</sup>, red trace). Note that for CD11c expression, YFP<sup>+</sup> IgA<sup>-</sup> dendritic cells were used as a positive control (grey trace). Representative plots are shown from  $n = 8$  mice. **e, f**, Sections of small intestines from wild-type versus double knockout mice (**e**) and AID-YFP<sup>+</sup> mice (**f**) were stained with specific fluorochrome-tagged antibodies for iNOS, TNF- $\alpha$  and IgA (or visualized for YFP) as indicated. Stained sections were then analysed by fluorescence microscopy at  $\times 200$ . Representative pictures are shown from at least three separate experiments. Arrows denote areas of co-localization and the rectangle indicates a villus that was enlarged to visualize simultaneous expression of each iNOS, TNF- $\alpha$  and YFP ( $\times 630$ ).

with monocytic and granulocytic cells, including Ly6C and Ly6G<sup>9</sup> and low levels of CD11c (Fig. 1d, for CD11c, dendritic cells (grey trace) were used as a comparator). By immunofluorescence microscopy, we found that YFP expression co-localizes with IgA expression as expected (Supplementary Fig. 4), and using these AID-YFP tissues we detected the expression of iNOS and TNF- $\alpha$  in some, but not all, YFP<sup>+</sup> cells in the small intestinal lamina propria tissue (Fig. 1f), and occasional co-expression of both iNOS and TNF- $\alpha$  was observed in YFP<sup>+</sup> cells, consistent with our flow cytometry data (Fig. 1f; see boxed insert). Taken together, we have found that a proportion of IgA<sup>+</sup> cells within the small intestinal lamina propria express the antimicrobial mediators TNF- $\alpha$  and iNOS. Although we do not detect significant expression of these molecules in other lamina propria cells (YFP<sup>+</sup> IgA<sup>-</sup> B cells, YFP<sup>-</sup> populations), it is possible that our detection methods are not sufficiently sensitive to pick up low levels of protein expression of TNF- $\alpha$  and iNOS in these cell types, or that expression of TNF- $\alpha$  and iNOS in these cells is induced during particular microbial encounters, as has been observed in non-mucosal tissues<sup>6</sup>.

Notably, not all IgA<sup>+</sup> cells expressed iNOS or TNF- $\alpha$ , or co-expressed both iNOS and TNF- $\alpha$  simultaneously (Fig. 1c, d and Supplementary Tables 2 and 4), which would make sense given the pro-inflammatory nature of these molecules. Indeed, cytospin analysis of IgA<sup>+</sup> cells that express iNOS and/or TNF- $\alpha$  revealed a different

morphology and cellular IgA localization than IgA<sup>+</sup>iNOS<sup>-</sup>TNF- $\alpha$ <sup>-</sup> cells, suggesting that acquisition of iNOS and TNF- $\alpha$  expression may be accompanied by additional activation steps beyond IgA CSR (Supplementary Figs 2 and 3). To understand further the necessary signals required for the induction of these two antimicrobial mediators in IgA<sup>+</sup> plasma cells, we assessed the expression of iNOS by IgA<sup>+</sup> plasma cells in germ-free mice. Although greatly reduced in number, IgA<sup>+</sup> cells in the lamina propria of germ-free mice did not express iNOS; however, the expression of iNOS could be recovered if germ-free mice were reconstituted with a limited microbiota (Fig. 2a). Even ‘reversible colonization’ of germ-free mice with a single species of *Escherichia coli* (HA107)<sup>10</sup> was sufficient to restore iNOS expression in IgA<sup>+</sup> cells. Therefore, microbial colonization of the gut is necessary for the expression of iNOS by IgA<sup>+</sup> plasma cells, and a single species of bacteria is sufficient.

To recapitulate what we observed *in vivo*, we assessed whether the acquisition of iNOS expression in IgA<sup>+</sup> cells could be supported by gut-derived support/stromal cells (see Methods where we describe the generation of stromal cell monolayers) compared with a bone-marrow-derived S17 stromal cell line or *ex vivo* preparations of bone marrow stroma<sup>11</sup>. In the presence of a combination of pro-IgA CSR factors, both bone marrow and gut stroma could support the development of YFP<sup>+</sup> IgA<sup>+</sup> cells from B220<sup>+</sup> bone marrow cells derived from



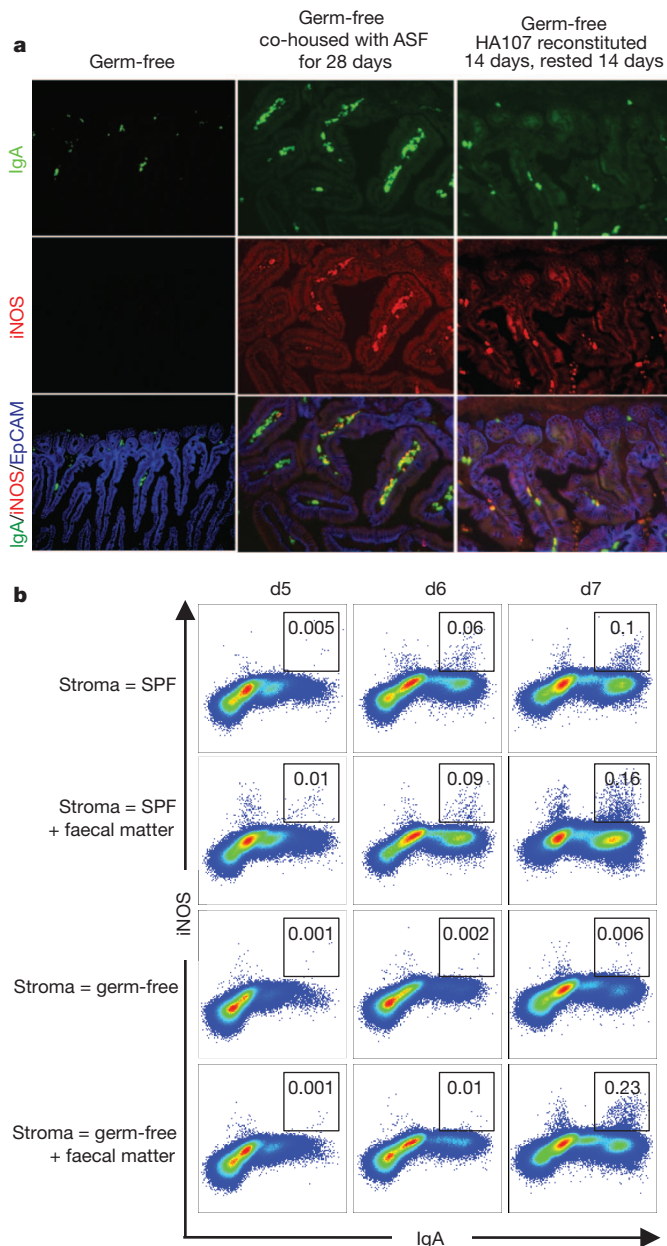


**Figure 2 | TNF- $\alpha$  and iNOS expression in IgA<sup>+</sup> plasma cells requires microbial exposure.** **a**, Sections of small intestines of germ-free mice and germ-free mice that were re-colonized with either a defined altered Schaedler flora (ASF) or reversibly re-colonized with HA107 *E. coli* by continual gavage administration for 14 days followed by 14 days without gavage returning them to a germ-free status<sup>10</sup>. All sections were stained with specific fluorochrome-tagged antibodies for IgA (green), iNOS (red) and EpCAM (blue) and analysed by fluorescence microscopy. Representative pictures are shown from 6 mice per group. **b**, B220<sup>+</sup> bone marrow cells from CD45.1<sup>+</sup> wild-type mice were co-cultured for 7 days with CD45.2<sup>+</sup> intestinal lamina propria cells (referred to as gut stroma) from either specific pathogen-free or germ-free animals in the presence of IL-7, TGF- $\beta$ , IL-21 and anti-CD40 antibody. In some cases faecal matter (intestinal wash) was added on the first day of the culture. The expression of IgA and iNOS was analysed by flow cytometry, and the black boxes indicate cells that are iNOS<sup>+</sup>. To ensure selective analysis of bone-marrow-derived precursors, cells were pre-gated on the CD45.2<sup>+</sup> population. Representative flow cytometry plots of cells are depicted. Data are representative of at least two independent experiments with 3–4 mice per group per experiment.

AID-YFP mice. However, only gut stroma, but not S17 or bone-marrow-derived stroma, was able to support the development of iNOS<sup>+</sup> IgA<sup>+</sup> cells (Supplementary Fig. 5a, b). Interestingly, gut stroma from *Ltbr*<sup>-/-</sup> mice was likewise able to support the development of

iNOS<sup>+</sup> IgA<sup>+</sup> cells in the presence of pro-IgA CSR factors, indicating that the defective CSR observed in *Ltbr*<sup>-/-</sup> mice can be overcome *in vitro* in the presence of exogenous cytokines and CD40 ligation (Supplementary Fig. 5b). Not unlike the *in vivo* scenario, microbes are required for *in vitro* development of iNOS<sup>+</sup> IgA<sup>+</sup> cells, as preparations of gut stroma from specific pathogen-free but not germ-free mice supports the development of iNOS<sup>+</sup> IgA<sup>+</sup> cells (Fig. 2b). Furthermore, co-incubation of germ-free gut stroma with faecal matter derived from specific pathogen-free mice restores the development of iNOS<sup>+</sup> IgA<sup>+</sup> cells (Fig. 2b). Thus, our *in vivo* and *in vitro* results suggest that the gut microenvironment, influenced by the local microbiota, supports the development of multifunctional B cells that express IgA and iNOS.

To examine the functional relevance of TNF- $\alpha$ /iNOS expression in IgA<sup>+</sup> cells, we created TNF- $\alpha$ /iNOS double knockout mice (*Tnfa*<sup>-/-</sup> *iNOS*<sup>-/-</sup> mice). *Tnfa*<sup>-/-</sup> *iNOS*<sup>-/-</sup> mice exhibited reduced levels of serum IgA (Fig. 3a), and this reduction was more marked than what we observed for *iNOS*<sup>-/-</sup> single knockout mice, which, in agreement with previous findings<sup>4</sup>, also exhibited decreased levels of serum IgA (data not shown). Bone marrow from double knockout mice, in combination with B-cell-deficient *JH*<sup>-/-</sup> bone marrow, was used to reconstitute B-cell-deficient, lethally irradiated recipients, thus creating mixed bone marrow chimaeras in which B cells are unable to produce TNF- $\alpha$ /iNOS (see Supplementary Fig. 6). *JH*<sup>-/-</sup> plus double knockout mixed chimaeric mice exhibited a normal complement of immune cells in the periphery, although we did note some changes in splenic microarchitecture (Supplementary Fig. 7), in agreement with the effects of B-cell-derived TNF- $\alpha$  on splenic stromal cell biology<sup>12</sup>. Consistent with a role for TNF- $\alpha$ /iNOS in the regulation of CSR to IgA (ref. 4), *JH*<sup>-/-</sup> plus double knockout mixed bone marrow chimaeric mice exhibited a significant drop in serum IgA but not IgG1 when compared with two groups of control mixed bone marrow chimaeric mice (double knockout plus wild type and *JH*<sup>-/-</sup> plus wild type mixed bone marrow chimaeric mice) (Fig. 3a, b), and this decrease in serum IgA tracked with significant reductions in IgA<sup>+</sup> cells within the lamina propria as quantified by immunofluorescence microscopy (Fig. 3c, d). Although all mixed bone marrow recipients were generated using the same cohort of recipient mice, we observed changes in the composition of the commensal bacterial community in the small intestine of *JH*<sup>-/-</sup> plus wild type versus *JH*<sup>-/-</sup> plus double knockout reconstituted mixed bone marrow chimaeric mice (Fig. 3e). Focusing on microbial populations that are known to influence immune cell function<sup>13</sup>, we noted that segmented filamentous bacteria were nearly absent from *JH*<sup>-/-</sup> plus double knockout mixed bone marrow chimaeras in small intestinal tissue ( $P < 0.05$ ), as well as in small intestinal 'scrapes' enriched for epithelial cells (not shown). In contrast, *Clostridium leptum* and *Bacillus* were increased in small intestinal tissue of *JH*<sup>-/-</sup> plus double knockout mixed chimaeras, and this may possibly account for the reduced frequency of segmented filamentous bacteria. The altered composition of commensal microbiota probably reflects the deficiency in TNF- $\alpha$ /iNOS rather than a reduction in IgA, as mice that are completely IgA-deficient exhibit excessive outgrowth of segmented filamentous bacteria<sup>14</sup>. Therefore, although our data do not eliminate the possibility that complete deletion of TNF- $\alpha$ /iNOS in all monocytes/dendritic cells would have an impact on IgA production, these results show that the expression of TNF- $\alpha$ /iNOS in B-lineage cells is essential for the homeostatic production of IgA and the maintenance of an appropriate representation of different commensal microbes within the small intestine.

We next assessed the impact of TNF- $\alpha$ /iNOS deletion in B cells on clearance of the mouse pathogen *Citrobacter rodentium*, which colonizes the caecum and large intestine following infection. First, using AID-YFP mice, we found that *C. rodentium* infection results in a significant accumulation of YFP<sup>+</sup> IgA<sup>+</sup> cells as well as YFP<sup>+</sup> CD11c<sup>+</sup> cells (but not IgA<sup>-</sup> B cells) in the caecum and large intestine as early as 36 h after infection (Fig. 4a–c). With these kinetics established, we infected *JH*<sup>-/-</sup> plus wild type versus *JH*<sup>-/-</sup> plus double knockout mixed bone marrow chimaeras with *C. rodentium*. Interestingly, *C.*



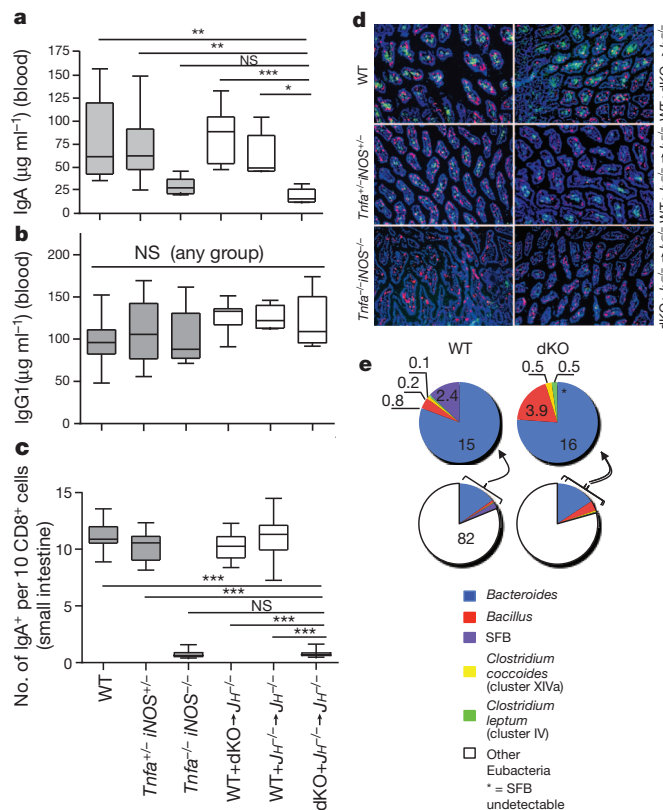


**Figure 3 | Reduced IgA production and altered commensal flora composition in iNOS/TNF-α double-deficient mixed chimaeric mice.**

**a, b**, Steady-state serum IgA, but not IgG1, levels are markedly decreased in double knockout and double knockout mixed chimaeras. Serum IgA and IgG1 levels were measured by ELISA in wild-type ( $n = 15$ ), *Tnfr1*<sup>+/+</sup> *iNOS*<sup>+/+</sup> ( $n = 12$ ) and *Tnfr1*<sup>-/-</sup> *iNOS*<sup>-/-</sup> (dKO,  $n = 7$ ) non-chimaeric mice as well as in wild-type plus double knockout ( $n = 8$ ), *JH*<sup>-/-</sup> plus wild-type ( $n = 5$ ) and *JH*<sup>-/-</sup> plus double knockout ( $n = 6$ ) mixed chimaeric mice. Similar results were obtained with two additional batches of mixed bone marrow chimaeric mice (not shown). Data represent median, quartiles and range values. **c**, The numbers of small intestinal lamina propria IgA<sup>+</sup> plasma cells and CD8α<sup>+</sup> cells were quantified from immunofluorescence microscopy images using ImageJ. A total of five different sections from 6 mice ( $n = 6$ ) per group was analysed. **d**, Representative images of frozen small intestinal tissue sections derived from the groups described in **a–c** stained for CD8α (red), IgA (green) and DAPI (blue). A total of five different sections from 6 mice per group were analysed. **e**, Seven weeks after bone-marrow reconstitution, the small intestines of wild-type and double knockout mixed chimaeras ( $n = 4$  for each group) were analysed for their commensal bacteria composition by quantitative real-time PCR amplification of 16S rRNA isolated from small intestinal preparations. Coloured pie graphs represent the percentages of the indicated bacteria species. A significant difference in the relative representation of segmented filamentous bacteria (SFB) was observed between wild-type and double knockout mice. Similar results for segmented filamentous bacteria were obtained in small intestinal scrapes of the epithelium (data not shown). Data represent means and s.d. values. \*\*\* $P = 0.001$ , \*\* $P = 0.01$ , \* $P < 0.05$ .

*rodentium* translocation to the spleen, enhanced weight loss and colonic pathology were all noted in *JH*<sup>-/-</sup> plus double knockout but not *JH*<sup>-/-</sup> plus wild type mixed chimaeric mice (Fig. 4d–f). Similar impaired clearance of *C. rodentium* was observed in *JH*<sup>-/-</sup> plus double knockout mixed bone marrow chimaeric mice when they were directly

compared with another control group (wild type plus double knockout mixed bone marrow chimaeras; see Supplementary Fig. 8a–c). Because we did not observe an accumulation of IgA<sup>+</sup> B cells at the site of infection, by inference we conclude that along with other dendritic-cell-mediated immune mechanisms, TNF-α/iNOS production by

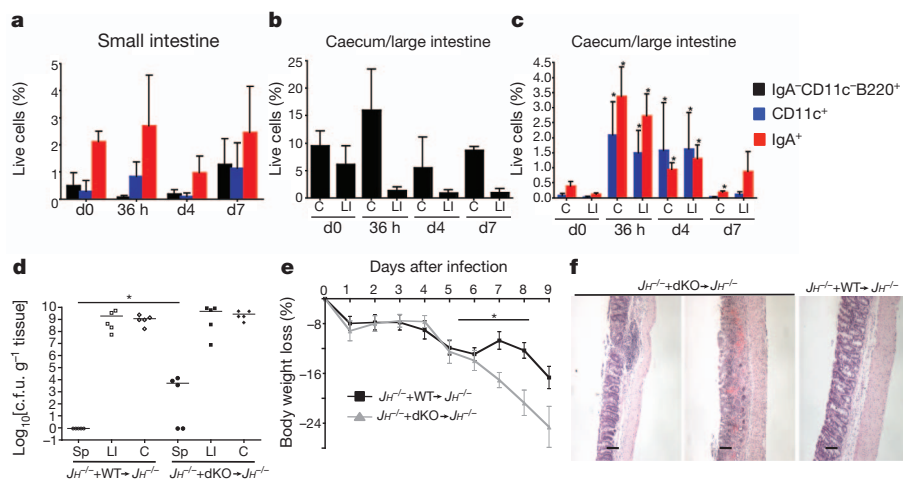


**Figure 4 | iNOS/TNF-α double-deficient mixed chimaeras are more susceptible to infection with *C. rodentium*.** AID-YFP animals were infected by oral gavage with  $1 \times 10^5$  colony-forming units (c.f.u.) of a nalidixic-acid-resistant strain of *C. rodentium* DBS100. **a–c**, The kinetics of accumulation of viable YFP<sup>+</sup> IgA<sup>+</sup> CD11c<sup>+</sup> B220<sup>+</sup> (black bars), YFP<sup>+</sup> CD11c<sup>+</sup> (blue bars) and YFP<sup>+</sup> IgA<sup>+</sup> (red bars) cells in the small intestine, the caecum (C) and the large intestine (LI) was analysed by flow cytometry (day 0 (d0), 36 h, day 4 (d4) and day 7 (d7)). The percentages of viable cells as mean and s.e.m. values are shown ( $n = 4$ ). A representative example of two individual experiments is shown. **d**, The colonization by *C. rodentium* was determined 9 days after infection. *C. rodentium* colonization of spleen (Sp) is significantly enhanced in double knockout (dKO) mice at day 9 after infection and at day 4 after infection (data not shown). Data are representative of two individual experiments from at least 5 mice per group in each experiment. Mean values are shown. **e**, The percentage of body weight loss in wild-type plus *JH*<sup>-/-</sup> *Rag*<sup>-/-</sup> and dKO + *JH*<sup>-/-</sup>

*JH*<sup>-/-</sup> *Rag*<sup>-/-</sup> mixed chimaeras after *C. rodentium* infection over time is depicted. Significantly increased body weight loss was observed in double knockout mice from day 6 to 9 after infection ( $n = 5–12$  per group). Note that double knockout plus *JH*<sup>-/-</sup> mixed chimaeric mice were killed 9 days after infection for humane reasons as weight loss exceeded 20% of their original body weight. Mean and s.e.m. values are shown. **f**, Large intestines from wild-type plus *JH*<sup>-/-</sup> and double knockout plus *JH*<sup>-/-</sup> mixed chimaeric mice were harvested 9 days after infection and the pathological scores were analysed by standard histological staining procedures using haematoxylin and eosin. Large intestines from double knockout plus *JH*<sup>-/-</sup> mice show more severe large intestine pathology. Haematoxylin and eosin stainings of two representative double knockout mice with a moderate and a more severe condition, as well as one representative wild-type plus *JH*<sup>-/-</sup> chimaeric mouse, are shown ( $n = 5$  mice per group). The panel shows the original magnification of  $\times 100$ . Scale bars represent 100 μm. \* $P < 0.05$ .

IgA<sup>+</sup> plasma cells is required, either directly or indirectly, for optimal control of *C. rodentium* in the gut, although it cannot be excluded at this stage that TNF- $\alpha$ /iNOS production by other B-lineage cells outside of the gut may have contributed to the observed phenotype. Moreover, we cannot eliminate the possibility that production of TNF- $\alpha$ /iNOS by B-lineage cells may have provoked the expression of TNF- $\alpha$ /iNOS in monocytes/dendritic cells to control the infection. Nevertheless, our findings show that B-cell-associated TNF- $\alpha$ /iNOS production is critical for control of *C. rodentium*, and this may explain why B-cell-deficient mice, but not IgA<sup>-/-</sup> mice or mice that lack secreted IgM, also fail to control *C. rodentium*<sup>15</sup>.

The immune system responds differently to antigens encountered systemically as opposed to at mucosal surfaces<sup>1</sup>. We postulate that in the process of differentiating to become IgA<sup>+</sup> plasma cells, the gut environment may have imprinted IgA<sup>+</sup> cells with more 'monocytic' potential, a phenomenon that has been previously observed *in vitro*<sup>16</sup>. Indeed, there is a precedent for B cells to display non-conventional 'monocyte/dendritic cell' functions in other species<sup>17</sup> and in response to TLR ligation<sup>18</sup>, and B cells have emerged as important effector<sup>19</sup> and regulatory cells<sup>20</sup> during innate responses to bacterial infection. Furthermore, B cells and monocytes share common precursors during their development<sup>21,22</sup>, and plasma cells have been recently shown to possess antigen-presenting capacity<sup>23</sup>. These results document a novel effector mechanism for IgA<sup>+</sup> plasma cells, which seems to arise in the unique environment of the gut, and may be critical to mount effective responses to microbial assault.

## METHODS SUMMARY

**Mice.** Mice were either purchased from commercial vendors or bred in-house at the University of Toronto. Germ-free wild-type mice were re-derived and maintained in the Germ-free Unit at McMaster University or the University of Bern, Switzerland. Germ-free wild-type mice were re-associated with a low-complexity microbiota, by co-housing with gnotobiotic mice that had been associated with the altered Schaedler flora. Reversible colonization experiments were carried out by gavaging germ-free mice with the *E. coli* K12 triple mutant strain HA107 and subsequently rested germ-free.

**Cell purification and flow cytometry.** Small intestine (free of Peyer's patches) as well as large intestine and the caecum were dissected, washed and epithelial cells were removed. Remaining tissue was digested with collagenase and the resulting suspension was filtered and analysed by flow cytometry or used for cytospin preparations. For flow cytometry, cells were subjected to aqua dead cell stain, then incubated with Fc-block followed by incubation with pre-determined concentrations of fluorochrome labelled antibodies to cell-surface markers, fixed/permeabilized and incubated with pre-determined concentrations of fluorochrome labelled antibodies to intracellular proteins. Cells were acquired using either a FACS Cailbur or a LSR-II (BD Biosciences). Acquired data were analysed and processed using FlowJo.

**Immunofluorescence microscopy.** Re-hydrated 5  $\mu$ m sections of small intestinal tissue were subjected to blocking with serum and Fc-block followed by staining with fluorochrome-labelled antibodies. Slides were then stained with DAPI before being mounted with Gel/Mount and visualized with a Leica DMRA2 microscope accompanied by OpenLab software (Improvision).

**Co-culture of stromal cells and bone marrow cells.** Bone-marrow- or lamina-propria-derived stromal cells were plated together with bone-marrow-derived B220<sup>+</sup> congenically disparate (CD45.1) cells. Co-cultures were supplemented with IgA switch factors including TGF- $\beta$ , IL-21 and anti-CD40 as well as IL-7. At the indicated times, cells were harvested and analysed by flow cytometry.

**Full Methods** and any associated references are available in the online version of the paper at [www.nature.com/nature](http://www.nature.com/nature).

**Received 11 June; accepted 4 November 2011.**

**Published online 11 December 2011.**

- Hooper, L. V. & Macpherson, A. J. Immune adaptations that maintain homeostasis with the intestinal microbiota. *Nature Rev. Immunol.* **10**, 159–169 (2010).
- Fagarasan, S., Kawamoto, S., Kanagawa, O. & Suzuki, K. Adaptive immune regulation in the gut: T cell-dependent and T cell-independent IgA synthesis. *Annu. Rev. Immunol.* **28**, 243–273 (2010).
- Lee, M. R., Seo, G. Y., Kim, Y. M. & Kim, P. H. iNOS potentiates mouse Ig isotype switching through AID expression. *Biochem. Biophys. Res. Commun.* **410**, 602–607 (2011).

- Tezuka, H. *et al.* Regulation of IgA production by naturally occurring TNF/iNOS-producing dendritic cells. *Nature* **448**, 929–933 (2007).
- Kang, H. S. *et al.* Signaling via LT $\beta$ R on the lamina propria stromal cells of the gut is required for IgA production. *Nature Immunol.* **3**, 576–582 (2002).
- Serbina, N. V., Salazar-Mather, T. P., Biron, C. A., Kuziel, W. A. & Pamer, E. G. TNF/iNOS-producing dendritic cells mediate innate immune defense against bacterial infection. *Immunity* **19**, 59–70 (2003).
- Muramatsu, M. *et al.* Class switch recombination and hypermutation require activation-induced cytidine deaminase (AID), a potential RNA editing enzyme. *Cell* **102**, 553–563 (2000).
- Crouch, E. E. *et al.* Regulation of AID expression in the immune response. *J. Exp. Med.* **204**, 1145–1156 (2007).
- Serbina, N. V. & Pamer, E. G. Monocyte emigration from bone marrow during bacterial infection requires signals mediated by chemokine receptor CCR2. *Nature Immunol.* **7**, 311–317 (2006).
- Hapfelmeier, S. *et al.* Reversible microbial colonization of germ-free mice reveals the dynamics of IgA immune responses. *Science* **328**, 1705–1709 (2010).
- Cumano, A., Dorshkind, K., Gillis, S. & Paige, C. J. The influence of S17 stromal cells and interleukin 7 on B cell development. *Eur. J. Immunol.* **20**, 2183–2189 (1990).
- Tumanov, A. V. *et al.* Cellular source and molecular form of TNF specify its distinct functions in organization of secondary lymphoid organs. *Blood* **116**, 3456–3464 (2010).
- Ivanov, I. I. & Littman, D. R. Modulation of immune homeostasis by commensal bacteria. *Curr. Opin. Microbiol.* **14**, 106–114 (2011).
- Suzuki, K. *et al.* Aberrant expansion of segmented filamentous bacteria in IgA-deficient gut. *Proc. Natl Acad. Sci. USA* **101**, 1981–1986 (2004).
- Maaser, C. *et al.* Clearance of *Citrobacter rodentium* requires B cells but not secretory immunoglobulin A (IgA) or IgM antibodies. *Infect. Immun.* **72**, 3315–3324 (2004).
- Delogu, A. *et al.* Gene repression by Pax5 in B cells is essential for blood cell homeostasis and is reversed in plasma cells. *Immunity* **24**, 269–281 (2006).
- Li, J. *et al.* B lymphocytes from early vertebrates have potent phagocytic and microbicidal abilities. *Nature Immunol.* **7**, 1116–1124 (2006).
- Johnson, B. A. *et al.* B-lymphoid cells with attributes of dendritic cells regulate T cells via indoleamine 2,3-dioxygenase. *Proc. Natl Acad. Sci. USA* **107**, 10644–10648 (2010).
- Kelly-Scumpia, K. M. *et al.* B cells enhance early innate immune responses during bacterial sepsis. *J. Exp. Med.* **208**, 1673–1682 (2011).
- Neves, P. *et al.* Signaling via the MyD88 adaptor protein in B cells suppresses protective immunity during *Salmonella typhimurium* infection. *Immunity* **33**, 777–790 (2010).
- Cumano, A., Paige, C. J., Iscove, N. N. & Brady, G. Bipotential precursors of B cells and macrophages in murine fetal liver. *Nature* **356**, 612–615 (1992).
- Montecino-Rodriguez, E., Leathers, H. & Dorshkind, K. Bipotential B-macrophage progenitors are present in adult bone marrow. *Nature Immunol.* **2**, 83–88 (2001).
- Pelletier, N. *et al.* Plasma cells negatively regulate the follicular helper T cell program. *Nature Immunol.* **11**, 1110–1118 (2010).

**Supplementary Information** is linked to the online version of the paper at [www.nature.com/nature](http://www.nature.com/nature).

**Acknowledgements** We thank D. White in the Faculty of Medicine Flow Cytometry core facility and H. Singh for critical reading of the manuscript. We thank E. Verdu for providing additional germ-free mice at short notice, and we also thank C. Guidos for numerous Rag2<sup>-/-</sup> mice for mixed bone marrow chimeras. C.J.P. is supported by a CIHR operating grant MOP number 9862. R.C. is supported in part by the Intramural Research Program of the National Institute of Arthritis and Musculoskeletal and Skin Diseases of the National Institutes of Health. I.I.I. is supported by NIH (R00 DK085329-02) and CCA (CDA #2388). A.M. is supported by a CIHR operating grant MOP number 89783. J.H.F. acknowledges support by an APART-fellowship of the Austrian Academy of Sciences, McGill start-up funds and a CIHR operating grant MOP number 114972. N.S. acknowledges the support of a CIHR Doctoral Award. J.L.G. is funded by the Canadian Institutes of Health Research (CIHR) and acknowledges the support of CIHR operating grant MOP number 67157 as well as infrastructure support from the Ontario Research Fund and that Canadian Foundation for Innovation. All authors have reviewed and agree with the content of the manuscript.

**Author Contributions** J.H.F. generated data in Figs 1d–f, 3a–d, 4d–f and Supplementary Figs 2–4, 7 and 8. O.L.R. contributed data in Figs 1a–d, 3a, b, 4, Supplementary Figs 7, 8 and Supplementary Tables 1–3. N.S. and C.J.P. contributed data in Fig. 2b and Supplementary Fig. 6. D.D.M. contributed data in Figs 1a, b, 2a and Supplementary Figs 1–3. S.H. contributed data in Fig. 2a. A.M. and M.L. contributed Supplementary Fig. 1b (D.M. did the sort). R.C. provided AID–YFP mice. I.I.I. originally suggested that we examine IgA<sup>+</sup> plasma cells as putative TNF- $\alpha$ /iNOS-producing cells and urged us to do the initial experiments. D.J.P. and S.J.R. contributed data in Fig. 3e and provided critical insights. S.E.G. and S.R. helped us set up the *Citrobacter rodentium* experiments and provided critical insights. A.J.M., S.H. and K.D.M. provided intestinal tissues from germ-free and re-colonized mice. J.G. provided gene-deficient mice. J.L.G. wrote the manuscript and obtained funding for the work from the Canadian Institutes of Health Research.

**Author Information** Reprints and permissions information is available at [www.nature.com/reprints](http://www.nature.com/reprints). The authors declare no competing financial interests. Readers are welcome to comment on the online version of this article at [www.nature.com/nature](http://www.nature.com/nature). Correspondence and requests for materials should be addressed to J.L.G. ([jen.gommerman@utoronto.ca](mailto:jen.gommerman@utoronto.ca)).



## METHODS

**Mice.** Wild-type C57BL/6.CD45.2 mice were obtained from in-house breeding or from commercial vendors. We compared the population of iNOS<sup>+</sup> cells in small intestinal lamina propria preparations from Charles River Laboratories, from Taconic and from Jackson Laboratories and found no significant differences in the frequency of iNOS<sup>+</sup> cells (data not shown). C57BL/6.CD45.1,  $\mu$ Mt, *Rag2*<sup>-/-</sup> and CD19-YFP were all purchased from Jackson Laboratories and bred in-house. *Tnfr*<sup>-/-</sup> and iNOS<sup>-/-</sup> deficient animals were purchased from Taconic and crossed. *Ltb*<sup>-/-</sup> mice were purchased from B&K Universal. *Ltbr*<sup>-/-</sup> mice were obtained from R. D. Newberry. AID-YFP<sup>8</sup> was provided by R. Casellas. *JH*<sup>-/-</sup> mice were obtained from S. Fillatreau. All animals were housed in specific pathogen-free conditions and all experiments were performed according to animal use protocols approved by the animal care committee of the Ontario Cancer Institute and the University of Toronto.

**Germ-free mice and microbiota re-associations.** C57BL/6 mice were re-derived to germ-free by two-cell embryo transfer and were maintained germ-free in flexible film isolators at the Farncombe Axenic and Germ-free Unit of the Central Animal Facility, McMaster University, Canada or in the Clean Animal Facility, University of Bern, Switzerland as previously described<sup>10</sup>. For re-colonization experiments, C57BL/6 mouse colonies were re-associated with a low-complexity microbiota, by co-housing with gnotobiotic mice that had been associated with the altered Schaedler flora (ASF, Taconic) consisting of eight different bacteria<sup>24</sup>, according to the protocol available at Taconic (<http://www.taconic.com/library>). These mice were used as ASF experimental mice and as sentinel colonizers for ASF re-associations of germ-free animals. Re-associated animals were maintained under barrier conditions in IVC cages in the Farncombe Axenic and Germ-free Unit or in the Clean Animal Facility, University of Bern, Switzerland, as previously described<sup>10</sup>. Reversible colonization experiments were carried out by gavaging germ-free mice four times with the *E. coli* K12 triple mutant strain HA107 (ref. 10) over 14 days and subsequently rested germ-free for 14 days. All animal experiments were carried out in accordance with the McMaster University animal utilization protocols and the Canadian Council on Animal Care (CCAC) guidelines or in accordance with Swiss federal regulations.

**Mixed bone marrow chimaeras.** *Rag2*<sup>-/-</sup> or *JH*<sup>-/-</sup> mice were irradiated with two consecutive doses of 550 rad using a MDS-Nordion Gammacell 40 irradiator and subsequently reconstituted by intravenous injection with  $1 \times 10^6$  red-blood-cell-depleted bone marrow cells (ratio 2:1 for all three groups: *JH*<sup>-/-</sup>:WT; *JH*<sup>-/-</sup>:*Tnfr*<sup>-/-</sup>:iNOS<sup>-/-</sup> and WT:*Tnfr*<sup>-/-</sup>:iNOS<sup>-/-</sup>) from sex-matched donors. Mice were then provided 2 mg ml<sup>-1</sup> neomycin-sulphate (Sigma-Aldrich) supplemented drinking water for 2 weeks after irradiation. Mice were further used for experiments following 8–10 weeks of reconstitution.

**Bacterial infection.** A nalidixic-acid-resistant strain of *C. rodentium* DBS100 (provided by B. Finlay) was grown overnight at 37 °C with moderate shaking.  $1 \times 10^9$  colony-forming units (c.f.u.) of the overnight culture, which was washed once in PBS, were used to inoculate mice by oral gavage. The mice were fasted for 3 h before challenge. The percentage of body weight loss of animals after infection was monitored. At indicated time points animals were killed and organ colonization by *C. rodentium* was determined by homogenizing tissues in sterile PBS using a rotor homogenizer followed by serial dilution plating on nalidixic-acid-containing LB plates. For pathological examination of tissues, large intestines were collected, the faecal content removed and washed twice in PBS and opened longitudinally. Tissues were fixed for 2 days in 10% formalin, washed twice with PBS and fixed for 18 h in 70% ethanol. Samples were embedded in paraffin, sectioned and analysed by standard histological staining procedures using haematoxylin and eosin.

**Immunofluorescence microscopy.** Small intestines were cut out and mesentery and fat removed. After gently pushing out the faecal content, small intestines were washed twice in PBS and cut open longitudinally and pieces were frozen in OCT compound (Sakura Finetek). Similarly, spleens from animals were removed and frozen in OCT. Spleens and intestinal tissue sections were cut at 5  $\mu$ m using a Leica CM3050 cryostat (Leica Microsystems), mounted on glass microscope slides and fixed in acetone. Sections were washed TBS followed by TBS-T (TBS plus 0.05% Tween-20 (Sigma Aldrich)), then incubated with TBS-T supplemented with 10% normal rabbit serum (Jackson Laboratories), 10% normal mouse serum (Jackson Laboratories), 5% BSA (Sigma) and 2  $\mu$ g ml<sup>-1</sup> of a rat anti-mouse CD16/CD32 antibody (Fc-block, clone: 2.4G2) for 30 min to block nonspecific staining. Fluorochrome labelled antibodies were applied for 45 min in the dark. The following antibodies were used: rat anti-mouse IgA-FITC (11-44-2, Southern Biotech), rabbit anti-mouse iNOS-PE (N-20, Santa Cruz Biotechnology), rat anti-mouse CD8 $\alpha$ -PE (53-6.7) rat anti-mouse EpCAM-APC (G8.8), rat anti-mouse TNF- $\alpha$ -APC (MP6-XT22), rabbit anti-mouse TNF- $\alpha$  (610325, R&D) followed by biotinylated anti-rabbit (Molecular probes) and Streptavidin-PE, rat anti-mouse CD21/CD35-biotin (8D9) followed by Streptavidin-Alexa488 (Invitrogen). Except otherwise mentioned, all antibodies were purchased from

eBioscience. After removal of the staining solution slides were washed three times with TBS-T, once with TBS and once with PBS. Finally, slides were stained with DAPI nucleic acid stain (Invitrogen) for 30 s and washed three times with PBS before being mounted with Gel/Mount (Biomeda Corp.). Images were acquired with a Leica DMRA2 microscope (Leica Microsystems) equipped with a Retiga EXi digital camera (Q Imaging) using OpenLab software (Improvision) and Adobe Photoshop. Quantification of IgA and CD8 $\alpha$ <sup>+</sup> cells was performed using Image J.

**Isolation of intestinal lamina propria cells.** Small and large intestines were cut out and mesentery and fat removed, flushed, Peyer's patches were removed and the intestine was cut open longitudinally and into pieces of ~5 mm. The caecum was opened, the content removed and the tissue cut in pieces. Tissue pieces were washed twice by gentle vortexing for a few seconds in ice-cold buffer (HBSS (Gibco) supplemented with 2% FBS (PAA) and 15 mM HEPES pH 7.4). The epithelial cells and intestinal epithelial lymphocytes were then removed by transferring the gut pieces to an EDTA-containing buffer (HBSS (Gibco) supplemented with 10% FBS (PAA), 5 mM EDTA, 15 mM HEPES, buffered with NaOH at pH 7.4) and shaken vigorously at room temperature for 10 min, vortexed gently for a few seconds, before decanting the supernatant. This wash step was repeated three times. Gut pieces were then washed three times in cold HBSS buffer (Gibco) to remove residual EDTA before transfer into RPMI 1640 supplemented with 10% FBS (PAA), 15 mM HEPES pH 7.4, collagenase type IV (0.25 mg ml<sup>-1</sup>, Sigma) and DNase I (0.05 mg ml<sup>-1</sup>, Roche) for digestion of tissue for approximately 1–2 h at 37 °C with occasional vortexing. The resulting suspension was filtered through a 70  $\mu$ m nylon cell strainer to obtain a single cell suspension. Finally cells were washed and re-suspended in ice-cold FACS buffer containing PBS supplemented with 2% FBS (PAA) and analysed by flow cytometry or used for cytospin preparations.

**Isolation of splenocytes.** Spleens were collected and fat was removed. Tissue was gently homogenized with glass slides in digestion buffer (HBSS (Gibco) supplemented with 10 mM HEPES, 150 mM NaCl, 5 mM KCl, 1 mM MgCl<sub>2</sub>, 1.8 mM CaCl<sub>2</sub>, 1 mg ml<sup>-1</sup> collagenase D (Roche) and 0.2 mg ml<sup>-1</sup> DNase I (Roche)) and incubated for 30 min at 37 °C. The cell suspension was homogenized by gentle pipetting before being incubated for an additional 15 min at 37 °C before the addition of EDTA (final concentration 1 mM) and incubation for 10 min at room temperature. Cells were pelleted and re-suspended in red blood cell lysis buffer for 1 min on ice (150 mM NH<sub>4</sub>Cl, 100 mM NaHCO<sub>3</sub>, 1 mM EDTA pH 8.0). Cells were then re-suspended in FACS buffer (PBS supplemented with 2% FBS (PAA)) and pelleted by centrifugation. Finally, cells were filtered through a 70  $\mu$ m nylon cell strainer and pelleted by centrifugation, re-suspended in FACS buffer (PBS supplemented with 2% FBS (PAA)) and analysed by flow cytometry.

**Flow cytometry.** Cells were washed with ice-cold PBS (no FBS) and before antibody staining a live/dead stain was applied using the fixable aqua dead cell stain kit (Invitrogen). After that, cells were transferred to ice-cold PBS + 2% FBS (PAA) and incubated with 1  $\mu$ g ml<sup>-1</sup> of a rat anti-mouse CD16/CD32 antibody (Fc-block, clone: 2.4G2) to block unspecific staining for 15 min at 4 °C. Predetermined concentrations of fluorochrome-labelled antibodies were added in a total volume of 100  $\mu$ l, thoroughly mixed with the cells and incubated for 15 min at 4 °C. The following antibodies were used: murine anti-mouse CD45.1-Pacific Blue (A20), murine anti-mouse CD45.2-Pacific blue (104, Biolegend), rat anti-mouse CD11b-FITC (M1/70), rat anti-mouse Ly6C-PerCP-Cy5.5 (HK1.4), rat anti-mouse CD11b-APC (M1/70), hamster anti-mouse CD11c-APC (N418), rat anti-mouse CD11b-PE-Cy7 (M1/70), hamster anti-mouse CD11c-PE-Cy7 (N418), rat anti-mouse CD19-FITC (ID3), rat anti-mouse CD4-PE (GK1.5), rat anti-mouse CD8 $\alpha$ -PerCP-Cy5.5 (53-6.7), rat anti-mouse CD45R (B220)-eFluor450 (RA3-6B2), rat anti-mouse Ly6G-PE (1A8, BD Biosciences), and rat anti-mouse CD138-APC (281-2, BD Biosciences). After washing with FACS buffer, cells were fixed and permeabilized using a cytofix/cytoperm kit from BD Biosciences according to the manufacturer's protocol. Intracellular staining was then performed for 30 min at 4 °C using the following antibodies: rat anti-mouse IgA-FITC (11-44-2, Southern Biotech), IgA-PE (11-44-2, Southern Biotech), rat anti-mouse IgA-biotin (11-44-2) followed by Streptavidin-APC-Cy7 or Streptavidin PerCP-Cy5.5, murine anti-mouse iNOS-FITC (6, BD Biosciences), mouse anti-mouse IgG1 iNOS-Alexa647 (C-11, Santa Cruz Biotechnology) used fresh at 1/25 and compared with an Alexa647-conjugated mouse anti-mouse IgG1 isotype control, rat anti-mouse TNF- $\alpha$ -PE (MP6-XT22, BD), rat anti-mouse TNF- $\alpha$ -APC (MP6-XT22, BD). Except otherwise mentioned, all antibodies have been purchased from eBioscience. Cells were then washed twice with Perm/Wash buffer and re-suspended in FACS buffer before analysis by flow cytometry using either a FACS Cailbur, or Canto II or an LSR-II (BD Biosciences). Acquired data were analysed and processed using FlowJo (Tree Star Inc.).

**Analysis of VDJ recombination.** Intestinal lamina propria cells and splenocytes were isolated and stained with the antibodies as described above. Lamina propria cells and splenocytes were sorted for CD3 $\epsilon$ <sup>+</sup> or CD19<sup>+</sup> populations. In addition,



lamina propria cells were stained for CD3 $\epsilon$  and B220 and the CD3 $\epsilon$ <sup>+</sup>B220<sup>+</sup> population was then sorted for CD11c<sup>lo</sup>iNOS<sup>+</sup> and CD11c<sup>hi</sup>iNOS<sup>+</sup> populations using a FACSaria (BD Biosciences) and placed in Trizol (Sigma-Aldrich). Genomic DNA from 10<sup>5</sup>–10<sup>6</sup> sorted cells of the shown phenotype were then subject to PCR to amplify all heavy chain V(D)J-rearranged products, however this PCR will preferentially amplify V-D-JH4 products as this product is the smallest among PCR products<sup>25</sup>. Briefly, the VH<sub>all</sub> primer and JH4-C intronic primer were used to amplify joints. Thirty-five cycles (94 °C for 30 s, 54 °C for 30 s, 72 °C for 2 min) were carried out. PCR products were separated on 0.9% agarose gels, Southern blotted and probed with an internal (coding region) JH4-specific probe.

**Analyses of serum immunoglobulin.** Sera from animals were prepared and analysed by sandwich ELISA on serially diluted samples by coating the primary antibody (goat anti-mouse immunoglobulin (H+L), Southern Biotechnologies) to 96-well plates (MaxiSorp; Nalgene Nunc). IgA (eBioscience) and IgG1 (15H6, Southern Biotechnologies) isotypes were used as standards. Standard and bound antibodies of plated sera samples were then detected by sequential incubation with biotinylated secondary antibodies (goat anti-mouse IgA-biotin and goat anti-mouse IgG1-biotin, both from Southern Biotechnologies), horseradish peroxidase-conjugated streptavidin (R&D Systems), and TMB (Sigma-Aldrich). Reaction was stopped by acidification with 0.5 M H<sub>2</sub>SO<sub>4</sub> (Sigma-Aldrich) and absorbance was read at 450 nm.

**Quantitative real-time PCR amplification of 16S rRNA.** DNA was extracted from the scraped epithelial content (small intestinal surface scrape), as well as from the remaining tissue (small intestinal tissue) of the terminal ileum using a QIAamp DNA Stool mini kit (Qiagen). Quantitative real time PCR (qRT-PCR) analysis was conducted using an AB 7300 system (Applied Biosystems) and sequence detection software (version 1.3.1, Applied Biosystems). The qRT-PCR program began with an initial step at 95 °C for 10 min, followed by 40 cycles of 95 °C for 15 s and 60 °C for 1 min, and a final dissociation stage of 95 °C for 15 s, 60 °C for 30 s and 95 °C for 15 s. Data was acquired in the final step at 60 °C. Each reaction mixture was run in duplicate in a total volume of 10 µl in 96-well optical reaction plates (Applied Biosystems) sealed with optical adhesive film (Applied Biosystems). Amplification reactions consisted of 5 µl Power SYBR green PCR master mix (Applied Biosystems) mixed with 1 µl of forward and reverse primers (0.5 µM) and 4 µl of genomic DNA (diluted to approximately 10 ng µl<sup>-1</sup>). Primer pairs were as follows: other Eubacteria, UniF340 (5'-ACTCCTACGGGAGGCAGCAGT-3') and UniR514 (5'-ATTACCGCGTCTGTC-3')<sup>26</sup>; *Bacteroides*, AllBac296f (5'-GAGAGGAAGTCCCCAC-3') and AllBac412r (5'-CGCTACTTGGCTG GTTCAG-3')<sup>27</sup>; *Bacillus*, (5'-GCGGCGTGCCTAATACATGC-3') and (5'-CTT CATCACTACGCGGCGT-3')<sup>27</sup>; *Clostridium coccoides* (*Clostridium* cluster IV), UniF338 (5'-ACTCCTACGGGAGGCAGC-3') and C.cocR491 (5'-GCTTCTTA GTCAGGTACCGTCAT-3')<sup>26</sup>; *Clostridium leptum* (*Clostridium* cluster XIVa), FClept09 (5'-CCTTCCGTGCCGAGTGA-3') and RClept08 (5'-GAATTAA ACCACATACTCCACTGCTT-3')<sup>28</sup>; segmented filamentous bacteria, SFB736F (5'-ACGCTGAGGCATGAGAGCAT-3') and SFB844R (5'-GACGGCACGGA TTGTTATTCA-3')<sup>26</sup>. The relative quantity of 16S rDNA for each bacterial group was calculated by the  $\Delta C_t$  method and normalized to the amount of total Eubacteria in the sample.

**Isolation of bone-marrow-derived B220<sup>+</sup> progenitors.** B220<sup>+</sup> progenitors were freshly isolated from the bones of C57BL/6.CD45.2, C57BL/6.CD45.1 or AID-Cre

× YFP mice. Briefly, a single-cell suspension of bone marrow was prepared by gentle grinding of femurs and tibiae using a mortar and pestle. The cells were then flushed with MACS buffer (Ca/Mg-free PBS supplemented with 1 mM EDTA, 0.25% BSA (Sigma)). B cell progenitors were positively selected using anti-B220-beads (clone RA3-6B2, Miltenyi) and a VarioMACS magnet with an LS adaptor (Miltenyi). Cells were washed three times with MACS buffer and eluted in OptiMEM (Life Technologies). Typically about 8–14 × 10<sup>6</sup> B220<sup>+</sup> cells were recovered from the bone marrow of one mouse (two femurs and two tibiae). In culture, IL-7 promotes the development of B cells from bone-marrow-derived B220<sup>+</sup> precursors<sup>29</sup>. Bone-marrow-derived differentiated B cells are ideal for these experiments as the secondary lymphoid organs contain a mixed population of innate, adaptive and antigen-experienced B cells.

**Co-culture of stromal cells and bone marrow cells.** For co-culture experiments, either 200 bone-marrow-derived S17 cells, or 80,000 (live) bone-marrow-derived stromal cells, or 80,000 (live) lamina-propria-derived stromal cells were plated together with 300,000 bone-marrow-derived B220<sup>+</sup> cells. For the lamina-propria-derived stromal cells, cells were isolated in the same manner as described above for lamina-propria-derived cells, washed two times in Opti-MEM and plated in 24-well plates. After 2 days, a slowly growing adherent monolayer is obtained. By day 7 of culture, the monolayer reaches confluence. In two cases, the stromal cell monolayer appeared less viable at day 7 when the B220<sup>+</sup> bone-marrow-derived cells expanded more rapidly than expected, and those experiments were discarded.

Cultures were performed in OptiMEM (Life Technologies) supplemented with 10% non-heat inactivated FBS (Gibco),  $\beta$ -mercaptoethanol (50 µM), NaHCO<sub>3</sub> (2.4 g l<sup>-1</sup>), penicillin-streptomycin (100 µg ml<sup>-1</sup>), IL-21 (30 ng ml<sup>-1</sup>, R&D Systems) TGF- $\beta$  (2.5 ng ml<sup>-1</sup>, R&D Systems), IL-7 (0.5 ng ml<sup>-1</sup>) and 2 µg of rat IgG2a anti-mouse CD40 (clone 3/23; BD Biosciences) or rat IgG2a (clone HB9419) as isotype control. The supernatant from the stably transfected J558 line was used as a source of IL-7 (supplied by A. Cumano). The co-culture was performed in 24-well plates in a total volume of 1 ml per well. On day 4, 0.5 ml of the above indicated culture mixture was added in addition, and on the indicated days, cells were collected and analysed by flow cytometry.

**Statistical analyses.** Statistical analyses were performed using Graphpad Prism software (GraphPad Software Inc.). Student's *t*-test was used for data with a normal distribution. Mann-Whitney *U*-test was used for non-Gaussian distributed data and 2-way analysis of variance for weight loss over time.

24. Peterson, D. A., McNulty, N. P., Guruge, J. L. & Gordon, J. I. IgA response to symbiotic bacteria as a mediator of gut homeostasis. *Cell Host Microbe* **2**, 328–339 (2007).
25. Marshall, A. J., Paige, C. J. & Wu, G. E. V. (H) repertoire maturation during B cell development *in vitro*: differential selection of Ig heavy chains by fetal and adult B cell progenitors. *J. Immunol.* **158**, 4282–4291 (1997).
26. Barman, M. *et al.* Enteric salmonellosis disrupts the microbial ecology of the murine gastrointestinal tract. *Infect. Immun.* **76**, 907–915 (2008).
27. Petnicki-Ocwieja, T. *et al.* Nod2 is required for the regulation of commensal microbiota in the intestine. *Proc. Natl Acad. Sci. USA* **106**, 15813–15818 (2009).
28. Furet, J. P. *et al.* Comparative assessment of human and farm animal faecal microbiota using real-time quantitative PCR. *FEMS Microbiol. Ecol.* **68**, 351–362 (2009).
29. Milne, C. D., Fleming, H. E. & Paige, C. J. IL-7 does not prevent pro-B/pre-B cell maturation to the immature/sIgM<sup>+</sup> stage. *Eur. J. Immunol.* **34**, 2647–2655 (2004).

# Cysteine methylation disrupts ubiquitin-chain sensing in NF- $\kappa$ B activation

Li Zhang<sup>1,2</sup>, Xiaojun Ding<sup>2</sup>, Jixin Cui<sup>2</sup>, Hao Xu<sup>2</sup>, Jing Chen<sup>2</sup>, Yi-Nan Gong<sup>2</sup>, Liyan Hu<sup>2</sup>, Yan Zhou<sup>2</sup>, Jianning Ge<sup>2</sup>, Qiuhe Lu<sup>2</sup>, Liping Liu<sup>2</sup>, She Chen<sup>2</sup> & Feng Shao<sup>2</sup>

NF- $\kappa$ B is crucial for innate immune defence against microbial infection<sup>1,2</sup>. Inhibition of NF- $\kappa$ B signalling has been observed with various bacterial infections<sup>3,4</sup>. The NF- $\kappa$ B pathway critically requires multiple ubiquitin-chain signals of different natures<sup>5,6</sup>. The question of whether ubiquitin-chain signalling and its specificity in NF- $\kappa$ B activation are regulated during infection, and how this regulation takes place, has not been explored. Here we show that human TAB2 and TAB3, ubiquitin-chain sensory proteins involved in NF- $\kappa$ B signalling, are directly inactivated by enteropathogenic *Escherichia coli* NleE, a conserved bacterial type-III-secreted effector responsible for blocking host NF- $\kappa$ B signalling. NleE harboured an unprecedented S-adenosyl-L-methionine-dependent methyltransferase activity that specifically modified a zinc-coordinating cysteine in the Npl4 zinc finger (NZF) domains in TAB2 and TAB3. Cysteine-methylated TAB2-NZF and TAB3-NZF (truncated proteins only comprising the NZF domain) lost the zinc ion as well as the ubiquitin-chain binding activity. Ectopically expressed or type-III-secretion-system-delivered NleE methylated TAB2 and TAB3 in host cells and diminished their ubiquitin-chain binding activity. Replacement of the NZF domain of TAB3 with the NleE methylation-insensitive Npl4 NZF domain resulted in NleE-resistant NF- $\kappa$ B activation. Given the prevalence of zinc-finger motifs and activation of cysteine thiol by zinc binding, methylation of zinc-finger cysteine might regulate other eukaryotic pathways in addition to NF- $\kappa$ B signalling.

Bacterial pathogens such as *Salmonella*, *Shigella* and enteropathogenic *E. coli* (EPEC) target the NF- $\kappa$ B pathway to counteract host defence<sup>3,4,7</sup>. Recent genetic studies reveal that EPEC suppression of host NF- $\kappa$ B signalling and NF- $\kappa$ B-dependent pro-inflammatory cytokine production requires a type-III-secreted effector called NleE<sup>8–10</sup> that also has homologues in *Shigella* and certain *Salmonella* species. Consistent with these studies, ectopic expression of NleE in HeLa cells efficiently blocked both IL-1 $\beta$  and TNF- $\alpha$ -induced NF- $\kappa$ B luciferase reporter activation (Fig. 1a) and nuclear translocation of NF- $\kappa$ B p65 subunit (Supplementary Fig. 1). NleE did not affect Ras-activated extracellular signal-activation regulated kinase 1 and 2 (Erk1/2) signalling (Supplementary Fig. 2a). NleE abolished I $\kappa$ B $\alpha$  degradation stimulated by TNF- $\alpha$  in 293T cells and IL-1 $\beta$  in HeLa cells<sup>8,9</sup> (Fig. 1b). The adaptor Myd88 and the ubiquitin ligase TRAF6 are downstream of the IL-1 $\beta$  receptor, whereas TRAF2 and TRAF5 ubiquitin ligases act downstream of the TNF- $\alpha$  receptor<sup>2</sup>. NleE efficiently blocked NF- $\kappa$ B activation stimulated with Myd88, TRAF6 or TRAF2 (Fig. 1c and Supplementary Fig. 2b). The TRAF-downstream TAK1 complex is composed of the kinase subunit TAK1, TAB1 and one of the homologous adaptors TAB2 and TAB3 (refs 11–13). TAB2 and TAB3 (TAB2/3) induce oligomerization-dependent auto-phosphorylation and activation of TAK1. Overexpression of TAK1 and TAB1 could stimulate the NF- $\kappa$ B signalling, but this activation was not inhibited by NleE (Fig. 1c). Thus, NleE alone is sufficient to block host NF- $\kappa$ B signalling by acting downstream of TRAF and upstream of TAK1.

The IL-1 $\beta$ -activated NF- $\kappa$ B pathway can be reconstituted in cell-free extracts by using recombinant TRAF6 protein. Addition of highly purified NleE into the cell extracts or pre-expression of NleE in cells abolished TRAF6-induced I $\kappa$ B $\alpha$  phosphorylation as well as phosphorylation of IKK $\alpha$ / $\beta$  in the IKK complex (Fig. 1d and Supplementary Fig. 3a, b). In agreement with the luciferase data, purified NleE diminished TRAF6-induced phosphorylation of TAK1 at Thr 187 (ref. 14) in the cell-free extracts (Fig. 1e). A previously identified non-functional NleE variant with deletion of <sub>209</sub>IDSYMK<sub>214</sub> (NleE $\Delta$ 6)<sup>9</sup> failed to block NF- $\kappa$ B signalling in all these assays (Fig. 1d, e and Supplementary Fig. 1). These results indicate that NleE directly targets and blocks TRAF-induced TAK1 activation.

NleE did not affect TRAF6-catalysed ubiquitin chain synthesis (Supplementary Fig. 4), which directed our focus to TAK1 complex components. In a yeast two-hybrid assay (Fig. 2a), NleE interacted specifically with TAB3, but not ubiquitin, TAK1 and TAB1. The interaction

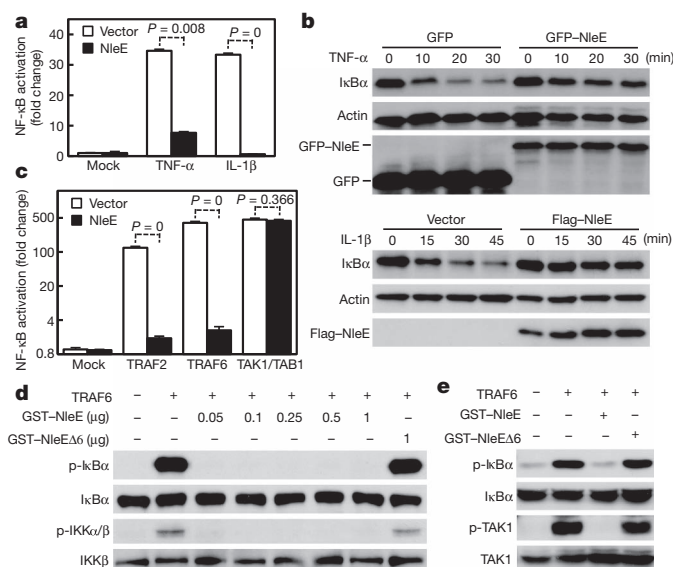


**Figure 1 | NleE blocks NF- $\kappa$ B signalling downstream of TRAFs and upstream of TAK1.** **a**, **b**, Effects of NleE expression on the NF- $\kappa$ B pathway. **a**, NF- $\kappa$ B-dependent luciferase activation shown as fold change normalized to that in unstimulated cells. Error bars indicate standard deviation. Experiments were performed at least three times with similar results obtained. **b**, Immunoblots of lysates of 293T (upper panels) and HeLa cells (lower panels) collected at indicated time points following treatment. **c**, Effects of NleE on NF- $\kappa$ B activation stimulated by TRAF2, TRAF6 or TAK1 plus TAB1.  $y$  axis is a logarithmic scale. Error bars indicate standard deviation. Experiments were performed at least three times with similar results obtained. **d**, **e**, Effects of purified NleE on NF- $\kappa$ B activation reconstituted in cell-free extract system. Recombinant TRAF6 protein together with GST-NleE was added into extracts prepared from MEF (**d**) or J774A.1 (**e**) cells. NleE $\Delta$ 6 is an NleE variant with a six-residue deletion of <sub>209</sub>IDSYMK<sub>214</sub>.

<sup>1</sup>Graduate Program in Chinese Academy of Medical Sciences and Peking Union Medical College, Beijing 100730, China. <sup>2</sup>National Institute of Biological Sciences, Beijing 102206, China.

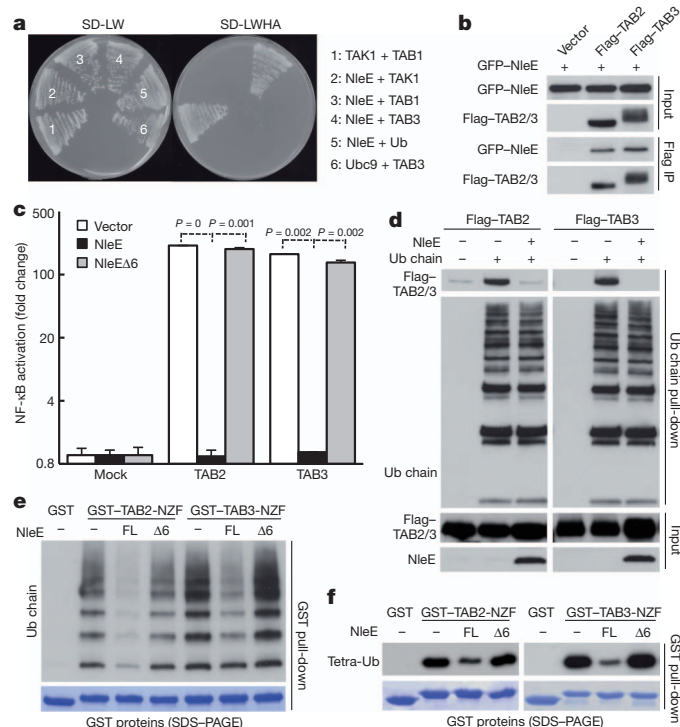


**Figure 2 | NleE directly targets TAB2 and TAB3 and impairs their ubiquitin-chain binding activity.** **a**, Yeast two-hybrid interaction assay of NleE and TAK1-complex components. Yeast strain was transformed with indicated plasmid combinations (bait plus prey). Activation of the *HIS3* and *ADE2* reporters was assessed by growth on SD-LWHA media. **b**, Co-immunoprecipitation assay of NleE and TAB2/3 interaction in 293T cells. Shown are immunoblots of anti-Flag immunoprecipitates (Flag IP) and total cell lysates (Input). **c**, Luciferase assays of effects of NleE on NF-κB activation stimulated by TAB2/3.  $y$  axis is shown on the logarithmic scale. Error bars indicate standard deviation. Experiments were performed at least three times with similar results obtained. **d**, Effects of NleE on ubiquitin-chain (Ub chain) binding of TAB2/3. Lysates of 293T cells transfected with Flag-TAB2/3 and NleE were subjected to Lys 63-linked ubiquitin-chain pull-down. Shown are immunoblots of the pull-down (Ub chain pull-down) and total cell lysates (Input). **e**, **f**, Effects of purified NleE on ubiquitin-chain binding of TAB2/3-NZF. Lys 63-linked ubiquitin chains (**e**) or tetra-ubiquitin (**f**) were subjected to pull-down by bacterially purified GST-TAB2/3-NZF in the presence or absence of recombinant NleE. FL, full-length; Δ6, NleEΔ<sub>209</sub>IDSYMK<sub>214</sub>.

was confirmed by co-immunoprecipitation of NleE with TAB3 as well as TAB2 from 293T cells (Fig. 2b). Consistently, NleE, but not NleEΔ6, completely blocked TAB2/3-stimulated NF-κB activation (Fig. 2c and Supplementary Fig. 5).

The effect of NleE on the integrity of the TAK1 signalling complex was then examined. NleE did not affect co-immunoprecipitation of endogenous TAB1 and TAK1 with TAB2 in both resting and Myd88-stimulated cells (Supplementary Fig. 6). TAB2 and TAB3 perceive the upstream Lys 63-linked polyubiquitin-chain signal for inducing TAK1 activation<sup>15–17</sup>. Lys 63-linked polyubiquitin chains readily precipitated TAB2/3 from 293T cells, which were largely abolished by NleE co-expression (Fig. 2d). Recombinant NleE also blocked precipitation of TAB2/3 by Lys 63-linked polyubiquitin chains from cell extracts (Supplementary Fig. 7a). The linear ubiquitin chain is known to have an important role in NF-κB signalling<sup>18–20</sup>. Linear tetra-ubiquitin could precipitate TAB3 from cell extracts, but much less proficiently than Lys 63-linked chains, and this binding was similarly sensitive to NleE treatment (Supplementary Fig. 7b). The carboxy-terminal conserved Npl4 zinc-finger (NZF) domains in TAB2/3 mediate TAB2/3 binding to polyubiquitin chains. When the NZF domain alone of TAB2 and TAB3 (TAB2/3-NZF) were assayed for Lys 63-linked ubiquitin chain binding, NleE had the same disruptive effect (Fig. 2e, f).

NleEΔ6 showed no inhibitory effect on ubiquitin-chain binding of TAB2/3 (Fig. 2e, f and Supplementary Fig. 7a). NleE by itself possessed little polyubiquitin-chain binding activity (Supplementary Fig. 8). Thus, NleE targets the NZF domains of TAB2/3 and disrupts their ubiquitin-chain binding activity.

Inhibition of NF-κB signalling in cell-free extracts required only a few nanograms of NleE (Fig. 1d and Supplementary Fig. 3a). Depleting most of NleE from cell extracts still resulted in a failed induction of TAK1 phosphorylation upon TRAF6 stimulation (Supplementary Fig. 9). These analyses indicate that NleE may act as an enzyme to impose a stable modification on TAB2/3, probably on their NZF domains. Purified TAB2/3-NZF domains were then incubated with recombinant NleE. Whereas no mobility shift of NleE-treated NZF domain occurred on an SDS-polyacrylamide gel electrophoresis (SDS-PAGE) gel, an evidently slower migration towards the anode appeared on a native gel (Fig. 3a). Mass spectrometry analysis identified a 14-dalton mass increase on NleE-treated TAB2/3-NZF compared with the control sample that showed an expected molecular mass (Supplementary Fig. 10). Tandem mass spectrometry further revealed that the 14-dalton mass increase occurred on Cys 673 in TAB2-NZF (Fig. 3b) and the equivalent Cys 692 in TAB3-NZF (Supplementary Fig. 11), indicating a methylation modification by NleE. A small molecule of 398 dalton, matching the mass of *S*-adenosyl-L-methionine (SAM), the most commonly used methyl donor by methyltransferases, was identified in bacterially purified NleE (Supplementary Fig. 12), indicating that SAM is co-purified with NleE from the bacteria. Consistently, addition of exogenous SAM decreased the minimal amount of NleE required for complete modification of TAB3-NZF by about 30-fold (Supplementary Fig. 13). NleE efficiently transferred <sup>3</sup>H-methyl from radiolabelled SAM onto TAB2/3-NZF domains (Fig. 3c) as well as full-length TAB2 and TAB3 purified from 293T cells *in vitro* (Fig. 3d and Supplementary Fig. 20a). Mass spectrometric analysis was performed to examine NleE

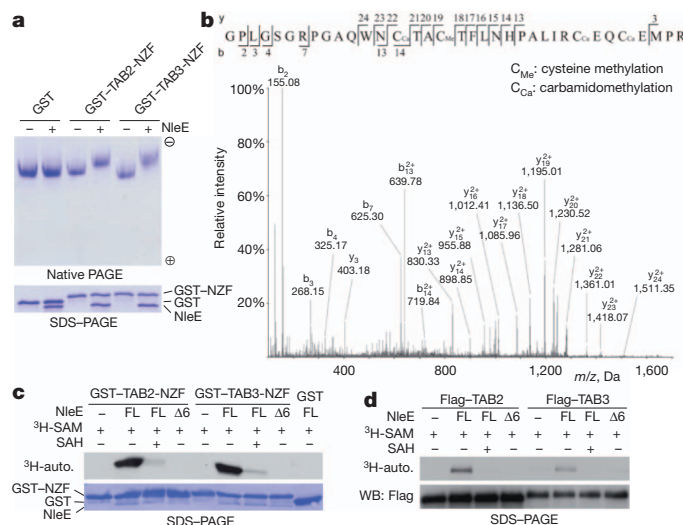


**Figure 3 | NleE is a SAM-dependent methyltransferase that specifically modifies Cys 673/692 in TAB2/3-NZF domains.** **a**, Native and SDS-PAGE analysis of GST and GST-TAB2/3-NZF treated with purified NleE protein. Coomassie-blue-stained gels are shown. **b**, Tandem mass (MS/MS) spectrum of a quadruply charged NleE-treated TAB2-NZF peptide. The *b*- and *y*-type product ions are marked in the spectrum, and also illustrated along the peptide sequence shown on top of the spectrum, which unambiguously identified the second cysteine as the methylated residue. The other three non-methylated cysteine residues were carbamidomethylated due to the iodoacetamide treatment during sample preparation as described in the Methods. **c**, **d**, <sup>3</sup>H-SAM labelling of TAB2/3-NZF and full-length TAB2/3 by purified NleE and the effects of *S*-adenosyl-L-homocysteine (SAH). GST-TAB2/3-NZF (**c**) and Flag-TAB2/3 (**d**) were purified from bacteria and 293T cells, respectively. FL, full-length; Δ6, NleEΔ<sub>209</sub>IDSYMK<sub>214</sub>. <sup>3</sup>H-auto., <sup>3</sup>H autoradiography; WB, western blot.



methylation of TAB2/3 in mammalian cells. The extracted ion chromatogram (XIC) identified the unmethylated form but not the methylated form of the Cys 673-containing peptide from Flag-TAB2 purified from vector-transfected cells (Supplementary Fig. 14). In marked contrast, only the methylated form of the corresponding peptide was identified from Flag-TAB2 purified from NleE-expressing cells, suggesting a nearly complete modification of TAB2 by NleE *in vivo*. NleE-catalysed methylation of TAB2/3-NZF domains and full-length TAB2/3 was effectively inhibited by *S*-adenosyl-L-homocysteine (SAH), the methyl transfer reaction product of SAM (Fig. 3c, d). Again, NleEΔ6 induced no mobility shift of TAB2/3-NZF on the native gel (Supplementary Fig. 13) and also failed to transfer <sup>3</sup>H-methyl onto TAB2/3 (Fig. 3c, d). NleE shows no sequence homology to any known methyltransferase<sup>21</sup>. The crystal structure of NleE (Q.Y., J.C. and F.S., unpublished data) reveals a new SAM-binding pocket, which involves Y212 (deleted in NleEΔ6) and more critically R107 in NleE. Mutation of either residue abolished NleE methylation of TAB3-NZF (Supplementary Fig. 15a). Thus, NleE is a new SAM-dependent methyltransferase that specifically modifies Cys 673 and Cys 692 in NZF domains of TAB2 and TAB3, respectively.

The approximately 30-residue NZF domain contains a zinc ion coordinated by four conserved cysteine residues<sup>22,23</sup> including the one modified by NleE in TAB2/3. In the TAB2-NZF and Lys 63-linked diubiquitin complex structure<sup>16,17</sup> (Fig. 4a), NleE-modified cysteine is involved in forming a hydrophobic surface that interacts with the Ile 44-centred hydrophobic patch in ubiquitin. In fact, the NleE-methylated NZF completely lost the ubiquitin-chain binding activity (Fig. 4b). Leucine or methionine substitution of Cys 673 in TAB2 (or Cys 692 in TAB3) abolished methylation of the corresponding NZF domain by NleE (Supplementary Fig. 16a), and both mutants were indeed devoid of ubiquitin-chain binding activity (Supplementary Fig. 16b). These mutations are expected to disrupt the zinc binding as leucine and methionine are not zinc ligands. NleE-methylated TAB3-NZF domain also lost the zinc ion, similarly to the effect of EDTA treatment (Supplementary Fig. 17). Thus, NleE methylation of a specific zinc-coordinating cysteine in TAB2/3-NZF domains and the consequent loss of zinc results in disruption of TAB2/3 ubiquitin-chain binding activity.

Mutation of any one of three other zinc-coordinating cysteines in TAB2/3-NZF domains also abolished the methylation by NleE (Supplementary Fig. 15b), indicating that NleE recognizes an intact zinc-finger structure. Notably, deletion of the NZF domain from TAB3 had little effect on NleE- and TAB3-binding in both yeast two-hybrid and co-immunoprecipitation assays (Supplementary Fig. 18a, b), indicating that structural information other than the NZF domain provides an additional docking interaction with NleE. This bipartite interaction mode is likely to be important for specific and highly efficient targeting of TAB2/3 by NleE.

The NZF domain is present in a number of proteins from different organisms, with members of this family being Npl4 and yeast Vps36 (Fig. 4a)<sup>22,23</sup>. NleE showed negligible activity towards Npl4-NZF, but methylated Vps36-NZF efficiently (Fig. 4c), raising the possibility that NleE targets other NZF-domain proteins in addition to TAB2/3. The NZF domain is also present in HOIL-1L, HOIP and Sharpin, the three components of the linear ubiquitin chain assembly complex (LUBAC) functioning in NF-κB signalling<sup>18–20</sup>. However, methylation of NZF domains from HOIL-1L, HOIP and Sharpin was hardly detected despite an excess amount of NleE used (Supplementary Fig. 19a). Linear ubiquitin binding activities of LUBAC-NZF domains were not affected by pre-incubation with excess NleE (Supplementary Fig. 19b). Full-length HOIL-1L, HOIP and Sharpin purified from 293T cells, as well as the active LUBAC complex, were all resistant to methylation by NleE (Supplementary Fig. 20a). The linear ubiquitin-chain synthesis activity of the LUBAC complex was not altered by co-incubation with NleE and SAM (Supplementary Fig. 21). NleE showed little effect on the ability of HOIL-1L, HOIP and Sharpin to bind linear tetra-ubiquitin

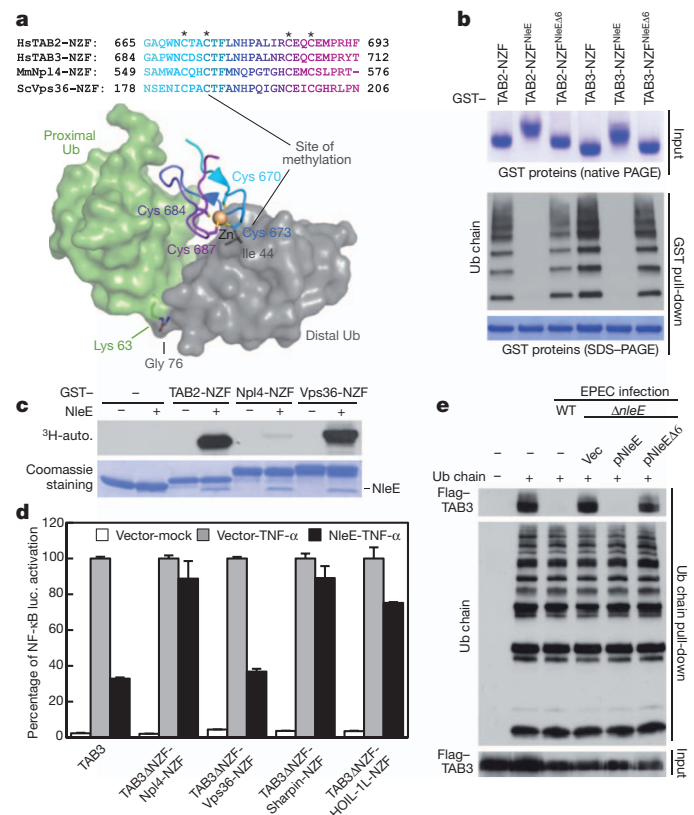


**Figure 4 | Cysteine methylation-induced loss of ubiquitin-chain binding of TAB2/3 contributes to NleE inhibition of host NF-κB signalling.**

**a**, Sequence alignment of representative NZF domains and structural illustration of TAB2-NZF in complex with Lys 63-linked diubiquitin. The four conserved zinc-coordinating cysteine residues are marked with asterisks in the alignment and shown as sticks with marks in the complex structure (PDB accession code 3A9J). **b**, Ubiquitin-chain binding of NleE-methylated TAB2/3-NZF. NleE fully methylated NZFs (GST-TAB2/3-NZF<sup>NleE</sup>) were used to pull-down Lys 63-linked polyubiquitin chains. **c**, <sup>3</sup>H-SAM labelling assay of other NZFs. Indicated bacterially purified GST-tagged NZF domains were incubated with recombinant NleE in the presence of <sup>3</sup>H-SAM. The reaction mixtures were loaded on an SDS-PAGE gel. The upper and lower panels are radiograph and Coomassie blue staining of the gel, respectively. **d**, Luciferase (luc.) assays of sensitivities of chimaeric TAB3 to NleE inhibition in TNF-α-induced NF-κB activation. TAB3ΔNZF-Vps36-NZF, TAB3ΔNZF-Npl4-NZF, TAB3ΔNZF-HOIL-1L-NZF and TAB3ΔNZF-Sharpin-NZF are chimaeric constructs with replacement of the NZF domain in TAB3 with that from Vps36, Npl4, HOIL-1L and Sharpin, respectively. Cells were transfected with chimaeric plasmids together with an NleE-expressing plasmid for 24 h and then subjected to a second transfection with NF-κB luciferase reporters. After 12 h, cells were treated with TNF-α for another 6 h before assaying the luciferase activity. Luciferase activation was shown as fold change normalized to that from TNF-α treatment without NleE expression. Error bars denote standard deviation. The *P* values for TAB3 versus TAB3ΔNZF-Npl4-NZF, TAB3ΔNZF-Vps36-NZF, TAB3ΔNZF-HOIL-1L-NZF and TAB3ΔNZF-Sharpin-NZF in TNF-α-treated NleE-expressing cells are 0.015, 0.082, 0 and 0.007, respectively. Experiments were performed at least three times with similar results obtained. **e**, Effects of type-III-delivered NleE on ubiquitin-chain binding of TAB3 during EPEC infection. 293T cells expressing Flag-TAB3 were infected with indicated EPEC strains. Cell lysates were subjected to Lys 63-linked ubiquitin-chain pull-down. WT, wild-type EPEC strain (E2348/69); Δ*nleE*, NleE-deletion strain. pNleE and pNleEΔ6 are rescue plasmids expressing wild-type NleE and the NleEΔ6 mutant, respectively.

(Supplementary Fig. 20b). The inability of NleE to target LUBAC *in vivo* agrees with the fact that NleE did not interact with HOIL-1, HOIP and Sharpin (Supplementary Fig. 18c), probably due to lack of the docking interaction provided by regions outside of the NZF domains in TAB2/3 (Supplementary Fig. 18a, b). Moreover, NleE could not methylate the C-terminal zinc-finger domain of NEMO

(Supplementary Fig. 22) that is also involved in ubiquitin-chain sensing in the NF- $\kappa$ B pathway<sup>24</sup>.

A subset of the NZF domains, including those from Npl4, Vps36 and LUBAC, bind the polyubiquitin chain<sup>19,22,23,25</sup>. Npl4-NZF and Vps36-NZF could functionally substitute TAB3-NZF in stimulating NF- $\kappa$ B signalling<sup>15</sup>. Notably, NF- $\kappa$ B activation by the TAB3 $\Delta$ NZF-Vps36-NZF chimaeric protein showed a similar sensitivity to NleE inhibition as that shown by wild-type TAB3, whereas TAB3 $\Delta$ NZF-Npl4-NZF was much more resistant to the inhibitory action of NleE on NF- $\kappa$ B activation (Supplementary Fig. 23a). The four LUBAC-NZF domains behaved similarly to Npl4-NZF in this assay (Supplementary Fig. 23b). The ability of TAB3 $\Delta$ NZF-Vps36-NZF and TAB3 to mediate TNF- $\alpha$ -induced NF- $\kappa$ B activation was sensitive to NleE inhibition; however, the LUBAC-NZF domains behaved similarly to Npl4-NZF and showed resistance to NleE inhibition (Fig. 4d and Supplementary Fig. 24). Furthermore, when the NZF domains in HOIL-1L and Sharpin were replaced with Npl4-NZF, no NleE-resistant effects in TNF- $\alpha$ -induced NF- $\kappa$ B activation were observed (Supplementary Fig. 25). These results agree well with the fact that these NZF domains, except for Vps36-NZF, are poor methylation substrates of NleE and further suggest that NleE-induced methylation of cellular TAB2/3 (Supplementary Fig. 14) is mainly responsible for the inhibition of the NF- $\kappa$ B signalling. Consistently, simultaneous knockdown of TAB2 and TAB3 severely attenuated TNF-induced NF- $\kappa$ B activation<sup>11,15</sup> (Supplementary Fig. 26), and expression of NleE in knockdown cells produced little additional effects (Supplementary Fig. 27). Interestingly, LUBAC-stimulated NF- $\kappa$ B activation is also sensitive to NleE inhibition as well as RNA-interference-mediated knockdown of TAB2/TAB3 expression (Supplementary Fig. 28). This indicates that LUBAC and TAB2/3-mediated ubiquitin-chain signalling might be linked together for full NF- $\kappa$ B activation.

NleE is mainly responsible for EPEC inhibition of host NF- $\kappa$ B signalling, and genetic deletion of NleE from the wild-type EPEC strain resulted in nuclear localization of p65 upon infection<sup>8,9</sup> (Supplementary Fig. 29). Polyubiquitin chains efficiently precipitated TAB3 from uninfected cells, but failed to do so from cells infected with wild-type EPEC (Fig. 4e). Importantly, deletion of NleE from EPEC resulted in efficient polyubiquitin-chain pull-down of TAB3. Complementation of the NleE-deletion strain with wild-type NleE, but not the methyltransferase-inactive NleE $\Delta$ 6, restored the inhibition of ubiquitin-chain pull-down of TAB3 (Fig. 4e). These data indicate that type-III-secreted NleE can target host TAB2/3 for methylation and inactivation, contributing to disruption of host NF- $\kappa$ B signalling by EPEC infection.

We have discovered a bacterial effector that uses an unprecedented methyltransferase activity to specifically modify a zinc-finger cysteine in host TAB2/3. This modification abolishes ubiquitin-chain binding of the NZF domains in TAB2/3 and thereby disrupts host NF- $\kappa$ B signalling. Methylation modification usually occurs on a lysine or an arginine as extensively exemplified by epigenetic modifications of histone. Our finding represents the first example of enzyme-catalysed cysteine methylation as a mechanism in regulating signal transduction. Two other instances of thiol methylation have been noted previously. The *E. coli* sacrificial DNA repair protein Ada transfers a methyl group from Sp-configured methyl phosphotriesters in damaged DNA to one of its own cysteines, thereby conferring cellular resistance to genotoxic effects of methylating agents<sup>26,27</sup>. The thiol group in small-molecule homocysteine is methylated by betaine-homocysteine S-methyltransferase (BHMT)<sup>28</sup> and methionine synthases<sup>29</sup> in homocysteine metabolism and methionine biosynthesis. In both instances, the methyl acceptor thiol is one of the four zinc-coordinating cysteines (occasionally three cysteines plus a histidine). Chemically, zinc binding can electronically activate the cysteine and generate a thiolate with high nucleophilicity<sup>30</sup>. The zinc thiolate is prone to undergo enzyme-catalysed methylation that usually uses S<sub>N</sub>2 nucleophilic attack on the donor methyl group by the substrate<sup>21</sup>. Given the wide presence of zinc-finger proteins and methyltransferase activities in

cells, cysteine methylation might be a previously underappreciated mechanism in regulating signal transduction.

## METHODS SUMMARY

**Reagents and NleE modification of TAB2/3-NZF domains.** DNA for NleE was amplified from enteropathogenic *E. coli* E2348/69 strain. For *in vitro* modification, 4  $\mu$ g of glutathione S-transferase-tagged TAB2/3-NZF were incubated with 3  $\mu$ g of NleE for 30 min at 37 °C in 30  $\mu$ l of buffer containing 50 mM Tris-HCl, pH 7.5, 150 mM NaCl, 5 mM DTT and 0.1% NP-40. For <sup>3</sup>H-SAM labelling, the reaction was supplemented with 0.55  $\mu$ Ci of <sup>3</sup>H-SAM (Perkin Elmer) and the amount of NleE was lowered to 0.6  $\mu$ g. For <sup>3</sup>H-SAM labelling of full-length TAB2/TAB3, Flag-TAB2/3 immunopurified from 293T cells was reacted with 0.2  $\mu$ g of NleE. To assay binding of NleE-methylated NZF to Lys 63 ubiquitin chains, 20  $\mu$ g of GST-TAB2/3-NZF were incubated with 3  $\mu$ g of NleE for 30 min at 37 °C in a 40  $\mu$ l reaction containing 0.8 mM SAM. Part of the reaction mixtures (3/8) were loaded onto a native PAGE gel to confirm the complete modification; the rest of the mixtures were subjected to Lys 63 ubiquitin-chain pull-down.

**Full Methods** and any associated references are available in the online version of the paper at [www.nature.com/nature](http://www.nature.com/nature).

Received 17 April; accepted 28 October 2011.

Published online 11 December 2011.

- Hayden, M. S. & Ghosh, S. Shared principles in NF- $\kappa$ B signaling. *Cell* **132**, 344–362 (2008).
- Vallabhapurapu, S. & Karin, M. Regulation and function of NF- $\kappa$ B transcription factors in the immune system. *Annu. Rev. Immunol.* **27**, 693–733 (2009).
- Bhavsar, A. P., Guttman, J. A. & Finlay, B. B. Manipulation of host-cell pathways by bacterial pathogens. *Nature* **449**, 827–834 (2007).
- Roy, C. R. & Mocarski, E. S. Pathogen subversion of cell-intrinsic innate immunity. *Nature Immunol.* **8**, 1179–1187 (2007).
- Terzic, J., Marinovic-Terzic, I., Ikeda, F. & Dikic, I. Ubiquitin signals in the NF- $\kappa$ B pathway. *Biochem. Soc. Trans.* **35**, 942–945 (2007).
- Skaug, B., Jiang, X. & Chen, Z. J. The role of ubiquitin in NF- $\kappa$ B regulatory pathways. *Annu. Rev. Biochem.* **78**, 769–796 (2009).
- Cui, J. & Shao, F. Biochemistry and cell signaling taught by bacterial effectors. *Trends Biochem. Sci.* **36**, 532–540 (2011).
- Nadler, C. et al. The type III secretion effector NleE inhibits NF- $\kappa$ B activation. *PLoS Pathog.* **6**, e1000743 (2010).
- Newton, H. J. et al. The type III effectors NleE and NleB from enteropathogenic *E. coli* and OspZ from *Shigella* block nuclear translocation of NF- $\kappa$ B p65. *PLoS Pathog.* **6**, e1000898 (2010).
- Vossenkamp, A. et al. Inhibition of NF- $\kappa$ B signaling in human dendritic cells by the enteropathogenic *Escherichia coli* effector protein NleE. *J. Immunol.* **185**, 4118–4127 (2010).
- Ishitani, T. et al. Role of the TAB2-related protein TAB3 in IL-1 and TNF signaling. *EMBO J.* **22**, 6277–6288 (2003).
- Cheung, P. C., Nebreda, A. R. & Cohen, P. TAB3, a new binding partner of the protein kinase TAK1. *Biochem. J.* **378**, 27–34 (2004).
- Jin, G. et al. Identification of a human NF- $\kappa$ B-activating protein, TAB3. *Proc. Natl Acad. Sci. USA* **101**, 2028–2033 (2004).
- Singh, R. N. et al. Suzuki, S., Kawasaki, N., Saiki, I. & Sakurai, H. Critical roles of threonine 187 phosphorylation in cellular stress-induced rapid and transient activation of transforming growth factor- $\beta$ -activated kinase 1 (TAK1) in a signaling complex containing TAK1-binding protein TAB1 and TAB2. *J. Biol. Chem.* **280**, 7359–7368 (2005).
- Kanayama, A. et al. TAB2 and TAB3 activate the NF- $\kappa$ B pathway through binding to polyubiquitin chains. *Mol. Cell* **15**, 535–548 (2004).
- Kulathu, Y., Akutsu, M., Bremm, A., Hofmann, K. & Komander, D. Two-sided ubiquitin binding explains specificity of the TAB2 NZF domain. *Nature Struct. Mol. Biol.* **16**, 1328–1330 (2009).
- Sato, Y., Yoshikawa, A., Yamashita, M., Yamagata, A. & Fukai, S. Structural basis for specific recognition of Lys 63-linked polyubiquitin chains by NZF domains of TAB2 and TAB3. *EMBO J.* **28**, 3903–3909 (2009).
- Gerlach, B. et al. Linear ubiquitination prevents inflammation and regulates immune signalling. *Nature* **471**, 591–596 (2011).
- Ikeda, F. et al. SHARPIN forms a linear ubiquitin ligase complex regulating NF- $\kappa$ B activity and apoptosis. *Nature* **471**, 637–641 (2011).
- Tokunaga, F. et al. SHARPIN is a component of the NF- $\kappa$ B-activating linear ubiquitin chain assembly complex. *Nature* **471**, 633–636 (2011).
- Schubert, H. L., Blumenthal, R. M. & Cheng, X. Many paths to methyltransferase: a chronicle of convergence. *Trends Biochem. Sci.* **28**, 329–335 (2003).
- Meyer, H. H., Wang, Y. & Warren, G. Direct binding of ubiquitin conjugates by the mammalian p97 adaptor complexes, p47 and Ufd1-Npl4. *EMBO J.* **21**, 5645–5652 (2002).
- Wang, B. et al. Structure and ubiquitin interactions of the conserved zinc finger domain of Npl4. *J. Biol. Chem.* **278**, 20225–20234 (2003).
- Laplante, E. et al. NEMO specifically recognizes K63-linked poly-ubiquitin chains through a new bipartite ubiquitin-binding domain. *EMBO J.* **28**, 2885–2895 (2009).

25. Alam, S. L. *et al.* Ubiquitin interactions of NZF zinc fingers. *EMBO J.* **23**, 1411–1421 (2004).
26. Sedgwick, B., Robins, P., Totty, N. & Lindahl, T. Functional domains and methyl acceptor sites of the *Escherichia coli* Ada protein. *J. Biol. Chem.* **263**, 4430–4433 (1988).
27. He, C. *et al.* A methylation-dependent electrostatic switch controls DNA repair and transcriptional activation by *E. coli* Ada. *Mol. Cell* **20**, 117–129 (2005).
28. Castro, C. *et al.* Dissecting the catalytic mechanism of betaine-homocysteine S-methyltransferase by use of intrinsic tryptophan fluorescence and site-directed mutagenesis. *Biochemistry* **43**, 5341–5351 (2004).
29. Koutmos, M. *et al.* Metal active site elasticity linked to activation of homocysteine in methionine synthases. *Proc. Natl Acad. Sci. USA* **105**, 3286–3291 (2008).
30. Matthews, R. G. & Goulding, C. W. Enzyme-catalyzed methyl transfers to thiols: the role of zinc. *Curr. Opin. Chem. Biol.* **1**, 332–339 (1997).

**Supplementary Information** is linked to the online version of the paper at [www.nature.com/nature](http://www.nature.com/nature).

**Acknowledgements** We thank I. Rosenshine for providing NleE deletion strains, K. Iwai for the HOIL-1L and HOIP expression plasmids, H. Sakurai for the phospho-TAK1 antibody, Z. Chen for TAB2/3 and Npl4-NZF chimera constructs, and S. Fukai for the NZF expression plasmid. We also thank members of the Shao laboratory for helpful discussions and technical assistance. This work was supported by the National Basic Research Program of China (973 Programs, 2010CB835400 and 2012CB518700).

**Author Contributions** L.Z. performed the majority of the experiments, assisted by J.C., H.X. and Y.-N.G.; X.D. and S.C. performed mass spectrometry analysis and analysed the data. J.C., L.H., Y. Z., J.G., Q.L. and L.L. generated reagents. L.Z. and F.S. analysed the data and wrote the manuscript. All authors discussed the results and commented on the manuscript.

**Author Information** Reprints and permissions information is available at [www.nature.com/reprints](http://www.nature.com/reprints). The authors declare no competing financial interests. Readers are welcome to comment on the online version of this article at [www.nature.com/nature](http://www.nature.com/nature). Correspondence and requests for materials should be addressed to F.S. ([shaofeng@nibs.ac.cn](mailto:shaofeng@nibs.ac.cn)).



## METHODS

**Plasmids, antibodies and reagents.** DNA for NleE amplified from enteropathogenic *E. coli* E2348/69 strain was inserted into pCS2-EGFP and pcDNA4-Flag-HA vectors for mammalian expression, and pGEX-6P-2 and pSUMO for recombinant expression in *E. coli*. The insert was also ligated into pBlueScript II SK (-) for rescue expression in EPEC. Expression plasmids for TRAF2, TRAF6, TAK1 and TAB1 were previously described<sup>31</sup>. cDNAs for TAB2, TAB3 and Sharpin were amplified from a HeLa cDNA library. HOIP and HOIL-1L cDNAs were provided by K. Iwai. TAB2/3 was inserted into pCS2-3×Flag vector and HOIP/HOIL-1L/Sharpin were cloned into pCS2-Flag vector. pCAGGS-E-MyD88 was from the BCCM/LMBP Plasmid collection. Luciferase assay plasmids were described previously<sup>32</sup>. For yeast two-hybrid analysis, DNA for NleE, TAK1 and HOIP was cloned into the bait vector pGBKT7; cDNA for TAK1, TAB1, TAB2, TAB3, TAB3ΔNZF, TAB3-NZF, ubiquitin, HOIP, HOIL-1L, Sharpin and NEMO was cloned into the prey vector pGAD-GH. TAB2/3-NZF, LUBAC-NZFs, NEMO-ZnF and NEMO-UBAN were cloned into pGEX-6P-2 for bacterial recombinant expression. pCold-GST-Npl4-NZF and pCold-GST-Vps36-NZF were provided by S. Fukai. TRAF6 baculovirus, bacterial expression constructs for Ubc13/Uev1, and pEF-Flag-TAB3ΔNZF-Npl4-NZF plasmid were gifts from Z. Chen. pEF-Flag-TAB3ΔNZF-Vps36-NZF/HOIL-1L-NZF/Sharpin-NZF/HOIP-NZF1/HOIP-NZF2 was constructed by replacing the Npl4-NZF with Vps36-NZF, HOIL-1L-NZF, Sharpin-NZF, HOIP-NZF1 and HOIP-NZF2, respectively, as previously described<sup>15</sup>. pCS2-Flag-HOIL-1LΔNZF-Npl4-NZF and pCS2-Flag-SharpinΔNZF-Npl4-NZF were generated by substituting Npl4-NZF for HOIL-1L-NZF and Sharpin-NZF, respectively, using overlapping PCR cloning strategy. All the mutations were generated with a QuikChange Site-Directed Mutagenesis Kit (Stratagene). All the plasmids were verified by DNA sequencing.

Antibodies for IκBα (sc-371), TAK1 (sc-7162), GFP (sc-8334), TAB2 (sc-11851), ubiquitin (P4D1, sc-8017), p65 (sc-372), and γPAK (sc-1519) (used in anti-TAK1 immunoprecipitation as the control antibody) were purchased from Santa Cruz; antibodies for p-IκBα (S32) (14D4, catalogue no. 2859), p-IκBα (S32/36) (5A5, catalogue no. 9246), p-IKKα/β (16A6, catalogue no. 2697), IKKβ (L570, catalogue no. 2678) were all from Cell Signaling Technology; p-TAK1 (Thr187) antibody was a gift from H. Sakurai; antibodies for TAK1 and TAB1 were provided by P. Cohen; the anti-GST antibody was generated by the antibody core facility at National Institute of Biological Sciences, Beijing, China; Flag (M2) and actin antibodies were from Sigma. ATP was purchased from Promega. HeLa, 293T and J774A.1 cells were obtained from the American Type Culture Collection (ATCC). The targeting sequences for RNAi are as follows: TAB2-1, 5'-CCTGAAGTACCTGAAGTTGTT-3'; TAB2-2, 5'-AGTCAACCTAAGGTCTA TATT-3'; TAB2-3, 5'-CACTCAGCCCAATACGAAATA-3'; TAB3-1, 5'-GCCTGAGGAAATGACAAGATT-3'; TAB2-A, 5'-TGGCTGGGTATCTCAG TTTAA-3'; TAB2-B, 5'-CAGTCAATAGCCAGACCTTAA-3'; TAB3-A, 5'-CCGGTTAATCATTCCTTA-3'. All other reagents were Sigma-Aldrich products unless noted.

**Transfection, immunoprecipitation and immunofluorescence.** Transfection was performed using Vigofect (Vigorous) unless otherwise specified. For anti-TAK1 immunoprecipitation, 293T cells were collected 24 h after transfection and lysed in buffer A (50 mM HEPES pH 7.4, 150 mM NaCl, 1% Triton X-100) supplemented with 1% protease inhibitor cocktail (Roche) for 30 min on ice. Supernatants were pre-cleared by Protein G Sepharose (4 °C, 30 min). Antibodies (1 μg) were added into the pre-cleared lysates. Following 2 h of incubation, 10 μl of Protein G Sepharose was added to precipitate the immuno-complex (4 °C, 1 h). The Sepharose was washed three times with buffer A. For anti-Flag immunoprecipitation, cells were harvested in buffer B (50 mM Tris-HCl pH 7.5, 150 mM NaCl and 0.5% Triton X-100) plus 1% protease inhibitor cocktail. To immunopurify Flag-TAB2/3 (for methylation by NleE), 4 × 10<sup>7</sup> 293T cells were transfected with pCS2-3×Flag-TAB2/3 for 24 h and anti-Flag immunoprecipitation was performed as above described except that the bound protein was eluted by 3×Flag peptides (400 μg ml<sup>-1</sup>). The eluted protein was verified by silver staining on an SDS-PAGE gel. p65 staining procedure has been described previously<sup>31,33</sup>.

**Bacterial strains and EPEC infection.** Enteropathogenic *E. coli* E2348/69 was used as wild-type strain<sup>34</sup>. NleE-deletion strain SC3908 generated from the E2348/69 background was provided by I. Rosenshine. Infection was performed with 293T cells at a multiplicity of infection of 200:1. 2.5 h after infection, cells were washed and the medium was supplemented with 200 μg ml<sup>-1</sup> gentamicin to kill the bacteria. Detailed procedures were essentially the same as described in ref. 34. To assay effects of NleE modification, 293T cells were transfected with pCS2-3×Flag-TAB3 by using the calcium phosphate precipitation method 20 h before infection. After 3 h, cells were collected and the lysates were subjected to Lys 63 ubiquitin-chains pull-down described below.

**Luciferase reporter and yeast two-hybrid assays.** Luciferase activity was determined 24 h after transfection by using the dual luciferase assay kit (Promega)

according to the manufacturer's instructions. Detailed procedures have been described previously<sup>31,32</sup>. To measure the sensitivity of TAB3 NZF domain-swapped variants to NleE inhibition in the context of TNF-α treatment, cells were first transfected with wild-type TAB3 or NZF domain-swapped chimaeric TAB3 for 24 h and then subjected to a second transfection with an empty vector or NleE-expressing plasmid together with NF-κB luciferase plasmids. After 12 h, cells were treated with 10 ng ml<sup>-1</sup> TNF-α for another 6 h before assaying the luciferase activation. The *P* value for the Student's *t*-test was calculated. Yeast two-hybrid interaction assay was performed using the Matchmaker Two-Hybrid System (Clontech) by following the manufacturer's instruction.

**Cell-free reconstitution and pull-down assays.** Cell-extract-based reconstitution of the NF-κB pathway was performed as previously described<sup>31</sup>. GST pull-down assays of ubiquitin-chain binding were also performed as previously described<sup>16</sup> with minor modifications. GST-tagged proteins (12.5 μg) were immobilized onto 15 μl of Glutathione Sepharose 4B beads in 250 μl of binding buffer (150 mM NaCl, 50 mM Tris pH 7.5, 5 mM DTT and 0.1% NP-40). The beads were incubated with 0.8 μg of Lys 63-linked tetra-ubiquitin (Boston Biochem) or 1 μg of Lys 63 ubiquitin chains in 250 μl of binding buffer supplemented with 0.5 mg ml<sup>-1</sup> BSA. Purified NleE, 4 μg or 8 μg, was added into the binding assays for tetra-ubiquitin or ubiquitin chains, respectively. After 2 h of incubation at 4 °C, beads were extensively washed and bound proteins were subjected to SDS-PAGE or immunoblotting analyses as indicated. To test the effect of EDTA treatment, binding of Lys 63 ubiquitin chains with Glutathione beads-immobilized GST-TAB2/3-NZF were performed in the presence of 10 mM EDTA at room temperature for 1 h and then 4 °C for another hour. To assay the effect of NleE on linear ubiquitin-chain binding of LUBAC-NZFs, 15 μg of GST-HOIP-NZF1/HOIL-1L-NZF/Sharpin-NZF was incubated with increasing amounts of NleE in a binding buffer containing 0.8 mM SAM at 37 °C for 30 min. GST proteins in the reaction mixture were then immobilized onto Glutathione Sepharose 4B beads and incubated with 0.8 μg of linear tetra-ubiquitin (Boston Biochem) following the typical GST pull-down protocol as above described.

For ubiquitin-chain pull-down, Lys 63 ubiquitin chains synthesized using SBP (streptavidin-binding peptide)-tagged ubiquitin or linear tetra-ubiquitin was immobilized onto Streptavidin Sepharose in the presence of 5 mg ml<sup>-1</sup> BSA. The Sepharose beads were washed twice with the buffer containing 20 mM Tris-HCl pH 7.5, 150 mM NaCl and 0.1% Triton X-100 before being subjected to pull-down Flag-TAB2/3 from cell lysates. Three types of Flag-TAB2/3-containing lysates were assayed. (1) 293T cells were co-transfected with Flag-TAB2/3 and NleE; (2) lysates of 293T cells transfected with Flag-TAB2/3 were further treated with 20 μg of recombinant NleE for 30 min at 37 °C; (3) 293T cells transfected with Flag-TAB2/3 were infected with indicated EPEC strains. For linear ubiquitin-chain pull-down of LUBAC components, 293T cells co-transfected with Sharpin/HOIL/HOIP and NleE were assayed; for linear ubiquitin-chain pull-down of Flag-TAB3, lysates of 293T cells transfected with Flag-TAB3 were further treated with 20 μg of recombinant NleE for 30 min at 37 °C. Cells were lysed in the buffer containing 20 mM Tris-HCl pH 7.5, 150 mM NaCl and 0.5% Triton X-100. The lysates were diluted five times with a buffer containing 20 mM Tris-HCl pH 7.5 and 150 mM NaCl, and BSA was added to a final concentration of 2 mg ml<sup>-1</sup>. Pre-cleared lysates were subjected to Lys 63 ubiquitin-chain pull-down at 4 °C overnight. The Streptavidin beads were extensively washed before being subjected to immunoblotting analysis.

**Linear tetra-ubiquitin and ubiquitination assays.** The construct of streptavidin binding peptide (SBP)-tagged linear tetra-ubiquitin was generated by following a previously described strategy with slight modifications<sup>35</sup>. Coding DNA sequences of SBP tag and ubiquitin were first joined together by overlapping PCR with an NdeI site at the very 5' end of ubiquitin, and inserted into pET28a to obtain pET28-His-SBP-NdeI-Ub. A fragment of ubiquitin with 5'-end NdeI site and 3'-end CviQI site was then inserted into the NdeI-digested pET28-SBP-NdeI-Ub to form pET28-SBP-di-Ub. This was repeated twice to generate pET28-His-SBP-tetra-Ub. Linear SBP-tetra-ubiquitin chain with an N-terminal 6×His tag was expressed in BL21 (DE3) and purified using Ni-NTA resin following the manufacturer's instruction.

*In vitro* ubiquitination assays involving TRAF6 were carried out in a 20-μl reaction containing 100 ng of E1, 0.8 μg of His-Ubc13, 0.8 μg of His-Uev1A, 0.3 μg of TRAF6, 2 μg of ubiquitin and 2 mM ATP in the presence or absence of recombinant NleE at 37 °C for 30 min. To assay the activity of the LUAC complex to synthesize linear ubiquitin chains and its sensitivity to NleE modification, a similar reaction system was adopted except that UbcH5c, Flag-HOIP/HOIL-1L/Sharpin immunopurified from 293T cells and K0-ubiquitin were used. The reaction mixture was also supplemented with 0.5 mM SAM to allow for complete modification by NleE. After incubation at 37 °C for 45 min, the reaction was stopped and the samples were analysed by western blotting.

**In vitro methylation of TAB2/3-NZF by NleE.** GST-TAB2/3-NZF (4 µg) was incubated with 3 µg of NleE for 30 min at 37 °C in 30 µl of buffer containing 50 mM Tris-HCl pH 7.5, 150 mM NaCl, 5 mM DTT and 0.1% NP-40. The reaction mixtures were separated on a 12% native PAGE gel followed by Coomassie blue staining. S-Adenosyl methionine (0.8 mM) was included in the reaction performed with indicated titrating amounts of NleE to test whether exogenously added SAM could promote the modification. To assay binding of NleE-methylated NZF to Lys 63 ubiquitin chains, 20 µg of GST-TAB2/3-NZF were incubated with 3 µg of NleE for 30 min at 37 °C in a 40 µl reaction containing 0.8 mM SAM. Part of the reaction mixtures (3/8) were loaded onto a native PAGE gel to confirm the complete modification by NleE; the rest of the reaction mixtures were then subjected to Lys 63 ubiquitin chain pull-down as described above.

For <sup>3</sup>H-SAM labelling, similar assays were carried out except that the cold SAM was substituted by 0.55 µCi of <sup>3</sup>H-SAM (PerkinElmer) and also that the amount of NleE were lowered down to 0.6 µg per reaction. The reaction was also performed in the presence of 1.2 mM S-adenosyl-L-homocysteine (SAH). Incorporation of <sup>3</sup>H-SAM into GST-TAB2/3-NZF by NleE was visualized by <sup>3</sup>H autoradiography. For <sup>3</sup>H-SAM labelling of full-length TAB2/TAB3, Flag-TAB2/3/HOIP/HOIL-1L/Sharpin immunopurified from 293T cells was used as the substrates and the amount of NleE used in each reaction is 0.2 µg.

**Mass spectrometry analysis.** To measure the mass measurement of TAB2/3-NZFs by matrix-assisted laser desorption/ionization-time of flight (MALDI-TOF), GST-TAB2/3-NZF recombinant proteins immobilized onto Glutathione Sepharose 4B were treated with NleE. The NZF domains were then released by PreScission protease cleavage. Following centrifugation, the supernatant containing NZF domains was subjected to molecular weight measurement on an Autoflex II TOF/TOF mass spectrometer equipped with a nitrogen pulsed laser (Bruker Daltonik). In brief, 1 µl of NZF domain solution was mixed with 1 µl of 2,5-dihydroxybenzoic acid matrix solution (Agilent Technologies) directly on a Bruker MTP 384 massive stainless steel MALDI target. The matrix spots were allowed to dry at room temperature after which each spot was washed on target with 1 µl of 0.1% trifluoroacetic acid to remove the salt. The spectra were acquired in positive reflector measurement mode with pulsed ion extraction.

The following procedure was followed to determine the mass of NleE, GST-TAB3-NZF, EDTA-treated GST-TAB3-NZF and NleE-modified GST-TAB3-NZF proteins in the native state by nano-electrospray ionisation (ESI) mass spectrometry. The buffer of the protein solution was changed to 150 mM ammonium acetate by Amicon Ultra centrifugal unit (Millipore) with 10K MW cutoff. The protein solution was loaded into nano-ES spray capillaries (Proxeon) and sprayed into a QSTAR XL mass spectrometer for protein mass measurement in the native state. The spray voltage was set at 800 V and the data was acquired in mass spectrometry mode. The protein charge envelop in each raw spectrum was deconvoluted into non-charged form through the BioAnalyst software provided by the manufacturer.

The methylation sites on NleE-treated TAB2/3-NZF domains were mapped by nano-liquid chromatography-MS/MS (LC-MS/MS). The NleE-treated TAB2/3-NZF domains were reduced in 2 mM DTT at 95 °C for 5 min and then alkylated in 5 mM iodoacetamide at room temperature for 10 min. DTT (10 mM final concentration) was then added to the reaction mixture to quench the excess iodoacetamide. The alkylated TAB2/3 NZF domain solution was digested with sequencing grade trypsin (Promega) for 3 h at 37 °C. An aliquot of NZF solution was analysed on an analytical capillary column (50 µm × 10 cm) packed with 5 µm spherical C18 reversed phase material (YMC). An Agilent 1100 binary pump was used to generate HPLC gradient as follows: 0–5% B in 5 min, 5–40% B in 25 min, 40–100% B in 15 min (A = 0.1 M acetic acid in water; B = 0.1 M acetic acid/70% acetonitrile). The eluted NZF peptides were sprayed into the QSTAR XL mass spectrometer (AB Sciex) equipped with a nano-ESI ion source. The mass spectrometer was operated in information-dependent mode with one MS scan followed by three MS/MS scans for each cycle. Database searches were performed on an in-house Mascot server (Matrix Science) against TAB2/3-NZF peptide sequences. Carbamidomethylation and methylation on cysteine residue were set as variable modifications.

For quantification of the *in vivo* TAB2-NZF domain peptide, the affinity-purified TAB2 protein was separated on SDS-PAGE gel. Protein bands corresponding to TAB2 were de-stained, and then reduced in 10 mM DTT at 56 °C for 30 min followed by alkylation in 55 mM iodoacetamide in the dark for 1 h. The protein bands were then digested in-gel with sequencing-grade trypsin (10 ng µl<sup>-1</sup> trypsin, 50 mM ammonium bicarbonate, pH 8.0) overnight at 37 °C. Peptides were extracted with 5% formic acid/50% acetonitrile and 0.1% formic acid/75% acetonitrile sequentially and then concentrated to approximately 10 µl. The extracted peptides were analysed by nano-LC-MS/MS on a LTQ Orbitrap Velos mass spectrometer (Thermo Fisher). The mass spectrometer was operated in data-dependent mode cycled with one MS scan followed by four collision-induced dissociation (CID) MS/MS scans and four higher-energy collisional dissociation (HCD) MS/MS scans. The extracted ion chromatograms (XICs) of the TAB2-NZF domain peptides were extracted from the raw data files with 0.01 Da mass window.

31. Ge, J. *et al.* A *Legionella* type IV effector activates the NF-κB pathway by phosphorylating the IκB family of inhibitors. *Proc. Natl Acad. Sci. USA* **106**, 13725–13730 (2009).
32. Li, H. *et al.* The phosphothreonine lyase activity of a bacterial type III effector family. *Science* **315**, 1000–1003 (2007).
33. Gong, Y. N. *et al.* Chemical probing reveals insights into the signaling mechanism of inflammasome activation. *Cell Res.* **20**, 1289–1305 (2010).
34. Cui, J. *et al.* Glutamine deamidation and dysfunction of ubiquitin/NEDD8 induced by a bacterial effector family. *Science* **329**, 1215–1218 (2010).
35. Reyes-Turcu, F. E., Shanks, J. R., Komander, D. & Wilkinson, K. D. Recognition of polyubiquitin isoforms by the multiple ubiquitin binding modules of isopeptidase T. *J. Biol. Chem.* **283**, 19581–19592 (2008).

# Basic amino-acid side chains regulate transmembrane integrin signalling

Chungho Kim<sup>1\*</sup>, Thomas Schmidt<sup>2\*</sup>, Eun-Gyung Cho<sup>3</sup>, Feng Ye<sup>1</sup>, Tobias S. Ulmer<sup>2</sup> & Mark H. Ginsberg<sup>1</sup>

Side chains of Lys/Arg near transmembrane domain (TMD)<sup>1–3</sup> membrane–water interfaces can ‘snorkel’, placing their positive charge near negatively charged phospholipid head groups<sup>4–6</sup>; however, snorkelling’s functional effects are obscure. Integrin  $\beta$  TMDs have such conserved basic amino acids. Here we use NMR spectroscopy<sup>7,8</sup> to show that integrin  $\beta_3$ (Lys 716) helps determine  $\beta_3$  TMD topography. The  $\alpha_{IIb}\beta_3$  TMD structure indicates that precise  $\beta_3$  TMD crossing angles enable the assembly of outer and inner membrane ‘clasps’ that hold the  $\alpha\beta$  TMD together to limit transmembrane signalling<sup>9</sup>. Mutation of  $\beta_3$ (Lys 716) caused dissociation of  $\alpha_{IIb}\beta_3$  TMDs and integrin activation. To confirm that altered topography of  $\beta_3$ (Lys 716) mutants activated  $\alpha_{IIb}\beta_3$ , we used directed evolution of  $\beta_3$ (K716A) to identify substitutions restoring default state. Introduction of Pro(711) at the midpoint of  $\beta_3$  TMD (A711P) increased  $\alpha_{IIb}\beta_3$  TMD association and inactivated integrin  $\alpha_{IIb}\beta_3$ (A711P,K716A).  $\beta_3$ (Pro 711) introduced a TMD kink of  $30 \pm 1^\circ$  precisely at the border of the outer and inner membrane clasps, thereby decoupling the tilt between these segments. Thus, widely occurring snorkelling residues in TMDs can help maintain TMD topography and membrane-embedding, thereby regulating transmembrane signalling.

Integrins are composed of  $\alpha$  and  $\beta$  type I transmembrane subunits<sup>10</sup>; association of the  $\alpha$  and  $\beta$  TMDs regulates bidirectional transmembrane signal transduction<sup>11</sup>. Most metazoan integrin  $\beta$  subunits contain a positively charged Lys or Arg (Fig. 1a) near the inner TMD boundary that precedes an additional hydrophobic patch, termed the ‘membrane proximal region’<sup>12</sup>. The membrane proximal region of integrin  $\beta_3$  and, in particular, Lys 716, is protected from paramagnetic  $Mn^{2+}$ EDDA<sup>2–</sup> and is therefore membrane-embedded. This region in other integrin  $\beta$  subunits is also embedded<sup>13</sup>; hence, the membrane proximal domain is the carboxy (C)-terminal limb of a long  $\alpha$ -helical TMD that is tilted at an angle of approximately  $25^\circ$ , thus enabling the  $\epsilon$ -amino group of  $\beta_3$ (Lys 716) to snorkel near phospholipid head groups<sup>7</sup>.

To assess the role of  $\beta_3$ (Lys 716) in TMD topography, we mutated it to a Glu residue and assessed embedding in phospholipid bicelles by measuring protection of the backbone amide protons from the electroneutral paramagnetic  $Mn^{2+}$ EDDA<sup>2–</sup> agent<sup>7,8</sup>. Lipid embedding on the extracellular side, defined by the protection pattern of Leu 694–Val 696, was unchanged in  $\beta_3$ (K716E) (Fig. 1b). In contrast,  $\beta_3$ (K716E) reduced protection on the intracellular side by approximately five residues, shifting the membrane border from residue 721 to 716 and decreasing membrane crossing angle. The absence of significant  $^{13}C^\alpha$  chemical shift changes between  $\beta_3$  and  $\beta_3$ (K716E) indicated no change in secondary structure as a consequence of the mutation (Supplementary Fig. 1a). At the level of  $H^N$  shifts, which are sensitive to surrounding chemical environment, relatively small  $H^N$  chemical changes between  $\beta_3$  and  $\beta_3$ (K716E) indicated limited rearrangements in bicelle structure (Fig. 1c), suggesting that Glu 716

still localized within the lipid–water interface. In analogy to the K716( $\epsilon$ -NH<sub>3</sub><sup>+</sup>)-lipid(PO<sub>4</sub><sup>–</sup>) snorkelling interaction, glutamate’s  $\gamma$ -COO<sup>–</sup> group may engage a POPC lipid’s choline N(CH<sub>3</sub>)<sub>3</sub><sup>+</sup> group or a POPS lipid’s amino NH<sub>3</sub><sup>+</sup> group within the lipid head group region (Fig. 1d).  $\beta_3$ (K716E) TMD-tail was not aggregated (Supplementary Fig. 1b), indicating that displacement of negatively charged Glu 716 from the hydrophobic core shifted Leu(717)–Ile(721) into a more polar environment. Thus, Lys 716 substitutions perturb  $\beta_3$  TMD membrane embedding and crossing angle.

Disruption of the interaction between integrin  $\alpha$  and  $\beta$  TMDs leads to allosteric rearrangements that result in increased ligand-binding affinity of the extracellular domain (integrin activation)<sup>10,11,14</sup> and activation of cytosolic signalling pathways<sup>15</sup>. A stable  $\alpha\beta$  TMD association, which is crucial in the regulation of and physiological functions of integrins, requires the simultaneous formation of two discrete assemblies, an inner and outer membrane clasp (IMC and OMC), respectively (Fig. 1e)<sup>9</sup>. Because the  $\beta_3$  TMD forms a continuous  $\alpha$ -helix, its crossing angle appears critical for the simultaneous assembly of these clasps<sup>9</sup>. To examine the effect of  $\beta_3$ (Lys 716) mutations on the  $\alpha_{IIb}\beta_3$  TMD association in mammalian cell membranes, we used a mini-integrin affinity capture assay<sup>16</sup> and chemical cross-linking. The latter experiments showed that the  $\alpha_{IIb}\beta_3$  TMD interaction is primarily a 1:1 heterodimer (Supplementary Fig. 2). For the capture assay, an  $\alpha_{IIb}$  mini-integrin bait containing the TMD and cytoplasmic tail of  $\alpha_{IIb}$  (Fig. 2a) joined to a C-terminal tandem affinity purification (TAP) tag<sup>16</sup> for rapid efficient purification was expressed with preys comprising the extracellular domain of the Tac (IL-2 receptor  $\alpha$ ) joined to the TMD and tail of  $\beta_3$  or  $\beta_3$ -bearing Lys 716 substitutions (Fig. 2a). When the cells were lysed and baits were captured using calmodulin beads, we found that the  $\alpha_{IIb}$  bait captured the  $\beta_3$  prey, as expected; however, neutral (Ala), polar (Cys, Ser), acidic (Glu), or hydrophobic (Leu) substitutions at  $\beta_3$ (Lys 716) blocked the  $\alpha_{IIb}\beta_3$  TMD association. In contrast, a basic amino-acid substitution (Arg) did not disrupt the association, consistent with the idea that a snorkelling residue in this position is required to the formation of the  $\alpha_{IIb}\beta_3$  TMD complex. To examine the potential effects of  $\beta_3$ (Lys 716) mutations on transmembrane signalling, we assayed their effects on the affinity state of integrin  $\alpha_{IIb}\beta_3$  by measuring binding to activation-specific  $\alpha_{IIb}\beta_3$  antibody (PAC1)<sup>17</sup> as in Fig. 2b. The results precisely correlated with the effects on  $\alpha\beta$  TMD interaction; all substitutions with the exception of Arg led to spontaneous integrin activation (Fig. 2c). The importance of this highly conserved Lys seems general because mutation of the paralogous residue in integrin  $\beta_{1A}$  (K732E) activated integrin  $\alpha_5\beta_1$  (Supplementary Fig. 3a–d) and inhibited the association of the  $\beta_1$  TMD with either the  $\alpha_5$  or  $\alpha_V$  TMD (Supplementary Fig. 3e). Thus, loss of a conserved basic residue in integrin  $\beta$  TMDs leads to disruption of the  $\alpha$ – $\beta$  TMD interaction and spontaneous transmembrane signalling.

The findings that  $\beta_3$ (Lys 716) substitutions that prohibit snorkelling alter TMD embedding, that such mutations dissociate the  $\alpha_{IIb}\beta_3$  TMD

<sup>1</sup>Department of Medicine, University of California, San Diego, La Jolla, California 92093, USA. <sup>2</sup>Department of Biochemistry and Molecular Biology, Zilkha Neurogenetic Institute, Keck School of Medicine, University of Southern California, Los Angeles, California 90033, USA. <sup>3</sup>Center for Neuroscience, Aging, and Stem Cell Research, Sanford-Burnham Medical Research Institute, La Jolla, California 92037, USA.

\*These authors contributed equally to this work.



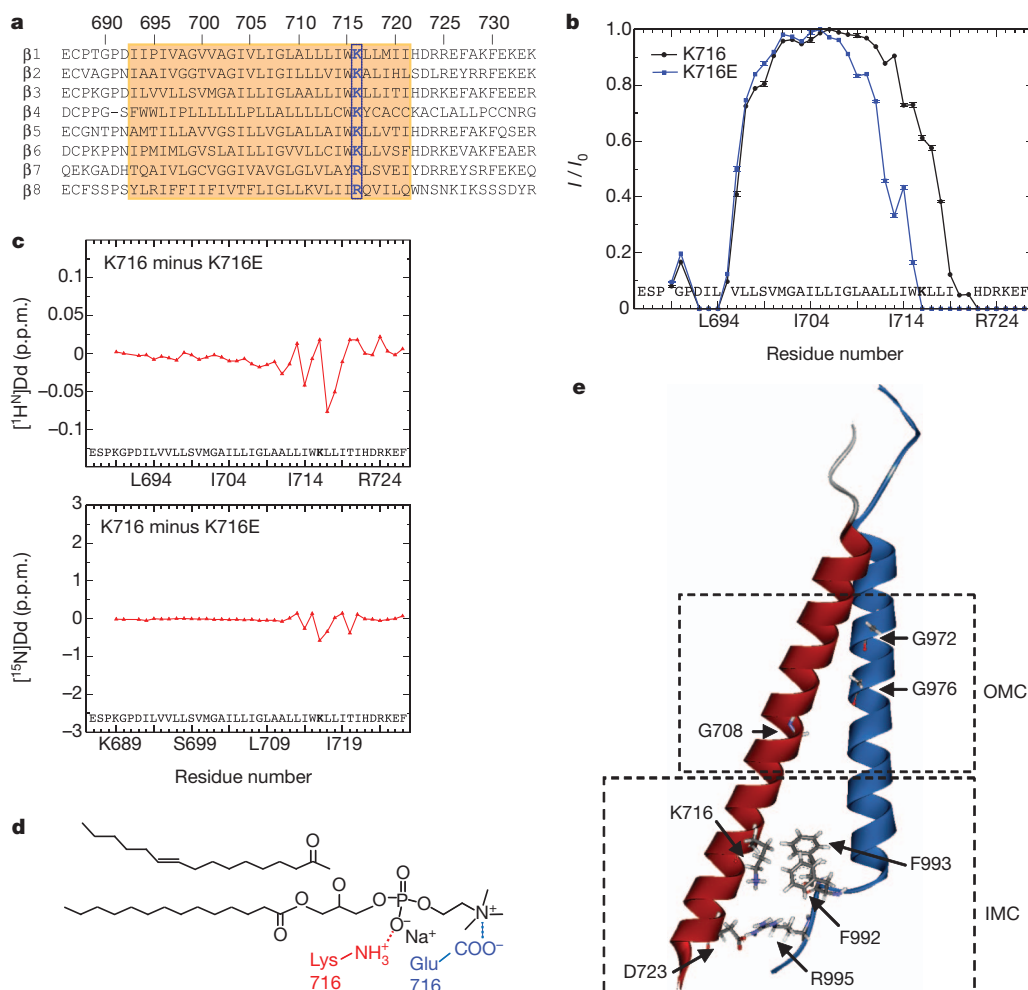


**Figure 1 | Loss of snorkelling lysine changes lipid embedding of  $\beta_3$  TMD.** **a**, Sequence alignment of TMD regions of integrin  $\beta$  subunits indicated with  $\beta_3$  numbering. Transmembrane domains are highlighted in orange. Conserved positive charged amino acids at position 716 (of  $\beta_3$ ) are bolded and boxed with blue line. **b**, Mutation of  $\beta_3$ (Lys 716) changes TMD membrane embedding. The TROSY H–N cross-peak signal intensity of a residue in the presence and absence of 1 mM  $\text{Mn}^{2+}$ EDDA $^{2-}$  in the aqueous phase,  $I/I_0$ , was measured to express quantitatively protection from the paramagnetic reagent. Experiments were performed in duplicates using independently prepared samples and quote the standard error between data sets. **c**, Chemical shift changes of K716E relative to the wild type. **d**, The predicted interaction of Lys 716 side chain  $\epsilon\text{-NH}_3^+$  with a lipid's  $\text{PO}_4^-$  group (red) and the interaction of glutamate's  $\gamma\text{-COO}^-$  with a POPS lipid's amino  $\text{NH}_3^+$  group (blue) are illustrated. **e**, NMR structure of integrin  $\alpha_{IIb}\beta_3$  TMD (PDB ID 2K9J). Side chains of residues essential to forming the OMC (Gly 972, Gly 976 in  $\alpha_{IIb}$  and Gly 708 in  $\beta_3$ ) and the IMC (Phe 992, Phe 993, Arg 995 in  $\alpha_{IIb}$ , Asp 723 in  $\beta_3$ ) are indicated.

complex and activate integrins, and the predicted importance of the crossing angle in maintenance of the two clasps that stabilize the  $\alpha\beta$  TMD association support the idea that the snorkelling Lys controls transmembrane signalling by specifying the embedding and crossing angle of the  $\beta_3$  TMD. Nevertheless, Rosetta modelling with sparse restraints provided by cystine cross-linking predicted seven clusters of integrin  $\alpha_{IIb}\beta_3$  TMD structures<sup>18</sup>, some of which resembled the calculated NMR structure<sup>9</sup>. The Rosetta structures suggested that  $\beta_3$ (Lys 716) can form hydrogen bonds with  $\alpha_{IIb}$  backbone carbonyl groups of Phe 992 and Phe 993, thereby stabilizing the  $\alpha$ – $\beta$

interaction<sup>18</sup>; the same paper reported that mutations at  $\beta_3$ (Lys 716) resulted in integrin activation<sup>18</sup>, a result we confirmed. However, NMR-based structural restraints<sup>9</sup> preclude  $\beta_3$ (Lys 716/ $\epsilon\text{-NH}_3^+$ )– $\alpha_{IIb}$ (Phe 993/CO) interactions (Supplementary Fig. 4). Furthermore, the embedding of the isolated  $\beta_3$  TMD was similar to that observed in the  $\alpha_{IIb}\beta_3$  complex<sup>9</sup> and, as shown, loss of the snorkelling  $\beta_3$ (Lys 716) alters  $\beta_3$  TMD embedding. We therefore sought a positive experimental confirmation that the effects of  $\beta_3$ (Lys 716) mutations on  $\alpha_{IIb}\beta_3$  TMD association and on integrin activation were dominated by changes in the  $\beta_3$  membrane topography.

If  $\beta_3$ (Lys 716) mutations changed topography to prevent the simultaneous formation of the IMC and OMC, thereby leading to integrin activation, we reasoned that compensating mutations within the  $\beta_3$  TMD might exist that would correct the crossing angle.

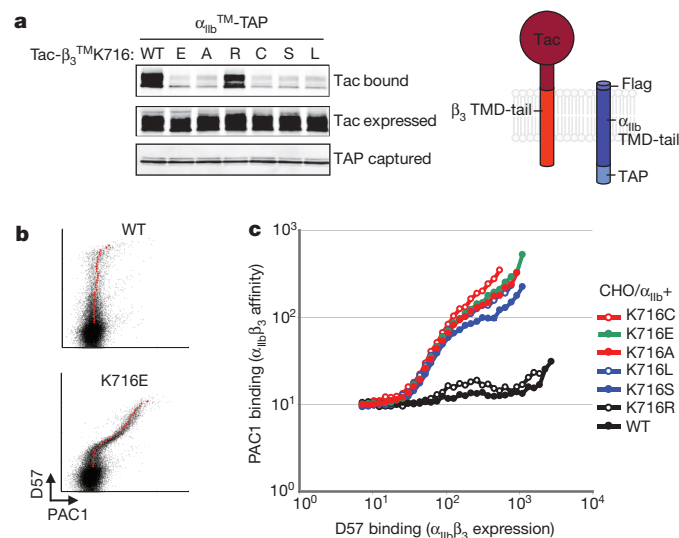


**Figure 2 | Mutations in the snorkelling lysine induce integrin activation and disrupt  $\alpha$ – $\beta$  TMD interaction.** **a**, Mutations of  $\beta_3$ (Lys 716) disrupt the  $\alpha_{IIb}\beta_3$  TMD interaction. CHO cells were co-transfected with  $\alpha_{IIb}$  TMD-tail construct fused with C-terminal TAP tag,  $\alpha_{IIb}$ <sup>TM</sup>-TAP, and  $\beta_3$  TMD-tail constructs fused with N-terminal Tac extracellular domain, Tac- $\beta_3$ <sup>TM</sup>, bearing various mutations at  $\beta_3$ (K716) as indicated.  $\alpha_{IIb}$ <sup>TM</sup>-TAP proteins were isolated and associated Tac- $\beta_3$ <sup>TM</sup> was detected by western blotting (upper panel). Expressed Tac- $\beta_3$ <sup>TM</sup> proteins (middle panel) and captured  $\alpha_{IIb}$ <sup>TM</sup>-TAP proteins (bottom panel) are also shown. **b**,  $\beta_3$ (K716E) activates integrin  $\alpha_{IIb}\beta_3$ . CHO cells stably expressing integrin  $\alpha_{IIb}$  (CHO/ $\alpha_{IIb}$ ) were transiently transfected with wild-type (WT) integrin  $\beta_3$  or  $\beta_3$ (K716E). Eighteen hours later, surface expression (D57 binding) and affinity of  $\alpha_{IIb}\beta_3$  (PAC1 binding) were analysed. Geometric means of PAC1 binding in cells expressing different quantities of  $\alpha_{IIb}\beta_3$  were plotted as larger red dots. **c**, Multiple  $\beta_3$ (K716) mutations activate integrin  $\alpha_{IIb}\beta_3$ . CHO/ $\alpha_{IIb}$  cells were transfected with integrin  $\beta_3$  bearing different mutations in the K716 residue as indicated. The geometric means of PAC1 binding to those CHO/ $\alpha_{IIb}$  cells were plotted against D57 binding.

Conversely, if  $\beta_3$ (Lys 716) formed hydrogen bonds with the  $\alpha_{IIB}$ , then a compensating mutation might introduce additional basic residues that could form such bonds.

We used random mutagenesis in a window of five residues amino (N)-terminal and 10 residues C-terminal to the  $\beta_3$ (K716) substitution (Fig. 3a and Supplementary Fig. 6a) to identify mutations that would complement the activating effects. We chose  $\beta_3$ (K716A) as the activating mutation; its effects may be less profound than  $\beta_3$ (K716E), thus favouring the discovery of weakly compensating mutations. Lentivirus particles carry two genomes<sup>19</sup>, making it possible that a single particle might encode two mutants. To test this possibility, we transfected packaging cells with a mixture of lentiviral plasmids encoding integrin  $\beta_3$  and  $\beta_3$ (K716A). When CHO cells bearing integrin  $\alpha_{IIB}$  were infected with the resulting viruses, we found only populations containing either fully active or fully inactive  $\alpha_{IIB}\beta_3$ , with no intermediate phenotype (Supplementary Fig. 5). Thus, the packaging cells incorporated two copies of identical genomes into each viral particle. We performed PCR using a primer that was synthesized with 9% contamination of incorrect nucleotides in the randomized windows. The contamination level was predicted by computer simulation to cover most single amino-acid changes within the window (Supplementary Fig. 6b and Supplementary

Table 1). We ligated the PCR fragments containing random mutations into a lentiviral vector encoding full-length integrin  $\beta_3$ , to create a randomized  $\beta_3$  complementary DNA (cDNA) library (Fig. 3b).

CHO/ $\alpha_{IIB}$  cells were infected with the mutant  $\beta_3$  lentiviral particles and the infected cells were analysed for integrin expression (D57 antibody binding) and activation (PAC1 antibody binding) by using flow cytometry (Fig. 3b). In contrast to the  $\beta_3$ (K716A)-infected cells, cells infected with the mutant  $\beta_3$  library exhibited a population of cells that expressed inactive  $\alpha_{IIB}\beta_3$  (R3 region in Fig. 3c). To identify those mutations, we collected approximately 7,000 cells in the R3 region and purified genomic DNAs from those cells and used PCR to isolate the region of integrin  $\beta_3$  containing the mutagenized window (Fig. 3b). Sequencing of the bulk product revealed that a  $\beta_3$ (A711P) mutation and stop codons at residues 724 and 725 were found in the mutagenized window (Fig. 3d). We performed NheI and BamHI digestion to isolate individual fragments containing the mutations and, after ligation into wild-type integrin  $\beta_3$ , confirmed the compensating effect of the mutations by transient transfection into cells expressing wild-type integrin  $\alpha_{IIB}$  and measuring PAC1 binding (Supplementary Fig. 7). The clones that showed a compensating effect were sequenced and fell into three major groups (Fig. 3e): clones containing Pro substitutions at

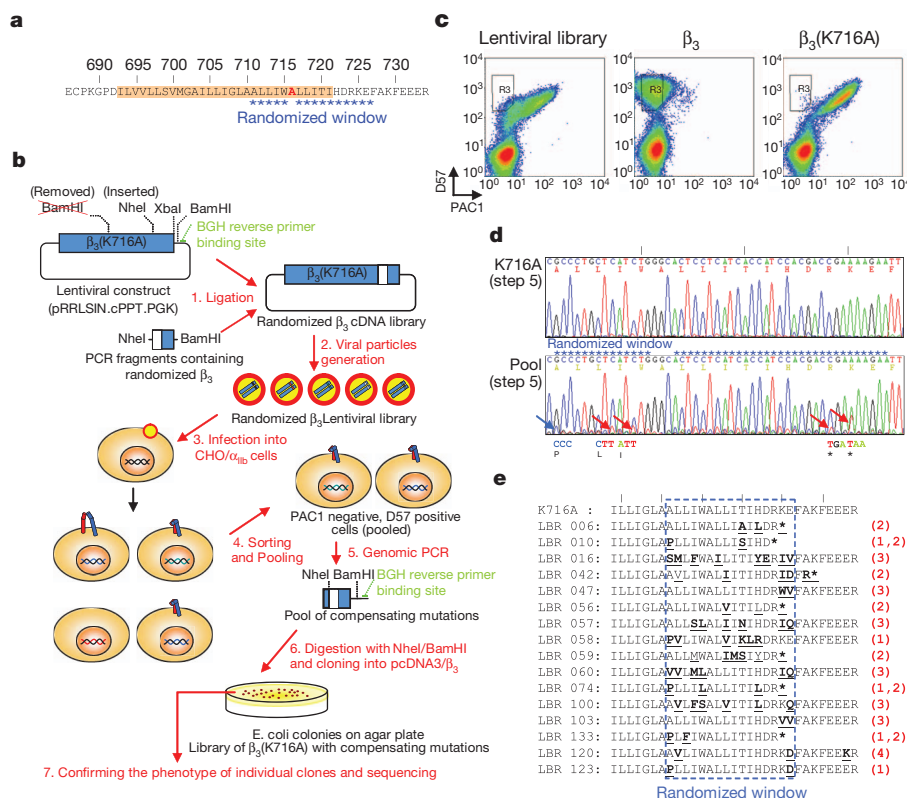


**Figure 3 | Directed evolution of the  $\beta_3$  integrin to identify mutations that complement the activating effect of snorkelling lysine mutation.**

**a**, Mutational window. The randomized amino-acid sequence in integrin  $\beta_3$ (K716A) is indicated by stars. **b–e**, Strategy and results of random mutagenesis. After removing BamHI and inserting NheI restriction enzyme sites by silent mutations, integrin  $\beta_3$ (K716A) was cloned into lentiviral vector. TMD-tail fragments of integrin  $\beta_3$  containing random mutations in the mutagenized window were produced by performing PCR with randomized forward primer and reverse primer containing a BamHI linker (Supplementary Fig. 6). The lentiviral  $\beta_3$ (K716A) construct and PCR fragments were digested with NheI and BamHI, and ligated to generate a randomized  $\beta_3$  cDNA library containing 310,000 independent clones. By transfecting the cDNA library into HEK293T cells with packaging vectors, viral particles were generated. CHO/ $\alpha_{IIB}$  cells were infected with the lentiviral particles, so that 10% of cells were infected to ensure that single lentiviral particle could be introduced into each cell (Supplementary Fig. 5). Cells infected with the lentiviral library, and cells infected with wild-type integrin  $\beta_3$  or  $\beta_3$ (K716A) lentivirus, were tested for D57

binding and PAC1 binding (**c**). Among  $10^7$  cells screened, approximately 7,000 with PAC1-negative and D57-positive phenotypes (cells in R3 in **c**) were sorted and pooled. Their genomic DNAs were prepared and TMD-tail regions of introduced integrin  $\beta_3$  were amplified by PCR using integrin- $\beta_3$ -specific forward primer and BGH reverse primer. The genomic PCR products from cells infected with lentiviral library or integrin  $\beta_3$ (K716A) mutant lentivirus were sequenced in bulk (**d**) to identify predominant mutations in the pool of compensating mutations. The genomic PCR products were ligated into integrin  $\beta_3$  to obtain individual compensating clones. Those individual clones (140 clones) were transiently transfected into CHO/ $\alpha_{IIB}$  cells to verify that they exhibited reduced PAC1 binding (Supplementary Fig. 7), and compensating clones were sequenced. Those clones were grouped according to the major mutation present (**e**). Clones were grouped into those that contained A711P mutations (group 1), R724X or K725X mutations (group 2), neutral residue substitutions for E726 (group 3) or spontaneous mutations that did not fall within the target window (group 4). The group number is depicted in red and the mutations are in bold type.

Ala 711 (group 1), stop codons at Arg 724 or Lys 725 (group 2) or a neutral residue substitution at Glu 726 (group 3).

The only compensating mutation consistently observed in the TMD was  $\beta_3$ (A711P) (group 1 in Fig. 3e). This represents an integrin TMD point mutation that inhibits transmembrane signalling. This residue is inaccessible to talin or other cytoplasmic proteins and is unlikely to provide a direct interaction with  $\alpha_{IIb}$  because it is not in the  $\alpha$ - $\beta$  TMD binding interface<sup>9</sup>. We confirmed that  $\beta_3$ (A711P) compensates both  $\beta_3$ (K716A) and  $\beta_3$ (K716E) mutations with respect to integrin activation (Fig. 4a and Supplementary Fig. 8b). In addition,  $\beta_3$ (A711P) increased interaction of the  $\beta_3$ (K716A) TMD with that of  $\alpha_{IIb}$  (Fig. 4b). In contrast, the two other groups of compensating mutations were in the  $\beta_3$  cytoplasmic domain. The truncated  $\beta_3$  caused by  $\beta_3$ (724X or 725X) (group 2) deletes the talin binding site in the  $\beta_3$  tail<sup>20</sup>. Furthermore,  $\beta_3$  Glu 726 can contribute to talin binding through electrostatic interactions with Lys 317 and Lys 364 in talin1 (ref. 21).

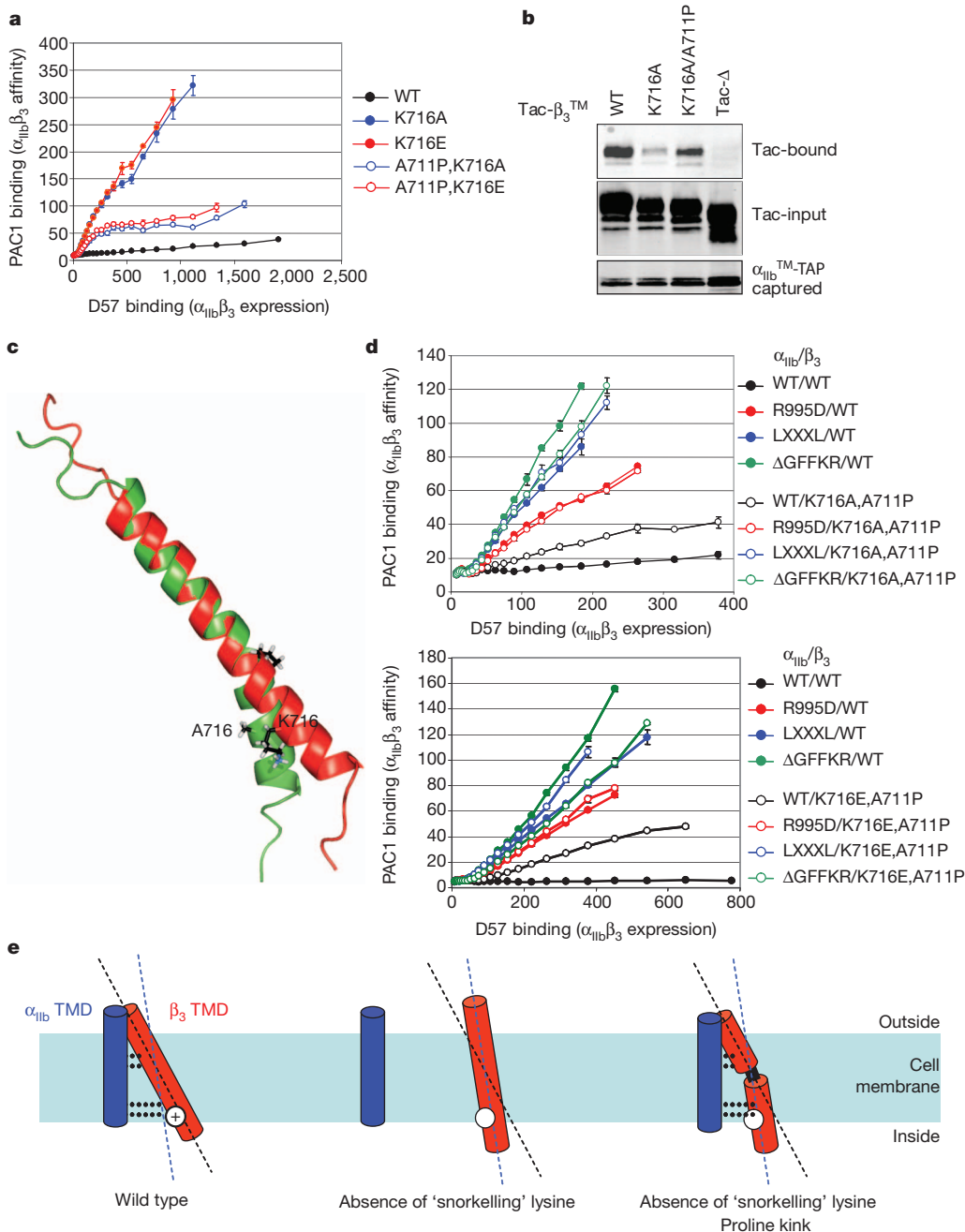


**Figure 4 | Proline introduced in the TMD forms a flexible kink that stabilizes the  $\alpha_{IIb}\beta_3$ (K716A) TMD interaction and reduces integrin activation.**

**a**,  $\beta_3$ (A711P) complements  $\beta_3$ (Lys 716) mutations in integrin activation. CHO/ $\alpha_{IIb}$  cells were transiently transfected with various integrin  $\beta_3$  constructs as indicated, and their binding to PAC1 and D57 was analysed as described above. Error bars, s.e.m. ( $n = 3$ ). **b**,  $\beta_3$ (A711P) stabilizes the TMD interactions of  $\alpha_{IIb}\beta_3$ (K716A). CHO cells were co-transfected with  $\alpha_{IIb}^{TM}$ -TAP constructs and wild type, or mutant Tac- $\beta_3^{TM}$  constructs as indicated, and the interaction between those integrin TMDs were analysed as previously reported<sup>16</sup>. **c**, Structure of the  $\beta_3$ (K716A,A711P) TMD. Structure of the bicelle-embedded integrin  $\beta_3$ (A711P,K716A) TMD segment (shown in green, Protein Data Bank ID 2L91) compared with the wild-type  $\beta_3$  TMD structure (shown in red)<sup>7</sup>. To illustrate the proline-induced kink, the structures were superimposed on the backbone heavy atom coordinates of Ile 693–Leu 709. Average structures are shown. **d**, The inactive state of  $\alpha_{IIb}\beta_3$ (A711P,K716A/E) requires formation of both IMC and OMC. Mutations in  $\alpha_{IIb}$  that disrupt either the OMC ( $\alpha_{IIb}$  G972L,G976L) (LXXXL) or IMC ( $\alpha_{IIb}$ R995D or  $\alpha_{IIb}$ ( $\Delta$ G<sup>991</sup>FFKR) reactivate the  $\alpha_{IIb}\beta_3$ (K716A,A711P) integrin (upper panel) or  $\alpha_{IIb}\beta_3$ (K716E,A711P) integrin (lower panel). Error bars, s.e.m. ( $n = 3$ ). **e**, Mechanism of proline-mediated compensation of snorkelling mutations. Snorkelling of positive-charged residue fixes the crossing angle of  $\beta_3$  TMD (left). Loss of snorkelling changes the crossing angle and preventing simultaneous formation of IMC and OMC, thereby disrupting TMD interaction (middle). The proline-induced kink restores the angle of N-terminal half of the helix (right), enabling reformation of both clasp.



these elements that is independent of the overall membrane  $\beta_3$  TMD crossing angle. Thus, even if the tilt angle of the inner helix is perturbed, this kink can aid the formation of both inner and outer membrane clasps<sup>9</sup> to stabilize the  $\alpha\beta$  dimer. To verify that both clasps still partake in maintaining the inactive state of the integrin, mutations that disrupted either clasp were examined. The OMC involves packing interactions of  $\alpha_{IIb}$ (Gly 972 and Gly 976) and  $\beta_3$ (Gly 708)<sup>9,23</sup>.  $\alpha_{IIb}$ (G972,976A) substitutions that disrupt the OMC overcame the compensating effect of  $\beta_3$ (A711P) in both K716A and K716E backgrounds (Fig. 4d). Similarly, the  $\alpha_{IIb}$ (R995D) mutation or  $\alpha_{IIb}$ ( $\Delta$ GFFKR) deletion, which disrupt the IMC, also overcame compensation (Fig. 4d). Thus, the kink introduced by  $\beta_3$ (A711P) allows the formation of the two membrane clasps required to stabilize the integrin in the off state (Fig. 4e).

In summary, we demonstrated that the loss of a snorkelling residue in integrin  $\beta$  TMDs can change membrane embedding and, thus, membrane-crossing angle, providing direct evidence that snorkelling can specify the topography of TMDs. Furthermore, we showed that snorkelling can affect transmembrane signalling by altering the stability of interactions between integrin TMDs. We have developed an efficient random lentiviral mutagenesis screening method, which was used to discover that a Pro-induced helix kink led to the stabilization of integrin  $\alpha$  and  $\beta$  TMDs interaction by facilitating the formation of the inner and outer membrane clasps. Thus, the long-appreciated snorkelling of basic residues in TMDs<sup>1–3</sup> can have an important role in their topography and lateral association and therefore in signal transduction.

## METHODS SUMMARY

**NMR spectroscopy.** Peptides encompassing human integrin  $\beta_3$ (P685–F727), either wild type or K716E mutant, were produced enriched in  $^{15}\text{N}$  or  $^2\text{H}/^{13}\text{C}/^{15}\text{N}$  isotopes as described previously<sup>7</sup>. Defined amounts of freeze-dried peptide were reconstituted in 25 mM HEPES·NaOH, pH 7.4, 6%  $\text{D}_2\text{O}$ , 0.02% w/v  $\text{NaN}_3$  solution containing 200 mM 1,2-dihexanoyl-*sn*-glycero-3-phosphocholine (DHPC), 40 mM 1-palmitoyl-2-oleoyl-*sn*-glycero-3-phosphocholine (POPC) and 20 mM 1-palmitoyl-2-oleoyl-*sn*-glycero-3-[phospho-L-serine] (Avanti Polar Lipids). Two-dimensional TROSY H–N experiments were recorded in the absence and presence of 1 mM  $\text{Mn}^{2+}$ EDDA<sup>2–</sup> using peptide concentrations of 0.2 mM (ref. 8). K716E assignment was transferred from the wild type using HNCA experiments.

**Random  $\beta_3$  library construction.** Integrin  $\beta_3$ (K716A) cDNA was mutated to remove the BamHI site and introduce an NheI site with silent mutations. The cDNA was cloned into lentiviral vector, which was modified from pRRLSIN.cPPT.PGK-IRES–GFP WPRE (Addgene) to have a BamHI site and BGH reverse primer binding site between PGK promoter and internal ribosome entry site/green fluorescent protein (IRES–GFP). The region between the NheI and BamHI sites was cut out and replaced with NheI- and BamHI-restricted mutagenized PCR products by ligation. The mutagenized PCR products were generated using BGH reverse primer and mutagenized forward primer (Supplementary Fig. 6a). A total of approximately 310,000 *Escherichia coli* colonies on plates from the ligation reaction were collected and pooled. Plasmids from those cells were purified to make the mutagenized  $\beta_3$  cDNA library.

**Full Methods** and any associated references are available in the online version of the paper at [www.nature.com/nature](http://www.nature.com/nature).

Received 14 February; accepted 3 November 2011.

Published online 18 December 2011.

1. Killian, J. A. & von Heijne, G. How proteins adapt to a membrane–water interface. *Trends Biochem. Sci.* **25**, 429–434 (2000).

2. von Heijne, G. Membrane proteins: from sequence to structure. *Annu. Rev. Biophys. Biomol. Struct.* **23**, 167–192 (1994).
3. Sipos, L. & von Heijne, G. Predicting the topology of eukaryotic membrane proteins. *Eur. J. Biochem.* **213**, 1333–1340 (1993).
4. Krishnakumar, S. S. & London, E. The control of transmembrane helix transverse position in membranes by hydrophilic residues. *J. Mol. Biol.* **374**, 1251–1269 (2007).
5. Strandberg, E. & Killian, J. A. Snorkeling of lysine side chains in transmembrane helices: how easy can it get? *FEBS Lett.* **544**, 69–73 (2003).
6. Strandberg, E. *et al.* Lipid dependence of membrane anchoring properties and snorkeling behavior of aromatic and charged residues in transmembrane peptides. *Biochemistry* **41**, 7190–7198 (2002).
7. Lau, T. L., Partridge, A. W., Ginsberg, M. H. & Ulmer, T. S. Structure of the integrin  $\beta_3$  transmembrane segment in phospholipid bicelles and detergent micelles. *Biochemistry* **47**, 4008–4016 (2008).
8. Lau, T. L., Dua, V. & Ulmer, T. S. Structure of the integrin  $\alpha_{IIb}$  transmembrane segment. *J. Biol. Chem.* **283**, 16162–16168 (2008).
9. Lau, T. L., Kim, C., Ginsberg, M. H. & Ulmer, T. S. The structure of the integrin  $\alpha_{IIb}\beta_3$  transmembrane complex explains integrin transmembrane signalling. *EMBO J.* **28**, 1351–1361 (2009).
10. Arnaout, M. A., Mahalingam, B. & Xiong, J. P. Integrin structure, allostery, and bidirectional signaling. *Annu. Rev. Cell Dev. Biol.* **21**, 381–410 (2005).
11. Shattil, S. J., Kim, C. & Ginsberg, M. H. The final steps of integrin activation: the end game. *Nature Rev. Mol. Cell Biol.* **11**, 288–300 (2010).
12. Ginsberg, M. H., Partridge, A. & Shattil, S. J. Integrin regulation. *Curr. Opin. Cell Biol.* **17**, 509–516 (2005).
13. Stefansson, A., Armulik, A., Nilsson, I., von Heijne, G. & Johansson, S. Determination of N- and C-terminal borders of the transmembrane domain of integrin subunits. *J. Biol. Chem.* **279**, 21200–21205 (2004).
14. Hynes, R. O. Integrins: bidirectional, allosteric signaling machines. *Cell* **110**, 673–687 (2002).
15. Zhu, J. *et al.* Requirement of  $\alpha$  and  $\beta$  subunit transmembrane helix separation for integrin outside-in signaling. *Blood* **110**, 2475–2483 (2007).
16. Kim, C., Lau, T. L., Ulmer, T. S. & Ginsberg, M. H. Interactions of platelet integrin  $\alpha_{IIb}$  and  $\beta_3$  transmembrane domains in mammalian cell membranes and their role in integrin activation. *Blood* **113**, 4747–4753 (2009).
17. Shattil, S. J., Hoxie, J. A., Cunningham, M. & Brass, L. F. Changes in the platelet membrane glycoprotein IIb/IIIa complex during platelet activation. *J. Biol. Chem.* **260**, 11107–11114 (1985).
18. Zhu, J. *et al.* The structure of a receptor with two associating transmembrane domains on the cell surface: integrin  $\alpha_{IIb}\beta_3$ . *Mol. Cell* **34**, 234–249 (2009).
19. Frankel, A. D. & Young, J. A. HIV-1: fifteen proteins and an RNA. *Annu. Rev. Biochem.* **67**, 1–25 (1998).
20. Tadokoro, S. *et al.* Talin binding to integrin  $\beta$  tails: a final common step in integrin activation. *Science* **302**, 103–106 (2003).
21. Anthis, N. J. *et al.* The structure of an integrin/talin complex reveals the basis of inside-out signal transduction. *EMBO J.* **28**, 3623–3632 (2009).
22. Senes, A., Engel, D. E. & DeGrado, W. F. Folding of helical membrane proteins: the role of polar, GxxxG-like and proline motifs. *Curr. Opin. Struct. Biol.* **14**, 465–479 (2004).
23. Berger, B. W. *et al.* Consensus motif for integrin transmembrane helix association. *Proc. Natl Acad. Sci. USA* **107**, 703–708 (2010).

**Supplementary Information** is linked to the online version of the paper at [www.nature.com/nature](http://www.nature.com/nature).

**Acknowledgements** This work was supported by grants from the National Institutes of Health of the USA. T.S.U. acknowledges support from the National Institutes of Health (HL089726) and M.H.G. was supported by HL078784, HL57900 and AR27214. C.K. is a recipient of a postdoctoral fellowship from the American Institute for Cancer Research.

**Author Contributions** The project was conceived by C.K. and M.H.G. All experiments with the exception of the NMR studies were performed by C.K. The NMR studies were conducted by T.S. under the supervision of T.S.U. E.C. and F.Y. contributed reagents. M.H.G. and C.K. wrote the paper, which was edited by T.S. and T.S.U.

**Author Information** Reprints and permissions information is available at [www.nature.com/reprints](http://www.nature.com/reprints). The authors declare no competing financial interests. Readers are welcome to comment on the online version of this article at [www.nature.com/nature](http://www.nature.com/nature). Correspondence and requests for materials should be addressed to M.H.G. ([mhginsberg@ucsd.edu](mailto:mhginsberg@ucsd.edu)) or T.S.U. ([tulmer@usc.edu](mailto:tulmer@usc.edu)).

## METHODS

**Plasmids, antibody and cell lines.**  $\alpha_{IIB}^{TM}$ -TAP, Tac- $\beta_3^{TM}$  constructs<sup>16</sup> and lentiviral cloning vector (pRRLSIN.cPPT.PGK-IRES-GFP.WPRE)<sup>24</sup> were described previously. Site-specific mutagenesis was performed using the QuikChange Site-Directed Mutagenesis Kit (Stratagene). Anti-Tac N19 (Santa Cruz Biotechnology), anti-Flag M2 (Sigma-Aldrich) and anti-HA 16B12 (Covance) antibodies were obtained commercially. Mouse monoclonal antibody specific for the human integrin  $\alpha_{IIB}\beta_3$  (D57) and activation-specific anti  $\alpha_{IIB}\beta_3$  antibody (PAC1) have been described previously<sup>13</sup>. Chinese hamster ovary (CHO) cell were maintained as described previously<sup>13</sup>. CHO/ $\alpha_{IIB}$  cells were prepared by infecting CHO cells with lentiviral particle containing integrin  $\alpha_{IIB}$ . Lipofectamine and Lipofectamine Plus reagents (Invitrogen) were used according to the manufacturer's recommendation for transient transfections.

**Affinity capture.** cDNA encoding  $\alpha_{IIB}^{TM}$ -TAP proteins were co-transfected into CHO cells with cDNA encoding Tac- $\beta_3^{TM}$  proteins bearing various mutations, and their affinities analysed as described previously<sup>16</sup>.

**Flow cytometry.** PAC1 binding assay was performed as described<sup>16,25</sup>. In brief, 1 day after transfection, suspended cells were incubated with D57 in combination with PAC1, followed by staining with allophycocyanin-conjugated anti-mouse IgG and with R-phycoerythrin-conjugated anti-mouse IgM. Five minutes before analysis, propidium iodide was added, and propidium-iodide-negative cells were analysed on FACSCalibur (BD Biosciences). The data were imported into MATLAB R2009a software, and the geometric means of PAC1 binding in cells expressing specified levels of  $\alpha_{IIB}\beta_3$  expression were calculated. Those mean values were indicated in the dot plots as larger red dots, and used for the line graphs.

**NMR spectroscopy.** Peptide encompassing human integrin  $\beta_3$ (P685–F727), including  $\beta_3$ (C687S), was produced enriched in  $^{15}\text{N}$  or  $^2\text{H}/^{13}\text{C}/^{15}\text{N}$  isotopes as described previously<sup>7</sup>. K716E substitution was introduced using QuikChange mutagenesis (Stratagene) and the peptide was produced analogously to wild-type  $\beta_3$ . Defined amounts of freeze-dried peptide was reconstituted in 25 mM

HEPES·NaOH, pH 7.4, 6%  $\text{D}_2\text{O}$ , 0.02% w/v  $\text{NaN}_3$  solution containing 200 mM DHPC, 40 mM POPC and 20 mM 1-palmitoyl-2-oleoyl-*sn*-glycero-3-[phospho-L-serine] (Avanti Polar Lipids). Two-dimensional TROSY H–N experiments were recorded in the absence and presence of 1 mM  $\text{Mn}^{2+}$ EDDA<sup>2–</sup> using peptide concentrations of 0.2 mM (ref. 8). K716E assignment was transferred from the wild type by using HNCA experiments. The structure of  $\beta_3$ (A711P, K716A) was determined in 350 mM DHPC, 105 POPC, as described previously for the corresponding wild-type peptide<sup>7</sup>. Structural statistics and spectral quality are summarized in Supplementary Tables 2 and 3 and Supplementary Fig. 10). All NMR experiments were conducted on a cryoprobe-equipped Bruker Avance 700 spectrometer at 35 °C.

**Random  $\beta_3$  library construction.** Integrin  $\beta_3$ (K716A) cDNA was mutated to remove BamHI site and introduce NheI site with silent mutations. The cDNA was cloned into lentiviral vector, which was modified from pRRLSIN.cPPT.PGK-IRES-GFP.WPRE (Addgene) to have the BamHI site and BGH reverse primer binding site between the PGK promoter and IRES-GFP. The region between the NheI and BamHI sites (corresponding to the integrin  $\beta_3$  region containing C-terminal TMD and full cytoplasmic tail, Supplementary Fig. 6a) were cut out and replaced with NheI- and BamHI-restricted mutagenized PCR products by ligation. The mutagenized PCR products were generated using BGH reverse primer and mutagenized forward primer (5'-cattgggtagccGCCCTGCTCATCTGGGcaCTCCTCATCACCATCCACGACCGAAAAGAAttcgctaaattgaggaag-3', where capital letters represent the position containing 9% of contaminating nucleotide, Supplementary Fig. 6a). A total approximately 310,000 *E. coli* colonies on plates from the ligation reaction were collected and pooled. Plasmids from those cells were purified to make the mutagenized  $\beta_3$  cDNA library.

24. Ye, F. *et al.* Recreation of the terminal events in physiological integrin activation. *J. Cell Biol.* **188**, 157–173 (2010).

25. Han, J. *et al.* Reconstructing and deconstructing agonist-induced activation of integrin  $\alpha_{IIB}\beta_3$ . *Curr. Biol.* **16**, 1796–1806 (2006).

# Subnanometre-resolution structure of the intact *Thermus thermophilus* H<sup>+</sup>-driven ATP synthase

Wilson C. Y. Lau<sup>1,2</sup> & John L. Rubinstein<sup>1,2,3</sup>

Ion-translocating rotary ATPases serve either as ATP synthases, using energy from a transmembrane ion motive force to create the cell's supply of ATP, or as transmembrane ion pumps that are powered by ATP hydrolysis<sup>1</sup>. The members of this family of enzymes each contain two rotary motors: one that couples ion translocation to rotation and one that couples rotation to ATP synthesis or hydrolysis. During ATP synthesis, ion translocation through the membrane-bound region of the complex causes rotation of a central rotor that drives conformational changes and ATP synthesis in the catalytic region of the complex. There are no structural models available for the intact membrane region of any ion-translocating rotary ATPase. Here we present a 9.7 Å resolution map of the H<sup>+</sup>-driven ATP synthase from *Thermus thermophilus* obtained by electron cryomicroscopy of single particles in ice. The 600-kilodalton complex has an overall subunit composition of A<sub>3</sub>B<sub>3</sub>CDE<sub>2</sub>FG<sub>2</sub>IL<sub>12</sub>. The membrane-bound motor consists of a ring of L subunits and the carboxy-terminal region of subunit I, which are equivalent to the c and a subunits of most other rotary ATPases, respectively. The map shows that the ring contains 12 L subunits<sup>2</sup> and that the I subunit has eight transmembrane helices<sup>3</sup>. The L<sub>12</sub> ring and I subunit have a surprisingly small contact area in the middle of the membrane, with helices from the I subunit making contacts with two different L subunits. The transmembrane helices of subunit I form bundles that could serve as half-channels across the membrane, with the first half-channel conducting protons

from the periplasm to the L<sub>12</sub> ring and the second half-channel conducting protons from the L<sub>12</sub> ring to the cytoplasm. This structure therefore suggests the mechanism by which a transmembrane proton motive force is converted to rotation in rotary ATPases.

To investigate how the structure of the *T. thermophilus* ATP synthase allows its rotary mechanism, we imaged the detergent-solubilized intact enzyme by electron cryomicroscopy (cryo-EM) and calculated a three-dimensional map to approximately 10 Å resolution (Supplementary Fig. 1). This resolution was sufficient to observe α-helices in the structure. Achieving this resolution required optimization of the specimen preparation and imaging conditions, and development of a new map refinement algorithm (Methods). Figure 1a shows the refined three-dimensional map. Available crystal structures of subunits and subcomplexes of the enzyme were fitted into the map with remarkably good agreement (Fig. 1b, c). A cross-section through the soluble region of the map shows that the α-helices that make up each of the E and G subunits of the two peripheral stalks can be resolved (Fig. 1d, purple and beige arrows, respectively), as can densities that correspond to α-helices in subunits with more complex folds, such as the A subunits (Fig. 1d, for example, circled in yellow). Map segments corresponding to subunits matched available crystal structures with high fidelity (Fig. 1e–g). If the protein particles imaged occupied all possible rotational states of the central rotor, the three-dimensional map would show the average conformation of each A and B subunit and the density corresponding to the DF subcomplex would

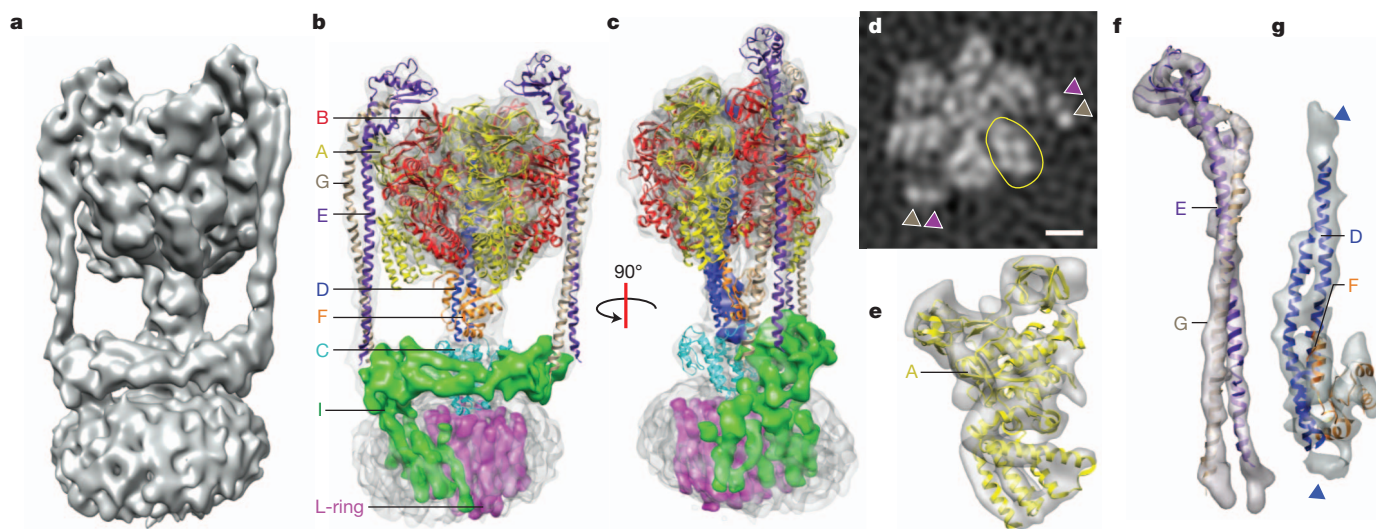


**Figure 1 | Three-dimensional map of the *T. thermophilus* ATP synthase.** **a**, A surface view of the three-dimensional map. **b**, **c**, The overall map (semi-transparent grey) with fitted crystal structures and segments corresponding to individual subunits. Segments of the cryo-EM map are shown for the L<sub>12</sub> ring, subunit I and residues of subunit D missing from its crystal structure. **d**, A cross-section through the soluble region of the map shows that α-helices from

the two E subunits (purple arrows) and two G subunits (beige arrows) can be resolved. Helices can also be resolved in other subunits, such as the A subunits (example circled in yellow). The map segments agree with crystal structures, such as subunit A (**e**), the EG subcomplex (**f**) and the DF subcomplex (**g**). Density corresponding to missing residues from the crystal structure of the D subunit is indicated with blue arrows. Scale bars, 25 Å.

<sup>1</sup>Molecular Structure and Function Program, The Hospital for Sick Children Research Institute, 555 University Avenue, Toronto, Ontario M5G 1X8, Canada. <sup>2</sup>Department of Biochemistry, The University of Toronto, Ontario M5S 1A8, Canada. <sup>3</sup>Department of Medical Biophysics, The University of Toronto, Ontario M5G 2M9, Canada.



appear as a rotational average of the structure of these subunits. However, docking an  $A_3B_3DF$  crystal structure<sup>4</sup> into the map (Fig. 1b, c and Supplementary Fig. 2) and fitting the DF-rotor subcomplex into its corresponding map segment (Fig. 1g) revealed that the enzyme was arrested in a single rotational state<sup>5</sup>. This homogeneity explains why we were able to extract nanometre-resolution information when averaging many different particles to calculate the map. The crystal structure of the  $A_3B_3DF$  subcomplex showed that two of the AB subunit pairs took on similar closed or narrow conformations, designated  $A_NB_N$  and  $A_{N'}B_{N'}$ , whereas the third adopted an open or wide conformation, designated  $A_WB_W$ <sup>4</sup>. From the position of the D and F subunits in the cryo-EM map, it is apparent that the  $A_NB_N$  pair, which corresponds to the  $\beta_{TP}\alpha_{TP}$  pair in mitochondrial  $F_1$ -ATPase<sup>6</sup>, is positioned at the A/B interface between the two peripheral stalks (Supplementary Fig. 2). Because we did not take any measures to stop the rotor in one rotational state, the existence of this unique position suggests that in the intact complex the observed state has a lower energy than other positions of the rotor. For the membrane-bound subunits I and L, where no crystal structures are available, segmented densities are shown in Fig. 1b, c.

The extramembranous portion of the map contains a wealth of information on how the different subunits interact in the intact enzyme. The two peripheral stalks of the complex have the same structures in the intact assembly, both adopting conformations that match the available crystal structure<sup>7</sup>. Contacts between the catalytic  $A_3B_3$  hexamer and the peripheral stalks exclusively involve the B subunits and E subunits of the stalks, and are mostly between the amino-terminal  $\beta$ -barrel domains of the B subunits and the C-terminal  $\alpha/\beta$ -domains of the E subunits. The N-terminal region of both subunits E and G in both of the peripheral stalks interact with the N-terminal region of subunit I. The funnel-shaped C subunit, which links the DF portion of the central rotor to the  $L_{12}$  ring and has been crystallized in isolation<sup>8</sup>, is significantly more open in the intact enzyme than in the crystal structure so that it can accept the DF subunits into its central cavity (Fig. 2). The three pseudo-symmetric domains of the C subunit can be differentiated in the map showing that interaction of the C subunit and the  $L_{12}$  ring strongly involves the N-terminal  $\alpha$ -helix of the first domain of subunit C. The C subunit sits asymmetrically on the  $L_{12}$  ring and does not penetrate significantly into the central pore of the ring. The cryo-EM map shows that the N-terminal region of subunit I consists of an elongated helical

bundle flanked by two domains, consistent with a crystal structure of a homologous protein that was published after submission of this manuscript<sup>9</sup> (Supplementary Fig. 3).

The map provides the first detailed insight into how the I subunit and  $L_{12}$  ring fit together to allow the generation of rotation (Fig. 3a). Cross-sections through the detergent-embedded region of the map show two concentric rings of densities, with the outer ring consisting of 12 well-resolved densities (Fig. 3b–e). These 12 densities undoubtedly correspond to the outer helices of the  $L_{12}$  ring, where each L subunit consists of a helical hairpin. The N-terminal inner helices of the  $L_{12}$  ring could not be resolved and appear as a nearly continuous density. Our ability to resolve the outer helices is consistent with the loose packing and gaps seen between the outer helices in crystal structures of related ring subcomplexes<sup>10–15</sup>. Although composed of similarly sized residues as the outer helices, the crystallographic studies suggest that the inner helices are more tightly packed and resolving them would require a resolution better than 9.7 Å. As shown previously<sup>5</sup>, the detergent used to keep the enzyme soluble, dodecylmaltoside, has a density higher than that of ice and is visible surrounding the transmembrane region of the complex (Fig. 3b, left panel, white bars). Features in the detergent micelle, which we expect to be mostly unstructured, may represent noise that is enhanced by construction of the map to nanometre resolution. Density is visible within the centre of the  $L_{12}$  ring (Fig. 3b, left panel, yellow circle) and probably corresponds to a detergent or lipid plug observed by atomic force microscopy of isolated rings<sup>16</sup>. The map presents the first determination of the ring structure within an intact rotary ATPase, providing insight into how the I subunit affects the  $L_{12}$  ring. This information is necessary to assess the likelihood of proposed catalytic models in which the L subunits undergo conformational changes when they contact the I subunit<sup>17</sup>. From the cryo-EM map it is evident that the 12-fold symmetry of the  $L_{12}$  ring is not broken significantly, even where the L subunits contact the I subunit (Fig. 3c, d). This preserved symmetry of the ring is inconsistent with models of proton translocation that require major conformational changes in the rotor, but could still be consistent with swivelling of the outer helices of the L subunits if this motion did not distort the ring significantly<sup>17</sup>.

Proton translocation facilitated by the I subunit drives rotation of the  $L_{12}$  ring, but until now there has been no structural information available for subunit I or its equivalent subunit from any rotary ATPase. Here we observe eight transmembrane densities that can be

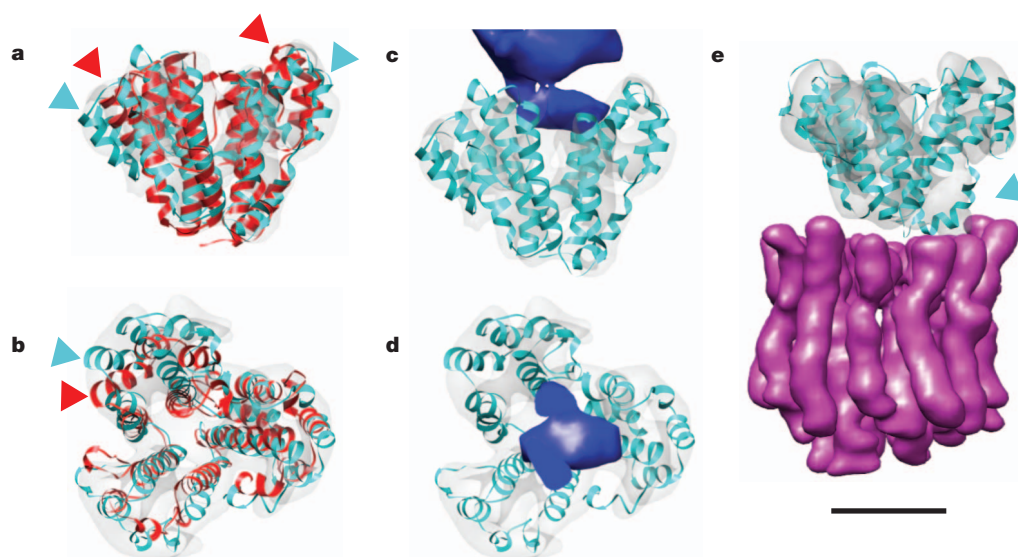


**Figure 2 | Fitting of the C subunit crystal structure.** a, b, Side (a) and top (b) views comparing rigid body fitting of the C subunit crystal structure (red) to flexible fitting of the crystal structure (cyan) into the corresponding map segment. Arrows indicate regions of major difference between the two atomic models. c, d, Side (c) and top (d) views showing that flexible fitting of the C

subunit gives it a more open conformation that allows it to accommodate the segment for the DF subcomplex (dark blue) into its central cavity. e, A side view of the C subunit, and the segment corresponding to the  $L_{12}$  ring (magenta), show that subunit C sits asymmetrically on the ring with its N-terminal  $\alpha$ -helix (cyan arrow) mediating most of the contact with the L subunits. Scale bar, 25 Å.

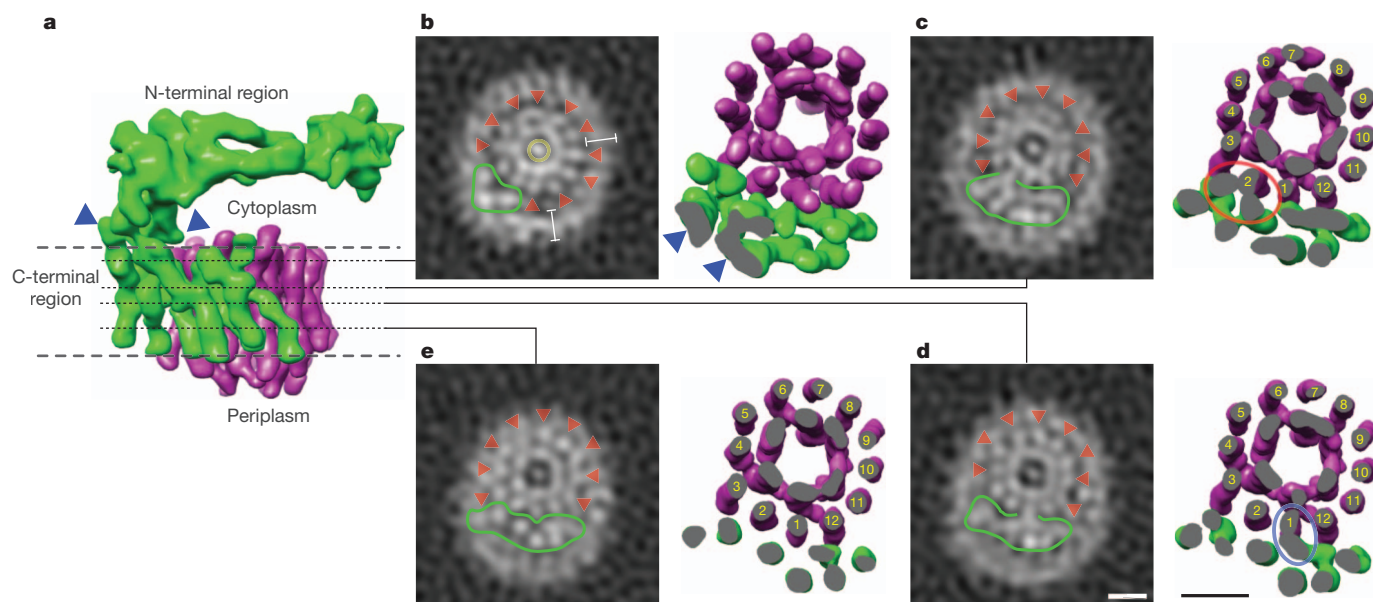


**Figure 3 | The membrane-bound region of the enzyme.** **a**, Map segments of the  $L_{12}$  ring (magenta) and subunit I (green) showing multiple contacts between the N- and C-terminal regions of subunit I (blue arrows). **b**, Cross-sections through the map (left panel) and map segments truncated at the same height (right panel) show subunit I separated from the  $L_{12}$  ring near the cytoplasm. Outer helices of the  $L_{12}$  ring are indicated (red arrows) and the transmembrane helices of subunit I are outlined (green). Cross-sections show

the detergent micelle (white bars) and detergent or lipid in the centre of the  $L_{12}$  ring (yellow circle). **c**, Near the middle of the membrane, subunit I contacts an L subunit, probably forming the mid-membrane end of the cytoplasmic half-channel (circle in red in right panel). **d**, Approximately 6 Å further towards the periplasm subunit I contacts a different L subunit, probably forming the mid-membrane end of the periplasmic half-channel (circled in blue in right panel). **e**, Subunit I is separated from the  $L_{12}$  ring near the periplasm. Scale bars, 25 Å.

attributed to  $\alpha$ -helices in the C-terminal region of subunit I (Fig. 3b–e). This number of transmembrane helices is consistent with an experimentally tested topology map of the *Saccharomyces cerevisiae* V-ATPase a subunit<sup>3</sup>, with which the I subunit sequence aligns well (Supplementary Fig. 4). Although we can trace the complete trajectories of the eight transmembrane densities of subunit I, our inability to resolve the helices in the tightly packed inner ring of the  $L_{12}$  oligomer means that we cannot rule out the possibility that we have missed a transmembrane helix in our analysis of subunit I. At the cytoplasmic surface of the membrane region, the densities from the N- and C-terminal regions of subunit I appear to be connected in more than one place (Fig. 3a and the right panel of Fig. 3b, blue arrows). These connections show that there must be protein–protein interactions between the N- and C-terminal regions of subunit I involved in keeping the two regions rigidly attached. Within the membrane, subunit I divides into two clusters of helices: one that is mostly perpendicular to the membrane, and another that contains tilted helices adjacent to the  $L_{12}$  ring. The first cluster contacts a single L subunit near the middle of the membrane region (right panel of Fig. 3c, circled in red) whereas the second cluster contacts the adjacent L subunit a small distance further towards the periplasm (right panel of Fig. 3d, circled in blue). The maximal separation of the I subunit helices from the outer helices of the  $L_{12}$  ring is of around the same distance, approximately 15 Å between helical axes, as is the maximal separation between adjacent outer helices of the  $L_{12}$  ring.

Proton translocation in rotary ATPases is thought to involve protonation and deprotonation of conserved mid-membrane glutamic acid or aspartic acid residues in the outer helices of the ring-forming subunits. In the L subunit from the *T. thermophilus* ATP synthase, this conserved protonatable residue is Glu 63. The contact of the I subunit with two different L subunits (Fig. 3c, d) places the two L subunits in distinct chemical environments and establishes the conditions necessary for a two half-channel model for proton translocation<sup>13,18</sup>, with one L subunit exchanging protons with the periplasm and another L subunit exchanging protons with the cytoplasm. One cluster of transmembrane helices in the I subunit could conduct protons from the periplasm to the

mid-membrane Glu 63 residue of an L subunit (Fig. 4a, blue circle). The other cluster of transmembrane helices in subunit I could conduct protons from the mid-membrane Glu 63 residue of the adjacent L subunit to the cytoplasm (Fig. 4a, red circle). Crystal structures of other membrane proteins indicate that four transmembrane helices are sufficient for forming a proton pore, with available examples showing proton<sup>19</sup> and sodium<sup>20</sup> conducting pores composed of four and three transmembrane helices, respectively. The structure suggests that protons flow from the periplasmic half-channel to the Glu 63 residue of the L subunit in contact with the periplasmic half-channel (the L subunit with an outer helix labelled '1' in Fig. 3c–e). Protonation of this Glu 63 neutralizes the negative charge of the residue and allows the anticlockwise rotation of the ring (viewed from the cytoplasm) that places the Glu 63 in the hydrophobic environment of the lipid bilayer (Fig. 4b). With the negative charge neutralized, Glu 63 can assume the proton-locked conformation seen in a crystal structure of the *Spirulina platensis*  $c_{15}$  ring<sup>13</sup>. In this conformation, both oxygen atoms in Glu 63 are involved in hydrogen bonding with other residues in the  $L_{12}$  ring and the neutral Glu 63 residue is tucked into the crevice between L subunits. The directionality of the rotation is explained by a Brownian ratchet mechanism where random thermal rotational fluctuations are biased to go in the correct direction by the direction of the proton motive force across the membrane<sup>18</sup>. Rotation of the  $L_{12}$  ring brings an L subunit bearing a protonated Glu 63 (on the helix labelled '2' in Fig. 3c–e) out of the lipid environment and into contact with the cytoplasmic half-channel of subunit I. Subunit I contains a conserved and essential arginine residue (Arg 563) of unknown function<sup>21,22</sup>. It has been postulated that Arg 563 causes a decrease in the  $pK_a$  of the Glu 63 residue on the L subunit in contact with the cytoplasmic half-channel, thereby causing it to lose its proton to the channel<sup>23</sup>. Arg 563 may also stabilize the deprotonated Glu 63 by forming a salt bridge<sup>12</sup>. This arrangement of half-channels is consistent with a model where L ring rotation could be driven in either direction, depending only on the direction of the proton motive force across the membrane. However, the specific arrangements of amino acids in the structure, which cannot be resolved in this map, could be such that proton translocation from



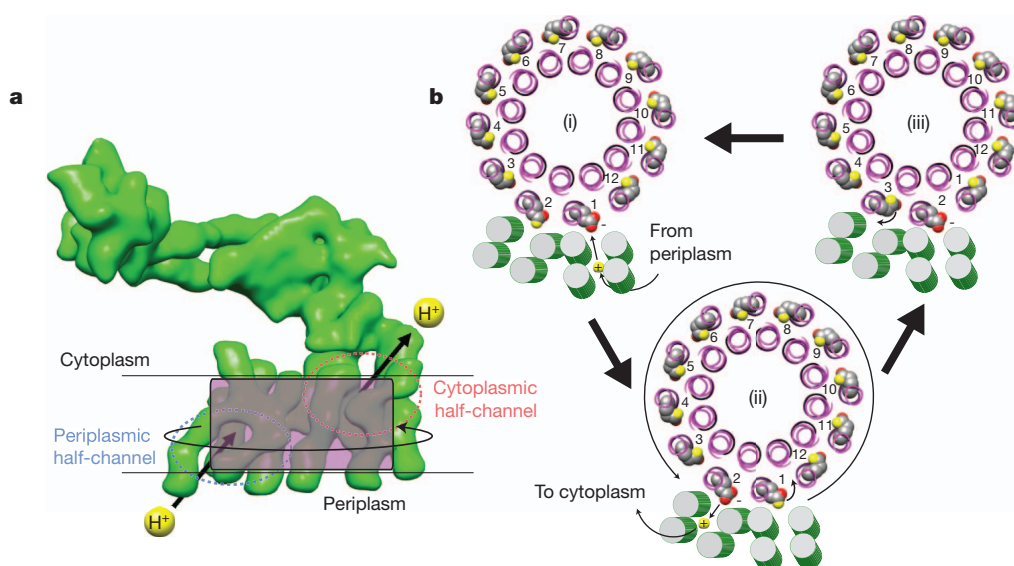


**Figure 4 | Model for proton translocation.** **a**, Subunit I (green) is shown parallel to the membrane with the  $L_{12}$  ring in front of it indicated by a semi-transparent magenta rectangle. During ATP synthesis, protons enter the periplasmic half-channel in subunit I (dashed blue oval) and are conducted to the centre of the lipid bilayer where they neutralize the Glu 63 residue of an L subunit. The ring rotates to bring a protonated Glu 63 residue into contact with the cytoplasmic half-channel (dashed red oval). **b**, Viewed from the cytoplasm, two half-channels in subunit I are depicted as clusters of green cylinders.

the cytoplasm to the periplasm is not able to induce rotation. At 9.7 Å resolution, it is not possible to relate unambiguously the sequence of the C-terminal region of subunit I and predicted transmembrane helices (shown in Supplementary Fig. 4) to the transmembrane densities in the map. Nonetheless, Arg 563 has been proposed to reside on transmembrane helix 7 and form part of the cytoplasmic half-channel<sup>3</sup>, which would identify transmembrane helix 7 as one of the two helices in contact with the L subunit labelled '2' in Fig. 3.

At both the cytoplasmic and periplasmic limits of the membrane-embedded region of the map (Fig. 3b, e) all helices from subunit I are well separated from the helices of the  $L_{12}$  ring, making it highly unlikely that an entire half-channel could be formed by the interface of helices from the I and L subunits<sup>24</sup>. F-type ATP synthases have been proposed to have five transmembrane helices<sup>25,26</sup>. If true, this topology would suggest that in those enzymes the two half-channels consist of three helices, that one or more helices contributes to both half-channels simultaneously, or that helices from the rotor are involved in formation of the half-channels. The observation that the two L subunits in contact with the I subunit are immediately adjacent to each other indicates that after a Glu 63 residue is deprotonated by the cytoplasmic half-channel it is immediately reprotonated by the periplasmic half-channel with a single 30° rotational step of the rotor. The small contact area between the I subunit and  $L_{12}$  ring suggests that these membrane-bound components rely on the two peripheral stalks to hold them together in the precise arrangement necessary for the complex's biological activity. This minimal contact is consistent with an important but fragile interaction that might easily be disrupted by non-physiological conditions such as those needed to make three-dimensional crystals, thus helping to explain why the membrane region of this class of enzyme has not been crystallized, despite significant efforts by many research groups. Knowledge of the precise residues involved in proton translocation will require construction of cryo-EM maps to higher resolution or formation of well-ordered crystals of this hitherto refractory protein complex. At subnanometre resolution, the complete structure of the *T. thermophilus*  $H^+$ -driven ATP synthase suggests the mechanism by which the energy stored in a transmembrane proton motive force is converted into rotation in rotary ATPases.

Deprotonated Glu 63 residues are shown with two red oxygen atoms whereas protonated Glu 63 residues are shown with one red and one yellow oxygen atom. Protonation of L subunit '1' by the periplasmic half-channel (i) and deprotonation of L subunit '2' by the cytoplasmic half-channel (ii) lead to rotation of the ring, with L subunit '1' assuming a proton-locked conformation as it enters the lipid bilayer. Rotation brings the proton-locked L subunit '3' to the cytoplasmic half-channel (iii) where it assumes an unlocked conformation, allowing the sequence of events to repeat.

## METHODS SUMMARY

*T. thermophilus* HB8 was grown and the  $H^+$ -driven ATP synthase purified as described previously<sup>5</sup>. Specimens were prepared for cryo-EM with a Vitrobot (FEI) and imaged with an FEI Tecnai F20 electron microscope equipped with a field emission gun and operating at 200 kV. An electron exposure of approximately 18 electrons Å<sup>-2</sup> was used during imaging to optimize the signal-to-noise ratio at relevant spatial frequencies<sup>27</sup>. Images were recorded on Kodak SO-163 film and digitized with a Photocan densitometer (Intergraph). The previously published cryo-EM map of the *T. thermophilus* V-ATPase<sup>5</sup> was filtered to 30 Å resolution and used as an initial model for refinement of the entirely new data set of 46,105 particle images. Initial particle orientations were determined by projection matching with FREALIGN<sup>28</sup> using information out to 20 Å resolution. The accuracy of particle orientations was refined further with a new program (Refine\_space), ultimately using information out to 11.2 Å resolution.

**Full Methods** and any associated references are available in the online version of the paper at [www.nature.com/nature](http://www.nature.com/nature).

Received 18 July; accepted 3 November 2011.

Published online 18 December 2011; corrected 11 January 2012 (see full-text HTML version for details).

- Muench, S. P., Trinick, J. & Harrison, M. A. Structural divergence of the rotary ATPases. *Q. Rev. Biophys.* **44**, 311–356 (2011).
- Toei, M. *et al.* Dodecamer rotor ring defines  $H^+$ /ATP ratio for ATP synthesis of prokaryotic V-ATPase from *Thermus thermophilus*. *Proc. Natl Acad. Sci. USA* **104**, 20256–20261 (2007).
- Toei, M., Toei, S. & Forgacs, M. Definition of membrane topology and identification of residues important for transport in subunit a of the vacuolar ATPase. *J. Biol. Chem.* **286**, 35176–35186 (2011).
- Numoto, N., Hasegawa, Y., Takeda, K. & Miki, K. Inter-subunit interaction and quaternary rearrangement defined by the central stalk of prokaryotic V1-ATPase. *EMBO Rep.* **10**, 1228–1234 (2009).
- Lau, W. C. & Rubinstein, J. L. Structure of intact *Thermus thermophilus* V-ATPase by cryo-EM reveals organization of the membrane-bound V(O) motor. *Proc. Natl Acad. Sci. USA* **107**, 1367–1372 (2010).
- Abrahams, J. P., Leslie, A. G., Lutter, R. & Walker, J. E. Structure at 2.8 Å resolution of F1-ATPase from bovine heart mitochondria. *Nature* **370**, 621–628 (1994).
- Lee, L. K. *et al.* The structure of the peripheral stalk of *Thermus thermophilus*  $H^+$ -ATPase/synthase. *Nature Struct. Mol. Biol.* **17**, 373–378 (2010).
- Iwata, M. *et al.* Crystal structure of a central stalk subunit C and reversible association/dissociation of vacuole-type ATPase. *Proc. Natl Acad. Sci. USA* **101**, 59–64 (2004).



9. Srinivasan, S., Vyas, N. K., Baker, M. L. & Quirocho, F. A. Crystal structure of the cytoplasmic N-terminal domain of subunit I, a homolog of subunit a, of V-ATPase. *J. Mol. Biol.* **412**, 14–21 (2011).
10. Murata, T. *et al.* Structure of the rotor of the V-type Na<sup>+</sup>-ATPase from *Enterococcus hirae*. *Science* **308**, 654–659 (2005).
11. Stock, D., Leslie, A. G. & Walker, J. E. Molecular architecture of the rotary motor in ATP synthase. *Science* **286**, 1700–1705 (1999).
12. Meier, T. *et al.* Structure of the rotor ring of F-type Na<sup>+</sup>-ATPase from *Ilyobacter tartaricus*. *Science* **308**, 659–662 (2005).
13. Pogoryelov, D., Yildiz, O., Faraldo-Gomez, J. D. & Meier, T. High-resolution structure of the rotor ring of a proton-dependent ATP synthase. *Nature Struct. Mol. Biol.* **16**, 1068–1073 (2009).
14. Watt, I. N. *et al.* Bioenergetic cost of making an adenosine triphosphate molecule in animal mitochondria. *Proc. Natl Acad. Sci. USA* **107**, 16823–16827 (2010).
15. Preiss, L. *et al.* A new type of proton coordination in an F<sub>1</sub>F<sub>0</sub>-ATP synthase rotor ring. *PLoS Biol.* **8**, e1000443 (2010).
16. Meier, T. *et al.* The central plug in the reconstituted undecameric c cylinder of a bacterial ATP synthase consists of phospholipids. *FEBS Lett.* **505**, 353–356 (2001).
17. Fillingame, R. H., Angevine, C. M. & Dmitriev, O. Y. Mechanics of coupling proton movements to c-ring rotation in ATP synthase. *FEBS Lett.* **555**, 29–34 (2003).
18. Junge, W., Lill, H. & Engelbrecht, S. ATP synthase: an electrochemical transducer with rotary mechanics. *Trends Biochem. Sci.* **22**, 420–423 (1997).
19. Stouffer, A. L. *et al.* Structural basis for the function and inhibition of an influenza virus proton channel. *Nature* **451**, 596–599 (2008).
20. Gonzales, E. B., Kawate, T. & Gouaux, E. Pore architecture and ion sites in acid-sensing ion channels and P2X receptors. *Nature* **460**, 599–604 (2009).
21. Cain, B. D. & Simoni, R. D. Proton translocation by the F<sub>1</sub>F<sub>0</sub>ATPase of *Escherichia coli*. Mutagenic analysis of the a subunit. *J. Biol. Chem.* **264**, 3292–3300 (1989).
22. Kawasaki-Nishi, S., Nishi, T. & Forgac, M. Arg-735 of the 100-kDa subunit a of the yeast V-ATPase is essential for proton translocation. *Proc. Natl Acad. Sci. USA* **98**, 12397–12402 (2001).
23. Pogoryelov, D. *et al.* Microscopic rotary mechanism of ion translocation in the F<sub>0</sub> complex of ATP synthases. *Nature Chem. Biol.* **6**, 891–899 (2010).
24. Steed, P. R. & Fillingame, R. H. Aqueous accessibility to the transmembrane regions of subunit c of the *Escherichia coli* F<sub>1</sub>F<sub>0</sub> ATP synthase. *J. Biol. Chem.* **284**, 23243–23250 (2009).
25. Long, J. C., Wang, S. & Vik, S. B. Membrane topology of subunit a of the F<sub>1</sub>F<sub>0</sub> ATP synthase as determined by labeling of unique cysteine residues. *J. Biol. Chem.* **273**, 16235–16240 (1998).
26. Valiyaveetil, F. I. & Fillingame, R. H. Transmembrane topography of subunit a in the *Escherichia coli* F<sub>1</sub>F<sub>0</sub> ATP synthase. *J. Biol. Chem.* **273**, 16241–16247 (1998).
27. Baker, L. A., Smith, E. A., Bueler, S. A. & Rubinstein, J. L. The resolution dependence of optimal exposures in liquid nitrogen temperature electron cryomicroscopy of catalase crystals. *J. Struct. Biol.* **169**, 431–437 (2010).
28. Grigorieff, N. FREALIGN: high-resolution refinement of single particle structures. *J. Struct. Biol.* **157**, 117–125 (2007).

**Supplementary Information** is linked to the online version of the paper at [www.nature.com/nature](http://www.nature.com/nature).

**Acknowledgements** We thank V. Kanelis, F. Sicheri, P. Rosenthal, L. Kay and R. Henderson for discussions and reading this manuscript, and J. Walker and R. Pomès for discussions. Computations were performed on the general-purpose cluster supercomputer at the SciNet HPC Consortium. W.C.Y.L. was supported by an Ontario Graduate Scholarship. J.L.R. was supported by a New Investigator Award from the Canadian Institutes of Health Research and an Early Researcher Award from the Ontario Ministry of Research and Innovation. This research was funded by operating grant MOP 81294 from the Canadian Institutes of Health Research.

**Author Contributions** J.L.R. and W.C.Y.L. designed the experiments and J.L.R. supervised the research. W.C.Y.L. performed protein purification and cryo-EM. J.L.R. wrote new computer programs. W.C.Y.L. and J.L.R. performed the image analysis, interpreted the data and wrote the manuscript.

**Author Information** The cryo-EM map of the *T. thermophilus* H<sup>+</sup>-driven ATP synthase is deposited in Electron Microscopy Data Bank under accession code EMD-5335; the docked atomic models are deposited in Protein Data Bank under accession number 3JQJ. Reprints and permissions information is available at [www.nature.com/reprints](http://www.nature.com/reprints). The authors declare no competing financial interests. Readers are welcome to comment on the online version of this article at [www.nature.com/nature](http://www.nature.com/nature). Correspondence and requests for materials should be addressed to J.L.R. ([john.rubinstein@utoronto.ca](mailto:john.rubinstein@utoronto.ca)).

## METHODS

**Specimen preparation and imaging.** *T. thermophilus* HB8 was grown and the H<sup>+</sup>-driven ATP synthase purified as described previously<sup>5</sup>. Specimens were prepared on glow-discharged Quantifoil R2/2 carbon-coated TEM grids (Quantifoil Microtools) with a Vitrobot grid freezing device (FEI Company) and imaged with a FEI Tecnai F20 electron microscope equipped with a field emission gun and operating at 200 kV. An electron exposure of approximately 18 electrons Å<sup>-2</sup> was used to optimize the signal-to-noise ratio at relevant spatial frequencies<sup>27</sup>. Images were recorded on Kodak SO-163 film with defocus values between 2.5 and 4.5 µm at ×50,000 magnification, developed in D19 for 8 min and digitized with a Photoscan densitometer (Intergraph). Only micrographs that showed high contrast from thin ice layers, no noticeable drift and oscillations of the contrast transfer function beyond 10 Å resolution were selected for further analysis. From these micrographs, contrast transfer function parameters were determined<sup>29</sup> and particle images were selected interactively with Ximdisp<sup>30</sup>.

**Three-dimensional map construction and segmenting.** Initial particle orientation parameters for the data set of 46,105 particle images were determined by projection matching with FREALIGN<sup>28</sup> using a reference map created by low-pass filtering the previously published map of the *T. thermophilus* H<sup>+</sup>-driven ATP synthase to 30 Å resolution. Orientation parameters were refined with FREALIGN using information out to 20 Å resolution. Further refinement of particle orientation parameters was achieved with a new program, Refine\_fspace, that performs projection matching in Fourier space while allowing continuous constrained optimization of the Euler angles and shifts with a simplex minimization algorithm<sup>31,32</sup>. Before projection matching with a normalized correlation coefficient, image Fourier transforms were multiplied by the contrast transfer function and the map projection Fourier transforms by the square of the contrast transfer function. To avoid influencing the measurement of resolution with noise bias, the highest spatial frequency used during refinement was kept below the resolution limit of the map, ultimately incorporating information out to 11.2 Å resolution.

From the data set of particle images, the top approximately 90% (42,075) with the best correlation coefficients at their determined orientations were selected and the final three-dimensional map was calculated by sinc function interpolation in Fourier space<sup>28</sup>. The resolution of the final map was assessed by Fourier shell correlation and Fourier neighbour correlation<sup>33</sup> with the 0.143 (ref. 34) and 0.5 thresholds. Fourier components were sharpened with an inverse B-factor of 750 Å<sup>2</sup> and weighted for the signal-to-noise ratio with a C<sub>ref</sub> filter<sup>35</sup>. Segmentation was performed automatically using Segger<sup>36</sup>, semiautomatically using Wateredge<sup>37</sup> and manually using EMAN qsegment<sup>38</sup>.

**Model building and fitting.** The Protein Data Bank accession numbers for atomic models used to interpret the three-dimensional cryo-EM map were 3A5C (A<sub>3</sub>B<sub>3</sub>DF complex<sup>4</sup>), 3K5B (EG complex<sup>7</sup>), 1R5Z (subunit C<sup>8</sup>) and 3RRK (the N-terminal domain of subunit I from *Meiothermus ruber*<sup>9</sup>). A comparative model of the L subunit in its proton-locked conformation was built with Phyre2 (ref. 39) using the two C-terminal transmembrane helices of the NtpK subunit of the sodium-driven V-ATPase from *Enterococcus hirae* (Protein Data Bank accession number 2BL2 (ref. 10)) as the template. This template was identified automatically by Phyre2 with 99.9% confidence and represents 90% coverage of subunit L. An atomic model of the L<sub>12</sub> ring was constructed in Situs<sup>40</sup>. Rigid-body fitting of atomic models into the cryo-EM map was done with UCSF Chimera<sup>41</sup>; flexible fitting of subunit C into the map was performed with IMODFIT (<http://chaconlab.org/imodfit/index.html>). All figures were rendered with UCSF Chimera<sup>41</sup>.

29. Mindell, J. A. & Grigorieff, N. Accurate determination of local defocus and specimen tilt in electron microscopy. *J. Struct. Biol.* **142**, 334–347 (2003).
30. Crowther, R. A., Henderson, R. & Smith, J. M. MRC image processing programs. *J. Struct. Biol.* **116**, 9–16 (1996).
31. Nelder, J. A. & Mead, R. A simplex method for function minimization. *Comput. J.* **7**, 308–313 (1965).
32. Press, W. H., Teukolsky, S. A., Vetterlin, W. T. & Flannery, B. P. *Numerical Recipes in Fortran 77* 2nd edn (Cambridge Univ. Press, 2003).
33. Sousa, D. & Grigorieff, N. Ab initio resolution measurement for single particle structures. *J. Struct. Biol.* **157**, 201–210 (2007).
34. Rosenthal, P. B., Crowther, R. A. & Henderson, R. An objective criterion for resolution assessment in single-particle electron microscopy (appendix). *J. Mol. Biol.* **333**, 743–745 (2003).
35. Rosenthal, P. B. & Henderson, R. Optimal determination of particle orientation, absolute hand, and contrast loss in single-particle electron cryomicroscopy. *J. Mol. Biol.* **333**, 721–745 (2003).
36. Pintilie, G. D. et al. Quantitative analysis of cryo-EM density map segmentation by watershed and scale-space filtering, and fitting of structures by alignment to regions. *J. Struct. Biol.* **170**, 427–438 (2010).
37. Baker, L. A. & Rubinstein, J. L. Edged watershed segmentation: a semi-interactive algorithm for segmentation of low-resolution maps from electron cryomicroscopy. *J. Struct. Biol.* **176**, 127–132 (2011).
38. Ludtke, S. J., Baldwin, P. R. & Chiu, W. EMAN: semiautomated software for high-resolution single-particle reconstructions. *J. Struct. Biol.* **128**, 82–97 (1999).
39. Kelley, L. A. & Sternberg, M. J. Protein structure prediction on the Web: a case study using the Phyre server. *Nature Protocols* **4**, 363–371 (2009).
40. Chacon, P. & Wriggers, W. Multi-resolution contour-based fitting of macromolecular structures. *J. Mol. Biol.* **317**, 375–384 (2002).
41. Goddard, T. D., Huang, C. C. & Ferrin, T. E. Visualizing density maps with UCSF Chimera. *J. Struct. Biol.* **157**, 281–287 (2007).

# An unanticipated architecture of the 750-kDa $\alpha_6\beta_6$ holoenzyme of 3-methylcrotonyl-CoA carboxylase

Christine S. Huang<sup>1</sup>, Peng Ge<sup>2</sup>, Z. Hong Zhou<sup>2</sup> & Liang Tong<sup>1</sup>

3-Methylcrotonyl-CoA carboxylase (MCC), a member of the biotin-dependent carboxylase superfamily, is essential for the metabolism of leucine, and deficient mutations in this enzyme are linked to methylcrotonylglycinuria (MCG) and other serious diseases in humans<sup>1–8</sup>. MCC has strong sequence conservation with propionyl-CoA carboxylase (PCC), and their holoenzymes are both 750-kilodalton (kDa)  $\alpha_6\beta_6$  dodecamers. Therefore the architecture of the MCC holoenzyme is expected to be highly similar to that of PCC<sup>9</sup>. Here we report the crystal structures of the *Pseudomonas aeruginosa* MCC (PaMCC) holoenzyme, alone and in complex with coenzyme A. Surprisingly, the structures show that the architecture and overall shape of PaMCC are markedly different when compared to PCC. The  $\alpha$ -subunits show trimeric association in the PaMCC holoenzyme, whereas they have no contacts with each other in PCC. Moreover, the positions of the two domains in the  $\beta$ -subunit of PaMCC are swapped relative to those in PCC. This structural information establishes a foundation for understanding the

disease-causing mutations of MCC and provides new insights into the catalytic mechanism and evolution of biotin-dependent carboxylases. The large structural differences between MCC and PCC also have general implications for the relationship between sequence conservation and structural similarity.

The  $\alpha$ - and  $\beta$ -subunits of human MCC have 42% and 34% sequence identity with those of human PCC (Supplementary Figs 1 and 2). The  $\alpha$ -subunit contains the biotin carboxylase (BC) and biotin carboxyl carrier protein (BCCP) domains (Fig. 1a), and a domain that mediates BC–CT interactions (BT domain)<sup>9</sup>. BC catalyses the MgATP-dependent carboxylation of biotin, and then a carboxyltransferase activity, supplied by the  $\beta$ -subunit, catalyses the transfer of the carboxyl group to the acceptor. The  $\beta$ -subunit contains two domains (Fig. 1a), N and C domains, with the same backbone fold, and its active site is located at the interface of a dimer.

Our initial interest in MCC stemmed from its distinct site of carboxylation in the substrate (Fig. 1b). To understand the molecular

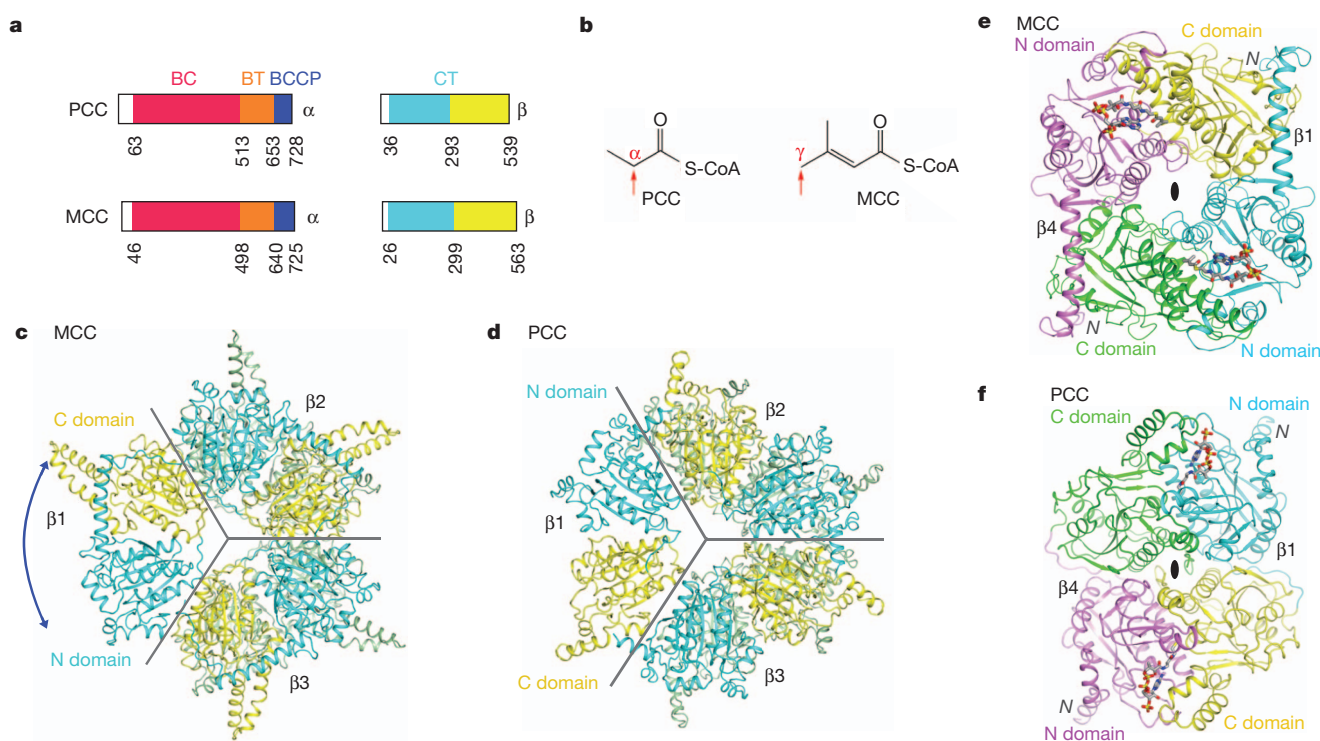


**Figure 1 | The domains of MCC $\beta$  are swapped compared to PCC $\beta$ .** **a**, Domain organization of human MCC and PCC. Residue numbers at the boundaries of the domains are indicated. **b**, Distinct carboxylation targets of MCC and PCC, indicated by the red arrow. **c**, Crystal structure of the  $\beta_6$  hexamer of PaMCC. The subunit beneath  $\beta_1$  is omitted for clarity, and the other two subunits in the bottom layer are coloured in green. The blue arrow indicates the swapping of the positions of the N and C domains relative to

PCC $\beta$ . Grey lines mark the boundaries of the subunits. **d**, Structure of *Roseobacter denitrificans* PCC $\beta$  (ref. 9). **e**, Structure of the  $\beta_2$  dimer of PaMCC. The N and C domains of the subunit in the bottom layer ( $\beta_4$ ) are coloured in magenta and green, respectively. N indicates N terminus. **f**, Structure of the  $\beta_2$  dimer of PCC. All the structure figures were produced with PyMOL (<http://www.pymol.org>) unless stated otherwise.

<sup>1</sup>Department of Biological Sciences, Columbia University, New York, New York 10027, USA. <sup>2</sup>Department of Microbiology, Immunology and Molecular Genetics, California NanoSystems Institute, University of California, Los Angeles, Los Angeles, California 90095, USA.



basis for this activity, we produced crystals of the MCC $\beta$  hexamer from *P. aeruginosa* (PaMCC $\beta$ ) that diffracted to 1.5-Å resolution (Supplementary Table 1). This bacterial enzyme is highly homologous to human MCC, with sequence identities of 47% and 65% for the  $\alpha$ - and  $\beta$ -subunits, respectively. To facilitate comparisons between these highly conserved enzymes, we numbered the residues in PaMCC according to their equivalents in human MCC. In *Pseudomonas* organisms, MCC is also involved in terpenoid metabolism<sup>10,11</sup>.

We solved the structure of PaMCC $\beta$  using *Roseobacter denitrificans* PCC $\beta$  as the model<sup>9</sup>. However, subsequent crystallographic analysis revealed that the positions of the N and C domains in PaMCC $\beta$  (Fig. 1c) are swapped relative to those in PCC $\beta$  (Fig. 1d), even though the overall shapes of the two  $\beta_6$  hexamers are similar. This distinct domain organization of PaMCC $\beta$  is primarily due to a different connectivity between its N and C domains, rather than a swap of these two domains in the primary sequence (Supplementary Fig. 3 and Supplementary Text). This also leads to a large difference in the organization of the PaMCC $\beta$  dimer compared to PCC $\beta$  (Fig. 1e, f). The closest structural homologue of PaMCC $\beta$  is the  $\alpha$ -subunit of glutacetyl-CoA decarboxylase (GCD $\alpha$ )<sup>12,13</sup> (Supplementary Fig. 4). However, the sequence conservation between PaMCC $\beta$  and GCD $\alpha$  (27% identity) is actually lower than that between PaMCC $\beta$  and

PCC $\beta$  (34% identity). The CoA binding sites, located in the N domain, are swapped between MCC $\beta$  and PCC $\beta$  as well (Fig. 1e, f). This may be related to the activity of MCC on the  $\gamma$  carbon of the substrate (Fig. 1b), as the activity of GCD $\alpha$  is also on the  $\gamma$  carbon (Supplementary Text).

Most importantly, the change in domain organization of MCC $\beta$  suggests that the overall architecture of the MCC holoenzyme may be different as well (Supplementary Text). Therefore, we next determined the structures of PaMCC free enzyme and CoA complex at 2.9- and 3.5-Å resolution, respectively (Fig. 2a and Supplementary Table 1). Like PCC, the holoenzyme of PaMCC contains a central  $\beta_6$  cylindrical core, with three  $\alpha$ -subunits at each end (Fig. 2b). The overall structures of the free enzyme and CoA complex of PaMCC are similar, although there are also recognizable differences (Supplementary Fig. 5 and Supplementary Text).

Notably, the positions of the  $\alpha$ -subunits in PaMCC, especially their BC domains, are entirely different from those in PCC (Fig. 2c). Rather than being splayed far apart from each other as in PCC (Fig. 2d), the three BC domains on either end of MCC are in direct contact with each other (Fig. 2b), burying 640 Å<sup>2</sup> of the surface area of each BC domain. Therefore, the BC domain shows trimeric association in the MCC holoenzyme, although this trimer is probably unstable on its own due to the relatively small buried surface area. Overall, the MCC

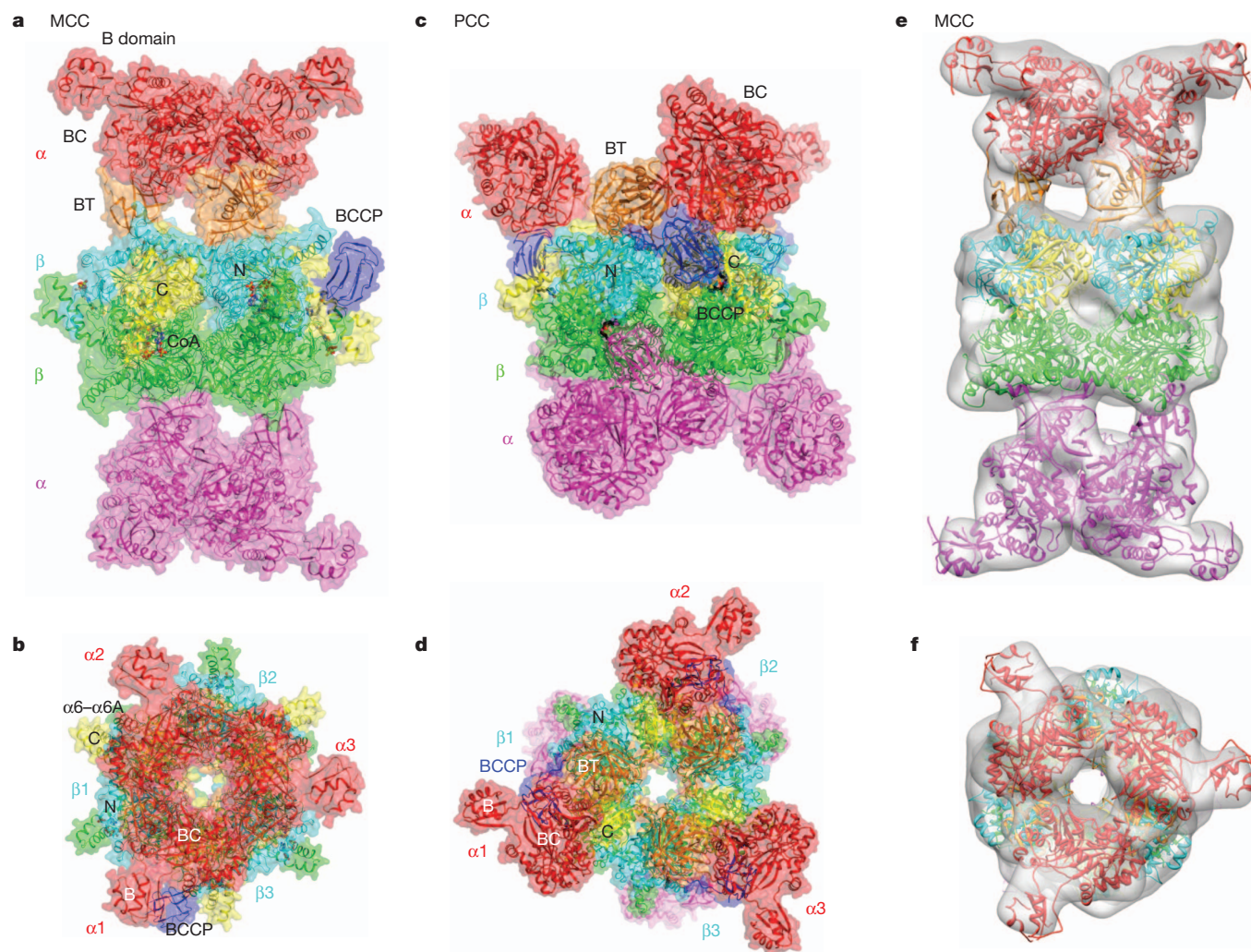


**Figure 2 | The MCC holoenzyme has a markedly different architecture compared to PCC.** **a**, Structure of the CoA complex of PaMCC holoenzyme, side view. Domains in the  $\alpha$ - and  $\beta$ -subunits in the top half of the structure are coloured as in Fig. 1a. The  $\alpha$ - and  $\beta$ -subunits in the bottom half are coloured in magenta and green, respectively. The molecular surface is shown in a semi-transparent rendering. **b**, Structure of the PaMCC holoenzyme, top view.

**c**, Structure of the PCC holoenzyme<sup>9</sup>, side view. **d**, Structure of the PCC holoenzyme, top view. **e**, Electron microscopy reconstruction of PaMCC at 12-Å resolution, side view. The crystal structure of the PaMCC free enzyme can be readily fit into the electron microscopy density. **f**, Electron microscopy reconstruction of PaMCC, top view. Panels **e** and **f** were produced with Chimera<sup>22</sup>.

holoenzyme has the shape of a cylinder, approximately 100 Å in diameter and 200 Å tall, and this shape is remarkably different from that of PCC (Supplementary Fig. 6)<sup>9</sup>.

As an independent verification for the crystal structure of PaMCC, we carried out electron microscopy studies on this holoenzyme and produced a reconstruction at 12-Å resolution (Supplementary Text and Supplementary Figs 7 and 8). The crystal structure and the electron microscopy density are in excellent agreement with each other (Fig. 2e, f), confirming the large structural differences between the MCC and PCC holoenzymes.

Interactions between the  $\alpha$ - and  $\beta$ -subunits in PaMCC are mediated predominantly by the BT domain, and by the BCCP domain when it is in the active site of the  $\beta$ -subunit for catalysis (see later). Approximately 3,000 Å<sup>2</sup> of the surface area of each  $\alpha$ -subunit is buried in the interface of the holoenzyme. The BT domain buries 1,500 Å<sup>2</sup> in the interface with the  $\beta$ -subunit, as well as 200 Å<sup>2</sup> in a contact with the BC domain of a neighbouring  $\alpha$ -subunit (see later). The BCCP domain in the active site of the  $\beta$ -subunit contributes 700 Å<sup>2</sup> to the surface area burial, primarily through residues around the biotinylated Lys 681 residue (Supplementary Fig. 1).

The BT domain in PaMCC contains a central  $\alpha$ -helix surrounded by a seven-stranded, highly twisted anti-parallel  $\beta$ -sheet (Fig. 3a and Supplementary Fig. 9). The overall structure of this domain is similar to that in PCC, with a root mean squared distance (r.m.s.d.) of 1.8 Å for their equivalent C $\alpha$  atoms. In addition, sequence comparisons suggest that the BT domain of human MCC and most other MCCs may have an eight-stranded  $\beta$ -barrel, which would be equivalent to that in PCC (Fig. 3a and Supplementary Text).

However, the position of the BT domain relative to the  $\beta$ -subunit and its interactions in the PaMCC holoenzyme are different compared to PCC (Fig. 3b and Supplementary Figs 10 and 11). The hook of the BT domain<sup>9</sup>, connecting the central helix to the first  $\beta$ -strand, is crucial for interactions with the  $\beta$ -subunit but has a markedly different conformation in PaMCC (Fig. 3a). The hook interacts with both the N and C domains of the  $\beta$ -subunit in PaMCC, and residues 542–544 in the hook form a parallel  $\beta$ -sheet with strand  $\beta$ 1 (residues 95–100) in the N domain of the  $\beta$ -subunit (Fig. 3c and Supplementary Fig. 10 and Supplementary Text). Consistent with these observations, we found

that structure-based mutations in the hook could destabilize the PaMCC holoenzyme (Supplementary Fig. 12).

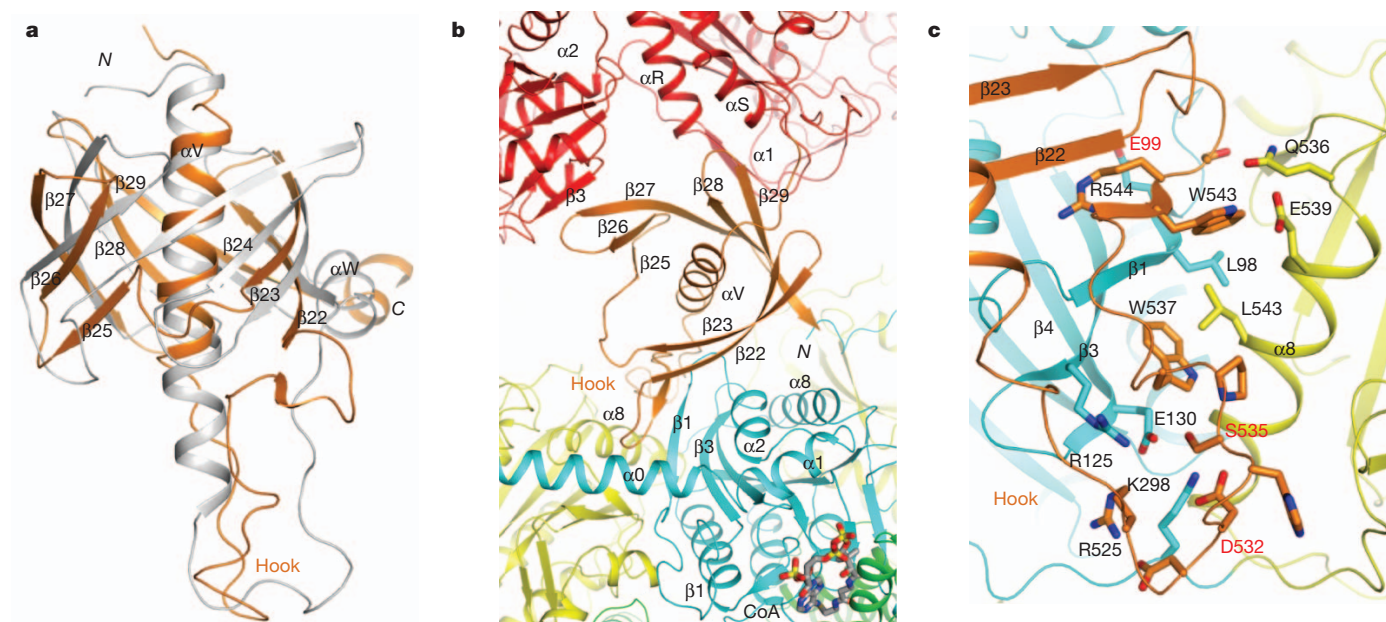
In addition to the hook, there is direct contact between the BT domain of one  $\alpha$ -subunit and the BC domain of a neighbouring  $\alpha$ -subunit, where residues 604–608 (strand  $\beta$ 27 of the BT domain) form an anti-parallel  $\beta$ -sheet with strand  $\beta$ 3 of the BC domain (Fig. 3b and Supplementary Text).

Overall, the unique interactions for the BT domain and the trimeric association of the BC domain in the MCC holoenzyme suggest that PCC cannot form a similar architecture, and therefore it is unlikely that the observed structural differences between MCC and PCC represent different stages of catalysis for these enzymes.

The distance between the active sites of BC and CT is approximately 80 Å in MCC (Fig. 4a). Therefore, the entire BCCP domain must translocate during MCC catalysis, as is the case with PCC<sup>9</sup> and pyruvate carboxylase (PC)<sup>14–17</sup>. On the other hand, MCC is distinct from PCC in that although the BT domain of an  $\alpha$ -subunit contacts its closest  $\beta$ -subunit, its BCCP domain is actually located in the active site of a neighbouring  $\beta$ -subunit (Fig. 4a), another consequence of the swapping of the N and C domains in the  $\beta$ -subunit of MCC.

We observed the binding of both CoA and BCCP-biotin to the active site of one of the  $\beta$ -subunits (Fig. 4a and Supplementary Fig. 13), and built a model for the bound conformation of methylcrotonyl-CoA (Fig. 4b and Supplementary Fig. 14 and Supplementary Text). The binding modes are consistent with the expected kinetic mechanism of the CT reaction<sup>18</sup>. The N1' atom of biotin is ~6 Å from the reactive  $\gamma$  carbon of methylcrotonyl-CoA in this model (Supplementary Fig. 14). There is a large conformational change for two helices in the active site upon CoA binding (Supplementary Fig. 15 and Supplementary Text).

The structure of PaMCC provides a foundation for understanding the molecular basis of its disease-causing mutations in human MCC, which represent one of the most frequently observed inborn errors of metabolism<sup>1–4,19–21</sup>. The missense mutations are distributed throughout the holoenzyme (Fig. 4c), but their effects can be interpreted based on the structure (Supplementary Text and Supplementary Table 2). Many of the mutations are located in or near the BC or CT active site (for example R385S in the  $\alpha$ -subunit, A218T and V375F in the  $\beta$  subunit;





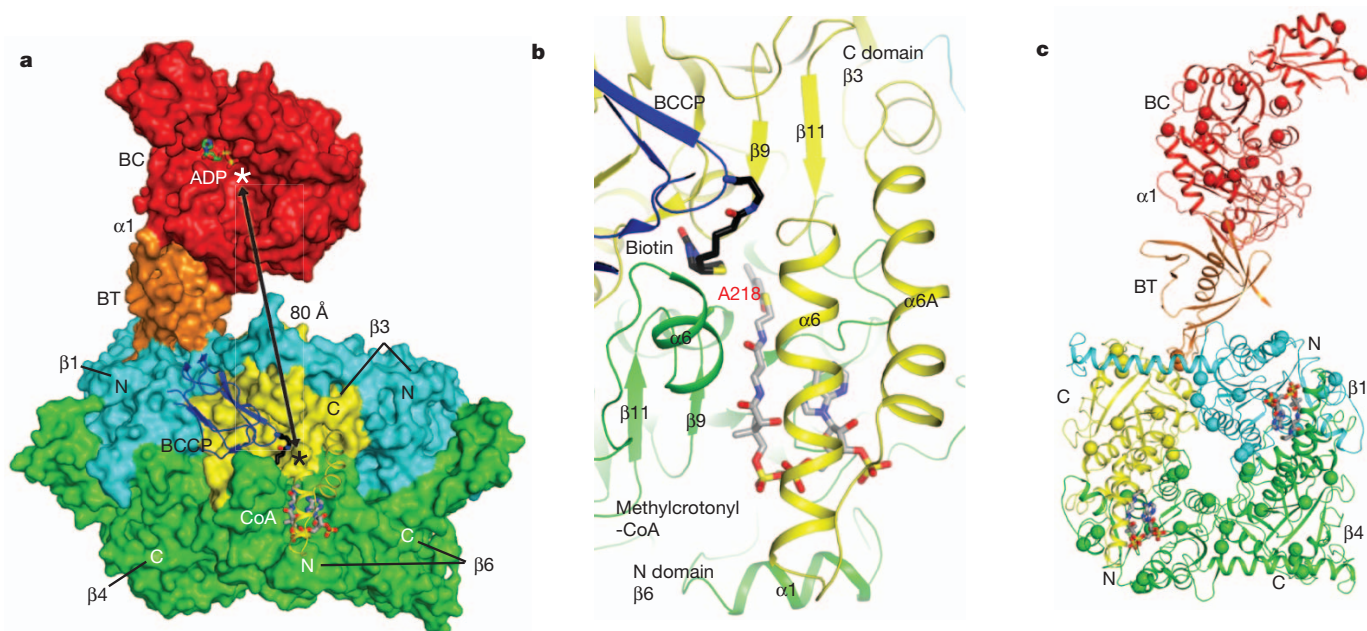


**Figure 4 | Molecular basis for catalysis and disease-causing mutations in the MCC holoenzyme.** **a**, The BC and CT active sites (indicated with asterisks) are separated by 80 Å in the PaMCC holoenzyme. Molecular surfaces of one  $\alpha$ -subunit and two  $\beta_2$  dimers are shown. The position of ADP bound to the BC subunit of *Escherichia coli* acetyl-CoA carboxylase<sup>23</sup> indicates the BC active site. Helices  $\alpha 6$ – $\alpha 6A$  are shown as a ribbon in order to make CoA visible.

Fig. 4b and Supplementary Figs 14, 16, 17). The V375F mutation may block the binding of BCCP to the active site of the  $\beta$ -subunit (Supplementary Fig. 17). A group of mutations are located in or near the subunit interface in the holoenzyme, such as S535F in the hook of the BT domain (Fig. 3c). Additional mutations are located in the hydrophobic core of the structure, and may disrupt folding and/or stability of the enzyme.

Our structure of the PaMCC holoenzyme also has implications for the evolution of biotin-dependent carboxylases. The structural differences between MCC and PCC suggest that there may be two separate lineages of such enzymes that carboxylate CoA esters of organic acids. One lineage includes PCC and acetyl-CoA carboxylase, which carboxylates the  $\alpha$  carbon of the acid. The other lineage targets the  $\gamma$  carbon of an  $\alpha$ - $\beta$  unsaturated acid and includes MCC, GCD $\alpha$  and possibly also geranyl-CoA carboxylase (Supplementary Fig. 18)<sup>10,11</sup>.

More importantly, the structures of MCC and PCC show that their strong sequence conservation only ensures that the backbone folds of the domains in the two enzymes are the same. On the other hand, the organization of these domains in the individual subunits and especially the architecture of the subunits in the holoenzymes are remarkably different. These observations may also have wide-ranging implications for the relationship between sequence conservation and structural similarity in general.

## METHODS SUMMARY

**Crystallography.** The  $\alpha$ - and  $\beta$ -subunits of PaMCC were co-expressed in *E. coli*, with a His-tag on the  $\beta$ -subunit. The PaMCC holoenzyme was purified by nickel affinity and gel filtration chromatography. Crystals were obtained by the microbatch method under oil, and the structures were determined by the molecular replacement method.

**Electron microscopy.** The PaMCC sample was stained with uranyl acetate and electron micrographs were recorded at  $\times 70,000$  magnification in a 200 kV electron microscope. A 12-Å-resolution three-dimensional reconstruction was obtained from  $\sim 12,000$  particle images.

**Mutagenesis and kinetic studies.** Site-specific mutants were designed based on the structural information, and their effects on the formation of the holoenzyme were assessed by nickel affinity chromatography. The catalytic activity of

**b**, Schematic drawing of the active site of the  $\beta$ -subunit. Biotin (black) and the modelled conformation of methylcrotonyl-CoA (grey) are shown as stick models. Residue Ala 218 is the site of a disease-causing mutation. For stereo version of this panel, see Supplementary Fig. 14. **c**, Disease-causing mutation sites are shown as spheres in the PaMCC structure. The mutations are distributed throughout the holoenzyme.

PaMCC was determined by a coupled enzyme assay, monitoring the hydrolysis of ATP.

**Full Methods** and any associated references are available in the online version of the paper at [www.nature.com/nature](http://www.nature.com/nature).

Received 22 August; accepted 1 November 2011.

Published online 11 December 2011.

- Baumgartner, M. R. *et al.* The molecular basis of human 3-methylcrotonyl-CoA carboxylase deficiency. *J. Clin. Invest.* **107**, 495–504 (2001).
- Gallardo, M. E. *et al.* The molecular basis of 3-methylcrotonylglycinuria, a disorder of leucine metabolism. *Am. J. Hum. Genet.* **68**, 334–346 (2001).
- Holzinger, A. *et al.* Cloning of the human MCCA and MCCB genes and mutations therein reveal the molecular cause of 3-methylcrotonyl-CoA carboxylase deficiency. *Hum. Mol. Genet.* **10**, 1299–1306 (2001).
- Desviat, L. R. *et al.* Functional analysis of MCCA and MCCB mutations causing methylcrotonylglycinuria. *Mol. Genet. Metab.* **80**, 315–320 (2003).
- Wakil, S. J., Stoops, J. K. & Joshi, V. C. Fatty acid synthesis and its regulation. *Annu. Rev. Biochem.* **52**, 537–579 (1983).
- Tong, L. Acetyl-coenzyme A carboxylase: crucial metabolic enzyme and attractive target for drug discovery. *Cell. Mol. Life Sci.* **62**, 1784–1803 (2005).
- Cronan, J. E., Jr & Waldrop, G. L. Multi-subunit acetyl-CoA carboxylases. *Prog. Lipid Res.* **41**, 407–435 (2002).
- Jitrapakdee, S. *et al.* Structure, mechanism and regulation of pyruvate carboxylase. *Biochem. J.* **413**, 369–387 (2008).
- Huang, C. S. *et al.* Crystal structure of the  $\alpha_6\beta_6$  holoenzyme of propionyl-coenzyme A carboxylase. *Nature* **466**, 1001–1005 (2010).
- Förster-Fromme, K. & Jendrossek, D. Catabolism of citronellol and related acyclic terpenoids in pseudomonads. *Appl. Microbiol. Biotechnol.* **87**, 859–869 (2010).
- Aguilar, J. A. *et al.* Substrate specificity of the 3-methylcrotonyl coenzyme A (CoA) and geranyl-CoA carboxylases from *Pseudomonas aeruginosa*. *J. Bacteriol.* **190**, 4888–4893 (2008).
- Wendt, K. S., Schall, I., Huber, R., Buckel, W. & Jacob, U. Crystal structure of the carboxyltransferase subunit of the bacterial sodium ion pump glutamyl-coenzyme A decarboxylase. *EMBO J.* **22**, 3493–3502 (2003).
- Kress, D. *et al.* An asymmetric model for Na<sup>+</sup>-translocating glutamyl-CoA decarboxylase. *J. Biol. Chem.* **284**, 28401–28409 (2009).
- St. Maurice, M. *et al.* Domain architecture of pyruvate carboxylase, a biotin-dependent multifunctional enzyme. *Science* **317**, 1076–1079 (2007).
- Xiang, S. & Tong, L. Crystal structures of human and *Staphylococcus aureus* pyruvate carboxylase and molecular insights into the carboxyltransfer reaction. *Nature Struct. Mol. Biol.* **15**, 295–302 (2008).
- Yu, L. P. C. *et al.* A symmetrical tetramer for *S. aureus* pyruvate carboxylase in complex with coenzyme A. *Structure* **17**, 823–832 (2009).
- Lasso, G. *et al.* Cryo-EM analysis reveals new insights into the mechanism of action of pyruvate carboxylase. *Structure* **18**, 1300–1310 (2010).



18. Knowles, J. R. The mechanism of biotin-dependent enzymes. *Annu. Rev. Biochem.* **58**, 195–221 (1989).
19. Stadler, S. C. *et al.* Newborn screening for 3-methylcrotonyl-CoA carboxylase deficiency: population heterogeneity of *MCCA* and *MCCB* mutations and impact on risk assessment. *Hum. Mutat.* **27**, 748–759 (2006).
20. Nguyen, K. V., Naviaux, R. K., Patra, S., Barshop, B. A. & Nyhan, W. L. Novel mutations in the human *MCCA* and *MCCB* gene causing methylcrotonylglycinuria. *Mol. Genet. Metab.* **102**, 218–221 (2011).
21. Uematsu, M. *et al.* Novel mutations in five Japanese patients with 3-methylcrotonyl-CoA carboxylase deficiency. *J. Hum. Genet.* **52**, 1040–1043 (2007).
22. Pettersen, E. F. *et al.* UCSF Chimera—a visualization system for exploratory research and analysis. *J. Comput. Chem.* **25**, 1605–1612 (2004).
23. Chou, C.-Y., Yu, L. P. C. & Tong, L. Crystal structure of biotin carboxylase in complex with substrates and implications for its catalytic mechanism. *J. Biol. Chem.* **284**, 11690–11697 (2009).

**Supplementary Information** is linked to the online version of the paper at [www.nature.com/nature](http://www.nature.com/nature).

**Acknowledgements** We thank Y. Shen for carrying out initial studies on MCC; N. Whalen and S. Myers for setting up the X29A beamline at the National Synchrotron Light Source. This research was supported in part by National Institutes of Health (NIH) grants DK067238 (to L.T.) and GM071940 (to Z.H.Z.). C.S.H. was also supported by an NIH training program in molecular biophysics (GM08281).

**Author Contributions** C.S.H. carried out protein expression, purification and crystallization experiments, mutagenesis and enzymatic assays. C.S.H. and L.T. carried out crystallographic data collection and processing, structure determination and refinement. P.G. and Z.H.Z. carried out electron microscopy experiments. All authors commented on the manuscript. L.T. supervised the project, analysed the data and wrote the paper.

**Author Information** Atomic coordinates have been deposited in the Protein Data Bank under accessions 3U9R, 3U9S and 3U9T. Reprints and permissions information is available at [www.nature.com/reprints](http://www.nature.com/reprints). The authors declare no competing financial interests. Readers are welcome to comment on the online version of this article at [www.nature.com/nature](http://www.nature.com/nature). Correspondence and requests for materials should be addressed to L.T. (ltong@columbia.edu).

## METHODS

**Protein expression and purification.** Full-length PaMCC $\beta$  was subcloned into the pET28a vector (Novagen). The expression construct contained an N-terminal hexa-histidine tag, which was not removed for crystallization. The native protein was overexpressed overnight in *E. coli* BL21 Rosetta (DE3) cells (Novagen) at 20 °C in the presence of 1 mM isopropyl- $\beta$ -D-thiogalactopyranoside (IPTG) (Gold Biotechnology). The soluble protein was eluted from nickel affinity beads (Qiagen) and was further purified by gel filtration chromatography with a running buffer of 25 mM Tris (pH 7.4), 250 mM NaCl and 2 mM dithiothreitol. The purified protein was concentrated to 20 mg ml<sup>-1</sup>, supplemented with 5% (v/v) glycerol, flash-frozen with liquid nitrogen and then stored at -80 °C.

The PaMCC holoenzyme was overexpressed using a bi-cistronic plasmid, with PaMCC $\alpha$  (untagged) placed downstream of PaMCC $\beta$  in the pET28a vector, similar to the strategy used for the co-expression of the PCC holoenzyme<sup>9</sup>. The holoenzyme was purified following the same protocol as that for PaMCC $\beta$ .

**Protein crystallization.** Crystals were obtained with the microbatch under-oil (paraffin oil, Hampton Research) method at 20 °C. The protein was at 20 mg ml<sup>-1</sup> concentration. For PaMCC $\beta$ , the precipitant solution contained 100 mM Tris (pH 8.5), 0.2 M (NH<sub>4</sub>)<sub>2</sub>HPO<sub>4</sub> and 30% (v/v) PEG 200.

For the PaMCC holoenzyme, the protein was first incubated with 2 mM methylcrotonyl-CoA for 30 min on ice. The precipitant solution contained 20% (w/v) PEG 3350 and 0.2 M sodium malonate (pH 7.0) or 0.2 M Na<sub>2</sub>SO<sub>4</sub>. Crystals with the shape of thin plates appeared after 10–14 days and belonged to space group P2<sub>1</sub>. Most of these crystals diffracted X-rays poorly. CoA was observed in the active site of the  $\beta$ -subunit based on the subsequent crystallographic analysis.

Under the same conditions, crystals with the shape of rhomboid blocks were observed after 6–8 weeks, after significant evaporation of the crystallization drops. These crystals belonged to space group R32, and showed better X-ray diffraction. They contained the free enzyme of PaMCC.

The crystals were flash-frozen in liquid nitrogen for diffraction analysis and data collection at 100 K.

**Data collection and structure determination.** X-ray diffraction data sets were collected on an ADSC Q315 CCD at the X29A beamline of the National Synchrotron Light Source (NSLS) at Brookhaven National Laboratory. The diffraction images were processed using the HKL package<sup>24</sup>. The data processing and refinement statistics are summarized in Supplementary Table 1.

Crystals of PaMCC $\beta$  contained one  $\beta$ -subunit in the asymmetric unit. The structure was determined by the molecular replacement method with the program Phaser<sup>25</sup>, using the structure of PCC $\beta$  as the model<sup>9</sup>. Structure refinement was carried out with the programs CNS<sup>26</sup> and Refmac<sup>27</sup>, and programs O<sup>28</sup> and Coot<sup>29</sup> were used for manual model rebuilding. Water molecules were located automatically with the program CNS.

Crystals of the CoA complex of PaMCC holoenzyme contained one dodecamer in the asymmetric unit. The structure was determined by the molecular replacement method with the program Phaser, using the structure of the PaMCC $\beta$  hexamer and the BC domain of PCC $\alpha$  (ref. 9) as the models. One copy of the BCCP domain was also located, using the BCCP domain of PCC as the model. However, molecular replacement calculations with the BT domain of PCC were not successful, and the BT domain model was built based on the (omit) electron density after structure refinement.

Crystals of the free enzyme of PaMCC contained one  $\alpha\beta$  protomer in the asymmetric unit. The structure was determined by the molecular replacement method, using the structure of one  $\alpha\beta$  protomer of PaMCC CoA complex as the model. No water molecules were included in the atomic models of the holoenzyme owing to the limited resolution.

**Electron microscopy.** The PaMCC sample was diluted to appropriate concentrations for electron microscopy with a buffer containing 25 mM Tris (pH 7.4) and 250 mM NaCl. An aliquot of 2.5  $\mu$ l of each of the diluted samples was placed onto a carbon-film-coated, glow-discharged 300-mesh copper grid. Excess sample was blotted away by filter paper after one minute. The sample was immediately stained with 2% uranyl acetate solution and air dried. Electron micrographs were recorded in an FEI TF20 electron microscope (operated at 200 kV) on a TVIPS 16-megapixel CCD camera at  $\times 70,000$  magnification. The sample with optimal particle concentration as shown in Supplementary Fig. 6 was used for extended imaging and in-depth three-dimensional reconstruction analysis.

First, we picked 500 particles manually from 5 CCD images with the EMAN boxer program and obtained a preliminary reconstruction to 22-Å resolution with EMAN<sup>30</sup>. Approximately 20,000 particles were subsequently picked automatically from 30 CCD images with SIGNATURE<sup>31</sup>, using the previous 22 Å structure as reference. D3 symmetry was imposed during refinement and three-dimensional reconstruction. Approximately 12,000 particles were selected for the final three-dimensional reconstruction. The resolution of the final three-dimensional reconstruction was assessed to be 12 Å based on the 0.5 cut-off in the Fourier shell correlation between three-dimensional reconstructions from the two half sets of the whole data set (Supplementary Fig. 7). The UCSF Chimera program was used to create three-dimensional graphical representations<sup>22</sup>. The atomic model of MCC was fitted to the density map using the 'fit-model-to-map' module of Chimera.

**Mutagenesis and kinetic studies.** Site-specific mutations were introduced with the QuikChange kit (Agilent) and sequenced for confirmation. The mutant plasmids were transformed into *E. coli*, and the formation of the PaMCC holoenzyme was assessed by nickel affinity chromatography.

The catalytic activity of PaMCC was determined using a coupled enzyme assay, converting the hydrolysis of ATP to the disappearance of NADH<sup>32,33</sup>. The reaction mixture contained 100 mM HEPES (pH 8.0), 0.5 mM ATP, 8 mM MgCl<sub>2</sub>, 40 mM NaHCO<sub>3</sub>, 0.5 mM methylcrotonyl-CoA or crotonyl-CoA, 0.2 mM NADH, 0.5 mM phosphoenolpyruvate, 7 units of lactate dehydrogenase, 4.2 units of pyruvate kinase and 200 mM NaCl. The absorbance at 340 nm was monitored for 5 min.

24. Otwinowski, Z. & Minor, W. Processing of X-ray diffraction data collected in oscillation mode. *Methods Enzymol.* **276**, 307–326 (1997).
25. McCoy, A. J. et al. Phaser crystallographic software. *J. Appl. Cryst.* **40**, 658–674 (2007).
26. Brünger, A. T. et al. Crystallography & NMR System: a new software suite for macromolecular structure determination. *Acta Crystallogr. D* **54**, 905–921 (1998).
27. Murshudov, G. N., Vagin, A. A. & Dodson, E. J. Refinement of macromolecular structures by the maximum-likelihood method. *Acta Crystallogr. D* **53**, 240–255 (1997).
28. Jones, T. A., Zou, J. Y., Cowan, S. W. & Kjeldgaard, M. Improved methods for building protein models in electron density maps and the location of errors in these models. *Acta Crystallogr. A* **47**, 110–119 (1991).
29. Emsley, P. & Cowtan, K. D. Coot: model-building tools for molecular graphics. *Acta Crystallogr. D* **60**, 2126–2132 (2004).
30. Ludtke, S. J., Baldwin, P. R. & Chiu, W. EMAN: semiautomated software for high-resolution single-particle reconstructions. *J. Struct. Biol.* **128**, 82–97 (1999).
31. Chen, J. Z. & Grigorieff, N. SIGNATURE: a single-particle selection system for molecular electron microscopy. *J. Struct. Biol.* **157**, 168–173 (2007).
32. Diacovich, L. et al. Crystal structure of the  $\beta$ -subunit of acyl-CoA carboxylase: structure-based engineering of substrate specificity. *Biochemistry* **43**, 14027–14036 (2004).
33. Blanchard, C. Z., Lee, Y. M., Frantom, P. A. & Waldrop, G. L. Mutations at four active site residues of biotin carboxylase abolish substrate-induced synergism by biotin. *Biochemistry* **38**, 3393–3400 (1999).

## ERRATUM

doi:10.1038/nature10773

### **Thermalization and its mechanism for generic isolated quantum systems**

Marcos Rigol, Vanja Dunjko & Maxim Olshanii

*Nature* **452**, 854–858 (2008).

In Figs 3b and e of this Letter, there were two points that could have been misinterpreted as outlying data points (they were inadvertently printed parts of a key to the figure that was incompletely removed). These points have been removed in the HTML and PDF versions. We thank David S. Weiss for drawing this to our attention.



## ERRATUM

doi:10.1038/nature10773

### **Thermalization and its mechanism for generic isolated quantum systems**

Marcos Rigol, Vanja Dunjko & Maxim Olshanii

*Nature* **452**, 854–858 (2008).

In Figs 3b and e of this Letter, there were two points that could have been misinterpreted as outlying data points (they were inadvertently printed parts of a key to the figure that was incompletely removed). These points have been removed in the HTML and PDF versions. We thank David S. Weiss for drawing this to our attention.

# CAREERS

**TURNING POINT** Social scientist hopes to engage the public in climate research **p.227**

**EUROPEAN UNION** Universities urge measures to improve researcher mobility **p.227**

**NATUREJOBS** For the latest career listings and advice [www.naturejobs.com](http://www.naturejobs.com)

MICHELANGELO



## BRIDGE FUNDING

# How to stay afloat

*When a lab runs out of money, there are a few strategies that it can use to get by.*

BY JEFFREY PERKEL

The world's economy is battered and bruised. More than three years after the start of the global recession, the European debt crisis threatens to derail a fragile financial recovery, and funding-agency budgets are suffering. Scientists are feeling the ill effects: many are having to make do with less, and there is a growing risk that researchers and laboratories will soon be caught between grants, unable to find new sources of funding when their current ones expire. "I'm not sure that I'm yet seeing the real impact of what's coming down the road," says John Kirby, dean of the College of the Environment and Life Sciences at the University of Rhode Island in Kingston, referring to the effects on his institution.

Across academia, scientists are planning for shortfalls, with mid-career researchers often the most at risk as funding agencies tailor grant programmes to younger researchers (see *Nature* 471, 399; 2011). "It is not clear

that this development is recession-related, but its emphasis on 'stellar' individuals may have the effect of reducing significantly the funding options for many mid-career scientists," says Charles Dorman, chair of the department of microbiology at Trinity College Dublin.

But young researchers are far from immune: in some cases, university start-up packages are being stretched to allow for the increasing amount of time that a researcher needs to secure a first independent grant. Richard Schultz, associate dean for the natural sciences at the University of Pennsylvania's School of Arts and Sciences in Philadelphia, says that some of his institution's start-up packages, which typically last three years, may soon be recalculated to last for four. "There's a greater likelihood that it may take [new recruits] longer than we anticipated before they get their own extramural funding," he says.

There are steps that researchers can take to make up for deficits. Internal bridge funding can help in the short term, but it is best

for scientists to plan ahead, broadening their search for support. Launching collaborations, varying funding sources and extending their work into unfamiliar areas could help anxious researchers to make their way out of the financial doldrums.

## CAUGHT BETWEEN GRANTS

Despite their best efforts, researchers can sometimes find themselves without funding for months or even years. In such cases, bridge funding can often be arranged from within the researcher's home institution. Usually cobbled together from overheads and small amounts of money set aside in department and college budgets, such funding is generally limited in availability and quantity, and is awarded on a case-by-case basis. An institution's stopgap resources can vary widely, from a few thousand dollars per researcher to perhaps US\$100,000. Before deciding whether to approve bridge funding, a department chair or college dean will assess the researcher's publication and ►

► service record, funding history and likelihood of eventually winning an extramural grant.

Kirby recalls a case that came up when he was working as an associate dean for research at South Dakota State University in Brookings. A private entity funding a research project suddenly went bankrupt, leaving two graduate students bereft of funds. The university stepped in and moved the students into research-assistantship posts so that they could complete their work, he says. In another case, a successful faculty member requested about \$50,000 to finalize a data set and strengthen a grant application. Bridge funding allowed him to win the grant and continue his work.

But in tough economic times, such opportunities can be difficult to find. In cash-strapped Ireland, for instance, “the ability of universities to offer significant support to researchers facing a funding gap is very limited or even non-existent”, says Dorman.

Carl Bauer, chair of the department of molecular and cellular biochemistry at Indiana University in Bloomington, helps to guide labs in his department out of financial straits. When a lab runs into trouble, the first thing Bauer does is to study its books carefully. Typically, such reviews don't entail micromanagement of reagent purchases or other equipment. Rather, the focus is on a lab's biggest expense: personnel. In the United States, graduate students can often be moved into teaching positions that require no funds from the principal investigator, but postdocs and technicians cannot. “Maybe I can keep them going for one more grant cycle, but after that point you have to let them go,” says Bauer. Downsizing is almost inevitable at that point, says Mary Collins, dean of the faculty of life sciences at University College London. Bauer adds that he also examines a struggling scientist's past grant applications, gauging whether they have been competitive, because this could affect whether they will be able to gain an independent grant in the future.

## A DIVERSIFIED PORTFOLIO

For those who have enough funding in the short term but worry about the medium and long term, experts recommend seeking money from multiple sources. A diverse portfolio of projects enables researchers to apply for a variety of grants. “It's like holding a basket of stocks in different areas,” says Bauer. If one grant falls through, research priorities might take a hit, but

the lab will survive on the others.

At any one time, Schultz aims to hold multiple grants with staggered start dates, to ensure that his lab's finances are relatively stable. He has several grants from the US National Institutes of Health coming up for renewal in the next few years; but given the current climate, he has “absolutely no confidence that any of them will be renewed. That, psychologically, is a bad place to be.” Schultz plans to submit several further grant applications in partnership with colleagues — not his usual practice.

Researchers are increasingly establishing collaborations to hedge their bets. This can improve their chances of getting funding by, for instance, making a project more exciting through the use of innovative approaches and technologies, or more relevant to practical applications, says Collins. “You have to think a bit laterally,” she adds. “The most important thing with a grant is to have a really interesting question. The second thing is to demonstrate that you have a clear means to providing some answers to that question. And if you have a technology that you really can't do or have never demonstrably done before, bringing in an expert who can do that as a collaborator is really helpful.”

There is a caveat: weak collaborations could put applicants at a disadvantage. Adam Zlotnick, a biochemist at Indiana University, moved to his current post from the University of Oklahoma Health Science Center in Oklahoma City, where he had applied for a grant renewal in collaboration with an organic chemist who was hoping to synthesize a series of antiviral compounds. The application was unsuccessful, in part because the reviewers felt that the collaboration wasn't strong enough. Once at Indiana, Zlotnick found himself working just across the hall from another organic chemist. The two researchers developed a close interaction, talking face-to-face almost daily and sharing graduate students and postdocs. They won a grant on the basis of an application that emphasized teamwork and the interdisciplinary nature of their science. Zlotnick was fortunate: despite missing one grant cycle, he had another grant and start-up funds from Indiana to see him through. However, the start-up money had been intended to jump-start another project, which had to be slowed considerably as he addressed his funding gap. Although he has now regained independent funding, Zlotnick says his enthusiasm for new projects has been tempered.



**“The most important thing with a grant is to have a really interesting question.”**

Mary Collins



**“If you don't have the track record, you don't stand a chance.”**

Gareth Leng

Mere marriages of convenience are not enough to ensure funding success for collaborations, says Gareth Leng, head of the School of Biomedical Sciences at the University of Edinburgh, UK. “Grant panels see through them and they don't work out. So you've got to have a kind of a real marriage of love and enthusiasm,” he says. “It's not a speed-dating thing,” Leng adds that researchers should be careful not to diverge too far from their familiar research path when forming a collaboration or expanding the scope of their grant search. A radical change of direction can be detrimental in the current economic environment. “If you don't have the track record, you don't stand a chance,” he notes.

## TUITION FEES

Scientists who can not only sell their research, but can also find ways to use its content and methods to contribute to graduate-student training, may be able to tap into sources of funding related to higher education, notes Alan Tessier, an environmental-biology programme officer at the US National Science Foundation (NSF) in Arlington, Virginia. For example, a researcher could apply to lead a grant under a scheme such as the multimillion-dollar NSF Integrated Graduate Education and Research Traineeship Program, or the NSF's Research Experience for Undergraduates initiative. “That includes support for graduate students in their lab,” says Tessier.

There are other strategies. For instance, biologists working *in vitro* might attempt to move their research to an *in vivo* model to demonstrate its potential impact and importance for human health, strengthening their case with funders and expanding their technical reach. Scientists in other areas could try to incorporate new informatics or modelling tools into their work to expand their repertoires, show that their work is not stagnant and demonstrate the ability to adapt to new scientific questions, says Collins. In the end, stopgap funding solutions are most useful when they allow the lab to retain personnel. Lab groups can be fragile, notes Schultz. Personnel retain knowledge of the group's past projects and investigative track, so losing just one member can be very disruptive. Even if someone must temporarily work part-time while money is sought, the hope is that the lab will soon recover. “Then they can get moving,” says Schultz, “and the lab won't go into what I call that death spiral.” Bridge funding is a means of ensuring survival until long-term measures are possible. And whether an investigator has to rely on bridge funding or run a lab on a smaller budget, what ultimately matters, Schultz notes, is that the lab is running. “It's not that you're flourishing,” he says. “Your purpose here is to survive.” ■

Jeffrey Perkel is a freelance writer based in Pocatello, Idaho.



# TURNING POINT

## Saffron O'Neill

*Saffron O'Neill, who studies the interactions between society, policy and climate change at the University of Melbourne in Australia, won the 2011 UK Scopus Young Researcher Award for the Social Sciences on 22 November.*

### What drew you to study climate change?

I see it as the most pressing environmental issue of our time, and there are lots of policy questions. After my undergraduate degree, my mentors advised me to go to the Tyndall Centre for Climate Research at the University of East Anglia in Norwich, UK. The centre was offering a PhD scholarship to determine how people engage with climate-change information.

### Was that meant to be in the social sciences?

It was open-ended, but the abstract focused on the physical sciences — modelling climate in ways that are amenable to public understanding. However, investigating why people didn't engage with this information was more interesting, so my PhD was turned on its head. That was a turning point, realizing that I could contribute from a social-sciences perspective.

### How did the 'Climategate' release of e-mails from researchers at the University of East Anglia affect your work?

Climategate happened in November 2009, five months after I left. My former colleagues were in the news all the time. I had moved to the University of Melbourne as a postdoc, but I still received hate mail, including death threats. The experience made me realize that scientists are keen to communicate with the public, but need to do a better job of explaining how scientific discoveries get made.

### Why did you decide to go to Australia?

One reason was so I could gain experience in a different country. It was challenging to learn about an unfamiliar policy arena, but it was rewarding to see how Australia and small island states are addressing policy challenges. And I had been working on climate-change mitigation, but had a growing interest in adaptation. My adviser here, Jon Barnett, is an international leader in this area. He focuses on how small island states will have to adapt. I also got a four-year postdoc, which gave me a lot of stability. I didn't have to scramble around for short-term contracts.

### What can your research do to advance climate-change policy-making?

The public has a lot of the scientific



information needed to start making decisions, yet isn't doing so effectively. Decision-making is the most important social dimension of any environmental problem, and that is where the most interesting questions lie. My research shows that people embrace climate-change information most if it is relevant to places they care about — for example, how sea-level rise may affect London — or if they can empathize with the affected animals, such as polar bears.

### What activities helped to raise your profile?

I served on a panel to assess whether an Australian preparedness strategy, known as Stay or Go, actually put people at increased risk during bush fires in the state of Victoria in 2009, which killed 173 people. Other countries mandate evacuation. The commission reviewing the policy drew on our panel's report when making its final recommendations. It was a rare opportunity to show how science — analysing the forensic data, statements, texts and phone calls made during the bush fires — can help to improve disaster-preparedness policies. I think that experience may have counted in my favour for the Scopus award, which takes citations into account.

### What is your next step?

I have a full-time lectureship on public perceptions of climate change lined up at the University of Exeter, UK, which is building a team of climate-change researchers. I've enjoyed being in Australia, but didn't realize how isolated it would feel here. Simply collaborating or going to meetings is really hard. A 24-hour plane ride to Europe is a big deal. Plus I'm trying not to fly too much, being a climate-change scientist. ■

INTERVIEW BY VIRGINIA GEWIN

## EUROPEAN UNION

### Call for more mobility

A group of universities has made recommendations on how to draw researchers to the European Union (EU). Among other things, the League of European Research Universities (LERU), based in Leuven, Belgium, has called for more transparency about visa regulations that affect researcher mobility, more incentives for companies to give venture funding to scientists and measures to promote gender equality in research. The group published the suggestions on 14 December, in response to a call by the European Commission (EC) for input on its proposal for a European Research Area Framework, to improve the European research environment and help to coordinate funding across the EU, set to be established by 2014. Katrien Maes, LERU's chief policy officer, expects to hear a response from the EC by spring 2012.

## COLLABORATION

### US–Russian pact

The US National Science Foundation (NSF) has inked an agreement with the Russian ministry of education and science to encourage collaborative research in areas such as energy, nanotechnology and information technology. Early-career scientists applying for NSF grants could improve their chances by collaborating with Russian researchers, suggests John Tsapogas, programme coordinator for the NSF's Office of International Science and Engineering in Arlington, Virginia. The agreement, co-signed on 16 December, allows the Russian ministry to fund US–Russian projects. Tsapogas says that the ministry has a larger budget than other Russian science agencies, so it has a high likelihood of collaborations.

## CANCER RESEARCH

### New York fellowships

The Memorial-Sloan Kettering Cancer Center in New York is creating ten five-year, early-career research fellowships. They will be funded with US\$15 million from \$50 million donated to the centre by the Robertson Foundation in New York. Fellows will get tenure-track appointments, says Charles Sawyers, chair of human oncology and pathogenesis at Sloan-Kettering. Investigators will be recruited in oncology and pathogenesis, cancer biology and genetics, pharmacology, and immunology. Sawyers expects much of the research to be translational.

# THE DRIVER

*On the road to freedom.*

BY RAHUL KANAKIA

Every day for the past 30 years, Vlad had woken up to find the black Lincoln town car already idling in front of his house. Today was no different. As Vlad made his coffee, the car slowly rolled up and down the block. When he walked to the spot where he'd parked his own car, it rolled along at his side like a well-trained dog. On the freeway, it was three car-lengths behind him. In the university parking lot, it pulled into the space right in front of Vlad, and the professor stared directly into the eyes of the driver. Vlad waved at him. The driver nodded.

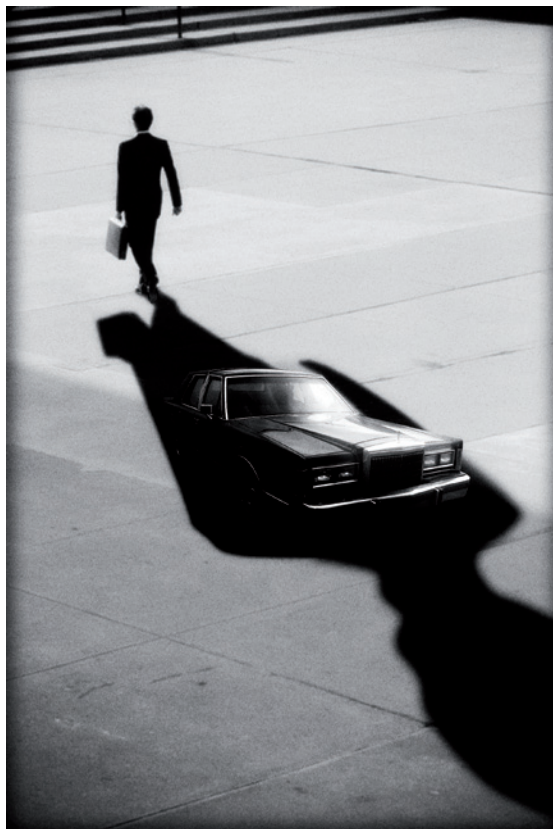
The driver was in his late forties, with a neatly trimmed salt-and-pepper beard and receding hairline. He was wearing a white polo shirt with an indistinct company logo over the right breast. Vlad didn't know how tall the driver was, because he had never seen the driver outside the car.

Over the years, Vlad had witnessed the driver ploughing through two pedestrians and ramming four cars off the road in three separate incidents. And once, when the child Vlad was on his bike, deciding which path to take, the window of the car opened up and the man said: "Left." When he got home, Vlad's worried mother told him of the gas explosion on the right-hand path that had killed three people.

By the time Vlad reached his ground-floor office, the car was parked in the quad, right next to the department's doors. It usually stayed there, within spitting distance of Vlad's window, until Vlad left. Bikes wove between it and the wall. Students stepped around it. Sometimes police officers came by and ticketed the car. Once, Vlad checked the citation number on several of these tickets. They were all paid promptly and electronically, within moments of the ticket being registered.

Vlad looked out of his window. It was a wonderful day. The birds were singing. The coeds were wearing sundresses. The sky was clear. The breeze was cool and vigorous. Vlad picked up the folding chair he kept in a corner of his office and decided to eat lunch with the driver.

It had taken years for Vlad to convince the driver to roll the window down at his approach. That had been such a triumph for the young Vlad. Now the driver smiled as Vlad walked up and unfolded his chair.



"How is your reading?" the driver said. "Don't you know better than me?" Vlad said. He unwrapped the sandwich he'd purchased from the deli and handed half through the open window to the man.

"The directorate has stopped contacting me," the driver said.

"What about the other Vlands? Have they made the breakthrough yet?"

"I don't know. Even the other drivers won't speak to me."

"For how long now?"

"A few months," the driver said. "I think they might have given up on you."

"So you're free now? You can finally leave the car?"

"I think so..." said the driver. "And you're free to start work again."

"I've been sitting in my office doing nothing for so long," said Vlad. "I'm not sure there's any work left in me."

"You've been reading. And you've been thinking," the driver said. "I know this isn't the end for you. I've seen how smart you are."

If anyone had seen

Vlad's potential, the driver had. They had spent so many afternoons just like this, with Vlad sitting at the window of the car. First it had been the child Vlad discussing his ambitions and his readings, and then the more adult Vlad seriously proposing grand theories to the driver's smiling face.

"Where will you go?" said Vlad.

"I think maybe I'll stay here, with you," the driver said. "At least for a few more years. Don't I owe that to you?"

Wouldn't that be fine? Vlad had sacrificed his whole future for the man. Didn't the driver owe Vlad something?

"No," said Vlad. "I'm not a slave-owner. You should go out into the world."

"Is that what you want?" said the driver. "It wouldn't be slavery, not really... not if I'm choosing it."

A tear fell from Vlad's left eye. "Do you ever wonder what will happen in the future you left behind?" Vlad said. "Why did they need the products of my mind so much? Why were others willing to kill in order to stop me?"

"I don't know," said the driver. "Maybe I wasn't even on the right side. But I did my duty. And I would've kept on doing it. You're the one who chose to set me free."

This tear was just the frailest echo of the thousands of tears the child Vlad had wept when he learned how the man was trapped in this car — perhaps forever — by those cruel directives. The student Vlad had formulated a plan. The adult Vlad had carried it out. And the plan had succeeded.

"Get out," Vlad said. "Go. Live."

The car door opened. The driver exited. He was huge. His shoulder was taller than Vlad's head. He was barefoot. Vlad smiled at that. The man hugged Vlad tightly and then walked to the exit of the quad, leaving his car open and empty.

Vlad slammed the car's door. He folded his chair up. He went back to his office and stood in front of his bookshelf. He put a hand on the last book he'd tried to read, and his fingers came away covered in dust.

All his life, Vlad had possessed a destiny. Now he knew that destiny was gone. He smiled. Tomorrow he'd probably feel empty. But today he felt free. ■

➤ **NATURE.COM**  
Follow Futures on  
Facebook at:  
[go.nature.com/mtoodm](https://www.facebook.com/mtoodm)

thinking," the driver said. "I know this isn't the end for you. I've seen how smart you are."

**Rahul Kanakia** is an international development consultant based in Oakland, California.

# Evolution of increased complexity in a molecular machine

Gregory C. Finnigan<sup>1\*</sup>, Victor Hanson-Smith<sup>2,3\*</sup>, Tom H. Stevens<sup>1</sup> & Joseph W. Thornton<sup>2,4,5</sup>

Many cellular processes are carried out by molecular ‘machines’—assemblies of multiple differentiated proteins that physically interact to execute biological functions<sup>1–8</sup>. Despite much speculation, strong evidence of the mechanisms by which these assemblies evolved is lacking. Here we use ancestral gene resurrection<sup>9–11</sup> and manipulative genetic experiments to determine how the complexity of an essential molecular machine—the hexameric transmembrane ring of the eukaryotic V-ATPase proton pump—increased hundreds of millions of years ago. We show that the ring of Fungi, which is composed of three paralogous proteins, evolved from a more ancient two-paralogue complex because of a gene duplication that was followed by loss in each daughter copy of specific interfaces by which it interacts with other ring proteins. These losses were complementary, so both copies became obligate components with restricted spatial roles in the complex. Reintroducing a single historical mutation from each paralogue lineage into the resurrected ancestral proteins is sufficient to recapitulate their asymmetric degeneration and trigger the requirement for the more elaborate three-component ring. Our experiments show that increased complexity in an essential molecular machine evolved because of simple, high-probability evolutionary processes, without the apparent evolution of novel functions. They point to a plausible mechanism for the evolution of complexity in other multi-paralogue protein complexes.

Comparative genomic approaches suggest that the components of many molecular machines have appeared sequentially during evolution and that complexity increased gradually by incorporating new parts into simpler assemblies<sup>2–8</sup>. Such horizontal analyses of extant systems, however, cannot decisively test these hypotheses or reveal the mechanisms by which additional parts became obligate components of larger complexes. In contrast, vertical approaches that combine computational phylogenetic analysis with gene synthesis and molecular assays allow changes in the sequence, structure and function of reconstructed ancestral proteins to be experimentally traced through time.<sup>9–11</sup> Here we apply this approach to characterize the evolution of a small molecular machine and dissect the mechanisms that caused it to increase in complexity.

The vacuolar H<sup>+</sup>-ATPase (V-ATPase) is a multisubunit protein complex that pumps protons across membranes to acidify subcellular compartments; this function is required for intracellular protein trafficking, coupled transport of small molecules and receptor-mediated endocytosis<sup>1</sup>. V-ATPase dysfunction has been implicated in human osteoporosis, in acquired drug resistance in human tumours, and in pathogen virulence<sup>12–14</sup>. A key subcomplex of the V-ATPase is the V<sub>0</sub> protein ring, a hexameric assembly that uses a rotary mechanism to move protons across organelle membranes (Fig. 1a)<sup>15,16</sup>. Although the V-ATPase is found in all eukaryotes, the V<sub>0</sub> ring varies in subunit composition among lineages. In animals and most other eukaryotes,

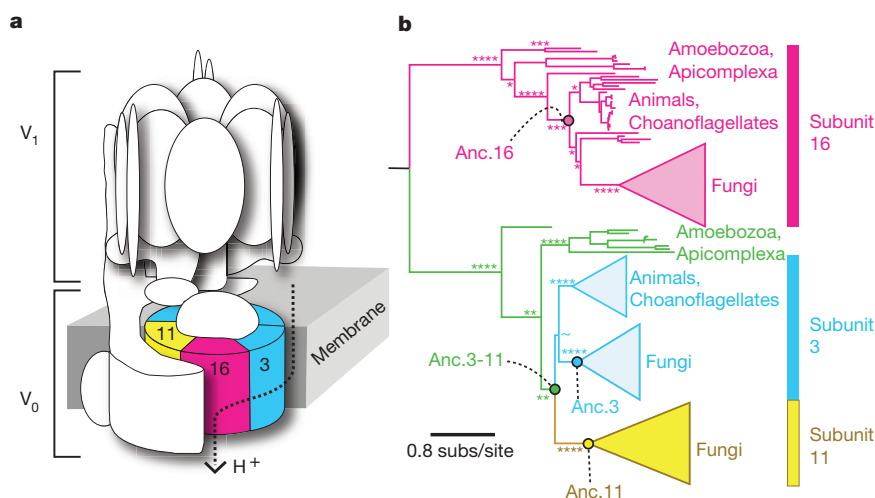


**Figure 1 | Structure and evolution of the V-ATPase complex.** **a**, In *S. cerevisiae*, the V-ATPase contains two subcomplexes: the octameric V<sub>1</sub> domain is on the cytosolic side of the organelle membrane, and the hexameric V<sub>0</sub> ring is membrane bound. Protein subunits Vma3, Vma11 and Vma16 are labelled and coloured. **b**, Maximum likelihood phylogeny of V-ATPase subunits Vma3, Vma11 and Vma16. All eukaryotes contain subunits 3 and 16, but Fungi also

contain subunit 11. Circles show ancestral proteins reconstructed in this study. Colours correspond to those of subunits in panel **a**; unduplicated orthologues of Vma3 and Vma11 are green. Asterisks show approximate likelihood ratios for major nodes: \*\*\*\*, >10<sup>3</sup>; \*\*\*, >10<sup>2</sup>; \*\*, >10; \*, <10; ~, <2. The complete phylogeny is presented in Supplementary Information, section 2.

<sup>1</sup>Institute of Molecular Biology, University of Oregon, Eugene, Oregon 97403, USA. <sup>2</sup>Institute for Ecology and Evolution, University of Oregon, Eugene, Oregon 97403, USA. <sup>3</sup>Department of Computer and Information Science, University of Oregon, Eugene, Oregon 97403, USA. <sup>4</sup>Howard Hughes Medical Institute, Eugene, Oregon 97403, USA. <sup>5</sup>Departments of Human Genetics and Ecology & Evolution, University of Chicago, Chicago, Illinois 60637, USA.

\*These authors contributed equally to this work.



the ring consists of one subunit of Vma16 protein and five copies of its paralogue, Vma3 (Fig. 1b)<sup>1</sup>. In Fungi, the ring consists of one Vma16 subunit, four copies of Vma3 and one Vma11 subunit, arranged in a specific orientation<sup>17</sup>. All three proteins are required for V-ATPase function in Fungi<sup>18,19</sup>, but the mechanisms are unknown by which both Vma3 and Vma11 became obligate components with specific positional roles in the complex.

To understand how the three-component ring evolved, we reconstructed ancestral  $V_0$  proteins from just before and after the increase in complexity, synthesized and functionally characterized them in a yeast genetic system, and used manipulative methods to identify the genetic and molecular mechanisms by which their functions changed. We first inferred the phylogeny and best-fit evolutionary model of the protein family of which Vma3, Vma11 and Vma16 are members, using the sequences of all 139 extant family members available in GenBank (Supplementary Table 1). The maximum likelihood phylogeny (Fig. 1b and Supplementary Information, section 2) indicates that Vma3 and Vma11 are sister proteins that were produced by duplication of an ancestral gene (Anc.3-11) before the last common ancestor of all Fungi (~800 million years ago<sup>20</sup>). Whether this duplication occurred before or after the divergence of Fungi from other eukaryotes (~1 billion years ago<sup>20</sup>) is not clearly resolved, although the latter scenario is more parsimonious. The Vma3/Vma11 and Vma16 lineages, in turn, descend from an older gene duplication deep in the eukaryotic lineage (Fig. 1b). We used a maximum likelihood algorithm<sup>21</sup> to infer the ancestral amino acid sequences with the highest probability of producing all the extant sequence data, given the best-fit phylogeny and model. We reconstructed the ancestral proteins (Anc.3-11 and Anc.16) that made up the ancient two-paralogue eukaryotic ring, as well as the duplicated subunits Anc.3 and Anc.11 from the three-component ring in the common ancestor of all Fungi (Supplementary Information, sections 3 and 4).

To characterize the functions of these reconstructed proteins, we synthesized coding sequences and transformed them into *Saccharomyces cerevisiae* deficient for various ring components and therefore incapable of growth in the presence of elevated  $\text{CaCl}_2$  (ref. 22). We found that the ancestral two-subunit ring can functionally replace the three-subunit ring of extant yeast. When the resurrected Anc.3-11 was transformed into yeast deficient for Vma3 (*vma3Δ*) or Vma11 (*vma11Δ*), growth in

the presence of elevated  $\text{CaCl}_2$  was rescued, indicating that the functions of the present-day Vma3 and Vma11 proteins were already present before the duplication that generated them (Fig. 2a). Furthermore, Anc.3-11—unlike either of its present-day descendants—can partially rescue growth in yeast that are doubly deficient for both Vma3 and Vma11 (*vma3Δ vma11Δ*). The reconstructed Anc.16 also rescued growth in Vma16-deficient *S. cerevisiae* (*vma16Δ*) (Fig. 2b), and co-expression of Anc.3-11 and Anc.16 together rescued cell growth in *vma3Δ vma11Δ vma16Δ* yeast, which lack all three ring subunits (Fig. 2c). The ancestral genes specifically restore proper V-ATPase function in acidification of the vacuolar lumen (Fig. 2g). In addition, mutation of the ancestral subunits to remove glutamic acid residues known to be essential for V-ATPase enzyme function<sup>17,23</sup> abolished their ability to rescue growth on  $\text{CaCl}_2$  (Supplementary Information, section 7). These inferences about the functions of Anc.3-11 and Anc.16 are robust to uncertainty about ancestral amino acid states. We reconstructed alternative versions of Anc.3-11 and Anc.16 by introducing amino acid states with posterior probability >0.2, but none of these abolished the ability of the ancestral genes to substitute functionally for the extant subunits (Supplementary Information, section 8). These results establish that during the increase in complexity, neither the  $V_0$  complex nor its component proteins evolved new functions required for growth under the conditions in which the ring is known to be important.

Similar experiments with the components of the ancestral three-component ring show that after the duplication of Anc.3-11, its descendants Anc.3 and Anc.11 both became necessary for a functional complex because of complementary losses of ancestral functions. Unlike Anc.3-11, expression of Anc.3 can rescue growth and vacuole acidification in *vma3Δ* but not *vma11Δ* yeast, and Anc.11 can rescue growth in *vma11Δ* but not *vma3Δ* yeast (Fig. 2d, e, g). Furthermore, both Anc.3 and Anc.11 are required to rescue growth fully in *vma3Δ vma11Δ* yeast (Fig. 2f). These data indicate that after its origin by gene duplication, Anc.11 lost the ancestral protein's ability to carry out at least some functions of Vma3, and Anc.3 lost the ancestral capacity to carry out those of Vma11.

We conjectured that Vma3 and Vma11 evolved their specialized roles because they lost specific interfaces present in their ancestor that are required for ring assembly. Previous experiments with fusions of

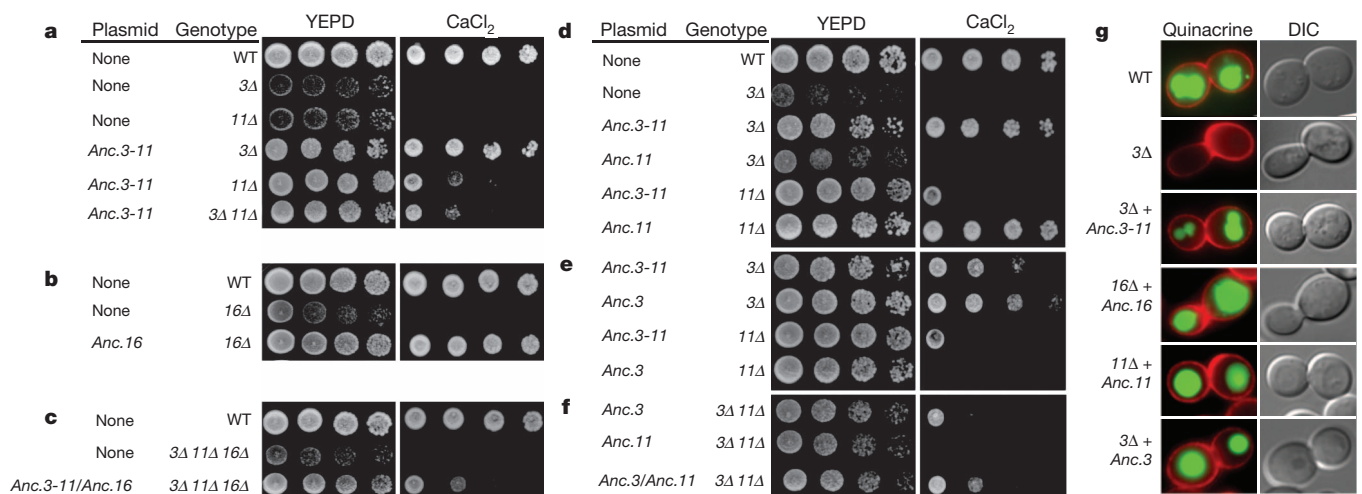


**Figure 2 | Two reconstructed ancestral  $V_0$  subunits functionally replace the three-paralogue ring in extant yeast.** *S. cerevisiae* were plated in decreasing concentrations on permissive medium (YEPD) buffered with elevated  $\text{CaCl}_2$ . **a**, Expression of Anc.3-11 rescues growth in yeast that are deficient for endogenous subunit Vma3 (3Δ), subunit Vma11 (11Δ) or both (3Δ 11Δ). Growth of wild-type (WT) yeast is shown for comparison. **b**, Anc.16 rescues growth in yeast that are deficient for subunit Vma16 (16Δ). **c**, Expression of Anc.3-11 and Anc.16 together rescues growth in yeast that are deficient for

Vma3, Vma11 and Vma16. **d**, Anc.11 rescues growth in *vma11Δ* but not in *vma3Δ* yeast. **e**, Anc.3 rescues growth in *vma3Δ* but not *vma11Δ* yeast. **f**, Anc.3 and Anc.11 together rescue growth in *vma3Δ vma11Δ* mutants. **g**, Yeast expressing reconstructed ancestral subunits properly acidified the vacuolar lumen. Red signal shows yeast cell walls; green signal (quinacrine) shows acidified compartments. Yeast were visualized by differential interference contrast microscopy.

extant yeast proteins have shown that the arrangement of subunits in the ring is constrained by the capacity of each subunit to form specific interfaces (which we labelled P, Q and R) with the other subunits<sup>24</sup>. Specifically, Vma11 is restricted to a single position between Vma16 and Vma3, because its clockwise interface can participate only in interface R with Vma16, and its anticlockwise interface can participate only in interface P with the clockwise side of Vma3 (Fig. 3). By contrast, copies of Vma3 occupy several positions in the ring, because they form interface P with other copies of Vma3 or Vma11, as well as interface Q with Vma16. However, Vma3 cannot form interface R with Vma16. As a result, both Vma3 and Vma11 are required in extant yeast to form a complete ring with Vma16.

To determine whether interaction interfaces were lost during evolution, we engineered fusions of ancestral ring proteins to assess the capacity of each to form the specific interfaces with other subunits that are required for a functional complex. Because Anc.3-11 can complement the loss of both Vma3 and Vma11, we proposed that the Anc.3-11 subunit could participate in all three specific interaction interfaces, and that these capacities were then partitioned between Anc.3 and Anc.11 after the duplication of Anc.3-11 (Fig. 3a, b). To test this hypothesis, we created six reciprocal gene fusions between yeast subunit Vma16 and ancestral subunits Anc.3-11, Anc.3 and Anc.11 (Fig. 3c and Supplementary Information, section 9). Each fusion constrains the structural position of subunits relative to subunit Vma16, making it possible to determine which arrangements yield a functional ring. As predicted, Anc.3-11 functioned on either side of Vma16 (Fig. 3d), indicating that it could form all three interfaces P, Q and R. By contrast, Anc.3 functioned when constrained to participate in interface Q with Vma16 and interface P with Vma3; however, ring function was lost when Anc.3 was constrained to form interface R with

Vma16 (Fig. 3e). Anc.11 functioned when constrained to participate in interface R with Vma16 and interface P with Vma3, but ring function was lost when Anc.11 was constrained to participate in interface Q with Vma16 and interface P with Vma3. This result indicates that Anc.11 lost the capacity to form one or both of these interfaces during its post-duplication divergence from Anc.3-11 (Fig. 3f).

Taken together, these data indicate that the specificity of the ring arrangement and the obligate roles of Vma3 and Vma11 evolved by complementary loss of asymmetric interactions with other members of the ring (Fig. 3g, h). Before Anc.3-11 duplicated, the protein ring contained copies of only undifferentiated subunit Vma3/Vma11 and subunit 16. Immediately after Anc.3-11 duplicated, the two descendant subunits must have been functionally identical, so the protein ring could have assembled with many possible combinations of the two descendants, including copies of only one of the descendant proteins. This flexibility disappeared when Anc.3 lost the ancestral interface that allowed it to interact with the anticlockwise side of Vma16, and Anc.11 lost the ability to interact with the clockwise side of Vma16 and/or the anticlockwise side of Vma3. These complementary losses are sufficient to explain the specific arrangement of contemporary subunits in reconstructed and present-day fungal transmembrane rings.

To establish the genetic basis for the partitioning of the functions of Anc.3-11 between Vma3 and Vma11, we introduced historical mutations into Anc.3.11 by directed mutagenesis and determined whether they recapitulated the shifts in function that occurred during the evolution of Anc.3 and Anc.11. The two phylogenetic branches leading from Anc.3-11 to Anc.3 and to Anc.11 contain 25 and 31 amino acid substitutions, respectively, but only a subset of these are strongly conserved in subunits Vma3 or Vma11 from extant Fungi (Fig. 4a). We introduced each of these 'diagnostic' substitutions into Anc.3-11 and

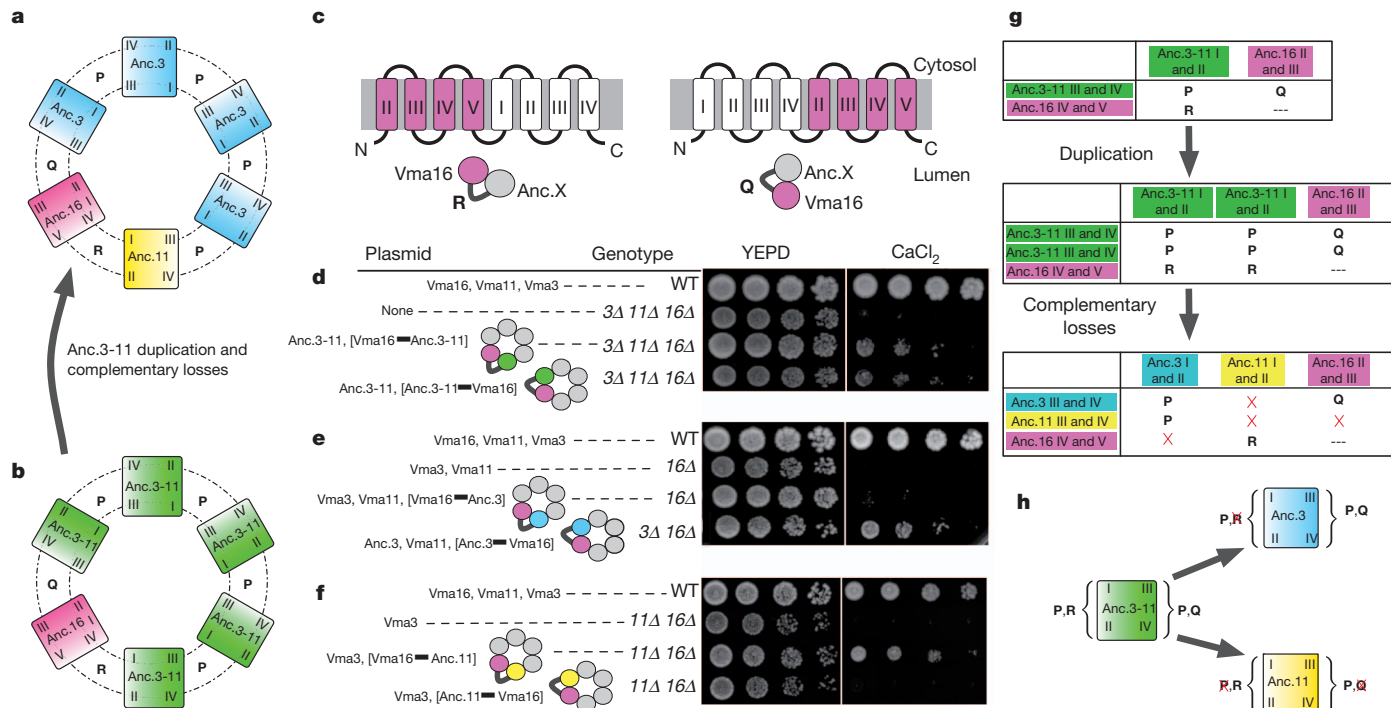


**Figure 3 | Increasing complexity by complementary loss of interactions in the fungal V<sub>0</sub> ring.** **a**, Model of the ancestral three-paralogue ring, arranged as in extant yeast<sup>24</sup>. Unique intersubunit interfaces are labelled P, Q and R. Subunits are colour-coded as in Fig. 1. **b**, Model of the ancestral two-paralogue ring, before duplication of Anc.3-11. **c**, To constrain the location of specific subunits, gene fusions were constructed by tethering an ancestral subunit to either the amino- or carboxy-terminal side of yeast Vma16. Roman numerals indicate the locations of transmembrane helices (I, II, III, IV and V)<sup>24</sup>. **d–f**, Growth assays of yeast with fused V<sub>0</sub> subunits identify the interfaces that ancestral subunits can

form. For each experiment, expressed V<sub>0</sub> subunits are listed. Tethered subunits are in brackets and connected by a thick line. Cartoons show the constrained location of the tethered subunit relative to Vma16. Anc.3-11 can function on either side of Vma16 (**d**). Anc.3 can function only on the clockwise side of Vma16 (**e**). Anc.11 can function only on the anticlockwise side of Vma16 (**f**). **g**, Interfaces that are formed by V<sub>0</sub> subunits before and after duplication and complementary loss of interfaces, based on the data in panels d–f. Red crosses indicate lost interfaces. **h**, Schematic of interfaces formed by Anc.3-11 that were lost in Anc.3 and Anc.11, based on data in panels d–f.

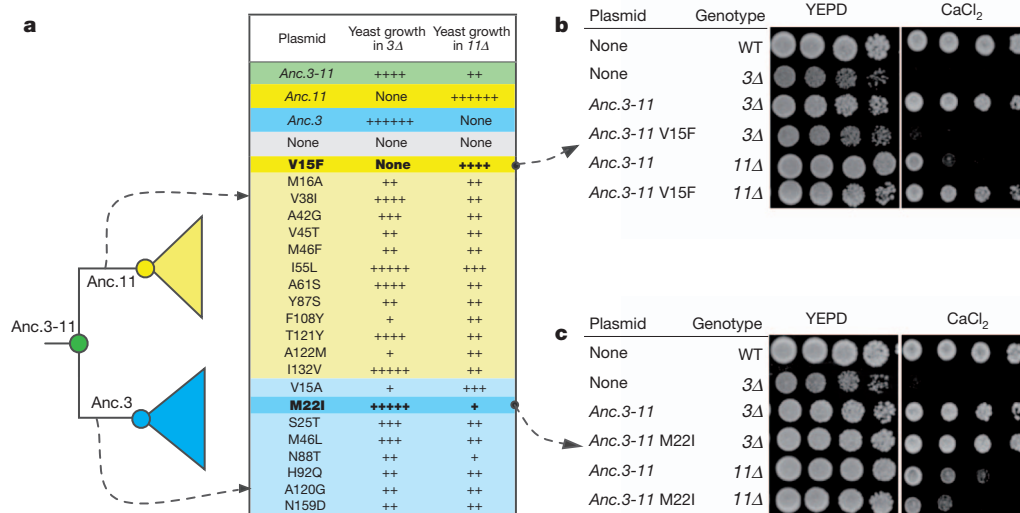


**Figure 4 | Genetic basis for functional differentiation of Anc.3 and Anc.11.**

**a**, Experimental analysis of historical amino acid replacements. The table lists replacements that occurred on the branches leading from Anc.3-11 to Anc.11 (yellow) or to Anc.3 (blue) and that were subsequently conserved. Each derived residue was introduced singly into Anc.3-11; the variant genes were transformed into *S. cerevisiae*, and growth was assayed on elevated CaCl<sub>2</sub>. The

experimentally evaluated whether they recapitulated the loss by Anc.3 or Anc.11 of the capacity to complement Vma gene deletions. We found that a single amino-acid replacement that occurred on the branch leading to Anc.11 (V15F) abolished the capacity of Anc.3-11 to function as subunit 3; it also enhanced the ability of Anc.3-11 to function as subunit 11 (Fig. 4b). V15F is located in transmembrane helix I, which participates in the P interface that our experiments indicate may have been lost on the same branch (Fig. 3 and Supplementary Information, section 4). Conversely, a single historical replacement (M22I) on the branch leading to Anc.3 radically reduced the capacity of Anc.3-11 to function as subunit 11 (Fig. 4c). M22I is also in transmembrane helix I, which participates in formation of the R interface that was lost on this branch (Fig. 3 and Supplementary Information, section 4). The Anc.3-11 M22I mutant retains some of the capacity of the ancestral protein to rescue growth in the Vma11-deficient background, suggesting that other mutations also contributed to the functional evolution of Vma3. One other historical mutation (N88T) on this branch also impaired the capacity of Anc.3-11 to function as subunit 11, but it reduced the capacity of the protein to function as Vma3 as well, suggesting that epistatic interactions with other residues allow this mutation to be tolerated in Anc.3 and its descendants. Several of the replacements on the branch leading to Anc.11 show a similar pattern, reducing the capacity of the protein to replace Vma3, indicating that these historical replacements function better together than in isolation.

How complexity and novel functions evolve has been a longstanding question in evolutionary biology<sup>25–27</sup>, because mutations that compromise existing functions are far more frequent than those that generate new ones<sup>28</sup>. Our results indicate that the architectural complexity of molecular assemblies can evolve because of a few simple, relatively high-probability mutations that degrade ancestral interfaces but leave other functions intact. The specific roles of subunits Vma3 and Vma11 seem to have been acquired when duplicated genes lost some, but not all, of the capacity of the ancestral protein to participate in interactions with copies of itself and another protein required for proper ring assembly. Because complementary losses occurred in both lineages, the two descendant subunits became obligate components, and the complexity of the ring increased. It is possible that specialization of the duplicated subunits allowed increases in fitness, but genome-wide

interaction screens and the phenotype of *vma11Δ* yeast provide no evidence that Vma11 evolved novel functions in addition to those that it inherited from Anc.3-11 in the V<sub>0</sub> ring<sup>29</sup>. We are aware of no other mechanistic analyses of a molecular machine's evolutionary trajectory, so the generality of our observations is unknown. By definition, however, all molecular machines involve differentiated parts in specific spatial orientations, and many such complexes are entirely or partially composed of paralogous proteins<sup>2–8</sup>. In the evolution of any such assembly, additional paralogues could become obligate components because of gene duplication<sup>30</sup> and subsequent mutations that cause specific interaction interfaces among them to degenerate.

This view of the evolution of molecular machines is related to recent models that explain other biological phenomena—such as the retention of large numbers of duplicate genes and mobile genetic elements within genomes—as the product of degenerative processes acting on modular biological systems<sup>27</sup>. Although mutations that enhanced the functions of individual ring components may have occurred during evolution, our data indicate that simple degenerative mutations are sufficient to explain the historical increase in complexity of a crucial molecular machine. There is no need to invoke the acquisition of 'novel' functions caused by low-probability mutational combinations.

## METHODS SUMMARY

Ancestral protein sequences were inferred using maximum-likelihood phylogenetics from an alignment of 139 protein sequences of extant subunits 3, 11 and 16 from Amoebozoa, Apicomplexa, Metazoa, Choanoflagellida and Fungi. Ancestral genes were synthesized, cloned into yeast expression vectors and tested for complementation in various *S. cerevisiae* mutants. V-ATPase function was assayed by growth tests on medium buffered with CaCl<sub>2</sub>, as described previously<sup>31</sup>. Steady-state levels of Vph1 were determined by western blot. Quinacrine staining and Vph1-GFP (green fluorescent protein) fusion constructs were visualized by fluorescence microscopy.

**Full Methods** and any associated references are available in the online version of the paper at [www.nature.com/nature](http://www.nature.com/nature).

Received 21 September; accepted 21 November 2011.

Published online 9 January 2012.

1. Forgac, M. Vacuolar ATPases: rotary proton pumps in physiology and pathophysiology. *Nature Rev. Mol. Cell Biol.* **8**, 917–929 (2007).



2. Pallen, M. J. & Matzke, N. J. From the origin of species to the origin of bacterial flagella. *Nature Rev. Microbiol.* **4**, 784–790 (2006).
3. Liu, R. & Ochman, H. Stepwise formation of the bacterial flagellar system. *Proc. Natl Acad. Sci. USA* **104**, 7116–7121 (2007).
4. Mulkidjanian, A. Y., Makarova, K. S., Galperin, M. Y. & Koonin, E. V. Inventing the dynamo machine: the evolution of the F-type and V-type ATPases. *Nature Rev. Microbiol.* **5**, 892–899 (2007).
5. Dolezal, P., Likic, V., Tachezy, J. & Lithgow, T. Evolution of the molecular machines for protein import into mitochondria. *Science* **313**, 314–318 (2006).
6. Clements, A. *et al.* The reducible complexity of a mitochondrial molecular machine. *Proc. Natl Acad. Sci. USA* **106**, 15791–15795 (2009).
7. Archibald, J. M., Logsdon, J. M. Jr & Doolittle, W. F. Origin and evolution of eukaryotic chaperonins: phylogenetic evidence for ancient duplications in CCT genes. *Mol. Biol. Evol.* **17**, 1456–1466 (2000).
8. Gabaldón, T., Rainey, D. & Huynen, M. A. Tracing the evolution of a large protein complex in the eukaryotes, NADH:ubiquinone oxidoreductase (complex I). *J. Mol. Biol.* **348**, 857–870 (2005).
9. Thornton, J. W. Resurrecting ancient genes: experimental analysis of extinct molecules. *Nature Rev. Genet.* **5**, 366–375 (2004).
10. Liberles, D. (ed.) *Ancestral Sequence Reconstruction* (Oxford Univ. Press, 2007).
11. Harms, M. J. & Thornton, J. W. Analyzing protein structure and function using ancestral gene reconstruction. *Curr. Opin. Struct. Biol.* **20**, 360–366 (2010).
12. Frattini, A. *et al.* Defects in TCIRG1 subunit of the vacuolar proton pump are responsible for a subset of human autosomal recessive osteopetrosis. *Nature Genet.* **25**, 343–346 (2000).
13. Pérez-Sayáns, M., Somoza-Martín, J. M., Barros-Angueira, F., Rey, J. M. & García-García, A. V-ATPase inhibitors and implication in cancer treatment. *Cancer Treat. Rev.* **35**, 707–713 (2009).
14. Xu, L. *et al.* Inhibition of host vacuolar H<sup>+</sup>-ATPase activity by a *Legionella pneumophila* effector. *PLoS Pathog.* **6**, e1000822 (2010).
15. Hirata, T. *et al.* Subunit rotation of vacuolar-type proton pumping ATPase: relative rotation of the g and c subunits. *J. Biol. Chem.* **278**, 23714–23719 (2003).
16. Imamura, H. *et al.* Rotation scheme of V<sub>1</sub>-motor is different from that of F<sub>1</sub>-motor. *Proc. Natl Acad. Sci. USA* **102**, 17929–17933 (2005).
17. Powell, B., Graham, L. A. & Stevens, T. H. Molecular characterization of the yeast vacuolar H<sup>+</sup>-ATPase proton pore. *J. Biol. Chem.* **275**, 23654–23660 (2000).
18. Umemoto, N., Yoshihisa, T., Hirata, R. & Anraku, Y. Roles of the VMA3 gene product, subunit c of the vacuolar membrane H<sup>+</sup>-ATPase on vacuolar acidification and protein transport. A study with VMA3-disrupted mutants of *Saccharomyces cerevisiae*. *J. Biol. Chem.* **265**, 18447–18453 (1990).
19. Umemoto, N., Ohya, Y. & Anraku, Y. VMA11, a novel gene that encodes a putative proteolipid, is indispensable for expression of yeast vacuolar membrane H<sup>+</sup>-ATPase activity. *J. Biol. Chem.* **266**, 24526–24532 (1991).
20. Taylor, J. W. & Berbee, M. L. Dating divergences in the fungal tree of life: review and new analyses. *Mycologia* **98**, 838–849 (2006).
21. Yang, Z., Kumar, S. & Nei, M. A new method of inference of ancestral nucleotide and amino acid sequences. *Genetics* **141**, 1641–1650 (1995).
22. Kane, P. M. The where, when, and how of organelle acidification by the yeast vacuolar H<sup>+</sup>-ATPase. *Microbiol. Mol. Biol. Rev.* **70**, 177–191 (2006).
23. Hirata, R., Graham, L. A., Takatsuki, A., Stevens, T. H. & Anraku, Y. Vma11 and vma16 encode second and third proteolipid subunits of the *Saccharomyces cerevisiae* vacuolar membrane H<sup>+</sup>-ATPase. *J. Biol. Chem.* **272**, 4795–4803 (1997).
24. Wang, Y., Cipriano, D. J. & Forgac, M. Arrangement of subunits in the proteolipid ring of the V-ATPase. *J. Biol. Chem.* **282**, 34058–34065 (2007).
25. Ohno, S. *Evolution by Gene Duplication* (Springer, 1970).
26. Jacob, F. Evolution and tinkering. *Science* **196**, 1161–1166 (1977).
27. Lynch, M. The frailty of adaptive hypotheses for the origins of organismal complexity. *Proc. Natl Acad. Sci. USA* **104**, 8597–8604 (2007).
28. Hietpas, R. T., Jensen, J. D. & Bolon, D. N. Experimental illumination of a fitness landscape. *Proc. Natl Acad. Sci. USA* **108**, 7896–7901 (2011).
29. Tong, A. H. Y. *et al.* Global mapping of the yeast genetic interaction network. *Science* **303**, 808–813 (2004).
30. Pereira-Leal, J. B., Levy, E. D., Kamp, C. & Teichmann, S. A. Evolution of protein complexes by duplication of homomeric interactions. *Genome Biol.* **8**, R51 (2007).
31. Ryan, M., Graham, L. A. & Stevens, T. H. Voa1p functions in V-ATPase assembly in the yeast endoplasmic reticulum. *Mol. Biol. Cell* **19**, 5131–5142 (2008).

**Supplementary Information** is linked to the online version of the paper at [www.nature.com/nature](http://www.nature.com/nature).

**Acknowledgements** This study was supported by National Institutes of Health (NIH) grants R01-GM081592 (to J.W.T.) and R01-GM38006 (to T.H.S.), National Science Foundation (NSF) grants IOB-0546906 (to J.W.T.) and DEB-0516530 (to J.W.T.), NIH Genetics Training grant T32-GM007257 (to G.C.F.), NSF IGERT grant DGE-9972830 (to V.H.-S.) and the Howard Hughes Medical Institute (J.W.T.). We thank L. Graham, G. Butler and B. Houser for generating yeast strains and other assistance. We thank members of the Stevens and Thornton laboratories for helpful comments.

**Author Contributions** V.H.-S. performed the phylogenetic analysis and statistical reconstructions. G.C.F. performed functional experiments. All authors conceived the experiments, interpreted the results and wrote the paper.

**Author Information** Reprints and permissions information is available at [www.nature.com/reprints](http://www.nature.com/reprints). The authors declare no competing financial interests. Readers are welcome to comment on the online version of this article at [www.nature.com/nature](http://www.nature.com/nature). Correspondence and requests for materials should be addressed to J.W.T. ([joet@uoregon.edu](mailto:joet@uoregon.edu)).

## METHODS

**In silico reconstruction of ancestral protein sequences.**  $V_0$  complex subunits Vma3, Vma11 and Vma16 are sometimes referred to as subunits c, c' and c'' in the literature. We searched GenBank for all eukaryote V-ATPase  $V_0$  ring sequences (Supplementary Information, section 1). Our query returned subunit 3, 11 and 16 protein sequences for 26 species in Fungi, and subunit 3 and 11 sequences for 35 species in Metazoa, Amoebozoa and Apicomplexa. We aligned the sequences using PRANK v0.081202 (refs 32, 33). We selected the best-fit model (WAG with gamma-distributed rate variation and a proportion of invariant sites) using the Akaike Information Criterion as implemented in PROTTEST<sup>34,35</sup>. With this model, we used PhyML v3.0 to infer the maximum likelihood topology, branch lengths and model parameters<sup>36</sup>. We optimized the topology using the best result from nearest-neighbour interchange and subtree pruning and regrafting; we optimized all other free parameters using the default hill-climbing algorithm in PhyML. Phylogenetic support was calculated as the approximate likelihood ratio (converted from the approximate likelihood ratio statistic (aLRS) for branches reported by PhyML, using the equation  $aLR = \exp[aLRS/2]$ ) and as the likelihood ratio-based SH-like branch supports<sup>37</sup>. Nematoda subunit 3 and 11 sequences were connected by a very long branch basal to the Chromalveolata lineages. This result is inconsistent with the expectation that Nematoda are animals<sup>38</sup>, so we excluded Nematoda data from further downstream analysis.

We inferred ML ancestral states and posterior probability distributions at each site for all ancestral nodes in the ML phylogeny using our own set of Python scripts, called Lazarus, which wraps PAML version 4.1 (ref. 39). Lazarus parsimoniously places ancestral gap characters according to Fitch's algorithm<sup>40</sup>. We characterized the overall support for Anc.3-11, Anc.16, Anc.3 and Anc.11 by binning the posterior probability of the ML state at each site into 5%-sized bins and then counting the proportion of total sites within each bin (Supplementary Information, section 2).

**Robustness to alignment uncertainty.** To assess the robustness of ancestral reconstructions to alignment uncertainty, we performed alignment using four algorithms: CLUSTAL version 2.0.10 (ref. 41), MUSCLE v3.7 (ref. 42), AMAP v2.2 (ref. 43), and PRANK v0.081202 (refs 32, 33). We then inferred the ML phylogeny and branch lengths for each alignment, using the methods described above. The resultant alignments varied in length from 347 sites (using CLUSTAL) to 683 sites (using PRANK), but all four alignments yielded the same ML topology with nearly identical ML branch lengths.

To determine which alignment algorithm yields the most accurate ancestral inferences under V-ATPase phylogenetic conditions, we simulated sequences across the V-ATPase ML phylogeny using insertion and deletion rates ranging from 0.0 to 0.1 indels per site. For each indel rate, we generated ten random unique indel-free ancestral sequences of 400 amino acids in length and then used INdelible<sup>44</sup> to simulate the ancestral sequence evolving along the branches of our ML phylogeny under the conditions of the WAG model with a proportion of invariant sites (+I) and a discrete gamma distribution of evolutionary rates (+G) with indel events randomly injected according to the specified indel rate. The size of each indel event was drawn from a Zipfian distribution with coefficient equal to 1.1 and the maximum length limited to 10 amino acids. We aligned the descendant sequences of each replicate using AMAP, CLUSTAL, MUSCLE and PRANK. For each alignment, we inferred the ML topology, branch lengths and model parameters using the methods described above. We used Lazarus to reconstruct all of the ancestral states, and queried Lazarus for the most-recent shared ancestor for opisthokont subunit 3/11 and opisthokont subunit 16 sequences. We measured the error of ancestral reconstructions as the proportion of ancestral sites that incorrectly contained an indel character (see Supplementary Information, section 6).

**Plasmids and yeast strains.** Bacterial and yeast manipulations were performed using standard laboratory protocols for molecular biology<sup>45</sup>. Plasmids that were used are listed in Supplementary Information, section 5. Ancestral sequences (pGF140, pGF139, pGF506 and pGF508) were synthesized by GenScript with a yeast codon bias. Triple haemagglutinin epitope tags were included before each stop codon. The Anc.3-11, Anc.16, Anc.3 and Anc.11 genes were subcloned to single-copy, CEN-based yeast vectors. The *ADH* terminator sequence (247 base pairs (bp)) and *Nat<sup>r</sup>* drug resistance marker<sup>46</sup> were amplified using polymerase-chain-reaction (PCR) containing 40-bp tails homologous to the 3' end of each coding region and vector sequence. Vectors were gapped, co-transformed into SF838-1D $\alpha$  yeast with PCR fragments and cells were selected for *Nat<sup>r</sup>*. A second round of *in vivo* ligation was used to place the ancestral genes under 500 bp of the *VMA3* or *VMA16* promoters to create pGF140 and pGF139, respectively. For vectors pGF240, pGF241, 1pGF252, pGF253, pGF503-pGF508, pGF510, pGF512-pGF515, pGF517-pGF519, pGF521, pGF523, pGF528, pGF529, pGF531, pGF534-pGF537 and pGF542, the relevant locus (Anc.3-11, Anc.16 or Anc.3) was PCR amplified with 5' and 3' untranslated flanking sequence and

cloned into pCR4Blunt-TOPO (Invitrogen). When necessary, a modified Quikchange protocol<sup>47</sup> was used to introduce point mutations before the gene was subcloned into a yeast vector (pRS316 or pRS415). To generate pGF502, sequence from codon 31 to the stop codon of Anc.16 was amplified with the *ADH::Nat<sup>r</sup>* cassette from pGF139, cloned into TOPO, and *in vivo* ligated downstream of the *VMA16* promoter (including a start codon) in pRS415.

A triple-fragment *in vivo* ligation was used to generate pGF646-pGF651. Gapped vector containing the *VMA16* promoter was transformed into yeast with two PCR fragments of the ring genes to be fused. For pGF646, the coding region of (1) *VMA16* (without codons 2–41) and (2) the coding region of Anc.11 (without codons 2–5) were amplified by PCR. The proteolipid on the C-terminal portion of the gene fusion also contained the *ADH* terminator and *Nat<sup>r</sup>* cassette; the amplified products contained PCR tails with homology to link the genes to both the gapped vector and to each other. Gene fusions were modelled after the experimental design of Wang *et al.* (2007)<sup>24</sup> in which the luminal protein sequence linking the two proteolipids was designed to be exactly 14 amino acids. To meet these criteria, additional amino acids were inserted into the following vectors linking the two subunits: pGF646 (Thr-Arg-Val-Asp), pGF648, pGF650 (Thr-Arg), pGF649, pGF651 (Gly-Ser).

Yeast strains that were used are listed in Supplementary Information, section 2. Strains containing deletion cassettes other than Kan<sup>R</sup><sup>45</sup> were constructed by PCR amplifying the *Hyg<sup>R</sup>* or *Nat<sup>r</sup>* cassette from pAG32 or pAG25, respectively, with primer tails with homology to flanking sequences to the *VMA11* or *VMA16* loci. *11A::Kan<sup>R</sup>* and *16A::Kan<sup>R</sup>* strains (SF838-1D $\alpha$ ) were transformed with the *Hyg<sup>R</sup>* and *Nat<sup>r</sup>* PCR fragments, respectively, and selected for drug resistance. The *11A::Hyg<sup>R</sup>* locus was amplified and transformed into LGY113 (to create LGY125) and LGY115 (to create LGY124). This was repeated with the *16A::Nat<sup>r</sup>* locus to create LGY139 and LGY143.

**Yeast Growth Assays.** Yeast were grown in liquid culture, diluted fivefold and spotted onto YEPD media buffered to pH 5.0 or yeast extract peptone dextrose media containing 25 mM (Figs 2, 3, 4) or 30 mM CaCl<sub>2</sub> (Fig. 2f).

**Whole-cell extract preparation and immunoblotting.** Yeast extracts and western blots were performed as previously described<sup>31</sup>. Antibodies that were used in this study included monoclonal primary anti-HA (Sigma-Aldrich), anti-Dpm1 (5C5; Invitrogen) and secondary horseradish-conjugated anti-mouse antibody (Jackson ImmunoResearch Laboratory, West Grove, Pennsylvania, USA).

**Fluorescence microscopy.** Staining with quinacrine was performed as previously described<sup>31</sup>. The cell wall (shown in red) was visualized using concanavalin A tetramethylrhodamine (Invitrogen). Microscopy images were obtained using an Axioplan 2 fluorescence microscope (Carl Zeiss). A  $\times 100$  objective, AxioVision software (Carl Zeiss) and Adobe Photoshop Creative Suite (v. 8.0) were used.

32. Löytynoja, A. & Goldman, N. An algorithm for progressive multiple alignment of sequences with insertions. *Proc. Natl Acad. Sci. USA* **102**, 10557–10562 (2005).
33. Löytynoja, A. & Goldman, N. Phylogeny-aware gap placement prevents errors in sequence alignment and evolutionary analysis. *Science* **320**, 1632–1635 (2008).
34. Whelan, S. & Goldman, N. A general empirical model of protein evolution derived from multiple protein families using a maximum-likelihood approach. *Mol. Biol. Evol.* **18**, 691–699 (2001).
35. Abascal, F., Zardoya, R. & Posada, D. Prottest: selection of best-fit models of protein evolution. *Bioinformatics* **21**, 2104–2105 (2005).
36. Guindon, S. & Gascuel, O. A simple, fast, and accurate algorithm to estimate large phylogenies by maximum likelihood. *Syst. Biol.* **52**, 696–704 (2003).
37. Anisimova, M. & Gascuel, O. Approximate likelihood-ratio test for branches: A fast, accurate, and powerful alternative. *Syst. Biol.* **55**, 539–552 (2006).
38. Aguinaldo, A. M. A. *et al.* Evidence for a clade of nematodes, arthropods, and other moulting animals. *Nature* **387**, 489–493 (1997).
39. Yang, Z. PAML 4: Phylogenetic analysis by maximum likelihood. *Mol. Biol. Evol.* **24**, 1586–1591 (2007).
40. Fitch, W. M. Toward defining the course of evolution: minimum change for a specific tree topology. *Syst. Zool.* **20**, 406–416 (1971).
41. Thompson, J. D., Higgins, D. G. & Gibson, T. J. CLUSTALW: improving the sensitivity of progressive multiple sequence alignment through sequence weighting position-specific gap penalties and weight matrix choice. *Nucleic Acids Res.* **22**, 4673–4680 (1994).
42. Edgar, R. C. MUSCLE: multiple sequence alignment with high accuracy and high throughput. *Nucleic Acids Res.* **32**, 1792–1797 (2004).
43. Do, C. B., Mahabhashyam, M. S., Brudno, M. & Batzoglou, S. ProbCons: Probabilistic consistency-based multiple sequence alignment. *Genome Res.* **15**, 330–340 (2005).
44. Fletcher, W. & Yang, Z. Indelible: a flexible simulator of biological sequence evolution. *Mol. Biol. Evol.* **26**, 1879–1888 (2009).
45. Sambrook, J. & Russell, D. W. *Molecular Cloning: A Laboratory Manual* 3rd edn (Cold Spring Harbor Laboratory Press, 2001).
46. Goldstein, A. L. & McCusker, J. H. Three new dominant drug resistance cassettes for gene disruption in *Saccharomyces cerevisiae*. *Yeast* **15**, 1541–1553 (1999).
47. Zheng, L., Baumann, U. & Reymond, J. L. An efficient one-step site-directed and site-saturation mutagenesis protocol. *Nucleic Acids Res.* **32**, e115 (2004).

# Structure of HDAC3 bound to co-repressor and inositol tetraphosphate

Peter J. Watson<sup>1</sup>, Louise Fairall<sup>1</sup>, Guilherme M. Santos<sup>1</sup> & John W. R. Schwabe<sup>1</sup>

Histone deacetylase enzymes (HDACs) are emerging cancer drug targets. They regulate gene expression by removing acetyl groups from lysine residues in histone tails, resulting in chromatin condensation. The enzymatic activity of most class I HDACs requires recruitment into multi-subunit co-repressor complexes, which are in turn recruited to chromatin by repressive transcription factors. Here we report the structure of a complex between an HDAC and a co-repressor, namely, human HDAC3 with the deacetylase activation domain (DAD) from the human SMRT co-repressor (also known as NCOR2). The structure reveals two remarkable features. First, the SMRT-DAD undergoes a large structural rearrangement on forming the complex. Second, there is an essential inositol tetraphosphate molecule—D-myo-inositol-(1,4,5,6)-tetrakisphosphate (Ins(1,4,5,6)P<sub>4</sub>)—acting as an ‘intermolecular glue’ between the two proteins. Assembly of the complex is clearly dependent on the Ins(1,4,5,6)P<sub>4</sub>, which may act as a regulator—potentially explaining why inositol phosphates and their kinases have been found to act as transcriptional regulators. This mechanism for the activation of HDAC3 appears to be conserved in class I HDACs from yeast to humans, and opens the way to novel therapeutic opportunities.

The acetylation of lysine residues in the tails of histone proteins plays an important role in the regulation of gene expression in eukaryotic cells<sup>1,2</sup>. The level of lysine acetylation is controlled through the opposing actions of histone acetyl transferases (HATs) and HDACs. Although chromatin is the best understood substrate for these enzymes, lysine acetylation is emerging as a general regulatory mechanism in a diverse array of cellular processes<sup>3</sup>.

There are four classes of HDACs in mammalian cells (reviewed in ref. 4). Class I HDACs are zinc-dependent enzymes, and include HDAC1, 2, 3 and 8. Of these, only HDAC8 is a fully functional enzyme in isolation<sup>5,6</sup>. HDAC1, 2 and 3 require recruitment into large multi-subunit co-repressor complexes for maximal activity<sup>7–12</sup>. These co-repressor complexes bring about the repression of gene expression when recruited to repressive transcription factors, but also contribute to the ‘resetting’ of chromatin after rounds of transcriptional activation<sup>13–16</sup>.

In recent years, HDACs have become important targets for the treatment of a number of cancers<sup>17</sup>. Cancer cell lines treated with HDAC inhibitors undergo terminal differentiation, growth arrest and/or apoptosis. Several HDAC inhibitors are at various stages in clinical trials, and two drugs, vorinostat and romidepsin, have been approved for the treatment of cutaneous T-cell lymphomas<sup>18</sup>.

HDAC1 and 2 are found in three co-repressor complexes: NuRD<sup>7,19</sup>, CoREST<sup>20,21</sup> and Sin3A<sup>22,23</sup>. In contrast, HDAC3 appears to be uniquely recruited to the SMRT complex (or to the homologous NCoR complex) where it interacts with a conserved DAD within SMRT or NCoR<sup>8,10,12,24–26</sup>. The DAD both recruits and activates HDAC3<sup>10–12</sup>. Recruitment of HDAC3 to the DAD is essential for repression by certain nuclear receptors and for the maintenance of normal circadian physiology<sup>27–29</sup>. It has been proposed that the assembly of the HDAC3 and SMRT-DAD requires a chaperone complex, because when these proteins are expressed in bacteria they do not form a complex<sup>30</sup>.

The DAD contains an extended SANT-like domain with an amino-terminal DAD-specific motif. Deletion of this motif results in both loss of binding and failure to activate HDAC3<sup>11</sup>. We have previously

reported the structure of the isolated DAD from SMRT<sup>31</sup>. This revealed that part of the DAD-specific motif forms an extra helix that is folded against the three helices of the SANT domain to form a four-helix bundle. The N-terminal portion of the DAD-specific motif is unstructured in solution<sup>31</sup>.

Here we report the structure of HDAC3 in complex with SMRT-DAD. This structure not only reveals the specificity and mechanism through which SMRT-DAD recruits and activates HDAC3, but also identifies Ins(1,4,5,6)P<sub>4</sub> as a key component of the complex that has the potential to regulate assembly of HDACs with their co-repressors.

## Overall architecture of the complex

As HDAC3 and SMRT-DAD do not form a complex when expressed in bacterial cells, full-length HDAC3 and Flag-tagged SMRT-DAD (amino acids 389–480) were expressed in suspension-grown mammalian HEK293 cells. The complex remained tightly associated during a three-step purification, including size exclusion chromatography (Supplementary Fig. 1). Interestingly, at salt concentrations higher than 50 mM, the complex dissociated and the HDAC3 predominantly took the form of aggregate or oligomers (Supplementary Fig. 2). Such oligomerization of HDAC3 has also been reported by others<sup>32</sup>. During crystallization, the HDAC3 tail is proteolysed but HDAC3 remains bound to SMRT-DAD and retains deacetylase activity (Supplementary Fig. 3). Small crystals (15 µm; Supplementary Fig. 1) diffracted to 2 Å and the structure was solved by molecular replacement with an HDAC8 structure<sup>33</sup>. Model building and refinement yielded an excellent map to 2.1 Å resolution with clear density for both HDAC3 and SMRT-DAD (Supplementary Fig. 1).

Overall, the HDAC3 structure is similar to the previously determined class I HDAC structures of HDAC8<sup>34</sup> and HDAC2<sup>35</sup>, and consists of an eight-stranded parallel β-sheet surrounded by a number of α-helices. The active site lies at the base of a tunnel leading from the surface of the protein. A solvent-exposed tyrosine residue is located on the surface of the enzyme immediately adjacent to the active site tunnel. This tyrosine is unique to HDAC3, and it seems that this

<sup>1</sup>Henry Wellcome Laboratories of Structural Biology, Department of Biochemistry, University of Leicester, Leicester LE1 9HN, UK.



residue might interact with the substrate and possibly contribute to substrate specificity (Supplementary Fig. 4).

### Structural rearrangement of SMRT-DAD

On forming a complex with HDAC3, the N-terminal helix of the DAD undergoes a major structural rearrangement (from that seen in the NMR structure), such that it no longer forms part of the core structure, but lies along the surface of HDAC3, making extensive intermolecular interactions (Fig. 1a, b). Along with a further extended region, this DAD-specific motif buries a surface of  $1,178 \text{ \AA}^2$ . The remaining three-helix bundle resembles a canonical SANT domain, and buries a further  $1,160 \text{ \AA}^2$  at the interface with HDAC3.

The SMRT-DAD interacts with the N-terminal region of HDAC3 (residues 9–49) that forms helix H1, loop L2, helix H2 and strand S2. This region differs between HDAC8 and HDAC3. Indeed, in HDAC3, helix H1 is distorted and can only be considered to be a pseudo-helix. These differences may explain why HDAC8 is active in the absence of an interacting co-repressor.

### An essential role for Ins(1,4,5,6)P<sub>4</sub>

At the earliest stages of refinement, the electron density difference map revealed a well-ordered small molecule bound at the interface between HDAC3 and the DAD (Fig. 2a). The electron density was

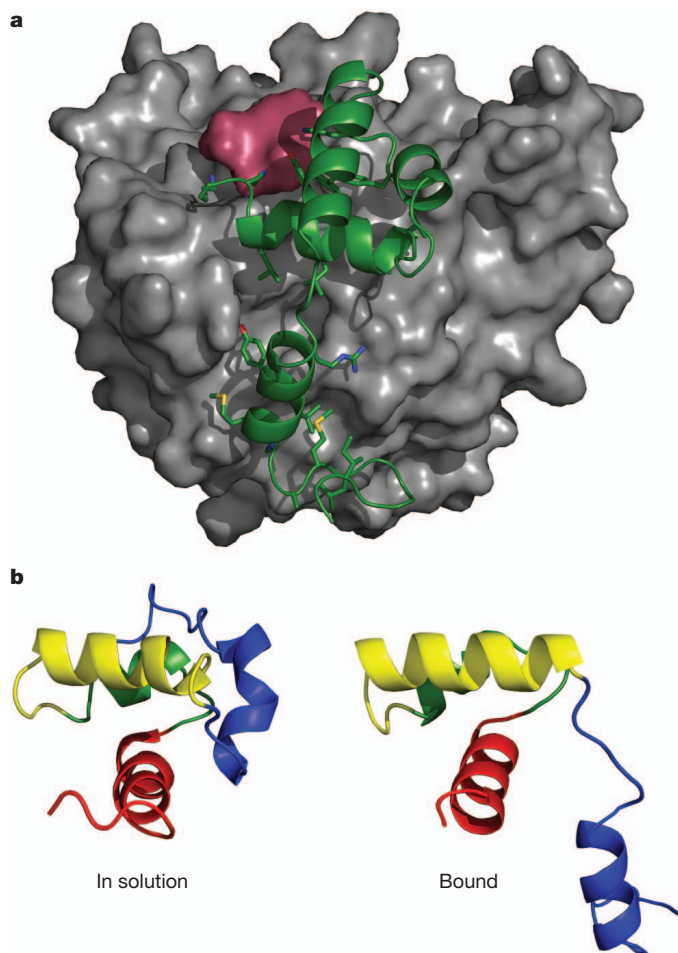


**Figure 1 | Structure of the HDAC3–SMRT-DAD complex.** **a**, Interaction of SMRT-DAD (green ribbon) with HDAC3 (grey surface). The Ins(1,4,5,6)P<sub>4</sub> at the interface is shown as a raspberry coloured surface. Side chains in the DAD that mediate interaction with HDAC3 and Ins(1,4,5,6)P<sub>4</sub> are shown as sticks. **b**, Structure of the DAD domain in solution (left; PDB code 1XC5) compared with that bound to HDAC3 (right); helices are individually coloured to facilitate comparison.

sufficiently well defined that the small molecule could be readily identified as inositol tetraphosphate. During further refinement, it could be unambiguously assigned as D-myo-inositol-1,4,5,6-tetrakisphosphate (based on the axial orientation of the hydroxyl group on carbon 2), referred to here as Ins(1,4,5,6)P<sub>4</sub> (Fig. 2b).

The Ins(1,4,5,6)P<sub>4</sub> molecule is sandwiched between HDAC3 and the DAD, in a highly basic pocket, making extensive contacts to both proteins, burying a surface of  $407 \text{ \AA}^2$  (Fig. 2c, d). HDAC3 and SMRT-DAD each contribute five hydrogen bonds and salt bridges to the Ins(1,4,5,6)P<sub>4</sub> (His 17, Gly 21, Lys 25, Arg 265, Arg 301 and Lys 449, Tyr 470, Tyr 471, Lys 474 and Lys 475, respectively) (Fig. 2e).

It is notable that the Ins(1,4,5,6)P<sub>4</sub> is sufficiently tightly bound to the complex that it is retained through the entire purification process. It is also striking that the binding is highly specific for Ins(1,4,5,6)P<sub>4</sub>, as the electron density shows that the ligand is uniquely Ins(1,4,5,6)P<sub>4</sub> rather than a mixture of inositol phosphates.

A careful examination of the structure suggests that Ins(1,4,5,6)P<sub>4</sub> binding is an essential requirement for the interaction between SMRT and HDAC3, acting as a ‘intermolecular glue’ that cements the complex together. If the Ins(1,4,5,6)P<sub>4</sub> ligand were not present, then the many basic residues on either side of the binding cleft would probably prevent interaction through charge repulsion. Indeed, at the base of the cleft, the  $\zeta$ -nitrogen atoms of SMRT Lys 449 and of HDAC3 Lys 25 are just  $4.4 \text{ \AA}$  from each other. Consequently, the assembly of the three-way SMRT–HDAC3–Ins(1,4,5,6)P<sub>4</sub> complex appears to be mutually interdependent, such that both SMRT-DAD and Ins(1,4,5,6)P<sub>4</sub> are required for activation of the HDAC3 enzymatic functionality.

These conclusions are supported by our previous mutagenesis study of SMRT-DAD, in which we looked at the effect of mutations on both the interaction with, and the deacetylase activity of, HDAC3. All mutations that failed to activate HDAC3 also abolished, or significantly impaired, interaction. These include mutations of Lys 449, Tyr 470 and Tyr 471, which play a key role in binding Ins(1,4,5,6)P<sub>4</sub> (ref. 31). The requirement for Ins(1,4,5,6)P<sub>4</sub> to enable complex formation may contribute to the explanation as to why recombinant HDAC3 and SMRT-DAD expressed in bacteria fail to interact, as bacteria probably do not contain sufficient Ins(1,4,5,6)P<sub>4</sub> to support complex formation.

Having discovered that Ins(1,4,5,6)P<sub>4</sub> plays a key role in HDAC3 activation, we asked whether inositol phosphates might contribute to the assembly and activation of other class I HDAC complexes. Significantly, the residues that mediate interaction with Ins(1,4,5,6)P<sub>4</sub> and the SANT domain from SMRT are conserved in both HDAC1 and 2, but not in HDAC8 (Fig. 3a), fitting with the observation that only HDAC8 is fully active in isolation.

Similarly, the co-repressor partners for HDAC1 and 2 (that is, MTA1, 2 and 3 and CoREST1, 2 and 3) contain SANT domains that are analogous to SMRT-DAD. The key Ins(1,4,5,6)P<sub>4</sub> binding residues are almost entirely conserved (Fig. 3b). It is likely that the specificity for the particular HDAC is conferred by the region N-terminal to the SANT domain: that is, the DAD specific motif in SMRT/NCOR and the ELM2 domains in the MTA and CoREST proteins.

Taken together, this suggests that inositol phosphate activation of class I HDACs is a general mechanism and, given that the key residues are also found in the yeast HDAC, Rpd3, and the Snt1 co-repressor, it would appear that this mechanism is also evolutionarily conserved.

### Mechanism of activation of HDAC3

The HDAC3–SMRT-DAD structure provides insight into the mechanism through which the DAD and Ins(1,4,5,6)P<sub>4</sub> contribute to the activation of HDAC3. In the crystal, the active site of HDAC3 resembles a product complex (Fig. 4a, b). An acetate molecule (present during purification) is bound at the active site, making hydrogen bonds to the catalytic zinc and side chains of Ty 298 and His 134. Furthermore, a methionine side chain (from an adjacent SMRT-DAD in the crystal lattice) is bound in the active site tunnel, mimicking a lysine residue.

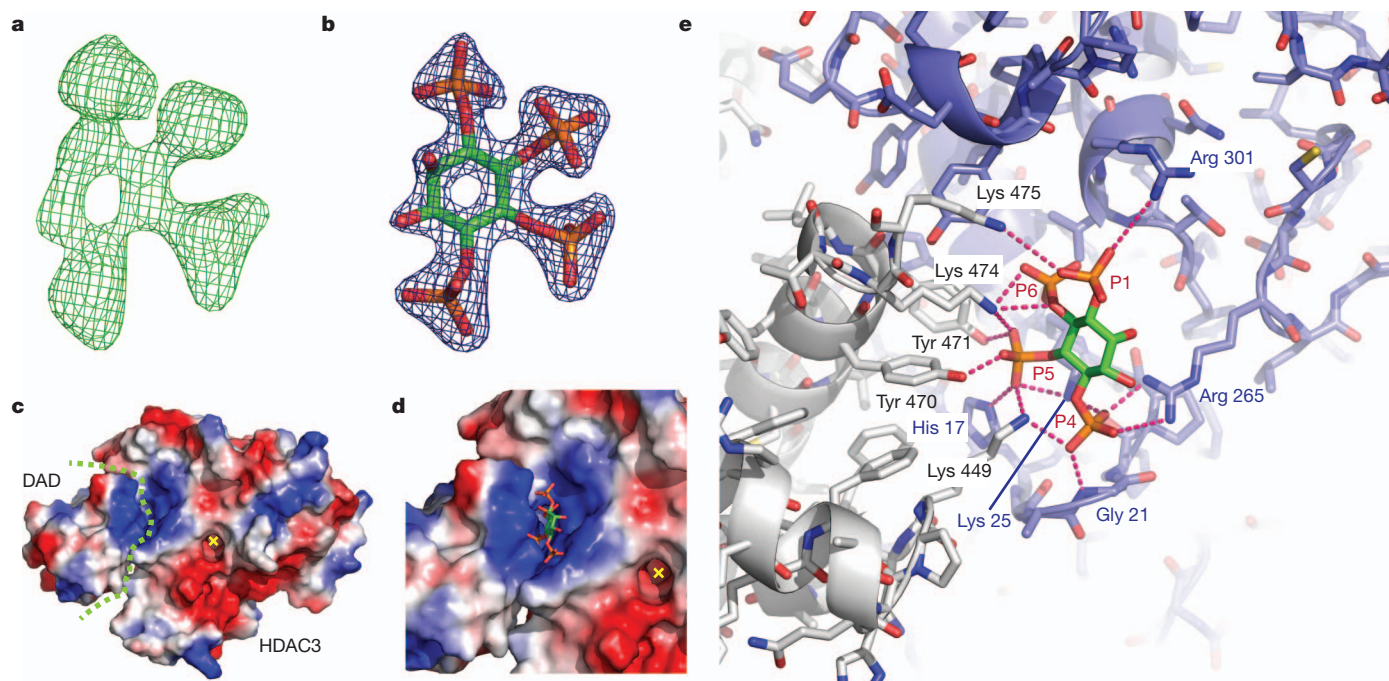


**Figure 2 | Ins(1,4,5,6)P<sub>4</sub> binding to the HDAC3-SMRT-DAD complex.**

**a**, A striking feature in the difference electron density map ( $F_o - F_c$  at  $3\sigma$ , green mesh) observed following molecular replacement. **b**, Electron density corresponding to the Ins(1,4,5,6)P<sub>4</sub> ligand following refinement ( $2F_o - F_c$  at  $2.25\sigma$ , blue mesh). The Ins(1,4,5,6)P<sub>4</sub> is shown as a stick model. **c**, Electrostatic surface representation of the HDAC3-SMRT-DAD complex (red indicates negative potential and blue positive). A strikingly basic pocket is located at the HDAC3-SMRT-DAD interface (indicated by a dashed green line). The active

site pocket of HDAC3 is indicated by a yellow cross. The Ins(1,4,5,6)P<sub>4</sub> is not shown for clarity. **d**, Ins(1,4,5,6)P<sub>4</sub> (shown as sticks) binding in the basic pocket at the HDAC3-SMRT-DAD interface. **e**, Detailed interactions of Ins(1,4,5,6)P<sub>4</sub> (sticks) with HDAC3 (blue) and SMRT-DAD (grey). Side chains from SMRT and HDAC3 which make contacts with the Ins(1,4,5,6)P<sub>4</sub> are labelled. The phosphate groups of the Ins(1,4,5,6)P<sub>4</sub> are labelled P1–6. Hydrogen bonds and/or salt bridges are indicated by dashed lines.

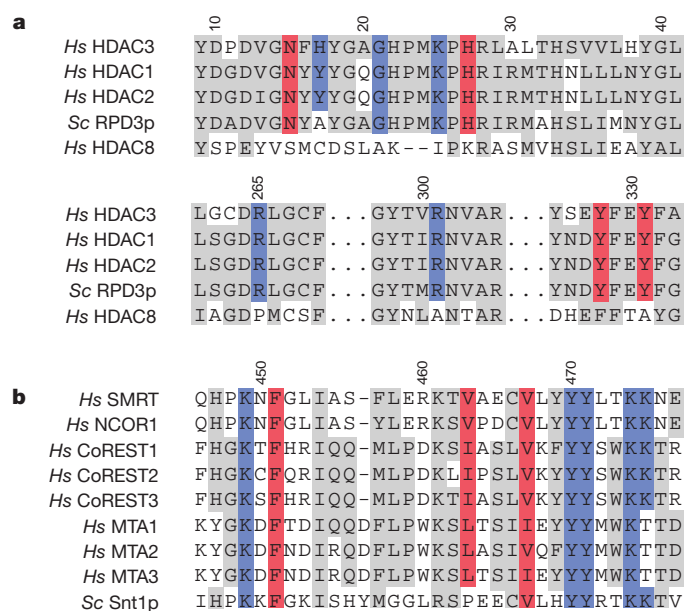


**Figure 3 | Sequence conservation suggests that class I HDACs, from yeast to man, require inositol phosphates for assembly and activation.** **a**, Alignments of key regions of class I HDACs from *Homo sapiens* (Hs) and *Saccharomyces cerevisiae* (Sc). Residues that mediate interaction with Ins(1,4,5,6)P<sub>4</sub> and SMRT-DAD are highlighted in blue and red, respectively. Other conserved residues are highlighted in grey. **b**, Alignment of SANT domains from known interaction partners for class I HDACs. Residues that mediate interaction with Ins(1,4,5,6)P<sub>4</sub> and HDAC3 are highlighted in blue and red, respectively. Green arrows indicate residues that impair HDAC3 recruitment and activation when mutated to alanine<sup>31</sup>.

The binding surfaces for DAD and Ins(1,4,5,6)P<sub>4</sub> are located to one side of the HDAC3 active site, involving pseudo helix H1 and loops L1 and L6 (Fig. 4a–c). We propose that changes in both conformation and dynamics occur when DAD and Ins(1,4,5,6)P<sub>4</sub> bind to HDAC3, and that these facilitate substrate access to the active site, resulting in enhanced enzyme activity.

There is a key interaction between Ins(1,4,5,6)P<sub>4</sub> and Arg 265 in loop L6 (coloured orange in Fig. 4b). This loop seems to be very important for access to the active site, because Leu 266 forms one wall of the active site tunnel, and in the absence of the Ins(1,4,5,6)P<sub>4</sub> this loop is likely to be relatively mobile.

Comparison of the HDAC3 structure with that of HDAC8, which does not require activation by complex formation, reveals that HDAC8 differs significantly in the region where HDAC3 interacts with SMRT-DAD and Ins(1,4,5,6)P<sub>4</sub> (Fig. 4d). In HDAC8, the equivalent helix to pseudo helix H1 in HDAC3 has a regular helical structure, loop L1 is two amino acids shorter and loop L6 contains a proline residue that partly orientates the loop away from the active site (Fig. 4d). We suggest that together these differences give substrate better access to that active site of HDAC8 than would be possible in the uncomplexed HDAC3. The pattern of crystallographic temperature factors for the various structures supports this interpretation (Supplementary Fig. 5).

To test the importance of Arg 265 as well as loops L1 and L6, we co-expressed mutant HDAC3 constructs with SMRT-DAD in mammalian cells. Strikingly, all the designed mutations resulted not only in total loss of deacetylase activity (Fig. 5a) but also abolished interaction with SMRT-DAD (Fig. 5b). These findings support our interpretation of the importance of these residues in the activation of HDAC3.

To support the conclusions that Ins(1,4,5,6)P<sub>4</sub> is essential for HDAC3 activity and to test the specificity for Ins(1,4,5,6)P<sub>4</sub>, we sought to establish an *in vitro* reconstitution assay. We expressed



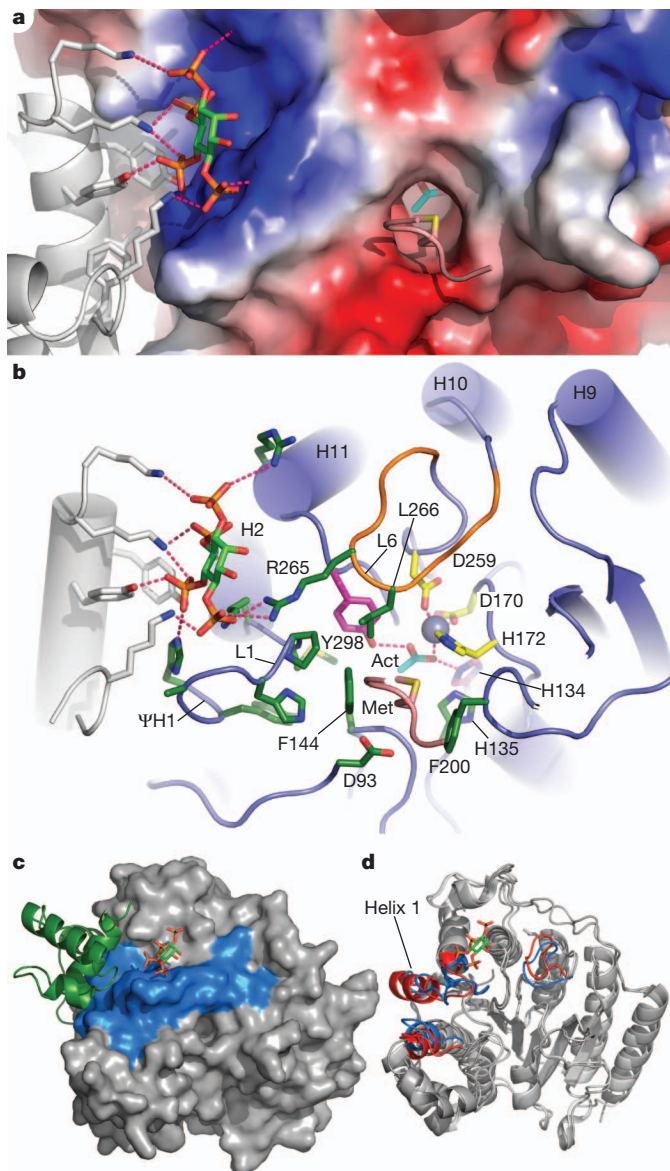


**Figure 4 | Mechanism of activation of HDAC3 by binding SMRT-DAD and Ins(1,4,5,6)P<sub>4</sub>.** **a**, SMRT-DAD (grey cartoon) and Ins(1,4,5,6)P<sub>4</sub> bind adjacent to the HDAC3 (charged surface representation) active site. Acetate and a methionine (lysine mimic) are located in the active site. **b**, Details of the HDAC3 active site. Key residues and loops are labelled—see text for details (hydrogen bonds and/or salt bridges are indicated by dashed lines). ΨH1, pseudo helix H1. **c**, Pseudo helix H1 and loops L1 and L6 are shown in blue on the surface of HDAC3 (grey). These regions are influenced or stabilized by binding of SMRT-DAD (green) and Ins(1,4,5,6)P<sub>4</sub> (shown as sticks). **d**, Comparison of the structures of HDAC3 and HDAC8. Regions of significant difference are coloured blue (HDAC3) and red (HDAC8). Helix 1 is indicated.

and purified HDAC3, Flag-tagged at the carboxy terminus, from mammalian cells and incubated the anti-Flag resin with bacterially expressed SMRT-DAD and various concentrations of Ins(1,4,5,6)P<sub>4</sub>, Ins(1,4,5)P<sub>3</sub> and Ins(1,2,3,4,5,6)P<sub>6</sub> (Fig. 5c). HDAC activity was very sensitive to inositol phosphate concentration and higher concentrations do not support reconstitution. This can be explained through high levels of free inositol phosphate competing with complex formation. This is analogous to moderate monovalent salt concentrations causing complex dissociation during purification (Supplementary Fig. 2).

A similar pattern of activation was seen using both Ins(1,4,5)P<sub>3</sub> and Ins(1,2,3,4,5,6)P<sub>6</sub>, but in both cases a tenfold higher concentration

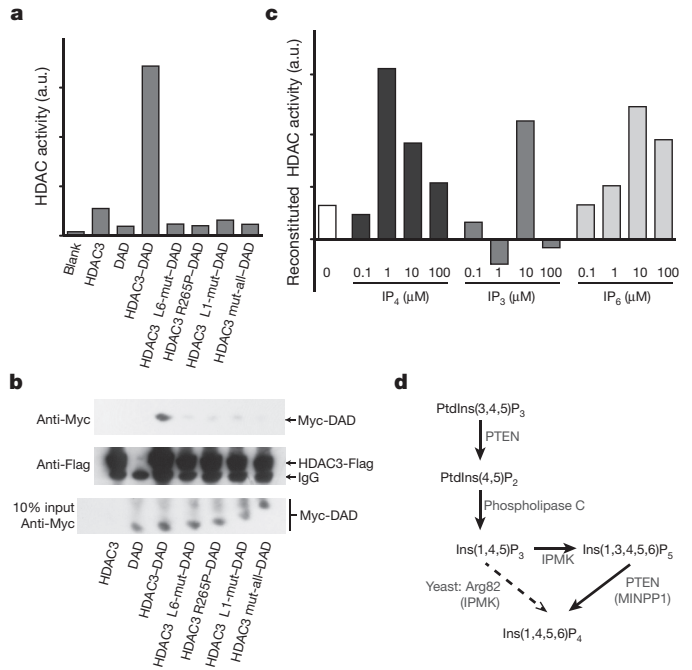


**Figure 5 | Exploring the role of Ins(1,4,5,6)P<sub>4</sub> in complex assembly and HDAC3 activation.** **a**, Effect of HDAC3 mutations on deacetylase activity of complexes with SMRT-DAD. Residues are mutated to their equivalents in HDAC8. Loop 1 mutation (L1-mut) is H17C/G21A/K25I. Loop 6 mutation (L6-mut) is R264P/L265M. 'Mut-all' is H17C/G21A/K25I/R264P/L265M/R301A. **b**, Immunoblots showing that HDAC3 mutations perturb interaction with SMRT-DAD. Recombinant proteins (Myc-DAD, HDAC3-Flag) and the IgG heavy chain are indicated. **c**, Deacetylase assays of HDAC3-Flag reconstituted with bacterially expressed SMRT-DAD in the presence of various inositol phosphates. IP<sub>4</sub>, IP<sub>3</sub> and IP<sub>6</sub> are Ins(1,4,5,6)P<sub>4</sub>, Ins(1,4,5)P<sub>3</sub> and Ins(1,2,3,4,5,6)P<sub>6</sub>, respectively. **d**, Synthesis pathway for Ins(1,4,5,6)P<sub>4</sub> from phosphatidylinositol-(3,4,5)-trisphosphate (PtdIns(3,4,5)P<sub>3</sub>) and phosphatidylinositol-(4,5)-bisphosphate (PtdIns(4,5)P<sub>2</sub>). Yeast Arg 82 converts Ins(1,4,5)P<sub>3</sub> to Ins(1,4,5,6)P<sub>4</sub>. In mammals, both IPMK and PTEN are required to make Ins(1,4,5,6)P<sub>4</sub>.

was required to achieve a similar level of HDAC activity to that seen with Ins(1,4,5,6)P<sub>4</sub>. This supports the interpretation that Ins(1,4,5,6)P<sub>4</sub> is the physiologically relevant assembly partner.

### Does Ins(1,4,5,6)P<sub>4</sub> regulate HDACs?

The finding that Ins(1,4,5,6)P<sub>4</sub> is essential for the assembly of class 1 HDAC repression complexes raises the question as to whether it is a signalling molecule with a role in regulating complex assembly, or if it is simply an essential structural cofactor.

The fact that Ins(1,4,5,6)P<sub>4</sub> remained bound during purification would seem to suggest that it is a structural cofactor. However, to retain an intact complex it was necessary to use low ionic strength buffers. At physiological ionic strengths, the Ins(1,4,5,6)P<sub>4</sub> is likely to dissociate readily and thus could regulate complex assembly.

Importantly, several studies have previously implicated Ins(1,4,5,6)P<sub>4</sub> as a regulator of gene expression and chromatin remodelling—although no molecular mechanism was identified. Yeast Arg 82 is a transcriptional regulator of genes involved in arginine metabolism. It has been shown<sup>36</sup> that Arg 82 is an inositol phosphate kinase that converts Ins(1,4,5)P<sub>3</sub> to Ins(1,4,5,6)P<sub>4</sub> and that kinase activity is required for its role in transcriptional regulation (Fig. 5d). Several further studies have supported the importance of Arg 82 kinase activity in transcriptional regulation and chromatin remodelling<sup>37–39</sup>, together suggesting that Ins(1,4,5,6)P<sub>4</sub> has an important regulatory role in yeast.

IPMK, the mammalian homologue of Arg 82, has been reported to phosphorylate Ins(1,4,5)P<sub>3</sub> to form Ins(1,3,4,5,6)P<sub>4</sub> and then



Ins(1,3,4,5,6)P<sub>5</sub> (refs 40, 41). Consequently, in mammalian cells, a phosphatase is required to generate Ins(1,4,5,6)P<sub>4</sub>. The most likely enzyme is the well-known tumour suppressor gene PTEN<sup>42,43</sup>, which is known to be active in the nucleus and to play a role in chromosome stability (reviewed in ref. 44). It is tempting to speculate that loss of HDAC complex function might be one of the routes through which PTEN mutations contribute to oncogenesis.

A final important question is whether the levels of Ins(1,4,5,6)P<sub>4</sub> are regulated in the cell. This is not easy to establish, as regulation could be temporally and/or spatially compartmentalized. However there is some evidence that both PTEN and InsP<sub>4</sub> levels change with progression through the cell cycle<sup>45</sup>. It is also possible that changing levels of Ins(1,4,5,6)P<sub>4</sub> may contribute to the circadian regulation of HDAC3 activity<sup>46</sup>. Further research will be needed to clarify these important questions.

## Discussion

We present the structure of a histone deacetylase in complex with its activating co-repressor. The structure reveals a striking structural rearrangement of the co-repressor and an unexpected inositol tetraphosphate molecule (Ins(1,4,5,6)P<sub>4</sub>) acting as an 'intermolecular glue', contributing to the stabilization and activation of HDAC3.

Sequence conservation suggests that Ins(1,4,5,6)P<sub>4</sub> plays a key role in co-repressor assembly and activation of class I HDACs from yeast to humans and is likely to act as a regulator of HDAC complex assembly. Although it remains to be established how the availability of Ins(1,4,5,6)P<sub>4</sub> might be controlled, the requirement of Ins(1,4,5,6)P<sub>4</sub> for co-repressor HDAC assembly presents novel opportunities for therapeutic intervention that may complement existing HDAC inhibitors. It may be possible to develop molecules that target the Ins(1,4,5,6)P<sub>4</sub> binding site itself, but it may also be possible to target the enzymes responsible for Ins(1,4,5,6)P<sub>4</sub> synthesis.

## METHODS SUMMARY

HDAC3 and Flag-tagged SMRT-DAD (residues 389–480) were expressed using transient transfection in suspension grown HEK293F cells. The HDAC3–SMRT-DAD complex was purified by Flag affinity chromatography, followed by TEV protease cleavage and size exclusion chromatography. Crystals of the HDAC3–DAD complex were grown by sitting drop vapour diffusion with a 10% propan-2-ol precipitant. The structure was determined by molecular replacement based on HDAC8 (PDB code 3EW8). Ligands, including Ins(1,4,5,6)P<sub>4</sub>, zinc, potassium, acetate and glycerol were added during the refinement process.

**Full Methods** and any associated references are available in the online version of the paper at [www.nature.com/nature](http://www.nature.com/nature).

**Received 5 July; accepted 23 November 2011.**

**Published online 9 January 2012.**

- Pogo, B. G., Allfrey, V. G. & Mirsky, A. E. RNA synthesis and histone acetylation during the course of gene activation in lymphocytes. *Proc. Natl Acad. Sci. USA* **55**, 805–812 (1966).
- Struhl, K. Histone acetylation and transcriptional regulatory mechanisms. *Genes Dev.* **12**, 599–606 (1998).
- Choudhary, C. *et al.* Lysine acetylation targets protein complexes and co-regulates major cellular functions. *Science* **325**, 834–840 (2009).
- Hildmann, C., Rieger, D. & Schwienhorst, A. Histone deacetylases — an important class of cellular regulators with a variety of functions. *Appl. Microbiol. Biotechnol.* **75**, 487–497 (2007).
- Hu, E. *et al.* Cloning and characterization of a novel human class I histone deacetylase that functions as a transcription repressor. *J. Biol. Chem.* **275**, 15254–15264 (2000).
- Lee, H., Rezai-Zadeh, N. & Seto, E. Negative regulation of histone deacetylase 8 activity by cyclic AMP-dependent protein kinase A. *Mol. Cell. Biol.* **24**, 765–773 (2004).
- Zhang, Y. *et al.* Analysis of the NuRD subunits reveals a histone deacetylase core complex and a connection with DNA methylation. *Genes Dev.* **13**, 1924–1935 (1999).
- Li, J. *et al.* Both corepressor proteins SMRT and N-CoR exist in large protein complexes containing HDAC3. *EMBO J.* **19**, 4342–4350 (2000).
- Lechner, T. *et al.* Sds3 (suppressor of defective silencing 3) is an integral component of the yeast Sin3-Rpd3 histone deacetylase complex and is required for histone deacetylase activity. *J. Biol. Chem.* **275**, 40961–40966 (2000).
- Zhang, J., Kalkum, M., Chait, B. T. & Roeder, R. G. The N-CoR-HDAC3 nuclear receptor corepressor complex inhibits the JNK pathway through the integral subunit GPS2. *Mol. Cell* **9**, 611–623 (2002).
- Guenther, M. G., Barak, O. & Lazar, M. A. The SMRT and N-CoR corepressors are activating cofactors for histone deacetylase 3. *Mol. Cell. Biol.* **21**, 6091–6101 (2001).
- Wen, Y. D. *et al.* The histone deacetylase-3 complex contains nuclear receptor corepressors. *Proc. Natl Acad. Sci. USA* **97**, 7202–7207 (2000).
- Métivier, R. *et al.* Estrogen receptor- $\alpha$  directs ordered, cyclical, and combinatorial recruitment of cofactors on a natural target promoter. *Cell* **115**, 751–763 (2003).
- Hoberg, J. E., Yeung, F. & Mayo, M. W. SMRT derepression by the I $\kappa$ B kinase  $\alpha$ : a prerequisite to NF- $\kappa$ B transcription and survival. *Mol. Cell. Biol.* **16**, 245–255 (2004).
- Billin, A. N., Thirlwell, H. & Ayer, D. E.  $\beta$ -catenin-histone deacetylase interactions regulate the transition of LEF1 from a transcriptional repressor to an activator. *Mol. Cell. Biol.* **20**, 6882–6890 (2000).
- Guan, H.-P., Ishizuka, T., Chui, P. C., Lehrke, M. & Lazar, M. A. Corepressors selectively control the transcriptional activity of PPAR $\gamma$  in adipocytes. *Genes Dev.* **19**, 453–461 (2005).
- Marks, P. A. & Breslow, R. Dimethyl sulfoxide to vorinostat: development of this histone deacetylase inhibitor as an anticancer drug. *Nature Biotechnol.* **25**, 84–90 (2007).
- Wagner, J. M., Hackanson, B., Lübbert, M. & Jung, M. Histone deacetylase (HDAC) inhibitors in recent clinical trials for cancer therapy. *Clin. Epigenet.* **1**, 117–136 (2010).
- Zhang, Y., LeRoy, G., Seelig, H. P., Lane, W. S. & Reinberg, D. The dermatomyositis-specific autoantigen Mi2 is a component of a complex containing histone deacetylase and nucleosome remodeling activities. *Cell* **95**, 279–289 (1998).
- Hakimi, M.-A. *et al.* A core-BRAF35 complex containing histone deacetylase mediates repression of neuronal-specific genes. *Proc. Natl Acad. Sci. USA* **99**, 7420–7425 (2002).
- Humphrey, G. W. *et al.* Stable histone deacetylase complexes distinguished by the presence of SANT domain proteins CoREST/kiaa0071 and Mta-L1. *J. Biol. Chem.* **276**, 6817–6824 (2001).
- Laherty, C. D. *et al.* Histone deacetylases associated with the mSin3 corepressor mediate mad transcriptional repression. *Cell* **89**, 349–356 (1997).
- Heinzel, T. *et al.* A complex containing N-CoR, mSin3 and histone deacetylase mediates transcriptional repression. *Nature* **387**, 43–48 (1997).
- Guenther, M. G. *et al.* A core SMRT corepressor complex containing HDAC3 and TBL1, a WD40-repeat protein linked to deafness. *Genes Dev.* **14**, 1048–1057 (2000).
- Yoon, H.-G. *et al.* Purification and functional characterization of the human N-CoR complex: the roles of HDAC3, TBL1 and TBLR1. *EMBO J.* **22**, 1336–1346 (2003).
- Oberoi, J. *et al.* Structural basis for the assembly of the SMRT/NCoR core transcriptional repression machinery. *Nature Struct. Mol. Biol.* **18**, 177–184 (2011).
- You, S.-H., Liao, X., Weiss, R. E. & Lazar, M. A. The interaction between nuclear receptor corepressor and histone deacetylase 3 regulates both positive and negative thyroid hormone action *in vivo*. *Mol. Endocrinol.* **24**, 1359–1367 (2010).
- Ishizuka, T. & Lazar, M. A. The nuclear receptor corepressor deacetylase activating domain is essential for repression by thyroid hormone receptor. *Mol. Endocrinol.* **19**, 1443–1451 (2005).
- Yin, L. *et al.* Rev-erb $\alpha$ , a heme sensor that coordinates metabolic and circadian pathways. *Science* **318**, 1786–1789 (2007).
- Guenther, M. G. Assembly of the SMRT-histone deacetylase 3 repression complex requires the TCP-1 ring complex. *Genes Dev.* **16**, 3130–3135 (2002).
- Codina, A. *et al.* Structural insights into the interaction and activation of histone deacetylase 3 by nuclear receptor corepressors. *Proc. Natl Acad. Sci. USA* **102**, 6009–6014 (2005).
- Yang, W.-M., Tsai, S.-C., Wen, Y.-D., Fejer, G. & Seto, E. Functional domains of histone deacetylase-3. *J. Biol. Chem.* **277**, 9447–9454 (2002).
- Dowling, D. P., Gantt, S. L., Gattis, S. G., Fierke, C. A. & Christianson, D. W. Structural studies of human histone deacetylase 8 and its site-specific variants complexed with substrate and inhibitors. *Biochemistry* **47**, 13554–13563 (2008).
- Somoza, J. R. *et al.* Structural snapshots of human HDAC8 provide insights into the class I histone deacetylases. *Structure* **12**, 1325–1334 (2004).
- Bressi, J. C. *et al.* Exploration of the HDAC2 foot pocket: synthesis and SAR of substituted N-(2-aminophenyl)benzamides. *Bioorg. Med. Chem. Lett.* **20**, 3142–3145 (2010).
- Odom, A. R. A role for nuclear inositol 1,4,5-trisphosphate kinase in transcriptional control. *Science* **287**, 2026–2029 (2000).
- Steger, D. J. Regulation of chromatin remodeling by inositol polyphosphates. *Science* **299**, 114–116 (2003).
- El Alami, M., Messenguy, F., Scherens, B. & Dubois, E. Arg82p is a bifunctional protein whose inositol polyphosphate kinase activity is essential for nitrogen and PHO gene expression but not for Mcm1p chaperoning in yeast. *Mol. Microbiol.* **49**, 457–468 (2003).
- Shen, X., Xiao, H., Ranallo, R., Wu, W.-H. & Wu, C. Modulation of ATP-dependent chromatin-remodeling complexes by inositol polyphosphates. *Science* **299**, 112–114 (2003).
- Saiardi, A. *et al.* Mammalian inositol polyphosphate multikinase synthesizes inositol 1,4,5-trisphosphate and an inositol pyrophosphate. *Proc. Natl Acad. Sci. USA* **98**, 2306–2311 (2001).

41. Nalaskowski, M. M., Deschermeier, C., Fanick, W. & Mayr, G. W. The human homologue of yeast ArgRll protein is an inositol phosphate multikinase with predominantly nuclear localization. *Biochem. J.* **366**, 549–556 (2002).
42. Craxton, A., Caffrey, J. J., Burkhart, W., Safrany, S. T. & Shears, S. B. Molecular cloning and expression of a rat hepatic multiple inositol polyphosphate phosphatase. *Biochem. J.* **328**, 75–81 (1997).
43. Caffrey, J. J., Darden, T., Wenk, M. R. & Shears, S. B. Expanding coincident signaling by PTEN through its inositol 1,3,4,5,6-pentakisphosphate 3-phosphatase activity. *FEBS Lett.* **499**, 6–10 (2001).
44. Di Cristofano, A. & Pandolfi, P. P. The multiple roles of PTEN in tumor suppression. *Cell* **100**, 387–390 (2000).
45. Mattingly, R. R., Stephens, L. R., Irvine, R. F. & Garrison, J. C. Effects of transformation with the v-src oncogene on inositol phosphate metabolism in rat-1 fibroblasts. D-myo-inositol 1,4,5,6-tetrakisphosphate is increased in v-src-transformed rat-1 fibroblasts and can be synthesized from D-myo-inositol 1,3,4-trisphosphate in cytosolic extracts. *J. Biol. Chem.* **266**, 15144–15153 (1991).
46. Feng, D. *et al.* A circadian rhythm orchestrated by histone deacetylase 3 controls hepatic lipid metabolism. *Science* **331**, 1315–1319 (2011).

**Supplementary Information** is linked to the online version of the paper at [www.nature.com/nature](http://www.nature.com/nature).

**Acknowledgements** We thank R. Owen and the other beamline staff at DIAMOND I24 for help with data collection; J. Goodchild for help with biochemical experiments; and S. Cowley, M. Lazar, P. Moody, L. Nagy, P. Tontoz and S. Shears for literature and discussions. This work was supported by the Wellcome Trust (grant WT085408).

**Author Contributions** P.J.W. expressed, purified and crystallized the protein and performed the biochemical studies. P.J.W., L.F. and J.W.R.S. performed the structural determination and wrote the paper. G.M.S. and L.F. performed early expression/purification trials in insect cells. J.W.R.S. conceived the study.

**Author Information** Atomic coordinates and structure factors are deposited in the Protein Data Bank under accession number 4A69. Reprints and permissions information is available at [www.nature.com/reprints](http://www.nature.com/reprints). The authors declare no competing financial interests. Readers are welcome to comment on the online version of this article at [www.nature.com/nature](http://www.nature.com/nature). Correspondence and requests for materials should be addressed to J.W.R.S. ([john.schwabe@le.ac.uk](mailto:john.schwabe@le.ac.uk)).

## METHODS

**Protein expression, purification and crystallization.** The DAD domain (SMRT 389–480) and full length HDAC3 were cloned into pcDNA3 vector. The DAD domain construct contained an N-terminal 10×His-3×Flag tag and a TEV protease cleavage site. HEK293F cells (Invitrogen) were co-transfected with both constructs using polyethylenimine (PEI) (Sigma). To transfect cells, 0.25 mg DNA total was diluted in 25 ml of PBS (Sigma) and vortexed briefly; 1 ml of 0.5 mg ml<sup>-1</sup> PEI was added, and the suspension was vortexed briefly, incubated for 20 min at room temperature, then added to the cells. (Final density was 1 × 10<sup>6</sup> cells per ml in a volume of 250 ml.) For larger volumes, multiple flasks were used. Cells were harvested 48 h after transfection and lysed by sonication in buffer containing 50 mM Tris pH 7.5, 100 mM potassium acetate, 5% v/v glycerol, 0.3% v/v Triton X-100, and Roche complete protease inhibitor (buffer A); the insoluble material was removed by centrifugation. The lysate was pre-cleared using Sepharose 4B (Sigma) and the complex was then bound to Flag resin (Sigma), washed three times with buffer A, three times with buffer B (50 mM Tris pH 7.5, 300 mM potassium acetate, 5% v/v glycerol) and three times with buffer C (50 mM Tris pH 7.5, 50 mM potassium acetate, 5% v/v glycerol, 0.5 mM TCEP). The complex was eluted from the resin by overnight cleavage at 4 °C with TEV protease in buffer C. The eluted protein was further purified by gel filtration on a Superdex S200 column (GE Healthcare) in buffer containing 25 mM Tris/HCl pH 7.5, 50 mM potassium acetate, 0.5 mM TCEP. The purified complex was concentrated to 7.5 mg ml<sup>-1</sup> for crystallization trials.

Crystals were grown by sitting drop vapour diffusion at 4 °C using 0.1 M HEPES pH 7.5, 0.2 M NaCl and 10% v/v propan-2-ol. Crystals were cubic in nature, grew to a final dimension of 15 × 15 × 15 µm and belong to space group C222<sub>1</sub>.

Comparison of a fresh protein sample with protein from within the crystallization drops (after 3 months) by SDS–PAGE showed the presence of a truncated form of HDAC3 (Supplementary Fig. 2). Analysis by liquid chromatography–tandem mass spectrometry showed that this HDAC3 was truncated at the C terminus to residue Q376.

**Structure determination.** Crystals were flash-frozen in mother liquor containing 40% glycerol as a cryoprotectant. Diffraction data were collected on a single crystal in two 45° wedges at the Diamond synchrotron microfocus beamline I24 and processed using XDS<sup>47</sup>. The structure was solved by molecular replacement using HDAC8 (PDB code 3EW8)<sup>33</sup> as a search model in Phaser<sup>48</sup>. Initial model building was performed with ARP/wARP (<http://www.embl-hamburg.de/>

ARP/), which was able to automatically build 95% of the HDAC3 protein chain, and two helices from the DAD. The additional HDAC3 and DAD sequences were fitted following multiple rounds of refinement and building using REFMAC and Coot<sup>49,50</sup>.  $F_o - F_c$  density consistent with the ligand, zinc/potassium ions and acetate/glycerol molecules observed during the refinement/model building process were fitted and refined as they became apparent. The final model contains amino acids 2–370 from chain A and 2–370 from chain B of HDAC3, and amino acids 408–476 from chain C and 408–475 from chain D of the DAD. The model also contains two Ins(1,4,5,6)P<sub>4</sub> molecules, two zinc ions, four potassium ions, two acetate molecules and four glycerol molecules. The final model has 97.8% residues in the favoured region, 2.0% in the allowed region and 0.2% in the outlier region of the Ramachandran plot.

**HDAC activity assays.** C-terminally Flag-tagged HDAC3 and Myc-tagged DAD were co-expressed in HEK 293 cells as described above. Cells were lysed in 50 mM Tris pH 7.5, 50 mM potassium acetate, 5% v/v glycerol, 0.3% v/v Triton X-100 and Roche complete protease inhibitor. In order to standardise the assay, 800 µg total protein was bound to 40 µl Flag resin (Sigma) for 2 h at 4 °C, then washed four times with lysis buffer. HDAC activity was measured using the HDAC Assay Kit (Active Motif) and read using a Victor X5 plate reader (Perkin Elmer).

**Reconstitution assays.** C-terminally Flag-tagged HDAC3 was expressed in HEK 293 cells and purified as described above. His<sub>6</sub>-tagged SMRT-DAD was expressed in *Escherichia coli* strain Rosetta (Novagen) and initial purification was carried out using Nickel NTA agarose (Qiagen) followed by gel filtration chromatography using a Superdex-S200 26/60 column (GE Healthcare) in buffer containing 50 mM Tris/HCl pH 7.5 and 50 mM potassium acetate. 40 µl of HDAC3-Flag resin was mixed with His-DAD, with or without phosphoinositide as required, in a final volume of 1 ml of buffer D (50 mM Tris/HCl pH 7.5, 50 mM potassium acetate, 5% glycerol, 0.3% v/v Triton X-100), and incubated for 2 h at 30 °C. The resin was then washed extensively with buffer D, and HDAC activity was measured using the HDAC Assay Kit (Active Motif) and read on a Victor X5 plate reader (Perkin Elmer).

47. Kabsch, W. XDS. *Acta Crystallogr. D* **66**, 125–132 (2010).

48. McCoy, A. J. *et al.* Phaser crystallographic software. *J. Appl. Crystallogr.* **40**, 658–674 (2007).

49. Collaborative Computational Project, Number 4. The CCP4 suite: programs for protein crystallography. *Acta Crystallogr. D* **50**, 760–763 (1994).

50. Emsley, P., Lohkamp, B., Scott, W. G. & Cowtan, K. Features and development of Coot. *Acta Crystallogr. D* **66**, 486–501 (2010).



# Differential oestrogen receptor binding is associated with clinical outcome in breast cancer

Caryn S. Ross-Innes<sup>1</sup>, Rory Stark<sup>1</sup>, Andrew E. Teschendorff<sup>2</sup>, Kelly A. Holmes<sup>1</sup>, H. Raza Ali<sup>1,8</sup>, Mark J. Dunning<sup>1</sup>, Gordon D. Brown<sup>1</sup>, Ondrej Gojis<sup>3,4,5</sup>, Ian O. Ellis<sup>6</sup>, Andrew R. Green<sup>6</sup>, Simak Ali<sup>3</sup>, Suet-Feung Chin<sup>1</sup>, Carlo Palmieri<sup>3</sup>, Carlos Caldas<sup>1,7,8,9</sup> & Jason S. Carroll<sup>1,7</sup>

Oestrogen receptor- $\alpha$  (ER) is the defining and driving transcription factor in the majority of breast cancers and its target genes dictate cell growth and endocrine response, yet genomic understanding of ER function has been restricted to model systems<sup>1–3</sup>. Here we map genome-wide ER-binding events, by chromatin immunoprecipitation followed by high-throughput sequencing (ChIP-seq), in primary breast cancers from patients with different clinical outcomes and in distant ER-positive metastases. We find that drug-resistant cancers still recruit ER to the chromatin, but that ER binding is a dynamic process, with the acquisition of unique ER-binding regions in tumours from patients that are likely to relapse. The acquired ER regulatory regions associated with poor clinical outcome observed in primary tumours reveal gene signatures that predict clinical outcome in ER-positive disease exclusively. We find that the differential ER-binding programme observed in tumours from patients with poor outcome is not due to the selection of a rare subpopulation of cells, but is due to the FOXA1-mediated reprogramming of ER binding on a rapid timescale. The parallel redistribution of ER and FOXA1 binding events in drug-resistant cellular contexts is supported by histological co-expression of ER and FOXA1 in metastatic samples. By establishing transcription-factor mapping in primary tumour material, we show that there is plasticity in ER-binding capacity, with distinct combinations of *cis*-regulatory elements linked with the different clinical outcomes.

Recent technological advances have allowed mapping of ER-binding events, with the goal of discovering the *cis*-regulatory elements and factors involved in mediating ER binding and transcription. Several genome-wide maps of ER in breast cancer cell-line models exist<sup>1–3</sup>, all showing that most ER-binding events occur at distal *cis*-regulatory elements. Forkhead motifs are enriched within the regions bound by ER binding and multiple studies have identified the forkhead protein FOXA1 as an important pioneer factor for ER–chromatin interactions<sup>4–6</sup>. However, the ER mapping studies have been restricted to breast cancer cell lines, mostly the MCF-7 cell line. We sought to interrogate ER-binding events, for the first time, in primary frozen breast cancer samples, to determine if ER binding is dynamic and if specific *cis*-regulatory elements can distinguish tumours from patients with distinct clinical outcomes.

ER ChIP-seq was performed in eight ER<sup>+</sup>, progesterone receptor (PR)<sup>+</sup>, HER2<sup>−</sup> primary breast tumours, representative of tumours from patients with better prognosis<sup>7</sup>, a conclusion supported by the available long-term clinical follow-up (Supplementary Fig. 1). Also included were seven primary breast tumours from patients with a poor outcome (ER<sup>+</sup> PR<sup>−</sup> HER2<sup>−</sup> or ER<sup>+</sup> PR<sup>+</sup> HER<sup>+</sup>), because PR<sup>−</sup> or HER2<sup>+</sup> tumours are more likely to be aggressive<sup>8,9</sup>. As expected, the poor outcome patients who had long-term clinical follow-up died of

breast cancer (Supplementary Fig. 1). Furthermore, three ER<sup>+</sup> distant metastatic samples from women with breast cancer were included. The metastatic locations and sample preparation can be found in Supplementary Fig. 1. As a control, we included two breast cancer samples that were ER<sup>−</sup> (ER- $\alpha$  negative), but expressed high transcript levels of ER- $\beta$ .

ER ChIP-seq was conducted and ER-binding peaks were called using two different algorithms, MACS<sup>10</sup> and SWEMBL (<http://www.ebi.ac.uk/~swilder/SWEMBL/>), to minimize peak caller bias. The number of sequencing reads and ER-binding events for each tumour is shown in Supplementary Fig. 2. ER binding could be mapped in all tumours, but total peak intensity and the number of identified binding events differed. Three tumours were split into two sections and ER ChIP-seq was conducted on the separate sections. We found very good concordance when comparing different sections of the same tumour ( $R^2 = 0.954$ ) suggesting that tumour heterogeneity did not substantially influence the ER-binding signal obtained from a sample (Supplementary Fig. 3).

We initially assessed whether a conserved set of breast cancer ER-binding events could be identified. We found a core set of 484 ER-binding events that were identified in at least 75% of all the tumours, but not in either of the ER<sup>−</sup> tumours (Fig. 1a). Peak calling details can be found in Supplementary Fig. 4. An example of a core ER-binding event is shown in Fig. 1b. This demonstrates that ER binding to chromatin still occurs even in tumours that are unlikely to respond to anti-oestrogen therapies, implying that drug resistance is not due to loss of ER binding to DNA. The average ER-binding signal intensity was highest in the metastatic samples and lowest in patients with good outcome tumours, a phenomenon observed both within the 484 core ER-binding regions (Fig. 1c) and globally (Supplementary Fig. 4). These data indicate that there is an acquisition of binding signal intensity in tumours that progress towards a poorer prognosis and ultimately metastasize. The only DNA motif found to be enriched in the core ER-binding events was an oestrogen responsive element (ERE) (Fig. 1d). The genes near (within 20 kilobases (kb): an optimal window between ER-binding events and target genes<sup>11</sup>) the 484 core ER-binding events exhibited elevated expression in the ER<sup>+</sup> tumours used for ChIP-seq, as compared to all other genes (data not shown) and were higher in ER<sup>+</sup> tumours relative to ER<sup>−</sup> tumours in nine independent data sets (Supplementary Fig. 5). The genes are provided in Supplementary Fig. 6 and include classic ER target genes such as *TFF1*, *GREB1* and *RARA*. A gene predictor was generated based on genes near the core ER-binding events. Patients were stratified and the tumours with the highest 'risk index' had a poor clinical outcome when compared to the tumours with the lowest 'risk index' (Fig. 1e shows the results based on one study<sup>12</sup> and additional data sets are shown in Supplementary Fig. 6; only ER<sup>+</sup> patients were considered). These conserved *cis*-regulatory elements

<sup>1</sup>Cancer Research UK, Cambridge Research Institute, Li Ka Shing Centre, Robinson Way, Cambridge CB2 0RE, UK. <sup>2</sup>UCL Cancer Institute, University College London, 72 Huntley Street, London WC1E 6BT, UK. <sup>3</sup>Imperial College London, Hammersmith Campus, London W12 0NN, UK. <sup>4</sup>Department of Gynaecology and Obstetrics, Third Faculty of Medicine, Charles University, Ruska 87, Prague 10, 100 00, Czech Republic. <sup>5</sup>Department of Pathology, Third Faculty of Medicine, Charles University, Ruska 87, Prague 10, 100 00, Czech Republic. <sup>6</sup>Department of Histopathology, Nottingham University Hospitals NHS Trust, Nottingham City Hospital, Nottingham NG5 1PB, UK. <sup>7</sup>Department of Oncology, University of Cambridge CB2 0XZ, UK. <sup>8</sup>Cambridge Breast Unit, Addenbrooke's Hospital, Cambridge University Hospital NHS Foundation Trust and NIHR Cambridge Biomedical Research Centre, Cambridge CB2 2QQ, UK. <sup>9</sup>Cambridge Experimental Cancer Medicine Centre (ECMC), Cambridge CB2 0RE, UK.

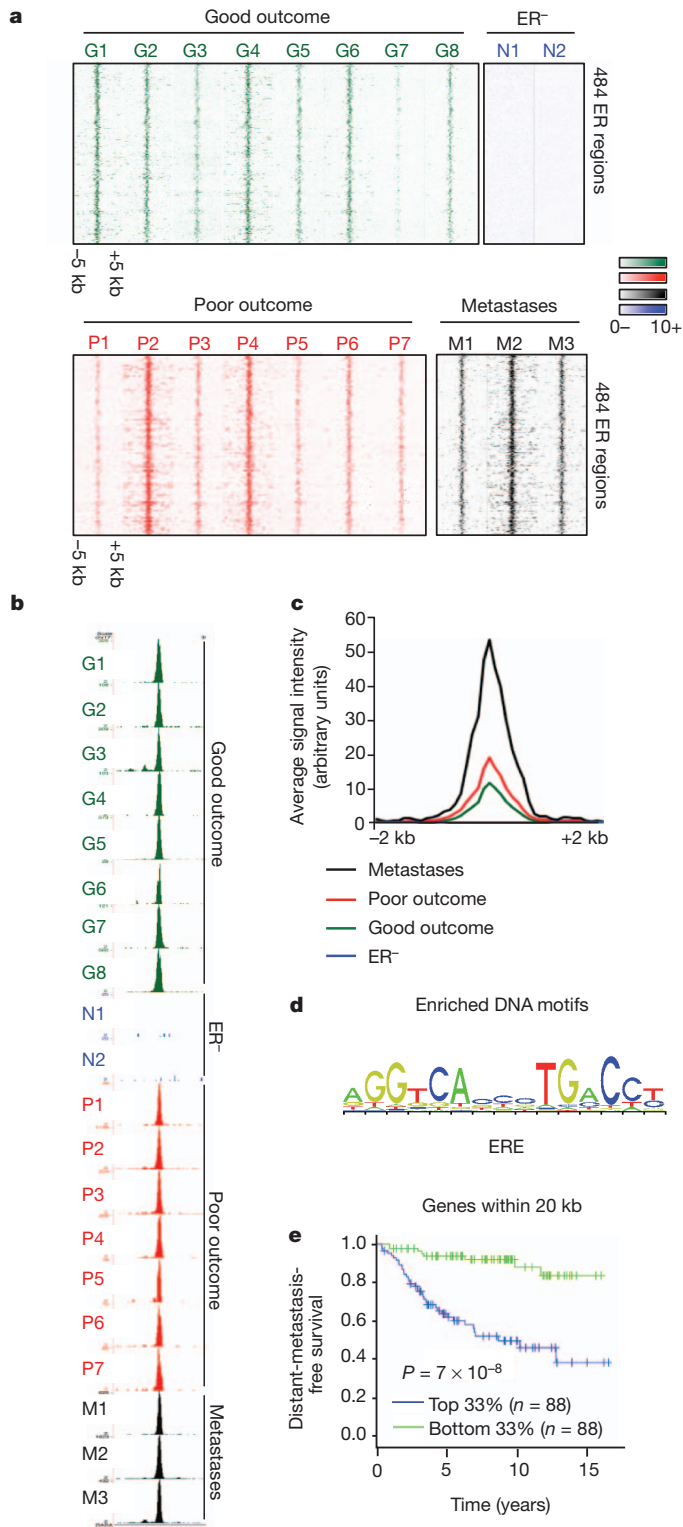


**Figure 1 | A subset of ER-binding events is conserved in primary breast tumours and distant metastases.** **a**, Heat map showing binding peak intensity of 484 core ER-binding events that are common to primary breast tumours and distant metastases. The window represents  $\pm 5$  kb regions from the centre of the binding events. **b**, Example of an ER-binding event at the *RARA* locus, which is present in all primary ER<sup>+</sup> breast tumours and metastases, but not the ER<sup>-</sup> tumours. **c**, Normalized average signal intensity of all core ER-binding events. Also included are the ER<sup>-</sup> tumours. **d**, Motif analysis revealed the enrichment of EREs. **e**, Genes within 20 kb of the core ER-binding events were used to generate a gene predictor that was tested in independent data sets for predictive value. Tumours were stratified according to expression of this gene signature and the top one third and bottom one third of tumours were compared. Results from one data set are shown<sup>12</sup> and additional data sets are provided in Supplementary Fig. 6.

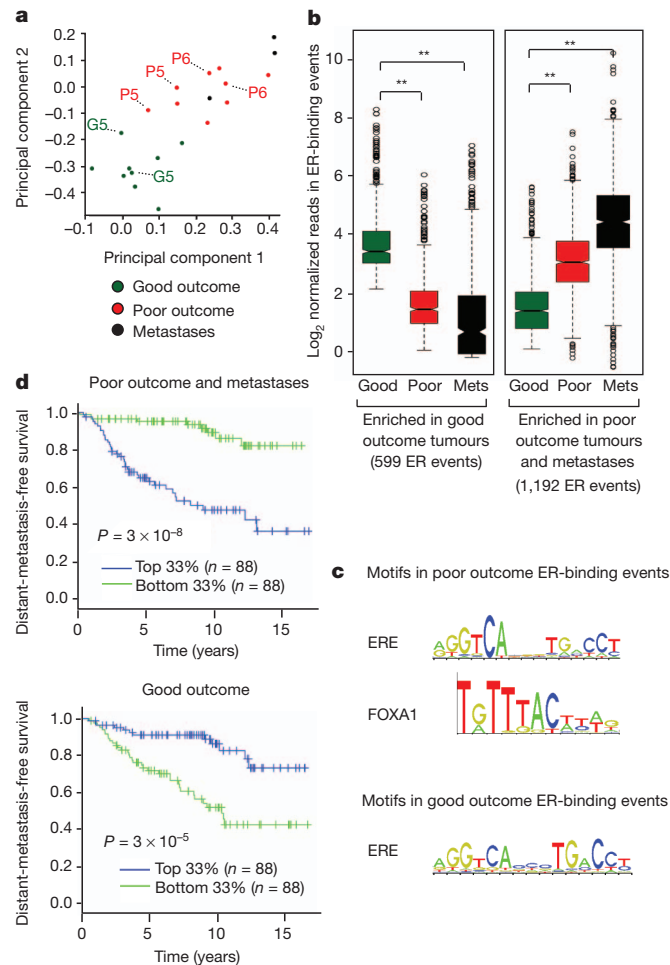


**Figure 2 | ER-binding profiles can discriminate between tumours from patients with different clinical outcomes.** **a**, Principal component analysis (44% of total variance) of the 1,791 ER-binding events that can discriminate between the patients with good outcome tumours and those with poor/met tumours. Included are the replicates from three tumours, which are highlighted. **b**, Box plot representing distribution of normalized read counts in differential ER-binding events that are statistically enriched in either the patients with good outcome tumours (599 ER-binding events) or the patients with poor outcome tumours and metastases (Mets) (1,192 ER-binding events). The samples were pre-normalized.  $**P < 1 \times 10^{-10}$ .  $P$  values were calculated using the Wilcoxon rank sum test. **c**, Enriched motifs in the poor/met and the good outcome ER-binding events. **d**, Genes within 20 kb of the differentially bound ER-binding events were used to generate a gene predictor. Tumours were stratified according to expression of this gene signature and the top one third and bottom one third of tumours were compared. Results from one data set are shown<sup>12</sup> and additional data sets are provided in Supplementary Fig. 12.

and their putative target genes may be the elements that contribute to tumorigenesis and are maintained regardless of the clinical outcome of the breast cancer patient. In contrast to the primary breast cancers and metastases, we mapped ER binding in three normal human mammary glands and two normal human liver samples and found limited numbers of ER-binding events, with almost no concordance in ER binding between individuals (data not shown).

We sought to determine if differential ER-binding events could discriminate the patients with good outcome (ER<sup>+</sup> PR<sup>+</sup> HER2<sup>-</sup> tumours), from patients with poor outcome or metastases (we described the combined set as poor/met tumours). After normalization of the data to account for global differences in ER binding, differential binding analysis (DBA) was used to identify ER-binding events that were statistically enriched in one category or the other. This resulted in a set of ER-binding events that could discriminate between the two groups when using principal component analysis

(Fig. 2a). In total, DBA revealed 1,192 genomic regions that had significantly more ER binding in the poor/met group compared to the good outcome patients (Fig. 2b), and 599 ER binding regions with more ER binding in the good outcome patients when compared to the poor/met patients (Fig. 2b). The clustering of the tumours on the basis of the 1,791 differential ER-binding events can be visualized in Supplementary Fig. 7. These findings suggest that there are specific and re-occurring *cis*-regulatory elements that are occupied by ER in breast cancers, but that these are different in tumours that respond to treatment versus those that relapse and metastasize. Analysis of enriched DNA motifs identified the presence of ERE and FOXA1 motifs in the differential poor outcome ER-binding events and ERE motifs in the good outcome ER-binding events (Fig. 2c). Correlation of the poor outcome ER-binding events with known processes revealed an association with endocrine resistance and luminal B status (Supplementary Fig. 8).

To investigate if the genes near the differential ER-binding events were potentially functional in breast cancer, we analysed genes within a 20 kb window around the 1,192 poor/met and 599 good outcome ER-binding events. Using a training set, we generated a gene expression predictor for each of the good and poor outcome gene lists. The probability calculation and comparisons between the good and poor outcome genes is shown in Supplementary Figs 9 and 10. Within the poor outcome gene list was the oncogene *ERBB2* (all genes are shown in Supplementary Fig. 11). As expected, genes in the poor outcome predictor were preferentially upregulated in poor outcome patients, whereas those in the good outcome predictor were preferentially downregulated (Supplementary Fig. 10). We next tested the predictors in an independent large cohort of breast cancer patients<sup>12</sup>, only considering ER<sup>+</sup> tumours. Using distant-metastasis-free survival as an endpoint, both gene sets predicted outcome ( $P = 3 \times 10^{-5}$  for good and  $3 \times 10^{-8}$  for poor outcome genes) in this data set<sup>12</sup> and with the expected opposite directionality (Fig. 2d). The gene predictors were associated with survival in additional data sets (Supplementary Fig. 12) and were largely independent of histopathological factors (Supplementary Fig. 13). We tested 1,000 randomizations from the entire list of genes and determined that the probability that a random set of genes would yield an equally robust predictor of clinical outcome was  $P = 0.004$ . Furthermore, the good and poor gene predictors had no predictive power in four cohorts of ER<sup>+</sup> patients (Supplementary Fig. 14). This suggests that the increased ER binding at distinct *cis*-regulatory elements is functionally and biologically relevant, resulting in altered gene expression profiles that contribute to differences in drug response and overall survival.

To validate the findings made in the tumours, we explored the possibility that ER-binding events were acquired in cell-line models of endocrine resistance. ER binding was mapped by ChIP-seq in three commonly used tamoxifen-responsive, ER<sup>+</sup> breast cancer cell lines (MCF-7, T-47D and ZR75-1), and two tamoxifen-resistant, ER<sup>+</sup> breast cancer cell lines, namely a tamoxifen-resistant MCF-7 derivative (TAM-R)<sup>13</sup> and BT-474 cells that are ER<sup>+</sup> and contain the *ERBB2* amplification (ER<sup>+</sup> HER2<sup>+</sup>). Similar to BT474 cells, TAM-R cells have increased *ERBB2* protein levels<sup>13</sup> and both represent cellular systems in which increased growth factor signalling results in endocrine resistance. For all five cell lines, ER ChIP-seq was performed in at least duplicate, in asynchronous cells to recapitulate the situation observed in primary tumours (Supplementary Fig. 2).

Almost 7,000 (6,920) ER-binding events were identified in all replicates of all cell lines (Fig. 3a and Supplementary Fig. 15). Almost all (98.9%) of the core ER-binding events that occurred in most primary tumours (Fig. 1a) overlapped with the cell-line core ER-binding events. DBA identified 8,188 ER-binding events with significantly stronger binding affinity in the tamoxifen-resistant cell lines, and 5,713 ER-binding events that were stronger in the tamoxifen-responsive cell lines (Fig. 3a). Examples of differentially bound regions are shown in Fig. 3b. Using the differential ER-binding events, the cell-line classification can be visualized by principal component analysis

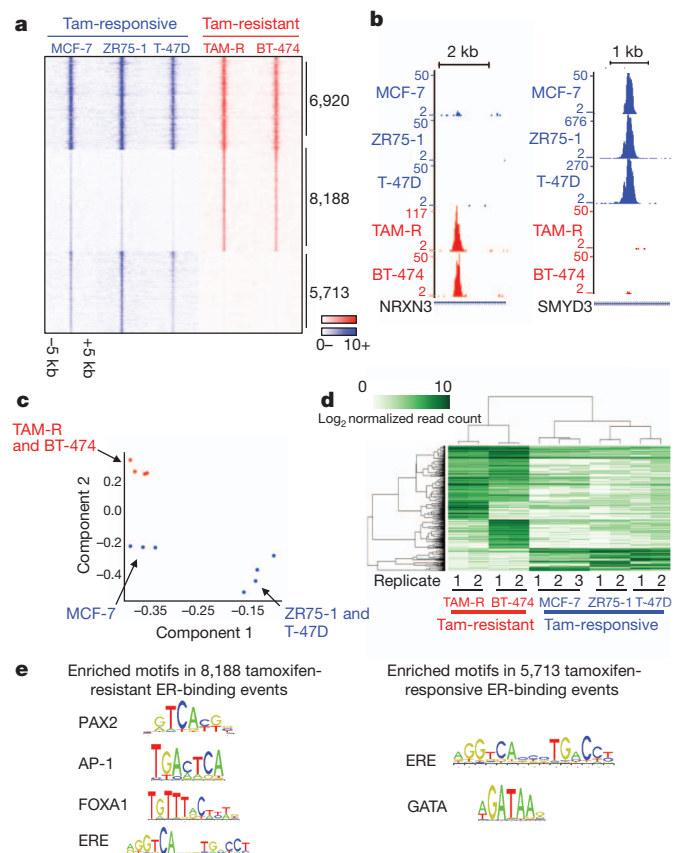


**Figure 3 | Identification of a tamoxifen-resistant ER-binding profile.**

**a**, Heat map representing ER-binding events found in all tamoxifen (Tam)-responsive and tamoxifen-resistant cell lines, or those enriched in either responsive or resistant cell lines. The window represents  $\pm 5$  kb regions from the centre of the binding events. Numbers indicate the total number of ER-binding events in each category. **b**, Examples of ER-binding events that are unique to either tamoxifen-responsive or tamoxifen-resistant cell lines. **c**, Principal component analysis (65% of total variance) of differential ER-binding events observed in responsive (blue) or resistant (red) breast cancer cells. **d**, Hierarchical clustering of the top 1,500 differentially bound ER-binding events (FDR < 0.006). **e**, Enriched motifs within the ER-binding events that discriminate between tamoxifen-sensitive and resistant cell lines.

(Fig. 3c) and hierarchical clustering (Fig. 3d). Enriched motif analysis revealed ERE and FOXA1 motifs in regions showing increased ER binding in tamoxifen-resistant cell lines (Fig. 3e), which are the same motifs observed in the poor outcome ER-binding events in primary tumours (Fig. 2c). GATA motifs were enriched in ER-binding events depleted during acquisition of drug resistance (Fig. 3e), possibly due to competition between FOXA1 and GATA3, another prominent breast cancer transcription factor.

We hypothesized that the ER-binding events induced in the tamoxifen-resistant breast cancer cell lines would be the same regions that were enriched in the poor/met clinical samples. However, 79.8% of the 1,192 ER binding events enriched in the poor/met samples (from Fig. 2b) overlap with ER-binding events in wild-type MCF-7 cells, suggesting that the cell-line models are closer to the tumours and metastases from poor outcome patients. In support of this, the 599 good outcome ER-binding events observed in primary tumours (Fig. 2b) overlap poorly with the ER binding observed in MCF-7 cells (30.2% versus 79.8% for the poor outcome). Interestingly, MCF-7 cells (plus T-47D and ZR75-1 cells) were derived from the pleural effusion of metastatic breast cancer patients, but were established before tamoxifen use in the clinic. We propose that MCF-7, ZR75-1 and T-47D cell lines possess an intermediate ER-binding profile with the acquisition of additional ER-binding regions required for resistance to anti-oestrogen treatment.



The differences in ER binding between responsive and resistant contexts may be due to selection and expansion of a resistant sub-population, or may be due to reprogramming of ER binding following specific stimuli. Growth factor pathways have long been implicated in modulating endocrine response<sup>14,15</sup> and have been shown to influence ER-binding potential and gene expression profiles<sup>14</sup>. We identified various stimuli (EGF, IL-6, TNF- $\alpha$  and IGF-I) shown to induce increased cellular invasion and drug resistance and treated asynchronous MCF-7 cells with control or the cocktail of mitogens for 90 min (Fig. 4a). Duplicate ER ChIP-seq replicates were performed (Supplementary Fig. 2).

Differential binding analysis identified 6,089 ER-binding regions that were differentially enriched ( $\geq 4$  fold change difference, false discovery rate (FDR)  $< 0.1$ ) following a 90 min treatment with the cocktail. These mitogen-induced ER-binding differences could be visualized using principal component analysis (Fig. 4b). Because FOXA1 is a pioneer factor required for ER–chromatin interactions<sup>4</sup> and FOXA1 motifs were enriched in both the mitogen-induced ER-binding events (Supplementary Fig. 16) and the tumours from the poor outcome patients (Fig. 2c), we assessed whether the rapid, reprogrammed ER binding occurred at regions pre-determined by FOXA1. We repeated the mitogen treatment, but mapped FOXA1 binding by

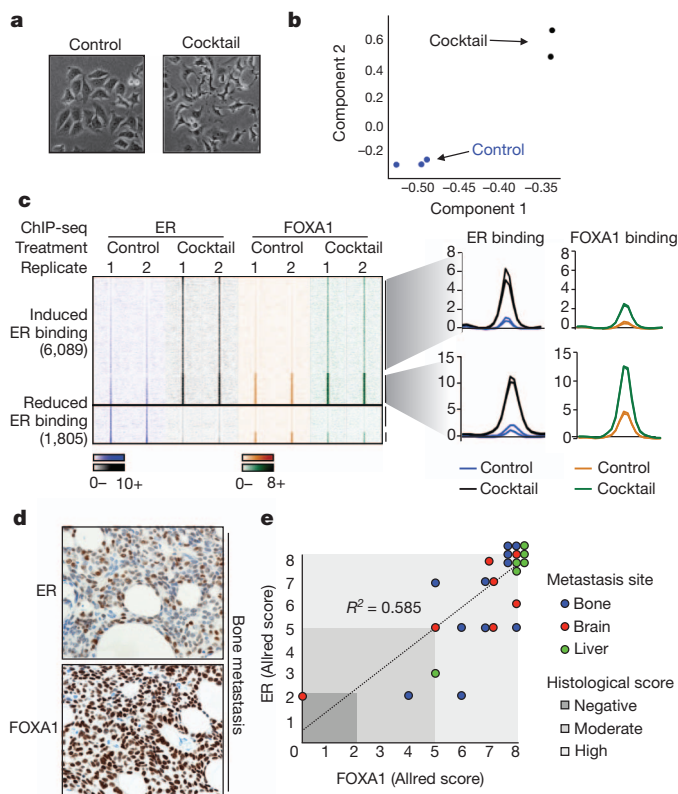


**Figure 4 | ER and FOXA1 binding is dynamic and their expression correlates in metastases.** **a**, Morphological changes in MCF-7 cells treated with a cocktail of mitogens (EGF, IGF-1, IL-6 and TNF- $\alpha$ ) for 90 min. Magnification,  $\times 40$ . **b**, Principal component analysis (93% of total variance) of differentially bound ER-binding events can discriminate between the control and mitogenic cocktail-treated samples in the first (and second) component. **c**, Heat map showing induction and loss of ER and FOXA1 binding after 90 min of treatment with the mitogenic cocktail. Also shown is the normalized average signal intensity of all ER- and FOXA1-binding events within the 'gained' ER-binding events. **d**, Metastatic samples from different sites were stained by immunohistochemistry for ER and FOXA1. Example of ER and FOXA1 expression in a breast cancer bone metastasis. Magnification,  $\times 40$ . **e**, Graphical representation of ER and FOXA1 co-expression in metastases. Location of metastases is provided, as is the Allred score.

ChIP-seq and found that  $\sim 25\%$  of the reprogrammed ER-binding events (1,515) occur at regions that are already bound by FOXA1, before mitogen treatment (Fig. 4c). A substantial proportion (37.6%) of the other reprogrammed ER-binding events occur at regions where FOXA1 binding is also induced by mitogens. As such,  $\sim 53\%$  of mitogen-induced ER-binding events occur at regions pre-bound by FOXA1 or at regions that also acquire FOXA1 binding (Fig. 4c), a level of concordance that mirrors the  $\sim 50\%$  overlap observed in wild-type cells<sup>6</sup>.

To determine if FOXA1 expression was present in ER<sup>+</sup> distant metastases, we obtained 24 metastatic samples (bone, brain and liver) from ER<sup>+</sup> breast cancer patients and performed immunohistochemistry for ER and FOXA1 (Fig. 4d). We found that  $\sim 87\%$  of the metastases retained ER expression and that FOXA1 expression occurred in  $\sim 95\%$  of the metastases (Fig. 4e). Importantly, the concordance between ER and FOXA1 was high ( $R^2 = 0.585$ ), regardless of the site of metastasis. Therefore, the co-expression of ER and FOXA1 in distant metastases supports our conclusions that FOXA1 mediates ER reprogramming.

By mapping ER binding in clinical samples, we provide a first glimpse of the primary regulatory regions that contribute to differences within ER<sup>+</sup> breast cancers, rather than secondary events such as gene expression profiles. Our findings suggest that there is plasticity in ER binding, with distinct ER-binding profiles associated with clinical outcome. These differential ER-binding profiles seem to be mediated by FOXA1. A remaining question is what dictates differential FOXA1 and subsequently ER binding. Possibilities include changes in the genomic landscape, alterations in co-factor levels or changes in FOXA1 structure and function, potentially by post-translational modifications. By establishing transcription factor mapping in primary samples, we find that differential ER-binding patterns govern gene expression programs and are associated with clinical outcome in ER<sup>+</sup> cancer.

## METHODS SUMMARY

MCF-7, ZR75-1, T-47D and BT-474 human cell lines were obtained from the American type culture collection (ATCC) and grown in the relevant media. TAM-R cells<sup>13</sup> were a gift from I. Hutcheson and R. Nicholson (Cardiff). The ER<sup>+</sup> breast cancer tumours were obtained from the Nottingham Tenovus primary breast cancer series, Addenbrooke's Hospital and Imperial College Healthcare NHS Trust, with appropriate ethical approval from the repositories. The malignant pericardial effusion and the two distant metastases were obtained from Imperial College Healthcare NHS Trust. For ChIP in the tumours and metastases, the frozen sample was cut into smaller pieces before ChIP, which was then performed as previously described<sup>16</sup>. For the malignant pericardial effusion, epithelial cells were first enriched using Dynabeads conjugated with Epcam<sup>17</sup>. For ChIPs from cell-line material, proliferating cells were cross-linked and processed for ChIP as previously described<sup>16</sup>. The antibodies used were anti-ER (sc-543) from Santa Cruz Biotechnologies and anti-FOXA1 (ab5089) from Abcam. Sequences generated by the Illumina Genome Analyzer were processed by the Illumina analysis pipeline version 1.6.1, and aligned to the Human Reference Genome (assembly hg18, NCBI build 36.1, March 2008) using BWA version 0.5.5 (ref. 18). Differential binding analysis was performed using the DiffBind package<sup>19</sup>. For immunohistochemical analyses, ER staining was conducted using the 6F11/2 mouse monoclonal antibody (Novocastra, Leica Microsystems) and FOXA1 staining was conducted using a rabbit polyclonal antibody (ab23738) from Abcam. An Allred scoring system was used to assess staining accounting for both staining intensity and the proportion of cells stained.

**Full Methods** and any associated references are available in the online version of the paper at [www.nature.com/nature](http://www.nature.com/nature).

Received 19 May; accepted 23 November 2011.

Published online 4 January 2012.

- Carroll, J. S. *et al.* Genome-wide analysis of estrogen receptor binding sites. *Nature Genet.* **38**, 1289–1297 (2006).
- Lin, C. Y. *et al.* Whole-genome cartography of estrogen receptor  $\alpha$  binding sites. *PLoS Genet.* **3**, e87 (2007).
- Welboren, W. J. *et al.* ChIP-Seq of ER $\alpha$  and RNA polymerase II defines genes differentially responding to ligands. *EMBO J.* **28**, 1418–1428 (2009).

4. Carroll, J. S. *et al.* Chromosome-wide mapping of estrogen receptor binding reveals long-range regulation requiring the forkhead protein FoxA1. *Cell* **122**, 33–43 (2005).
5. Lupien, M. *et al.* FoxA1 translates epigenetic signatures into enhancer-driven lineage-specific transcription. *Cell* **132**, 958–970 (2008).
6. Hurtado, A., Holmes, K. A., Ross-Innes, C. S., Schmidt, D. & Carroll, J. S. FOXA1 is a key determinant of estrogen receptor function and endocrine response. *Nature Genet.* **43**, 27–33 (2011).
7. EBCTCG. Effects of chemotherapy and hormonal therapy for early breast cancer on recurrence and 15-year survival: an overview of the randomised trials. *Lancet* **365**, 1687–1717 (2005).
8. Kun, Y. *et al.* Classifying the estrogen receptor status of breast cancers by expression profiles reveals a poor prognosis subpopulation exhibiting high expression of the ERBB2 receptor. *Hum. Mol. Genet.* **12**, 3245–3258 (2003).
9. Arpino, G. *et al.* Estrogen receptor-positive, progesterone receptor-negative breast cancer: association with growth factor receptor expression and tamoxifen resistance. *J. Natl Cancer Inst.* **97**, 1254–1261 (2005).
10. Zhang, Y. *et al.* Model-based Analysis of ChIP-Seq (MACS). *Genome Biol.* **9**, R137 (2008).
11. Fullwood, M. J. *et al.* An oestrogen-receptor- $\alpha$ -bound human chromatin interactome. *Nature* **462**, 58–64 (2009).
12. Loi, S. *et al.* Definition of clinically distinct molecular subtypes in estrogen receptor-positive breast carcinomas through genomic grade. *J. Clin. Oncol.* **25**, 1239–1246 (2007).
13. Knowlden, J. M. *et al.* Elevated levels of epidermal growth factor receptor/c-erbB2 heterodimers mediate an autocrine growth regulatory pathway in tamoxifen-resistant MCF-7 cells. *Endocrinology* **144**, 1032–1044 (2003).
14. Lupien, M. *et al.* Growth factor stimulation induces a distinct ER $\alpha$  cistrome underlying breast cancer endocrine resistance. *Genes Dev.* **24**, 2219–2227 (2010).
15. Nagashima, T. *et al.* Quantitative transcriptional control of ErbB receptor signaling undergoes graded to biphasic response for cell differentiation. *J. Biol. Chem.* **282**, 4045–4056 (2007).
16. Schmidt, D. *et al.* ChIP-seq: using high-throughput sequencing to discover protein–DNA interactions. *Methods* **48**, 240–248 (2009).
17. Gomm, J. J. *et al.* Isolation of pure populations of epithelial and myoepithelial cells from the normal human mammary gland using immunomagnetic separation with Dynabeads. *Anal. Biochem.* **226**, 91–99 (1995).
18. Li, H. & Durbin, R. Fast and accurate short read alignment with Burrows–Wheeler transform. *Bioinformatics* **25**, 1754–1760 (2009).
19. Stark, R. & Brown, G. D. DiffBind: differential binding analysis of ChIP-seq peak data. *Bioconductor* <http://bioconductor.org/packages/release/bioc/html/DiffBind.html>.

**Supplementary Information** is linked to the online version of the paper at [www.nature.com/nature](http://www.nature.com/nature).

**Acknowledgements** The authors would like to thank D. Schmidt for assistance with figures, J. Hadfield for Illumina sequencing, S. MacArthur, O. Rueda, S. Vowler, R. Russell and M. Wilson for technical and bioinformatics help. We thank J. Stingl and his laboratory for help with the normal mammary gland work. We would like to acknowledge the support of The University of Cambridge, Cancer Research UK and Hutchison Whampoa Limited. The authors would like to thank Imperial College Healthcare NHS Trust, Human Biomaterials Resource Centre (Tissue Bank). Tumour samples from Cambridge were obtained with support from NIHR Biomedical Research Centre and the Experimental Cancer Medicine Centre. C.S.R.-I. is supported by a Commonwealth Scholarship. O.G. is part funded by a grant awarded by the Ministry of Education of the Czech Republic (Project ‘‘Oncology’’ MSM 0021620808) and is also a recipient of a Translational Research Fellowship from the European Society of Medical Oncology. C.P. is funded by Cancer Research UK. J.S.C. is supported by an ERC starting grant and an EMBO Young investigator award.

**Author Contributions** C.S.R.-I., R.S., C.C. and J.S.C. designed all experiments. Experimental work was conducted by C.S.R.-I. with help from K.A.H. Computational analysis was conducted by R.S. and A.E.T., with help from M.J.D. and G.D.B. All clinical samples, clinical information and help with sample processing was provided by C.C., C.P., S.-F.C., S.A., A.R.G., I.O.E. and O.G. Histological analysis was conducted by H.R.A. The manuscript was written by C.S.R.-I., R.S., C.C. and J.S.C. with assistance from other authors.

**Author Information** Alignment and peak data are deposited in the Gene Expression Omnibus under accession number GSE32222. Reprints and permissions information is available at [www.nature.com/reprints](http://www.nature.com/reprints). The authors declare no competing financial interests. Readers are welcome to comment on the online version of this article at [www.nature.com/nature](http://www.nature.com/nature). Correspondence and requests for materials should be addressed to J.S.C. ([jason.carroll@cancer.org.uk](mailto:jason.carroll@cancer.org.uk)) or C.C. ([carlos.caldas@cancer.org.uk](mailto:carlos.caldas@cancer.org.uk)).

## METHODS

**Cell culture.** MCF-7, ZR75-1, T-47D and BT-474 human cell lines were obtained from the American type culture collection (ATCC). MCF-7 cells were grown in DMEM containing 10% heat-inactivated FBS, 2 mM L-glutamine, 50 U ml<sup>-1</sup> penicillin and 50 µg ml<sup>-1</sup> streptomycin. ZR75-1, T-47D and BT-474 cells were grown in RPMI containing 10% heat-inactivated FBS, 2 mM L-glutamine, 50 U ml<sup>-1</sup> penicillin and 50 µg ml<sup>-1</sup> streptomycin. To validate the cell lines, samples were genotyped by the Health Protection Agency (<http://www.hpa.org.uk>) (MCF-7, ZR75-1, T-47D) or by in-house genotyping (BT-474). TAM-R cells<sup>13</sup> were obtained from I. Hutcheson and R. Nicholson (Cardiff) and were maintained in phenol-red-free DMEM containing 5% charcoal dextran-treated FBS, 2 mM L-glutamine, 50 U ml<sup>-1</sup> penicillin and 50 µg ml<sup>-1</sup> streptomycin and 10 nM 4-hydroxytamoxifen.

**Primary tumour material.** The ER<sup>+</sup> breast cancer tumours were obtained from the Nottingham Tenovus primary breast cancer series, Addenbrooke's Hospital and Imperial College Healthcare NHS Trust, with appropriate ethical approval from the repositories. The malignant pericardial effusion and the two distant metastases were obtained from Imperial College Healthcare NHS Trust. See Supplementary Fig. 2 for clinical details.

**Chromatin immunoprecipitations.** The antibodies used were anti-ER (sc-543) from Santa Cruz Biotechnologies and anti-FOXA1 (ab5089) from Abcam. For ChIP in the tumours and metastases, the frozen sample was cut into smaller pieces and thawed in 1% (final concentration) formaldehyde for 20 min at room temperature (20 °C). The reaction was quenched by adding 0.1 volume of 2 M glycine for 10 min. The sample was disaggregated by Dounce homogenization and processed according to standard ChIP procedures<sup>16</sup>. The DNA was subsequently amplified as previously described<sup>16</sup>. For the malignant pericardial effusion, epithelial cells were first enriched using Dynabeads conjugated with Epcam<sup>17</sup>. For ChIPs from cell-line material, proliferating cells were cross-linked and processed for ChIP as previously described<sup>16</sup>. For the TAM-R cells, ER ChIP-seq was performed on cells grown in DMEM containing 10% FBS and 10 nM tamoxifen for 24 h. For the cocktail experiments, cells were treated with 100 ng ml<sup>-1</sup> IGF-1, 100 ng ml<sup>-1</sup> EGF, 1 ng ml<sup>-1</sup> TNF-α and 10 ng ml<sup>-1</sup> IL-6 for 90 min.

**High-throughput sequencing and enrichment analysis.** Sequences generated by the Illumina Genome Analyzer were processed by the Illumina analysis pipeline version 1.6.1, and aligned to the Human Reference Genome (assembly hg18, NCBI build 36.1, March 2008) using BWA version 0.5.5 (ref. 18). Reads were filtered by removing those with a BWA alignment quality score less than 15. Enriched regions of the genome were identified by comparing the ChIP samples to input samples using the MACS peak caller version 1.3.7.1 (ref. 10). Additional peak calls were determined for the tumour samples using the SWEMBL peak caller version 3.2 (S. Wilder *et al.*, manuscript in preparation) with default parameters except with  $-R = 0.005$ . For tumours without a corresponding input, all the available tumour input reads were combined and down sampled to derive a control track for peak calling purposes.

**Differential binding analysis.** After identifying a common set of peaks (see Supplementary Figs 4A and 15), significantly differentially bound sites were identified by first counting the number of reads in the ChIP samples overlapping each identified peak (subtracting the number of overlapping reads from the corresponding input sample). Differential analysis was performed using the edgeR package<sup>20</sup>. Normalization factors were computed using the TMM technique, after which tagwise dispersions were calculated and subjected to an exact test<sup>20</sup>. Resulting *P* values were subjected to Benjamini–Hochberg multiple testing correction to derive FDRs; only sites differentially bound with a FDR < 0.1 (cell line samples) or a *P* value < 0.01 were considered for further analysis. The differential binding analysis and related plots were performed using the DiffBind package<sup>19</sup>.

**Heat-map generation.** To generate the heat maps of the raw ChIP-seq data, ER-binding peaks in the different samples were used as targets to centre each window. Each window was divided into 100 bins of 100 bp in size. An enrichment value was assigned to each bin, counting the number of sequencing reads in that bin normalized to 10,000,000 sequencing reads, after subtracting the number of normalized input reads per bin.

**Motif analysis.** For analysis of enriched DNA motifs, Weeder was used, with the default settings<sup>21</sup>.

**Distant-metastasis-free-survival analysis.** First, we computed for each gene in the given ER-binding list (ER-core-binding events, good outcome ER binding, poor/met ER binding) a *P* value and statistic from a univariate Cox regression, individually in nine independent data sets<sup>12,22–29</sup>. This was done to ascertain if the

observed directionalities of association between gene expression and outcome were consistent with the predictions from the differential ER-binding events. Histograms of *P* values over all cohorts clearly confirmed the association of the ER-binding events with distant-metastasis-free survival (DMFS; Supplementary Fig. 9). Moreover, genes more bound in poor prognosis and metastatic tumours were generally more highly expressed in poor prognosis tumours (Supplementary Fig. 10).

We adopted a two-step strategy to first learn from the pool of genes in a given ER-binding list, a subset with patterns of gene expression that are associated with DMFS in a training set, and second to then validate this predictor in completely independent data. We used the ER<sup>+</sup> breast cancer samples from two independent data sets as training sets<sup>22,23</sup>, re-normalized the gene expression profiles to mean zero and unit variance and applied a singular value decomposition to the resulting reduced expression matrices. For each of the top 10 eigenvectors (principal components) we correlated their profiles across samples to DMFS using a Cox regression, and next identified DMFS-associated eigenvectors, which were also highly correlated (or anticorrelated) between the two training sets. Thus, our algorithm is similar to the supervised principal components algorithm (SPCA) previously described<sup>30</sup>, but differs in that we extend this procedure to two training sets. We consistently identified DMFS-associated eigenvectors that were also highly correlated between the two training sets. A prognostic predictor was constructed by averaging the DMFS-associated eigenvectors from each training set. The predictor was subsequently tested in seven independent ER<sup>+</sup> breast cancer cohorts<sup>12,24–29</sup>. Specifically, for each sample we computed the Pearson correlation of the predictor with the sample expression profile over the genes that could be mapped. The resulting correlation can be viewed as the risk index. In each cohort this risk index was then evaluated in a Cox regression to test ability to predict DMFS. The data shown in Fig. 1e and Fig. 2d is derived from the Loi data set<sup>12</sup>, but the additional data sets are provided in Supplementary Fig. 6 and 12.

The Sweave document describing all analyses can be found at <http://c3315341.r41.cf0.rackcdn.com/Data.tar.gz>.

**Immunohistochemistry.** Immunohistochemistry of full-face sections was performed using a BondMax Autoimmunostainer (Leica Microsystems). ER staining was conducted using the 6F11/2 mouse monoclonal antibody (Novocastra, Leica Microsystems) at 1 in 70 and antigen retrieval was performed by heating with pH 6 citrate buffer for 30 min. FOXA1 staining was conducted using a rabbit polyclonal antibody (ab23738) from Abcam, at 1 in 800 with antigen retrieval performed by heating with pH 6 citrate buffer for 20 min. Bound primary antibody was detected using a BOND polymer detection kit (Leica) and developed with 3-3'-diaminobenzidine (DAB). The degree of staining was assessed by a pathologist (H.R.A.) using a standard light microscope. An Allred scoring system was used to assess staining accounting for both staining intensity (0 = none, 1 = weak, 2 = moderate, 3 = strong) and the proportion of cells stained (0 = 0%, 1 < 1%, 2 = 1–10%, 3 = 11–33%, 4 = 34–66%, 5 > 66%), providing a composite score (intensity + proportion = 0–8).

- Robinson, M. D., McCarthy, D. J. & Smyth, G. K. edgeR: a Bioconductor package for differential expression analysis of digital gene expression data. *Bioinformatics* **26**, 139–140 (2010).
- Pavesi, G. *et al.* MoD Tools: regulatory motif discovery in nucleotide sequences from co-regulated or homologous genes. *Nucleic Acids Res.* **34**, W566–W570 (2006).
- Wang, Y. *et al.* Gene-expression profiles to predict distant metastasis of lymph-node-negative primary breast cancer. *Lancet* **365**, 671–679 (2005).
- van de Vijver, M. J. *et al.* A gene-expression signature as a predictor of survival in breast cancer. *N. Engl. J. Med.* **347**, 1999–2009 (2002).
- Sotiriou, C. *et al.* Gene expression profiling in breast cancer: understanding the molecular basis of histologic grade to improve prognosis. *J. Natl. Cancer Inst.* **98**, 262–272 (2006).
- Chin, K. *et al.* Genomic and transcriptional aberrations linked to breast cancer pathophysiologies. *Cancer Cell* **10**, 529–541 (2006).
- Schmidt, M. *et al.* The humoral immune system has a key prognostic impact in node-negative breast cancer. *Cancer Res.* **68**, 5405–5413 (2008).
- Buffa, F. M. *et al.* microRNA associated progression pathways and potential therapeutic targets identified by integrated mRNA and microRNA expression profiling in breast cancer. *Cancer Res.* **71**, 5635 (2011).
- Naderi, A. *et al.* A gene-expression signature to predict survival in breast cancer across independent data sets. *Oncogene* **26**, 1507–1516 (2007).
- Hoadley, K. A. *et al.* EGFR associated expression profiles vary with breast tumor subtype. *BMC Genomics* **8**, 258 (2007).
- Bair, E. & Tibshirani, R. Semi-supervised methods to predict patient survival from gene expression data. *PLoS Biol.* **2**, e108 (2004).



# Cysteinyl leukotriene type I receptor desensitization sustains $\text{Ca}^{2+}$ -dependent gene expression

Siaw-Wei Ng<sup>1</sup>, Daniel Bakowski<sup>1</sup>, Charmaine Nelson<sup>1</sup>, Ravi Mehta<sup>1</sup>, Robert Almeyda<sup>2</sup>, Grant Bates<sup>2</sup> & Anant B. Parekh<sup>1</sup>

Receptor desensitization is a universal mechanism to turn off a biological response; in this process, the ability of a physiological trigger to activate a cell is lost despite the continued presence of the stimulus. Receptor desensitization of G-protein-coupled receptors involves uncoupling of the receptor from its G-protein or second-messenger pathway followed by receptor internalization<sup>1</sup>. G-protein-coupled cysteinyl leukotriene type I (CysLT1) receptors regulate immune-cell function and CysLT1 receptors are an established therapeutic target for allergies, including asthma<sup>2</sup>. Desensitization of CysLT1 receptors arises predominantly from protein-kinase-C-dependent phosphorylation of three serine residues in the receptor carboxy terminus<sup>3</sup>. Physiological concentrations of the receptor agonist leukotriene  $\text{C}_4$  ( $\text{LTC}_4$ ) evoke repetitive cytoplasmic  $\text{Ca}^{2+}$  oscillations, reflecting regenerative  $\text{Ca}^{2+}$  release from stores, which is sustained by  $\text{Ca}^{2+}$  entry through store-operated calcium-release-activated calcium (CRAC) channels<sup>4</sup>. CRAC channels are tightly linked to expression of the transcription factor *c-fos*<sup>5</sup>, a regulator of numerous genes important to cell growth and development<sup>6</sup>. Here we show that abolishing leukotriene receptor desensitization suppresses agonist-driven gene expression in a rat cell line. Mechanistically, stimulation of non-desensitizing receptors evoked prolonged inositol-trisphosphate-mediated  $\text{Ca}^{2+}$  release, which led to accelerated  $\text{Ca}^{2+}$ -dependent slow inactivation of CRAC channels and a subsequent loss of excitation–transcription coupling. Hence, rather than serving to turn off a biological response, reversible desensitization of a  $\text{Ca}^{2+}$  mobilizing receptor acts as an ‘on’ switch, sustaining long-term signalling in the immune system.

The paradox of receptor desensitization is how long-term responses can be evoked if the receptor is inactivated. This is a particularly acute problem in immune cells, in which cell differentiation and clonal selection develop over hours in the continued presence of external cues.

Stimulation of rat basophilic leukaemia (RBL-1) cells with  $\text{LTC}_4$ , acting exclusively on CysLT1 receptors<sup>7,8</sup> (Supplementary Fig. 1), led to cytoplasmic  $\text{Ca}^{2+}$  signals (Fig. 1a) followed by robust expression of *c-fos* at both messenger RNA (Fig. 1b, c)<sup>4</sup> and protein levels (Fig. 1d, e). Maximal activation of CRAC channels with thapsigargin led to a similar increase in *c-fos* expression (Fig. 1b–e). Both  $\text{LTC}_4$  and thapsigargin induce *c-fos* expression through the build-up of  $\text{Ca}^{2+}$  microdomains near open store-operated CRAC channels<sup>4,5</sup>. Thapsigargin led to a larger, more sustained  $\text{Ca}^{2+}$  signal than  $\text{LTC}_4$  (Fig. 1a)<sup>4,5</sup> and the rate of  $\text{Ca}^{2+}$  entry through CRAC channels was approximately twofold more for thapsigargin than  $\text{LTC}_4$  (Fig. 1f), consistent with patch-clamp recordings<sup>7</sup>. The similar increase in  $\text{Ca}^{2+}$ -dependent *c-fos* expression to  $\text{LTC}_4$  and thapsigargin was therefore surprising, given the significant difference in CRAC channel activation.

We considered various explanations for why CysLT1 receptor activation and thapsigargin evoked similar *c-fos* levels despite marked differences in the extent of CRAC channel activation. These included: (1) CysLT1 receptors tapped into a different signalling mechanism linking CRAC channel microdomains to *c-fos* expression; (2) local  $\text{Ca}^{2+}$  entry through CRAC channels was larger after receptor activation

because  $\text{LTC}_4$  hyperpolarized the membrane potential; and (3) cytoplasmic  $\text{Ca}^{2+}$  and protein kinase C (PKC) interacted synergistically to drive gene expression in response to CysLT1 receptor activation. Evidence against these possibilities is presented in Supplementary Figs 2–4. Instead, gene expression showed high sensitivity to  $\text{Ca}^{2+}$  entry, enabling CysLT1 receptor activation to couple effectively to *c-fos* transcription (Supplementary Fig. 5), as well as rapidly and high gain. Combined, this ensures efficient gene expression to bursts of CRAC channel activity after physiological levels of receptor stimulation.

Experiments described in Fig. 1g and h revealed an important role for PKC in receptor-dependent gene expression. The structurally distinct PKC blockers G06983 and calphostin C abolished *c-fos* expression (Fig. 1g, h). PKC block had a marked effect on the  $\text{Ca}^{2+}$  signal evoked by agonist. Whereas cytoplasmic  $\text{Ca}^{2+}$  oscillations were routinely observed with  $\text{LTC}_4$  (Fig. 1i), the response was converted into a large, single, slowly decaying  $\text{Ca}^{2+}$  spike after PKC inhibition (Fig. 1i, j). Acute stimulation with PMA in the absence of  $\text{LTC}_4$  failed to induce significant *c-fos* expression (data not shown)<sup>9</sup>, demonstrating that PKC activity per se was not sufficient to induce *c-fos* expression in these cells. The PKC inhibitors had no effect on thapsigargin-evoked *c-fos* expression (Fig. 1k) or cytoplasmic  $\text{Ca}^{2+}$  signals (Fig. 1l). Thapsigargin (2  $\mu\text{M}$ ) activates CRAC channels maximally (Supplementary Fig. 5) and, by blocking SERCA pumps (which can be located near CRAC channels<sup>10</sup>), reduces the decay of  $\text{Ca}^{2+}$  gradients radiating from the plasma membrane. It is possible that other non-receptor-dependent stimuli, which raise local  $\text{Ca}^{2+}$  levels less effectively than 2  $\mu\text{M}$  thapsigargin, might activate *c-fos* in a manner dependent on basal PKC activity, but this activity would be unusual in that it is not stimulated acutely by PMA in the presence of sub-maximal CRAC channel activation (Supplementary Fig. 4).

In RBL cells, exposure to the phorbol ester PMA for several hours downregulates several PKC isozymes<sup>11</sup>. Using this protocol, we found that *c-fos* expression was substantially reduced in response to CysLT1 receptor stimulation (Fig. 1m), whereas no significant reduction was seen when thapsigargin was used instead (Fig. 1m) or when inactive 4 $\alpha$ -phorbol replaced PMA (data not shown). Similar to PKC blockers, the  $\text{Ca}^{2+}$  signal to  $\text{LTC}_4$  was prolonged after PKC downregulation (Fig. 1n). This prolonged  $\text{Ca}^{2+}$  signal did not reflect a change in  $\text{Ca}^{2+}$  clearance mechanisms (Supplementary Fig. 6); instead, it is characteristic of loss of receptor desensitization, particularly for CysLT1 receptors, in which desensitization is mediated predominantly by PKC<sup>3</sup> and prevention of desensitization leads to broader  $\text{Ca}^{2+}$  signals<sup>12</sup>. Inhibition of CysLT1 receptor desensitization is predicted to lead to greater inositol trisphosphate ( $\text{InsP}_3$ ) production and hence more extensive  $\text{Ca}^{2+}$  store emptying. Several findings are consistent with this. First,  $\text{Ca}^{2+}$  release to  $\text{LTC}_4$  lasted approximately five times longer when PKC was blocked than in control cells (Fig. 2a, expanded in inset). Second, the amount of  $\text{Ca}^{2+}$  remaining within the stores, measured as the ionomycin-sensitive  $\text{Ca}^{2+}$  response<sup>13</sup>, was substantially less after activation of CysLT1 receptors in the presence of PKC block than in control cells (Fig. 2a). Third,  $\text{InsP}_3$  production, measured using the green fluorescent protein–pleckstrin homology

<sup>1</sup>Department of Physiology, Anatomy and Genetics, University of Oxford, Parks Road, Oxford OX1 3PT, UK. <sup>2</sup>Department of Ear-Nose-Throat Surgery, John Radcliffe Hospital, Oxford OX3 9DH, UK.

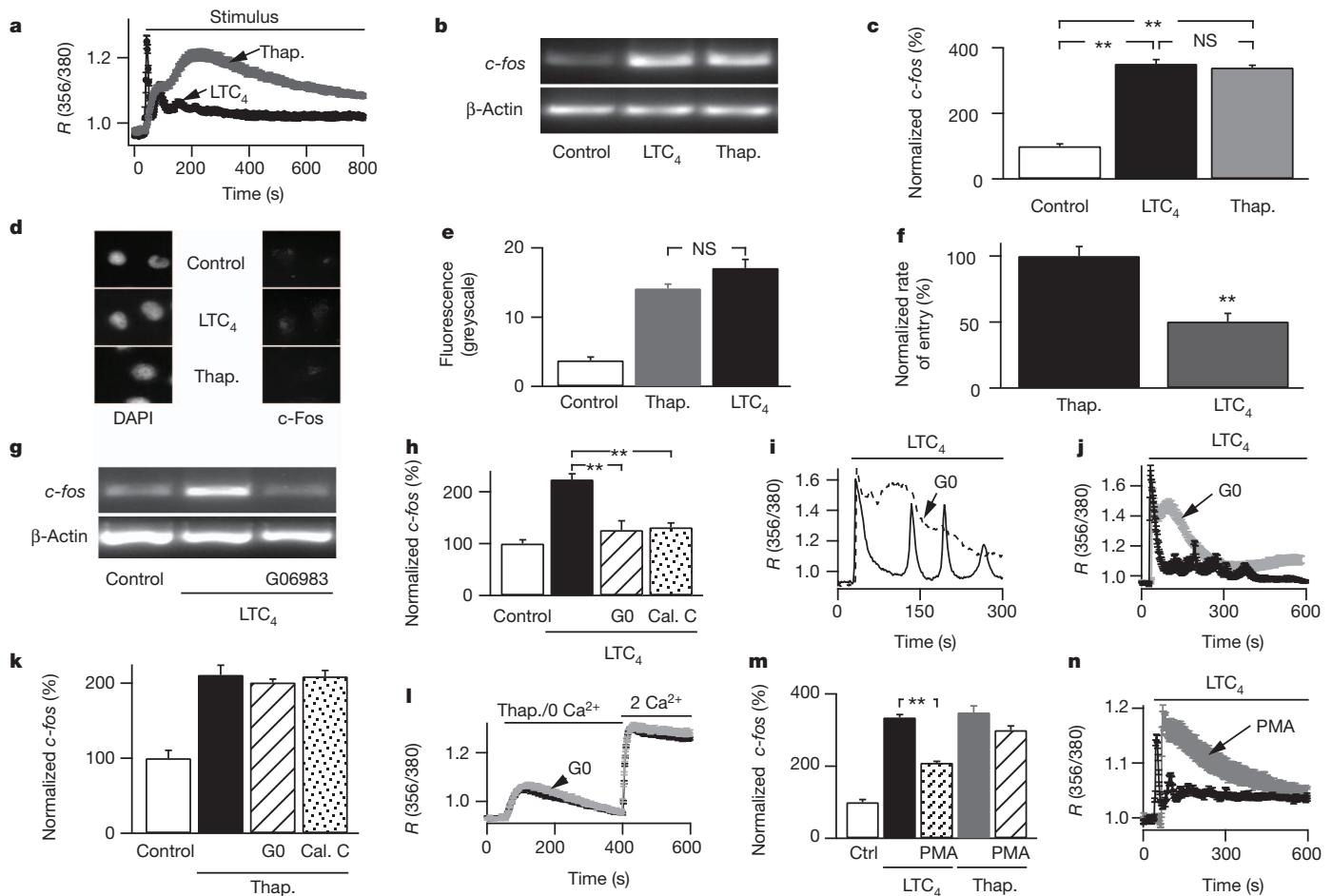


**Figure 1 | CysLT1-receptor-dependent  $c$ -fos expression requires PKC.**

**a**, Averaged  $\text{Ca}^{2+}$  signals to  $\text{LTC}_4$  and thapsigargin (Thap.) are compared ( $>50$  cells per graph).  $R$  (356/380), ratio of fluorescence measured at 356 and 380 nm. Stimulus was present for 8 min. **b**,  $c$ -fos expression is compared between control (non-stimulated), 160 nM  $\text{LTC}_4$ - and 2  $\mu\text{M}$  thapsigargin-stimulated cells. Stimulus was present for 8 min. **c**, Histograms show averaged responses from three independent experiments.  $\text{LTC}_4$  and thapsigargin groups were different from control ( $P < 0.001$ ), but not from one another ( $P > 0.3$ ; analysis of variance (ANOVA)). **d**, Cells stained with antibody against  $c$ -Fos protein. DAPI, 4',6-diamidino-2-phenylindole. **e**, Aggregate data are compared ( $n > 20$  per bar). Thapsigargin and  $\text{LTC}_4$  groups were different from control ( $P < 0.001$ ) but not from one another ( $P = 0.11$ ). **f**,  $\text{Ca}^{2+}$  entry rate was measured after readmission of  $\text{Ca}^{2+}$  to cells stimulated with  $\text{LTC}_4$  or thapsigargin in  $\text{Ca}^{2+}$ -free solution ( $*P < 0.01$ ). **g**, G06983 (1  $\mu\text{M}$ ; 10 min pre-treatment) suppresses  $\text{LTC}_4$ -induced  $c$ -fos expression. **h**, Histogram comparing the effects of PKC blockers.  $\text{LTC}_4$  control group ( $\text{LTC}_4$  in the absence of PKC block) was different from the other groups

( $P < 0.01$ ). There were no significant differences between the other groups. G0, G06983. Cal. C, calphostin C. **i**, Single-cell  $\text{Ca}^{2+}$  signals to  $\text{LTC}_4$  are compared for the conditions shown. **j**, Averaged data are compared ( $>45$  cells for each condition). **k**, Histogram showing  $c$ -fos expression to thapsigargin in the presence of PKC blockers. All thapsigargin-treated groups were significantly different from control ( $P < 0.001$ ) but were not significantly different from one another. **l**,  $\text{Ca}^{2+}$  signals to thapsigargin are unaffected by PKC block. 0  $\text{Ca}^{2+}$ ,  $\text{Ca}^{2+}$ -free external solution; 2  $\text{Ca}^{2+}$ , external solution containing 2 mM  $\text{Ca}^{2+}$ . **m**, Downregulation of PKC (PMA; 500 nM, 24 h) reduces  $\text{LTC}_4$ - but not thapsigargin-induced  $c$ -fos expression (data from four independent experiments). All stimulated groups were significantly different from control ( $P < 0.01$ ). For  $\text{LTC}_4$  the PMA group was different from the  $\text{LTC}_4$  control ( $P < 0.01$ ). For thapsigargin, the PMA groups was not different from the thapsigargin control ( $P = 0.07$ ). **n**, PKC downregulation alters the  $\text{LTC}_4$ -evoked  $\text{Ca}^{2+}$  signal. Error bars show data  $\pm$  s.e.m. NS, not significant.

(GFP-PH) construct<sup>14</sup>, increased to a greater extent when PKC was inhibited (Fig. 2b).

Cytoplasmic  $\text{Ca}^{2+}$  inhibits CRAC channels through mechanisms of fast and slow inactivation<sup>15</sup>. The prolonged  $\text{Ca}^{2+}$  release evoked by  $\text{LTC}_4$  in the presence of non-desensitizing receptors could therefore inactivate CRAC channels to suppress agonist-evoked gene expression. In support of this, accumulation of the slow  $\text{Ca}^{2+}$  chelator EGTA in the cytoplasm rescued gene expression to CysLT1 receptor activation in the presence of PKC block (Fig. 2c, d).  $\text{Ca}^{2+}$ -dependent fast inactivation of CRAC channels is unlikely to contribute here because (1) it is unaffected by the slow chelator EGTA<sup>16,17</sup>, which reversed the inhibitory effects of PKC block (Fig. 2c, d), and (2) the rate and extent of fast inactivation were unaltered by CysLT1 receptor activation in the presence of PKC downregulation (Fig. 3a). Instead,  $\text{Ca}^{2+}$ -dependent slow inactivation is likely to be the dominant mechanism because (1) it too is suppressed by cytoplasmic EGTA<sup>18,19</sup>, (2) the

$\text{Ca}^{2+}$  dependence of slow inactivation has a dissociation constant ( $K_d$ ) of  $\sim 0.5 \mu\text{M}$  and full block occurs at  $\sim 1 \mu\text{M}$  (Fig. 3b), which is similar to the peak  $\text{Ca}^{2+}$  rise evoked by  $\text{LTC}_4$  in the presence of PKC inhibitors or following downregulation of PKC ( $0.87 \pm 0.1 \mu\text{M}$ ), and (3)  $\text{Ca}^{2+}$ -dependent slow inactivation develops with a time course similar to the duration of the prolonged  $\text{Ca}^{2+}$  rise caused by  $\text{LTC}_4$  following loss of PKC activity<sup>18,19</sup>.

If prolonged  $\text{Ca}^{2+}$  release to non-desensitizing CysLT1 receptors leads to slow inactivation of CRAC channels, then development of a calcium-release-activated calcium current ( $I_{\text{CRAC}}$ ) to a subsequent stimulus should be impaired. Pre-activation of CysLT1 receptors reduced  $I_{\text{CRAC}}$  evoked by thapsigargin but only in the presence of PKC block (Fig. 3c). No such inhibitory effect was seen when cells were dialysed with a strongly buffered  $\text{Ca}^{2+}$ -containing pipette solution, which prevents the development of slow inactivation (Fig. 3d). Increasing the time between the termination of  $\text{Ca}^{2+}$  release and

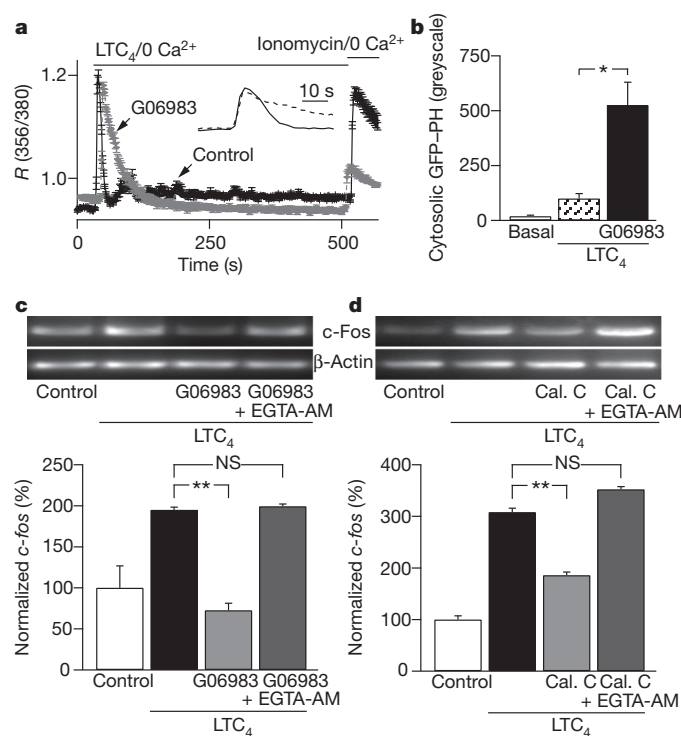


**Figure 2 | Gene expression to non-desensitizing CysLT1 receptors is rescued by preventing a cytoplasmic Ca<sup>2+</sup> rise.** **a**, Stimulation with LTC<sub>4</sub> in the presence of G06983 evokes a more sustained Ca<sup>2+</sup> release response, and this leads to more extensive store depletion (measured through the extent of Ca<sup>2+</sup> release evoked by 5 μM ionomycin). Both LTC<sub>4</sub> and ionomycin were applied in Ca<sup>2+</sup>-free external solution. Inset compares the kinetics of Ca<sup>2+</sup> release. **b**, Cytosolic GFP-PH levels, a measure of InsP<sub>3</sub> levels, rise when CysLT1 receptors are stimulated in the presence of G06983. **c**, Top, loading cells with the Ca<sup>2+</sup> chelator EGTA prevents loss of gene expression to agonist when PKC is blocked. Bottom, aggregate data from five independent gels are summarized. **d**, As in **c**, but calphostin C was used to block PKC instead. Bottom, aggregate data from three independent gels are summarized. Error bars show data ± s.e.m. NS, not significant.

subsequent store-operated Ca<sup>2+</sup> entry should enable some recovery from Ca<sup>2+</sup>-dependent slow inactivation and this should partially rescue gene expression. When Ca<sup>2+</sup> influx was evoked a few minutes after Ca<sup>2+</sup> release, significant, albeit incomplete, rescue of Ca<sup>2+</sup> entry (Fig. 3e) and *c-fos* transcription (Fig. 3f) occurred in cells stimulated with LTC<sub>4</sub> in the presence of PKC inhibition. Hence, allowing CRAC channels time to recover from Ca<sup>2+</sup>-dependent inactivation results in partial rescue of agonist-driven gene expression.

Our attempts to express the PKC-insensitive CysLT1 receptor, in which S313, S315 and S316 had been mutated to alanines, were thwarted by the difficulty of expressing these receptors<sup>3</sup>, although in a few cells we observed that Ca<sup>2+</sup> oscillations to LTC<sub>4</sub> were less frequent (3.1 ± 0.5 versus 5.4 ± 0.4, 4 and 6 cells, respectively) and the initial spike was a little broader (~1.25-fold) than mock-transfected cells.

To place our findings in a physiological context, we turned to the human nasal polyp, which is rich in mast cells<sup>20</sup>. The polyp and associated nasal mucosa are largely self-contained, providing an excellent 'quasi *in vivo* human system'. Mast cells from polyps, acutely isolated from patients undergoing surgery, respond to LTC<sub>4</sub> and express functional CRAC channels<sup>7,8</sup>. Stimulation with LTC<sub>4</sub> activated *c-Fos* protein expression in mast cells isolated from polyps (Fig. 3g) and this was reduced by pre-treatment with either calphostin C or G06983 (Fig. 3h). PKC inhibitors had no inhibitory effect when thapsigargin was used instead.

Western blots revealed the presence of Ca<sup>2+</sup>-dependent PKC-α, -β and -ζ isozymes<sup>11,21</sup> but only faint expression of PKC-δ and -ε (Fig. 4a).

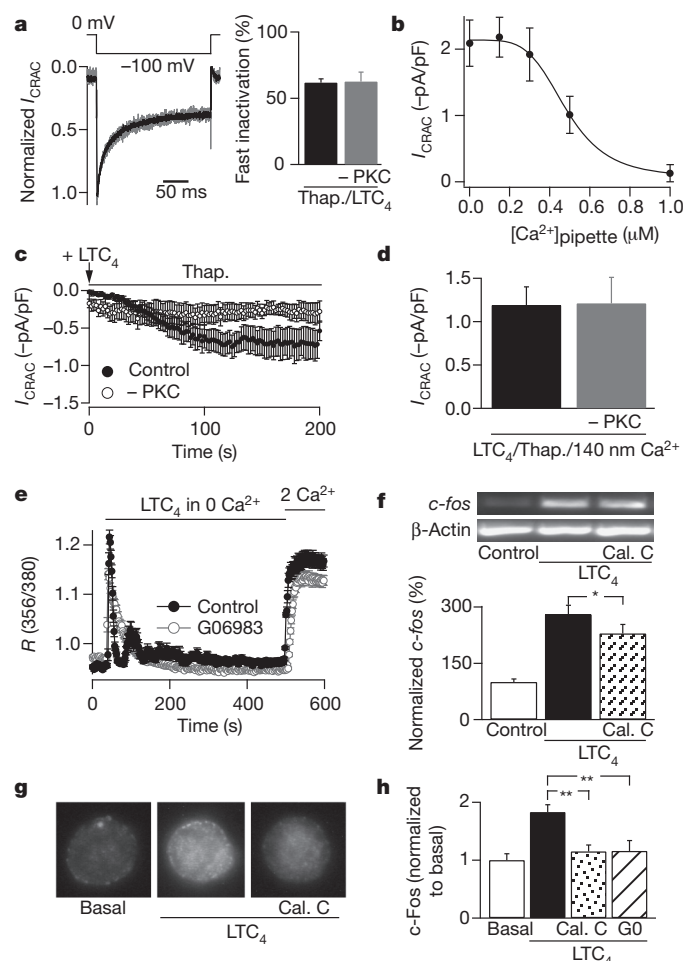


**Figure 3 | Ca<sup>2+</sup>-dependent slow inactivation underlies suppression of *c-Fos* expression to non-desensitizing CysLT1 receptors.** **a**, Ca<sup>2+</sup>-dependent fast inactivation is unaffected by non-desensitizing receptors (labelled -PKC). Cells were stimulated with LTC<sub>4</sub> (160 nM) before breaking in with a pipette solution containing thapsigargin and buffered Ca<sup>2+</sup> (140 nM) and fast inactivation was measured within 60 s of break-in. **b**, Dependence of Ca<sup>2+</sup>-dependent slow inactivation on patch pipette Ca<sup>2+</sup> concentration. pA, picoamperes; pF, picrofarads. [Ca<sup>2+</sup>]<sub>pipette</sub>, concentration of Ca<sup>2+</sup> in pipette. **c**, Stimulation of non-desensitizing receptors with LTC<sub>4</sub> before break-in significantly reduced the size of I<sub>CRAC</sub> that developed in response to dialysis with thapsigargin in weak buffer (0.2 mM EGTA). **d**, As in **c**, but cells were dialysed with a pipette solution containing strong Ca<sup>2+</sup> buffer (10 mM EGTA, 140 nM free Ca<sup>2+</sup>). **e**, Store-operated Ca<sup>2+</sup> entry recovers partially by increasing the time interval between Ca<sup>2+</sup> release and subsequent Ca<sup>2+</sup> entry. **f**, *c-fos* expression to non-desensitizing receptor stimulation is rescued partially when Ca<sup>2+</sup> entry occurs several minutes after Ca<sup>2+</sup> release has reached completion. **g**, *c-Fos* expression in human nasal mast cells after CysLT1 receptor activation is suppressed by PKC inhibition. **h**, Aggregate data are compared (12–17 cells per bar; three patients each). Error bars show data ± s.e.m. NS, not significant.

Overnight PMA exposure significantly reduced PKC-α and -β expression, but not PKC-ζ (Fig. 4a, b). Their weak expression made PKC-δ and -ε difficult to quantify. Confocal microscope studies confirmed robust expression of PKC-α, -β and -ζ (Fig. 4c), with barely detectable levels of PKC-δ and -ε (data not shown). Overnight PMA exposure significantly reduced PKC-α and -β but not -ζ at the cellular level (Fig. 4d). Knockdown of PKC-α using a targeted short interfering RNA (siRNA) approach (Fig. 4e) resulted in a broadening of the first Ca<sup>2+</sup> oscillation evoked by LTC<sub>4</sub>, indicative of less receptor desensitization, and fewer Ca<sup>2+</sup> oscillations in each cell (Supplementary Fig. 7). Knockdown of PKC-β had a much weaker effect on the Ca<sup>2+</sup> oscillations (Supplementary Fig. 7). Knockdown of PKC-α or PKC-α plus -β simultaneously, but not PKC-β alone, reduced LTC<sub>4</sub>-driven



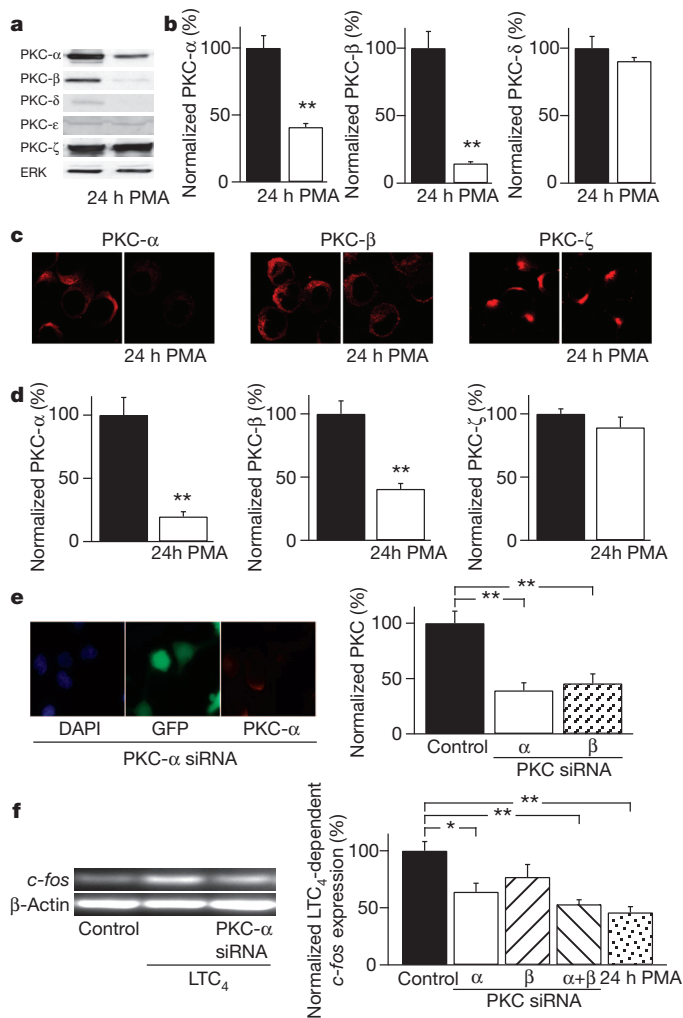


**Figure 4 | PKC- $\alpha$  regulates CysLT1 receptor-driven *c-fos* transcription.**

**a**, Expression of PKC- $\alpha$ , - $\beta$  and - $\zeta$  (western blot) is shown in control cells and cells exposed to PMA for 24 h. **b**, Quantification of data from three independent experiments, as in **a**. **c**, Confocal microscope images of PKC expression for the conditions shown. Cells were fixed before analysis. Original magnification,  $\times 100$ . **d**, Quantification of images from experiments, as in **c**. **e**, siRNA against PKC- $\alpha$  or - $\beta$  significantly reduces corresponding protein expression. Left, DAPI staining of nuclei; middle, GFP expression (indicating transfection); and right, PKC- $\alpha$  expression after siRNA-mediated knockdown. Right, aggregate data from four experiments are depicted. Both siRNA groups were different from control ( $P < 0.005$ ). Error bars show data  $\pm$  s.e.m. NS, not significant. **f**, Knockdown of PKC- $\alpha$ , - $\beta$  and PKC- $\alpha$  plus - $\beta$  on LTC<sub>4</sub>-dependent *c-fos* expression. Data are compared with mock-transfected cells. For comparison, 24 h exposure to PMA is included. All treated groups were significantly different from the LTC<sub>4</sub> control (black bar) group except siRNA PKC- $\beta$  knockdown ( $P > 0.1$ ). PKC- $\alpha$  plus - $\beta$  and 24 h PMA groups had  $P < 0.01$ ; PKC- $\alpha$  group had  $P < 0.05$ . Error bars show data  $\pm$  s.e.m. NS, not significant.

*c-fos* expression to an extent similar to that seen after overnight PMA treatment (Fig. 4f). Stimulation of non-G-protein-coupled FC $\epsilon$ RI antigenic receptors in RBL-2H3 cells activates *c-fos* expression primarily through PKC- $\delta$  and - $\epsilon$ <sup>22</sup>. Although it is possible that these PKC isoforms also contribute to gene expression under our conditions, our results nevertheless suggest a major role for PKC- $\alpha$  in G-protein-coupled-receptor desensitization, and thus coupling to the nucleus.

Collectively, our findings reveal a counterintuitive function for desensitization of a phospholipase-C-coupled receptor. Rather than terminating a response, homologous receptor desensitization is essential for maintaining excitation–transcription coupling. Desensitization of CysLT1 receptors is mediated principally by PKC-dependent phosphorylation<sup>3</sup>. Prevention of receptor desensitization through either

acute block or degradation of PKC or after knockdown of PKC- $\alpha$  all led to loss of Ca<sup>2+</sup>-dependent gene expression, despite potentiation of Ca<sup>2+</sup> release to agonist. Mechanistically, the prolonged Ca<sup>2+</sup> release phase accelerated Ca<sup>2+</sup>-dependent slow inactivation of CRAC channels, resulting in loss of Ca<sup>2+</sup> entry. Because Ca<sup>2+</sup> microdomains near open CRAC channels drive *c-fos* expression, the decline in CRAC channel activity abolishes excitation–transcription coupling. The interval between Ca<sup>2+</sup> oscillations after CysLT1 receptor activation is  $\sim 25$  s (ref. 4). Because InsP<sub>3</sub> has a short half-life in the cytoplasm ( $\sim 1$  s)<sup>23</sup>, receptor desensitization will presumably lower InsP<sub>3</sub> levels during the interspike interval. Store refilling will occur quickly and CRAC channel activity will be transient after CysLT1 receptor stimulation. The short duration of Ca<sup>2+</sup> release and thus Ca<sup>2+</sup> entry, determined by receptor desensitization, will ensure Ca<sup>2+</sup>-dependent slow inactivation does not develop, as this inhibitory mechanism requires a sustained Ca<sup>2+</sup> rise for several seconds. It is therefore the kinetics of receptor desensitization and recovery from desensitization within a highly Ca<sup>2+</sup> sensitive and high-gain system that ensures bursts of store-operated Ca<sup>2+</sup> entry occur that are sufficient for the activation of *c-fos* expression, without the build-up of the Ca<sup>2+</sup>-dependent slow inactivation pathway that would abolish the response.

## METHODS SUMMARY

Cultured RBL-1 cells and acutely isolated human nasal polyps were prepared as described previously<sup>7</sup>. Transfection with siRNA constructs was achieved using the AMAXA system. Patch-clamp recordings and cytoplasmic Ca<sup>2+</sup> measurements followed standard methods<sup>7</sup>. RT-PCR, western blotting and confocal microscopy were carried out as described previously<sup>5</sup>. Error bars are s.e.m.

**Full Methods** and any associated references are available in the online version of the paper at [www.nature.com/nature](http://www.nature.com/nature).

**Received 8 April; accepted 23 November 2011.**

**Published online 9 January 2012.**

- Pierce, K. L., Premont, R. T. & Lefkowitz, R. J. Seven-transmembrane receptors. *Nature Rev. Mol. Cell Biol.* **3**, 639–650 (2002).
- Funk, C. D. Leukotriene modifiers as potential therapeutics for cardiovascular disease. *Nature Rev. Drug Discov.* **4**, 664–672 (2005).
- Naik, S. *et al.* Regulation of cysteinyl leukotriene type 1 receptor internalization and signaling. *J. Biol. Chem.* **280**, 8722–8732 (2005).
- Di Capite, J., Ng, S.-W. & Parekh, A. B. Decoding of cytoplasmic Ca<sup>2+</sup> oscillations through the spatial signature drives gene expression. *Curr. Biol.* **19**, 853–858 (2009).
- Ng, S.-W., Nelson, C. & Parekh, A. B. Coupling of Ca<sup>2+</sup> microdomains to spatially and temporally distinct cellular responses by the tyrosine kinase Syk. *J. Biol. Chem.* **284**, 24767–24772 (2009).
- Foletta, V. C., Segal, D. H. & Cohen, D. R. Transcriptional regulation in the immune system: all roads lead to AP-1. *J. Leukoc. Biol.* **63**, 139–152 (1998).
- Di Capite, J. L., Shirley, A., Nelson, C., Bates, G. & Parekh, A. B. Intercellular calcium wave propagation involving positive feedback between CRAC channels and cysteinyl leukotrienes. *FASEB J.* **23**, 894–905 (2009).
- Di Capite, J., Nelson, C., Bates, G. & Parekh, A. B. Targeting CRAC channels and leukotriene receptors provides a novel combination strategy for treating nasal polyposis. *J. Allergy Clin. Immunol.* **124**, 1014–1021 (2009).
- Stephan, V., Seibt, A., Koerholz, D. & Wahn, V. Expression of mRNA for the proto-oncogene *c-fos* in rat basophilic leukemia cells. *Cell. Signal.* **9**, 65–70 (1997).
- Jousset, H., Frieden, M. & Demareux, N. STIM1 knockdown reveals that store-operated Ca<sup>2+</sup> channels located close to sarco/endoplasmic Ca<sup>2+</sup> ATPases (SERCA) pumps silently refill the endoplasmic reticulum. *J. Biol. Chem.* **282**, 11456–11464 (2007).
- Ozawa, K. *et al.* Ca<sup>2+</sup>-dependent and Ca<sup>2+</sup>-independent isoforms of protein kinase C mediate exocytosis in antigen-stimulated rat basophilic RBL-2H3 cells. Reconstitution of secretory responses with Ca<sup>2+</sup> and purified isoforms in washed permeabilized cells. *J. Biol. Chem.* **268**, 1749–1756 (1993).
- Deshpande, D. A. *et al.* PKC-dependent regulation of the receptor locus dominates functional consequences of cysteinyl leukotriene type 1 receptor activation. *FASEB J.* **21**, 2335–2342 (2007).
- Bird, G. S. & Putney, J. W. J. Capacitative calcium entry supports calcium oscillations in human embryonic kidney cells. *J. Physiol.* **562**, 697–706 (2005).
- Stauffer, T. P., Ahn, S. & Meyer, T. Receptor-induced transient reduction in plasma membrane PtdIns(4,5)P<sub>2</sub> concentration monitored in living cells. *Curr. Biol.* **8**, 343–346 (1998).
- Parekh, A. B. & Putney, J. W. J. Store-operated calcium channels. *Physiol. Rev.* **85**, 757–810 (2005).
- Zweifach, A. & Lewis, R. S. Rapid inactivation of depletion-activated calcium current (ICRAC) due to local calcium feedback. *J. Gen. Physiol.* **105**, 209–226 (1995).

17. Fierro, L. & Parekh, A. B. Fast calcium-dependent inactivation of calcium release-activated calcium current (CRAC) in RBL-1 cells. *J. Membr. Biol.* **168**, 9–17 (1999).
18. Zweifach, A. & Lewis, R. S. Slow calcium-dependent inactivation of depletion-activated calcium current. *J. Biol. Chem.* **270**, 14445–14451 (1995).
19. Parekh, A. B. Slow feedback inhibition of calcium release-activated calcium current by calcium entry. *J. Biol. Chem.* **273**, 14925–14932 (1998).
20. Takasaka, T., Kaku, Y. & Hozawa, K. Mast cell degranulation in nasal polyps. *Acta Otolaryngol. Suppl.* **430**, 39–48 (1986).
21. Ozawa, K., Yamada, K., Kazanietz, M. G., Blumberg, P. M. & Beaven, M. A. Different isoforms of protein kinase C mediate feedback inhibition of phospholipase C and stimulatory signals for exocytosis in RBL-2H3 cells. *J. Biol. Chem.* **268**, 2280–2283 (1993).
22. Razin, E., Szallasi, Z., Kazanietz, M. G., Blumberg, P. M. & Rivera, J. Protein kinases C- $\beta$  and C- $\epsilon$  link the mast cell high-affinity receptor for IgE to the expression of c-fos and c-jun. *Proc. Natl Acad. Sci. USA* **91**, 7722–7726 (1994).
23. Kasai, H. & Petersen, O. H. Spatial dynamics of second messengers: IP<sub>3</sub> and cAMP as long-range and associative messengers. *Trends Neurosci.* **17**, 95–101 (1994).

**Supplementary Information** is linked to the online version of the paper at [www.nature.com/nature](http://www.nature.com/nature).

**Acknowledgements** This work was supported by Medical Research Council grant support to A.B.P. S.-W. N. held a BBSRC-Glaxo-Smith-Kline studentship. We thank G. Miesenboeck and J. Putney for comments on the manuscript.

**Author Contributions** S.-W.N. performed and analysed Ca<sup>2+</sup> measurements, RT-PCR, western blots and siRNA knockdown. D.B. performed and analysed patch-clamp recordings. C.N. carried out immunocytochemistry. R.M. helped with Ca<sup>2+</sup> measurements. R.A. and G.B. supplied human nasal polyps. A.B.P. carried out some patch-clamp experiments, discussed the results, supervised the project and wrote the paper.

**Author Information** Reprints and permissions information is available at [www.nature.com/reprints](http://www.nature.com/reprints). The authors declare no competing financial interests. Readers are welcome to comment on the online version of this article at [www.nature.com/nature](http://www.nature.com/nature). Correspondence and requests for materials should be addressed to A.B.P. ([anant.parekh@dpag.ox.ac.uk](mailto:anant.parekh@dpag.ox.ac.uk)).

## METHODS

**Cell culture and transfection.** RBL-1 cells were bought from ATCC and were cultured (37 °C, 5% CO<sub>2</sub>) in Dulbecco's modified Eagle medium with 10% fetal bovine serum, 2 mM L-glutamine and penicillin-streptomycin, as previously described<sup>24</sup>. Cells were transfected with siRNA against Syk (purchased from Invitrogen; 5'-3' sense, CCCUCUGGCAGCUAGUGGAACAUUA; antisense, UAAUGUCCACUAGCUGCCAGAGGG) using the Amaxa nucleofection system<sup>25</sup>. siRNA against PKC isozymes were purchased from Invitrogen; PKC- $\alpha$  sense, GCGACACCUGCGACAUGAUGUUA; antisense, UGAACAUAUCU GUCGAGGUGUCGC; PKC- $\beta$  sense, GGCUAAUGACCAAACACCCAGGC AA; antisense, UUGCCUGGGUGUUGGUCAUUAAGCC. Cells were used 36–48 h after plating.

**Human tissue.** Human polyps were removed from patients with full ethical consent and with approval from the National Research Ethics Service (REC number 07/H0607/104). Polyps were treated as described<sup>7</sup> and used within 6 h of surgical removal.

**ICRAC recordings.** Patch-clamp experiments were conducted in the tight-seal whole-cell configuration at room temperature (20–24 °C) as previously described<sup>7,24</sup>. Sylgard-coated, fire-polished pipettes had resistances of 4.2–5.5 M $\Omega$  when filled with standard internal solution that contained (in mM): Cs<sup>+</sup> glutamate 145, NaCl 8, MgCl<sub>2</sub> 1, Mg-ATP 2, EGTA 10, CaCl<sub>2</sub> 4.6 mM (free Ca<sup>2+</sup> ~140 nM), HEPES 10, pH 7.2 with CsOH. In some experiments, weak Ca<sup>2+</sup> buffer was used instead (0.2 mM EGTA and no added CaCl<sub>2</sub>). A correction of +10 mV was applied for the subsequent liquid junction potential that arose from this glutamate-based internal solution. The composition of the extracellular solution was (in mM): NaCl 145, KCl 2.8, CaCl<sub>2</sub> 10, MgCl<sub>2</sub> 2, CsCl 10, D-glucose 10, HEPES 10, pH 7.4 with NaOH.

$I_{CRAC}$  was measured by applying voltage ramps (–100 to +100 mV in 50 ms) at 0.5 Hz from a holding potential of 0 mV. For fast inactivation, step pulses (250 ms duration) were applied from 0 mV to –100 mV every 2 s. Currents were filtered using an 8-pole Bessel filter at 2.5 kHz and digitized at 100  $\mu$ s. Currents were normalized by dividing the amplitudes (measured from the voltage ramps at –80 mV) by the cell capacitance. Capacitive currents were compensated before each ramp by using the automatic compensation of the EPC-9/2 (HEKA Elektronik) patch-clamp amplifier. For  $I_{CRAC}$ , leak currents were subtracted by averaging 2–3 ramp currents obtained just before  $I_{CRAC}$  had started to develop, and then subtracting this from all subsequent currents.

**Ca<sup>2+</sup> imaging.** Ca<sup>2+</sup> imaging experiments were carried out at room temperature (21–24 °C) using the IMAGO CCD camera-based system from TILL Photonics, as described previously<sup>25</sup>. Cells were alternately excited at 356 and 380 nm (20 ms exposures) and images were acquired every 2 s. Images were analysed offline using IGOR Pro for Windows. Cells were loaded with Fura 2-AM (2  $\mu$ M) for 40 min at room temperature in the dark and then washed three times in standard external solution of composition (in mM) NaCl 145, KCl 2.8, CaCl<sub>2</sub> 2, MgCl<sub>2</sub> 2, D-glucose 10, HEPES 10, pH 7.4 with NaOH. Cells were left for 15 min to allow further de-esterification. Ca<sup>2+</sup>-free solution had the following composition (in mM) NaCl 145, KCl 2.8, MgCl<sub>2</sub> 2, D-glucose 10, HEPES 10, EGTA 0.1, pH 7.4 with NaOH).

**EGTA-AM loading.** Cells were loaded with EGTA by incubation for 45 min with EGTA-AM as described<sup>5</sup>.

**Confocal microscopy.** Cells were fixed in 4% paraformaldehyde in phosphate buffer for 30 min at room temperature. All the washes used 0.01% PBS (137 mM NaCl, 2.7 mM KCl, 8 mM Na<sub>2</sub>HPO<sub>4</sub>, 1 mM KH<sub>2</sub>PO<sub>4</sub>). The cells were blocked with 2% BSA and 10% goat serum for 1 h. Anti-c-Fos, -PKC- $\delta$ , -PKC- $\epsilon$  and -PKC- $\zeta$  were used in carrier (0.2% BSA, 1% goat serum) and left overnight at 4 °C and were purchased from Cell Signalling. Anti-PKC- $\alpha$  and - $\beta$  were used in carrier (0.2% BSA, 1% goat serum) and left overnight at 4 °C and were purchased from Santa Cruz. The secondary anti-rabbit IgG was a HandL chain-specific (goat) fluorescein conjugate (Alexa Fluor 568, excitation at 578 nm, emission at 603 nm wavelength) from Invitrogen. This was used in PBS for 2 h at room temperature. The cells were mounted in Vectashield mounting medium. Images were obtained using a Leica confocal microscope, as described<sup>5</sup>.

**Western blotting.** Total cell lysates (50  $\mu$ g) were separated by SDS-PAGE on a 10% gel and electrophoretically transferred to nitrocellulose membrane, as described<sup>2</sup>. Membranes were blocked with 5% non-fat dry milk in TBS plus 0.1% Tween 20 (TBST) buffer for 1 h at room temperature. Membranes were washed with TBST three times and then incubated with primary antibody overnight at 4 °C. Anti-PKC- $\delta$ , - $\epsilon$  and - $\zeta$  antibodies were obtained from New England Biolabs and used at 1:2,500 dilution. Anti-PKC- $\alpha$ , - $\beta$  and total ERK2 antibodies were purchased from Santa Cruz Biotechnology. PKC- $\alpha$  and - $\beta$  antibodies were used at 1:2,500 dilution and total ERK antibody was used at a dilution of 1:5,000. The membranes were then washed with TBST again and incubated with a 1:2,500 dilution of goat anti-rabbit secondary antibody IgG from Santa Cruz Biotechnology for 1 h at room temperature. After washing with TBST, the bands were developed for visualization using ECL-plus western blotting detection system (GE Healthcare). Gels were quantified using the UN-SCAN-IT software package (Silk Scientific). Total ERK2 is widely used as a control for gel loading. The antibody does not discriminate between phosphorylated (and hence active) and non-phosphorylated ERK2 and therefore detects the total amount of this protein, regardless of whether the kinase has been activated. The extent of PKC was therefore normalized to the total amount of ERK2 present in each lysate, to correct for any differences in amount of cells used for each experiment.

**RT-PCR.** Total RNA was extracted from RBL cells by using an RNeasy Mini Kit (Qiagen), as described<sup>4,5</sup>. RNA was quantified spectrophotometrically by absorbance at 260 nm. Total RNA (1  $\mu$ g) was reverse-transcribed using the iScript<sup>TM</sup> cDNA Synthesis Kit (Bio-Rad), according to the manufacturer's instructions. Following cDNA synthesis, PCR amplification was then performed using BIO-X-ACT<sup>TM</sup> Short DNA Polymerase (Bioline) with primers specific for the detection of *c-fos* were synthesized by Invitrogen. The PCR products were electrophoresed through an agarose gel and visualized by ethidium bromide staining.

**Statistics.** Results are presented as means  $\pm$  s.e.m. Statistical significance was assessed using Student's *t*-test for comparison between two groups or ANOVA followed by a post-hoc Newman Keuls multiple comparison test for the difference between groups and results were considered significant at \**P* < 0.05, \*\**P* < 0.01.

24. Glitsch, M. D., Bakowski, D. & Parekh, A. B. Activation of the store-operated Ca<sup>2+</sup> current ICRAC is compromised by inhibitors of the lipoxygenase family of enzymes. *J. Physiol. (Lond.)* **539**, 93–106 (2002).

25. Ng, S.-W., Di Capite, J. L., Singaravelu, K. & Parekh, A. B. Sustained activation of the tyrosine kinase Syk by antigen in mast cells requires local Ca<sup>2+</sup> influx through Ca<sup>2+</sup> release-activated Ca<sup>2+</sup> channels. *J. Biol. Chem.* **283**, 31348–31355 (2008).



# A novel retinoblastoma therapy from genomic and epigenetic analyses

Jinghui Zhang<sup>1\*</sup>, Claudia A. Benavente<sup>2\*</sup>, Justina McEvoy<sup>2\*</sup>, Jacqueline Flores-Otero<sup>2\*</sup>, Li Ding<sup>3,4</sup>, Xiang Chen<sup>1</sup>, Anatoly Ulyanov<sup>1</sup>, Gang Wu<sup>1</sup>, Matthew Wilson<sup>5,6</sup>, Jianmin Wang<sup>7</sup>, Rachel Brennan<sup>2</sup>, Michael Rusch<sup>1</sup>, Amity L. Manning<sup>8</sup>, Jing Ma<sup>9</sup>, John Easton<sup>1</sup>, Sheila Shurtleff<sup>9</sup>, Charles Mullighan<sup>9</sup>, Stanley Pounds<sup>10</sup>, Suraj Mukatira<sup>7</sup>, Pankaj Gupta<sup>7</sup>, Geoff Neale<sup>7</sup>, David Zhao<sup>11</sup>, Charles Lu<sup>3</sup>, Robert S. Fulton<sup>3,4</sup>, Lucinda L. Fulton<sup>3,4</sup>, Xin Hong<sup>3,4</sup>, David J. Dooling<sup>3,4</sup>, Kerri Ochoa<sup>3,4</sup>, Clayton Naeve<sup>11</sup>, Nicholas J. Dyson<sup>8</sup>, Elaine R. Mardis<sup>3,4,12</sup>, Armita Bahrami<sup>9</sup>, David Ellison<sup>9</sup>, Richard K. Wilson<sup>3,4,13</sup>, James R. Downing<sup>9</sup> & Michael A. Dyer<sup>2,5,14</sup>

**Retinoblastoma is an aggressive childhood cancer of the developing retina that is initiated by the biallelic loss of *RB1*. Tumours progress very quickly following *RB1* inactivation but the underlying mechanism is not known. Here we show that the retinoblastoma genome is stable, but that multiple cancer pathways can be epigenetically deregulated. To identify the mutations that cooperate with *RB1* loss, we performed whole-genome sequencing of retinoblastomas. The overall mutational rate was very low; *RB1* was the only known cancer gene mutated. We then evaluated the role of *RB1* in genome stability and considered non-genetic mechanisms of cancer pathway deregulation. For example, the proto-oncogene *SYK* is upregulated in retinoblastoma and is required for tumour cell survival. Targeting *SYK* with a small-molecule inhibitor induced retinoblastoma tumour cell death *in vitro* and *in vivo*. Thus, retinoblastomas may develop quickly as a result of the epigenetic deregulation of key cancer pathways as a direct or indirect result of *RB1* loss.**

Retinoblastoma is a rare childhood cancer of the retina that can develop in a sporadic or a heritable form and is fatal if untreated. When the *RB1* gene was first cloned, it was found to undergo biallelic inactivation in virtually all retinoblastoma tumours<sup>1</sup>. Since then, hundreds of genetic lesions have been identified in human cancer. These genetic lesions can be grouped on the basis of the signalling pathways they affect that have direct or indirect mechanistic links to many of the common cellular properties, or hallmarks, of cancer. Thus, the rate of cancer progression is related to the kinetics of acquisition of multiple genetic lesions and/or epigenetic changes that ultimately lead to activation of growth-signalling pathways, evasion of cell death and senescence, acquisition of limitless replicative potential, sustained angiogenesis, and local tissue invasion and metastasis<sup>2</sup>.

*RB1* inactivation confers limitless replicative potential to retinoblasts and is rate limiting for retinoblastoma tumorigenesis<sup>3</sup>. However, the mechanisms that enable retinoblastoma cells to acquire the additional hallmarks of cancer remain unknown. Evidence from molecular, cellular and cytogenetic studies suggest that *RB1* is required for maintaining chromosomal stability<sup>4,5</sup>, and that its loss leads to chromosome instability in cells maintained in culture. These data raise the possibility that *RB1* inactivation may underlie the rapid acquisition of cooperating mutations in key cancer pathways through chromosome instability. Alternatively, epigenetic changes may have a more dominant role in cooperating with the loss of *RB1* retinoblastoma tumorigenesis. *RB1* has been implicated in regulating most major epigenetic processes, including microRNA regulation, DNA methylation, histone modification and ATP-dependent chromatin reorganization<sup>6–10</sup>. Thus, inactivation of *RB1* in retinoblasts may lead to the rapid epigenetic

deregulation of cancer genes that contribute to the essential cellular properties of retinoblastoma.

In this study, the St Jude Children's Research Hospital – Washington University Pediatric Cancer Genome Project characterized the genetic landscape of retinoblastoma. Whole-genome sequencing (WGS) of four retinoblastomas and their paired germline DNA samples showed no genetic lesions in known tumour suppressor genes or oncogenes, other than *RB1* and *MYCN*. More importantly, an orthotopic xenograft derived from one of the primary tumours showed no evidence of clonal variation or new coding-region mutations. This finding suggests that the retinoblastoma genome is more stable than previously believed.

Unlike the genetic landscape of retinoblastoma, the epigenetic profile shows profound changes relative to that observed in normal retinoblasts. One of the most striking results was the induction of the expression of the proto-oncogene spleen tyrosine kinase (*SYK*) in human retinoblastoma. *SYK* is required for tumour cell survival, and inhibition of *SYK* with a small-molecule inhibitor caused the degradation of MCL1 and caspase-mediated cell death in retinoblastoma cells in culture and *in vivo*. These findings highlight how comprehensive genetic and epigenetic analyses of tumours can be integrated, leading to the discovery of promising new therapeutic approaches and shedding light on the mechanisms underlying the rapid progression of retinoblastoma following *RB1* inactivation.

## Retinoblastoma whole-genome sequencing

We performed WGS analysis on four primary human retinoblastoma samples (Supplementary Information, section 1, and Supplementary Table 1) and on matched normal tissue. Local tumour cell invasion,

<sup>1</sup>Department of Computational Biology and Bioinformatics, St Jude Children's Research Hospital, Memphis, Tennessee 38105, USA. <sup>2</sup>Department of Developmental Neurobiology, St Jude Children's Research Hospital, Memphis, Tennessee 38105, USA. <sup>3</sup>The Genome Institute, Washington University School of Medicine in St Louis, St Louis, Missouri 63108, USA. <sup>4</sup>Department of Genetics, Washington University School of Medicine in St Louis, St Louis, Missouri 63108, USA. <sup>5</sup>Department of Ophthalmology, University of Tennessee Health Science Center, Memphis, Tennessee 38163, USA. <sup>6</sup>Department of Surgery, St Jude Children's Research Hospital, Memphis, Tennessee 38105, USA. <sup>7</sup>Hartwell Center for Biotechnology & Bioinformatics, St Jude Children's Research Hospital, Memphis, Tennessee 38105, USA. <sup>8</sup>Massachusetts General Hospital, Charlestown, Massachusetts 02129, USA. <sup>9</sup>Department of Pathology, St Jude Children's Research Hospital, Memphis, Tennessee 38105, USA. <sup>10</sup>Department of Biostatistics, St Jude Children's Research Hospital, Memphis, Tennessee 38105, USA. <sup>11</sup>Department of Information Sciences, St Jude Children's Research Hospital, Memphis, Tennessee 38105, USA. <sup>12</sup>Siteman Cancer Center, Washington University School of Medicine in St Louis, St Louis, Missouri 63108, USA. <sup>13</sup>Department of Medicine, Washington University School of Medicine in St Louis, St Louis, Missouri 63108, USA. <sup>14</sup>Howard Hughes Medical Institute, Chevy Chase, Maryland 20815, USA.

\*These authors contributed equally to this work.

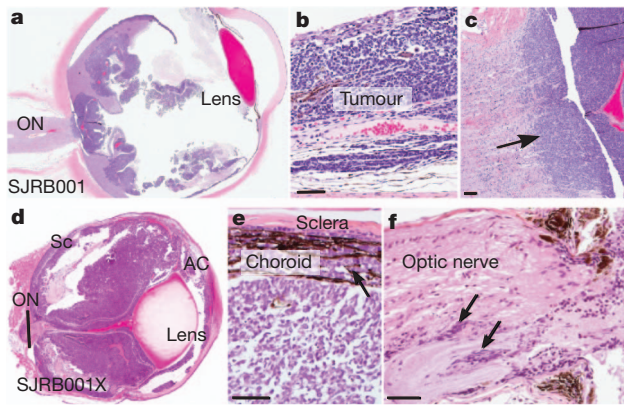


**Figure 1 | Characterization of retinoblastoma samples.** **a–c**, Representative retinoblastoma tumour section (SJRB001) stained with haematoxylin and eosin (H&E), showing choroidal and optic nerve invasion (arrow). **d–f**, H&E-stained section of the SJRB001X orthotopic xenograft with choroidal (**e**) and optic nerve (**f**) invasion (arrows). AC, anterior chamber; ON, optic nerve; Sc, sclera. Scale bars, 25  $\mu$ m.

but not metastasis, was evident in each patient (Fig. 1a–c and Supplementary Fig. 1). We generated an orthotopic xenograft, SJRB001X, of the primary tumour SJRB001 by inoculating primary tumour cells into the vitreous humour of the eyes of immunocompromised mice (Supplementary Information, section 2). SJRB001X had molecular, genetic and histopathologic features similar to those of SJRB001 (Fig. 1d–f; Supplementary Figs 2–4; Supplementary Tables 2–4; and Supplementary Information, section 3).

Using a paired-end sequencing approach, we generated 1,040.9 gigabase pairs (Gb) of sequence data for the samples described; 956.8 Gb (92%) was successfully mapped to the NCBI 36.1 reference genome (Supplementary Information, section 4, and Supplementary Table 5). The average genome coverage was  $\times 28.9$ , and the average exon coverage was  $\times 23.8$  with 98.4% of single nucleotide polymorphisms (SNPs) detected across all nine genomes showing concordance with their corresponding SNP array genotype calls at the same genomic positions (Supplementary Table 5). To provide additional sequence coverage, we performed transcriptome sequencing of all four primary tumours (Supplementary Information, section 5, and Supplementary Table 6).

We identified 668 validated somatic sequence mutations and 40 structural variations across the four cases (Table 1). These included 23 tier-1 mutations in genes, 35 tier-2 mutations in evolutionarily conserved regions of the genome (Supplementary Information, section 6), 309 tier-3 mutations in non-repetitive regions of the genome that are not part of tiers 1 and 2, and 301 tier-4 mutations in repetitive sequences in the genome (Table 1 and Supplementary Table 7). The average number of sequence mutations was 167 per case (range, 56–258), with

only 3.25 mutations per case (range, 0–5) resulting in amino-acid changes (Table 1). The estimated mean mutation rate was  $6.7 \times 10^{-8}$  per base (range,  $1.03 \times 10^{-7}$ – $2.17 \times 10^{-8}$ ), which is 15-fold less than that in adult tumours analysed by WGS, except for acute myeloid leukaemia<sup>11</sup>. The predominant changes were C  $\rightarrow$  A and G  $\rightarrow$  T transversions (Supplementary Fig. 5), which is consistent with the possibility that some of the transversions result from production of 8-oxoguanine during oxidative stress. Tumour SJRB002 had no somatic sequence variations that resulted in amino-acid changes; the only structural variations were the loss of heterozygosity (LOH) at the *RB1* locus on chromosome 13 and a gain of chromosome 6p. This suggests that very few genetic lesions are required for retinoblastoma progression after *RB1* inactivation.

### *RB1* inactivation in retinoblastoma

Both *RB1* alleles were inactivated in each sample (Supplementary Figs 6 and 7). Tumours SJRB002 and SJRB003 had mutations in *RB1* combined with copy-number-neutral LOH, and SJRB001 and SJRB004 had somatic sequence mutations combined with *RB1*-promoter hypermethylation (Supplementary Figs 6–8). Deep-sequence analysis of the germline sample from SJRB002 revealed that about 10% of reads contained the R445 nonsense mutation, suggesting the presence of germline chimaerism for the *RB1* mutation (Supplementary Fig. 6). Combining the WGS data with SNP array data of an additional 42 samples, we found that tumours from patients with lower regional nucleotide diversity were much less likely to undergo LOH at the *RB1* locus (Supplementary Tables 8 and 9 and Supplementary Information, section 7). These data show a significant association ( $P = 8 \times 10^{-8}$ , Fisher's exact test) between a germline genetic variation and mechanism of biallelic *RB1* inactivation in retinoblastoma.

### Recurrent lesions in retinoblastoma

To determine whether any of the 11 genes with somatic mutations that caused amino-acid changes or a frameshift in the coding region (Table 1; Fig. 2a, b; Supplementary Figs 9 and 10; Supplementary Information, section 8; and Supplementary Table 10) were recurrently mutated in retinoblastoma, we sequenced all exons from the 11 genes in our recurrent screening cohort of 42 retinoblastomas (Supplementary Information, section 4). Only *BCOR* was recurrently mutated in retinoblastoma (6 of 46, or 13%). Five of the samples had *BCOR* mutations that resulted in truncation of the encoded protein, and one sample had a focal gene deletion (Fig. 2c, Supplementary Table 11 and Supplementary Fig. 11).

We also used the WGS data to identify somatic structural variations including whole-chromosome gains and losses, focal deletions (DEL), insertions (INS), inversions (INV), intrachromosomal rearrangements (ITX), interchromosomal rearrangements (CTX) and regions of LOH (Fig. 2a–c; Supplementary Information, section 9; Supplementary Table 12; and Supplementary Fig. 12). The average

**Table 1 | Somatic mutations and structural alterations in retinoblastoma**

Sample*	Tier 1†	Non-silent tier 1‡	Genes	Tier 2	Tier 3¶	Tier 4#	Total	Mutation rate	Structural variations**
SJRB001 D, G	7	4	<i>RB1</i> , <i>CCNC</i> , <i>AGMO</i> , <i>RHBG</i>	16	117	85	225	$1.03 \times 10^{-7}$	4
SJRB001 X, D§	0	0	NA	8	68	9	85	$5.87 \times 10^{-8}$	4
SJRB002 D, G	1	0	NA	1	25	29	56	$2.17 \times 10^{-8}$	0
SJRB003 D, G	7	4	<i>RB1</i> , <i>HNMT</i> , <i>LHX8</i> , <i>STOML2</i>	5	67	50	129	$5.79 \times 10^{-8}$	24
SJRB004 D, G	8	5	<i>RB1</i> , <i>CD300LG</i> , <i>SDK1</i> , <i>TXK</i> , <i>DMWD</i>	13	100	137	258	$8.63 \times 10^{-8}$	12

Background mutation rate was calculated on the basis of the ratio of tier-3 mutations to tier-3 bases covered at least tenfold in tumour and germline samples for each pair.

\*D, diagnostic tumour sample; G, germline (blood DNA) sample; X, xenograft sample.

†Tier 1 mutations are found in genes and include exons, 5' and 3' untranslated regions, and splice sites. Introns are not included.

‡Non-silent tier-1 mutations change amino acids in genes.

§All of the somatic mutations in SJRB001 D, G were identified in SJRB001X. This row highlights the new mutations acquired in the xenograft relative to the primary tumour.

||Tier-2 mutations are found in regions of the genome that are conserved between humans and mice.

¶Tier-3 mutations are found in regions of the genome that are not evolutionarily conserved.

#Tier-4 mutations are found in repetitive regions of the genome.

\*\*Structural variations include focal amplifications and deletions, LOH, and interchromosomal and intrachromosomal translocations.

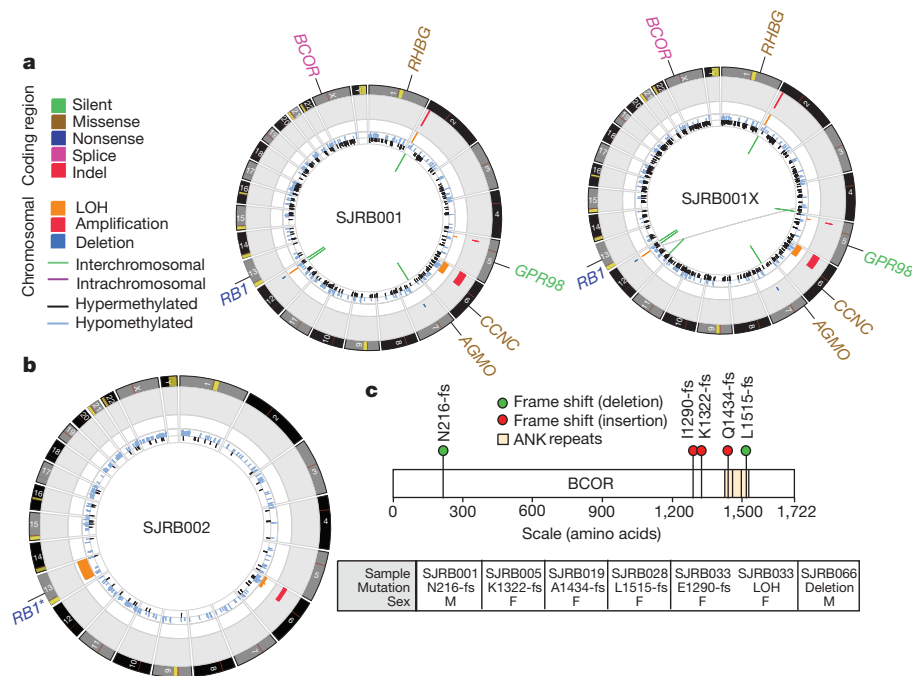


**Figure 2 | Genomic profiles of SJRB001, SJRB002 and SJRB001X.**

**a, b,** CIRCOS plots of genetic alterations in two retinoblastomas and the matched orthotopic xenograft. Loss of heterozygosity (orange), amplifications (red) and deletions (blue) are shown. Interchromosomal translocations (green lines) and intrachromosomal translocations (purple lines) are indicated.

number of structural variations was ten per case (range, 0–24) (Supplementary Table 1). Tumour SJRB001 had four structural variations (two DEL and ins INS) including a gain of a region of chromosome 2 spanning *MYCN* (Supplementary Table 12), and the only chromosomal lesion in SJRB002 was a gain of chromosome 6p, which occurs in about 40% of human retinoblastomas<sup>12</sup> (Fig. 2b). Only a few genomic regions were affected by the structural variations in SJRB003 and SJRB004 (Supplementary Figs 10, 13 and 14 and Supplementary Table 12).

### Orthotopic retinoblastoma xenograft

The genomic landscape of the orthotopic xenograft was remarkably similar to that of the primary tumour, despite continuous growth and multiple passages *in vivo* over nine months (Fig. 2 and Supplementary Table 1). All of the sequence mutations and structural variations detected in SJRB001 were retained in SJRB001X. Only 67 new SNVs and four structural variations were identified in the xenograft, and none affected annotated genes (Fig. 2 and Supplementary Table 1). Moreover, each mutation was identified at a subclonal level (range, 20–30%) and the mutant allele frequency for the lesions in tiers 1–4 in SJRB001 was retained in SJRB001X (Supplementary Fig. 15).

This result was surprising because several studies in mice and cell cultures have linked *RB1* inactivation to defects in chromosome segregation that result in aneuploidy<sup>4,5,13–15</sup> and chromosome instability<sup>4</sup>. We measured the distance between sister chromatids, the distance between kinetochores and the proportion of lagging chromatids in two *RB1*-deficient human retinoblastoma orthotopic xenografts<sup>16</sup> (SJRB001X and SJRB002X). Consistent with results from *RB1*-deficient retinal pigmented epithelium cells<sup>4</sup>, the distances between sister chromatids and between kinetochores were increased, and there was evidence of lagging chromosomes (Supplementary Figs 16 and 17). However, less variation in ploidy was observed during spectral karyotype analysis of SJRB001X and SJRB002X, which was more consistent with the ploidy of wild-type cells (Fig. 3a, b and Supplementary Table 13). Moreover, copy number variations were much lower in our cohort of 46 retinoblastomas than in tumours with known genome instability such as ovarian cancer

(Fig. 3c). Together, the cytogenetic data and WGS data suggest that the genome is stable and that newly acquired lesions do not provide a selective growth advantage and are thus probably passenger mutations (Supplementary Information, section 9).

Sequence mutations in NCBI RefSeq genes included silent single nucleotide variants (SNVs; green), missense SNVs (brown), nonsense SNVs (dark blue), splice-site mutations (pink) and insertion/deletion mutations (indels, red).

\*Germline mosaic. **c,** *BCOR* mutations identified in the discovery and

recurrency cohort.

### Identifying deregulated cancer pathways

There are many examples over the past several decades of epigenomic changes such as DNA methylation contributing to tumorigenesis<sup>17–19</sup>. Indeed, a recent study demonstrated changes in DNA methylation in Wilms' tumours<sup>20</sup>, which tend, like retinoblastomas, to have stable genomes. To explore whether epigenetic deregulation of genes or pathways promotes tumorigenesis in retinoblastoma, we carried out an integrative analysis of chromatin immunoprecipitation (ChIP) data, DNA methylation data and gene expression data using order statistics. The SJRB001X sample was used for ChIP assay (Supplementary Figs 18–20), and primary tumour and xenograft samples were used for both DNA methylation and gene expression assays. In all three analyses, experimental results in retinoblastoma tumours were compared with those from human fetal retinae. In this comparison, a total of 104 genes, including 15 known cancer genes (Fig. 4a and Supplementary Tables 14 and 15), were found to have significant differences, indicating that several key cancer genes were epigenetically deregulated.

### SYK is a novel therapeutic target

SYK is the fifth most significant gene identified by the integrative analysis and the only upregulated kinase gene (Supplementary Table 15 and Fig. 4a). *SYK* is expressed throughout the haematopoietic system, regulates immunomodulatory signalling and has been implicated in several haematologic malignancies<sup>21–24</sup>. Small-molecule inhibitors of SYK have been developed to treat autoimmune disorders<sup>25</sup>, and two of those agents, BAY 61-3606 and R406, have shown efficacy in preclinical leukaemia studies<sup>26–28</sup>.

ChIP-on-chip analysis showed increased activating histone modifications (H3K4me3 and K3K9/14Ac) at *SYK*'s promoter, and the repressive histone marker (H3K9me3) was unchanged. Binding of



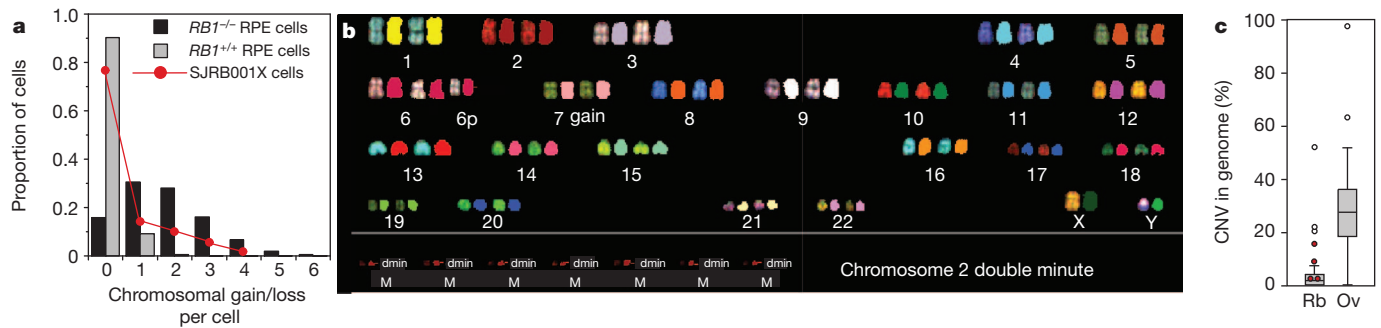


**Figure 3 | Analysis of aneuploidy and chromosome instability in retinoblastoma.** **a**, Chromosomal mis-segregation of SJRB001X cells after at least 21 rounds of cell division is plotted in red. RPE, retinal pigment epithelium. **b**, Representative spectral karyotype image of SJRB001X after the third passage in mice. **c**, Alterations in the 46 retinoblastoma (Rb) cases relative

to 153 high-grade serous ovarian cancer (Ov) cases from The Cancer Genome Atlas. The median percentage of the genome involved in copy number variations (CNVs) was 1.5% for retinoblastoma and 27.7% for ovarian cancer. Red circles, samples used for WGS.

RNA polymerase II to the SYK promoter was also increased (Fig. 4b and Supplementary Tables 14 and 15). These ChIP-on-chip results were validated in independent samples by real-time PCR analysis with reverse transcription (Fig. 4c), and we confirmed the increase in SYK gene expression (Fig. 4d). SYK protein levels were higher in human retinoblastoma orthotopic xenografts and cell lines than in human fetal retinae (Fig. 4e). To determine whether SYK is expressed in primary human retinoblastomas, we performed immunohistochemistry on a retinoblastoma tissue microarray or whole-eye sections. In total,

100% (82 of 82) showed very strong expression (3+) of SYK in all tumour cells; SYK was not expressed in normal retina (Fig. 4f). SYK's kinase activity is regulated through autophosphorylation at the Tyr 525 and Tyr 526 residues within its catalytic domain. These sites were phosphorylated in retinoblastoma cells, and this phosphorylation was reversed by exposure to BAY 61-3606 or R406 (Fig. 4g and data not shown).

To determine whether SYK expression is required for retinoblastoma growth, survival or both, we generated a short hairpin RNA (shRNA)

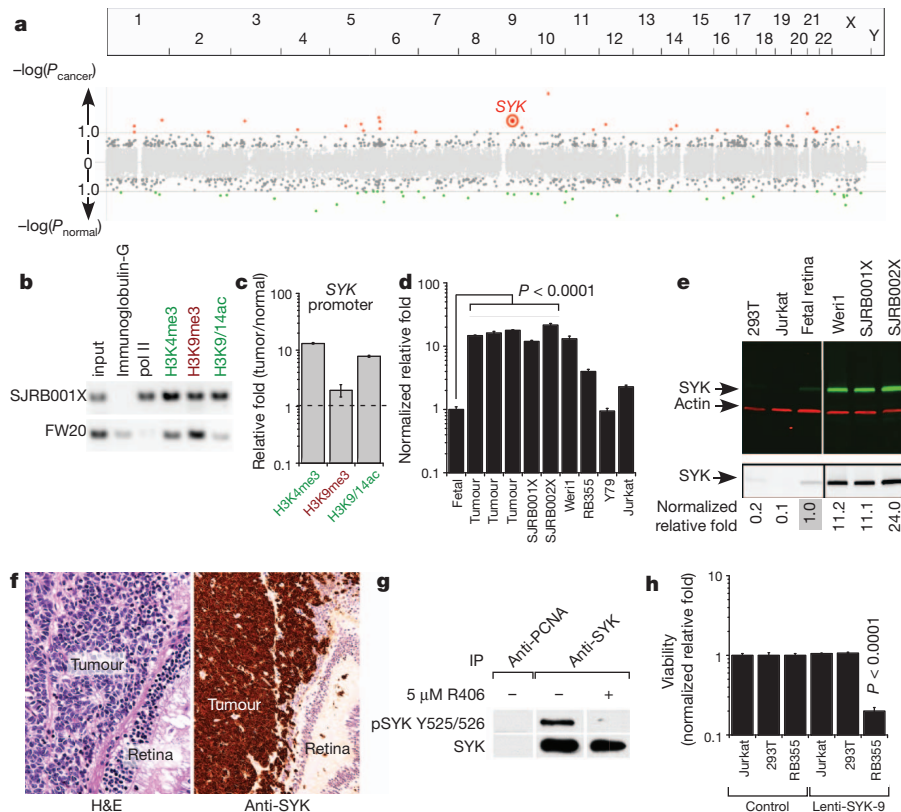


**Figure 4 | SYK is expressed in retinoblastoma and is required for survival.** **a**, Whole-genome view of the gene ranks based on integrating ChIP-on-chip, methylation and gene expression results. The y axis shows  $-\log(P)$ , where  $P$  is the  $P$  value of the  $Q$  statistic corrected for multiple testing. Significantly (false discovery rate,  $\leq 10\%$ ) downregulated (green) or upregulated (red) genes are shown. **b**, **c**, ChIP validation of histone markers of the SYK promoter including quantification by quantitative PCR with TaqMan probes. In **c**, each bar shows mean  $\pm$  s.d. of triplicate samples. **d**, SYK expression measured by quantitative PCR in fetal-week-20 retina (fetal), primary retinoblastoma (tumour), orthotopic xenografts (SJRB001X and SJRB002X) and cell lines. Each bar is

mean  $\pm$  s.d. of duplicate samples normalized to GPI1 expression.

**e**, Immunoblot of SYK (green) and actin (red) in orthotopic xenografts, human fetal retina and representative cell lines; black and white representation of the SYK immunoblot is in the lower panel. **f**, H&E (purple) and anti-SYK (brown) immunohistochemistry of retinoblastoma tissue. **g**, Immunoprecipitation analysis of SYK and pSYK Y525/526 from Wer11 retinoblastoma cells. **h**, Viability was measured in triplicate cultures 72 h after infection of retinoblastoma cells with a lentivirus vector expressing either a control lentivirus or an shRNA against SYK. Scale bars, 10  $\mu$ m.

against SYK and cloned it into the lentiviral vector Lenti-SYK-9. Lenti-SYK-9 efficiently knocked down SYK in retinoblastoma cell lines (Supplementary Fig. 21) and drastically increased apoptosis in retinoblastoma cells (Fig. 4h and Supplementary Fig. 21). Similar results were obtained *in vivo* using SJRB001X (data not shown). We used an empty lentiviral vector and a lentiviral vector encoding an SYK shRNA that less effectively reduced SYK expression (Lenti-SYK-6) as controls. Cell lines that do not express SYK (BJ, 293T and uninduced Jurkat cells) were used as controls and the Lenti-SYK-9 lentivirus had no effect on the growth or apoptosis of the control cells.

We exposed retinoblastoma cell lines that express high levels of SYK (Wer1 and RB355) to various concentrations of the SYK inhibitors BAY 61-3606 and R406 for 72 h and then measured cell viability. Jurkat (uninduced) and 293T cells were used as negative controls. Wer1 and RB355 cells were sensitive to both SYK inhibitors, but the Jurkat and 293T cells were unaffected (Fig. 5a). Transmission electron microscopy of retinoblastoma cells treated with the SYK inhibitors showed morphologic features consistent with cell death and mitochondrial defects (Supplementary Fig. 22); this was confirmed by scoring the proportion of activated caspase 3<sup>+</sup> cells (Fig. 5b, c and Supplementary Fig. 22). Jurkat cells showed no increase in activated caspase 3<sup>+</sup> cells after treatment with 10  $\mu$ M R406 or BAY 61-3606 (data not shown).

The proportions of cells from each line that incorporated EdU were similar, suggesting that retinoblastoma's cell cycle is not affected by SYK inhibition (Fig. 5d, e and Supplementary Fig. 22). The effects of targeting SYK were partly rescued by the pan-caspase inhibitor Q-VD-OPH (Supplementary Fig. 22). Less MitoTracker Red accumulated in retinoblastoma cells exposed to the SYK inhibitors (Supplementary Fig. 22), yet treatment of Jurkat cells with either inhibitor had no effect on MitoTracker Red accumulation (data not shown). Inhibiting SYK in B-CLL cells reduced their autophosphorylation of

SYK and destabilized MCL1<sup>26,29</sup>, the only anti-apoptotic member of the BCL2 family that is upregulated in retinoblastoma (data not shown). Both inhibitors reduced autophosphorylation of SYK on Y525/526 (Fig. 4g) and reduced MCL1 expression coincident with apoptosis (Fig. 5f).

We tested the efficacy of BAY 61-3606 *in vivo* using our SJRB001X model<sup>30</sup>. The chemotherapy regimen consisted of a single subconjunctival dose of BAY 61-3606 on day 1 and daily doses of topotecan (TPT) on days 1–5 until either six courses (21 days per course) were administered or the tumour had progressed and surgical enucleation was required (Fig. 5g, h). BAY 61-3606 plus TPT significantly improved the outcome ( $P = 0.003$ ; Fig. 5i), and its efficacy was correlated with an increase in activated caspase 3<sup>+</sup> cells in the treated eyes (Fig. 5j). Previous studies using this model have shown that TPT combined with subconjunctival carboplatin had no effect on tumour response or outcome<sup>30</sup>, so the improvement seen here can be attributed to targeting SYK. MCL1 expression was also reduced in the treated eyes, which is consistent with increased apoptosis and targeting of SYK *in vivo* (Fig. 5k). Together, these results suggest that SYK is a promising new target for treating retinoblastoma.

## Discussion

Genome sequencing reveals that retinoblastomas have a relatively stable genome. The mutational rate and number of structural variations per case that we assessed were among the lowest reported in human cancer to date. Moreover, in one example (SJRB002) the only non-silent mutation found was in *RB1*, and only two structural variations were detected. The minimal increase in passenger mutations in SJRB001X cells, despite prolonged passage, was also consistent with a relatively stable genome. These results are surprising because previous studies have shown that the functional inactivation of *RB1* can cause

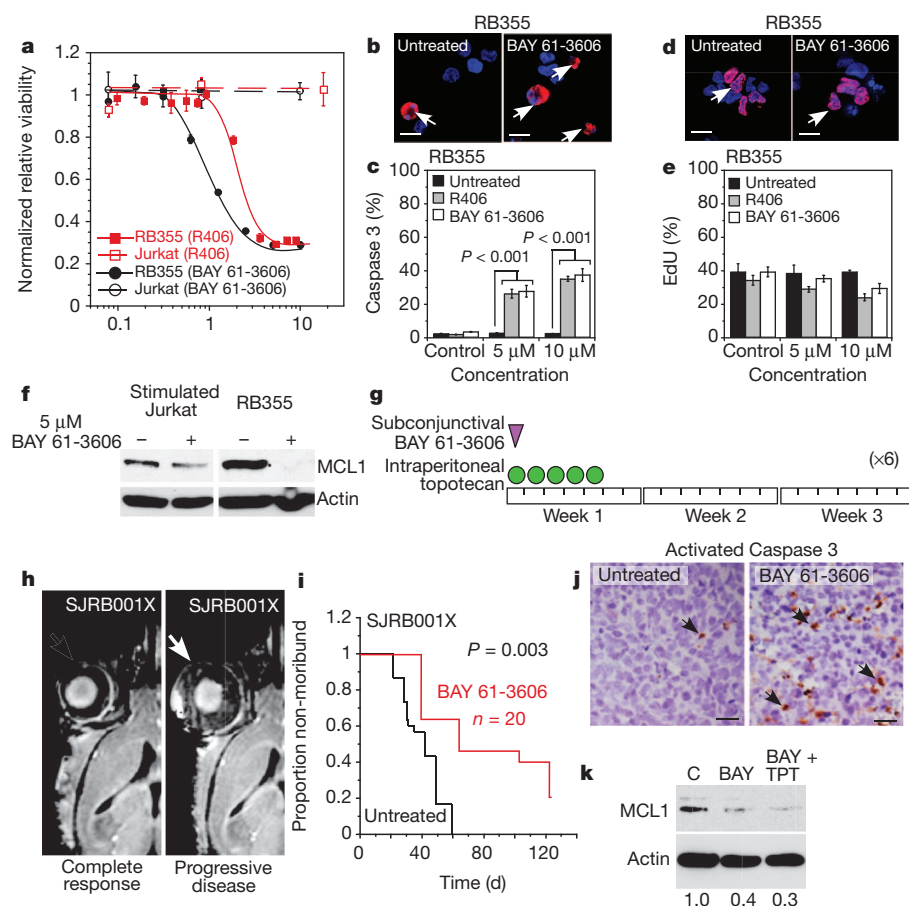


**Figure 5 | Retinoblastoma cells are sensitive to SYK inhibitors.** **a**, Dose response for SYK inhibitors R406 (red) and BAY 61-3606 (black) in RB355 retinoblastoma cells and a negative control (Jurkat). Each data point is mean  $\pm$  s.d. of triplicate samples. **b–e**, Immunofluorescence of activated caspase 3 (**b, c**) or EdU (**d, e**) (red) before and after treatment of RB355 cells with R406 or BAY 61-3606. A total of 250 cells were scored in duplicate for each sample and each treatment condition to derive the mean and s.d. Nuclei were stained with 4',6-diamidino-2-phenylindole (DAPI, blue). **f**, Treatment of stimulated Jurkat or RB355 cells with 5  $\mu$ M BAY 61-3606 for 24 h reduced MCL1 expression. **g**, Schematic of the treatment schedule for mice with SJRB001X tumours.

**h**, Representative magnetic resonance images of a mouse whose tumour responded after four courses of treatment with BAY 61-3606 (left) and another whose disease progressed during treatment (right). **i**, Survival curves show that treatment with BAY 61-3606 plus TPT improved outcome.

**j**, Immunostaining for activated caspase 3 (arrows) in eyes either untreated or treated with BAY 61-3606. **k**, Immunoblot showing reduction in MCL1 after treatment with BAY 61-3606 (BAY) or BAY 61-3606 plus TPT. C, control. Scale bars: (b, d); 10  $\mu$ m (j).

genomic instability. Although retinoblastoma cells show the mitotic defects that can lead to errors in chromosome segregation, the ploidy of retinoblastoma cells is stable *in vitro* and *in vivo*<sup>31,32</sup>. We do not exclude the possibility that RB1 inactivation promotes change in other contexts, but our data show that genomic instability is not a hallmark of retinoblastoma and do not explain how retinoblastomas progress so rapidly.

We propose that epigenetic mechanisms contribute to retinoblastoma tumorigenesis. We identified several known oncogenes and tumour suppressor genes with histone modifications and altered DNA methylation that correlated with changes in gene expression. Our key discovery was that SYK is important in retinoblastoma. Retinal progenitor cells and retinal neurons express little or no SYK, and SYK has no known function in the developing visual system. Moreover, no recurrent genetic lesions in SYK were identified by WGS or SNP array analysis to suggest that this gene drives retinoblastoma tumorigenesis. Only by integrating epigenetic and gene expression analyses did we identify SYK as an important oncogene in retinoblastoma. This is important not only for expanding our understanding of the biology of retinoblastoma but also for advancing immediate therapeutic options that were not previously considered, such as the use of BAY 61-3606 or R406. This study highlights the value of integrating WGS analyses of the genetic and epigenetic features of tumour genomes to finding a cure for cancers such as retinoblastoma.

## METHODS SUMMARY

Full details of sample acquisition, molecular and biochemical procedures, informatics and whole genome sequencing, and animal and drug studies are provided in Supplementary Information. The St Jude Children's Research Hospital Institutional Review Board approved experiments involving human subjects and informed consent was obtained from all subjects. For animal studies, all experiments were performed in accordance with federal guidelines and regulations. The St Jude Children's Research Hospital Institutional Animal Care and Use Committee approved all animal experiments. Lentiviral vectors (GIPZ with Lenti-SYK-9 #V3LHS-366147 and Lenti-SYK-6 #V3LHS-366143) encoding shRNAs against SYK were purchased from OpenBiosystems.

Received 27 March; accepted 24 November 2011.

Published online 11 January 2012.

1. Friend, S. H. *et al.* A human DNA segment with properties of the gene that predisposes to retinoblastoma and osteosarcoma. *Nature* **323**, 643–646 (1986).
2. Hanahan, D. & Weinberg, R. A. Hallmarks of cancer: the next generation. *Cell* **144**, 646–674 (2011).
3. Knudson, A. Mutation and cancer: statistical study of retinoblastoma. *Proc. Natl Acad. Sci. USA* **68**, 820–823 (1971).
4. Manning, A. L., Longworth, M. S. & Dyson, N. J. Loss of pRB causes centromere dysfunction and chromosomal instability. *Genes Dev.* **24**, 1364–1376 (2010).
5. Hernandez, E. *et al.* Rb inactivation promotes genomic instability by uncoupling cell cycle progression from mitotic control. *Nature* **430**, 797–802 (2004).
6. Chi, P., Allis, C. D. & Wang, G. G. Covalent histone modifications – miswritten, misinterpreted and mis-erased in human cancers. *Nature Rev. Cancer* **10**, 457–469 (2010).
7. Lu, J., Ruhf, M. L., Perrimon, N. & Leder, P. A genome-wide RNA interference screen identifies putative chromatin regulators essential for E2F repression. *Proc. Natl Acad. Sci. USA* **104**, 9381–9386 (2007).
8. Benetti, R. *et al.* A mammalian microRNA cluster controls DNA methylation and telomere recombination via Rbl2-dependent regulation of DNA methyltransferases. *Nature Struct. Mol. Biol.* **15**, 998 (2008).
9. Wen, H., Andrejka, L., Ashton, J., Karess, R. & Lipsick, J. S. Epigenetic regulation of gene expression by *Drosophila* Myb and E2F2-RBF via the Myb-MuvB/dREAM complex. *Genes Dev.* **22**, 601–614 (2008).
10. Bourgo, R. J. *et al.* SWI/SNF deficiency results in aberrant chromatin organization, mitotic failure, and diminished proliferative capacity. *Mol. Biol. Cell* **20**, 3192–3199 (2009).
11. Ley, T. J. *et al.* DNA sequencing of a cytogenetically normal acute myeloid leukaemia genome. *Nature* **456**, 66–72 (2008).
12. Corson, T. W. & Gallie, B. L. One hit, two hits, three hits, more? Genomic changes in the development of retinoblastoma. *Genes Chromosom. Cancer* **46**, 617–634 (2007).
13. Ganem, N. J., Godinho, S. A. & Pellman, D. A mechanism linking extra centrosomes to chromosomal instability. *Nature* **460**, 278–282 (2009).
14. Iovino, F., Lentini, L., Amato, A., & Di Leonardo, A. RB acute loss induces centrosome amplification and aneuploidy in murine primary fibroblasts. *Mol. Cancer* **5**, 38 (2006).

15. Amato, A., Lentini, L., Schillaci, T., Iovino, F. & Di Leonardo, A. RNAi mediated acute depletion of retinoblastoma protein (pRB) promotes aneuploidy in human primary cells via micronuclei formation. *BMC Cell Biol.* **10**, 79 (2009).
16. McEvoy, J. *et al.* Coexpression of normally incompatible developmental pathways in retinoblastoma genesis. *Cancer Cell* **16**, 260–275 (2011).
17. Feinberg, A. P. & Tycko, B. The history of cancer epigenetics. *Nature Rev. Cancer* **4**, 143–153 (2004).
18. Jones, P. A. & Laird, P. W. Cancer epigenetics comes of age. *Nature Genet.* **21**, 163–167 (1999).
19. Laird, P. W. Cancer epigenetics. *Hum. Mol. Genet.* **14** (suppl. 1), R65–R76 (2005).
20. Hansen, K. D. *et al.* Increased methylation variation in epigenetic domains across cancer types. *Nature Genet.* **43**, 768–775 (2011).
21. Hahn, C. K. *et al.* Proteomic and genetic approaches identify SYK as an AML target. *Cancer Cell* **16**, 281–294 (2009).
22. Chen, L. *et al.* SYK-dependent tonic B-cell receptor signaling is a rational treatment target in diffuse large B-cell lymphoma. *Blood* **111**, 2230–2237 (2008).
23. Feldman, A. L. *et al.* Overexpression of Syk tyrosine kinase in peripheral T-cell lymphomas. *Leukemia* **22**, 1139–1143 (2008).
24. Young, R. M. *et al.* Mouse models of non-Hodgkin lymphoma reveal Syk as an important therapeutic target. *Blood* **113**, 2508–2516 (2009).
25. Weinblatt, M. E. *et al.* An oral spleen tyrosine kinase (Syk) inhibitor for rheumatoid arthritis. *N. Engl. J. Med.* **363**, 1303–1312 (2010).
26. Baudot, A. D. *et al.* The tyrosine kinase Syk regulates the survival of chronic lymphocytic leukemia B cells through PKC $\delta$  and proteasome-dependent regulation of Mcl-1 expression. *Oncogene* **28**, 3261–3273 (2009).
27. Suljagic, M. *et al.* The Syk inhibitor fostamatinib disodium (R788) inhibits tumor growth in the E $\mu$ -TCL1 transgenic mouse model of CLL by blocking antigen-dependent B-cell receptor signaling. *Blood* **116**, 4894–4905 (2010).
28. Buchner, M. *et al.* Spleen tyrosine kinase inhibition prevents chemokine- and integrin-mediated stromal protective effects in chronic lymphocytic leukemia. *Blood* **115**, 4497–4506 (2010).
29. Gobessi, S. *et al.* Inhibition of constitutive and BCR-induced Syk activation downregulates Mcl-1 and induces apoptosis in chronic lymphocytic leukemia B cells. *Leukemia* **23**, 686–697 (2009).
30. Brennan, R. C. *et al.* Targeting the p53 pathway in retinoblastoma with subconjunctival Nutlin-3a. *Cancer Res.* **71**, 4205–4213 (2011).
31. Yan, Y. *et al.* Engraftment and growth of patient-derived retinoblastoma tumour in severe combined immunodeficiency mice. *Eur. J. Cancer* **36**, 221–228 (2000).
32. Squire, J., Gallie, B. L. & Phillips, R. A. A detailed analysis of chromosomal changes in heritable and non-heritable retinoblastoma. *Hum. Genet.* **70**, 291–301 (1985).

**Supplementary Information** is linked to the online version of the paper at [www.nature.com/nature](http://www.nature.com/nature).

**Acknowledgements** The WGS was supported as part of the St Jude Children's Research Hospital – Washington University Pediatric Cancer Genome Project. We thank J. Lahti, J. Dalton and M. Valentine for help with FISH analysis, L. Holmfeldt, J. Zhang and M. Barbato for help with sample preparation, and V. Valentine for spectral karyotype analysis. We thank I. Qaddoumi, C. Rodriguez-Galindo and B. Haik for the support of the St Jude Children's Research Hospital retinoblastoma clinical research and W. Lei, D. McGoldrick, D. Alford, S. Espy, J. Obenauer and K. Johnson for assistance with data acquisition, handling and analysis. We thank A. McArthur and C. Guss for editing the manuscript, J. Temirov for help with sister chromatid analysis, J. Thurman for help with histology, F. Krafcik for help with cell culture, J. Wu and C. Billups for statistical analysis, J. Jeon for help with lentiviral preparations and C. Bradley for assistance with preclinical testing. This work was supported, in part, by Cancer Center Support (CA21765) from the NCI; grants to M.A.D. from the NIH (EY014867 and EY018599), the American Cancer Society and the Research to Prevent Blindness Foundation; and the American Lebanese Syrian Associated Charities. M.A.D. is a Howard Hughes Medical Institute Early Career Scientist. This work was also supported by an American Cancer Society Fellowship to A.L.M., the MGH Cancer Center Saltonstall Foundation Scholarship to N.J.D. and funding from AstraZeneca and NIH grants GM81607 and CA64402 to N.J.D.

**Author Contributions** M.A.D., C.A.B., J. McEvoy, J.F.-O., R.B. and A.L.M. designed the experiments. L.D. and J.Z. led the data analysis. M.A.D., L.D., J.Z., X.C., A.U., G.W., J.W., M.R., J. Ma, S.P., S.M., P.G., G.N., D.Z., C.L., R.S.F., L.L.F., X.H., D.J.D. and K.O. performed the data analysis and provided bioinformatics support. M.A.D., J.Z., A.U., C.A.B., J. McEvoy, J.F.-O., R.B. and A.L.M. prepared the figures and tables. C.A.B., J.M., J.F.-O., R.B. and A.L.M. performed the laboratory experiments. J.F.-O. created the xenograft. M.W. provided samples. J.E., S.S. and C.M. provided assistance with sample processing and handling. A.B. and D.E. provided pathology support. M.A.D., C.N., E.R.M., R.K.W. and J.R.D. supervised the project. M.A.D. wrote the manuscript. J.Z., C.A.B., J. McEvoy, J.F.-O., L.D., M.W., E.R.M., S.S., C.M. and J.R.D. read and commented on the manuscript. J.Z., L.D., X.C., A.U., G.W., J.W., M.R., J. Ma, J.E., S.S., C.M., S.P., S.M., P.G., G.N., D.Z., C.L., R.S.F., L.L.F., X.H., D.J.D., K.O., C.N., E.R.M., A.B., D.E., R.K.W., J.R.D. and M.A.D. are part of the St Jude Children's Research Hospital – Washington University Pediatric Cancer Genome Project.

**Author Information** The whole-genome sequence data and SNP 6.0 data have been deposited in the NCBI dbGaP under accession number phs000352.v1.p1. Reprints and permissions information is available at [www.nature.com/reprints](http://www.nature.com/reprints). The authors declare no competing financial interests. This paper is distributed under the terms of the Creative Commons Attribution-Non-Commercial-Share Alike licence, and is freely available to all readers at [www.nature.com/nature](http://www.nature.com/nature). Readers are welcome to comment on the online version of this article at [www.nature.com/nature](http://www.nature.com/nature). Correspondence and requests for materials should be addressed to M.A.D. (michael.dyer@stjude.org), J.R.D. (james.downing@stjude.org) or R.K.W. (rwilson@wustl.edu).



# Structure of the carboxy-terminal region of a KCNH channel

Tinatin I. Brelidze<sup>1</sup>, Anne E. Carlson<sup>1</sup>, Banumathi Sankaran<sup>2</sup> & William N. Zagotta<sup>1</sup>

The KCNH family of ion channels, comprising *ether-à-go-go* (EAG), EAG-related gene (ERG), and EAG-like (ELK) K<sup>+</sup>-channel subfamilies, is crucial for repolarization of the cardiac action potential<sup>1</sup>, regulation of neuronal excitability<sup>2</sup> and proliferation of tumour cells<sup>3</sup>. The carboxy-terminal region of KCNH channels contains a cyclic-nucleotide-binding homology domain (CNBHD) and C-linker that couples the CNBHD to the pore<sup>4</sup>. The C-linker/CNBHD is essential for proper function and trafficking of ion channels in the KCNH family<sup>5–9</sup>. However, despite the importance of the C-linker/CNBHD for the function of KCNH channels, the structural basis of ion-channel regulation by the C-linker/CNBHD is unknown. Here we report the crystal structure of the C-linker/CNBHD of zebrafish ELK channels at 2.2-Å resolution. Although the overall structure of the C-linker/CNBHD of ELK channels is similar to the cyclic-nucleotide-binding domain (CNBD) structure of the related hyperpolarization-activated cyclic-nucleotide-modulated (HCN) channels<sup>10</sup>, there are marked differences. Unlike the CNBD of HCN, the CNBHD of ELK displays a negatively charged electrostatic profile that explains the lack of binding and regulation of KCNH channels by cyclic nucleotides<sup>4,11</sup>. Instead of cyclic nucleotide, the binding pocket is occupied by a short  $\beta$ -strand. Mutations of the  $\beta$ -strand shift the voltage dependence of activation to more depolarized voltages, implicating the  $\beta$ -strand as an intrinsic ligand for the CNBHD of ELK channels. In both ELK and HCN channels the C-linker is the site of virtually all of the intersubunit interactions in the C-terminal region. However, in the zebrafish ELK structure there is a reorientation in the C-linker so that the subunits form dimers instead of tetramers, as observed in HCN channels. These results provide a structural framework for understanding the regulation of ion channels in the KCNH family by the C-linker/CNBHD and may guide the design of specific drugs.

KCNH channels are voltage-gated K<sup>+</sup> channels that regulate the electrical excitability of heart and nerve cells. Similar to other K<sup>+</sup>-selective channels, KCNH channels are composed of four subunits surrounding a centrally located pore. Each subunit contains a voltage-sensor domain (transmembrane segments S1–S4), and a pore domain (transmembrane segments S5–S6 and an intervening pore-forming loop)<sup>4</sup> (Fig. 1a). KCNH channels have a Per-Arnt-Sim (PAS) domain in the amino-terminal region and a C-linker and CNBHD in the C-terminal region<sup>4,12</sup> (Fig. 1a). Many of the unique gating properties of KCNH channels arise from these intracellular domains<sup>3–7,13,14</sup>. Whereas the structure of the N-terminal region has been solved for ERG channels<sup>12,15–17</sup>, there is no structural information on the C-linker/CNBHD for any of the KCNH channels.

KCNH channels are part of a large family of cyclic-nucleotide-regulated channels that includes the HCN and cyclic-nucleotide-gated (CNG) channels (Supplementary Fig. 1a). Unlike HCN and CNG channels<sup>18</sup>, KCNH channels are not regulated by direct binding of cyclic nucleotides<sup>4,11</sup>. Instead, it has been suggested that the CNBHD of KCNH channels may be an orphan receptor for an as yet unidentified

channel regulator<sup>19</sup>. Indeed, it has been recently shown that mouse EAG1 channels are regulated by the direct binding of flavonoids to the C-linker/CNBHD<sup>19</sup>. In addition, the C-linker/CNBHD has been shown to interact with the N-terminal PAS domain and regulate gating<sup>6–8</sup>. Mutations in both of these regions in human ERG1 channels cause long-QT syndrome (LQTS), a heart arrhythmia that can cause cardiac death<sup>20</sup>. Therefore the C-linker/CNBHD is an important regulatory domain in KCNH channels.

To understand the role of the C-linker/CNBHD in KCNH channel function, we sought to determine the X-ray structure of the C-linker/CNBHD of an ion channel in the KCNH family. Using a screen based on fluorescence-detection size-exclusion chromatography (FSEC)<sup>21</sup>,

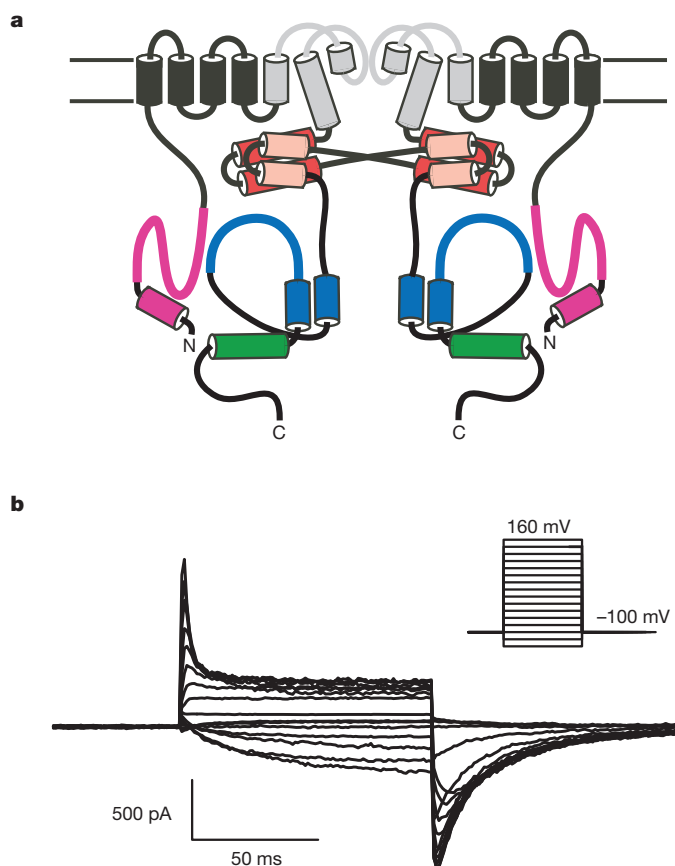


**Figure 1 | Topology and electrophysiological properties of zebrafish ELK channels.** **a**, Cartoon of two of the four subunits of ELK channels. The pore-forming loop and S5–S6 transmembrane domains are grey. The N-terminal  $\alpha$ -helix and PAS domain are magenta. The ‘elbow’ and ‘shoulder’ regions of the C-linker are represented by the red and pink cylinders, respectively. The  $\alpha$ -helix, represented by a cylinder, is green and the rest of the CNBHD is blue. **b**, Currents from zebrafish ELK channels recorded in the inside-out patch configuration.

<sup>1</sup>Department of Physiology and Biophysics, University of Washington School of Medicine, Box 357290, Seattle, Washington 98195-7290, USA. <sup>2</sup>Berkeley Center for Structural Biology, Lawrence Berkeley National Laboratory, 1 Cyclotron Road, BLDG 6R2100, Berkeley, California 94720, USA.

we identified the C-linker/CNBHD of *Danio rerio* (zebrafish) ELK as a potential candidate for crystallization. Zebrafish ELK shares substantial sequence similarity with mammalian ELK channels (Supplementary Fig. 1c).

Expression of zebrafish ELK channels in *Xenopus laevis* oocytes gave rise to robust voltage-activated  $K^+$  currents with electrophysiological characteristics similar to the ones reported previously for mammalian ELK channels<sup>22–25</sup> (Fig. 1b). Zebrafish ELK channels were activated by depolarizing voltage steps and showed inactivation at voltages  $> +40$  mV (Fig. 1b). The half-maximal activation voltage ( $V_{1/2}$ ) was  $-45.3 \pm 3.2$  mV ( $n = 18$ ) with a slope of e-fold per  $13.8 \pm 0.6$  mV ( $n = 18$ ) (Supplementary Fig. 1b). In comparison, human ELK2 channels activate with  $V_{1/2}$  of  $-22.8 \pm 0.5$  mV and a slope of  $18.1 \pm 0.4$  mV, and inactivate at voltages  $> +20$  mV (ref. 22). As previously observed for mouse EAG and human ERG channels<sup>4,11</sup>, application of cAMP had no

effect on the currents through zebrafish ELK channels (Supplementary Fig. 1b).

The C-linker/CNBHD of zebrafish ELK channels crystallized in two space groups,  $C222_1$  and  $P12_11$ , and diffracted X-rays to 2.2- and 2.3-Å resolution, respectively (Supplementary Table 1). The structure of the zebrafish ELK C-linker/CNBHD was solved by the single-wavelength anomalous dispersion (SAD) phasing method using selenomethionine derivative crystals.

The crystal structure revealed that the C-linker of zebrafish ELK channels consists of six  $\alpha$ -helices ( $\alpha A' - \alpha F'$ ) with  $\alpha A'$  and  $\alpha B'$  helices forming an antiparallel helix–turn–helix motif. The CNBHD consists of eight  $\beta$ -strands forming an antiparallel  $\beta$ -roll, three  $\alpha$ -helices ( $\alpha A - \alpha C$ ), and a short  $\beta$ -strand ( $\beta 9$ ) after the  $\alpha C$ -helix (Fig. 2a). The general architecture of the CNBHD of ELK is similar to the fold of CNBDs in other proteins<sup>26</sup>.

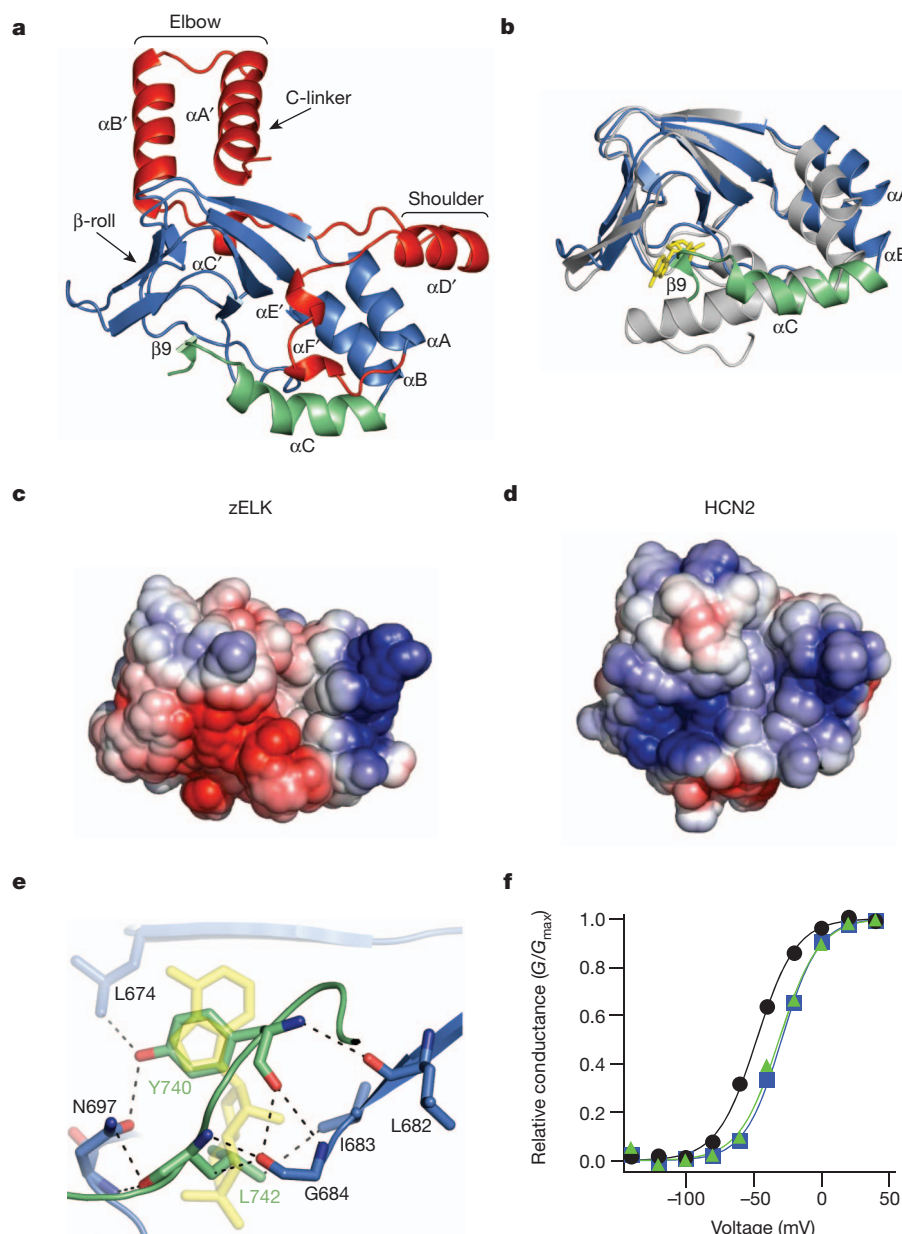


**Figure 2 | Structure of the C-linker/CNBHD.** **a**, Ribbon representation of a monomer of the C-linker/CNBHD of zebrafish ELK (zELK) channels. **b**, Alignment of the CNBHD of zebrafish ELK (the  $\alpha C$ -helix is green and the rest is blue) and mouse HCN2 (grey) channels<sup>10</sup>. cAMP in the HCN2 structure is yellow. **c**, **d**, Electrostatic potential surface of the CNBHD of zebrafish ELK (**c**) and HCN2 channels (**d**), viewed in the same orientation as in **b**. **e**, Residues

in the  $\beta$ -roll cavity interacting with residues Y740 and L742 of the intrinsic ligand. Dashed lines show both polar and non-polar interactions. cAMP from the HCN2 structure is shown in yellow. **f**, Representative conductance–voltage relationships for wild-type (black), Y740A mutant (blue) and  $\Delta 740$ –742 mutant (green) zebrafish ELK channels.

Although the overall folds of the CNBHDs of ELK and HCN2 channels are similar, superposition of the two structures reveals remarkable differences (Fig. 2b and Supplementary Fig. 2a). The root mean squared deviation (r.m.s.d.) for the  $\alpha$ -carbons of the two structures (residues 626–740 of zebrafish ELK and residues 523–635 of mouse HCN2; ref. 10) is 4.7 Å with the largest differences observed for the three  $\alpha$ -helices in the CNBHD. The  $\alpha$ A- and  $\alpha$ B-helices of ELK are moved away from the cavity formed by the  $\beta$ -roll that serves as the cyclic-nucleotide-binding pocket in other CNBD-containing proteins. The  $\alpha$ A-helix is moved by about 4.5 Å and the  $\alpha$ B-helix is moved by about 3.4 Å relative to their positions in the cAMP-bound form of HCN2. The position of the  $\alpha$ A-helix of ELK is similar to the position of the  $\alpha$ A-helix in cAMP-bound MlotiK channels<sup>27</sup> and the position of the  $\alpha$ B-helix is similar to the unliganded MlotiK channels<sup>27–29</sup> (Supplementary Fig. 3). The differences in the  $\alpha$ C-helix are even more marked. The  $\alpha$ C-helix of ELK is shorter and bent, and is followed by a short  $\beta$ -strand,  $\beta$ 9 (Fig. 2b). These differences all reside in the  $\alpha$ -helices of the CNBD that undergo ligand-dependent conformational changes in HCN and CNG channels.

Out of the ten residues that directly interact with cAMP in HCN2 channels, only three (V667, L677 and G684) are conserved in zebrafish ELK channels (Supplementary Fig. 4). Moreover, most of the residues in the phosphate-binding cassette of HCN2, including R591, are not conserved, and the  $\alpha$ P-helix is missing in zebrafish ELK. The electrostatic profiles of the CNBHD of ELK and HCN2 channels reveal that the putative ligand-binding pocket formed by the  $\beta$ -roll cavity is negatively charged for ELK but positively charged for HCN2 channels (Fig. 2c, d). The negatively charged electrostatic profile would not be favourable for binding of a negatively charged cyclic nucleotide. Consistent with this, crystallization of zebrafish ELK in the presence of 5 mM cAMP did not reveal any new electron density corresponding to cAMP (Supplementary Table 1 and data not shown). These differences in the CNBD structures probably account, at least in part, for the lack of cyclic nucleotide regulation of KCNH channels<sup>4,11</sup>.

The zebrafish ELK CNBHD structure displays another unique feature: the  $\beta$ 9-strand after the  $\alpha$ C-helix forms direct interactions with the  $\beta$ -roll cavity in ELK channels (Fig. 2e and Supplementary Figs 2b and 5). Interestingly, the phenyl ring of Y740 on the  $\beta$ 9-strand is positioned in an analogous place to the purine ring of cAMP in HCN2 channels and L742 is positioned in an analogous place to the cyclic phosphate of cAMP<sup>10</sup>. Virtually all ion channels in the KCNH family have either tyrosine or phenylalanine at the position corresponding to Y740 in zebrafish ELK and a leucine at position corresponding to L742 (Supplementary Fig. 1c). These observations raise an intriguing possibility that the  $\beta$ 9-strand might act as an intrinsic ligand, a portion of the protein that occupies the ligand-binding site whose displacement regulates the channel.

To explore a possible regulatory role of the  $\beta$ 9-strand, we examined the effect of mutations in the  $\beta$ 9-strand on the function of intact zebrafish ELK channels. Zebrafish ELK channels with either a point mutation Y740A or deletion of the  $\beta$ 9-strand ( $\Delta$ 740–742) exhibited robust voltage-activated currents that inactivated at voltages  $> +40$  mV, similar to wild-type ELK channels (Supplementary Fig. 6a). However, for both mutations, the  $V_{1/2}$  values for activation were significantly larger ( $P < 0.01$ , Student's  $t$ -test) than the  $V_{1/2}$  of wild-type channels (wild type:  $-45.3 \pm 3.2$  mV,  $n = 18$ ; Y740A:  $-29.8 \pm 4.4$  mV,  $n = 19$ ;  $\Delta$ 740–742:  $-28.3 \pm 4.4$  mV,  $n = 11$ ) (Fig. 2f and Supplementary Fig. 6b). This 15 mV shift in the voltage dependence of activation in the mutants is similar in magnitude to the effect of cAMP on HCN channels, lending further support to the possibility that the  $\beta$ 9-strand may function as an intrinsic ligand for ELK channels. Interestingly, mutations in the region corresponding to the  $\beta$ 9-strand of human ERG channels are associated with LQTS<sup>20,30</sup>. Additional experiments will need to be done to further test the intrinsic ligand hypothesis.

Similar to HCN channels, the C-linker of zebrafish ELK channels is the primary region of intersubunit interactions in the crystal structure

with a buried solvent accessible surface area of about 2,520 Å<sup>2</sup> for each subunit (Fig. 3a). The intersubunit interface can be likened to an 'elbow on the shoulder', where the 'elbow' formed by the  $\alpha$ A'- and  $\alpha$ B'-helices of one subunit is resting on the 'shoulder' formed by the  $\alpha$ D'-helix and the  $\alpha$ C'- $\alpha$ D' loop of the neighbouring subunit (Figs 2a, 3a, d and Supplementary Fig. 7). The structure of the elbow-on-the-shoulder interface between neighbouring subunits is very similar between ELK and HCN2 channels (Fig. 3d), except that the region before the  $\alpha$ D'-helix is not  $\alpha$ -helical in ELK.

Unexpectedly, however, the elbow-on-the-shoulder interface in zebrafish ELK occurs with a two-fold related subunit (rotated by 180°), instead of a four-fold related subunit (rotated by 90°) like in HCN channels (Fig. 3a, b). This difference results from a  $\sim 55^\circ$  rotation in the region after the  $\alpha$ B'-helix in ELK relative to HCN2 channels (Fig. 3c). The implication of this marked rotation of the 'elbow' is a dimeric assembly of the C-linker/CNBHDs in the zebrafish ELK structure (Fig. 3a), as opposed to the tetrameric assembly of the C-linker/CNBHDs in HCN channels<sup>10</sup> (Fig. 3b). The intersubunit interface and the dimeric assembly are preserved in both sets of molecules in the asymmetric unit and for both crystal forms of zebrafish ELK (Supplementary Fig. 8), suggesting that they are independent of crystal contacts. FSEC experiments also revealed that the GFP-tagged C-linker/CNBHD of zebrafish ELK channels dimerizes at sufficiently

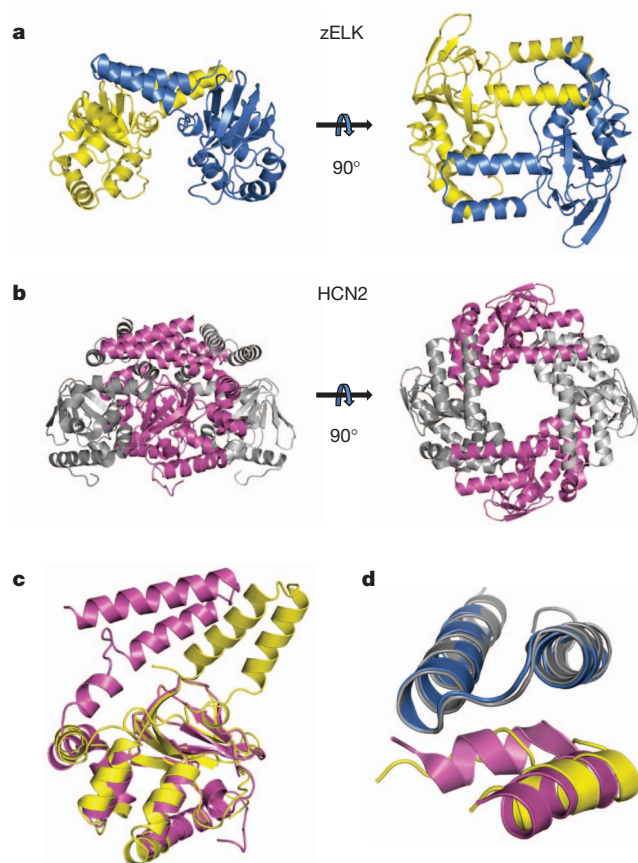


**Figure 3 | Structural comparison of the C-linker regions and quaternary arrangement of the C-linker/CNBHDs of zebrafish ELK and HCN2 channels.** **a**, A dimer formed by the C-linker/CNBHD of zebrafish ELK (zELK) channels viewed perpendicular (left) and parallel (right) to the two-fold axis. **b**, A tetramer formed by the C-linker/CNBHD of HCN2 channels viewed perpendicular (left) and parallel (right) to the four-fold axis. **c**, Superposition of the ribbon representations of the C-linker/CNBHD monomers of zebrafish ELK (yellow) and mouse HCN2 channels (magenta) using the alignment of the  $\alpha$ -carbons of the CNBDs of these structures. **d**, Superposition of the elbow-on-the-shoulder interface of zebrafish ELK (blue, elbow; yellow, shoulder) and mouse HCN2 channels (grey, elbow; magenta, shoulder).



high concentrations in solution (Supplementary Fig. 9). Additional experiments would be required to determine if the quaternary state of the C-linker/CNBHD in intact channels has a two-fold or four-fold symmetry (Supplementary Discussion and Supplementary Fig. 10).

Here we present the first crystal structure, to our knowledge, of the C-linker/CNBHD of a KCNH channel. The structure reveals a putative ligand-binding pocket that differs markedly from the cyclic-nucleotide-binding pocket of HCN channels and does not appear to bind cyclic nucleotides. Instead of a ligand, the putative ligand-binding pocket of zebrafish ELK channels is occupied by a novel  $\beta$ 9-strand after the  $\alpha$ C-helix. Mutations of the  $\beta$ 9-strand shifted the voltage dependence of activation, suggesting that the  $\beta$ 9-strand is a regulatory element for ELK channels that acts as an intrinsic ligand. The crystal structure also displays an unexpected conformation of the C-linker that leads to dimerization of the C-linker/CNBHDs of zebrafish ELK channels. These findings provide a structural framework to understand the regulation of KCNH channels by the C-linker/CNBHD.

## METHODS SUMMARY

**Protein purification.** The C-linker/CNBHD of zebrafish ELK (amino acids Q543–L750) was subcloned into a modified pMalc2T vector (New England Biolabs) containing an N-terminal MBP affinity tag followed by a thrombin cleavage site. The protein was expressed in BL21 (DE3) *Escherichia coli* cells as previously described<sup>11</sup>, purified on an amylose affinity column and then on an ion-exchange column after an overnight cleavage with thrombin at 4 °C. The purified protein was concentrated to 20–30 mg ml<sup>-1</sup> for crystallization. Selenomethionine derivatives were generated as previously described<sup>10</sup>.

**Crystallography.** Crystals were grown at 20 °C using the sitting-drop vapour diffusion method. 150-nl drops of the concentrated protein and reservoir solutions were mixed 1:1 by a Mosquito (TTP LABTECH). The final protein solution contained: ~250 mM KCl, 1 mM TCEP, 30 mM HEPES, 100 mM citric acid, pH 3.5. The reservoir solution contained: 6% w/v 1,5-diaminopentane dihydrochloride, 180 mM ammonium acetate, 22.5% (w/v) PEG 3350, 90 mM Tris; pH 8.5 for crystal T141; 1.8 M non-detergent sulphobetaine (NDSB)-211, 180 mM ammonium acetate, 22.5% (w/v) PEG 3350, 90 mM Tris, pH 8.5 for crystal T42; 6% (w/v) D-(+)-galactose, 180 mM ammonium sulphate, 22.5% (w/v) PEG 3350, 90 mM HEPES, pH 7.5 for crystal T26; and 5 mM cAMP, 180 mM ammonium acetate, 22.5% (w/v) PEG 3350, 90 mM Tris, pH 8.5 for crystal T84.

The crystallographic data are summarized in Supplementary Table 1 and details of the structure determination are described in Methods.

**Electrophysiology.** The full-length zebrafish ELK channel (GenInfo Identifier (GI) 159570347) with a C-terminal Flag epitope was generated by Bio Basic Inc. and subcloned into the pGEMHE oocyte expression vector. Expression of the wild-type and mutant zebrafish ELK channels in *Xenopus* oocytes and current recordings were done as previously described<sup>11</sup>. Both pipette and bath solutions contained 130 mM KCl, 10 mM HEPES, 0.2 mM EDTA, pH 7.2. 1 mM cAMP was added to the bath solution as indicated.

**Full Methods** and any associated references are available in the online version of the paper at [www.nature.com/nature](http://www.nature.com/nature).

Received 29 May; accepted 23 November 2011.

Published online 9 January 2012.

1. Sanguinetti, M. C. & Tristani-Firouzi, M. hERG potassium channels and cardiac arrhythmia. *Nature* **440**, 463–469 (2006).
2. Zhang, X. *et al.* Deletion of the potassium channel Kv12.2 causes hippocampal hyperexcitability and epilepsy. *Nature Neurosci.* **13**, 1056–1058 (2010).
3. Camacho, J. *Ether-à-go-go* potassium channels and cancer. *Cancer Lett.* **233**, 1–9 (2006).
4. Ganetzky, B., Robertson, G. A., Wilson, G. F., Trudeau, M. C. & Titus, S. A. The Eag family of K<sup>+</sup> channels in *Drosophila* and mammals. *Ann. NY Acad. Sci.* **868**, 356–369 (1999).
5. Al-Owais, M., Bracey, K. & Wray, D. Role of intracellular domains in the function of the hERG potassium channel. *Eur. Biophys. J.* **38**, 569–576 (2009).
6. Stevens, L., Ju, M. & Wray, D. Roles of surface residues of intracellular domains of hERG potassium channels. *Eur. Biophys. J.* **38**, 523–532 (2009).
7. Gustina, A. S. & Trudeau, M. C. hERG potassium channel gating is mediated by N- and C-terminal region interactions. *J. Gen. Physiol.* **137**, 315–325 (2011).
8. Muskett, F. W. *et al.* Mechanistic insight into human *ether-à-go-go*-related gene (hERG) K<sup>+</sup> channel deactivation gating from the solution structure of the EAG domain. *J. Biol. Chem.* **286**, 6184–6191 (2011).

9. Zhou, Z., Gong, Q., Epstein, M. L. & January, C. T. hERG channel dysfunction in human long QT syndrome. Intracellular transport and functional defects. *J. Biol. Chem.* **273**, 21061–21066 (1998).
10. Zagotta, W. N. *et al.* Structural basis for modulation and agonist specificity of HCN pacemaker channels. *Nature* **425**, 200–205 (2003).
11. Brelidze, T. I., Carlson, A. E. & Zagotta, W. N. Absence of direct cyclic nucleotide modulation of mEAG1 and hERG1 channels revealed with fluorescence and electrophysiological methods. *J. Biol. Chem.* **284**, 27989–27997 (2009).
12. Morais Cabral, J. H. *et al.* Crystal structure and functional analysis of the hERG potassium channel N terminus: a eukaryotic PAS domain. *Cell* **95**, 649–655 (1998).
13. Schonherr, R. & Heinemann, S. H. Molecular determinants for activation and inactivation of hERG, a human inward rectifier potassium channel. *J. Physiol. (Lond.)* **493**, 635–642 (1996).
14. Wang, J., Trudeau, M. C., Zappia, A. M. & Robertson, G. A. Regulation of deactivation by an amino terminal domain in human *ether-à-go-go*-related gene potassium channels. *J. Gen. Physiol.* **112**, 637–647 (1998).
15. Muskett, F. W. *et al.* Mechanistic insight into hERG K<sup>+</sup> channel deactivation gating from the solution structure of the EAG domain. *J. Biol. Chem.* **286**, 6184–6191 (2011).
16. Li, Q. *et al.* NMR solution structure of the N-terminal domain of hERG and its interaction with the S4–S5 linker. *Biochem. Biophys. Res. Commun.* **403**, 126–132 (2010).
17. Ng, C. A. *et al.* The N-terminal tail of hERG contains an amphipathic  $\alpha$ -helix that regulates channel deactivation. *PLoS ONE* **6**, e16191 (2011).
18. Craven, K. B. & Zagotta, W. N. CNG and HCN channels: two peas, one pod. *Annu. Rev. Physiol.* **68**, 375–401 (2006).
19. Brelidze, T. I., Carlson, A. E., Davies, D. R., Stewart, L. J. & Zagotta, W. N. Identifying regulators for EAG1 channels with a novel electrophysiology and tryptophan fluorescence based screen. *PLoS ONE* **5**, e12523 (2010).
20. Splawski, I. *et al.* Spectrum of mutations in long-QT syndrome genes. *KVLQT1*, *HERG*, *SCN5A*, *KCNK1*, and *KCNK2*. *Circulation* **102**, 1178–1185 (2000).
21. Kawate, T. & Gouaux, E. Fluorescence-detection size-exclusion chromatography for precrystallization screening of integral membrane proteins. *Structure* **14**, 673–681 (2006).
22. Becchetti, A. *et al.* The functional properties of the human *ether-à-go-go*-like (hELK2) K<sup>+</sup> channel. *Eur. J. Neurosci.* **16**, 415–428 (2002).
23. Engeland, B., Neu, A., Ludwig, J., Roeper, J. & Pongs, O. Cloning and functional expression of rat *ether-à-go-go*-like K<sup>+</sup> channel genes. *J. Physiol. (Lond.)* **513**, 647–654 (1998).
24. Trudeau, M. C., Titus, S. A., Branchaw, J. L., Ganetzky, B. & Robertson, G. A. Functional analysis of a mouse brain Elk-type K<sup>+</sup> channel. *J. Neurosci.* **19**, 2906–2918 (1999).
25. Zou, A. *et al.* Distribution and functional properties of human KCNH8 (Elk1) potassium channels. *Am. J. Physiol. Cell Physiol.* **285**, C1356–C1366 (2003).
26. Rehmann, H., Wittinghofer, A. & Bos, J. L. Capturing cyclic nucleotides in action: snapshots from crystallographic studies. *Nature Rev. Mol. Cell Biol.* **8**, 63–73 (2007).
27. Altieri, S. L. *et al.* Structural and energetic analysis of activation by a cyclic nucleotide binding domain. *J. Mol. Biol.* **381**, 655–669 (2008).
28. Clayton, G. M., Silverman, W. R., Heginbotham, L. & Morais-Cabral, J. H. Structural basis of ligand activation in a cyclic nucleotide regulated potassium channel. *Cell* **119**, 615–627 (2004).
29. Schunke, S., Stoldt, M., Lecher, J., Kaupp, U. B. & Willbold, D. Structural insights into conformational changes of a cyclic nucleotide-binding domain in solution from *Mesorhizobium loti* K1 channel. *Proc. Natl Acad. Sci. USA* **108**, 6121–6126 (2011).
30. Napolitano, C. *et al.* Genetic testing in the long QT syndrome: development and validation of an efficient approach to genotyping in clinical practice. *J. Am. Med. Assoc.* **294**, 2975–2980 (2005).

**Supplementary Information** is linked to the online version of the paper at [www.nature.com/nature](http://www.nature.com/nature).

**Acknowledgements** We thank M. Munari, S. Camp, S. Cunnington and G. Sheridan for excellent technical assistance. We thank the beamline staff at the Advanced Light Source (ALS) and especially P. Zwart for help with data analysis. We also thank the members of the Zagotta laboratory for helpful discussions. This work was supported by the Howard Hughes Medical Institute, National Institutes of Health (NIH) grant R01 EY010329 (W.N.Z.) and NIH grant F32 HL095241 (A.E.C.). The Berkeley Center for Structural Biology is supported in part by the NIH, National Institute of General Medical Sciences and the Howard Hughes Medical Institute. The ALS is supported by the Director, Office of Science, Office of Basic Energy Sciences, of the US Department of Energy under contract no. DE-AC02-05CH11231.

**Author Contributions** T.I.B. and W.N.Z. conceived the experiments. T.I.B. performed the crystallographic experiments, and B.S. helped with the crystallographic data analysis. A.E.C. and W.N.Z. performed the electrophysiology experiments and data analysis. T.I.B. and W.N.Z. wrote the manuscript.

**Author Information** Atomic coordinates and structure factors for the reported crystal structures have been deposited with the Protein Data Bank under accession codes 3UKN, 3UKT and 3UKV (see Supplementary Table 1 for identifications). Reprints and permissions information is available at [www.nature.com/reprints](http://www.nature.com/reprints). The authors declare no competing financial interests. Readers are welcome to comment on the online version of this article at [www.nature.com/nature](http://www.nature.com/nature). Correspondence and requests for materials should be addressed to W.N.Z. ([zagotta@u.washington.edu](mailto:zagotta@u.washington.edu)).

## METHODS

**FSEC.** The C-linker/CNBHD of zebrafish ELK channels (amino acids Q543–L750) was covalently fused to a C-terminal GFP in the pCGFP-BC bacterial expression vector provided by T. Kawate and E. Gouaux<sup>21</sup>. The construct was transformed into BL21 (DE3) cells. 5 ml cultures of the cells were grown at 37 °C, induced with IPTG and harvested by centrifugation. The cell pellets were resuspended in a lysis buffer (500 mM KCl, 1 mM TCEP, 30 mM HEPES, 1 mM PMSF and 2.5 mg ml<sup>−1</sup> DNase; pH 8.0) and sonicated. Insoluble protein was separated by centrifugation and the supernatant was analysed on a Superdex 200 10/300 GL column (GE Healthcare).

**Scale-up protein purification.** The C-linker/CNBHD of zebrafish ELK (amino acids Q543–L750) was subcloned into a modified pMALc2T vector (New England Biolabs) containing an N-terminal MBP affinity tag followed by a thrombin cleavage site. The protein was expressed in BL21 (DE3) *Escherichia coli* cells as previously described<sup>11</sup>. The cells were harvested by centrifugation, resuspended in a lysis buffer (500 mM KCl, 1 mM TCEP, 30 mM HEPES, 1 mM PMSF and 2.5 mg ml<sup>−1</sup> DNase; pH 8.0) and lysed in an Emulsiflex-C5 (Avestin). Insoluble protein was separated by centrifugation. The C-linker/CNBHD of zebrafish ELK was purified on an amylose affinity column and was then loaded on a HiTrap SP FF ion-exchange column following an overnight cleavage with thrombin at 4 °C. The protein was eluted with a linear KCl gradient and 100 mM citric acid (pH 3.5) was added to the final protein solution to increase the solubility of the protein at high concentrations. The protein was concentrated to 20–30 mg ml<sup>−1</sup> for crystallization. Selenomethionine derivatives were generated as previously described<sup>10,31</sup>.

**Crystallization.** Crystals were grown at 20 °C using the sitting-drop vapour diffusion method. 150-nl drops of the concentrated protein and reservoir solution were mixed 1:1 by a Mosquito (TTP LABTECH). The final protein solution contained: ~250 mM KCl, 1 mM TCEP, 30 mM HEPES, 100 mM citric acid, pH 3.5. The reservoir solution contained: 6% w/v 1,5-diaminopentane dihydrochloride, 180 mM ammonium acetate, 22.5% (w/v) PEG 3350, 90 mM Tris; pH 8.5 for crystal T141; 1.8 M non-detergent sulphobetaine (NDSB)-211, 180 mM ammonium acetate, 22.5% (w/v) PEG 3350, 90 mM Tris, pH 8.5 for crystal T42; 6% (w/v) D-(+)-galactose, 180 mM ammonium sulphate, 22.5% (w/v) PEG 3350, 90 mM HEPES, pH 7.5 for crystal T26; and 5 mM cAMP, 180 mM ammonium acetate, 22.5% (w/v) PEG 3350, 90 mM Tris, pH 8.5 for crystal T84. The crystals were cryoprotected in reservoir solution supplemented with 25% glycerol before being flash frozen in liquid nitrogen.

**Data collection and structure determination.** Diffraction data sets were collected at the Advanced Light Source (beamline 8.2.1) at Lawrence Berkeley National Laboratory in Berkeley, California. Data were analysed with Mosfilm<sup>32</sup> and HKL2000<sup>33</sup> software. Molecular replacement using the structure of the C-linker/CNBHD of HCN2 channels as a search model failed to find a solution. Therefore, the structure of the zebrafish ELK C-linker/CNBHD was solved by the SAD phasing of selenomethionine derivative crystal T141 using PHENIX<sup>34</sup> followed by phase extension to 2.25 Å resolution using a native data set. Structures for the rest of the data sets were solved by molecular replacement using this structure as a search model followed by numerous cycles of refinement in PHENIX and manual model building in Coot<sup>35</sup>. The molecular replacement was carried out using Phaser in PHENIX<sup>34</sup>. The asymmetric unit contained three molecules in the C222<sub>1</sub> space group and four in the P12<sub>1</sub>1 space group. The structures of different ELK molecules in the asymmetric unit and molecules in the two different space groups were very similar, with r.m.s.d. values for the  $\alpha$ -carbons calculated for the entire sequence of the resolved C-linker/CNBHD ranging from 0.4–0.7 Å (Supplementary Fig. 8). The crystallographic data and refinement statistics are summarized in Supplementary Table 1. Electron density was visible for all but

several terminal residues in molecules A and B of the native structure in the C222<sub>1</sub> space group. Molecules A and B of the native C222<sub>1</sub> structure were used for analysis in this paper. Analysis with Molprobity<sup>36</sup> of the final models indicated no Ramachandran outliers for T42 and T26 structures, and 0.59 (%) for T84. Figures were made using PyMOL<sup>37</sup>. The topology of the C-linker/CNBHD of zebrafish ELK was defined by PROCHECK (<http://www.ebi.ac.uk/pdbsum/>). The phylogenetic tree in Supplementary Fig. 1a was computed with Cobalt<sup>38</sup> (<http://www.ncbi.nlm.nih.gov/tools/cobalt/>). The GI numbers for the amino acid sequences aligned in Supplementary Fig. 1c were: zebrafish ELK, 159570347; human ELK1, 27886667; human ELK2, 26006814; human ERG1, 103488986; mouse EAG1, 487740; bovine CNGA1, 231739; mouse HCN2, 148699724. The electrostatic potential surface calculations were carried out using the APBS<sup>39</sup> plugin for PyMOL and the PARSE force field, and coloured from red (−3 kT/e) to blue (+3 kT/e) where k is Boltzmann's constant, T is absolute temperature, and e is the charge on an electron.

**Electrophysiology.** The full-length zebrafish ELK channel (GI: 159570347) with a C-terminal Flag epitope was generated by Bio Basic Inc. and subcloned into the pGEMHE oocyte expression vector. The cRNA was transcribed using the T7 mMessage mMachine Ultra kit (Ambion). Expression of the wild-type and mutant (Y740A and  $\Delta$ 740–742) zebrafish ELK channels in *Xenopus* oocytes and current recordings from inside-out patches allowing 10 min for run up following excision were done as described before<sup>11</sup>. Both pipette and bath solutions contained 130 mM KCl, 10 mM HEPES, 0.2 mM EDTA, pH 7.2. 1 mM cAMP was added to the bath solution as indicated. Zebrafish ELK currents were elicited by applying a series of 100-ms voltage pulses (ranging from −140 to +160 mV in 20 mV increments) from a pre-pulse potential of −140 mV, followed by a 150 ms tail pulse to −100 mV. Currents were leak-subtracted with P/4 protocol. To obtain conductance versus voltage curves, peak tail current amplitudes at −100 mV were normalized to the largest peak conductance amplitude, which followed a step to +40 mV. These normalized data were then plotted against the test voltage, and were fit with a Boltzmann equation:

$$\frac{G}{G_{\max}} = \frac{1}{1 + e^{\left(\frac{V - V_{1/2}}{s}\right)}}$$

where V represents the test voltage, V<sub>1/2</sub> is the midpoint activation voltage, and s is the slope of the relation.

- Guerrero, S. A., Hecht, H. J., Hofmann, B., Biebl, H. & Singh, M. Production of selenomethionine-labelled proteins using simplified culture conditions and generally applicable host/vector systems. *Appl. Microbiol. Biotechnol.* **56**, 718–723 (2001).
- Collaborative Computation Project 4. The CCP4 suite: programs for protein crystallography. *Acta Crystallogr. D* **50**, 760–763 (1994).
- Otwinowski, Z. & Minor, W. Processing X-ray diffraction data collected in oscillation mode. *Methods Enzymol.* **276**, 307–326 (1997).
- Adams, P. D. et al. PHENIX: a comprehensive Python-based system for macromolecular structure solution. *Acta Crystallogr. D* **66**, 213–221 (2010).
- Emsley, P. & Cowtan, K. Coot: model-building tools for molecular graphics. *Acta Crystallogr. D* **60**, 2126–2132 (2004).
- Chen, V. B. et al. MolProbity: all-atom structure validation for macromolecular crystallography. *Acta Crystallogr. D* **66**, 12–21 (2010).
- DeLano, W. L. The PyMOL molecular graphics system. <http://www.pymol.org> (DeLano Scientific, 2002).
- Huson, D. H. et al. Dendroscope: an interactive viewer for large phylogenetic trees. *BMC Bioinformatics* **8**, 460 (2007).
- Baker, N. A., Sept, D., Joseph, S., Holst, M. J. & McCammon, J. A. Electrostatics of nanosystems: application to microtubules and the ribosome. *Proc. Natl Acad. Sci. USA* **98**, 10037–10041 (2001).

# X-ray structures of LeuT in substrate-free outward-open and apo inward-open states

Harini Krishnamurthy<sup>1</sup> & Eric Gouaux<sup>1,2</sup>

Neurotransmitter sodium symporters are integral membrane proteins that remove chemical transmitters from the synapse and terminate neurotransmission mediated by serotonin, dopamine, noradrenaline, glycine and GABA ( $\gamma$ -aminobutyric acid). Crystal structures of the bacterial homologue, LeuT, in substrate-bound outward-occluded and competitive inhibitor-bound outward-facing states have advanced our mechanistic understanding of neurotransmitter sodium symporters but have left fundamental questions unanswered. Here we report crystal structures of LeuT mutants in complexes with conformation-specific antibody fragments in the outward-open and inward-open states. In the absence of substrate but in the presence of sodium the transporter is outward-open, illustrating how the binding of substrate closes the extracellular gate through local conformational changes: hinge-bending movements of the extracellular halves of transmembrane domains 1, 2 and 6, together with translation of extracellular loop 4. The inward-open conformation, by contrast, involves large-scale conformational changes, including a reorientation of transmembrane domains 1, 2, 5, 6 and 7, a marked hinge bending of transmembrane domain 1a and occlusion of the extracellular vestibule by extracellular loop 4. These changes close the extracellular gate, open an intracellular vestibule, and largely disrupt the two sodium sites, thus providing a mechanism by which ions and substrate are released to the cytoplasm. The new structures establish a structural framework for the mechanism of neurotransmitter sodium symporters and their modulation by therapeutic and illicit substances.

Chemical neurotransmission in the central nervous system is terminated through re-uptake of neurotransmitters from the synapse into surrounding neuronal and glial cells, a process first characterized in 1961 (ref. 1). Transmitter uptake is mediated by neurotransmitter sodium symporters (NSSs)<sup>2,3</sup>, integral membrane proteins that exploit energetically favourable  $\text{Na}^+$  electrochemical gradients for the thermodynamically uphill transport of neurotransmitters. Members of the NSS family include transporters for GABA, glycine, noradrenaline, serotonin and dopamine—chemical transmitters that have fundamental roles in the function of the nervous system. Accordingly, dysfunction of these transporters is implicated in diseases such as depression<sup>4,5</sup>, schizophrenia<sup>4</sup>, epilepsy<sup>6</sup> and Parkinson's disease<sup>4</sup>, and they are targets for therapeutic drugs including tricyclic antidepressants (TCAs) and selective serotonin re-uptake inhibitors (SSRIs) as well as addictive substances such as cocaine and amphetamines<sup>7</sup>. Understanding the substrate translocation mechanism of NSSs is central to the development of accurate models of substrate and drug complexes and to the discovery of new therapeutic agents.

The mechanism of NSS transport is generally described by the thermodynamically coupled binding of substrate and ion(s) to a central binding site that is alternately accessible to either side of the membrane<sup>8,9</sup> (Supplementary Fig. 1). Crystal structures of LeuT, a bacterial NSS homologue, elucidated the architecture of NSS proteins, demonstrated the existence of a substrate- and ion-bound occluded conformation, and illustrated how competitive and non-competitive inhibitors stabilize an outward-facing conformation<sup>10–14</sup>. LeuT is, at present, the best template for modelling the structure of NSSs and their complexes with therapeutic and illicit drugs. However, our understanding of

mechanism and structure/function relationships in NSSs is incomplete due to the absence of LeuT structures in outward-open and inward-open states.

In the absence of structural knowledge of transporter intermediates, general mechanisms of transport have been proposed based on structures of other secondary transporters bearing the LeuT fold and crystallized in distinct conformational states<sup>15–19</sup>. However, low amino acid sequence identity compromises the extent to which this approach can generate a detailed and accurate mechanism for NSSs. Concomitantly, spectroscopic and computational methods have focused on characterization of conformational changes accompanying substrate and ion association/dissociation events in LeuT<sup>20–23</sup>. Although these approaches have yielded new insights into localized movements, they have not revealed the three-dimensional, atomic-level details of conformational changes associated with substrate binding, isomerization of the transporter to the inward-open conformation, and release of substrate and sodium ion(s). Here, we present crystal structures of the outward-open and inward-open states of LeuT and thereby establish the structural basis for transport in the NSS family and provide accurate templates for modelling eukaryotic NSSs and their complexes with substrates, ions and drugs.

## Substrate-free and inward-open conformations

To stabilize the substrate-free and inward-open states of LeuT, we mutated residues in transmembrane domains (TMs) 3 and 8, helices comprising part of the 'scaffold' domain (TMs 3, 4, 8 and 9) and in TM6, one of the 'core' domain helices (TMs 1, 2, 6 and 7)<sup>10,22,24</sup> in the background of the wild-type-like K288A variant (LeuT<sup>K</sup>)<sup>25</sup> (Supplementary Table 1 and Supplementary Fig. 2). To enhance

<sup>1</sup>Vollum Institute, Oregon Health and Science University, 3181 SW Sam Jackson Park Road, Portland, Oregon 97239, USA. <sup>2</sup>Howard Hughes Medical Institute, Oregon Health and Science University, 3181 SW Sam Jackson Park Road, Portland, Oregon 97239, USA.



crystallization behaviour, we raised conformation-specific antibodies, exploiting fluorescence-detection size-exclusion chromatography (FSEC)<sup>26</sup> to select the antibodies and to demonstrate state-dependent binding. Well-diffracting crystals of substrate-free LeuT were obtained using the Tyr 108 to Phe mutant in TM3 (LeuT<sup>K</sup>(Y108F))<sup>25</sup> and the 2B12 antibody fragment (Fab). Stabilization of LeuT in an inward-open conformation required weakening of the sodium 2 (Na2) site<sup>10</sup> by mutation of Thr 354 to Val and Ser 355 to Ala (TM8), as well as the cytoplasmic gate by changing Tyr 268 to Ala (TM6; LeuT<sup>K</sup>(TSY))<sup>23,27,28</sup>, together with the 6A10 Fab.

### Sodium-bound state is outward-open

The substrate-free LeuT<sup>K</sup>(Y108F) structure (Supplementary Table 2 and Supplementary Fig. 3) adopts an outward-open conformation as a consequence of hinge-like movements in TMs 1b, 2a (residues 41–55), and 6a, relative to the outward-occluded state (Fig. 1a–c, e). Extracellular loop 3 (EL3) and TM11 are displaced by as much as 2.8 Å and 2.2 Å, respectively, due to the movements of TM1b and TM6a (Fig. 1a). Notably, TMs 1b, 2a and 6a pivot at Val 23, Gly 55 and Leu 257, respectively, suggesting that when substrate no longer forges interactions between the core and scaffold domains, constraints on TM1b and TM6a are released, allowing them to move outward and the transporter to adopt an outward-open conformation. The LeuT<sup>K</sup>(Y108F) structure is similar to the previously reported Trp-bound LeuT structure<sup>12</sup> with a root mean squared deviation (r.m.s.d.) value of 0.4 Å for all C $\alpha$  atoms (Supplementary Fig. 4), supporting the

general principle that inhibitors bind to conformational states populated by the wild-type transporter.

The ‘thin’ extracellular gate<sup>19</sup> of the outward-occluded state is ruptured in the LeuT<sup>K</sup>(Y108F) structure. Residues that bridge TM1b/TM6a to TM3/TM10 in the outward-occluded state have separated, opening a pathway to the extracellular solution (Fig. 1d, e). Arg 30 no longer forms a water-mediated salt bridge with Asp 404 (TM10) and the side chain of Phe 253 has rotated away from the binding site by a  $\sim 90^\circ$  rotation about the  $\chi_1$  dihedral angle, in agreement with molecular dynamics simulations<sup>21,29</sup>. The coordinated movement of Arg 30 and Phe 253 enables the retention of an important cation- $\pi$  interaction between their respective guanidinium and phenyl groups. The phenyl ring of residue 253 now occupies the same position as the indole ring of Trp 602 bound to the extracellular vestibule in the Trp-bound LeuT complex<sup>12</sup>.

Prominent electron density peaks ( $4.0\sigma$ ) observed in the Na1 and Na2 sites together with ion-oxygen distances of  $\sim 2.4$  Å (ref. 30) are consistent with sodium occupancy of these sites, although higher resolution diffraction data will be required to confirm their identity (Fig. 2). Most importantly, the outward-open structure suggests that the presence of sodium ions keeps the intracellular thick gate<sup>19</sup> closed by bridging interactions between the intracellular halves of the core and scaffold domains. Even though the Na1 site is located close to the pivot points for TM1b and TM6a (Fig. 2a), the concerted movement of the helices allows for retention of ion coordination geometry, excepting the loss of the carboxylate oxygen from the absent substrate.

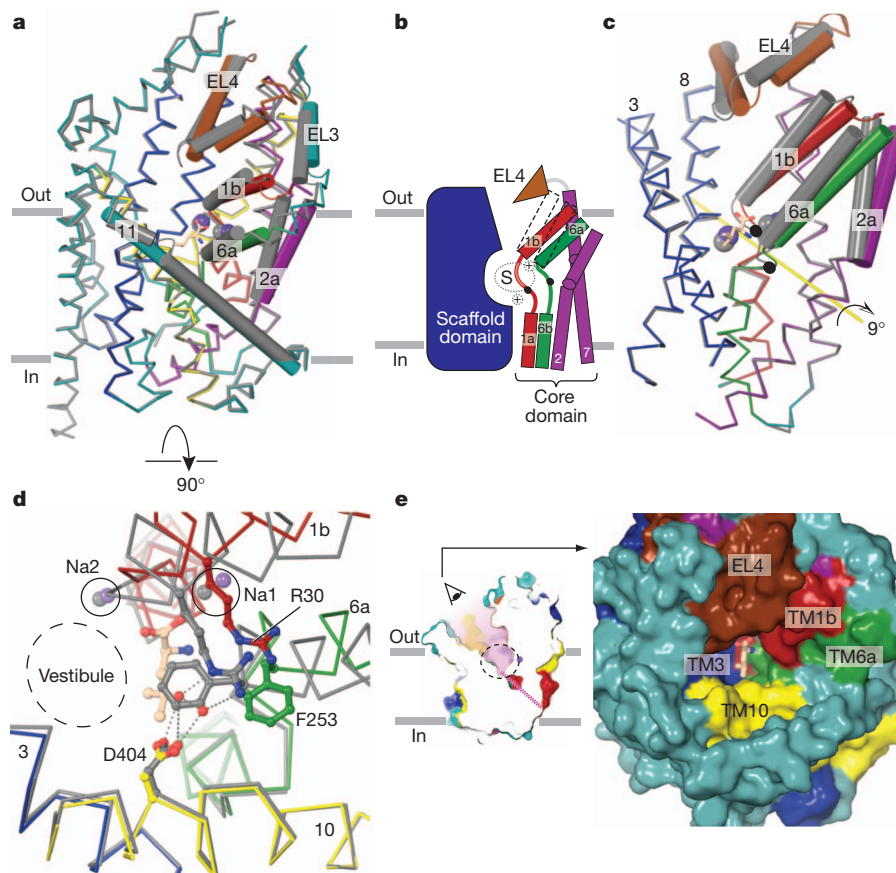


**Figure 1 | The substrate-free, Na<sup>+</sup>-bound state is outward-open.**

**a**, Superposition of the outward-open and leucine-bound outward-occluded conformations. Outward-open structure is coloured with Na<sup>+</sup> ions as purple spheres. The outward-occluded structure with Na<sup>+</sup> ions (spheres) is grey and leucine is shown in stick representation. **b**, Schematic of scaffold and core domains, EL4, the pivot points of hinge movements in TMs 1 and 6 (solid black circles) and the substrate (S) and sodium sites (+). **c**, Superposition, as in panel **a**, illustrating that a  $\sim 9^\circ$  rotation about an axis passing through the middle of

the core domain (yellow arrow) describes the conformational change associated with opening to the outside. Pivot points are shown as in panel **b**. **d**, Rupture of extracellular gate interactions (grey dashed lines) in the outward-open structure. Two water molecules that bridge Arg 30 and Asp 404 in the outward-occluded state are shown as red spheres. **e**, Surface representation of the outward-open structure with the zig-zag pink line indicating a closed intracellular pathway. Leucine, where shown, is from the outward-occluded Leu-bound structure.

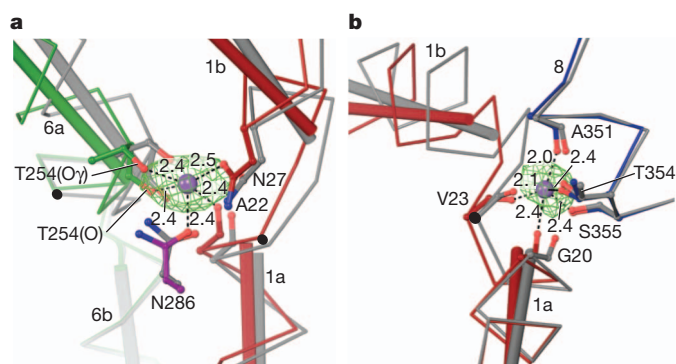


**Figure 2 | Sodium sites in the outward-open state.** **a**, The Na1 site showing positions of the coordinating residues within the framework of global changes in the outward-open structure. **b**, The Na2 site.  $F_o - F_c$  omit density is contoured at  $4\sigma$  and represented as green mesh. Colour scheme and representations are the same as in Fig. 1. Dashed lines indicate interactions between sodium ions and coordinating atoms with distances in Å, solid black circles are approximate pivot points for hinge movement of helices and red and green cylinders define the TM1 and six helix axes, respectively.

Binding of  $\text{Na}^+$  at this site may precede substrate binding, as also suggested by simulation studies<sup>29</sup>, thereby stabilizing local conformations of TMs 1 and 6 and engaging the main-chain carbonyl oxygen of Ala 22 (TM1a) with side-chain oxygens of Asn 27 (TM1b) and Thr 254 (TM6a). The Na2 site is located towards the intracellular region of TM1, stitching TM1a to TM8 through the main-chain carbonyls of Gly 20 and Val 23 (Fig. 2b). Thus, the  $\text{Na}^+$  ions, through their interaction with TM1a, stabilize an intracellular-closed conformation, a finding supported by single-molecule Förster resonance energy transfer (FRET) studies<sup>23</sup>.

### Structure of the inward-open conformation

We hypothesized that weakening of the Na2 binding site by mutation of Thr 354 and Ser 355 to valine and alanine, respectively, and perturbation of the intracellular gate by mutation of Tyr 268 to Ala<sup>27</sup>,

together yielding the LeuT<sup>K</sup>(TSY) variant, would shift the conformational equilibrium of LeuT towards the inward-open state (Supplementary Discussion and Supplementary Figs 2, 5, 8 and 9). We proceeded to crystallize the LeuT<sup>K</sup>(TSY)-6A10 Fab complex in the presence of lipids and solved the structure by molecular replacement at 3.2 Å resolution (Supplementary Table 2 and Supplementary Figs 10 and 11). Electron density for LeuT residues 1–10 was not observed and that for amino acids 11–24 was weak (mean  $B$  factor of 158.0 Å<sup>2</sup> versus 121.2 Å<sup>2</sup> for the rest of LeuT). The Fab fragment binds on the intracellular side of LeuT<sup>K</sup>(TSY) (Supplementary Fig. 11).

LeuT<sup>K</sup>(TSY) adopts an inward-open conformation as a consequence of large hinge-like movements within the core domain relative to the scaffold domain, and shifts in extracellular loops (Figs 3a–c). Perhaps the most notable change involves TM1a. Tilted by  $\sim 45^\circ$  from its position in the closed state, it protrudes into the predicted location of the membrane. TM6b, in comparison, is rotated away from the central binding site by only  $17^\circ$ . In contrast to the uncoupled movements of TMs 1a and 6b, TMs 1b and 6a tilt by a similar extent ( $24^\circ$  and  $21^\circ$ , respectively) towards the scaffold domain, blocking the extracellular pathway. Because TM1 and TM6 do not move as a unit, we superimposed the inward-open and outward-occluded structures using only the scaffold domain, resulting in an r.m.s.d. in  $\text{C}\alpha$  positions of 3.0 Å. Helices buttressing TM1 and TM6, namely TM2, TM7 and TM5, also undergo substantial rearrangements but their extracellular and intracellular halves move to significantly different extents (Fig. 3c). Thus, these helices bend, rather than tilt as rigid bodies, facilitated by either a glycine or proline residue located in their midsections. Movement of TM7 causes EL4 to dip down further into the extracellular vestibule, thus closing off the extracellular solvent pathway. To make room for TM6a, TM11 moves away from the centre of the transporter, a direction opposite to that seen in the outward-open state (Fig. 3b).

### Access to the substrate-binding site

In the inward-open LeuT structure, formation of a thick extracellular gate cuts off solvent access from the extracellular side while the thick

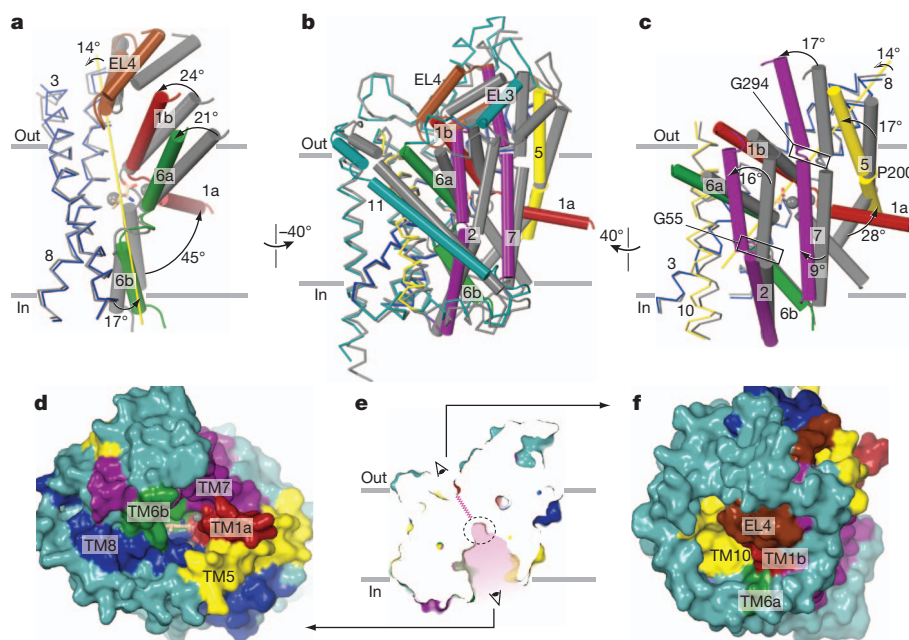


**Figure 3 | Inward-open conformation.** **a–c**, Superposition of inward-open and outward-occluded state structures using the scaffold domain. The overall changes shown in **b** are divided in two parts, **a** and **c**, for clarity. The extent of rotation for the key TMs between the outward-occluded and inward-open conformations are indicated in **a** and **c**. The axis of rotation of core domain with the exclusion of TM1a is depicted in yellow. **d**, Surface representation of the

inward-open structure looking 'up' into the binding site from the intracellular side, as depicted in **e**, **f**, Surface representation of the inward-open structure showing the elements forming the extracellular thick gate. Colour coding and representations are as in Fig. 1. Leucine and sodium, where shown, are from the outward-occluded Leu-bound structure.



intracellular gate opens, allowing access to the substrate binding site from the inside (Figs 3d–f). Consistent with cysteine accessibility studies on the serotonin (SERT)<sup>22,31,32</sup> and GABA (GAT-1)<sup>33</sup> transporters, TM1a, TM5 and TM8 line the intracellular cavity. In particular, residues Leu 14 and Ala 19 of TM1a are solvent accessible, in line with the marked increase in reactivity observed for the corresponding residues in SERT in the inward-open conformation<sup>22</sup>. Accessibility and cross-linking studies also indicate that TM1b and TM6a move closer to TM3 (ref. 34) and, together with EL4, become inaccessible in the absence of sodium<sup>35–38</sup>. Consistent with its essential role in substrate transport<sup>39</sup>, EL4 occludes the extracellular pathway by packing tightly against TM1b and TM7 on one side and TM3, TM8 and EL2 on the other side, making extensive contacts that include hydrophobic interactions and a hydrogen bond between Asp 401 (TM10) and Ala 319 (EL4).

The collapse of the extracellular vestibule in the inward-open state is central to our understanding of how therapeutic agents, including TCAs and SSRIs, inhibit NSSs. Large, bulky molecules such as tryptophan<sup>12</sup>, the cocaine analogue 2 $\beta$ -carbomethoxy-3 $\beta$ -(4-iodophenyl)tropane<sup>31</sup> and SKF-8997A<sup>40</sup> arrest LeuT, SERT and GAT-1, respectively, in the outward-facing conformation by blocking collapse of the extracellular vestibule, which in turn precludes opening of the intracellular gate. The inward-open LeuT structure now provides a new template for designing novel therapeutic agents that arrest NSS transporters in the inward-facing conformation. Ibogaine, shown to bind in the intracellular vestibule of SERT<sup>41</sup>, is the only known inhibitor of this type.

The closure of the extracellular gate radically changes the nature of the proposed S2 substrate-binding site, which is hypothesized to be occupied by substrate in occluded and inward-facing conformational states<sup>42,43</sup>. Residues Ile 111 and Leu 400, stated to line the S2 site, are now deeply buried (Supplementary Fig. 12). Although we do see a

small non-protein electron density feature near EL4, it is probably not a substrate molecule, not only because no substrates were included in the protein preparation, but also because the density cannot be well fit by leucine or a related amino acid. We suggest that the density is due to buffer, detergent or several water molecules.

## Rupture and formation of gating interactions

The extracellular gate of the inward-open state is closed through interactions between residues of TM1b (Arg 30) and TM10 (Asp 404, Gly 408, Thr 409), EL4 (Ala 319) and TM10 (Asp 401) (Fig. 4a) and TM6a (Asp 240) and TM11 (Tyr 471). The guanidinium group of Arg 30, riding 'on top' of the aromatic ring of Phe 253 (TM6a), makes multiple interactions with TM10 that include a direct salt bridge with Asp 404 and hydrogen bonds to Thr 409 and the carbonyl oxygen of Gly 408. In GAT-1, conservative mutation to Lys of the residue equivalent to Arg 30 severely compromises uptake activity<sup>44</sup>, an outcome in accord with the manner in which interactions of Arg 30 are modulated in the outward-open, outward-occluded and inward-open states of LeuT (Fig. 4a, b).

In contrast to the extracellular gate, a network of interactions within the thick intracellular gate of outward-facing and outward-occluded states is disrupted (Fig. 4b, c). Ionic interactions linking the N terminus and TM1a (Arg 5, Trp 8) to TM6b (Ser 267, Tyr 268) and TM8 (Gln 361, Asp 369) on the intracellular side no longer exist. The splaying apart of TM5, TM7 and TM1a also abrogates interactions between Lys 196 and Thr 10 and between Ser 278 and Arg 11. Consistent with the disruption of these interactions, mutation of residues homologous to Arg 5 or Trp 8 (ref. 45), Tyr 268 (refs 27, 28), Asp 369, Lys 196 and Ser 278 (refs 46, 47) in eukaryotic transporters alters substrate uptake and shifts the conformational equilibrium of the transporter towards an inward-open state.

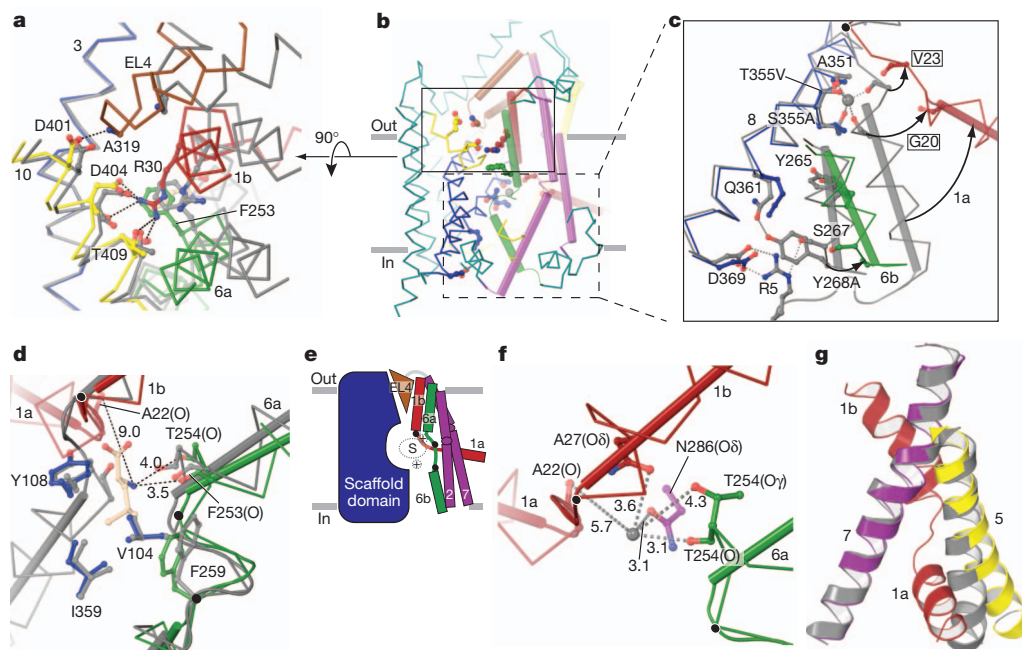


**Figure 4 | Changes in gate, substrate and ion site interactions and coupling to helix movements.** **a**, Comparison of the extracellular gating interactions in the inward-open and outward-occluded structures. View is from extracellular side. Polar contacts in the inward-open structure are shown as black dashed lines. **b**, Overall view of inward-open structure showing closed extracellular gate (box with solid lines) and open intracellular gate (box with dashed lines). **c**, Comparison of the intracellular gating interactions in the inward-open and outward-occluded structures. Interactions forming the intracellular gate in the outward-occluded state are shown as grey dashed lines. **d**, Changes in the central substrate-binding site. In comparing the outward-occluded and inward-

open structures, A22, T254 and F253 move away from the binding site. Distances were measured relative to leucine from the outward-occluded structure. **e**, A cartoon representing changes in the core domain relative to the scaffold domain and the location of hinges relative to the position of substrate- and ion-binding sites is shown. **f**, Changes in the Na1 site. Distances of the coordinating residues from the sodium ion of the outward-occluded structure are shown. **g**, Superposition of the inward-open and outward-occluded structures using TM7. TM1a of only the inward-open structure is shown for clarity. Colour scheme is as in Fig. 1. Location of TM1 and TM6 hinges are shown as black spheres in c–f.



## Perturbation of ion and substrate sites

The location of hinges for the conformational changes in TM1 and TM6 of the inward-open state has profound consequences for the substrate and sodium ion sites. The hinge for TM1a is located at Leu 25, considerably 'above' the Na2 site, leading to separation of residues on TM1a and TM8 that define this site, thus demonstrating how the release of sodium from the Na2 site, the movement of TM1a and the opening of the transporter to the cytoplasm are coupled (Fig. 4c), a mechanism that has also been suggested for the *Vibrio parahaemolyticus* sodium/galactose transporter (vSGLT)<sup>48</sup>. There are two hinges in TM6, Ser 256 for TM6a and Phe 259 for TM6b, while TM1b also pivots at Leu 25. Because these residues are all close to the substrate-binding site but further away from the Na1 site (Fig. 4e), there is minimal perturbation of the former (Fig. 4d) but considerable weakening of the latter (Fig. 4e, f). Thus, although changes in TM1 and TM6 affect residues coordinating the  $\alpha$ -amino group of leucine and cause small shifts in the side chains of Phe 253 and Phe 259, residues from TM3 and TM8 that engage the aliphatic moiety of the substrate maintain their positions. Consequently, an important portion of the substrate-binding pocket is retained in the inward-open state, preserving the ability of the transporter to bind substrate under conditions of reversed substrate flux.

## Structural principles of transporter mechanism

The pseudo two-fold symmetric relationship of TMs 1–5 and 6–10 together with the organization of TMs 1, 2, 6 and 7 as a four-helix bundle led to the rocking bundle mechanism of transport, in which the core moves as a unit about a rotation axis oriented approximately parallel to the membrane and intersecting the substrate-binding site<sup>22</sup>. Detailed analysis of the inward-open state, however, indicates that only a portion of the core moves as a unit and that there is not strict adherence to the pseudo two-fold symmetry. The conformational transition from the outward-occluded to the inward-open state is brought about by multiple adjustments in individual TM helices, including the bending of TM2 and TM7 at conserved glycine residues and the independent movements of TMs 1a and 6b. Indeed, the core domains in the inward-open and outward-occluded states align with a r.m.s.d. of 3.5 Å (C $\alpha$  atoms), whereas the scaffold domains align with a r.m.s.d. of 0.7 Å. If TM1a is excluded from consideration, however, the core domain helices superpose with a r.m.s.d. of 0.83 Å (C $\alpha$  atoms), thus demonstrating that a portion of the core helices do reorient as a unit, undergoing a rotation of  $\sim 14^\circ$  about an axis passing through Leu 25 and Phe 259 in the plane of the membrane (Fig. 3a, c). The intracellular loop 1 (IL1) and EL4 are also related by the pseudo two-fold symmetry axis, yet whereas EL4 undergoes large relative movements, the position of IL1 is constant.

The structural rearrangement of TM1a in the inward-open conformation of LeuT is different from that seen in Mhp1 (refs 15, 18), in which TM1 moves as a rigid body (Supplementary Fig. 13)<sup>22</sup>. At present it is unclear whether the extent to which TM1a is seen to tilt away from its position in the occluded state reflects its true position in a native membrane environment. The fact that TM1a is neither involved in crystal contacts nor interacts with the Fab (Supplementary Fig. 11) diminishes the possibility that its position is a crystallization artefact. The weak density of TM1a suggests that it is highly flexible in the detergent/lipid micelles in which LeuT<sup>K</sup>(TSY) was crystallized. Indeed, the apparent mobility and large extent of movement of TM1a are in general agreement with findings of single-molecule FRET studies and molecular dynamics simulations<sup>23,49,50</sup>.

## Coupling of binding sites and helix movements

The inward-open structure of LeuT suggests the manner by which changes in the sodium- and substrate-binding pockets are coupled to the larger structural changes that simultaneously open the intracellular side and close the extracellular side. The location of the TM1 hinge at Leu 25 in the inward-open state, at a position extracellular to the

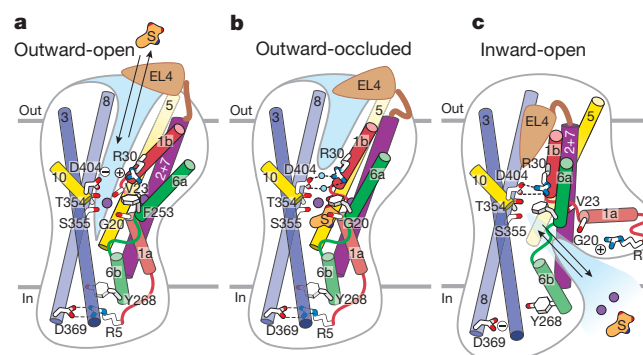


**Figure 5 | Schematic of transport in LeuT.** a–c, Shown are structural elements and gating residues instrumental to conformational changes associated with the transition from the outward-open (a) to the outward-occluded state (b) and the inward-open state (c). At present there is no crystal structure for an inward-occluded state and thus no schematic is provided.

substrate and sodium sites, is consistent with the observation that in the absence of Na<sup>+</sup> ions TM1a moves away from the scaffold domain and TM6b, not only initiating conformational changes that open an intracellular pathway, but also resulting in the disruption of the sodium ion sites. We propose that it is energetically unfavourable for TM1a to remain in an intracellular gate 'closed' conformation without the compensating contributions from bound Na<sup>+</sup>. We further suggest that the movement of TM1a initiates a cascade of structural rearrangements that result in closure of the extracellular gate as follows. A change in the position of TM1a requires movement of the intracellular region of TM5 (Fig. 4g). Yet because TM5 lacks the hinge-like regions of TM1 and TM6, the entire helix tilts, 'pushing' TM7 and TM1b and closing the extracellular gate (Fig. 3c). Similar structural adjustments involving TM2 and TM6a also occur, ensuring that the intracellular gate cannot open without simultaneous closure of the extracellular gate.

## Mechanism

Crystal structures of LeuT captured in three distinct conformational states show how both local conformational changes and rigid body movements of groups of helices are associated with the transport mechanism (Fig. 5). Opening and closure of the extracellular and intracellular gates exploit hinge-like bending of helices at pivot points within short non-helical regions halfway across the bilayer, together with the rigid body rotation of helical bundles, movements of extracellular loops and flexing of numerous transmembrane helices (Supplementary Movie). General principles emerging from these studies are that local hinge-like movements of transmembrane helices are coupled to the formation and disruption of substrate- and sodium-binding sites, which are translated through nearly rigid body movements of groups of helices and loops into opening and closing of the 'thick' extracellular and intracellular gates. Most importantly, the relative locations of substrate/ion-binding sites and hinge pivots define the extent to which hinge motions perturb the sites. More broadly, these structures demonstrate how the overall conformation and shape of LeuT changes during the transport cycle, thereby providing a general mechanistic framework to understand how substrates, ions, mutations and drugs modulate the conformational equilibria and transport activity of LeuT and related NSS proteins.

## METHODS SUMMARY

LeuT mutants were expressed as previously described<sup>10</sup>, monoclonal antibodies and Fab fragments were generated by standard methods, and X-ray crystal structures of the Fab complexes were solved by molecular replacement. Final models were obtained by an iterative process of manual model building and refinement against X-ray diffraction data. The functional properties of LeuT mutants were examined using scintillation proximity binding assays and uptake or exchange assays with LeuT reconstituted into proteoliposomes.

**Full Methods** and any associated references are available in the online version of the paper at [www.nature.com/nature](http://www.nature.com/nature).

**Received 5 August; accepted 28 November 2011.**

**Published online 9 January 2012.**

- Hertting, G. & Axelrod, J. Fate of tritiated noradrenaline at the sympathetic nerve endings. *Nature* **192**, 172–173 (1961).
- Nelson, N. The family of Na<sup>+</sup>/Cl<sup>-</sup> neurotransmitter transporters. *J. Neurochem.* **71**, 1785–1803 (1998).
- Saier, M. H. J. A functional-phylogenetic classification system for transmembrane solute transporters. *Microbiol. Mol. Biol. Rev.* **64**, 354–411 (2000).
- Hahn, M. K. & Blakely, R. D. Monoamine transporter gene structure and polymorphisms in relation to psychiatric and other complex disorders. *Pharmacogenomics J.* **2**, 217–235 (2002).
- Klimek, V. *et al.* Reduced levels of norepinephrine transporters in the locus coeruleus in major depression. *J. Neurosci.* **17**, 8451–8458 (1997).
- Richerson, G. B. & Wu, Y. Role of the GABA transporter in epilepsy. *Adv. Exp. Med. Biol.* **548**, 76–91 (2004).
- Amara, S. G. & Sonders, M. S. Neurotransmitter transporters as molecular targets for addictive drugs. *Drug Alcohol Depend.* **51**, 87–96 (1998).
- Mitchell, P. A general theory of membrane transport from studies of bacteria. *Nature* **180**, 134–136 (1957).
- Jardetzky, O. Simple allosteric model for membrane pumps. *Nature* **211**, 969–970 (1966).
- Yamashita, A., Singh, S. K., Kawate, T., Jin, Y. & Gouaux, E. Crystal structure of a bacterial homologue of Na<sup>+</sup>/Cl<sup>-</sup>-dependent neurotransmitter transporters. *Nature* **437**, 215–223 (2005).
- Singh, S., Yamashita, A. & Gouaux, E. Antidepressant binding site in a bacterial homologue of neurotransmitter transporters. *Nature* **448**, 952–956 (2007).
- Singh, S. K., Piscitelli, C. L., Yamashita, A. & Gouaux, E. A competitive inhibitor traps LeuT in an open-to-out conformation. *Science* **322**, 1655–1661 (2008).
- Zhou, Z. *et al.* LeuT-desipramine structure reveals how antidepressants block neurotransmitter uptake. *Science* **317**, 1390–1393 (2007).
- Zhou, Z. *et al.* Antidepressant specificity of serotonin transporter suggested by three LeuT–SSRI structures. *Nature Struct. Mol. Biol.* **16**, 652–657 (2009).
- Weyand, S. *et al.* Structure and molecular mechanism of a nucleobase–cation–symport-1 family transporter. *Science* **322**, 709–713 (2008).
- Faham, S. *et al.* The crystal structure of a sodium galactose transporter reveals mechanistic insights into Na<sup>+</sup>/sugar symport. *Science* **321**, 810–814 (2008).
- Shaffer, P. L., Goehring, A., Shankaranarayanan, A. & Gouaux, E. Structure and mechanism of a Na<sup>+</sup>-independent amino acid transporter. *Science* **325**, 1010–1014 (2009).
- Shimamura, T. *et al.* Molecular basis of alternating access membrane transport by the sodium-hydantoin transporter Mhp1. *Science* **328**, 470–473 (2010).
- Krishnamurthy, H., Piscitelli, C. L. & Gouaux, E. Unlocking the molecular secrets of sodium-coupled transporters. *Nature* **459**, 347–355 (2009).
- Shaikh, S. A. & Tajkhorshid, E. Modeling and dynamics of the inward-facing state of a Na<sup>+</sup>/Cl<sup>-</sup> dependent neurotransmitter transporter homologue. *PLOS Comput. Biol.* **6**, e1000905 (2010).
- Claxton, D. P. *et al.* Ion/substrate-dependent conformational dynamics of a bacterial homologue of neurotransmitter:sodium symporters. *Nature Struct. Mol. Biol.* **17**, 822–829 (2010).
- Forrest, L. R. *et al.* Mechanism for alternating access in neurotransmitter transporters. *Proc. Natl Acad. Sci. USA* **105**, 10338–10343 (2008).
- Zhao, Y. *et al.* Single-molecule dynamics of gating in a neurotransmitter transporter homologue. *Nature* **465**, 188–193 (2010).
- Boudker, O. & Verdon, G. Structural perspectives on secondary active transporters. *Trends Pharmacol. Sci.* **31**, 418–426 (2010).
- Piscitelli, C. L., Krishnamurthy, H. & Gouaux, E. Neurotransmitter/sodium symporter orthologue LeuT has a single high-affinity substrate site. *Nature* **468**, 1129–1132 (2010).
- Kawate, T. & Gouaux, E. Fluorescence-detection size-exclusion chromatography for precrystallization screening of integral membrane proteins. *Structure* **14**, 673–681 (2006).
- Kniazeff, J. *et al.* An intracellular interaction network regulates conformational transitions in the dopamine transporter. *J. Biol. Chem.* **283**, 17691–17701 (2008).
- Loland, C. J., Norregaard, L., Litman, T. & Gether, U. Generation of an activating Zn<sup>2+</sup> switch in the dopamine transporter: mutation of an intracellular tyrosine constitutively alters the conformational equilibrium of the transport cycle. *Proc. Natl Acad. Sci. USA* **99**, 1683–1688 (2002).
- Celik, L., Schiott, B. & Tajkhorshid, E. Substrate binding and formation of an occluded state in the leucine transporter. *Biophys. J.* **94**, 1600–1612 (2008).
- Harding, M. M. Small revisions to predicted distances around metal sites in proteins. *Acta Crystallogr. D* **62**, 678–682 (2006).
- Zhang, Y.-W. & Rudnick, G. The cytoplasmic substrate permeation pathway of serotonin transporter. *J. Biol. Chem.* **281**, 36213–36220 (2006).
- Rudnick, G. The cytoplasmic permeation pathway of neurotransmitter transporters. *Biochemistry* **50**, 7462–7475 (2011).
- Ben-Yona, A. & Kanner, B. I. Transmembrane domain 8 of the  $\gamma$ -aminobutyric acid transporter GAT-1 lines a cytoplasmic accessibility pathway into its binding pocket. *J. Biol. Chem.* **284**, 9727–9732 (2009).
- Tao, Z., Zhang, Y. W., Agyiri, A. & Rudnick, G. Ligand effects on cross-linking support a conformational mechanism for serotonin transport. *J. Biol. Chem.* **284**, 33807–33814 (2009).
- Rosenberg, A. & Kanner, B. I. The substrates of the  $\gamma$ -aminobutyric acid transporter GAT-1 induce structural rearrangements around the interface of transmembrane domains 1 and 6. *J. Biol. Chem.* **283**, 14376–14383 (2008).
- Henry, L. K., Adkins, E. M., Han, Q. & Blakely, R. D. Serotonin and cocaine-sensitive inactivation of human serotonin transporters by methanethiosulfonates targeted to transmembrane domain I. *J. Biol. Chem.* **278**, 37052–37063 (2003).
- Zomot, E. & Kanner, B. I. The interaction of the  $\gamma$ -aminobutyric acid transporter GAT-1 with the neurotransmitter is selectively impaired by sulfhydryl modification of a conformationally sensitive cysteine residue engineered into extracellular loop IV. *J. Biol. Chem.* **278**, 42950–42958 (2003).
- Mitchell, S. M., Lee, E., Garcia, M. L. & Stephan, M. M. Structure and function of extracellular loop 4 of the serotonin transporter as revealed by cysteine-scanning mutagenesis. *J. Biol. Chem.* **279**, 24089–24099 (2004).
- Smicun, Y., Campbell, S. D., Chen, M. A., Gu, H. & Rudnick, G. The role of external loop regions in serotonin transport. Loop scanning mutagenesis of the serotonin transporter external domain. *J. Biol. Chem.* **274**, 36058–36064 (1999).
- Hirayama, B. A., Diez-Sampedro, A. & Wright, E. M. Common mechanisms of inhibition for the Na<sup>+</sup>/glucose (hSGLT1) and Na<sup>+</sup>/Cl<sup>-</sup>/GABA (hGAT1) cotransporters. *Br. J. Pharmacol.* **134**, 484–495 (2001).
- Jacobs, M. T., Zhang, Y. W., Campbell, S. D. & Rudnick, G. Ibogaine, a noncompetitive inhibitor of serotonin transport, acts by stabilizing the cytoplasm-facing state of the transporter. *J. Biol. Chem.* **282**, 29441–29447 (2007).
- Shi, L., Quick, M., Zhao, Y., Weinstein, H. & Javitch, J. A. The mechanism of a neurotransmitter:sodium symporter-inward release of Na<sup>+</sup> and substrate is triggered by a substrate in a second binding site. *Mol. Cell* **30**, 667–677 (2008).
- Zhao, Y. *et al.* Substrate-modulated gating dynamics in a Na<sup>+</sup>-coupled neurotransmitter transporter homologue. *Nature* **474**, 109–113 (2011).
- Pantanowitz, S., Bendahan, A. & Kanner, B. I. Only one of the charged amino acids located in the transmembrane  $\alpha$ -helices of the  $\gamma$ -aminobutyric acid transporter (subtype A) is essential for its activity. *J. Biol. Chem.* **268**, 3222–3225 (1993).
- Bennett, E. R., Su, H. & Kanner, B. I. Mutation of arginine 44 of GAT-1, a (Na<sup>+</sup> + Cl<sup>-</sup>)-coupled  $\gamma$ -aminobutyric acid transporter from rat brain, impairs net flux but not exchange. *J. Biol. Chem.* **275**, 34106–34113 (2000).
- Loland, C. J., Granas, C., Javitch, J. A. & Gether, U. Identification of intracellular residues in the dopamine transporter critical for regulation of transporter conformation and cocaine binding. *J. Biol. Chem.* **279**, 3228–3238 (2004).
- Chen, N., Rickey, J., Berfield, J. L. & Reith, M. E. Aspartate 345 of the dopamine transporter is critical for conformational changes in substrate translocation and cocaine binding. *J. Biol. Chem.* **279**, 5508–5519 (2004).
- Watanabe, A. *et al.* The mechanism of sodium and substrate release from the binding pocket of vSGLT. *Nature* **468**, 988–991 (2010).
- Quick, M. *et al.* State-dependent conformations of the translocation pathway in the tyrosine transporter Tyt1, a novel neurotransmitter:sodium symporter from *Fusobacterium nucleatum*. *J. Biol. Chem.* **281**, 26444–26454 (2006).
- Shi, L. & Weinstein, H. Conformational rearrangements to the intracellular open states of the LeuT and ApcT transporters are modulated by common mechanisms. *Biophys. J.* **99**, L103–L105 (2010).

**Supplementary Information** is linked to the online version of the paper at [www.nature.com/nature](http://www.nature.com/nature).

**Acknowledgements** We thank D. Cawley for monoclonal antibody production, L. Vaskalis for help with illustrations and the staff at the Advanced Photon Source beamline 24-ID-E and at the Advanced Light Source beamline 5.0.2 for their assistance with X-ray data collection and processing. We are grateful to E. Haddadian, T. Sosnick and K. Freed for assistance in refining the backbone torsional and side-chain angles using their unpublished TOP algorithm. We thank all Gouaux laboratory members, especially C. Piscitelli and S. K. Singh, for discussions and helpful suggestions throughout the project. This work was supported by the National Institutes of Health. E.G. is an investigator with the Howard Hughes Medical Institute.

**Author Contributions** H.K. and E.G. contributed to all aspects of the project.

**Author Information** Atomic coordinates and structure factors have been deposited with the Protein Data Bank under accession codes 3TT1, 3TT3 and 3TU0 for the LeuT<sup>K</sup>(Y108F)–2B12 complex, the LeuT<sup>K</sup>(TSY)–6A10 complex and the LeuT<sup>K</sup>(TS) complex with alanine, respectively. Reprints and permissions information is available at [www.nature.com/reprints](http://www.nature.com/reprints). The authors declare no competing financial interests. Readers are welcome to comment on the online version of this article at [www.nature.com/nature](http://www.nature.com/nature). Correspondence and requests for materials should be addressed to E.G. ([gouauxe@ohsu.edu](mailto:gouauxe@ohsu.edu)).



## METHODS

**Purification of LeuT mutants.** The site-directed mutants LeuT<sup>K</sup>(Y108F), LeuT<sup>K</sup>(TS) and LeuT<sup>K</sup>(TSY) were produced by polymerase chain reaction (PCR) and subcloned into a pET16b plasmid containing a thrombin-cleavage site and a C-terminal octa-histidine tag. All mutants were verified by DNA sequencing. The resulting proteins were expressed and purified as previously described<sup>10,25</sup> with the following modifications. To obtain leucine-free transporter, buffers for purification did not contain sodium salts and membranes were washed three times in sodium-free buffer to ensure that no endogenously bound leucine was carried along. LeuT mutants were solubilized with *n*-dodecyl- $\beta$ -D-maltopyranoside (C<sub>12</sub>M) and purified by Ni-affinity chromatography. Protein for functional and biochemical assays was further purified by gel filtration in buffer containing C<sub>12</sub>M.

**Monoclonal antibodies and Fab fragments.** Mouse monoclonal antibodies against LeuT<sup>K</sup>(Y108F) and LeuT<sup>K</sup>(TSY) were raised by standard methods using corresponding purified protein in detergent as antigen. Antibodies recognizing a conformational epitope in LeuT<sup>K</sup>(Y108F) were selected using FSEC<sup>26</sup> and western blot analysis, resulting in the identification of the 2B12 monoclonal antibody. Antibodies specific to the inward-facing mutant LeuT<sup>K</sup>(TSY) were selected based on their relative affinities for LeuT<sup>K</sup>(TSY) and wild-type LeuT as determined by FSEC. From these screens we isolated the 6A10 monoclonal antibody. All FSEC analysis relied on C-terminal GFP fusions of the LeuT variants. Antibodies were purified from hybridoma supernatants using a SP sepharose cation-exchange column. Fab fragments were generated by papain digestion at 37 °C in 50 mM sodium phosphate pH 7.2, 1 mM EDTA and a papain to monoclonal antibody ratio of 1:20 w/w (2B12) or 1:100 w/w (6A10). Cysteine at 10 mM final concentration was added to the digestion reaction for 6A10. Digestion of 2B12 was stopped with 30 mM iodoacetamide after 4 h, while digestion of 6A10 was quenched by transferring the reaction to 4 °C after 2 h. Fab fragments were purified on a Protein A column, followed by ion-exchange chromatography. DNA encoding the light and heavy chains of 2B12 (IgG2a,  $\kappa$ ) and 6A10 (IgG1,  $\kappa$ ) Fab fragments were cloned and sequenced from hybridoma cells using rapid amplification of 5' complementary DNA ends (5'-RACE).

**Purification of Fab complexes for crystallization.** The His-tag of LeuT destined for crystallization was cleaved by thrombin. Transporter was then mixed with excess Fab and the complex was subjected to gel filtration in *n*-octyl- $\beta$ -D-thiogluco-pyranoside (C<sub>8</sub>SG)-containing buffer. The buffer consisted of 20 mM Tris, pH 8.0, 50 mM (LeuT<sup>K</sup>(TSY)-Fab) or 100 mM (LeuT<sup>K</sup>(Y108F)-Fab) KCl and 12 mM (LeuT<sup>K</sup>(TSY)-Fab) or 15 mM (LeuT<sup>K</sup>(Y108F)-Fab) C<sub>8</sub>SG. For crystallization of LeuT<sup>K</sup>(TSY)-Fab complex, the protein was then supplemented with a fivefold molar excess of 1,2-dimyristoyl-*sn*-glycero-3-phosphoethanolamine (DMPE) and incubated at 4 °C for 1 h before removing insoluble lipids by centrifugation. A 55 mM DMPE stock was prepared in 20% DMSO and 80% gel filtration buffer. Protein was concentrated to 3.0–3.2 mg ml<sup>-1</sup> (LeuT<sup>K</sup>(Y108F)-Fab) or 4.5–5 mg ml<sup>-1</sup> (LeuT<sup>K</sup>(TSY)-Fab) for crystallization.

**Crystallization.** Crystallization was carried out by vapour diffusion in hanging drops at 20 °C. LeuT<sup>K</sup>(Y108F)-Fab crystals were grown in 40 mM Tris pH 7.5, 23–26% PEG 550 monomethyl ether and 50–100 mM NaCl, and cryo-protected in 35% PEG 550 monomethyl ether. Crystals were allowed to sit in the final cryo-solution for 4–5 h before flash freezing in liquid nitrogen.

Different crystal forms were obtained for the LeuT<sup>K</sup>(TSY)-Fab complex in similar crystallization conditions with the best crystals belonging to space group C222<sub>1</sub>. These crystals were grown in 100 mM HEPES pH 7.6, 0.1 M Mg(NO<sub>3</sub>)<sub>2</sub>, 12–14% PEG 1500 and 1.5% w/v trimethylamine *N*-oxide dehydrate in a protein to precipitant ratio of 1:2. LeuT<sup>K</sup>(TSY)-Fab crystals were cryo-protected with 15% PEG 1500 and 20% glycerol before flash-freezing.

Crystals of alanine-bound LeuT<sup>K</sup>(TS) were obtained from protein purified in 20 mM Tris pH 8.0, 100 mM L-Ala, 200 mM NaCl and 40 mM *n*-octyl- $\beta$ -D-glucoside ( $\beta$ -OG). Purification and crystallization were carried out as described for wild-type LeuT<sup>10</sup>.

**Data collection and structure determination.** For the LeuT<sup>K</sup>(Y108F)-Fab complex, X-ray diffraction data sets for the crystals were indexed, integrated and scaled using HKL2000 and the CCP4 suite of computer programs<sup>51,52</sup>. The crystals diffract to ~3.1 Å resolution, belong to the space group P2<sub>1</sub>2<sub>1</sub>2<sub>1</sub> and harbour two LeuT<sup>K</sup>(Y108F)-Fab complexes per asymmetric unit, giving a Matthews coefficient<sup>53</sup> of 3.9 Å Da<sup>-3</sup>. The structure was determined by molecular replacement using the program PHASER<sup>54</sup>. The search probes were the tryptophan-bound LeuT structure (PDB accession 3F3A) and a Fab homology model built using SWISS-MODEL<sup>55</sup>. The model was built using COOT<sup>56</sup> into 2F<sub>o</sub> - F<sub>c</sub> maps, cross-validated using simulated annealing composite omit maps and refined with PHENIX<sup>57</sup> using non-crystallographic symmetry, individual atomic displacement parameters and translation/libration/screw (TLS)<sup>58</sup> subdomains. Six TLS groups composed of two LeuT molecules, two Fab constant domains and two

Fab variable domains were defined. This iterative model building and refinement procedure yielded a structure with good crystallographic and stereochemical statistics. Regions of weak or no electron density were excluded from the model such that the final structure consists of LeuT residues 5–129 and 135–507, Fab light chain residues 1–215, and Fab heavy chain residues 1–135, 143–219.

For the LeuT<sup>K</sup>(TSY)-Fab complex, the crystals diffract to ~3.2 Å resolution and belong to the space group C222<sub>1</sub>. There is one complex in the asymmetric unit, resulting in a Matthews coefficient of 3.4 Å Da<sup>-3</sup>. Initial phases were derived from a molecular replacement solution using PHASER<sup>54</sup> in which a partial structure of leucine-bound LeuT (PDB accession 2A65) and a high-resolution IgG1 Fab structure (PDB accession 1Q9Q) were used as search probes. The partial LeuT search probe was obtained by deleting TMs 1, 6 and 12 from the 2A65 structure. Electron density maps calculated using the 'prime and switch' method<sup>59</sup> clearly showed the LeuT regions where there were deviations from the 2A65 structure. This initial molecular replacement solution was used as a starting point for automated building using Phenix. Further changes were made to the LeuT portion using COOT<sup>56</sup>. At this stage, electron density for the Fab portion was poor, making it difficult for manual building. A homology model built using PDB accession 1EJO for the light chain and PDB accession 2Z4Q for the heavy chain by PHYRE<sup>60</sup> resulted in a substantial decrease in the crystallographic *R* factors, yielding *R*<sub>work</sub> and *R*<sub>free</sub> values of 0.33 and 0.36, respectively. This model and a 2F<sub>o</sub> - F<sub>c</sub> map calculated with exclusion of the test set of reflections (*R*<sub>free</sub> set) were then submitted to a crystallographic refinement server (<http://godzilla.uchicago.edu>). The resulting model had improved stereochemistry and *R*<sub>work</sub> and *R*<sub>free</sub> values of 0.29 and 0.32, respectively.

Further improvements to the model were made until the *R*<sub>work</sub>/*R*<sub>free</sub> values converged to 0.26/0.30 and structure quality assessed using Molprobity<sup>61</sup> was satisfactory. Throughout the model building procedure, bias-minimized 'prime and switch' maps<sup>59</sup> and simulated annealing composite omit maps were used. Individual isotropic *B* factors and TLS parameters were refined using 11 TLS groups identified using Phenix<sup>57</sup>: three LeuT domains comprised of residues 11–184, 185–254 and 255–511, four Fab heavy-chain domains involving residues 1–83, 84–140, 141–180 and 181–219, together with residues 1–94, 95–131, 132–177 and 178–215 forming the 4 Fab light-chain domains. The final model consists of LeuT residues 11–511, Fab light-chain residues 1–216, Fab heavy-chain residues 1–102, 104–219, and several detergent molecules.

The changes in helix and domain orientation were analysed using the program Interhlx (K. Yap, University of Toronto) and DynDom, respectively, and molecular figures were prepared using PyMOL.

**Saturation binding assays.** Dissociation constants of LeuT mutants for leucine were determined by scintillation proximity assays as described previously<sup>25</sup> at a protein concentration of 1  $\mu$ M in 20 mM Tris-MES pH 7.0, 200 mM NaCl and 1 mM C<sub>12</sub>M. Non-specific binding was measured in duplicate using 1 mM L-leucine as cold competitor and total binding was measured in triplicate. Data were fit with GraphPad Prism.

**Transport time course.** LeuT mutants were reconstituted into liposomes as previously described<sup>25</sup>, at a protein to lipid ratio of 1:100, and loaded with either Buffer 1 (20 mM Tris-MES pH 6.0 and 500 mM KCl) for uptake or Buffer 2 (20 mM Tris-MES pH 6.0, 500 mM NaCl and 10 mM L-leucine) for exchange. Transport was initiated at 27 °C by diluting proteoliposomes to 10  $\mu$ g ml<sup>-1</sup> into external buffer (20 mM Tris-MES pH 6.0, 500 mM NaCl) containing either 200 nM (for LeuT<sup>K</sup>(Y108F)) or 400 nM (for LeuT<sup>K</sup>(TS) and LeuT<sup>K</sup>(TSY)) or 10 nM [<sup>3</sup>H]-leucine. Uptake or exchange was followed by quenching 100  $\mu$ l samples of the reaction mixture in 1.8 ml of ice-cold Buffer 1 for uptake or Buffer 2 for exchange. Background counts were measured with control reactions performed in the absence of sodium. Reactions were measured in replicates of 3–5 and analysed using GraphPad Prism.

**FSEC.** FSEC experiments<sup>26</sup> were carried out using a Superose 6 10/300 column with the mobile phase consisting of 20 mM Tris, pH 8.0, 1 mM C<sub>12</sub>M, and either 200–400 mM NaCl and 10 mM leucine or 200 mM KCl for analyses of LeuT in substrate-bound and apo states, respectively. Fab-LeuT complexes were prepared by mixing LeuT and Fab in a molar ratio of 1:2. Elution was followed using tryptophan fluorescence with excitation and emission wavelengths at 280 nm and 335 nm, respectively.

- Otwinowski, Z. & Minor, W. Processing of X-ray diffraction data collected in oscillation mode. *Methods Enzymol.* **276**, 307–326 (1997).
- Collaborative Computational Project 4. The CCP4 suite: programs for protein crystallography. *Acta Crystallogr. D* **50**, 760–763 (1994).
- Matthews, B. W. Solvent content of protein crystals. *J. Mol. Biol.* **33**, 491–497 (1968).
- McCoy, A. J. Solving structures of protein complexes by molecular replacement with Phaser. *Acta Crystallogr. D* **63**, 32–41 (2007).
- Kopp, J. & Schwede, T. The SWISS-MODEL Repository: new features and functionalities. *Nucleic Acids Res.* **34**, D315–D318 (2006).



56. Emsley, P. & Cowtan, K. Coot: model-building tools for molecular graphics. *Acta Crystallogr. D* **60**, 2126–2132 (2004).
57. Adams, P. D. *et al.* PHENIX: building new software for automated crystallographic structure determination. *Acta Crystallogr. D* **58**, 1948–1954 (2002).
58. Painter, J. & Merritt, E. A. Optimal description of a protein structure in terms of multiple groups undergoing TLS motion. *Acta Crystallogr. D* **62**, 439–450 (2006).
59. Terwilliger, T. C. Using prime-and-switch phasing to reduce model bias in molecular replacement. *Acta Crystallogr. D* **60**, 2144–2149 (2004).
60. Kelley, L. A. & Sternberg, M. J. Protein structure prediction on the Web: a case study using the Phyre server. *Nature Protocols* **4**, 363–371 (2009).
61. Chen, V. B. *et al.* MolProbity: all-atom structure validation for macromolecular crystallography. *Acta Crystallogr. D* **66**, 12–21 (2010).

# Clonal evolution in relapsed acute myeloid leukaemia revealed by whole-genome sequencing

Li Ding<sup>1,2\*</sup>, Timothy J. Ley<sup>1,3,4\*</sup>, David E. Larson<sup>1</sup>, Christopher A. Miller<sup>1</sup>, Daniel C. Koboldt<sup>1</sup>, John S. Welch<sup>3</sup>, Julie K. Ritchey<sup>3</sup>, Margaret A. Young<sup>3</sup>, Tamara Lamprecht<sup>3</sup>, Michael D. McLellan<sup>1</sup>, Joshua F. McMichael<sup>1</sup>, John W. Wallis<sup>1,2</sup>, Charles Lu<sup>1</sup>, Dong Shen<sup>1</sup>, Christopher C. Harris<sup>1</sup>, David J. Dooling<sup>1,2</sup>, Robert S. Fulton<sup>1,2</sup>, Lucinda L. Fulton<sup>1,2</sup>, Ken Chen<sup>1,2</sup>, Heather Schmidt<sup>1</sup>, Joelle Kalicki-Weizer<sup>1</sup>, Vincent J. Magrini<sup>1,2</sup>, Lisa Cook<sup>1</sup>, Sean D. McGrath<sup>1</sup>, Tammi L. Vickery<sup>1</sup>, Michael C. Wendt<sup>1,2</sup>, Sharon Heath<sup>3</sup>, Mark A. Watson<sup>5</sup>, Daniel C. Link<sup>3,4</sup>, Michael H. Tomasson<sup>3,4</sup>, William D. Shannon<sup>6</sup>, Jacqueline E. Payton<sup>5</sup>, Shashikant Kulkarni<sup>2,4,5</sup>, Peter Westervelt<sup>3,4</sup>, Matthew J. Walter<sup>3,4</sup>, Timothy A. Graubert<sup>3,4</sup>, Elaine R. Mardis<sup>1,2,4</sup>, Richard K. Wilson<sup>1,2,4</sup> & John F. DiPersio<sup>3,4</sup>

**Most patients with acute myeloid leukaemia (AML) die from progressive disease after relapse, which is associated with clonal evolution at the cytogenetic level<sup>1,2</sup>. To determine the mutational spectrum associated with relapse, we sequenced the primary tumour and relapse genomes from eight AML patients, and validated hundreds of somatic mutations using deep sequencing; this allowed us to define clonality and clonal evolution patterns precisely at relapse. In addition to discovering novel, recurrently mutated genes (for example, *WAC*, *SMC3*, *DIS3*, *DDX41* and *DAXX*) in AML, we also found two major clonal evolution patterns during AML relapse: (1) the founding clone in the primary tumour gained mutations and evolved into the relapse clone, or (2) a subclone of the founding clone survived initial therapy, gained additional mutations and expanded at relapse. In all cases, chemotherapy failed to eradicate the founding clone. The comparison of relapse-specific versus primary tumour mutations in all eight cases revealed an increase in transversions, probably due to DNA damage caused by cytotoxic chemotherapy. These data demonstrate that AML relapse is associated with the addition of new mutations and clonal evolution, which is shaped, in part, by the chemotherapy that the patients receive to establish and maintain remissions.**

To investigate the genetic changes associated with AML relapse, and to determine whether clonal evolution contributes to relapse, we performed whole-genome sequencing of primary tumour–relapse pairs and matched skin samples from eight patients, including unique patient identifier (UPN) 933124, whose primary tumour mutations were previously reported<sup>3</sup>. Informed consent explicit for whole-genome sequencing was obtained for all patients on a protocol approved by the Washington University Medical School Institutional Review Board. We obtained >25× haploid coverage and >97% diploid coverage for each sample (Supplementary Table 1 and Supplementary Information). These patients were from five different French–American–British haematological subtypes, with elapsed times of 235–961 days between initial diagnosis and relapse (Supplementary Table 2a, b).

Candidate somatic events in the primary tumour and relapse genomes were identified<sup>4,5</sup> and selected for hybridization capture-based validation using methods described in Supplementary Information. Deep sequencing of the captured target DNAs from skin (the matched normal tissue), primary tumour and relapse tumour specimens<sup>6</sup> (Supplementary Table 3) yielded a median of 590-fold coverage per site. The average number of mutations and structural variants was 539 (range 118–1,292) per case (Fig. 1a).

The general approach for relapse analysis is exemplified by the first sequenced case (UPN 933124). A total of 413 somatic events from tiers

1 to 3 were validated (see ref. 7 for tier designations; Supplementary Fig. 1a and Supplementary Tables 4a and 5). Of these, 78 mutations were relapse-specific (63 point mutations, 1 dinucleotide mutation, 13 indels and 1 translocation; relapse-specific criteria described in Supplementary Information and shown in Supplementary Fig. 1b), 5 point mutations were primary-tumour-specific, and 330 (317 point mutations and 13 indels) were shared between the primary tumour and relapse samples (Fig. 1a, b and Supplementary Fig. 2). The skin sample was contaminated with leukaemic cells for this case (peripheral white blood cell count was 105,000 cells mm<sup>-3</sup> when the skin sample was banked), with an estimated tumour content in the skin sample of 29% (Supplementary Information). In addition to the ten somatic non-synonymous mutations originally reported for the primary tumour sample<sup>3</sup>, we identified one deletion that was not detected in the original analysis (*DNMT3A* L723fs (ref. 8)) and three mis-sense mutations previously misclassified as germline events (*SMC3* G662C, *PDXDC1* E421K and *TTN* E14263K) (Fig. 1b, Table 1 and Supplementary Table 4b).

A total of 169 tier 1 coding mutations (approximately 21 per case) were identified in the eight patients (Table 1 and Supplementary Tables 4b and 6), of which 19 were relapse-specific. In addition to mutations in known AML genes such as *DNMT3A* (ref. 8), *FLT3* (ref. 9), *NPM1* (ref. 10), *IDH1* (ref. 7), *IDH2* (ref. 11), *WT1* (ref. 12), *RUNX1* (refs 13, 14), *PTPR* (ref. 3), *PHF6* (ref. 15) and *ETV6* (ref. 16) in these eight patients, we also discovered novel, recurring mutations in *WAC*, *SMC3*, *DIS3*, *DDX41* and *DAXX* using 200 AML cases whose exomes were sequenced as part of the Cancer Genome Atlas AML project (Table 1, Supplementary Table 4b and Supplementary Fig. 3; T.J.L., R.K.W. and The Cancer Genome Atlas working group on AML, unpublished data). Details regarding the novel, recurrently mutated genes are provided in Table 1, Supplementary Tables 4b and 7 and Supplementary Figs 3 and 4. Structural and functional analyses of structural variants are presented in the Supplementary Information (Supplementary Figs 5–10 and Supplementary Tables 2, 8 and 9).

The generation of high-depth sequencing data allowed us to quantify accurately mutant allele frequencies in all cases, permitting estimation of the size of tumour clonal populations in each AML sample. On the basis of mutation clustering results, we inferred the identity of four clones having distinct sets of mutations (clusters) in the primary tumour of AML1/UPN 933124 (Supplementary Information). The median mutant allele frequencies in the primary tumour for clusters 1 to 4 were 46.86%, 24.89%, 16.00% and 2.39%, respectively (Fig. 1b and Supplementary Table 5c). Clone 1 is the ‘founding’ clone (that is, the other subclones are derived from it), containing the cluster 1 mutations; assuming that nearly all of these mutations are heterozygous, they must

<sup>1</sup>The Genome Institute, Washington University, St Louis, Missouri 63108, USA. <sup>2</sup>Department of Genetics, Washington University, St Louis, Missouri 63110, USA. <sup>3</sup>Department of Internal Medicine, Division of Oncology, Washington University, St Louis, Missouri 63110, USA. <sup>4</sup>Siteman Cancer Center, Washington University, St Louis, Missouri 63110, USA. <sup>5</sup>Department of Pathology and Immunology, Washington University, St Louis, Missouri 63110, USA. <sup>6</sup>Division of Biostatistics, Washington University, St Louis, Missouri 63110, USA.

\*These authors contributed equally to this work.

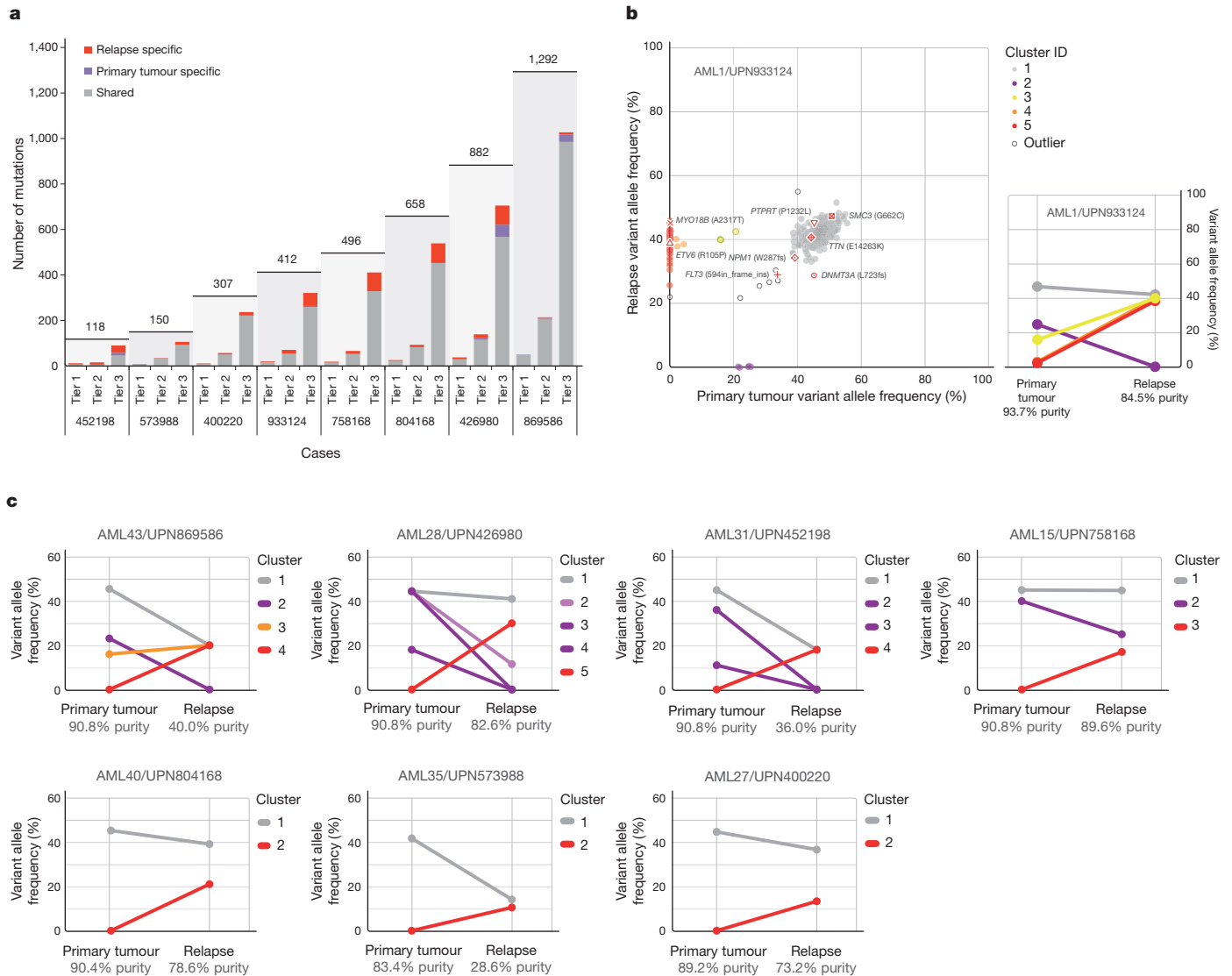


**Figure 1 | Somatic mutations quantified by deep sequencing of capture validation targets in eight acute myeloid leukaemia primary tumour and relapse pairs.** **a**, Summary of tier 1–3 mutations detected in eight cases (not including translocations). All mutations shown were validated using capture followed by deep sequencing. Shared mutations are in grey, primary tumour-specific mutations in blue and relapse-specific mutations in red. The total number of tier 1–3 mutations for each case is shown above the light-grey rectangle. **b**, Mutant allele frequency distribution of validated mutations from tier 1–3 in the primary tumour and relapse of case UPN 933124 (left). Mutant allele frequencies for five primary-tumour-specific mutations were obtained from a 454 deep read-count experiment. Four mutation clusters were identified

in the primary tumour, and one was found at relapse. Five low-level mutations in both the primary tumour and relapse (including four residing in known copy number variable regions) were excluded from the clustering analysis. Non-synonymous mutations from genes that are recurrently mutated in AML are shown. The change of mutant allele frequencies for mutations from the five clusters is shown (right) between the primary tumour and relapse. The orange and red lines are superimposed. **c**, The mutation clusters detected in the primary tumour and relapse samples from seven additional AML patients. The relationship between clusters in the primary tumour and relapse samples are indicated by lines linking them.

**Table 1 | Coding mutations identified in eight primary tumour–relapse pairs**

UPN	Total tier 1 mutations (primary/relapse)	Recurrently mutated genes in primary tumour	Relapse-specific non-synonymous somatic mutations
452198	9/9	<i>DNMT3A, NPM1, FLT3, IDH1</i>	None
573988	6/8	<i>NPM1, IDH2</i>	<i>STOX2</i>
804168	22/26	<i>FLT3, WT1, PHF6, FAM5C, TTC39A</i>	<i>SLC25A12, RIPK4, ABCD2</i>
933124	14/17	<i>DNMT3A, NPM1, FLT3, TTN, SMC3, PTPRT</i>	<i>ETV6*, MYO18B*, WAC*†, STK4</i>
400220	12/13	<i>FLT3, RUNX1, WT1, PLEKHH1</i>	None
426980	32/35	<i>IDH2, MYO1F, DDX4</i>	<i>GBP4, DCLK1, IDH2*, DCLK1*, ZNF260</i>
758168	15/19	<i>DNAH9, DIS3, CNTN5, PML-RARA†</i>	<i>ENSGO0000180144, DAGLA*</i>
869586	51/50	<i>RUNX1, WT1, TTN, PHF6, NF1, SUZ12, NCOA7, EED, DAXX, ACSS3, WAC, NUMA1</i>	None

Tier 1 mutation counts exclude RNA genes.

\* Recurrent mutations occurring in relapse sample.

† Translocations were not included in tier 1 mutation counts.



be present in virtually all the tumour cells at presentation and at relapse, as the variant frequency of these mutations is  $\sim 40\text{--}50\%$ . Clone 2 (with cluster 2 mutations) and clone 3 (with cluster 3 mutations) must be derived from clone 1, because virtually all the cells in the sample contain the cluster 1 mutations (Fig. 2a). It is likely that a single cell from clone 3 gained a set of mutations (cluster 4) to form clone 4: these survived chemotherapy and evolved to become the dominant clone at relapse. We do not know whether any of the cluster 4 mutations conferred chemotherapy resistance; although none had translational consequences, we cannot rule out a relevant regulatory mutation in this cluster.

Assuming that all the mutations detected are heterozygous in the primary tumour sample (with a malignant cellular content at 93.72% for the primary bone marrow sample, see Supplementary Information), we were able to calculate the fraction of total malignant cells in each clone. Clone 1 is the founding clone; 12.74% of the tumour cells contain only this set of mutations. Clones 2, 3 and 4 evolved from clone 1. The additional mutations in clones 2 and 3 may have provided a growth or survival advantage, as 53.12% and 29.04% of the tumour cells belonged to these clones, respectively. Only 5.10% of the tumour cells were from clone 4, indicating that it may have arisen last (Fig. 2a). However, the relapse clone evolved from clone 4. A single clone

containing all of the cluster 5 mutations was detected in the relapse sample; clone 5 evolved from clone 4, but gained 78 new somatic alterations after sampling at day 170. As all mutations in clone 5 appear to be present in all relapse tumour cells, we suspect that one or more of the mutations in this clone provided a strong selective advantage that contributed to relapse. The *ETV6* mutation, the *MYO18B* mutation, and/or the *WNK1-WAC* fusion are the most likely candidates, as *ETV6*, *MYO18B* and *WAC* are recurrently mutated in AML.

We evaluated the mutation clusters in the seven additional primary tumour–relapse pairs by assessing peaks of allele frequency using kernel density estimation (Supplementary Fig. 11 and Supplementary Information). We thus inferred the numbers and malignant fractions of clones in each primary tumour and relapse sample. Similar to UPN 933124, multiple mutation clusters (2–4) were present in each of the primary tumours from four patients (UPN 869586, UPN 426980, UPN 452198 and UPN 758168). However, only one major cluster was detected in each of the primary tumours from the three other patients (UPN 804168, UPN 573988 and UPN 400220) (Fig. 1c and Supplementary Table 10). Importantly, all eight patients gained relapse-specific mutations, although the number of clusters in the relapse samples varied (Fig. 1).

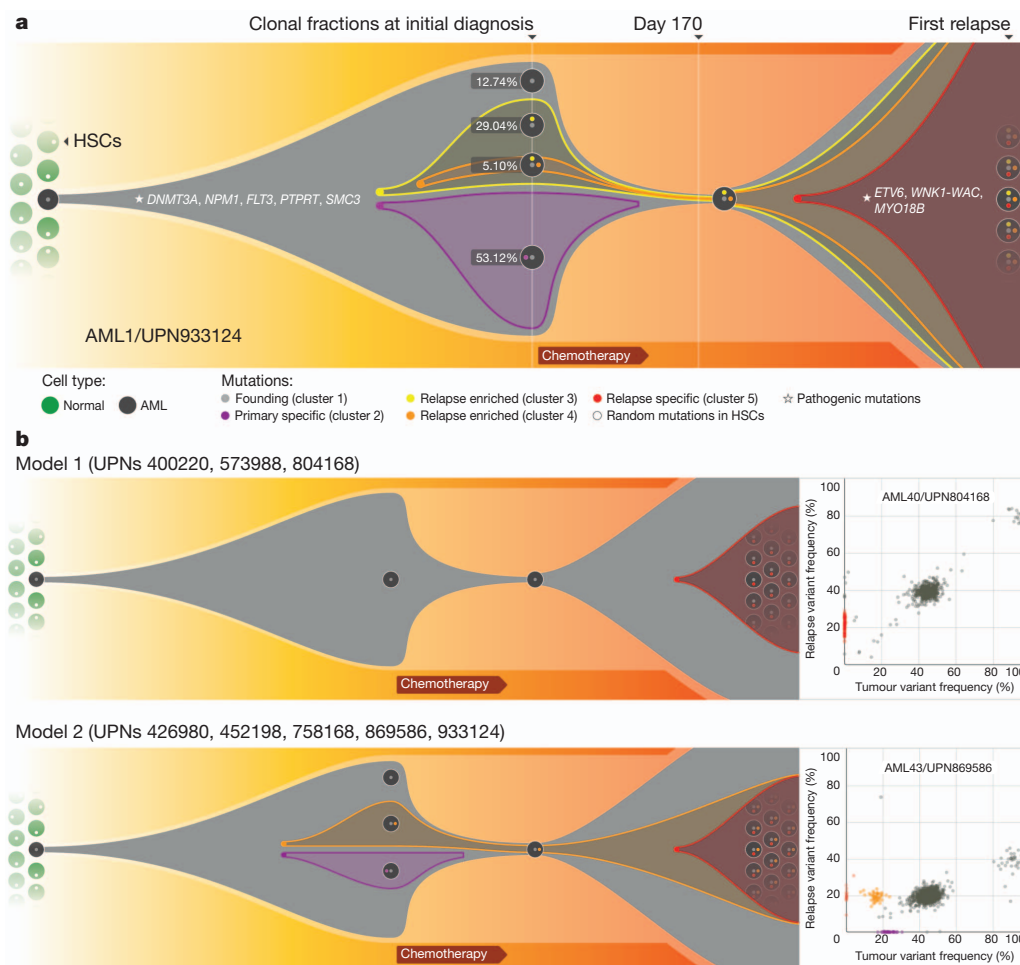


**Figure 2 | Graphical representation of clonal evolution from the primary tumour to relapse in UPN 933124, and patterns of tumour evolution observed in eight primary tumour and relapse pairs. a**, The founding clone in the primary tumour in UPN 933124 contained somatic mutations in *DNMT3A*, *NPM1*, *PTPRT*, *SMC3* and *FLT3* that are all recurrent in AML and probably relevant for pathogenesis; one subclone within the founding clone evolved to become the dominant clone at relapse by acquiring additional mutations, including recurrent mutations in *ETV6* and *MYO18B*, and a *WNK1-WAC* fusion gene. HSC, haematopoietic stem cell. **b**, Examples of the

two major patterns of tumour evolution in AML. Model 1 shows the dominant clone in the primary tumour evolving into the relapse clone by gaining relapse-specific mutations; this pattern was identified in three primary tumour and relapse pairs (UPN 804168, UPN 573988 and UPN 400220). Model 2 shows a minor clone carrying the vast majority of the primary tumour mutations survived and expanded at relapse. This pattern was observed in five primary tumour and relapse pairs (UPN 933124, UPN 452198, UPN 758168, UPN 426980 and UPN 869586).

Two major patterns of clonal evolution were detected at relapse (Fig. 2b and Supplementary Fig. 3): in cases with pattern 1, the dominant clone in the primary tumour gained additional mutations and evolved into the relapse clone (UPN 804168, UPN 573988 and UPN 400220). These patients may simply be inadequately treated (for example, elderly patients who cannot tolerate aggressive consolidation, like UPN 573988), or they may have mutations in their founding clones (or germline variants) that make these cells more resistant to therapy (UPN 804168 and UPN 400220). In patients with pattern 2, a minor subclone carrying the vast majority (but not all) of the primary tumour mutations survived, gained mutations, and expanded at relapse; a subset of primary tumour mutations was often eradicated by therapy, and were not detected at relapse (UPN 758168, UPN 933124, UPN 452198, UPN 426980 and UPN 869586). Specific mutations in a key subclone may contribute to chemotherapy resistance, or the mutations important for relapse may be acquired during tumour evolution, or both. Notably, in cases 426980 and 758168, a second primary tumour clone survived chemotherapy and was also present at relapse (Fig. 1c and Supplementary Fig. 3). Owing to current technical limits in our ability to detect mutations in rare cells (mostly related to currently achievable levels of coverage with whole genome sequencing), our models represent a minimal estimate of the clonal heterogeneity in AML.

All eight patients received cytarabine and anthracycline for induction therapy, and additional cytotoxic chemotherapy for consolidation; treatment histories are summarized in Supplementary Table 2 and described in Supplementary Information. To investigate the potential impact of treatment on relapse mutation types, we compared the six classes of transition and transversion mutations in the primary tumour with the relapse-specific mutations in all eight patients (Fig. 3a). Although C•G→T•A transitions are the most common mutations found in both primary and relapse AML genomes, their frequencies are significantly different between the primary tumour mutations (51.1%) and relapse-specific mutations (40.5%) ( $P = 2.99 \times 10^{-7}$ ). Moreover, we observed an average of 4.5%, 5.3% and 4.2% increase in A•T→C•G ( $P = 9.13 \times 10^{-7}$ ), C•G→A•T ( $P = 0.00312$ ) and C•G→G•C ( $P = 0.00366$ ) transversions, respectively, in relapse-specific mutations. Notably, an increased A•T→C•G transversion rate has also been observed in cases of chronic lymphocytic leukaemia with mutated immunoglobulin genes<sup>17</sup>. C•G→A•T transversions are the most common mutation in lung cancer patients who were exposed to tobacco-borne carcinogens<sup>18</sup> (Fig. 3b and Supplementary Table 11). We

examined the 456 relapse-specific mutations and 3,590 primary tumour point mutations from all eight cases as a group, and found that the transversion frequency is significantly higher for relapse-specific mutations (46%) than for primary tumour mutations (30.7%) ( $P = 3.71 \times 10^{-11}$ ), indicating that chemotherapy has a substantial effect on the mutational spectrum at relapse. Similar results were obtained when we limited the analysis to the 213 mutations that had 0% variant frequency in the primary tumour samples (Supplementary Fig. 1b); the transversion frequency for relapse-specific mutations was 50.4%, versus 31.4% for primary tumour samples ( $P = 3.89 \times 10^{-9}$ ). Very few copy-number alterations were detected in the eight relapse samples, suggesting that the increased transversion rate is not associated with generalized genomic instability (Supplementary Fig. 12).

We first described the use of deep sequencing to define precisely the variant allele frequencies of the mutations in the AML genome of case 933124 (ref. 3), and here have refined and extended this technique to examine clonal evolution at relapse. The analysis of eight primary AML and relapse pairs has revealed unequivocal evidence for a common origin of tumour subpopulations; a dominant mutation cluster representing the founding clone was discovered in the primary tumour sample in all cases. The relationship of the founding clone (and subclones thereof) to the 'leukaemia initiating cell' is not yet clear—purification of clonal populations and functional testing would be required to establish this relationship. We observed the loss of primary tumour subclones at relapse in four of eight cases, suggesting that some subclones are indeed eradicated by therapy (Figs 1 and 2 and Supplementary Fig. 3). Some mutations gained at relapse may alter the growth properties of AML cells, or confer resistance to additional chemotherapy. Regardless, each tumour displayed clear evidence of clonal evolution at relapse and a higher frequency of transversions that were probably induced by DNA damage from chemotherapy. Although chemotherapy is required to induce initial remissions in AML patients, our data also raise the possibility that it contributes to relapse by generating new mutations in the founding clone or one of its subclones, which then can undergo selection and clonal expansion. These data demonstrate the critical need to identify the disease-causing mutations for AML, so that targeted therapies can be developed that avoid the use of cytotoxic drugs, many of which are mutagens.

This study extends the findings of previous studies<sup>19–21</sup>, which recently described patterns of clonal evolution in ALL patients using fluorescence *in situ* hybridization and/or copy number alterations detected by SNP arrays, and it enhances the understanding of genetic changes acquired during disease progression, as previously described for breast and pancreatic cancer metastases<sup>22–25</sup>. Our data provide complementary information on clonal evolution in AML, using a much larger set of mutations that were quantified with deep sequencing; this provides an unprecedented number of events that can be used to define precisely clonal size and mutational evolution at relapse. Both ALL and AML share common features of clonal heterogeneity at presentation followed by dynamic clonal evolution at relapse, including the addition of new mutations that may be relevant for relapse pathogenesis. Clonal evolution can also occur after allogeneic transplantation (for example, loss of mismatched HLA alleles via a uniparental disomy mechanism), demonstrating that the type of therapy itself can affect clonal evolution at relapse<sup>26,27</sup>. Taken together, these data demonstrate that AML cells routinely acquire a small number of additional mutations at relapse, and suggest that some of these mutations may contribute to clonal selection and chemotherapy resistance. The AML genome in an individual patient is clearly a 'moving target'; eradication of the founding clone and all of its subclones will be required to achieve cures.

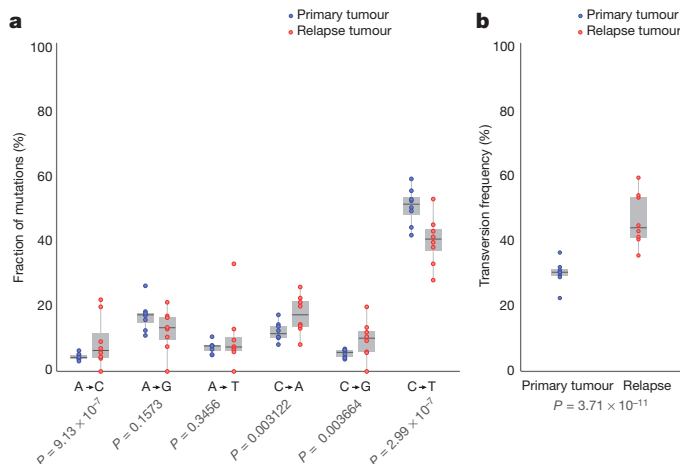


**Figure 3 | Comparison of mutational classes between primary tumours and relapse samples.** **a**, Fraction of the primary tumour and relapse-specific mutations in each of the transition and transversion categories. **b**, Transversion frequencies of the primary tumour and relapse-specific mutations from eight AML tumour and relapse pairs. 456 relapse-specific mutations and 3,590 primary tumour mutations from eight cases were used for assessing statistical significance using proportion tests.

## METHODS SUMMARY

Illumina paired-end reads were aligned to NCBI build36 using BWA 0.5.5 (<http://sourceforge.net/projects/bio-bwa/>). Somatic mutations were identified using SomaticSniper<sup>28</sup> and a modified version of the SAMtools indel caller. Structural

variations were identified using BreakDancer<sup>5</sup>. All predicted non-repetitive somatic SNVs, indels and all structural variants were included on custom sequence capture arrays from Roche Nimblegen. Illumina 2 × 100-bp paired-end sequencing reads were produced after elution from capture arrays. VarScan<sup>6</sup> and a read remapping strategy using Crossmatch (P. Green, unpublished data) and BWA were used for determining the validation status of predicted SNVs, indels and structural variants. A complete description of the materials and methods is provided in Supplementary Information. All sequence variants for the AML tumour samples from eight cases have been submitted to dbGaP (accession number phs000159.v4.p2).

Received 29 March; accepted 29 November 2011.

Published online 11 January 2012.

- Testa, J. R., Mintz, U., Rowley, J. D., Vardiman, J. W. & Golomb, H. M. Evolution of karyotypes in acute nonlymphocytic leukemia. *Cancer Res.* **39**, 3619–3627 (1979).
- Garson, O. M. *et al.* Cytogenetic studies of 103 patients with acute myelogenous leukemia in relapse. *Cancer Genet. Cytogenet.* **40**, 187–202 (1989).
- Ley, T. J. *et al.* DNA sequencing of a cytogenetically normal acute myeloid leukaemia genome. *Nature* **456**, 66–72 (2008).
- Li, H. *et al.* The Sequence Alignment/Map format and SAMtools. *Bioinformatics* **25**, 2078–2079 (2009).
- Chen, K. *et al.* BreakDancer: an algorithm for high-resolution mapping of genomic structural variation. *Nature Methods* **6**, 677–681 (2009).
- Koboldt, D. C. *et al.* VarScan: variant detection in massively parallel sequencing of individual and pooled samples. *Bioinformatics* **25**, 2283–2285 (2009).
- Mardis, E. R. *et al.* Recurring mutations found by sequencing an acute myeloid leukemia genome. *N. Engl. J. Med.* **361**, 1058–1066 (2009).
- Ley, T. J. *et al.* DNMT3A mutations in acute myeloid leukemia. *N. Engl. J. Med.* **363**, 2424–2433 (2010).
- Nakao, M. *et al.* Internal tandem duplication of the *flt3* gene found in acute myeloid leukemia. *Leukemia* **10**, 1911–1918 (1996).
- Falini, B. *et al.* Cytoplasmic nucleophosmin in acute myelogenous leukemia with a normal karyotype. *N. Engl. J. Med.* **352**, 254–266 (2005).
- Ward, P. S. *et al.* The common feature of leukemia-associated IDH1 and IDH2 mutations is a neomorphic enzyme activity converting alpha-ketoglutarate to 2-hydroxyglutarate. *Cancer Cell* **17**, 225–234 (2010).
- King-Underwood, L., Renshaw, J. & Pritchard-Jones, K. Mutations in the Wilms' tumor gene *WT1* in leukemias. *Blood* **87**, 2171–2179 (1996).
- Gao, J. *et al.* Isolation of a yeast artificial chromosome spanning the 8;21 translocation breakpoint t(8;21)(q22;q22.3) in acute myelogenous leukemia. *Proc. Natl Acad. Sci. USA* **88**, 4882–4886 (1991).
- Kirito, K. *et al.* A novel RUNX1 mutation in familial platelet disorder with propensity to develop myeloid malignancies. *Haematologica* **93**, 155–156 (2008).
- Van Vlierberghe, P. *et al.* PHF6 mutations in adult acute myeloid leukemia. *Leukemia* **25**, 130–134 (2011).
- Barjesteh van Waalwijk van Doorn-Khosrovani, S. *et al.* Somatic heterozygous mutations in ETV6 (TEL) and frequent absence of ETV6 protein in acute myeloid leukemia. *Oncogene* **24**, 4129–4137 (2005).
- Puente, X. S. *et al.* Whole-genome sequencing identifies recurrent mutations in chronic lymphocytic leukaemia. *Nature* **475**, 101–105 (2011).
- Ding, L. *et al.* Somatic mutations affect key pathways in lung adenocarcinoma. *Nature* **455**, 1069–1075 (2008).
- Mullighan, C. G. *et al.* Genomic analysis of the clonal origins of relapsed acute lymphoblastic leukemia. *Science* **322**, 1377–1380 (2008).
- Anderson, K. *et al.* Genetic variegation of clonal architecture and propagating cells in leukaemia. *Nature* **469**, 356–361 (2011).
- Notta, F. *et al.* Evolution of human BCR-ABL1 lymphoblastic leukaemia-initiating cells. *Nature* **469**, 362–367 (2011).
- Ding, L. *et al.* Genome remodelling in a basal-like breast cancer metastasis and xenograft. *Nature* **464**, 999–1005 (2010).
- Shah, S. P. *et al.* Mutational evolution in a lobular breast tumour profiled at single nucleotide resolution. *Nature* **461**, 809–813 (2009).
- Yachida, S. *et al.* Distant metastasis occurs late during the genetic evolution of pancreatic cancer. *Nature* **467**, 1114–1117 (2010).
- Navin, N. *et al.* Tumour evolution inferred by single-cell sequencing. *Nature* **472**, 90–94 (2011).
- Vago, L. *et al.* Loss of mismatched HLA in leukemia after stem-cell transplantation. *N. Engl. J. Med.* **361**, 478–488 (2009).
- Villalobos, I. B. *et al.* Relapse of leukemia with loss of mismatched HLA resulting from uniparental disomy after haploidentical hematopoietic stem cell transplantation. *Blood* **115**, 3158–3161 (2010).
- Larson, D. E. *et al.* SomaticSniper: identification of somatic point mutations in whole genome sequencing data. *Bioinformatics* (in the press).

**Supplementary Information** is linked to the online version of the paper at [www.nature.com/nature](http://www.nature.com/nature).

**Acknowledgements** We thank the Analysis Pipeline group for developing the automated sequence analysis pipelines; the LIMS group for developing tools and software to manage samples and sequencing; the Systems group for providing the IT infrastructure and HPC solutions required for sequencing and analysis; and R. T. Demeter for experimental support. We also thank The Cancer Genome Atlas for allowing us to use unpublished data for this study, and the Washington University Cancer Genome Initiative for their support. This work was funded by grants to R.K.W. and the National Human Genome Research Institute (NHGRI U54 HG003079), and grants to T.J.L. from the National Cancer Institute (PO1 CA101937) and the Barnes-Jewish Hospital Foundation (00335-0505-02).

**Author Contributions** T.J.L., L.D., J.F.D., E.R.M. and R.K.W. designed the experiments. L.D. and T.J.L. led data analysis. L.D., D.E.L., C.A.M., D.C.K., J.S.W., M.D.M., J.W.W., C.L., D.S., C.C.H., K.C., H.S., J.K.-V., M.C.W., M.A.W., W.D.S., J.E.P. and S.K. performed data analysis. J.F.M., M.D.M. and L.D. prepared figures and tables. J.S.W., J.K.R., M.A.Y., T.L., R.S.F., L.L.F., V.J.M., L.S., L.C., S.D.M. and T.L.V. performed laboratory experiments. S.H. and P.W. provided samples and clinical data. D.J.D. provided informatics support. T.J.L., D.C.L., M.H.T., E.R.M., R.K.W. and J.F.D. developed project concept. L.D., T.J.L., M.J.W., T.A.G. and J.F.D. wrote the manuscript.

**Author Information** All sequence variants for the AML tumour samples from eight cases have been submitted to dbGaP under accession number phs000159.v4.p2. Reprints and permissions information is available at [www.nature.com/reprints](http://www.nature.com/reprints). This paper is distributed under the terms of the Creative Commons Attribution-Non-Commercial-Share Alike licence, and is freely available to all readers at [www.nature.com/nature](http://www.nature.com/nature). The authors declare no competing financial interests. Readers are welcome to comment on the online version of this article at [www.nature.com/nature](http://www.nature.com/nature). Correspondence and requests for materials should be addressed to T.J.L. ([timley@wustl.edu](mailto:timley@wustl.edu)).



# Molecular recognition of a single sphingolipid species by a protein's transmembrane domain

F.-Xavier Contreras<sup>1\*</sup>, Andreas M. Ernst<sup>1\*</sup>, Per Haberkant<sup>1†</sup>, Patrik Björkholm<sup>2,3</sup>, Erik Lindahl<sup>2,4</sup>, Başak Gönen<sup>1</sup>, Christian Tischer<sup>5</sup>, Arne Elofsson<sup>2,3</sup>, Gunnar von Heijne<sup>2,3</sup>, Christoph Thiele<sup>6</sup>, Rainer Pepperkok<sup>5</sup>, Felix Wieland<sup>1</sup> & Britta Brügger<sup>1</sup>

**Functioning and processing of membrane proteins critically depend on the way their transmembrane segments are embedded in the membrane<sup>1</sup>. Sphingolipids are structural components of membranes and can also act as intracellular second messengers. Not much is known of sphingolipids binding to transmembrane domains (TMDs) of proteins within the hydrophobic bilayer, and how this could affect protein function. Here we show a direct and highly specific interaction of exclusively one sphingomyelin species, SM 18, with the TMD of the COPI machinery protein p24 (ref. 2). Strikingly, the interaction depends on both the headgroup and the backbone of the sphingolipid, and on a signature sequence (VXXTLXXIY) within the TMD. Molecular dynamics simulations show a close interaction of SM 18 with the TMD. We suggest a role of SM 18 in regulating the equilibrium between an inactive monomeric and an active oligomeric state of the p24 protein<sup>3,4</sup>, which in turn regulates COPI-dependent transport. Bioinformatic analyses predict that the signature sequence represents a conserved sphingolipid-binding cavity in a variety of mammalian membrane proteins. Thus, in addition to a function as second messengers, sphingolipids can act as cofactors to regulate the function of transmembrane proteins. Our discovery of an unprecedented specificity of interaction of a TMD with an individual sphingolipid species adds to our understanding of why biological membranes are assembled from such a large variety of different lipids.**

Lipidomics of Golgi-derived COPI vesicles unravelled a partial segregation of cholesterol and most sphingomyelin species except for one (*N*-stearoyl sphingomyelin) from the vesicle fraction<sup>5</sup>. To understand the molecular mechanisms of SM 18 enrichment in vesicles, we investigated *in vivo* binding of lipids to p24 and p23, membrane proteins involved in COPI vesicle biogenesis (Supplementary Fig. 1)<sup>6</sup>. Lipid crosslinking<sup>7,8</sup> revealed a strong sphingolipid labelling of p24 (Fig. 1a, b, see also Supplementary Fig. 2), with a fivefold higher recovery of radioactivity per mole of protein compared to p23. To analyse if this interaction of p24 with sphingomyelin is specific for SM 18, we established a liposomal assay to study TMD–lipid interactions (see Supplementary Fig. 3). Maltose-binding protein (MBP) fusions of the TMDs of p23 and p24 were analysed in a liposomal Förster resonance energy transfer (FRET) system for their interaction with pentaenoyl-SM 18 (SM 18:5, as a fluorescently labelled analogue of endogenous SM 18:O (ref. 9), see Supplementary Information), pentaenoyl-ceramide 18, or pentaenoyl-phosphatidylcholine (PC) 18 (Fig. 1c). Distinct FRET was observed between the TMD of p24 and SM 18:5, but not with the TMD of p23. A mutant lacking the single Trp residue within the TMD (p24(TMD)W4A) did not trigger a FRET. With ceramide 18:5 no FRET was observed for any TMD. With PC 18:5 weak FRET was observed with the p24(TMD), and a slightly stronger signal was obtained with p23(TMD). Together these results show a marked specificity of p24 for

sphingomyelin, with both the hydrophobic moiety and the hydrophilic choline phosphate headgroup needed for the interaction. We next analysed the extent of FRET obtained between the TMDs of p24 and p23 and pentaenoyl-sphingomyelins covering the range of the major endogenous molecular species from C14 to C24. A remarkable specificity was observed for the interaction of p24 with SM 18 in liposomes composed of di-oleoyl-phosphatidylcholine/phosphatidylethanolamine/pentaenoyl-sphingomyelin (Fig. 1d, left panel). In liposomes more closely reflecting the lipid composition of the mammalian Golgi apparatus we again observed a striking specificity for SM 18, with weak but significant signals for SM 20 and SM 22 (Fig. 1d, right panel). In contrast, the TMD of p23 did not give rise to comparable FRET with any of the sphingomyelin species.

To define the structural prerequisites for SM 18 binding, we performed an Ala scan across the TMD of p24 starting with position 8 within the TMD, leaving three amino acids before and after W4 unchanged, to minimise a direct influence on the biophysical properties of the FRET donor. Two groups of mutants were observed, with a strong inhibition of FRET with Ala substitutions in positions 8, 10, 11, 12, 15, 19 and 20 (group 1), and less inhibition in positions 13, 16, 17, 18 and 21 (group 2) (Supplementary Fig. 4). Although group 1 mutants showed a strong inhibition of FRET, they maintained a high degree of specificity for SM 18:5 (for example, V11A, Supplementary Fig. 5a). In contrast, group 2 mutants V13, T16, L17 and Y21 showed strongly compromised species specificity (Supplementary Fig. 5c–f). Mutant G18A was not further investigated, because G18W had not shown an alteration of SM 18 binding (Supplementary Fig. 3d), indicating that G18 is not directly involved in the lipid–p24 interaction. From the above data we deduced that a carboxy-terminal motif made of amino acid residues V13, T16, L17 and Y21 of the p24 TMD (V181, T184, L185 and Y189 in the full-length protein) represents a structural determinant for the specific binding of SM 18 (see also Supplementary Discussion). An energy-minimised projection of the TMD yielded the structure depicted in Fig. 2a (left). In this model, a groove is formed from the Tyr residue in position 21 to the Val residue in position 13. Within the sphingomyelin-binding motif, the  $\beta$ -branched residue Ile is found in position 20 of the TMD.  $\beta$ -branched residues were shown to contribute to TMD–TMD interactions<sup>10,11</sup> by conveying higher rigidity and thereby allowing for stronger London dispersion forces. In the model, this residue is part of the cavity and thus is likely to contribute to the binding motif. If this groove indeed accommodates the backbone of SM 18, the insertion of a bulky hydrophobic residue in position 17 should prevent lipid binding. To fill this cavity with minimal alterations of the helical structure<sup>12</sup> we introduced a Phe residue in position 17 of the TMD. FRET analysis showed that binding of SM 18 was completely inhibited (Fig. 2b). To challenge the existence of a C-terminal binding motif, we transferred the C-terminal half of the p24 TMD to the amino-terminal half of the non-sphingomyelin-binding TMD of p23. The

<sup>1</sup>Heidelberg University Biochemistry Center, Im Neuenheimer Feld 328, 69120 Heidelberg, Germany. <sup>2</sup>Center for Biomembrane Research, Department of Biochemistry and Biophysics, Stockholm University, SE-106 91 Stockholm, Sweden. <sup>3</sup>Stockholm Bioinformatics Center, Science for Life Laboratory Stockholm University, Box 1031, SE-171 21 Solna, Sweden. <sup>4</sup>Theoretical & Computational Biophysics, Royal Institute of Technology, AlbaNova University Centre, SE-106 91 Stockholm, Sweden. <sup>5</sup>ALMF, EMBL, Meyerhofstrasse 1, 69117 Heidelberg, Germany. <sup>6</sup>LIMES Life and Medical Sciences Institute, Carl-Troll-Strasse 31, 53115 Bonn, Germany. <sup>†</sup>Present address: Cell Biology and Biophysics Unit EMBL, Meyerhofstrasse 1, 69117 Heidelberg, Germany.

\*These authors contributed equally to this work.

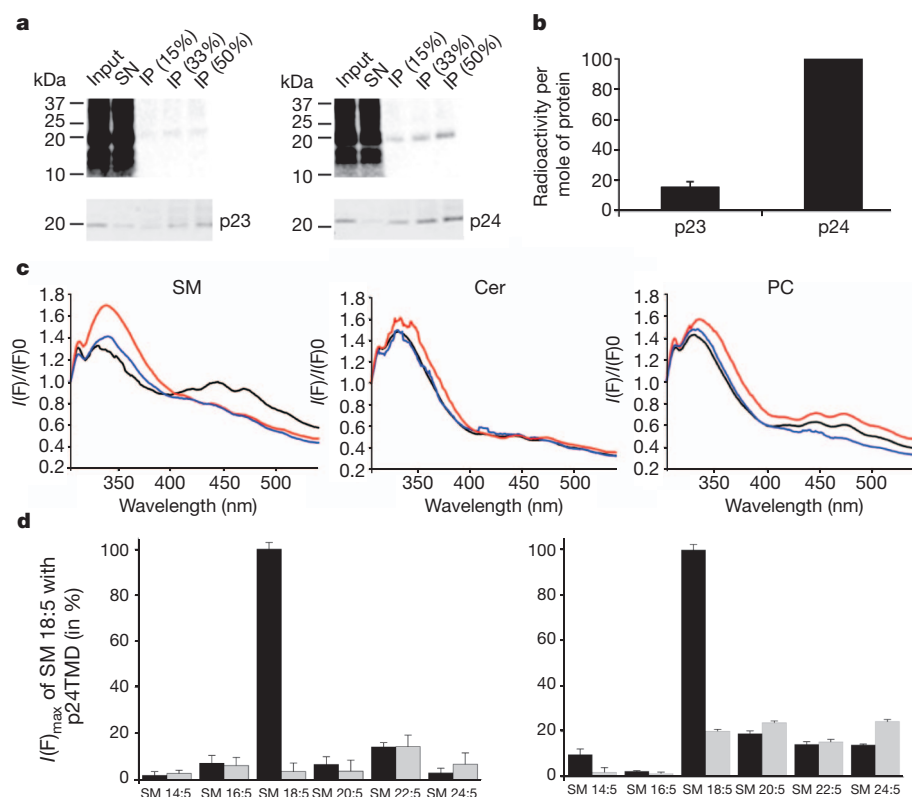


**Figure 1 | p24 specifically interacts with SM 18.**  
**a**, CHO cells were grown in the presence of 200  $\mu$ Ci of [ $^3$ H]-photo-sphingosine. Cells were ultraviolet-irradiated, lysed and subjected to immunoprecipitation using antibodies against p23 or p24. Radioactivity recovered from input, supernatant (SN) and immunoprecipitation (IP) was visualized by autoradiography (upper panels). Lower panels, western blot analysis.  
**b**, Quantification of immunoprecipitated radioactivity. **c**, *In vitro* FRET analysis of MBP-TMD fusion proteins and pentaenoyl-lipids. Proteoliposomes contained either SM 18:5, pentaenoyl-ceramide 18:5 (Cer) or PC 18:5. Red curve, p23(TMD); black curve, p24(TMD); blue curve, p24(TMD)W4A. **d**, Proteoliposomes were prepared in the presence of p24(TMD) (black bars) or p23(TMD) (grey bars) and 1 mol% of pentaenoyl-sphingomyelins, mimicking a liquid-disordered phase (left panel) or a mammalian Golgi membrane (right panel). Background-subtracted fluorescence data are normalized to SM 18:5, and are the mean  $\pm$  s.d. of three experiments.

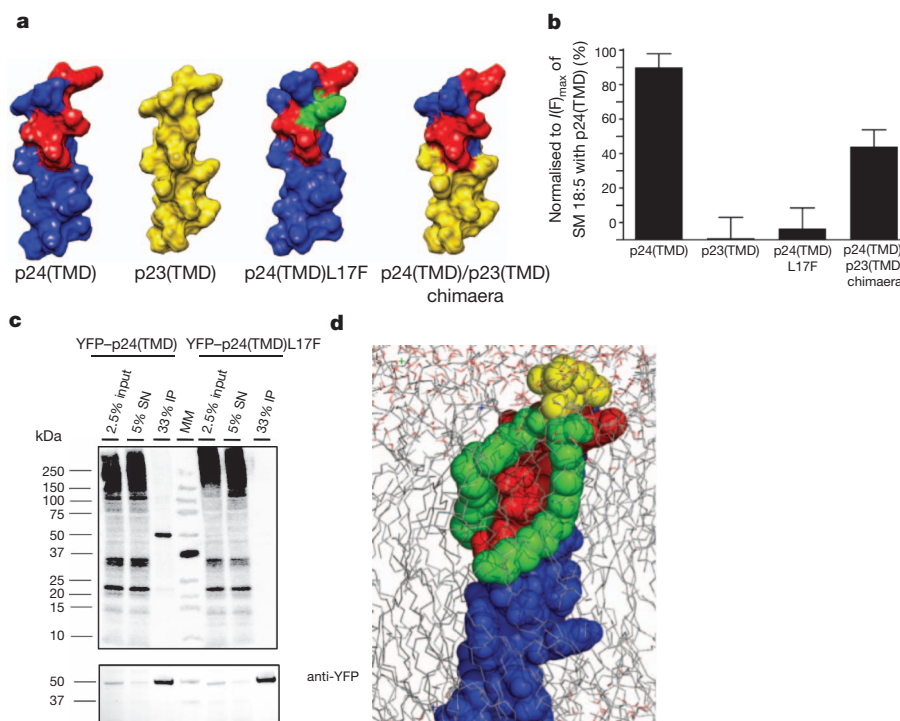


**Figure 2 | Characterization of the sphingomyelin-binding pocket.**

**a**, Energy-minimised structure of p24(TMD), p23(TMD), p24(TMD)L17F, and p24/p23 chimaeric TMD. Residues of p24 involved in SM 18 recognition are depicted in red, the L17F mutation is highlighted in green.  
**b**, Proteoliposomes containing p24(TMD), p23(TMD), p24(TMD)L17F or the p24(TMD)/p23(TMD) chimaera were prepared in the presence of 1 mol% of pentaenoyl-SM (18:5) (di-oleoyl-phosphatidylcholine/phosphatidylethanolamine/pentaenoyl-sphingomyelin, molar ratio 89:10:1).

FRET measurements were performed as described above. Data are the mean  $\pm$  s.d. of three independent experiments. **c**, *In vivo* binding of [ $^3$ H]-sphingolipids to YFP-p24 and YFP-p24L17F. Upper panel, autoradiography; lower panel, western blot. MM, molecular mass marker. **d**, Molecular dynamics simulations: snapshot of a SM 18-p24(TMD) interaction. The interacting lipid and residues displaying the signature are highlighted. Blue, p24(TMD); red, sphingomyelin-binding pocket, yellow; SM 18:0 head group; green, SM 18:0 backbone and N-acylated fatty acid.

chimaeric TMD yielded 50% of the level of FRET compared to the TMD of p24 (Fig. 2b). Interestingly, the chimaera shows promiscuity with regard to the sphingomyelin molecular species, binding significant amounts of SM 20 and SM 22 in addition to SM 18 (Supplementary Fig. 5b), pointing at a contribution of the N-terminal residues to the orientation of the sphingomyelin-binding pocket. The loss of FRET by mutant p24(TMD)L17F suggested a loss of SM 18 binding. To test loss of binding *in vivo*, full-length wild-type p24 and p24L17F were expressed as yellow fluorescent protein (YFP) fusion proteins (Supplementary Fig. 6a). Sphingolipid labelling showed that p24L17F has lost the capability to bind sphingomyelin *in vivo* (Fig. 2c). Sphingomyelin is known to be synthesized in the luminal leaflet; however, *in vitro* experiments suggest that sphingolipids can flip between the two leaflets stimulated by free ceramide that translocates from the cytoplasmic to the luminal leaflet of membranes<sup>13</sup> (see also Supplementary Fig. 6b). In addition, *in vivo* analyses using the sphingomyelin-binding toxin equinatoxin II point to an occurrence of sphingomyelin in the cytoplasmic leaflet of the Golgi membrane<sup>14</sup>.

To understand binding selectivity at the molecular level, we compared the structural features of sphingomyelin molecular species (see Supplementary Fig. 7). Molecular dynamics simulations and monolayer experiments<sup>15–17</sup> suggest that only the sphingomyelin species with a suitable dynamic volume would fit into the cavity of the p24 TMD formed by V13, T16 and L17, excluding lipids with larger dynamic volume (SM 14 and 16, see Supplementary Fig. 7). Sphingomyelin species with smaller dynamic volumes, however, would need to be excluded from the hydrophobic cavity by a different mechanism (see Supplementary Discussion).

We next investigated the binding signature through a series of five molecular simulations of the TMD of p24 embedded in a POPC bilayer including sphingomyelins with fatty acids of C14 to C22. By extending

all atomistic simulations to 1  $\mu$ s we observe spontaneous diffusion of sphingomyelins to the TMD and close interaction with the proposed binding site primarily for SM 18, and to a minor extent also SM 16 and SM 20 (Supplementary Fig. 8). The polar head group of sphingomyelin ‘wraps around’ the Y21 side chain, while the C18 chain continues down around the helix and packs in the groove between V13, T16 and L17 (Fig. 2d and Supplementary Movie 1). The sphingosine chain packs in the groove below V13. The other sphingomyelin molecular species also approach the p24 TMD, but steric effects seem to make interactions more difficult in these cases. For instance, the SM 14 lipid head group rather interacts with Y21 by packing mostly below the side chain, which rotates both lipid chains away from the helix and prevents efficient packing (Supplementary Movie 2). The lifetime of the SM 18–p24 (TMD) complex in the molecular dynamics simulation was of the order of 250 ns, which is five times longer than observed for the other sphingomyelin species. Likewise, as compared to SM 18, the relative dissociation constant of SM 14 was 6.5-fold higher (Supplementary Fig. 9). Notably, although the TMD of p24 is highly conserved in higher eukaryotes, it is not conserved in yeast, in agreement with the absence of sphingomyelin in this organism.

To search for other candidate sphingolipid-interacting proteins, we defined a binding signature where either a  $\beta$ -branched residue (I, T, V) or Leu is allowed in any of the first four positions, and an aromatic residue (F, W, Y) is allowed in the last position (Fig. 3a). The signature represents  $4^4 \times 3 = 768$  unique sequence motifs, 13 of which were found to be overrepresented in a set of mammalian membrane proteins (see Full Methods in Supplementary Information). These 13 motifs identified 48 candidate proteins (Supplementary Table 1), mostly localized to the plasma membrane (Fig. 3b).

Three recombinant candidates and, as a negative control, the non-signature containing asialo-glycoprotein receptor, were expressed in

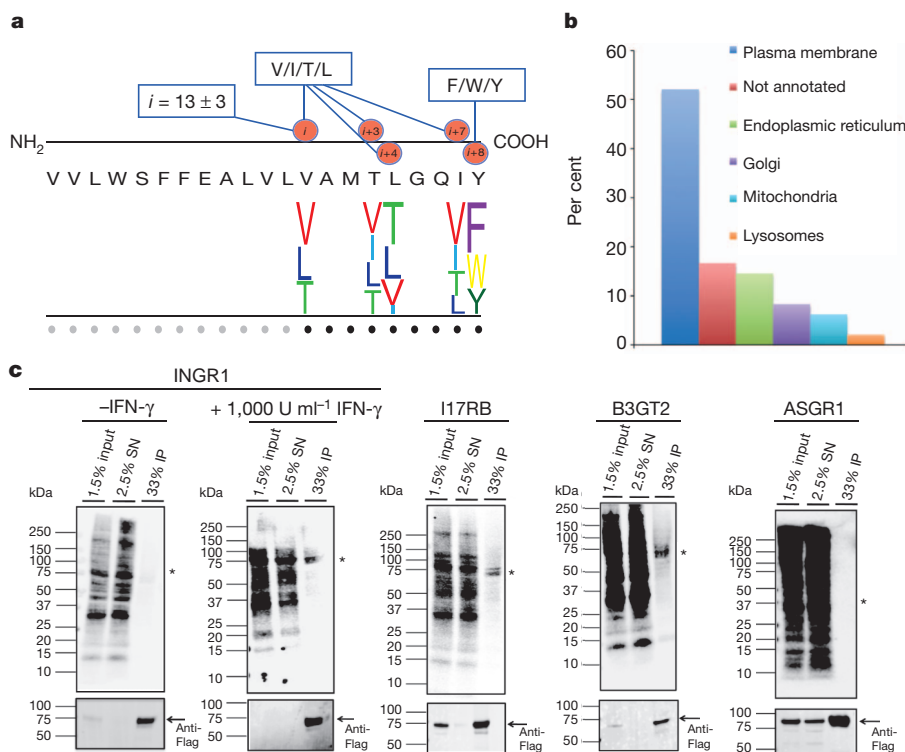


**Figure 3 | A conserved sphingolipid binding signature.** **a**, Signature patterns used for both randomization/shuffling approach and screening for potential sphingolipid-binding proteins (upper panel). All possible combinations were analysed for significant overrepresentations in TMDs. Motifs overrepresented with a  $P$ -value  $\leq 0.05$  were used to generate the sequence logo (lower panel). The letter size corresponds to the probability to find this amino acid at that position. Each dot below the line represents an amino acid position.

**b**, Intracellular distribution of signature-containing transmembrane protein candidates. **c**, *In vivo* labelling of Flag-tagged constructs of human INGR1, I17RB, B3GT2 and ASGR1. Cells were labelled with [ $^3$ H]-photo-sphingosine, ultraviolet-irradiated, lysed and subjected to IP using an antibody against the Flag tag. Radioactivity recovered with protein candidates was visualized by autoradiography. The corresponding proteins were detected by western blot analysis. Asterisk, expected size of proteins.



HeLa cells (Supplementary Fig. 10). In *in vivo* labelling all three candidates showed strong binding to a sphingolipid (Fig. 3c). Interestingly, INGR1 binds to a sphingolipid only upon activation by its ligand interferon  $\gamma$ .

What may be the function of the highly specific interaction of SM 18 with p24? As p24 acts as membrane machinery for the formation of COPI vesicles, we analysed if a loss of binding of SM 18 would affect transport of biosynthetic cargo<sup>18,19</sup>. We analysed transport of vesicular stomatitis G (VSV-G) protein<sup>20,21</sup> to determine the transport rates in HeLa cells stably transfected with full-length wild-type p24 or p24L17F, N-terminally fused to YFP. Expression of p24L17F caused an acceleration of VSV-G protein transport (Fig. 4a), resulting in a 2.5-fold increase of the fraction of total VSV-G that reached the plasma membrane at  $t = 45$  min (see also Supplementary Fig. 11a, b).

How can a marked acceleration of transport be caused by a lack of binding of SM 18 to p24? A decrease in recycling efficiency would cause an increased anterograde transport of this cargo, and should affect Golgi export. To test this possibility, we measured Golgi export kinetics using fluorescence loss in photobleaching (FLIP). Whereas Golgi-associated fluorescence of YFP-wild-type p24 was reduced to 50% within 4.5 min, the half-life of Golgi residence of YFP-p24L17F was significantly prolonged to 7 min (Fig. 4b, for controls see Supplementary Fig. 11c). To analyse if indeed retrograde transport from the Golgi to the ER is affected we monitored trafficking to the

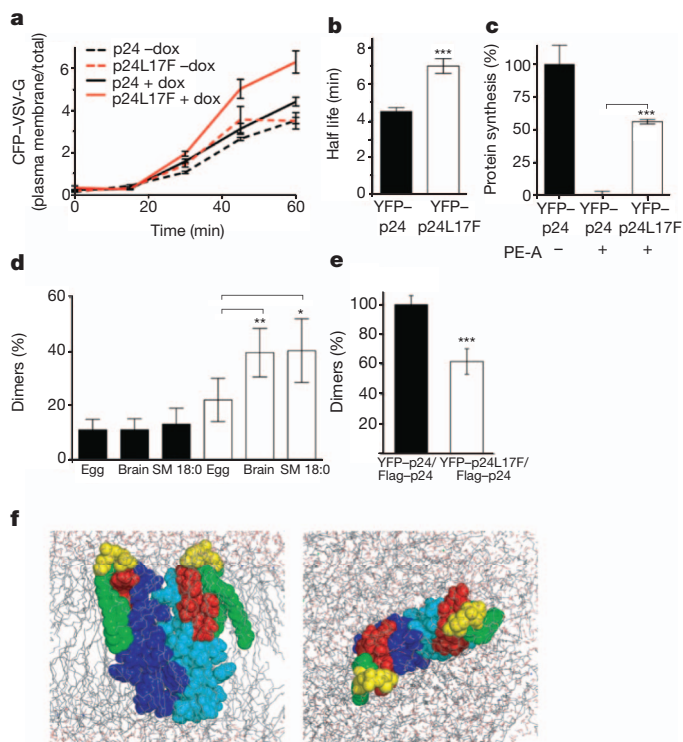


**Figure 4 | Binding of SM 18 to p24(TMD) affects protein transport and triggers p24 dimerization.** **a**, Expression of p24L17F accelerates transport of ts-O45-G protein. For each time point and experiment ( $n = 3$ ), at least 600 cells were analysed. CFP-VSV-G, cyan-fluorescent-protein-tagged ts-O45-G protein. **b**, Comparison of the average half lives of decay in fluorescence in Golgi of YFP-p24 and YFP-p24L17F. Data represent the mean of  $n = 22$ –24 experiments  $\pm$  s.e.  $P$ -value of two-tailed, unpaired  $t$ -test  $< 0.0001$  (\*\*\*) is given. **c**, Expression of YFP-p24L17F reduces toxicity of PE-A. Error bars, s.e.m. Statistics: two-tailed, unpaired  $t$ -test. **d**, SM 18:0 induces dimerization of p24(TMD) (white bars) but not of p23(TMD) (black bars). TMDs reconstituted into proteoliposomes with indicated sphingomyelin species subjected to chemical crosslinking ( $n = 4$ ). Results of paired, two-tailed  $t$ -tests are given. **e**, Quantification of homodimers in CHO cells *in situ*. Error bars, s.e.m. Statistics: two-tailed, unpaired  $t$ -test. \*\*\* $P < 0.001$  **f**, Model of p24(TMD) SM 18 complexes. Left, side view; right, top view.

endoplasmic reticulum of *Pseudomonas aeruginosa* exotoxin A (PE-A). The toxin is transported from the Golgi to the endoplasmic reticulum in a COPI-dependent manner<sup>22</sup>. In contrast to cells expressing YFP-p24, YFP-p24L17F-cells showed a significant reduction of PE-A-dependent inhibition of protein biosynthesis, the readout for exotoxin transport to the endoplasmic reticulum (Fig. 4c, for controls see Supplementary Fig. 11d). Together, these data imply that efficient retrograde COPI-dependent transport depends on binding of p24 to sphingomyelin.

To test if binding to SM 18 might help organize the dimeric, transport active state of p24, by affecting its monomer/oligomer equilibrium via the TMD, we used a chemical crosslinking assay with proteoliposomes reconstituted from p24 family-TMD fusion proteins and sphingomyelins of various species compositions. Indeed, dimerization is significantly induced only in liposomes containing both SM 18 and p24 (Fig. 4d and Supplementary Fig. 12a–c). To analyse if dimerization of p24 is also affected *in vivo* in the presence of full-length p24L17F, we monitored dimerization of p24 using an *in situ* protein–protein interaction assay. Signals were significantly reduced in the presence of p24L17F (Fig. 4e, for representative images and western blots see Supplementary Fig. 12d). Similar results were obtained when cells expressing either YFP-p24 or YFP-p24L17F were subjected to chemical crosslinking (Supplementary Fig. 12e).

How might a complex of dimeric p24 and SM 18 be organized? We performed molecular dynamics simulations starting from different models based on the sphingomyelin-bound monomeric structures from the initial simulations. The most stable model was one with a rather polar dimerization interface not overlapping with the sphingomyelin binding site (Fig. 4f); this complex remained intact for at least 200 ns. Besides a direct role of sphingomyelin in stabilizing a p24 dimer, other mechanisms of sphingomyelin-triggered dimerization might apply, such as a sphingomyelin-dependent conformational change of p24 or build-up of high concentrations of p24 in SM 18 microdomains.

In summary, we have uncovered an unprecedented specificity of interaction between an individual sphingolipid species and a TMD, and have defined a structural signature within the TMD for this binding. Specific binding of individual lipid species to TMDs of membrane proteins may serve different functions and help to understand the need for the complexity of membrane lipid compositions at a functional level.

## METHODS SUMMARY

***In vivo* photoaffinity labelling of CHO cells.** Cells were labelled with the different photoactivatable precursors as described<sup>7,8</sup>. Briefly, cells were washed with PBS, followed by addition of freshly prepared delipidated medium containing lipid precursors. After labelling, the medium was removed and cells were washed twice with PBS. After ultraviolet irradiation, cells were collected and lysed in lysis buffer (50 mM HEPES-NaOH, pH 7.4, 100 mM NaCl, 5 mM EDTA, 1% Triton X-100 (v/v), 0.5% deoxycholate (w/v) and protease inhibitor cocktail). After lysis, samples were subjected to immunoprecipitation. After SDS-PAGE and western blotting, radioactively labelled proteins were detected by digital autoradiography ( $\beta$ -Imager 2000, Biospace).

**FRET assay.** FRET was used to probe the interaction of TMDs with pentaenoyl-lipids directly. FRET experiments were conducted on a Jasco 6500 unit spectrofluorometer (Jasco). Proteoliposomes (protein/lipid, 1:5,000) were diluted in a quartz cuvette in buffer (10 mM HEPES/KOH pH 7.4) to a final concentration of 0.1 mM. The proteoliposomes were incubated at 25 °C for 5 min under continuous stirring. The extent of FRET between TMD and pentaenoyl-lipids was determined by recording emission spectra from 310 to 540 nm. Emission spectra were collected, exciting at 280 nm the Trp present in the TMD. Slit widths of 5 nm were used for both excitation and emission.

**Full Methods** and any associated references are available as Supplementary information.

Received 12 January; accepted 30 November 2011.

Published online 9 January 2012.

1. Coskun, U. & Simons, K. Cell membranes: the lipid perspective. *Structure* **19**, 1543–1548 (2011).

2. Popoff, V., Adolf, F., Brugger, B. & Wieland, F. COPI budding within the Golgi stack. *Cold Spring Harb. Perspect. Biol.* doi:10.1101/cshperspect.a005231 (15 August 2011).
3. Béthune, J. *et al.* Coatamer, the coat protein of COPI transport vesicles, discriminates endoplasmic reticulum residents from p24 proteins. *Mol. Cell. Biol.* **26**, 8011–8021 (2006).
4. Reinhard, C. *et al.* Receptor-induced polymerization of coatamer. *Proc. Natl Acad. Sci. USA* **96**, 1224–1228 (1999).
5. Brügger, B. *et al.* Evidence for segregation of sphingomyelin and cholesterol during formation of COPI-coated vesicles. *J. Cell Biol.* **151**, 507–518 (2000).
6. Beck, R., Ravet, M., Wieland, F. T. & Cassel, D. The COPI system: molecular mechanisms and function. *FEBS Lett.* **583**, 2701–2709 (2009); corrigendum **583**, 3541 (2009).
7. Haberkant, P. *et al.* Protein-sphingolipid interactions within cellular membranes. *J. Lipid Res.* **49**, 251–262 (2008).
8. Thiele, C., Hannah, M. J., Fahrenholz, F. & Huttner, W. B. Cholesterol binds to synaptophysin and is required for biogenesis of synaptic vesicles. *Nature Cell Biol.* **2**, 42–49 (2000).
9. Kuerschner, L. *et al.* Polyene-lipids: a new tool to image lipids. *Nature Methods* **2**, 39–45 (2005).
10. Russ, W. P. & Engelman, D. M. The GxxxG motif: a framework for transmembrane helix-helix association. *J. Mol. Biol.* **296**, 911–919 (2000).
11. Senes, A., Gerstein, M. & Engelman, D. M. Statistical analysis of amino acid patterns in transmembrane helices: the GxxxG motif occurs frequently and in association with  $\beta$ -branched residues at neighboring positions. *J. Mol. Biol.* **296**, 921–936 (2000).
12. Jones, D. T., Taylor, W. R. & Thornton, J. M. A mutation data matrix for transmembrane proteins. *FEBS Lett.* **339**, 269–275 (1994).
13. Contreras, F. X., Basanez, G., Alonso, A., Herrmann, A. & Goni, F. M. Asymmetric addition of ceramides but not dihydroceramides promotes transbilayer (flip-flop) lipid motion in membranes. *Biophys. J.* **88**, 348–359 (2005).
14. Bakrac, B. *et al.* A toxin-based probe reveals cytoplasmic exposure of Golgi sphingomyelin. *J. Biol. Chem.* **285**, 22186–22195 (2010).
15. Li, X. M., Smaby, J. M., Momsen, M. M., Brockman, H. L. & Brown, R. E. Sphingomyelin interfacial behavior: the impact of changing acyl chain composition. *Biophys. J.* **78**, 1921–1931 (2000).
16. Niemelä, P., Hyvönen, M. T. & Vattulainen, I. Structure and dynamics of sphingomyelin bilayer: insight gained through systematic comparison to phosphatidylcholine. *Biophys. J.* **87**, 2976–2989 (2004).
17. Niemelä, P. S., Hyvönen, M. T. & Vattulainen, I. Influence of chain length and unsaturation on sphingomyelin bilayers. *Biophys. J.* **90**, 851–863 (2006).
18. Presley, J. F. *et al.* ER-to-Golgi transport visualized in living cells. *Nature* **389**, 81–85 (1997).
19. Scales, S. J., Pepperkok, R. & Kreis, T. E. Visualization of ER-to-Golgi transport in living cells reveals a sequential mode of action for COPII and COPI. *Cell* **90**, 1137–1148 (1997).
20. Keller, P., Toomre, D., Diaz, E., White, J. & Simons, K. Multicolour imaging of post-Golgi sorting and trafficking in live cells. *Nature Cell Biol.* **3**, 140–149 (2001).
21. Simpson, J. C. *et al.* An RNAi screening platform to identify secretion machinery in mammalian cells. *J. Biotechnol.* **129**, 352–365 (2007).
22. Jackson, M. E. *et al.* The KDEL retrieval system is exploited by *Pseudomonas* exotoxin A, but not by Shiga-like toxin-1, during retrograde transport from the Golgi complex to the endoplasmic reticulum. *J. Cell Sci.* **112**, 467–475 (1999).

**Supplementary Information** is linked to the online version of the paper at [www.nature.com/nature](http://www.nature.com/nature).

**Acknowledgements** The authors would like to thank T. Sachsenheimer for technical assistance, A. Brodde for help with lipid synthesis, D. Cassel for comments on the manuscript, and the members of the Wieland laboratory for discussion. This work was supported by a grant of the German research foundation (DFG, TRR83) to B.B. and F.W. and by ERC grants to E.L. (209825) and G.v.H. (AdG232648); F.-X.C. was supported by a FEBS fellowship and A.M.E. by the Peter and Traudl Engelhorn foundation.

**Author Contributions** F.-X.C., A.M.E. and P.H. designed and performed the experiments. P.B. performed the bioinformatics analyses under the supervision of A.E., G.v.H. and A.M.E.; E.L. designed, performed and interpreted molecular dynamics simulation experiments. B.G. performed *in vivo* crosslinking experiments. C.Th. provided reagents and helped to establish photolabelling and FRET experiments. C.Ti. and R.P. provided reagents and tools and supported A.M.E. concerning VSV-G experiments. F.W. and B.B. designed the experiments and wrote the manuscript.

**Author Information** Reprints and permissions information is available at [www.nature.com/reprints](http://www.nature.com/reprints). The authors declare no competing financial interests. Readers are welcome to comment on the online version of this article at [www.nature.com/nature](http://www.nature.com/nature). Correspondence and requests for materials should be addressed to F.W. ([felix.wieland@bzh.uni-heidelberg.de](mailto:felix.wieland@bzh.uni-heidelberg.de)) and B.B. ([britta.bruegger@bzh.uni-heidelberg.de](mailto:britta.bruegger@bzh.uni-heidelberg.de)).

# Transiting circumbinary planets Kepler-34 b and Kepler-35 b

William F. Welsh<sup>1</sup>, Jerome A. Orosz<sup>1</sup>, Joshua A. Carter<sup>2</sup>, Daniel C. Fabrycky<sup>3</sup>, Eric B. Ford<sup>4</sup>, Jack J. Lissauer<sup>5</sup>, Andrej Prša<sup>6</sup>, Samuel N. Quinn<sup>2,7</sup>, Darin Ragozzine<sup>2</sup>, Donald R. Short<sup>1</sup>, Guillermo Torres<sup>2</sup>, Joshua N. Winn<sup>8</sup>, Laurance R. Doyle<sup>9</sup>, Thomas Barclay<sup>5,10</sup>, Natalie Batalha<sup>5,11</sup>, Steven Bloemen<sup>12</sup>, Erik Brugamyer<sup>13</sup>, Lars A. Buchhave<sup>14,15</sup>, Caroline Caldwell<sup>13</sup>, Douglas A. Caldwell<sup>9</sup>, Jessie L. Christiansen<sup>5,9</sup>, David R. Ciardi<sup>16</sup>, William D. Cochran<sup>13</sup>, Michael Endl<sup>13</sup>, Jonathan J. Fortney<sup>17</sup>, Thomas N. Gautier III<sup>18</sup>, Ronald L. Gilliland<sup>19</sup>, Michael R. Haas<sup>5</sup>, Jennifer R. Hall<sup>20</sup>, Matthew J. Holman<sup>2</sup>, Andrew W. Howard<sup>21</sup>, Steve B. Howell<sup>5</sup>, Howard Isaacson<sup>21</sup>, Jon M. Jenkins<sup>5,9</sup>, Todd C. Klaus<sup>20</sup>, David W. Latham<sup>2</sup>, Jie Li<sup>5,9</sup>, Geoffrey W. Marcy<sup>21</sup>, Tsevi Mazeh<sup>22</sup>, Elisa V. Quintana<sup>5,9</sup>, Paul Robertson<sup>13</sup>, Avi Shporer<sup>23,24</sup>, Jason H. Steffen<sup>25</sup>, Gur Windmiller<sup>1</sup>, David G. Koch<sup>5</sup> & William J. Borucki<sup>5</sup>

**Most Sun-like stars in the Galaxy reside in gravitationally bound pairs of stars<sup>1,2</sup> (binaries). Although long anticipated<sup>3–8</sup>, the existence of a ‘circumbinary planet’ orbiting such a pair of normal stars was not definitively established until the discovery<sup>9</sup> of the planet transiting (that is, passing in front of) Kepler-16. Questions remained, however, about the prevalence of circumbinary planets and their range of orbital and physical properties. Here we report two additional transiting circumbinary planets: Kepler-34 (AB)b and Kepler-35 (AB)b, referred to here as Kepler-34 b and Kepler-35 b, respectively. Each is a low-density gas-giant planet on an orbit closely aligned with that of its parent stars. Kepler-34 b orbits two Sun-like stars every 289 days, whereas Kepler-35 b orbits a pair of smaller stars (89% and 81% of the Sun’s mass) every 131 days. The planets experience large multi-periodic variations in incident stellar radiation arising from the orbital motion of the stars. The observed rate of circumbinary planets in our sample implies that more than ~1% of close binary stars have giant planets in nearly coplanar orbits, yielding a Galactic population of at least several million.**

The new planets were identified using 671 days of data from the NASA Kepler spacecraft<sup>10</sup>. As part of its mission<sup>11</sup> to detect Earth-like planets via the transit method, Kepler is monitoring more than 2,000 eclipsing binary stars<sup>12,13</sup>. From these, we selected a sample of 750 systems with orbital periods ranging from 0.9 to 276 days, and for which eclipses of both stars occur. For each system, we measured the eclipse times for both stars and searched for departures from strict periodicity, as would be produced by gravitational perturbations from a third body.

All 750 systems were searched by eye for planetary transits, with particular attention being paid to a subset (18% of the total) that exhibited significant differences between the periods derived from the deeper primary eclipses, and those derived from the shallower secondary eclipses (for details, see Supplementary Information). (Here ‘primary eclipse’ indicates the eclipse of the primary star by the secondary star.) This led to the discovery of Kepler-34 and

Kepler-35, and a candidate system KOI-2939. KOI-2939 (Kepler Input Catalog<sup>14</sup> number 05473556) exhibited a single transit at BJD (barycentric Julian date)  $2,454,996.995 \pm 0.010$  of duration 2.5 h and depth 0.18%. The transit duration constrains the size and velocity of the third body and is consistent with a Jovian planet transiting the secondary star, but we cannot verify its planetary nature. We defer discussion for a future investigation.

The stars of Kepler-34 (denoted A and B, where A is the brighter, more massive primary star) have an orbital period of 28 days, with a period difference between primary and secondary eclipses of  $4.91 \pm 0.59$  s. Three transits were detected (Fig. 1), with the first and second being transits of the primary star, while the third is of the secondary star. Notably the transit durations are all different, ruling out the most common type of ‘false positive’, a background eclipsing binary. Circumbinary transits naturally vary in duration as a consequence of the changing velocity of the stars. The Kepler photometry was supplemented by spectroscopic observations of the radial-velocity variations of both stars (Fig. 1f), in order to determine the orbital scale and sizes of all three bodies. The photometric and spectroscopic data were fitted with a model<sup>9,15</sup> that accounts for the three-body gravitational dynamics and the loss of light due to eclipses and transits (see Supplementary Information). The model fit confirms that the transiting body is a planet with 22% of the mass of Jupiter (69 Earth masses) and 76% of the radius of Jupiter (8.6 Earth radii). The primary and secondary stars are similar to the Sun. Using the spectra, we also measured the effective temperature and abundance of heavy elements (metallicity) of both stars. The observed stellar parameters match the Yonsei-Yale theoretical models of stellar evolution<sup>16</sup> for an age of 5–6 Gyr. The parameters and uncertainties are given in Table 1, with details in Supplementary Information.

The stars of Kepler-35 (A and B) have an orbital period of 21 days, with a period difference between primary and secondary eclipses of  $1.89 \pm 0.48$  s. Four transits were detected (Fig. 2 b–e). The first, second and fourth events are transits of the primary star, and the weaker third

<sup>1</sup>Astronomy Department, San Diego State University, 5500 Campanile Drive, San Diego, California 92182, USA. <sup>2</sup>Harvard-Smithsonian Center for Astrophysics, 60 Garden Street, Cambridge, Massachusetts 02138, USA. <sup>3</sup>UCO/Lick Observatory, University of California, Santa Cruz, California 95064, USA. <sup>4</sup>University of Florida, 211 Bryant Space Science Center, Gainesville, Florida 32611-2055, USA. <sup>5</sup>NASA Ames Research Center, Moffett Field, California 94035, USA. <sup>6</sup>Villanova University, Department of Astronomy and Astrophysics, 800 E. Lancaster Avenue, Villanova, Pennsylvania 19085, USA. <sup>7</sup>Department of Physics and Astronomy, Georgia State University, PO Box 4106, Atlanta, Georgia 30302, USA. <sup>8</sup>Massachusetts Institute of Technology, Physics Department and Kavli Institute for Astrophysics and Space Research, 77 Massachusetts Avenue, Cambridge, Massachusetts 02139, USA. <sup>9</sup>Carl Sagan Center for the Study of Life in the Universe, SETI Institute, 189 Bernardo Avenue, Mountain View, California 94043, USA. <sup>10</sup>Bay Area Environmental Research Institute, Inc., 560 Third Street West, Sonoma, California 95476, USA. <sup>11</sup>Department of Physics and Astronomy, San Jose State University, One Washington Square, San Jose, California 95192, USA. <sup>12</sup>Instituut voor Sterrenkunde, Katholieke Universiteit Leuven, Celestijnenlaan 200D, B-3001 Leuven, Belgium. <sup>13</sup>McDonald Observatory, The University of Texas at Austin, Austin, Texas 78712-0259, USA. <sup>14</sup>Niels Bohr Institute, Copenhagen University, Juliane Maries Vej 30, DK-2100 Copenhagen, Denmark. <sup>15</sup>Centre for Star and Planet Formation, Natural History Museum of Denmark, University of Copenhagen, DK-1350 Copenhagen, Denmark. <sup>16</sup>NASA Exoplanet Science Institute/Caltech, 770 South Wilson Avenue, Pasadena, California 91125, USA. <sup>17</sup>Department of Astronomy and Astrophysics, University of California, Santa Cruz, Santa Cruz, California 95064, USA. <sup>18</sup>Jet Propulsion Laboratory, 4800 Oak Grove Drive, Pasadena, California 91109, USA. <sup>19</sup>Space Telescope Science Institute, 3700 San Martin Drive, Baltimore, Maryland 21218, USA. <sup>20</sup>Orbital Sciences Corporation/NASA Ames Research Center, Moffett Field, California 94035, USA. <sup>21</sup>Astronomy Department, University of California, Berkeley, California 94720, USA. <sup>22</sup>School of Physics and Astronomy, Tel Aviv University, Tel Aviv 69978, Israel. <sup>23</sup>Las Cumbres Observatory Global Telescope Network, 6740 Cortona Drive, Suite 102, Santa Barbara, California 93117, USA. <sup>24</sup>Department of Physics, Broida Hall, University of California, Santa Barbara, California 93106, USA. <sup>25</sup>Fermilab Center for Particle Astrophysics, MS 127, PO Box 500, Batavia, Illinois 60510, USA.



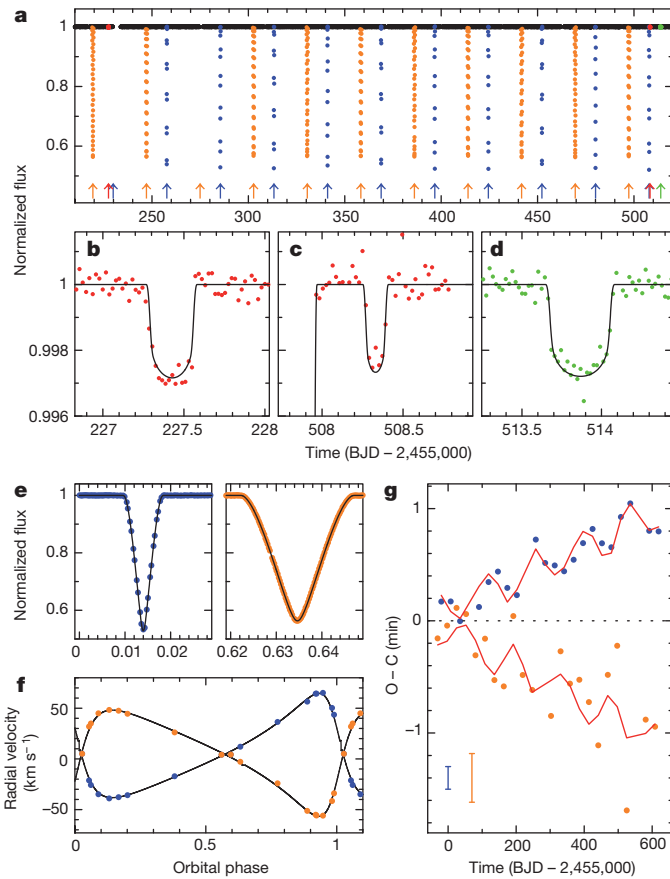


**Figure 1 | Observations of Kepler-34.** **a**, A portion of the normalized light curve, showing the relative brightness versus time (in units of barycentric Julian days, BJD). Low-frequency variations and instrumental drifts have been removed (Supplementary Information). The blue points show the primary eclipses (star B eclipses star A), orange points show the secondary eclipses, red points show the primary transits (planet transits star A), and green shows the secondary transit. The times of each event are indicated by the arrows. Owing to gaps in the observations, one primary and one secondary eclipse were missed. **b–d**, Close-up views of the three transit events. The solid curve is the photometric-dynamical model. Variations in transit widths are mainly due to differences in the transverse velocity of the stars during transit. The large drop before the transit in **c** is due to a primary eclipse. **e**, Close-up views of the phase-folded primary and secondary eclipses plotted versus orbital phase (time modulo the orbital period  $P$ , where  $P = 27.795794795$  d and the time of periastron is BJD 2,455,007.5190). Only Kepler Quarter 4 data are shown. **f**, Radial velocities of the primary star (blue points), secondary (orange points), and the model curve, versus orbital phase. **g**, Observed (O) minus computed (C) diagram, showing the deviations between the measured eclipse times and those predicted assuming strict periodicity. Primary eclipses are shown as blue points, secondaries by orange points, and the corresponding models by the red curves. A period of 27.79578193 days and an epoch of BJD 2,454,979.72301 were used to compute the primary eclipse times, and a phase offset of 0.6206712 for the secondary eclipse times. The divergence indicates the primary and secondary periods are different. The two vertical bars in the lower left denote the median  $\pm 1\sigma$  uncertainties of the primary and secondary eclipse times: 0.10 and 0.22 min.

event is a transit of the secondary star. Transits do not occur every planetary orbit, placing a strong constraint on the mutual orbital inclination and its evolution. The transits differ in duration, and the interval between transits is not constant, again signalling a circumbinary body. Modelling the photometry and radial velocities yields the system parameters given in Table 1. The transiting body is a planet with 13% of the mass and 73% of the radius of Jupiter (respectively 41 Earth

**Table 1 | Circumbinary planet system parameters**

	Kepler-34 (this work)	Kepler-35 (this work)	Kepler-16 (ref. 9)
<b>Planetary properties</b>			
Mass of planet, $M_p$ ( $M_{\text{Jupiter}}$ )	$0.220^{+0.011}_{-0.010}$	$0.127^{+0.020}_{-0.020}$	$0.333^{+0.016}_{-0.016}$
Radius of planet, $R_p$ ( $R_{\text{Jupiter}}$ )	$0.764^{+0.012}_{-0.014}$	$0.728^{+0.014}_{-0.014}$	$0.7538^{+0.0026}_{-0.0023}$
Mean density of planet, $\rho_p$ ( $\text{g cm}^{-3}$ )	$0.613^{+0.045}_{-0.041}$	$0.410^{+0.070}_{-0.069}$	$0.964^{+0.047}_{-0.046}$
Planet surface gravity, $g_p$ ( $\text{cm s}^{-2}$ )	$936^{+57}_{-54}$	$596^{+98}_{-98}$	$1,452^{+70}_{-69}$
<b>Properties of the planetary orbit</b>			
Reference epoch (BJD)	2,454,969.20000	2,454,965.85000	2,455,212.12316
Period, $P$ (days)	$288.822^{+0.063}_{-0.081}$	$131.458^{+0.077}_{-0.105}$	$228.776^{+0.020}_{-0.037}$
Semi-major axis length, $a$ (AU)	$1.0896^{+0.0009}_{-0.0009}$	$0.60347^{+0.00101}_{-0.00103}$	$0.7048^{+0.0011}_{-0.0011}$
Eccentricity, $e$	$0.182^{+0.016}_{-0.020}$	$0.042^{+0.007}_{-0.004}$	$0.00685^{+0.00101}_{-0.00146}$
$e \sin(\omega)$	$0.025^{+0.007}_{-0.007}$	$0.035^{+0.009}_{-0.011}$	$-0.00448^{+0.00088}_{-0.00090}$
$e \cos(\omega)$	$0.180^{+0.016}_{-0.021}$	$0.017^{+0.021}_{-0.018}$	$0.0051^{+0.0014}_{-0.0028}$
Mean longitude, $\lambda \equiv M + \omega$ (deg)	$106.5^{+2.5}_{-2.0}$	$136.4^{+2.1}_{-2.7}$	$106.51^{+0.32}_{-0.16}$
Inclination, $i$ (deg)	$90.355^{+0.026}_{-0.018}$	$90.76^{+0.12}_{-0.09}$	$90.0322^{+0.0022}_{-0.0023}$
Relative nodal longitude, $\Omega$ (deg)	$-1.74^{+0.14}_{-0.16}$	$-1.24^{+0.24}_{-0.33}$	$0.003^{+0.013}_{-0.013}$
<b>Properties of the stars in the stellar binary</b>			
Mass of A, $M_A$ ( $M_{\text{Sun}}$ )	$1.0479^{+0.0033}_{-0.0030}$	$0.8877^{+0.0051}_{-0.0053}$	$0.6897^{+0.0035}_{-0.0034}$
Radius of A, $R_A$ ( $R_{\text{Sun}}$ )	$1.1618^{+0.0027}_{-0.0031}$	$1.0284^{+0.0020}_{-0.0019}$	$0.6489^{+0.0013}_{-0.0013}$
Mass of B, $M_B$ ( $M_{\text{Sun}}$ )	$1.0208^{+0.0022}_{-0.0022}$	$0.8094^{+0.0042}_{-0.0045}$	$0.20255^{+0.00066}_{-0.00065}$
Radius of B, $R_B$ ( $R_{\text{Sun}}$ )	$1.0927^{+0.0032}_{-0.0027}$	$0.7861^{+0.0020}_{-0.0022}$	$0.22623^{+0.00059}_{-0.00053}$
Flux ratio in the Kepler bandpass, $F_B/F_A$	$0.8475^{+0.0110}_{-0.0076}$	$0.3941^{+0.0111}_{-0.0010}$	$0.01555^{+0.00010}_{-0.00006}$
<b>Properties of the stellar binary orbit</b>			
Period, $P$ (days)	$27.7958103^{+0.0000016}_{-0.0000015}$	$20.733666^{+0.000012}_{-0.000012}$	$41.079220^{+0.000078}_{-0.000077}$
Semi-major axis length, $a$ (AU)	$0.22882^{+0.00019}_{-0.00018}$	$0.17617^{+0.00029}_{-0.00030}$	$0.22431^{+0.00035}_{-0.00034}$
Eccentricity, $e$	$0.52087^{+0.00052}_{-0.00055}$	$0.1421^{+0.0014}_{-0.0015}$	$0.15944^{+0.00061}_{-0.00062}$
$e \sin(\omega)$	$0.49377^{+0.00057}_{-0.00060}$	$0.1418^{+0.0014}_{-0.0015}$	$-0.15840^{+0.00063}_{-0.00061}$
$e \cos(\omega)$	$0.165828^{+0.000065}_{-0.000061}$	$0.0086413^{+0.0000031}_{-0.0000031}$	$-0.0181481^{+0.0000045}_{-0.0000044}$
Mean longitude, $\lambda \equiv M + \omega$ (deg)	$300.1970^{+0.0099}_{-0.0105}$	$89.1784^{+0.0011}_{-0.0012}$	$92.3520^{+0.0011}_{-0.0011}$
Inclination, $i$ (deg)	$89.8584^{+0.0075}_{-0.0083}$	$90.4238^{+0.0076}_{-0.0073}$	$90.3401^{+0.0016}_{-0.0019}$

Results of the photometric-dynamical model for Kepler-34 (KIC 8572936) and Kepler-35 (KIC 9837578). The orbital parameters listed are the osculating Jacobian parameters, that is, the instantaneous Keplerian elements for the listed epoch. In general, unlike the simple two-body Keplerian case, the orbital elements are functions of time. In particular, the orbital period of Kepler-34 b varies from 280 to 312 days on secular timescales; the median period is  $\sim 291$  days. See Supplementary Information for details. For direct comparison, values<sup>a</sup> for Kepler-16 are listed. The mean longitude ( $\lambda$ ) is the sum of the mean anomaly ( $M$ ) and the argument of periastron ( $\omega$ ).

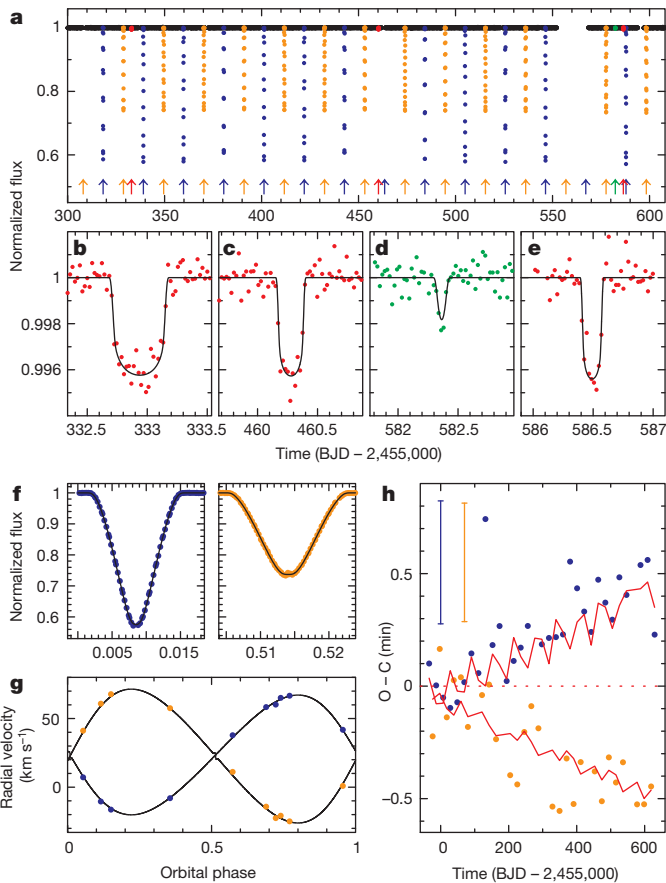


**Figure 2 | Observations of Kepler-35.** The representation of data is similar to that in Fig. 1. **a**, A portion of the light curve for Kepler-35. Owing to interruptions in the data acquisition, two primary and two secondary eclipses were not observed. **b–e**, Close-up views of the four transit events. Red points denote primary transits, green points denote a secondary transit. Note the differences in transit duration. **f**, Close-up views of the primary eclipses and secondary eclipses, plotted versus orbital phase where  $P = 20.733762175$  days and the time of periastron passage is BJD 2,455,007.3131. Only Kepler Quarter 4 data are shown (BJD 2,455,183 through to 2,455,275). **g**, Radial velocities of the primary star (blue points), secondary (orange points) and model fit. **h**, Observed minus computed diagram, where a period of 20.73373997 days and an epoch of BJD 2,454,965.84579 were used to predict the primary eclipses, and a phase offset of 0.5055680 for the secondary eclipses. The two vertical bars in the upper left denote the median  $\pm 1\sigma$  uncertainties of the primary and secondary eclipse times, 0.27 and 0.26 min, respectively

Kepler-16 b, but all are consistent with low-density gas-giant planets. Figure 3 gives a visual comparison of the systems' orbits. For all three systems, the planetary and stellar orbits are aligned to within  $2^\circ$ , suggesting that each system formed from a flat disk of material. The period ratios (planetary to stellar) for Kepler-34, Kepler-35 and Kepler-16 are 10.4, 6.3 and 5.6, respectively, only 21%, 24% and 14% larger than analytic estimates for stability against three-body interactions<sup>17–19</sup>. Long-term integration of the equations of motion confirms that these two new systems are stable for at least 10 Myr (Supplementary Information). Note that the planets' locations bracket the habitable zone<sup>20</sup> (where liquid water would be stable on the surface of a rocky planet), with Kepler-34 b and Kepler-35 b lying interior to the habitable zone and Kepler-16 b lying exterior to it.

A simple argument suggests that circumbinary giant planets are not extremely rare, as three such objects have been seen in our sample of 750 systems. Given the orbital geometry of Kepler-34, Kepler-35 and Kepler-16, the probability<sup>21</sup> that a randomly placed observer who sees stellar eclipses would also see planetary transits is approximately 12%, 14% and 21%, respectively (Supplementary Information). If this probability of roughly  $\sim 15\%$  were constant across all 750 target systems, then the fraction of binaries with circumbinary gas giant planets at similar periods would be  $(3/750) \times (0.15)^{-1}$ , or a few per cent. However, this does not account for the period distribution of binaries in our sample, and the search is not complete; consequently a lower limit of  $\sim 1\%$  is reasonable. With  $\sim 2.6\%$  of all Sun-like stars in

masses and 8.2 Earth radii). Comparison to stellar-evolutionary models suggests a system age of  $\sim 8$ –12 Gyr, although, interestingly, the models do not provide a satisfactory match to the stellar masses and radii under the assumption of a common age and metallicity (Supplementary Information).

The mean densities of Kepler-34 b and Kepler-35 b are respectively  $0.61$  and  $0.41 \text{ g cm}^{-3}$ , somewhat lower than the  $0.96 \text{ g cm}^{-3}$  of

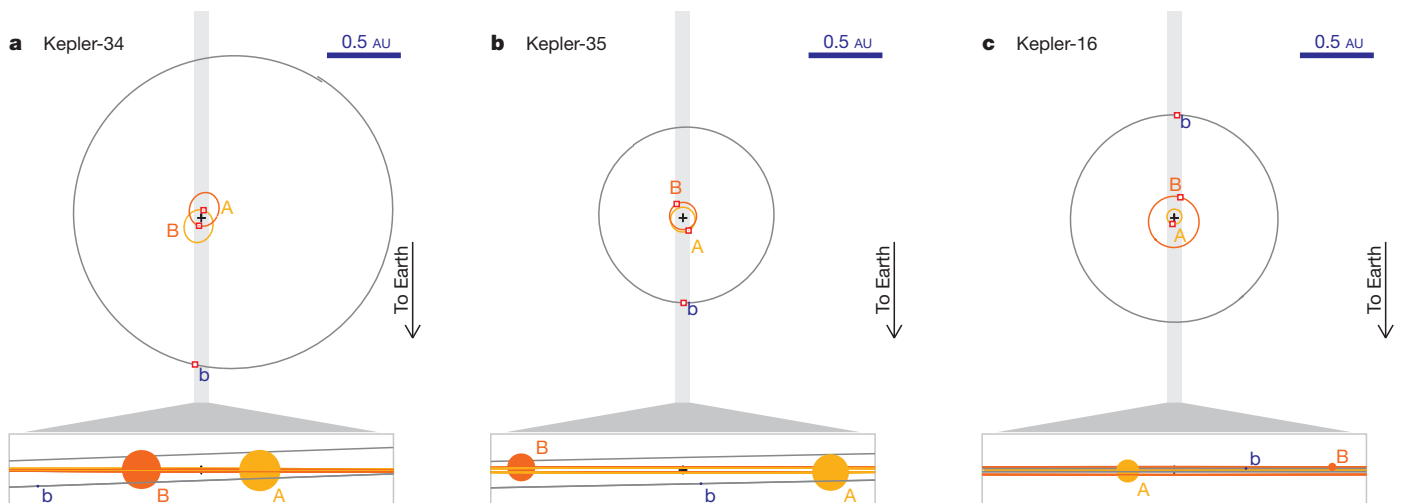


**Figure 3 | Orbital configurations.** **a**, Scale view of the orbits of the Kepler-34 system seen face-on (top) and also as seen from Earth (boxed, bottom). In the face-on view, the stars and planet are too small to be seen relative to their orbit curves, and so are represented as dots and marked with symbols A, B, and b denoting the primary star, secondary star, and planet. This view is correct for a given epoch (BJD 2,455,507.50). Because of the dynamical interactions between the three bodies, this orbital configuration will evolve. For example, the orbits precess, and hence the orbits do not actually close. The line-of-sight view shown

in the box depicts the stars and planet with correct relative sizes and orientation. More importantly, the orbits and the orbital tilts are accurately portrayed, showing how transits do not necessarily occur at every conjunction. The grey shaded area in the top panel denotes the limits of the view shown in the expanded bottom panel. **b**, As for **a**, but for Kepler-35 at epoch BJD 2,455,330.60. Note that the relative sizes of the bodies are drawn to scale for each panel (**a–c**), not just within a panel. **c**, As for **a**, but for Kepler-16 at epoch BJD 2,455,213.0.

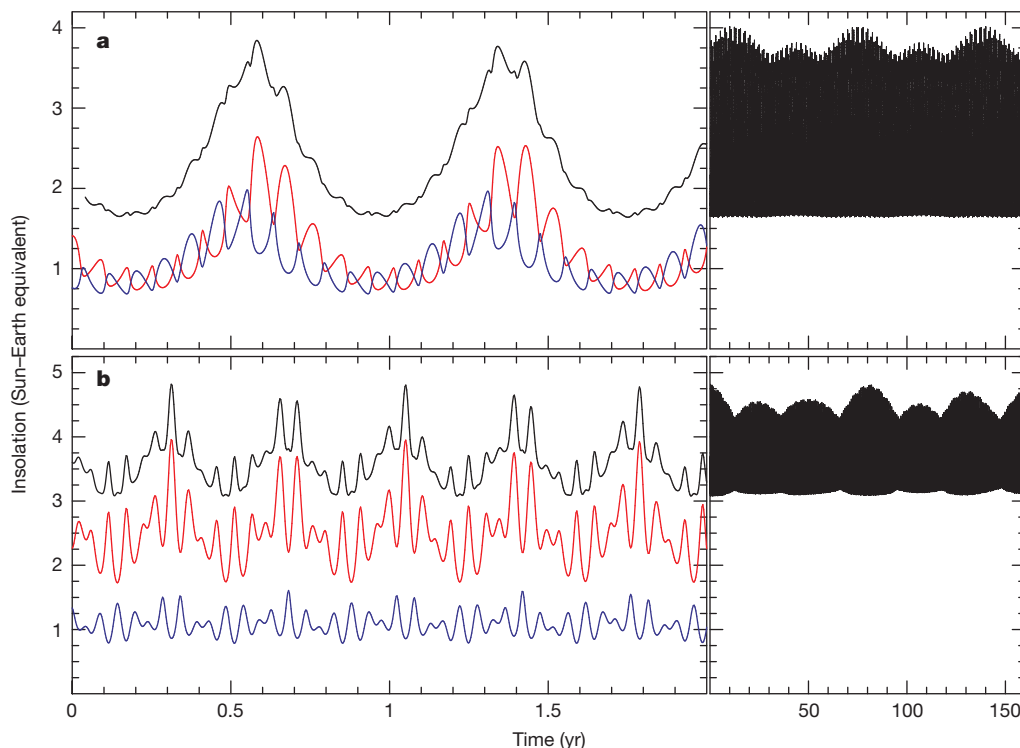


**Figure 4 | Variations in insolation received by Kepler-34 b and Kepler-35 b.** **a**, Left panel, the black curve shows the incident flux (insolation) received by Kepler-34 b from its two stars. The insolation is in units of the solar constant  $S$  (solar flux received at a distance of 1 AU;  $S = 1.0$  for the Sun–Earth system). The contribution from star A is shown in red and the contribution from star B in

the Galaxy residing in binary star systems similar to the three discussed here<sup>2,22</sup> (Supplementary Information), a conservative estimate yields millions of nearly coplanar circumbinary planets in the Galaxy like the ones reported here.

Orbital motion of the central stars causes complex time variations in stellar insolation for circumbinary planets. Figure 4 shows the calculated insolation for Kepler-34 b and Kepler-35 b. The variation is multi-periodic, with changes on the timescales of the stellar orbit, the planetary orbit, and the long-term precession of the orbits due to three-body effects. For Kepler-34 b and Kepler-35 b, the average insolation is (respectively) 2.4 and 3.6 times the Earth's insolation, with maximum-to-minimum ratios of 250% and 160%. By comparison, for Venus the insolation is 1.9 times the Earth's with only a 2.7% variation. These highly variable, multi-periodic fluctuations in insolation are unique to circumbinary planets, and can lead to complex climate cycles. It will be interesting to explore the effects of these swings in insolation on the atmospheric dynamics (Supplementary Information), and ultimately on the evolution of life on habitable circumbinary planets.

Received 15 November; accepted 5 December 2011.

Published online 11 January 2012.

1. Binnendijk, L. *Properties of Double Stars* (Univ. Pennsylvania Press, 1960).
2. Raghavan, D. *et al.* A survey of stellar families: multiplicity of solar-type stars. *Astrophys. J.* **190** (Suppl.), 1–42 (2010).
3. Schneider, J. & Chevreton, M. The photometric search for Earth-sized extrasolar planets by occultation in binary systems. *Astron. Astrophys.* **232**, 251–257 (1990).
4. Quintana, E. V. & Lissauer, J. J. Terrestrial planet formation surrounding close binary stars. *Icarus* **185**, 1–20 (2006).
5. Deeg, H.-J. *et al.* Extrasolar planet detection by binary stellar eclipse timing: evidence for the third body around CM Draconis. *Astron. Astrophys.* **480**, 563–571 (2008).
6. Haghighipour, N. *Planets in Binary Star Systems* (Astrophysics and Space Science Library, Vol. 366, Springer, 2010).
7. Sybilski, P., Konacki, M. & Kozłowski, S. Detecting circumbinary planets using eclipse timing of binary stars — numerical simulations. *Mon. Not. R. Astron. Soc.* **405**, 657–665 (2011).

blue. The most rapid variations are caused by the orbital motion of the stars. The slower variations are due to the orbital motion of the planet. Right panel, a longer timescale view of the insolation. The long-timescale quasi-periodicity is caused by the mutual precession of the orbits of the stars and planet, but is dominated by the precession of the planet. **b**, As for **a**, but for Kepler-35 b.

8. Schwarz, R. *et al.* Prospects of the detection of circumbinary planets with Kepler and CoRoT using the variations of eclipse timing. *Mon. Not. R. Astron. Soc.* **414**, 2763–2770 (2011).
9. Doyle, L. R. *et al.* Kepler-16: a transiting circumbinary planet. *Science* **333**, 1602–1606 (2011).
10. Koch, D. *et al.* Kepler mission design. *Astrophys. J.* **713**, L79–L86 (2010).
11. Borucki, W. J. *et al.* Kepler planet-detection mission: introduction and first results. *Science* **327**, 977–980 (2010).
12. Prša, A. *et al.* Kepler eclipsing binary stars. I. Catalog and principal characterization of 1879 eclipsing binaries in the first data release. *Astron. J.* **141**, 83–98 (2011).
13. Slawson, R. W. *et al.* Kepler eclipsing binary stars. II. 2165 Eclipsing binaries in the second data release. *Astron. J.* **142**, 160–173 (2011).
14. Brown, T. M. *et al.* Kepler input catalog: photometric calibration and stellar classification. *Astron. J.* **142**, 112–129 (2011).
15. Carter, J. A. *et al.* KOI-126: a triply eclipsing hierarchical triple with two low-mass stars. *Science* **331**, 562–565 (2011).
16. Yi, S. K. *et al.* Toward better age estimates for stellar populations: the  $Y^2$  isochrones for solar mixture. *Astrophys. J. Suppl. Ser.* **136**, 417–437 (2001).
17. Holman, M. J. & Wiegert, P. A. Long-term stability of planets in binary systems. *Astron. J.* **117**, 621–628 (1999).
18. Eggleton, P. & Kiseleva, L. An empirical condition for stability of hierarchical triple systems. *Astrophys. J.* **455**, 640–645 (1995).
19. Doolin, S. & Blundell, K. M. The dynamics and stability of circumbinary orbits. *Mon. Not. R. Astron. Soc.* (in the press); preprint at <http://arXiv.org/abs/1108.4144> (2011).
20. Kasting, J. F., Whitmire, D. P. & Reynolds, R. T. Habitable zones around main sequence stars. *Icarus* **101**, 108–128 (1993).
21. Ragozzine, D. & Holman, M. J. The value of systems with multiple transiting planets. *Astrophys. J.* (submitted); preprint at <http://arXiv.org/abs/1006.3727> (2010).
22. Chabrier, G. Galactic stellar and substellar initial mass function. *Publ. Astron. Soc. Pacif.* **115**, 763–795 (2003).

**Supplementary Information** is linked to the online version of the paper at [www.nature.com/nature](http://www.nature.com/nature).

**Acknowledgements** Kepler was selected as the tenth NASA Discovery mission with funding provided by NASA's Science Mission Directorate. We thank the many people who made the Kepler mission a reality. W.F.W., J.A.O., E.B.F., A.P., L.R.D., J.J.F., M.J.H., T.M. and J.H.S. were supported by the Kepler Participating Scientist Program. W.F.W., J.A.O., D.R.S. and G.W. were supported by the NSF. D.C.F. and J.A.C. acknowledge NASA support through Hubble Fellowship grants, awarded by STScI, operated by AURA. J.N.W. was supported by the NASA Origins programme. S.B. acknowledges funding from the European Research Council under the European Community's Seventh Framework Programme (PROSPERITY) and from the Research Council of KU Leuven.



Some of the reported computations were run on the Odyssey cluster supported by the FAS Science Division Research Computing Group at Harvard University. This Letter is based in part on observations made with the Nordic Optical Telescope (operated on the island of La Palma jointly by Denmark, Finland, Iceland, Norway and Sweden, in the Spanish Observatorio del Roque de los Muchachos of the Instituto de Astrofísica de Canarias), the W. M. Keck Observatory (operated by the University of California and the California Institute of Technology) and the Hobby-Eberly Telescope (HET; a joint project of the University of Texas at Austin, the Pennsylvania State University, Stanford University, Ludwig-Maximilians-Universität München, and Georg-August-Universität Göttingen).

**Author Contributions** W.F.W. led the research effort on these transiting circumbinary planets (CBPs) and wrote much of the Letter. J.A.O. led the ETV (eclipse timing variation) investigation, measured  $O - Cs$ , inspected light curves, measured EB (eclipsing binary) properties, measured radial velocities and flux ratios, generated Figs 1 and 2, and assembled the Supplementary Information. J.A.C. created and used the photometric-dynamical code to model the light curve and RVs (radial velocities), measured system parameters, and generated Table 1 and Fig. 3. D.C.F. produced initial dynamical models to interpret the timing of eclipse and transit events leading to the planet interpretation, and developed criteria for non-eclipsing CBP searches. E.B.F. contributed to interpretation and text, checked long-term stability, and did insolation calculations. J.J.L. contributed to interpretation and text, and initiated study of variations in insolation on CBPs. A.P. measured mass, radii and other properties of the EBs, including contamination and flux ratios. S.N.Q. obtained and analysed spectra, and determined stellar parameters and luminosity ratios. D.R. computed the estimated frequency of CBPs. D.R.S. developed the automated ETV code to measure eclipse times and  $O - C$  deviations. G.T. contributed to the discussion of the stellar parameters and carried out the comparison with stellar evolution models. J.N.W. contributed to the text, estimated age via gyrochronology, and contributed to topics related to pseudosynchronicity. L.R.D. contributed to the habitable zone discussion and led the initial search for CBPs. T.B. examined pixel level data and contributed basis-vector corrected light curves. N.B. directed EB target selection and identification. S.B. contributed to the text and Supplementary Information. E.B. carried out an independent spectroscopic investigation to measure stellar parameters. L.A.B. gathered spectroscopic observations for the RV and spectroscopic parameter determination. C.C. contributed three nights of spectroscopic observations at the McDonald 2.7 m observatory. D.A.C. contributed to calibration of the Kepler

photometer and pipeline necessary for data acquisition. J.L.C. supported the science operations to collect and calibrate the Kepler data. D.R.C. coordinated ground-based follow-up observations. W.D.C. obtained the HET spectra, and processed all McDonald 2.7 m and HET spectra. M.E. contributed HET and McDonald 2.7 m spectra. J.J.F. contributed calculations and discussion regarding the characteristics of the planets' atmospheres. T.N.G. coordinated the Kepler follow-up observation effort. R.L.G. provided mission support and contributed to the text and discussion of results. M.R.H. led the effort to gather, process and distribute the data necessary for this investigation. J.R.H. contributed to the collection, validation and management of the Kepler data used here. M.J.H. contributed to the discussion of the dynamical stability. A.W.H. made spectroscopic observations using Keck-HIRES. S.B.H. contributed reconnaissance spectroscopy. H.I. obtained spectroscopic observations of targets. J.M.J. developed observation/analysis techniques and calibration software that enables the Kepler photometer to operate successfully. T.C.K. led the design and development of the Science Processing Pipeline Infrastructure needed to process the data used here. D.W.L. contributed spectroscopy and preparation of the Kepler Input Catalog. J.L. contributed to the development of the Data Validation component of the Kepler Science Operations Center pipeline necessary to obtain these data. G.W.M. obtained Keck-HIRES spectra. T.M. analysed the beaming effect in Kepler-35 and participated in the discussion of statistical inference and the spectroscopic light ratio. E.V.Q. developed calibration/validation software necessary for the Kepler data in this paper. P.R. contributed ten nights of spectroscopic observations at the McDonald 2.7 m telescope. A.S. contributed ground-based follow-up imaging of the targets. J.H.S. contributed to the text, scope and interpretation. G.W. ran the ETV code, developed tools for analysing  $O - C$  variations, and assisted with text. D.G.K. designed major portions of the Kepler photometer that acquired these data. W.J.B. led the design and development of the Kepler mission that acquired these data, and contributed to the text.

**Author Information** The Kepler light curves used in this work can be downloaded from the MAST (Multimission Archive at Space Telescope Science Institute) at <http://archive.stsci.edu/kepler/>. Reprints and permissions information is available at [www.nature.com/reprints](http://www.nature.com/reprints). The authors declare no competing financial interests. Readers are welcome to comment on the online version of this article at [www.nature.com/nature](http://www.nature.com/nature). Correspondence and requests for materials should be addressed to W.F.W. ([wfw@sciences.sdsu.edu](mailto:wfw@sciences.sdsu.edu)) or J.A.C. ([jacarter@cfa.harvard.edu](mailto:jacarter@cfa.harvard.edu)), for questions regarding the photometric-dynamical modelling).

# Reconfigurable self-assembly through chiral control of interfacial tension

Thomas Gibaud<sup>1</sup>, Edward Barry<sup>1</sup>, Mark J. Zakhary<sup>1</sup>, Mir Henglin<sup>1</sup>, Andrew Ward<sup>1</sup>, Yasheng Yang<sup>1</sup>, Cristina Berciu<sup>2</sup>, Rudolf Oldenbourg<sup>3</sup>, Michael F. Hagan<sup>1</sup>, Daniela Nicastro<sup>2</sup>, Robert B. Meyer<sup>1</sup> & Zvonimir Dogic<sup>1</sup>

From determining the optical properties of simple molecular crystals to establishing the preferred handedness in highly complex vertebrates, molecular chirality profoundly influences the structural, mechanical and optical properties of both synthetic and biological matter on macroscopic length scales<sup>1,2</sup>. In soft materials such as amphiphilic lipids and liquid crystals, the competition between local chiral interactions and global constraints imposed by the geometry of the self-assembled structures leads to frustration and the assembly of unique materials<sup>3–6</sup>. An example of particular interest is smectic liquid crystals, where the two-dimensional layered geometry cannot support twist and chirality is consequently expelled to the edges in a manner analogous to the expulsion of a magnetic field from superconductors<sup>7–10</sup>. Here we demonstrate a consequence of this geometric frustration that leads to a new design principle for the assembly of chiral molecules. Using a model system of colloidal membranes<sup>11</sup>, we show that molecular chirality can control the interfacial tension, an important property of multi-component mixtures. This suggests an analogy between chiral twist, which is expelled to the edges of two-dimensional membranes, and amphiphilic surfactants, which are expelled to oil–water interfaces<sup>12</sup>. As with surfactants, chiral control of interfacial tension drives the formation of many polymorphic assemblages such as twisted ribbons with linear and circular topologies, starfish membranes, and double and triple helices. Tuning molecular chirality *in situ* allows dynamical control of line tension, which powers polymorphic transitions between various chiral structures. These findings outline a general strategy for the assembly of reconfigurable chiral materials that can easily be moved, stretched, attached to one another and transformed between multiple conformational states, thus allowing precise assembly and nanosculpting of highly dynamical and designable materials with complex topologies.

In experiments on chiral self-assembly, we used a two-component mixture consisting of 880-nm-long rod-like fd viruses and the non-adsorbing polymer Dextran. In aqueous suspension, fd viruses alone have purely repulsive interactions<sup>13</sup>. Adding non-adsorbing polymer to a dilute isotropic suspension of fd rods induces attractive interactions by the depletion mechanism and leads to their condensation into colloidal membranes, which are equilibrium structures consisting of one-rod-length-thick, liquid-like monolayers of aligned rods<sup>11</sup> (Fig. 1a). Despite having different structures on molecular length scales, the coarse-grained properties of colloidal membranes are identical to those of conventional lipid bilayers. However, unlike their amphiphilic counterparts, colloidal membranes do not form vesicles and are instead observed as freely suspended disks with exposed edges. Here we investigate the behaviour of these exposed edges in a manner analogous to previously studied liquid–liquid domains embedded in lipid bilayers<sup>14–16</sup>. For our experiments, it is essential that fd viruses are chiral, that is, a pair of aligned viruses minimizes their interaction energy when they are slightly twisted with respect to each other in a preferred direction. The strength of chiral interactions can be continuously tuned to zero through either genetic or physical methods<sup>13,17</sup> (Supplementary Fig. 1).

Before investigating chiral membranes, we determined the edge structure of a membrane composed of simpler, achiral rods using three complementary imaging techniques, namely two-dimensional (2D) and three-dimensional (3D) polarization microscopy and electron microscopy. The local tilting of the rods within a membrane was determined using a 2D LC-PolScope, which produces images in which the intensity of each pixel represents the local retardance of the membrane<sup>18</sup> (Fig. 1d). Such images can be quantitatively related to the tilting of the rods away from the layer normal<sup>19</sup> (the *z* axis). Rods in the bulk of a membrane are aligned along the *z* axis, and it follows that 2D LC-PolScope images appear black in that region (Fig. 1e). By contrast, the bright, birefringent ring along the membrane's periphery reveals local tilting of the rods (Fig. 1e and Supplementary Fig. 2). For achiral rods, this indicates that a membrane has a hemi-toroidal curved edge (Fig. 1b, c). By comparison with an untilted edge, a curved edge structure lowers the area of the rod–polymer interface, thus reducing interfacial tension, at the cost of increasing the elastic energy due to a twist distortion. This hypothesis is confirmed by visualizing the 3D membrane structure using electron tomography, which shows that the viruses' long-axis transitions from being parallel to the *z* axis in the membrane bulk to being perpendicular to the *z* axis and tangential to the edge along the membrane periphery (Fig. 1d and Supplementary Fig. 3). For achiral viruses, the spontaneous twist at the edges is equally likely to be clockwise or anticlockwise. However, the 2D LC-PolScope records only 2D projections of the birefringence map and thus cannot distinguish between these two possibilities. For this reason, we used a 3D LC-PolScope<sup>20</sup>, which reveals that achiral rods are equally likely to tilt in either direction, thus confirming the spontaneously broken chiral symmetry at the edge of an achiral membrane (Fig. 1f–h and Supplementary Fig. 4). Simulations of hard, achiral spherocylinders and depletant molecules provide additional verification that interfacial effects alone cause spontaneous twisting of achiral rods at the membrane's edge (Supplementary Fig. 5).

When viewed with optical microscopy, a membrane's edge shows pronounced thermal fluctuations, the analysis of which yields the line tension,  $\gamma_{\text{eff}}$ , which is the energetic cost required to move rods from the membrane interior to the periphery<sup>12,21,22</sup> (Fig. 2a). A typical fluctuation spectrum for an achiral edge is shown in Fig. 2b. In the regime of small wavevector, *q*, the mean square Fourier amplitudes,  $\langle a_q^2 \rangle$ , are independent of *q*, allowing us to extract the effective line tension,  $\gamma_{\text{eff}} = k_B T / \langle a_q^2 \rangle$  (ref. 12), where  $k_B$  is the Boltzmann constant and *T* is the temperature. In the large-*q* limit, fluctuations scale as  $1/q^2$  and are therefore substantially suppressed relative to those of a simple interface. One possible explanation is that fluctuations are suppressed as a result of a quasi-one-dimensional (quasi-1D) nematic phase at the edge, which is a direct consequence of rod tilting (Fig. 1e). At large wavelengths, the elastic energy required to deform the quasi-1D nematic phase is negligible and the fluctuations are dominated by the line tension. With decreasing wavelength, there is an increasing energetic penalty associated with bending the quasi-1D nematic phase, resulting in the suppression of fluctuations.

<sup>1</sup>The Martin Fisher School of Physics, Brandeis University, 415 South Street, Waltham, Massachusetts 02454, USA. <sup>2</sup>Department of Biology, Brandeis University, 415 South Street, Waltham, Massachusetts 02454, USA. <sup>3</sup>Marine Biological Laboratory, 7 MBL Street, Woods Hole, Massachusetts 02543, USA.

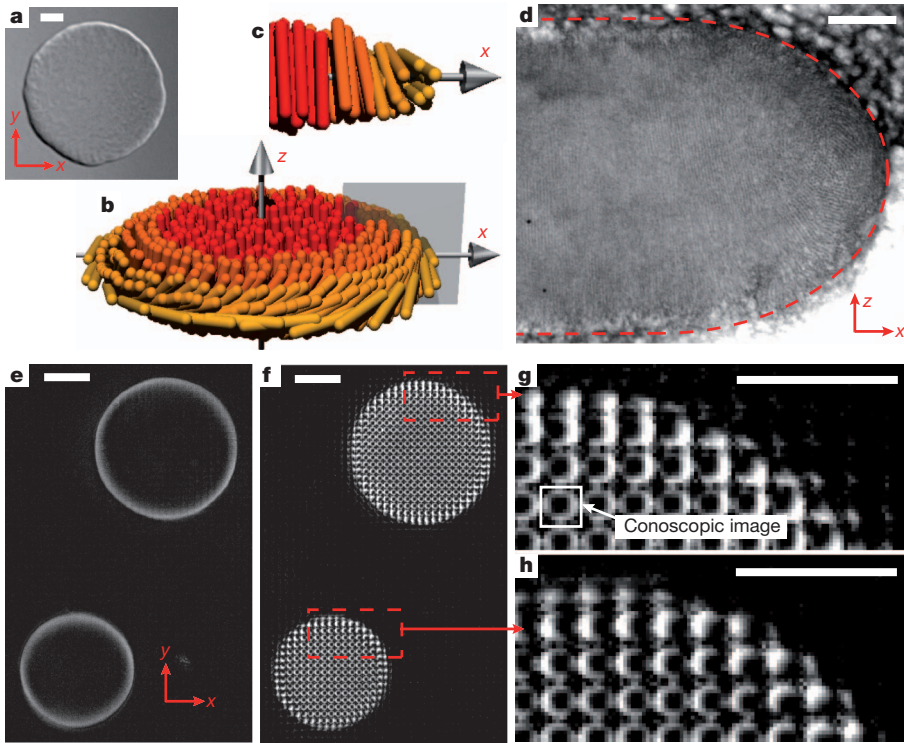


**Figure 1 | Edge structure of membranes assembled from an achiral mixture of wild-type and Tyr21Met fd phages.** **a**, Differential interference contrast (DIC) image of a colloidal membrane. **b**, Illustration of colloidal membrane indicating that its edge adopts a surface-tension-minimizing curved profile, forcing rods to twist locally. For clarity, the aspect ratio of rods has been reduced. **c**, Cross-section shown in **b**. **d**, Electron micrograph of a membrane directly visualizing the curved edge profile (Supplementary Fig. 3). **e**, 2D LC-PolScope birefringence map of two membranes. The bright band associated with the edges indicates local rod tilting (Supplementary Fig. 2). **f**, 3D LC-PolScope image composed of an array of conoscopic microimages, each sampling the local orientation of the rods. In each microimage, the displacement of the dark spot away from the centre determines the local tilting of the rods with respect to the layer normal (the  $z$  axis; Supplementary Fig. 4). **g**, **h**, Sections of 3D LC-PolScope images of two edges with clockwise (**g**) and anticlockwise (**h**) twists, respectively, illustrating the broken chiral symmetry found at the edge of achiral membranes. Scale bars, 5  $\mu\text{m}$  (**a**, **e**–**g**, **h**); 0.2  $\mu\text{m}$  (**d**).

Next we demonstrated that the chirality of the constituent rods controls the magnitude of  $\gamma_{\text{eff}}$ . The global constraints imposed by the 2D membrane topology are fundamentally incompatible with local twisting (chiral interactions) between constituent rods, leading to the expulsion of chirality from the bulk of the membrane<sup>7</sup> (untwisting of rods). It follows that introducing chirality raises the energy of rods in the membrane bulk while simultaneously lowering the energy of rods close to the edge, where they are free to twist and satisfy chiral interactions. Therefore, we propose that there are two contributions to the effective line tension,  $\gamma_{\text{bare}}$  and  $\gamma_{\text{chiral}}$ , such that  $\gamma_{\text{eff}} = \gamma_{\text{bare}} - \gamma_{\text{chiral}}$ , where  $\gamma_{\text{bare}}$  is the line tension of a membrane edge composed of achiral rods and  $\gamma_{\text{chiral}}$  is the chiral contribution to the line tension<sup>19,23</sup>. To measure  $\gamma_{\text{bare}}$  and  $\gamma_{\text{chiral}}$  independently, we used the temperature dependence of fd chirality (Supplementary Fig. 1). We measured  $\gamma_{\text{bare}}$  at high

temperature (60 °C), where rods are achiral ( $\gamma_{\text{chiral}} = 0$ ) and, therefore,  $\gamma_{\text{eff}} = \gamma_{\text{bare}}$  (Fig. 2c). Decreasing the temperature increases the strength of chiral interactions, resulting in a smaller  $\gamma_{\text{eff}}$  value and demonstrating that chirality indeed reduces line tension (Fig. 2c). Temperature-dependent chiral contributions ( $\gamma_{\text{chiral}}(T) = -\gamma_{\text{eff}}(T) + \gamma_{\text{bare}}$ ) were converted into a function that depends on the chiral wavevector,  $q_0$ , using measurements of the temperature dependence of the cholesteric twist (Supplementary Fig. 1). Notably, measurements of  $\gamma_{\text{chiral}}$  at different depletant concentrations collapse onto a universal curve (Fig. 2d), confirming that the two contributions to  $\gamma_{\text{eff}}$  are uncorrelated. Our data show that chirality can reduce the line tension by as much as  $450k_{\text{B}}T$  per micrometre of edge length (Fig. 2d). To test this hypothesis independently, we measured  $\gamma_{\text{eff}}$  for membranes composed of the Tyr21Met mutant fd virus. By contrast with wild-type fd virus, the chirality of this mutant fd virus is temperature independent (Supplementary Fig. 6). We find that  $\gamma_{\text{eff}}$  for the Tyr21Met mutant membranes is temperature independent over the entire measurement range, unambiguously demonstrating chiral control of line tension and ruling out any intrinsic temperature effects.

Our findings raise the possibility that at sufficiently low temperatures the chiral contribution to interfacial energy could dominate the bare line tension, lowering the energetic cost of creating edges and leading to

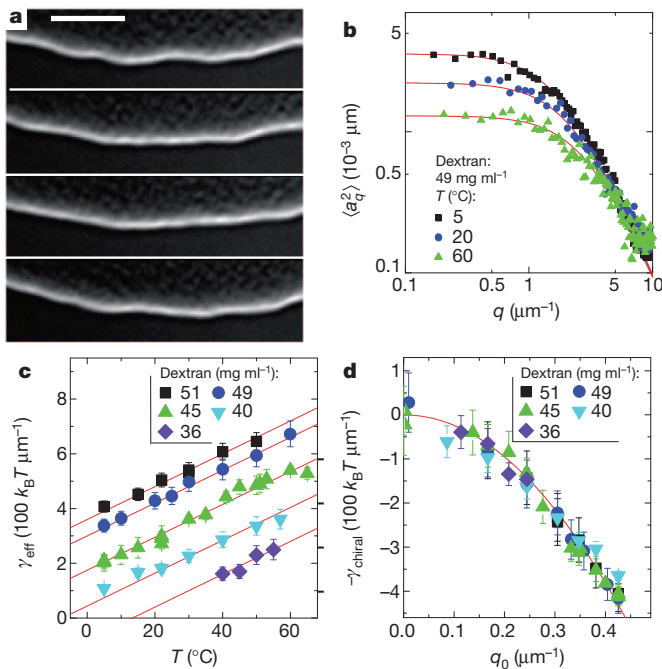


**Figure 2 | Chiral control of effective line tension,  $\gamma_{\text{eff}}$ .** **a**, DIC images, taken 1 s apart, illustrating the fluctuations of the membrane's edge. Scale bar, 5  $\mu\text{m}$ . **b**, Fluctuation spectrum ( $\langle a_q^2 \rangle$ ) versus  $q$  plotted for three different temperatures. For small  $q$ ,  $\langle a_q^2 \rangle$  is independent of  $q$  and inversely proportional to the effective line tension,  $\gamma_{\text{eff}} = k_{\text{B}}T/\langle a_q^2 \rangle$ . For large  $q$ , the suppressed fluctuations are independent of depletant concentration (osmotic pressure) and sample temperature (fd chirality) and scale as  $1/q^2$ . Red lines are fits using equation (3) (Methods). **c**,  $\gamma_{\text{eff}}$  extracted from the low- $q$  regime, plotted for a range of sample temperatures (fd chirality) and Dextran concentrations (osmotic pressures). In the achiral limit at 60 °C,  $\gamma_{\text{chiral}} = 0$  and  $\gamma_{\text{bare}} = \gamma_{\text{eff}}$ . Increasing the Dextran concentration increases  $\gamma_{\text{bare}}$ . Decreasing the temperature reduces  $\gamma_{\text{eff}}$  because  $\gamma_{\text{chiral}}$  increases. The red lines of fixed slope are guides to the eyes illustrating the universal scaling of  $\gamma_{\text{eff}}$  with chirality. **d**,  $\gamma_{\text{chiral}}$  as a function of the twist wavevector,  $q_0$  (measured in the cholesteric phase), for various depletant concentrations. The temperature dependence of  $q_0$  is extracted from Supplementary Fig. 1. The red curve is quadratic fit to the data:  $\gamma_{\text{chiral}} = Cq_0^2$ . Error bars, s.d.;  $n = 10$ .



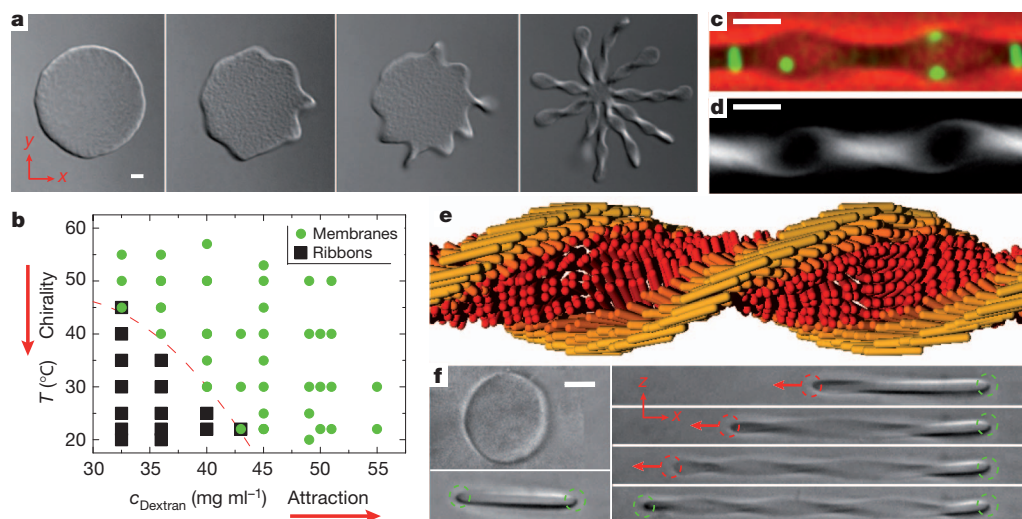


**Figure 3 | Transition of a 2D disk into 1D twisted ribbons.** **a**, A temperature quench reduces the line tension, inducing a transition of the 2D membrane into 1D twisted ribbons (Supplementary Movie 1). **b**, The stability diagram indicates regions of phase space where ribbons and membranes are observed as a function of temperature (chirality) and Dextran concentration ( $c_{\text{Dextran}}$ ). The boundary indicates the temperature above which no stable or metastable ribbons are observed at a given Dextran concentration. **c**, An overlaid phase contrast (red)/fluorescence (green) image of a stable ribbon containing a low volume fraction of

fluorescently labelled rods (Supplementary Movie 2). **d**, LC-PolScope image indicating rod tilting that penetrates from the edge of the ribbon towards its centre. The intensity at each pixel is proportional to  $\sin^2(\theta)$ , where  $\theta$  is the local rod tilt angle away from the image plane. **e**, Schematic structure of twisted ribbons as deduced from optical microscopy. **f**, A 2D colloidal membrane is trapped with a dual-beam optical trap and stretched, inducing the transition to a 1D twisted ribbon (Supplementary Movie 3). Red circles indicate moving traps and green circles indicate fixed traps. Scale bars, 2  $\mu\text{m}$ .

their spontaneous formation. In this respect, we expect chirality to have a role similar to that of amphiphilic surfactants in oil–water mixtures. Such surfactants lower surface tension and lead to the formation of excess interfaces through the assembly of microemulsions. To investigate this possibility, we quenched a membrane assembled at low depletant (Dextran) concentration from the high-temperature achiral phase. With decreasing temperature, fluctuations of the membrane edge become more pronounced, indicating that  $\gamma_{\text{eff}}$  is decreasing. Eventually the edge becomes unstable, resulting in a remarkable polymorphic transition in which twisted, ribbon-like structures grow along the entire periphery of the disk, generating a starfish-shaped membrane (Fig. 3a and Supplementary Movie 1). This polymorphic transition is reversible; with increasing temperature, the starfish membrane collapses back into a disk. The stability diagram indicates that 1D twisted ribbons are stable at low Dextran concentrations and low temperatures (small  $\gamma_{\text{bare}}$  values and large  $\gamma_{\text{chiral}}$  values), whereas flat 2D membranes are stable for large  $\gamma_{\text{bare}}$  values or small  $\gamma_{\text{chiral}}$  values (Fig. 3b). DIC microscopy reveals the overall structure of the ribbons, such as their pitch and width (Fig. 3a); fluorescence microscopy shows the liquid-like dynamics of single rods within the assemblage (Fig. 3c and Supplementary Movie 2); and 2D LC-PolScope imaging quantitatively determines the local tilt of the rods (Fig. 3d). A schematic representation of the twisted ribbons based on this information, indicating inhomogeneous tilting of the rods within a ribbon, is shown in Fig. 3e. Such data are in agreement with recent theoretical predictions<sup>24</sup>.

Chiral self-assembly produces structures that combine seemingly divergent properties of high elasticity and fluidity. To demonstrate these properties, we trapped two opposite sides of a flat disk with a dual-beam optical trap and applied an extensional force, causing the transition from a stretched disk into a twisted ribbon (Fig. 3f and Supplementary Movie 3). This mechanically induced disk-to-ribbon transition is reversible; on removal of the optical trap, the highly elastic ribbon relaxes back into its original shape. Furthermore, using optical tweezers it is possible to change the architecture of the chiral assemblages systematically, allowing new pathways for assembling nanomaterials with highly complex topologies. For example, two ends of a linear twisted ribbon are easily joined together to assemble a closed, ring-like polymeric structure. The disk-to-ribbon transition is tightly coupled to the assemblage topology

(Fig. 4d). On increasing the temperature, all linear ribbons transform into achiral disks (Supplementary Movie 4), whereas closed, ring-like ribbons remain twisted owing to the constraint imposed by the ring topology (Supplementary Movie 5).

The chiral assembly pathways described here are hierarchical, opening up the possibility that simple changes on microscopic (ångström) length scales can be used to control structures on macroscopic (millimetre) length scales<sup>25,26</sup>. At the smallest relevant length scale, each virus is assembled from DNA that is coated with thousands of

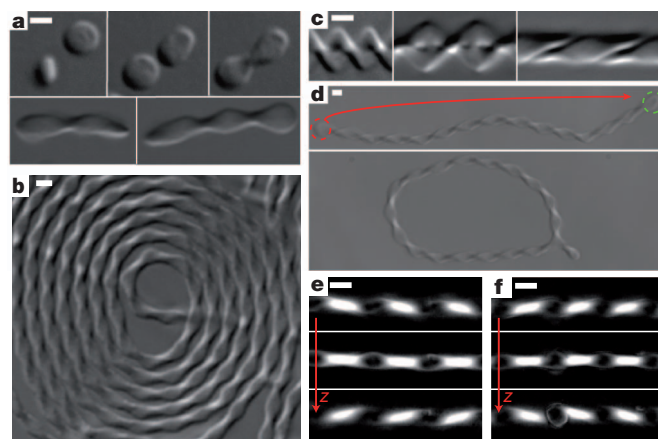


**Figure 4 | Hierarchical self-assembly: from isolated viruses and metastable disks to singly and doubly twisted ribbons.** **a**, In the ribbon region of the phase diagram in Fig. 3b, fd viruses condense into metastable, self-limited disks. On longer timescales, these disks coalesce and form 1D twisted ribbons. **b**, Image of a single ribbon that has collapsed into a toroid. **c**, Doubly twisted ribbons are assembled by wrapping around each other two singly twisted ribbons with a well-defined phase difference (Supplementary Fig. 8). **d**, Directed assembly of a ring-like supramolecular polymer from a linear twisted ribbon using optical tweezers. **e**, **f**, Single point mutation of the major coat protein permits microscopic control of ribbon chirality. Wild-type fd virus assembles into left-handed ribbons (**e**), whereas the Tyr21Met fd virus forms right-handed ribbons (**f**), as demonstrated by the z-stack series of 2D LC-PolScope images. Scale bars, 2  $\mu\text{m}$ .

copies of the major coat protein. At the mesoscopic length scale, attractive depletion interactions condense dilute, rod-like viruses into self-limited, metastable, mesoscopic colloidal disks whose diameter is approximately one twist penetration length<sup>19,23,27,28</sup> (Fig. 4a). Once assembled, mesoscopic disks themselves experience mutual attractions, resulting in lateral coalescence and formation of twisted doublets. On longer timescales, this coalescence process continues, producing ribbons with complex topologies and multiple branching points (Supplementary Fig. 7). The length of these ribbons can reach macroscopic (millimetre) dimensions. This hierarchical assembly process describes a robust synthesis of ribbons that behave as supramolecular polymers and can assemble into even more-complex structures at higher levels of hierarchy, such as toroids (Fig. 4b). Under certain conditions, ribbons also wrap around each other to produce a great variety of double- and triple-helical structures (Fig. 4c and Supplementary Fig. 8). A challenge associated with hierarchical assembly pathways is to control the final macroscopic assemblage by specific modification of relevant microscopic parameters. Previous work showed that even a single amino-acid mutation of the major coat protein can alter the microscopic chirality of individual viruses<sup>13</sup>. We used this finding to demonstrate that such amino-acid exchange propagates across all hierarchical levels, switching the ribbon handedness and allowing for microscopic control of macroscopic ribbon chirality (Fig. 4e, f).

We have shown that the chirality of the constituent molecules can be used to tune the line tension associated with the exposed edge of a colloidal monolayer membrane. The potential of hierarchical chiral self-assembly is demonstrated by assembling reconfigurable materials with unique mechanical properties and complex topologies that can easily switch between multiple polymorphic forms<sup>29,30</sup>.

## METHODS SUMMARY

Wild-type and Tyr21Met fd viruses were purified according to previously published protocols<sup>13</sup>. To reduce the number of longer viruses, which destabilize monolayer structures such as colloidal membranes or twisted ribbons, virus suspensions were cycled through isotropic–nematic phase coexistence. Only the isotropic portion of the samples, enriched in shorter viruses, was used for experiments<sup>11</sup>. The polydispersity of viruses was quantified using gel electrophoresis (Supplementary Fig. 9). All samples were prepared in a buffer containing 20 mM Tris and 100 mM NaCl at pH 8.0. Addition of the non-adsorbing polymer Dextran (relative molecular mass, 500,000; Sigma-Aldrich) induces condensation of rod-like viruses into either flat colloidal membranes or various other chiral assemblages. The strength of chiral interactions between rods was tuned either by changing the sample temperature or by varying the ratio of wild-type fd virus to Tyr21Met fd virus in membranes containing a mixture of the two<sup>13</sup>. Optical microscopy data was taken with an inverted microscope (Nikon TE-2000) equipped with DIC optics, a homemade heating/cooling stage and a cooled charged-coupled-device camera (QImaging, Retiga EXi). The 2D and 3D LC-PolScope imaging set-ups have been described elsewhere<sup>18,20</sup>. To prevent binding of viruses to surfaces, microscope slides and coverslips were cleaned and subsequently coated with a silane agent (3-(trimethoxysilyl) propyl methacrylate, Sigma Aldrich) to which a polyacrylamide brush was polymerized from methacrylate groups.

**Full Methods** and any associated references are available in the online version of the paper at [www.nature.com/nature](http://www.nature.com/nature).

**Received 31 July; accepted 6 December 2011.**

**Published online 4 January 2012.**

1. Pasteur, L. On the relations that can exist between crystalline form, and chemical composition and the sense of rotary polarization. *Ann. Chim. Phys.* **24**, 442–459 (1848).
2. Hirokawa, N., Tanaka, Y., Okada, Y. & Takeda, S. Nodal flow and the generation of left-right asymmetry. *Cell* **125**, 33–45 (2006).
3. Harris, A. B., Kamien, R. D. & Lubensky, T. C. Molecular chirality and chiral parameters. *Rev. Mod. Phys.* **71**, 1745–1757 (1999).

4. Oda, R., Huc, I., Schmutz, M., Candau, S. J. & MacKintosh, F. C. Tuning bilayer twist using chiral counterions. *Nature* **399**, 566–569 (1999).
5. Aggeli, A. *et al.* Hierarchical self-assembly of chiral rod-like molecules as a model for peptide beta-sheet tapes, ribbons, fibrils, and fibers. *Proc. Natl Acad. Sci. USA* **98**, 11857–11862 (2001).
6. Kamien, R. D. & Selinger, J. V. Order and frustration in chiral liquid crystals. *J. Phys. Condens. Matter* **13**, R1–R22 (2001).
7. de Gennes, P. G. An analogy between superconductors and smectics A. *Solid State Commun.* **88**, 1039–1042 (1993).
8. Renn, S. R. & Lubensky, T. C. Abrikosov dislocation lattice in a model of the cholesteric to smectic-A transition. *Phys. Rev. A* **38**, 2132–2147 (1988).
9. Matsumoto, E. A., Alexander, G. P. & Kamien, R. D. Helical nanofilaments and the high chirality limit of smectics A. *Phys. Rev. Lett.* **103**, 257804 (2009).
10. Hough, L. E. *et al.* Helical nanofilament phases. *Science* **325**, 456–460 (2009).
11. Barry, E. & Dogic, Z. Entropy driven self-assembly of nonamphiphilic colloidal membranes. *Proc. Natl Acad. Sci. USA* **107**, 10348–10353 (2010).
12. Safran, S. *Statistical Thermodynamics of Surfaces, Interfaces, and Membranes* 79–85 (Addison Wesley, 1994).
13. Barry, E., Beller, D. & Dogic, Z. A model liquid crystalline system based on rodlike viruses with variable chirality and persistence length. *Soft Matter* **5**, 2563–2570 (2009).
14. Baumgart, T., Hess, S. T. & Webb, W. W. Imaging coexisting fluid domains in biomembrane models coupling curvature and line tension. *Nature* **425**, 821–824 (2003).
15. Honerkamp-Smith, A. R. *et al.* Line tensions, correlation lengths, and critical exponents in lipid membranes near critical points. *Biophys. J.* **95**, 236–246 (2008).
16. Lee, K. Y. C. & McConnell, H. M. Quantized symmetry of liquid monolayer domains. *J. Phys. Chem.* **97**, 9532–9539 (1993).
17. Dogic, Z. & Fraden, S. Cholesteric phase in virus suspensions. *Langmuir* **16**, 7820–7824 (2000).
18. Oldenbourg, R. & Mei, G. New polarized light microscope with precision universal compensator. *J. Microsc.* **180**, 140–147 (1995).
19. Barry, E., Dogic, Z., Meyer, R. B., Pelcovits, R. A. & Oldenbourg, R. Direct measurement of the twist penetration length in a single smectic A layer of colloidal virus particles. *J. Phys. Chem. B* **113**, 3910–3913 (2009).
20. Oldenbourg, R. Polarized light field microscopy: an analytical method using a microlens array to simultaneously capture both conoscopic and orthoscopic views of birefringent objects. *J. Microsc.* **231**, 419–432 (2008).
21. Aarts, D. G. A. L., Schmidt, M. & Lekkerkerker, H. N. W. Direct visual observation of thermal capillary waves. *Science* **304**, 847–850 (2004).
22. Fradin, C. *et al.* Reduction in the surface energy of liquid interfaces at short length scales. *Nature* **403**, 871–874 (2000).
23. Pelcovits, R. A. & Meyer, R. B. Twist penetration in single-layer smectic A discs of colloidal virus particles. *Liq. Cryst.* **36**, 1157–1160 (2009).
24. Kaplan, C. N., Tu, H., Pelcovits, R. A. & Meyer, R. B. Theory of depletion-induced phase transition from chiral smectic-A twisted ribbons to semi-infinite flat membranes. *Phys. Rev. E* **82**, 021701 (2010).
25. Srivastava, S. *et al.* Light-controlled self-assembly of semiconductor nanoparticles into twisted ribbons. *Science* **327**, 1355–1359 (2010).
26. Chung, W. J. *et al.* Biomimetic self-templating supramolecular structures. *Nature* **478**, 364–368 (2011).
27. Grason, G. M. & Bruinsma, R. F. Chirality and equilibrium biopolymer bundles. *Phys. Rev. Lett.* **99**, 098101 (2007).
28. Claessens, M., Semmrich, C., Ramos, L. & Bausch, A. R. Helical twist controls the thickness of F-actin bundles. *Proc. Natl Acad. Sci. USA* **105**, 8819–8822 (2008).
29. Nguyen, T. D. & Glotzer, S. C. Switchable helical structures formed by the hierarchical self-assembly of laterally tethered nanorods. *Small* **5**, 2092–2098 (2009).
30. Nguyen, T. D. & Glotzer, S. C. Reconfigurable assemblies of shape-changing nanorods. *ACS Nano* **4**, 2585–2594 (2010).

**Supplementary Information** is linked to the online version of the paper at [www.nature.com/nature](http://www.nature.com/nature).

**Acknowledgements** This work was supported by the US National Science Foundation (NSF-MRSEC-0820492, NSF-DMR-0955776, NSF-MRI-0923057, NSF-CMMI-1068566) and the Petroleum Research Fund (ACS-PRF 50558-DNI7). We acknowledge use of the Brandeis MRSEC optical microscopy facility.

**Author Contributions** T.G., E.B., M.J.Z., R.B.M. and Z.D. designed the experiments and interpreted the results. T.G., E.B. and M.J.Z. performed the experiments. A.W. performed the optical trapping experiments. E.B., C.B. and D.N. performed the electron microscopy imaging. M.H. performed the experiments on mutant viruses. R.O. performed the LC-PolScope imaging. Y.Y. and M.F.H. designed and performed the computer simulations. T.G., E.B., M.J.Z. and Z.D. wrote the manuscript.

**Author Information** Reprints and permissions information is available at [www.nature.com/reprints](http://www.nature.com/reprints). The authors declare no competing financial interests. Readers are welcome to comment on the online version of this article at [www.nature.com/nature](http://www.nature.com/nature). Correspondence and requests for materials should be addressed to Z.D. ([zdogic@brandeis.edu](mailto:zdogic@brandeis.edu)).



## METHODS

**Virus stock solutions.** Filamentous viruses were grown using standard biological techniques that have been discussed elsewhere<sup>31</sup>. The resulting virus suspensions contain a low fraction of multimeric virus particles (dimers and trimers) with longer contour lengths. Because high monodispersity in particle length is essential for assembly of membranes and ribbons, the polydispersity was reduced by fractionating the samples through the isotropic–nematic phase transition, as longer viruses preferentially dissolve in the nematic liquid-crystalline phase. Suspensions of fd viruses (2–8 ml) were prepared at isotropic–nematic phase coexistence. Only the isotropic (top) portion of the sample, enriched in monomeric viruses, was used for subsequent experiments. The fractionation was repeated once or twice to obtain sufficiently monodisperse suspensions that reproducibly assemble into colloidal membranes and ribbons. The polydispersity of virus suspensions was quantified using gel electrophoresis of intact viruses. Approximately 20  $\mu\text{l}$  of a 0.5  $\text{mg ml}^{-1}$  virus solution was loaded into a 1.8% agarose gel and run at 1.4  $\text{V cm}^{-1}$  for approximately 8 h (ref. 31). The virus coat protein was dissolved by immersing gels in 0.2 M NaOH for 30 min, and the remaining DNA was visualized with ultraviolet light after staining with ethidium bromide<sup>31</sup> (Supplementary Fig. 9). Only virus suspensions with a monodispersity greater than 95% were used for experiments. For fluorescence microscopy, viruses were labelled with fluorescent dyes as described previously<sup>32</sup>. The wild-type fd virus was labelled with Alexa 488-NHS ester (Invitrogen) and the Tyr21Met fd virus was labelled with DyLight 546-NHS ester (Pierce). All samples were buffered in 20 mM Tris, pH 8.0, to which 100 mM NaCl was added to screen electrostatic repulsion between viruses. The concentration of the viruses was determined using absorption spectroscopy<sup>13</sup>.

**Tuning the twist of the cholesteric phase.** The strength of chiral interactions between viruses was quantified by measuring the pitch of a cholesteric liquid-crystalline sample. Glass cylindrical capillaries, 0.7 mm in diameter (Charles Supper Company), were filled with fd virus suspensions. For the cholesteric texture to develop properly, it was necessary to clean the capillaries in a hot detergent solution (Hellmanex) after soaking them in 5 M NaOH. After equilibration for several hours, the samples show a well-known fingerprint texture, seen by polarization microscopy, that is characteristic of cholesteric liquid-crystalline phases<sup>13,17</sup> (Supplementary Fig. 1). The twist wavevector,  $q_0 = 2\pi/P$ , was determined by measuring the cholesteric pitch,  $P$ . Bulk samples were prepared at 100  $\text{mg ml}^{-1}$ . Previous work, as well as experiments described in Supplementary Fig. 4, indicate that this is the effective virus concentration in membranes and ribbons<sup>11</sup>. We assume that  $q_0$  is the same for bulk cholesteric phase and 2D membranes.

Two complimentary methods were used to tune the strength of chiral interactions between fd viruses: genetic mutations of the major coat protein and physical control of sample temperature. Most aspects of the wild-type fd virus phase behaviour, such as the location of the isotropic–nematic phase transition, are independent of temperature, as is expected for entropic suspensions of hard, rod-like particles. An exception is that the wild-type fd virus persistence length is weakly dependent on temperature<sup>33</sup>. Data shown in Supplementary Fig. 1 indicates that decreasing temperature increases the strength of chiral interactions between the viruses, as evidenced by the measurements of the cholesteric pitch<sup>17</sup>. Notably, the twist wavevector shows evidence of a second-order phase transition from a high-temperature achiral phase to a low-temperature cholesteric phase. By contrast with the temperature-dependent chirality of wild-type fd virus, the chirality of Tyr21Met fd virus does not show any temperature dependence (Supplementary Fig. 6).

An alternative control of chirality involves modifying the composition of the major coat protein. For example, Tyr21Met fd virus, a mutant that differs from wild-type fd virus by a single point mutation of the major coat protein, forms a cholesteric helix with the opposite handedness<sup>13</sup>. By controlling the ratio of wild-type to Tyr21Met fd virus, it is possible to tune the chirality of the resulting suspension<sup>13</sup>. Such mixtures still form colloidal membranes, and fluorescence microscopy indicates that the two components are uniformly dispersed on optically resolvable length scales ( $\sim 300$  nm). We have used both temperature and genetic methods to tune the chirality of the constituent rods.

**Light microscopy sample preparation.** Light microscopy chambers were assembled using glass slides and coverslips (Goldseal, Fisher Scientific) with a layer of unstretched Parafilm as a spacer. Glass slides and coverslips were coated with an acrylamide brush to prevent non-specific binding of viruses to the glass surfaces, by a procedure described elsewhere<sup>34</sup>. We mixed fd virus with the non-adsorbing polymer Dextran (relative molecular mass, 500,000; Sigma-Aldrich) to form membrane and ribbons samples. The virus concentration remained fixed at 10  $\text{mg ml}^{-1}$ , and the Dextran concentration varied between 30 and 50  $\text{mg ml}^{-1}$  as indicated in the main text. The samples, sealed using ultraviolet-cured glue (Norland Optical) and stored at 4 °C, remained good for weeks to months.

**Optical microscopy.** Samples were characterized using a number of complimentary optical microscopy techniques. Except those made using the 3D LC-PolScope, all observations were made using a  $\times 100$  oil-immersion objective (Plan Fluor; numerical aperture, 1.3) on an inverted microscope (Nikon TE-2000). Images were recorded with cooled charge-coupled-device (CCD) cameras (CoolSnap HQ, Photometrics, or Retiga Exi, QImaging). The microscope was equipped with traditional polarization optics, a DIC module, a fluorescence imaging module and 2D LC-PolScope microscopy<sup>18</sup>. For 3D PolScope measurements, we used a Zeiss Axiovert 200M microscope with a Plan ApoChomat oil-immersion objective ( $\times 63$ ; numerical aperture, 1.4) and a monochrome CCD camera<sup>20</sup> (Retiga 4000R, QImaging).

Sample temperature was tuned between 4 and 60 °C with a home-made Peltier module equipped with a proportional–integral–derivative temperature controller (ILX Lightwave LPT 5910). The temperature-controlling side of the Peltier device was attached to a copper ring fitted around the microscope objective, which heats or cools the sample through the immersion oil. A thermistor, placed in the copper ring adjacent to the sample, enabled the proportional–integral–derivative feedback necessary to adjust the temperature. Excess heat was removed using a constant flow of room-temperature water.

**3D LC-PolScope microscopy.** Membrane edges with left-handed and right-handed twists appear indistinguishable when viewed with 2D LC-PolScope because this technique provides only a 2D projection of the sample birefringence. To determine the 3D orientation of rods, we used 3D LC-PolScope microscopy<sup>20</sup>. The 3D LC-PolScope extends the capabilities of the 2D LC-PolScope by placing a microlens array in the image plane of the objective lens. The microlens array generates a hybrid image consisting of a series of conoscopic microimages, each probing a different spatial area in the image plane. Analysis of each conoscopic microimage reveals the local birefringence as a function of the propagation direction of transmitted light rays. Supplementary Fig. 4a illustrates the path of the optical rays from the specimen plane to the back focal plane of the 3D LC-PolScope microlens array. Rays shown in green and red pass perpendicularly through the membrane, parallel to its optical axis, and experience no differential retardation. Rays shown in black pass at an angle to the optical axis and are differentially retarded. Rays with the same tilt angle in the specimen plane are focused at the same point in the back focal plane of the objective. The array of microlenses, placed in the image plane of the objective, refocuses these rays into a plane behind the microlens array. Behind each microlens, an image of the objective's aperture appears containing multiple conoscopic images, each specific to rays that have passed through a small region of the specimen. For example, rays emanating from the region  $X$  of the sample fall onto the microlens  $X'$ . Therefore, only rays that passed through  $X$  contribute to the conoscopic image behind  $X'$ . The same argument applies to rays passing through  $Y$  and  $Y'$ , and so on.

The conoscopic image of a single microlens focused on the bulk portion of the membrane shows a radially symmetric distribution of the retardance that increases away from the centre of the image (Supplementary Fig. 4b). In the centre, the rays of light are aligned with the orientation of the viruses and the retardance is zero. Away from the centre, the retardance increases because the rays of light become tilted with respect to the orientation of the viruses. When the viruses are tilted with respect to the optical axis, for example near the edge of the membrane, the radial profile obtained from a conoscopic image becomes asymmetric and indicates local tilting of the molecules. For colloidal membranes composed of an achiral mixture of wild-type and Tyr21Met fd viruses, the viruses at the edge of a membrane are found to twist in clockwise and anticlockwise directions with equal probability (Supplementary Fig. 4c–e).

Analysis of the 3D LC-PolScope retardance profile is used to determine the concentration of viruses within a membrane, because the membrane birefringence is proportional to the local rod concentration. It follows that the local retardance of the membrane is given by  $R = \Delta n_{\text{sat}} d c S \sin^2(\theta) / \sin(\alpha)$ , where  $\theta$  is the local tilting of the rods,  $c$  is the concentration of rods within a membrane,  $d$  is the thickness of the colloidal membrane,  $S$  is the local order parameter (assumed to be  $\sim 1$ ),  $\Delta n_{\text{sat}}$  is the specific birefringence of a fully aligned bulk sample of fd virus at unit concentration as determined by X-ray scattering experiments<sup>35</sup> and  $\alpha$  is the orientation of the rays of light as a function of the distance,  $r$ , to the centre of the conoscopic image. This orientation is given by  $\sin(\alpha) = r N_A / r_{NA} N$ , where  $r_{NA} = 3.9 \mu\text{m}$  is the size of the conoscopic image,  $NA = 1.4$  is the numerical aperture and  $n = 1.33$  is the index of refraction of the solvent. The fitting of this functional form to the retardance profile yields a mean concentration of viruses in the bulk of the membrane of  $c = 103 \pm 10 \text{ mg ml}^{-1}$  (Supplementary Fig. 4f). Similar values were obtained by an independent method that involves counting the number of fluorescently labelled particles<sup>11</sup>. Finally, we also note that the concentration of the viruses does not appreciably change with varying Dextran concentration (Supplementary Fig. 4g).

**Measurement of the line tension.** Line tension was measured by directly imaging and analysing thermal fluctuations of the membrane's edge with DIC optical microscopy using well-established methods<sup>12</sup>. Lower line tension indicates that



less energy is required to place the particles at an interface, resulting in larger fluctuations of the membrane's edge. The conformation of the membrane's edge is described by  $h(x)$ , the local height of the interface, where  $x$  is the lateral position along the interface. The total length of the interface is

$$L = \int dx \sqrt{1 + \left(\frac{dh}{dx}\right)^2} \quad (1)$$

For small fluctuations ( $dh/dx = \tan(\theta) \approx \theta$ ), the expression for the excess length of the edge relative to a flat interface can be approximated as

$$\Delta L = \int dx \sqrt{1 + \theta^2} - L \approx \frac{1}{2} \int dx \theta^2(x)$$

If line tension,  $\gamma$ , is the energetic cost per unit length of the edge, the free-energy difference between fluctuating and straight edges is given by  $\Delta F = \gamma \Delta L$ . Next we decompose  $\theta(x)$  into a Fourier series:

$$\theta(x) = \sum_q \sqrt{\frac{2}{L}} a_q \cos(qx)$$

Here  $L$  is the length of the interface and the wavevector,  $q$ , is given by  $q = n\pi/L$ . The energetic cost of the membrane conformation specified by Fourier amplitudes  $a_q$  is given by

$$\Delta F = \gamma \Delta L = \frac{\gamma}{2} \int_0^L dx \theta^2(x) = \frac{\gamma}{2} \sum_q a_q^2$$

By invoking the equipartition theorem, it is possible to relate the line tension to fluctuations of the interface:

$$\langle a_q^2 \rangle = k_B T / \gamma \quad (2)$$

To measure  $\langle a_q^2 \rangle$  experimentally, we acquired a series of uncorrelated images of the interfacial contour. To ensure optimal contrast, the DIC shear axis was always perpendicular to the membrane's edge. Under these conditions, intensity profile cuts taken perpendicular to the edge could be fitted to a Gaussian, yielding the conformation of the edge with subpixel accuracy. Each conformation is described in terms of the Fourier amplitudes,  $a_q$ . Averaging over a sufficient number of uncorrelated images yields a fluctuation spectrum as shown in Fig. 2b, where the mean square amplitudes,  $\langle a_q^2 \rangle$ , are plotted as functions of  $q$ . In the limit of small  $q$ ,  $\langle a_q^2 \rangle$  is independent of wavenumber as predicted by equation (2). As  $q$  increases, the fluctuations are suppressed and scale as  $q^{-2}$ . The entire fluctuation spectrum can be quantitatively described by the following equation:

$$\langle a_q^2 \rangle = \frac{k_B T}{\gamma + \kappa q^2} \quad (3)$$

The  $1/q^2$  regime can be obtained by including terms that are proportional to the square of the gradient of  $\theta(x)$  in equation (1). This indicates that there is a bending energy,  $\kappa$ , associated with fluctuations of the interface, which might be related to the existence of a thin, quasi-1D nematic phase located at the edge of the membrane, where the rods are tilted and the layer's smectic ordering is destroyed.

**Laser tweezers.** Colloidal membranes and ribbons are easily manipulated using optical tweezers. The laser tweezer set-up was built around an inverted Nikon TE-2000 microscope. A 1,064-nm laser beam (Compass 1064, Coherent) is time-shared between two points by means of a pair of orthogonally oriented paratellurite ( $\text{TeO}_2$ ) acousto-optic deflectors (Intra-Action). The laser is projected onto the back focal plane of an oil-immersion objective (Plan Fluor  $\times 100$ , NA = 1.3) and subsequently focused onto the imaging plane. Using custom LABVIEW software, multiple trap locations were specified and used to stretch and manipulate membranes and ribbons.

**Electron microscopy.** For transmission electron microscopy, membranes were assembled as described above but with the following differences. The monolayer membranes are relatively small and only stable in solution; therefore, to keep them intact throughout fixation and staining, we immobilized the membrane assemblies by embedding them in 1% low-melting-temperature agarose (SeaKem; gelation temperature,  $25 \pm 5^\circ\text{C}$ ), in 100 mM NaCl, 20 mM Tris, pH 8.15, and 150 mM sucrose as a cryoprotectant. Virus samples were mixed in 1.5-ml Eppendorf tubes with fluid agarose at  $30^\circ\text{C}$  and kept warm for 3–6 h to allow formation of relatively large membranes as confirmed by light microscopy. Subsequently, a drop of the fluid sample containing membranes was transferred into the 0.1-mm-high cavity of an aluminium planchette for high-pressure freezing (Wohlgend), which was then closed. Then the sample temperature was decreased to  $4^\circ\text{C}$  for 30–45 min. The gelled samples were rapidly frozen using a Leica HPM-100 high-pressure freezer (Leica Microsystems). Using a Leica AFS-2 device, the frozen samples were freeze-substituted at low temperatures (starting at  $-90^\circ\text{C}$ ) over the course of three days in a solution containing 1% osmium tetroxide (EMS), 0.5% anhydrous glutaraldehyde (EMS) and 2% water in anhydrous acetone (AC32680-0010, Fisher Scientific). After the temperature was raised to  $4^\circ\text{C}$ , the sample was infiltrated and embedded in EMBED 812-Resin (EMS). Ultrathin, 70-nm, sections were collected on slot grids covered with Formvar support film and post-stained with uranyl acetate (supersaturated solution) and 0.2% lead citrate, before inspection on a FEI Morgan 268 transmission electron microscope with a 1k CCD camera (GATAN) and on a 300-keV Tecnai F30 intermediate-voltage transmission electron microscope (FEI) with a 4k CCD camera (GATAN). For electron tomography, we used 150-nm-thick sections that were coated with 10-nm colloidal gold particles. Tilt series were recorded over an angular range of  $\pm 60^\circ$  with  $1^\circ$  increments on the Tecnai F30 using the microscope control software SERIAL-EM<sup>36</sup>. Tomographic reconstructions were calculated with the IMOD software using fiducial alignment and weighted back-projection<sup>37</sup>.

**Computer simulations of the rod/polymer mixture.** In the computational model, the rods were represented as hard spherocylinders and the non-adsorbing polymers (depletant) were modelled as ghost spheres, which act as hard spheres when interacting with rods but can freely interpenetrate one another<sup>38</sup>. We performed Metropolis Monte Carlo simulation with periodic boundary conditions. The system contained 6,000 rods in a box with dimensions  $140 \times 140 \times 50$  (in units of the rod diameter). A constant osmotic pressure was maintained by coupling ghost spheres to a constant-chemical-potential bath through insertion and deletion moves. The simulations thus sampled the  $N_{\text{rod}}\mu_{\text{sphere}}VT$  ensemble, where  $N_{\text{rod}}$  is the number of rods,  $\mu_{\text{sphere}}$  is the sphere chemical potential and  $V$  is the volume. The rod aspect ratio was 20, the ghost-sphere diameter was 1.5 and on average there were about 520,000 spheres. Simulations were initialized with rods in a monolayer, and Monte Carlo simulation was performed until rod density within the membrane and rod orientations equilibrated. Rods at the membrane edge twisted spontaneously regardless of the initial rod orientations in the membrane.

31. Maniatis, T., Sambrook, J. & Fritsch, E. *Molecular Cloning* Ch. 3 (1989).
32. Lettinga, M. P., Barry, E. & Dogic, Z. Self-diffusion of rod-like viruses in the nematic phase. *Europhys. Lett.* **71**, 692–698 (2005).
33. Tang, J. X. & Fraden, S. Nonmonotonic temperature dependence of the flexibility of bacteriophage fd. *Biopolymers* **39**, 13–22 (1996).
34. Lau, A. W. C., Prasad, A. & Dogic, Z. Condensation of isolated semi-flexible filaments driven by depletion interactions. *Europhys. Lett.* **87**, 48006 (2009).
35. Purdy, K. R. *et al.* Measuring the nematic order of suspensions of colloidal fd virus by X-ray diffraction and optical birefringence. *Phys. Rev. E* **67**, 031708 (2003).
36. Mastrorade, D. N. Automated electron microscope tomography using robust prediction of specimen movements. *J. Struct. Biol.* **152**, 36–51 (2005).
37. Kremer, J. R., Mastrorade, D. N. & McIntosh, J. R. Computer visualization of three-dimensional image data using IMOD. *J. Struct. Biol.* **116**, 71–76 (1996).
38. Yang, Y., Barry, E., Dogic, Z. & Hagan, M. F. Self-assembly of 2D membranes from mixtures of hard rods and depleting polymers. *Soft Matter* **8**, 707–714 (2012).

# Complete subunit architecture of the proteasome regulatory particle

Gabriel C. Lander<sup>1\*</sup>, Eric Estrin<sup>2\*</sup>, Mary E. Matyskiela<sup>2\*</sup>, Charlene Bashore<sup>2</sup>, Eva Nogales<sup>1,3,4</sup> & Andreas Martin<sup>2,4</sup>

**The proteasome is the major ATP-dependent protease in eukaryotic cells, but limited structural information restricts a mechanistic understanding of its activities. The proteasome regulatory particle, consisting of the lid and base subcomplexes, recognizes and processes polyubiquitinated substrates. Here we used electron microscopy and a new heterologous expression system for the lid to delineate the complete subunit architecture of the regulatory particle from yeast. Our studies reveal the spatial arrangement of ubiquitin receptors, deubiquitinating enzymes and the protein unfolding machinery at subnanometre resolution, outlining the substrate's path to degradation. Unexpectedly, the ATPase subunits within the base unfoldase are arranged in a spiral staircase, providing insight into potential mechanisms for substrate translocation through the central pore. Large conformational rearrangements of the lid upon holoenzyme formation suggest allosteric regulation of deubiquitination. We provide a structural basis for the ability of the proteasome to degrade a diverse set of substrates and thus regulate vital cellular processes.**

The ubiquitin–proteasome system is the major pathway for selective protein degradation in eukaryotic cells. Covalent modification with a polyubiquitin chain targets damaged, misfolded and short-lived regulatory proteins for ATP-dependent destruction by the 26S proteasome, a massive 1.5 MDa proteolytic machine. The proteasome thus controls a myriad of essential cellular processes, including the cell cycle, transcription and protein quality control<sup>1</sup>. Despite intensive study, however, the structural basis for substrate recognition and processing by the proteasome remains poorly understood.

The proteasome contains at least 32 different subunits that form a barrel-shaped 20S proteolytic core capped on either end by a 19S regulatory particle. The active sites of the peptidase are sequestered in an internal chamber, and access is controlled by the regulatory particle, which functions in substrate recognition, deubiquitination, unfolding and translocation of the unfolded chains into the core<sup>2–5</sup>.

The regulatory particle is composed of 19 subunits and can be divided into two subcomplexes, the lid and the base. The lid consists of nine non-ATPase proteins (Rpn3, Rpn5–Rpn9, Rpn11, Rpn12 and Sem1 in yeast), including the deubiquitinating enzyme (DUB) Rpn11, whose activity is essential for efficient substrate degradation<sup>6,7</sup>. The base contains six distinct AAA+ ATPases, Rpt1–Rpt6, that form a hetero-hexameric ring (in the order Rpt1, Rpt2, Rpt6, Rpt3, Rpt4, Rpt5; ref. 8) and constitute the molecular motor of the proteasome. The ATPases are predicted to use the energy of ATP binding and hydrolysis to exert a pulling force on substrate proteins, unfold them, and translocate the polypeptides through a narrow central pore into the peptidase chamber. In the presence of ATP, the carboxy termini of the ATPases bind dedicated sites on the  $\alpha$ -subunit ring ( $\alpha$ 1– $\alpha$ 7) of the 20S core, triggering the opening of a gated access channel and facilitating substrate entry<sup>5,9–11</sup>. Besides Rpt1–Rpt6, the base contains four non-ATPase subunits: Rpn1, Rpn2 and the ubiquitin receptors Rpn10 and Rpn13. Additional ubiquitin shuttle receptors (Rad23, Ddi1 and Dsk2) are recruited to the base through interactions with Rpn1, which also binds a second, non-essential DUB, Ubp6 (refs 12–14).

Whereas the proteolytic core has been well studied, there is only limited structural characterization of the regulatory particle<sup>11,15–17</sup>.

None of the 13 non-ATPase subunits, including the ubiquitin receptors and deubiquitinating enzymes, have been localized within this assembly. Although it has been shown that efficient degradation depends on the length, linkage type and placement of an ubiquitin chain, as well as the presence of an unstructured initiation site on a substrate<sup>3,18,19</sup>, we are missing the topological information needed to explain these requirements. Thus, elucidating the architecture of the regulatory particle and the spatial arrangement of individual subunits is crucial to understanding the molecular mechanisms for substrate recognition and processing.

Here, we present the electron microscopy structure of the proteasome holoenzyme and the lid subcomplex. A new heterologous expression system for the lid facilitated the localization of all subunits within the regulatory particle, providing a complete architectural picture of the proteasome. The resulting structural understanding offers novel insight into the mechanisms of ubiquitin binding, deubiquitination, substrate unfolding and translocation by this major eukaryotic proteolytic machine.

## Recombinant expression of yeast lid in *Escherichia coli*

We developed a system for the heterologous coexpression of all nine lid subunits from *Saccharomyces cerevisiae* in *Escherichia coli*. This system allowed us to generate truncations, deletions and fusion constructs that were used to localize individual subunits and delineate their boundaries within the lid. The recombinant, purified lid was analysed in its subunit composition and stoichiometry by SDS–polyacrylamide gel electrophoresis (SDS–PAGE; Supplementary Figs 1 and 2) and tandem mass spectrometry. The small, non-essential subunit Sem1 could not be detected, neither for the recombinant nor the endogenous lid that was isolated from yeast. All other subunits were present with the expected stoichiometry, and gel-filtration analyses showed indistinguishable elution profiles for the heterologously expressed lid and its endogenous counterpart (data not shown). Furthermore, atomic emission spectroscopy confirmed that the essential Zn<sup>2+</sup> ion was incorporated in Rpn11, indicating proper folding in *E. coli*.

<sup>1</sup>Life Sciences Division, Lawrence Berkeley National Laboratory, University of California, Berkeley, California 94720, USA. <sup>2</sup>Department of Molecular and Cell Biology, University of California, Berkeley, California 94720, USA. <sup>3</sup>Howard Hughes Medical Institute, University of California, Berkeley, California 94720, USA. <sup>4</sup>QB3 Institute, University of California, Berkeley, California 94720, USA.

\*These authors contributed equally to this work.

To compare the functionalities of recombinant and endogenous lid, we established conditions for their *in vitro* reconstitution with base and 20S core subcomplexes from yeast to yield 26S holoenzyme. These reassembled particles were assayed for their activity in ubiquitin-dependent substrate degradation by using a polyubiquitinated green fluorescent protein (GFP)–cyclin fusion protein and following the decrease in GFP fluorescence. Proteasome reconstituted with *E. coli*-expressed lid supported robust substrate degradation (Supplementary Fig. 3). Importantly, the three-dimensional electron microscopy reconstructions from negative-stained samples of both lid subcomplexes are practically identical (Fig. 1a and Supplementary Fig. 4), establishing this recombinant system as an ideal tool for our structural studies of the regulatory particle.

### Localization of regulatory particle subunits

As a first step in elucidating the architecture of the regulatory particle, we compared the single-particle electron microscopy reconstructions of the yeast holoenzyme and the isolated lid subcomplex obtained at 9- and 15-Å resolution, respectively (Fig. 1b, Supplementary Figs 5–7 and Supplementary Movie 1). Docking the five-lobed, hand-shaped structure of the lid into the electron density of the holoenzyme revealed the lid's position on one side of the regulatory particle, forming extensive interactions with the base subcomplex, but also contacting the 20S core. The lid subunits Rpn3, Rpn5, Rpn6, Rpn7, Rpn9 and Rpn12 contain a C-terminal PCI (Proteasome-CSN-eIF3) domain that is assumed to have scaffolding functions and allow inter-subunit contacts<sup>1</sup>. Our reconstruction provided sufficient resolution to unambiguously locate the winged-helix fold and the flanking helical segments of individual PCIs (Fig. 1c and Supplementary Movie 1). The C-terminal PCI domains of the six Rpn subunits thus interact laterally to form a horseshoe-shaped anchor from which the amino-terminal domains extend radially. This arrangement demonstrates

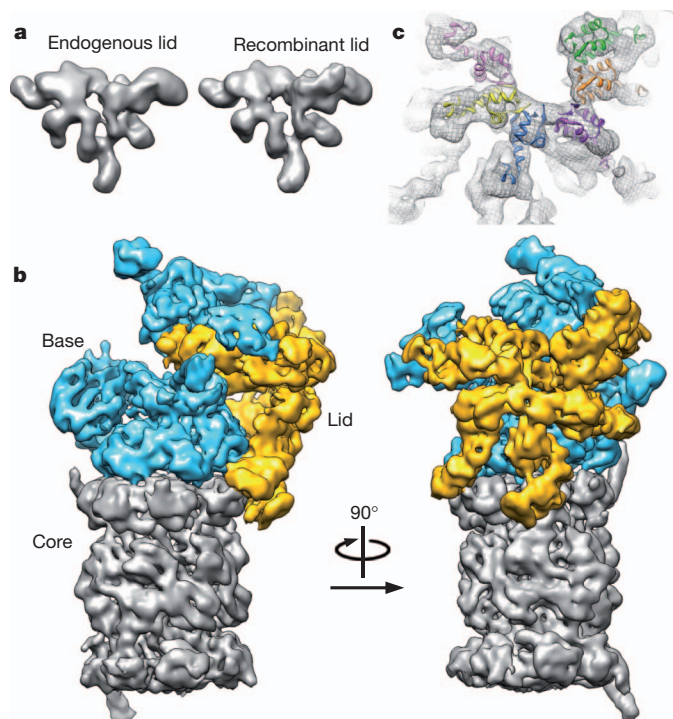


**Figure 1 | The lid subcomplex within the holoenzyme assembly.** **a**, Negative-stain three-dimensional reconstruction at approximately 15-Å resolution shows resemblance between endogenous (left) and recombinant (right) lid. **b**, Locations of lid (yellow) and base (cyan) within the subnanometre holoenzyme reconstruction. **c**, Six copies of the crystal structure of a PCI domain (PDB ID: 1RZ4) are docked into the lid electron density, showing a horseshoe-shaped arrangement of the winged-helix domains. Each domain is coloured according to its respective lid subunit (Fig. 2).

the scaffolding function of PCI domains in the lid, and we predict that similar interactions underlie the architecture of other PCI-containing complexes.

To determine the subunit topology of the lid, we used our heterologous *E. coli* expression system, fused maltose-binding protein (MBP) to the N or C terminus of individual subunits (Supplementary Fig. 1), and localized the MBP within the tagged lid particles by negative-stain electron microscopy (Supplementary Fig. 8a). None of the MBP fusions notably affected the lid structure, and we were able to identify the positions of all eight essential lid subunits and the relative orientation of their N and C termini. In combination with the PCI docking, the resolution of secondary structures in the cryoelectron density and known molecular weights, this information allowed us to delineate approximate subunit boundaries (Fig. 2a and Supplementary Movie 1).

Overall, Rpn3, Rpn7, Rpn6, Rpn5 and Rpn9 form the fingers of the hand-shaped lid structure. Rpn8 shows an extended conformation that connects Rpn3 and Rpn9, and thus closes the PCI horseshoe. In addition, it interacts with Rpn11, the only essential DUB of the proteasome, which lies in the palm of the hand and makes extensive contacts with Rpn8, Rpn9 and Rpn5.

Using the topology determined for the isolated lid subcomplex, we delineated the individual lid subunits in the context of the holoenzyme (Fig. 2b). To complete the subunit assignment for the entire regulatory particle, the positions of Rpt1–Rpt6 in the base subcomplex were assigned according to established interactions with the core particle<sup>15,20</sup>, whose crystal structure could be docked unambiguously into the electron microscopy density (Supplementary Fig. 9). We localized the two large non-ATPases Rpn1 and Rpn2 of the base subcomplex by antibody-labelling of a C-terminal Flag tag and N-terminal fusion of glutathione-S-transferase (GST), respectively (Supplementary Figs 2 and 10a–c). Rpn1 and Rpn2 had been predicted to contain numerous tetratricopeptide repeat (TPR)-like motifs and adopt  $\alpha$ -solenoid structures<sup>21</sup>. Indeed, we found a high structural resemblance between Rpn1 and Rpn2, both consisting of a strongly curled solenoid that transitions into an extended arm towards the C terminus (Fig. 3a). Rpn1 contacts the C-terminal helix of the 20S core subunit  $\alpha$ 4 and, based on the variability observed in our electron microscopy images, is likely to be flexible or loosely attached to the side of the base. Previous crystallography studies of the archaeal proteasome homologue PAN revealed that the N-terminal domains of the ATPases form a separate hexameric ring (N-ring) that consists of OB domains and three protruding coiled-coil segments<sup>17,22</sup>. Each coiled coil is formed by the far N-terminal residues of two neighbouring ATPases in the hexamer. Although Rpt1 and Rpt2 do not seem to form an extended coiled coil, we find that the N-terminal helical portion of Rpt1 interacts with the solenoid and the C-terminal arm of Rpn1. Rpn2 is located above the N-ring and mounted atop the longest of the protruding coiled coils, formed by Rpt3 and Rpt6. These interactions strongly resemble those observed between Rpt1 and Rpn1 (Fig. 3a).

Localizing the ubiquitin receptors and DUBs within the regulatory particle is of particular interest. In addition to the DUB Rpn11 in the lid, we identified the positions of both intrinsic ubiquitin receptors, Rpn10 and Rpn13, and of the base-associated DUB Ubp6 by imaging proteasome particles from yeast deletion strains (Fig. 3b and Supplementary Fig. 10d–f). The ubiquitin receptor Rpn13 binds to Rpn2 as expected<sup>23,24</sup>. The globular VWA domain of the second receptor Rpn10 has been shown previously to stabilize the lid–base interaction<sup>25,26</sup>; however, we found that it does not contact the base directly. This domain bridges Rpn11 and Rpn9, which might increase the lid–base affinity indirectly by stabilizing Rpn11 in its Rpn2-bound conformation (see below). The flexibly attached ubiquitin interacting motif (UIM) of Rpn10 probably contacts the coiled coil formed by Rpt4 and Rpt5, stabilizing its position relative to other subunits and potentially communicating with the AAA+ motor. The DUB Ubp6 seems to be flexible and does not give rise to ordered density. Nonetheless, variance



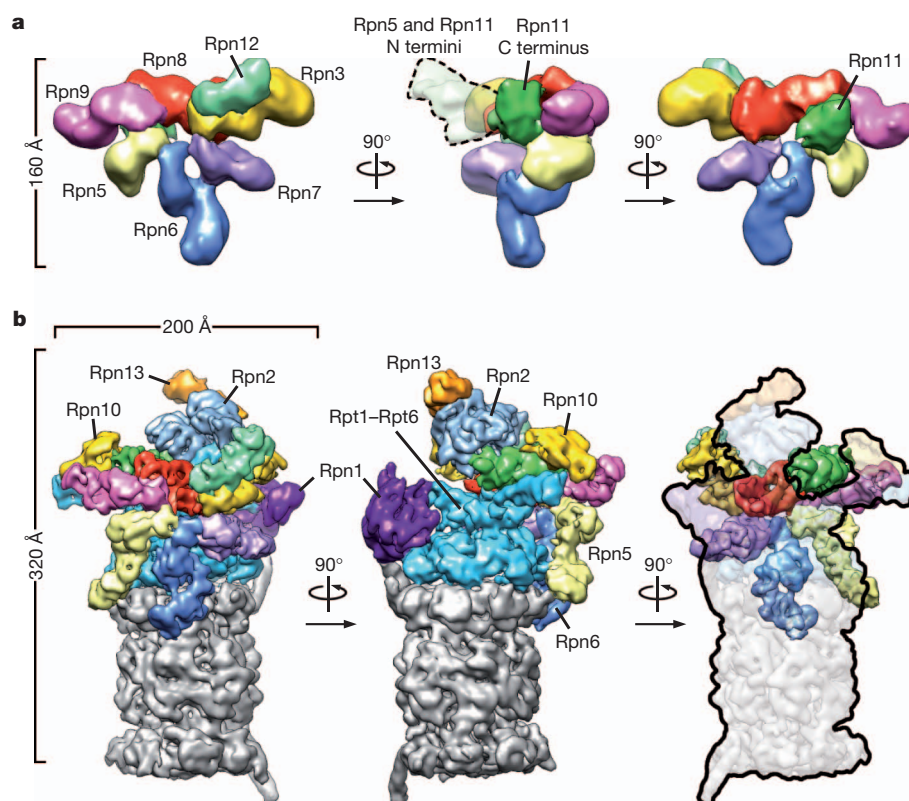


**Figure 2 | Three-dimensional reconstructions of the recombinant lid subcomplex and the yeast 26S proteasome.** **a**, Negative-stain reconstruction of the isolated lid subcomplex at 15-Å resolution, coloured by subunit and shown from the exterior (left), the side (middle) and the interior, base-facing side (right). A dotted line (middle) indicates the highly variable electron density

for the flexible N-terminal domains of Rpn5 and Rpn11. **b**, Subnanometre cryoelectron microscopy reconstruction of the holoenzyme, shown in three views corresponding to the isolated lid and coloured as above, with the core particle in grey.

maps indicate that it interacts with the C-terminal arm of Rpn1, as suggested by immunoprecipitations<sup>14</sup>.

### Inter-subcomplex contacts

The complete localization of subunits within the holoenzyme revealed unexpected contacts between the lid and core subcomplexes. Rpn5 and Rpn6 form fingers that touch the C termini of the core subunits  $\alpha 1$  and  $\alpha 2$ , respectively. We confirmed the interaction between Rpn6 and  $\alpha 2$  by *in vitro* crosslinking, using an engineered cysteine in  $\alpha 2$  and a 7-Å heterobifunctional crosslinker (Supplementary Fig. 11). These previously unknown direct interactions between lid and core may stabilize the entire holoenzyme assembly, and/or be part of an allosteric network that modulates the activities of either subcomplex.

Our holoenzyme structure shows that Rpn3, Rpn7, Rpn8 and Rpn11 make extensive contacts with the base. Compared to their positions in the isolated lid, Rpn8 and Rpn11 have undergone significant conformational changes in the holoenzyme (Fig. 4). The C terminus of Rpn8 is detached from Rpn3 to interact with the coiled coil of Rpt3/Rpt6, while the N-terminal MPN domain of Rpn11 extends towards the centre of the regulatory particle to bind the solenoid portion of Rpn2. Similarly, the N-terminal region of Rpn3 is more elongated than in the isolated lid and also contacts the Rpn2 solenoid, but from the opposite side. In turn, the extended C-terminal arm of Rpn2 interacts with Rpn3 and Rpn12, and thus forms a direct connection between the solenoid section of Rpn2, the coiled coil of Rpt3/Rpt6, and the lid (Fig. 3b).

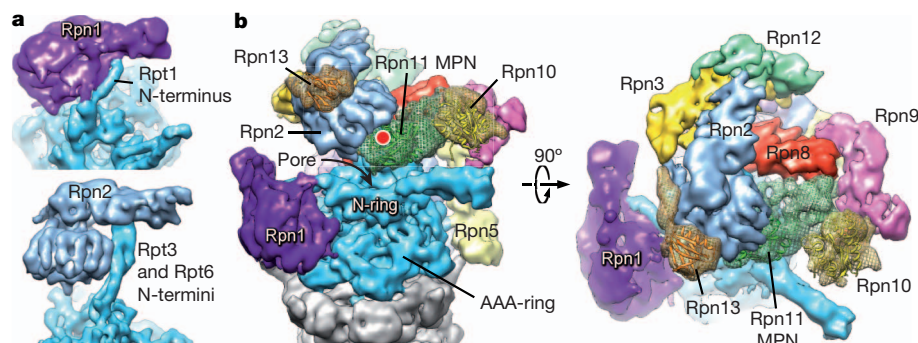


**Figure 3 | Localization of Rpn1 and Rpn2, and ubiquitin-interacting subunits.** **a**, Rpn1 (top) and Rpn2 (bottom) are oriented to emphasize similarities in their domain structure and solenoid attachment to the extended N-terminal helices of Rpt1 and Rpt3/Rpt6, respectively. **b**, Side and top views of the regulatory particle, showing the locations of the ubiquitin receptors Rpn10

and Rpn13, and the DUB Rpn11 relative to the central pore. Crystal structures for Rpn10 (PDB ID: 2X5N), Rpn13 (PDB ID: 2R2Y), and an MPN domain homologous to Rpn11 (AMSH-LP, PDB ID: 2ZNR) are shown docked into the electron microscopy density. The predicted active site of Rpn11 is indicated (red dot).

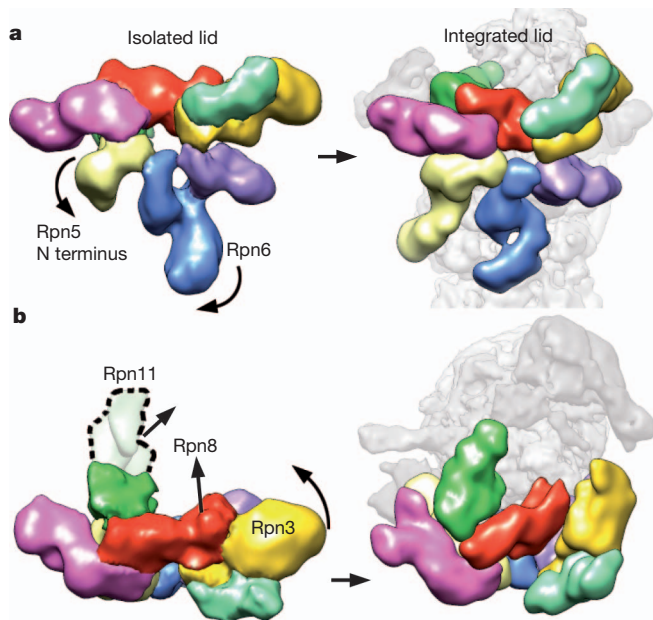


**Figure 4 | Conformational rearrangements of the lid subcomplex upon integration into the holoenzyme.** **a, b,** The lid complex in its isolated (left) and integrated (right) state is shown as viewed from the exterior (**a**) and top (**b**) of the regulatory particle. Major subunit rearrangements are depicted by arrows. The N terminus of Rpn5 (light yellow) interacts with Rpn11 in the isolated complex, and swings down to contact the core particle upon incorporation into the holoenzyme. The N-terminal domain of Rpn6 swings to the left to interact similarly with the core particle. Rpn3, Rpn8 and Rpn11 undergo notable rearrangements, in which they move towards the centre of the regulatory particle.

We speculate that Rpn2 stabilizes a lid conformation in which Rpn3, Rpn8 and the DUB Rpn11 extend towards the base (Fig. 4b). Together, the lid, Rpn2 and the coiled coils of the N-ring seem to function as a scaffold that positions the two intrinsic ubiquitin receptors Rpn10 and Rpn13, and the DUB Rpn11 for substrate binding, deubiquitination and transfer to the subjacent central pore of the AAA+ motor (Fig. 3b). Interestingly, several lid subunits interact directly with AAA+ domains of the Rpt subunits. Rpn7 contacts the AAA+ domains of Rpt2 and Rpt6, while Rpn6 and Rpn5 touch Rpt3. These interactions with contiguous motor domains are surprising, because current models for ATP-dependent unfoldases suggest significant conformational changes of individual subunits in the hexamer during ATP hydrolysis and substrate translocation<sup>27–29</sup>. The observed contacts between lid and the motor domains might form only transiently; alternatively, the AAA+ ring of the proteasome may be much more static than previously assumed.

### Lid conformational changes may regulate DUB activity

Comparing the structures of the lid in isolation and when bound to holoenzyme revealed major conformational changes that suggest an allosteric mechanism for the regulation of Rpn11 DUB activity (Fig. 4). In the isolated lid, the N-terminal MPN domain of Rpn11 forms extensive interactions with Rpn9 and the curled up Rpn5 finger. Upon lid binding to the holoenzyme, this Rpn5 finger swings down to contact the  $\alpha 1$  subunit of the 20S core and thereby releases Rpn11, which then extends towards the Rpn2 solenoid. Docking the MPN domain of a related DUB (PDB ID: 2ZNR) into the electron density of Rpn11 indicates the approximate location of the active site (Fig. 3b). The interactions of Rpn11 with Rpn9 and Rpn5 in the free lid probably restrict access to this active site, which would prevent futile substrate deubiquitination in the absence of base and 20S core, and explain previous observations that the lid subcomplex has DUB activity only within the holoenzyme<sup>7</sup> (and our unpublished data).

### Functional asymmetry in the AAA+ unfoldase

Our subnanometre structure of the holoenzyme provides new insights into the architecture and potential mechanisms of the base AAA+ unfoldase. As suggested by previous electron microscopy studies<sup>15,16</sup>, the ring of the base and the 20S core are slightly offset from a coaxial alignment, with the base shifted by approximately 10 Å towards the lid (Fig. 5a). Despite or perhaps because of this offset, the C-terminal tails of Rpt2, Rpt3 and Rpt5 are docked into their cognate 20S binding pockets at the interfaces of the subunits  $\alpha 3$  and  $\alpha 4$ ,  $\alpha 1$  and  $\alpha 2$ , and  $\alpha 5$  and  $\alpha 6$ , respectively. Those three Rpt tails contain the terminal HbYX motif, which is critical for triggering gate opening in the 20S core<sup>5,10</sup>, and indeed our structure is consistent with an open-gate conformation. The tails of Rpt1, Rpt4 and Rpt6 lack this motif and were not observed to interact statically with 20S in our holoenzyme structure.

Current mechanistic models for AAA+ unfoldases predict that ATPase subunits in the hexamer are in different nucleotide states and undergo significant conformational changes driven by coordinated ATP hydrolysis<sup>27,30,31</sup>. Because we determined the structure of wild-type proteasome in the presence of saturating ATP, we expected that different complexes would have any given Rpt subunit in different conformations, leading to reduced electron density or low resolution when averaging thousands of these unsynchronized motors. However, our reconstruction shows highly ordered density throughout the AAA+ domains of all six Rpt subunits. Whereas the C-terminal ‘small AAA+’ subdomains (except for Rpt6) arrange in one plane above the 20S core, the ‘large AAA+’ subdomains of Rpt1–Rpt5 are oriented in a spiral staircase around the hexameric ring, with Rpt3 at the highest and Rpt2 at the lowest position (Fig. 5b and Supplementary Movie 1). The AAA+ domain of Rpt6 adopts a tilted orientation, bridging Rpt2 and Rpt3. Similar staircase arrangements have been observed previously for helicases of the AAA+ and RecA superfamilies<sup>32,33</sup>. It was suggested that during ATP hydrolysis, individual subunits progress through the different conformational stages of the staircase, thereby translocating substrate through the pore. The particular staircase orientation we observed identically for all proteasome particles may represent a low-energy state of the base, adopted under our experimental conditions. Alternatively, this staircase arrangement of Rpt1–Rpt6 may be static and reflect the functional state of the base, in which substrates are translocated by local motions of the pore loops while the relative positions of the motor subunits remain fixed. Future biochemical and structural studies will be required to distinguish between these two models.

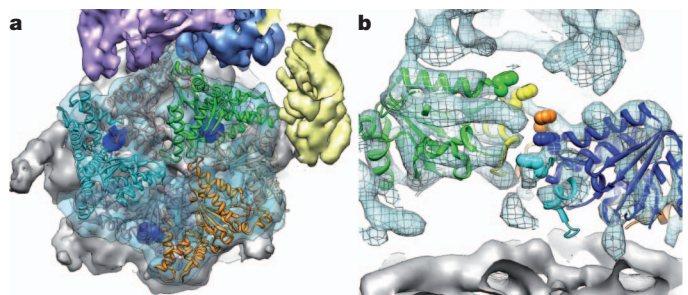


**Figure 5 | Structural features of the base ATPase subunits.** **a,** Positions of Rpt2 (cyan), Rpt3 (green) and Rpt5 (orange) within the base hexameric ring and relative to the 20S core (grey) are shown using fitted crystal structures of the homologous PAN AAA+ domain (PDB ID: 3H4M). The electron microscopy density contains the molecular envelope of the C-terminal tails (dark blue), docked into their cognate binding sites on the 20S core. Corresponding densities were not found for the tails of Rpt1, Rpt4 and Rpt6 (grey ribbon structure). **b,** Cutaway side view of the holoenzyme electron microscopy density with Rpt1–Rpt5 visible. Individually docked copies of the PAN crystal structure reveal a spiral staircase arrangement of the Rpt subunits, emphasized by space-filling representations of the PAN pore-1 loop residues (not resolved in the Rpt subunits).



## Spatial arrangement of ubiquitin receptors and DUBs

Localizing all subunits of the regulatory particle enabled us to infer the requirements and potential mechanisms for the recognition and degradation of ubiquitin-tagged substrates (Fig. 6). After a substrate binds to an ubiquitin receptor, its polyubiquitin chain must be removed by Rpn11 cleavage at the proximal ubiquitin to permit subsequent fast degradation<sup>6,7</sup>. To allow cleavage without disengaging from the receptor, an ubiquitin chain must be long enough to span the distance between receptor and DUB. Based on our structure, both Rpn13 and the UIM of Rpn10 are located 70–80 Å from the predicted position of the Rpn11 MPN domain (Fig. 3b). The shuttle receptors Rad23, Ddi1 and Dsk2 are expected to reside ~80–120 Å away from Rpn11, depending on where they bind Rpn1 (ref. 13). For receptor interaction, at least part of the ubiquitin chain has to be in an extended conformation with the hydrophobic patches exposed<sup>24,34,35</sup>. Because a single ubiquitin moiety in an extended K48-linked chain contributes approximately 30 Å in length<sup>36</sup>, it would take three ubiquitins to span the distance between Rpn10 or Rpn13 and Rpn11. Moreover, both Rpn10 and Rpn13 bind between two consecutive ubiquitin moieties<sup>24,34</sup>, such that at least a tetra-ubiquitin chain would be required on a substrate to allow interaction with a receptor and simultaneous deubiquitination by Rpn11 (Fig. 6). This model agrees with *in-vitro* studies that indicate a minimum of four K48-linked ubiquitins is necessary for efficient substrate degradation<sup>3</sup>, although this number may differ for other chain types<sup>37</sup>. Given the arrangement of Rpn10 and Rpn13, an ubiquitin chain would have to be significantly longer to interact with both receptors. However, knockout studies have shown that ubiquitin chains are not required to bind to multiple receptors simultaneously<sup>38</sup>.

In contrast to Rpn11, Ubp6 is known to cleave within polyubiquitin chains or trim them from their distal end<sup>39</sup>. Of all the ubiquitin-interacting subunits in the regulatory particle, we found Ubp6 to be the furthest away from the entrance to the pore, which may allow it to clip extended or unnecessary ubiquitin chains from substrates. Because Ubp6 is located closer to Rad23, Dsk2 or Ddi1 than to Rpn10 or Rpn13, it may act preferentially on substrates delivered by these shuttle receptors.

To avoid dissociation upon deubiquitination, a substrate polypeptide must be engaged with the unfolding machinery of the base before or

shortly after removal of its ubiquitin chain. Engagement by the base is known to depend on an unstructured initiation site or “tail” on the substrate<sup>40</sup>, which needs to be long enough to reach through the narrow N-ring and into the AAA+ pore (Fig. 6). In addition, this tail would have to be sufficiently spaced from the attachment point of the polyubiquitin chain to allow concurrent substrate engagement by the pore and deubiquitination by Rpn11. The distance between the predicted active site of Rpn11 and the AAA+ pore below the N-ring is approximately 60 Å, which could easily be bridged by 40–45 unstructured residues or a shorter tail combined with a folded structure.

As an alternative to the above model for simultaneous receptor binding and deubiquitination, it has been proposed that commencing substrate translocation by the base might move the proximal ubiquitin from a receptor towards Rpn11 for cleavage<sup>7</sup>. Our structure suggests for this model that efficient substrate processing would only require a mono- or diubiquitin for receptor binding and a 50–60 Å longer spacing between the ubiquitin and the flexible tail to reach the AAA+ pore. This length dependence of engagement is consistent with recent *in vitro* degradation studies, using model substrates with different lengths and ubiquitin modifications<sup>19</sup>. Future experiments will be required to assess whether substrates get deubiquitinated in a translocation-dependent or -independent manner.

## Concluding remarks

The work presented here defines the architecture of the entire proteasome regulatory particle and provides a much-needed structural framework for the mechanistic understanding of ubiquitin-dependent protein degradation. We localized Rpn11 directly above the entrance of the pore, surrounded by the ubiquitin receptors Rpn10 and Rpn13. This insight allows us to visualize the substrate's path towards degradation and will be critical in elucidating how the characteristics of ubiquitin modifications affect substrate recognition and processing. Moreover, our study significantly furthers the understanding of the heterohexameric AAA+ motor of the proteasome. Individual ATPase subunits were found in a spiral staircase arrangement and may operate with more limited dynamics than previously assumed for AAA+ protein unfoldases.

Unexpectedly, the lid is bound to the side of the holoenzyme and interacts with both the base and core particle. These interactions induce major conformational changes in lid subunits that may allosterically activate the DUB Rpn11, allowing critical removal of ubiquitin chains during substrate degradation in the holoenzyme, while preventing futile deubiquitination by the isolated lid. In addition, contacts between the subcomplexes could have unexplored roles in coordinating individual substrate processing steps, for instance ubiquitin binding, deubiquitination, and the onset of translocation. The intricate architecture of the proteasome highlights the complex requirements for this proteolytic machine, which must accommodate and specifically regulate a highly diverse set of substrates in the eukaryotic cell.

## METHODS SUMMARY

**Protein expression and purification.** Endogenous holoenzyme, core particle<sup>41</sup> and lid subcomplex<sup>42</sup> were purified from *S. cerevisiae* essentially as described. The base subcomplex was purified according to protocols for the holoenzyme preparation, but with minor modifications as described in the Methods. Details of yeast strain construction are provided in Supplementary Table 1.

Yeast lid was recombinantly expressed from three plasmids in *E. coli* BL21-star (DE3), and purified on anti-Flag M2 resin and by size-exclusion chromatography (see Methods).

**Electron microscopy and image analysis.** All electron microscopy data were collected using the Legicon data collection software<sup>43</sup> and processed in the Appion electron microscopy processing environment<sup>44</sup>. Three-dimensional maps were calculated using libraries from the EMAN2 and SPARX software packages<sup>45,46</sup>. UCSF Chimera was used for volume segmentation, atomic coordinate docking and figure generation<sup>47</sup>.

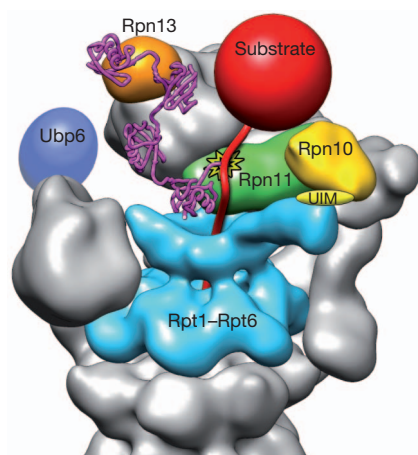


**Figure 6 | Model for the recognition, deubiquitination and engagement of a polyubiquitinated substrate by the 26S proteasome.** A K48-linked tetra-ubiquitin chain (magenta, PDB ID: 2KDE) is conjugated to the unstructured initiation region of a substrate (red) and bound to the ubiquitin receptor Rpn13 (orange). The substrate is poised for deubiquitination by Rpn11 (green, active site indicated by star), and its unstructured initiation region is engaged by the translocation machinery of the base (cyan). A polyubiquitin chain could alternatively bind to the UIM of Rpn10 (yellow) or interact with both receptors simultaneously. The DUB Ubp6 is localized further from the central pore, in a position to trim excess ubiquitin chains.



**Full Methods** and any associated references are available in the online version of the paper at [www.nature.com/nature](http://www.nature.com/nature).

**Received 25 October; accepted 12 December 2011.**

**Published online 11 January 2012.**

- Finley, D. Recognition and processing of ubiquitin-protein conjugates by the proteasome. *Annu. Rev. Biochem.* **78**, 477–513 (2009).
- Glickman, M. H., Rubin, D. M., Fried, V. A. & Finley, D. The regulatory particle of the *Saccharomyces cerevisiae* proteasome. *Mol. Cell. Biol.* **18**, 3149–3162 (1998).
- Thrower, J. S., Hoffman, L., Rechsteiner, M. & Pickart, C. M. Recognition of the polyubiquitin proteolytic signal. *EMBO J.* **19**, 94–102 (2000).
- Groll, M. *et al.* A gated channel into the proteasome core particle. *Nature Struct. Biol.* **7**, 1062–1067 (2000).
- Smith, D. M. *et al.* Docking of the proteasomal ATPases' carboxyl termini in the 20S proteasome's  $\alpha$  ring opens the gate for substrate entry. *Mol. Cell* **27**, 731–744 (2007).
- Yao, T. & Cohen, R. E. A cryptic protease couples deubiquitination and degradation by the proteasome. *Nature* **419**, 403–407 (2002).
- Verma, R. *et al.* Role of Rpn11 metalloprotease in deubiquitination and degradation by the 26S proteasome. *Science* **298**, 611–615 (2002).
- Tomko, R. J. Jr, Funakoshi, M., Schneider, K., Wang, J. & Hochstrasser, M. Heterohexameric ring arrangement of the eukaryotic proteasomal ATPases: implications for proteasome structure and assembly. *Mol. Cell* **38**, 393–403 (2010).
- Rabl, J. *et al.* Mechanism of gate opening in the 20S proteasome by the proteasomal ATPases. *Mol. Cell* **30**, 360–368 (2008).
- Gillette, T. G., Kumar, B., Thompson, D., Slaughter, C. A. & DeMartino, G. N. Differential roles of the COOH termini of AAA subunits of PA700 (19S regulator) in asymmetric assembly and activation of the 26S proteasome. *J. Biol. Chem.* **283**, 31813–31822 (2008).
- da Fonseca, P. C. & Morris, E. P. Structure of the human 26S proteasome: subunit radial displacements open the gate into the proteolytic core. *J. Biol. Chem.* **283**, 23305–23314 (2008).
- Elsasser, S. *et al.* Proteasome subunit Rpn1 binds ubiquitin-like protein domains. *Nature Cell Biol.* **4**, 725–730 (2002).
- Gomez, T. A., Kolawa, N., Gee, M., Sweredoski, M. J. & Deshaies, R. J. Identification of a functional docking site in the Rpn1 LRR domain for the UBA-UBL domain protein Ddi1. *BMC Biol.* **9**, 33 (2011).
- Leggett, D. S. *et al.* Multiple associated proteins regulate proteasome structure and function. *Mol. Cell* **10**, 495–507 (2002).
- Bohn, S. *et al.* Structure of the 26S proteasome from *Schizosaccharomyces pombe* at subnanometer resolution. *Proc. Natl Acad. Sci. USA* **107**, 20992–20997 (2010).
- Nickell, S. *et al.* Insights into the molecular architecture of the 26S proteasome. *Proc. Natl Acad. Sci. USA* **106**, 11943–11947 (2009).
- Förster, F. *et al.* An atomic model AAA-ATPase/20S core particle sub-complex of the 26S proteasome. *Biochem. Biophys. Res. Commun.* **388**, 228–233 (2009).
- Xu, P. *et al.* Quantitative proteomics reveals the function of unconventional ubiquitin chains in proteasomal degradation. *Cell* **137**, 133–145 (2009).
- Inobe, T., Fishbain, S., Prakash, S. & Matouschek, A. Defining the geometry of the two-component proteasome degron. *Nature Chem. Biol.* **7**, 161–167 (2011).
- Tian, G. *et al.* An asymmetric interface between the regulatory and core particles of the proteasome. *Nature Struct. Mol. Biol.* **18**, 1259–1267 (2011).
- Effantin, G., Rosenzweig, R., Glickman, M. H. & Steven, A. C. Electron microscopic evidence in support of  $\alpha$ -solenoid models of proteasomal subunits Rpn1 and Rpn2. *J. Mol. Biol.* **386**, 1204–1211 (2009).
- Zhang, F. *et al.* Structural insights into the regulatory particle of the proteasome from *Methanocaldococcus jannaschii*. *Mol. Cell* **34**, 473–484 (2009).
- Hamazaki, J. *et al.* A novel proteasome interacting protein recruits the deubiquitinating enzyme UCH37 to 26S proteasomes. *EMBO J.* **25**, 4524–4536 (2006).
- Schreiner, P. *et al.* Ubiquitin docking at the proteasome through a novel pleckstrin-homology domain interaction. *Nature* **453**, 548–552 (2008).
- Glickman, M. H. *et al.* A subcomplex of the proteasome regulatory particle required for ubiquitin-conjugate degradation and related to the COP9-signalosome and eIF3. *Cell* **94**, 615–623 (1998).
- Verma, R., Oania, R., Graumann, J. & Deshaies, R. J. Multiubiquitin chain receptors define a layer of substrate selectivity in the ubiquitin-proteasome system. *Cell* **118**, 99–110 (2004).
- Glynn, S. E., Martin, A., Nager, A. R., Baker, T. A. & Sauer, R. T. Structures of asymmetric ClpX hexamers reveal nucleotide-dependent motions in a AAA+ protein-unfolding machine. *Cell* **139**, 744–756 (2009).
- Maillard, R. A. *et al.* ClpX(P) generates mechanical force to unfold and translocate its protein substrates. *Cell* **145**, 459–469 (2011).
- Aubin-Tam, M. E., Olivares, A. O., Sauer, R. T., Baker, T. A. & Lang, M. J. Single-molecule protein unfolding and translocation by an ATP-fueled proteolytic machine. *Cell* **145**, 257–267 (2011).
- Martin, A., Baker, T. A. & Sauer, R. T. Rebuilt AAA+ motors reveal operating principles for ATP-fueled machines. *Nature* **437**, 1115–1120 (2005).
- Hersch, G. L., Burton, R. E., Bolon, D. N., Baker, T. A. & Sauer, R. T. Asymmetric interactions of ATP with the AAA+ ClpX6 unfoldase: allosteric control of a protein machine. *Cell* **121**, 1017–1027 (2005).
- Thomsen, N. D. & Berger, J. M. Running in reverse: the structural basis for translocation polarity in hexameric helicases. *Cell* **139**, 523–534 (2009).
- Enemark, E. J. & Joshua-Tor, L. Mechanism of DNA translocation in a replicative hexameric helicase. *Nature* **442**, 270–275 (2006).
- Riedinger, C. *et al.* Structure of Rpn10 and its interactions with polyubiquitin chains and the proteasome subunit Rpn12. *J. Biol. Chem.* **285**, 33992–34003 (2010).
- Eddins, M. J., Varadan, R., Fushman, D., Pickart, C. M. & Wolberger, C. Crystal structure and solution NMR studies of Lys48-linked tetraubiquitin at neutral pH. *J. Mol. Biol.* **367**, 204–211 (2007).
- Cook, W. J., Jeffrey, L. C., Carson, M., Chen, Z. & Pickart, C. M. Structure of a diubiquitin conjugate and a model for interaction with ubiquitin conjugating enzyme (E2). *J. Biol. Chem.* **267**, 16467–16471 (1992).
- Bremm, A., Freund, S. M. & Komander, D. Lys11-linked ubiquitin chains adopt compact conformations and are preferentially hydrolyzed by the deubiquitinase Cezanne. *Nature Struct. Mol. Biol.* **17**, 939–947 (2010).
- Husnjak, K. *et al.* Proteasome subunit Rpn13 is a novel ubiquitin receptor. *Nature* **453**, 481–488 (2008).
- Hanna, J. *et al.* Deubiquitinating enzyme Ubp6 functions noncatalytically to delay proteasomal degradation. *Cell* **127**, 99–111 (2006).
- Prakash, S., Tian, L., Ratliff, K. S., Lehotzky, R. E. & Matouschek, A. An unstructured initiation site is required for efficient proteasome-mediated degradation. *Nature Struct. Mol. Biol.* **11**, 830–837 (2004).
- Verma, R. *et al.* Proteasomal proteomics: identification of nucleotide-sensitive proteasome-interacting proteins by mass spectrometric analysis of affinity-purified proteasomes. *Mol. Biol. Cell* **11**, 3425–3439 (2000).
- Leggett, D. S., Glickman, M. H. & Finley, D. Purification of proteasomes, proteasome subcomplexes, and proteasome-associated proteins from budding yeast. *Methods Mol. Biol.* **301**, 57–70 (2005).
- Suloway, C. *et al.* Automated molecular microscopy: the new Leginon system. *J. Struct. Biol.* **151**, 41–60 (2005).
- Lander, G. C. *et al.* Appion: an integrated, database-driven pipeline to facilitate EM image processing. *J. Struct. Biol.* **166**, 95–102 (2009).
- Tang, G. *et al.* EMAN2: an extensible image processing suite for electron microscopy. *J. Struct. Biol.* **157**, 38–46 (2007).
- Hohn, M. *et al.* SPARX, a new environment for Cryo-EM image processing. *J. Struct. Biol.* **157**, 47–55 (2007).
- Goddard, T. D., Huang, C. C. & Ferrin, T. E. Visualizing density maps with UCSF Chimera. *J. Struct. Biol.* **157**, 281–287 (2007).

**Acknowledgements** We thank the members of the Martin and Nogales labs for helpful discussions, and G. Cardone for help with local resolution calculations. G.C.L. acknowledges support from Damon Runyon Cancer Research Foundation, M.E.M. acknowledges support by the American Cancer Society grant 121453-PF-11-178-01-TBE, C.B. acknowledges support from the NSF Graduate Research Fellowship. This research was funded in part by the Searle Scholars Program (A.M.), start-up funds from the UC Berkeley MCB Department (A.M.), the NIH grant R01-GM094497-01A1 (A.M.), the Lawrence Berkeley National Laboratory (G.C.L.), and the Howard Hughes Medical Institute (E.N.). Some of the work presented here was conducted at the National Resource for Automated Molecular Microscopy, which is supported by the NIH through the NCRP P41 program (RR017573).

**Author contributions** E.E., M.E.M. and C.B. designed, expressed and purified proteasome constructs, and performed biochemical experiments. G.C.L. performed the electron microscopy, processing and segmentation analysis. All authors contributed to experimental design, data analysis and manuscript preparation.

**Author information** The cryoelectron microscopy density map for the 26S proteasome can be found at the Electron Microscopy Data Bank under accession number EMD-1992. The negative stain reconstructions of the recombinantly expressed and yeast-purified lid have been assigned accession numbers EMD-1993 and EMD-1994, respectively. Reprints and permissions information is available at [www.nature.com/reprints](http://www.nature.com/reprints). The authors declare no competing financial interests. Correspondence and requests for materials should be addressed to A.M. ([a.martin@berkeley.edu](mailto:a.martin@berkeley.edu)).

## METHODS

**Recombinant lid construction and purification.** Yeast Rpn5, Rpn6, Rpn8, Rpn9 and Rpn11–6×His were cloned into pETDuet-1 (Novagen), yeast Rpn3, Flag–Rpn7 and Rpn12 were cloned into pCOLADuet-1 (Novagen), and yeast Sem1 and Hsp90 were cloned into pACYCDuet-1 (Novagen). A T7 promoter preceded each gene and each plasmid contained a T7 terminator following the multiple cloning site. Genes for select rare transfer RNAs were included in the pACYCDuet-1 plasmid to account for codon-usage differences between yeast and *E. coli*. To ensure full-length of Rpn6 in lid particles used for biochemical experiments and the negative stain reconstruction of recombinant lid, we used a construct with the Flag tag moved from Rpn7 to Rpn6. *E. coli* BL21-star (DE3) cells were co-transformed with the three plasmids mentioned above. Lid proteins and the chaperone Hsp90 were coexpressed overnight at 18 °C after inducing cells with 0.5 mM isopropyl-β-D-thiogalactopyranoside at  $D_{600} = 0.7$ . Cells were collected by centrifugation (4,000g for 30 min), resuspended in Flag buffer (50 mM HEPES, pH 7.6, 100 mM NaCl, 100 mM KCl and 5% glycerol) supplemented with protease inhibitors and 2 mg ml<sup>-1</sup> lysozyme, and sonicated on ice for 2 min in 15-s bursts. The lysate was clarified by centrifugation (27,000g for 30 min), and the complex was affinity-purified on anti-Flag M2 resin (Sigma-Aldrich) using an N-terminal Flag-tag on Rpn6 or Rpn7. The protein was concentrated in a 30,000 MWCO concentrator (Amicon) for further purification on a Superose 6 size-exclusion column (GE Healthcare) equilibrated in Flag buffer. Intact, assembled lid particles eluted at 13.1 ml, similar to lid purified from yeast.

His<sub>6</sub>-tagged yeast Rpn10 was expressed in *E. coli* and purified by Ni-NTA affinity and size-exclusion chromatography.

**Yeast strain construction.** Wild-type holoenzyme was purified from the strain YYS40 (*MATa ade2-1 his3-11,15 leu2-3,112 trp1-1 ura3-1 can1 RPN11::RPN11-3XFLAG (HIS3)*)<sup>48</sup>. To generate *RPN10*, *RPN13* and *UBP6* deletion strains, the kanMX6 sequence was integrated at the respective genomic locus, replacing the gene in YYS40. To generate the strains used to purify GST–Rpn2, GFP–Rpn5 and GFP–Rpn8 holoenzyme, sequences encoding the respective tags under the control of the  $P_{GAL1}$  promoter were integrated 5' of the respective genes in YYS40. To generate the strain used to purify Rpn1–Flag holoenzyme, a sequence encoding the Flag-tag was integrated 3' to *RPN1* in a W303 background strain (*MATa ade2-1 his3-11 leu2-3,112 trp1-1 ura3-1 can1-100 bar1*).

To generate the strains used to purify α2 mutant-containing core particle for the crosslinking experiments shown in Supplementary Fig. 11, pRS305 (*LEU2*) containing the mutant α2 and the genomic sequences found 500 nucleotides upstream and 100 nucleotides downstream of the gene was integrated at the *LEU2* locus of RJD1144 (*MATa, his3Δ200 leu2-3,112 lys2-801 trpΔ63 ura3-52 PRE1-FLAG-6xHIS::Ylplac211 (URA3)*)<sup>41</sup>, and the chromosomal copy of α2 was deleted. To generate the strain used to purify lid with Rpn6 tagged with three haemagglutinin (HA) for crosslinking, the 3×HA sequence was integrated 3' of *RPN6* in YYS40.

**Expression and purification of yeast holoenzyme and subcomplexes.** Endogenous holoenzyme, core particle<sup>41</sup> and lid subcomplex<sup>42</sup> were purified from *S. cerevisiae* essentially as described. Frozen yeast cells were lysed in a Spex SamplePrep 6870 Freezer/Mill. For holoenzyme purification, lysed cells of a strain containing a Flag-tag on Rpn11 were resuspended in lysis buffer containing 60 mM HEPES pH 7.6, 50 mM NaCl, 50 mM KCl, 5 mM MgCl<sub>2</sub>, 0.5 mM EDTA, 10% glycerol, 0.2% NP-40, and ATP regeneration mix (5 mM ATP, 0.03 mg ml<sup>-1</sup> creatine kinase, 16 mM creatine phosphate). Holoenzyme was bound to anti-Flag M2 resin and washed with wash buffer (60 mM HEPES pH 7.6, 50 mM NaCl, 50 mM KCl, 5 mM MgCl<sub>2</sub>, 0.5 mM EDTA, 10% glycerol, 0.1% NP-40 and 500 μM ATP) before elution with 3×Flag peptide and separation over Superose-6 in gel-filtration buffer (60 mM HEPES pH 7.6, 50 mM NaCl, 50 mM KCl, 5 mM MgCl<sub>2</sub>, 0.5 mM EDTA, 10% glycerol and 500 μM ATP). Lid, base or core particle were purified similarly but from different yeast strains and including a salt wash to separate subcomplexes. Lid was purified from a yeast strain containing Rpn11–Flag using a 900 mM NaCl wash. Base was purified from a yeast strain containing a C-terminal Flag tag on Rpn2 and including a 500 mM NaCl wash, with 500 μM ATP present throughout the purification. Core particle was purified from a yeast strain containing a Flag–6×His tag on Pre1 and including a 500 mM NaCl wash. All subcomplexes were further purified by size-exclusion chromatography on Superose-6 in gel filtration buffer (see above).

**GFP degradation assay.** Proteasome holoenzyme was reconstituted from 20S core, base, Rpn10 and recombinant or endogenous yeast lid in the presence of ATP. A GFP–titin–cyclin fusion protein was modified with a K48-linked polyubiquitin chain<sup>49</sup> and degraded by reconstituted proteasome at 30 °C in Flag buffer with an ATP-regeneration system (5 mM ATP, 16 mM creatine phosphate, 6 μg ml<sup>-1</sup> creatine phosphokinase). Degradation was monitored by the loss of fluorescence using a QuantaMaster spectrofluorimeter (PTI).

**Protein crosslinking.** Sulfo-MBS (Thermo Scientific) is a short (7.3 Å), heterobifunctional crosslinker, whose maleimide moiety reacts primarily with sulphhydryls between pH 6.5 and 7.5, and whose NHS ester reacts with primary amines between pH 7 and 9. We purified core particle from yeast strains in which the only copy of the core α2 subunit was either wild type, a D245C mutant, or an A249C mutant. Other intrinsic cysteines of the core were found largely non-reactive towards sulphhydryl-modifying agents (not shown). 10 μM reduced core particle purified from strains containing wild type, A249C and D245C α2 was incubated with 150 μM sulphy-MBS for 15 min at pH 6.5, allowing conjugation of the crosslinker to cysteines. Core particle was buffer-exchanged to remove excess crosslinker and increase the pH to 7.5, activating the amine-reactive functional group on sulphy-MBS. This core particle was added at a final concentration of 2 μM to a proteasome reconstitution mixture, containing 2 μM purified base, 10 μM purified Rpn10, 0.5 mM ATP, and 2 μM lid purified from a yeast strain in which Rpn6 was C-terminally tagged with a 3×HA tag. Crosslinking was allowed to proceed for 15 min before reactions were stopped by the addition of 0.5 mM glycine pH 7.5 and divided equally for separation by SDS–PAGE, followed by either Coomassie staining or anti-HA western blotting.

**Electron microscopy.** Sample preparation: negative-stain analysis of both the purified proteasome lid and holoenzyme complexes was performed using 400 mesh continuous carbon grids that had been plasma-cleaned in a 75% argon/25% oxygen atmosphere for 20 s using a Solarus plasma cleaner (Gatan). Due to the tendency for holoenzyme to adopt a preferential orientation on the carbon substrate, 5 μl of 0.1% poly L-lysine hydrobromide (Polysciences catalogue no. 09730) was placed onto the hydrophilized carbon grids and adsorbed for 90 s, washed twice with 5 μl drops of water, and allowed to dry completely. This polylysine step was skipped when preparing grids containing the lid samples, as the lid does not adopt a preferred orientation on the carbon substrate. The remaining steps were identical for both holoenzyme and lid. A 4-μl drop of sample at a concentration of 25 μM was placed onto the grid and allowed to adsorb for 1 min. The grid was blotted to near-dryness and a 4-μl drop of fresh 2% (w/v) uranyl formate was quickly placed onto the grid. To reduce the amount of glycerol remaining on the grids, they were subsequently floated on four successive 25-μl drops of the uranyl formate solution, waiting 10 s on each drop. The grids were then blotted to dryness.

Preservation of both lid and holoenzyme complexes in vitreous ice was performed in the same manner. 400-mesh C-flats containing 2 μm holes with a spacing of 2 μm (Protochips) were plasma cleaned in a 75% argon/25% oxygen atmosphere for 8 s using a Solarus plasma cleaner (Gatan). The purified sample, at a concentration of 5 μM in a buffer containing 5% glycerol, was first diluted 1:5 from 60 mM HEPES, pH 7.6, 50 mM NaCl, 50 mM KCl, 5 mM MgCl<sub>2</sub>, 0.5 mM EDTA, 10% glycerol, 1 mM DTT, 0.5 mM ATP into a buffer containing 20 mM HEPES, pH 7.6, 50 mM NaCl, 50 mM KCl, 1 mM ATP, 1 mM DTT and 0.05% NP40, and 4-μl aliquots were placed onto the grids. Grids were immediately loaded into a Vitrobot (FEI company) whose climate chamber had equilibrated to 4 °C and 100% humidity. The grids were blotted for 3 s at an offset of –1 mm, and plunged into liquid ethane. The frozen grids were transferred to a grid box and stored in liquid nitrogen until retrieved for data collection.

Data collection: negative-stain analysis of the lid and holoenzyme samples was performed using a Tecnai T12 Bio-TWIN and a Tecnai F20 TWIN transmission electron microscope operating at 120 keV. Lid samples were imaged at a nominal magnification of ×68,000 (1.57 Å per pixel at the specimen level) on the T12, and ×80,000 (1.45 Å per pixel) on the F20. Holoenzyme samples were imaged at a magnification of ×49,000 (2.18 Å per pixel) on the T12, and ×50,000 (2.16 Å per pixel) on the F20. T12 data were acquired on a F416 CMOS 4Kx4K camera (TVIPS), F20 data were acquired on a Gatan 4Kx4K camera, and all micrographs were collected using an electron dose of 20 e<sup>-</sup> Å<sup>-2</sup> with a randomly set focus ranging from –0.5 to –1.2 μm. The automatic rastering application of the Legicon data collection software was used for data acquisition. Between 300 and 500 micrographs were collected for each of the negatively stained data sets.

For cryoelectron microscopy, individual grids were loaded into a 626 single-tilt cryotransfer system (Gatan) and inserted into a Tecnai F20 TWIN transmission electron microscope operating at 120 keV. Data were acquired at a nominal magnification of ×100,000 (1.08 Å per pixel) using an electron dose of 20 e<sup>-</sup> Å<sup>-2</sup> with a randomly set focus ranging from –1.2 to –2.5 μm. A total of 9,153 micrographs were collected of the holoenzyme using the MSI-T application of the Legicon software. While the holoenzyme was remained intact during the freezing process, the isolated lid specimen became completely disassembled during the freezing process. In an attempt to overcome this, the isolated lid was also frozen using grids onto which a thin carbon film was floated. Due to the elevated background noise from the addition of a carbon substrate, the resulting images lacked the sufficient signal-to-noise ratio necessary to solve a cryoelectron

microscopy structure of the isolated lid to a better resolution than the negative-stain structure.

**Image processing of negative-stain data.** All image pre-processing and two-dimensional classification was performed in the Appion image processing environment<sup>44</sup>. Due to the large number of data sets acquired for both the negatively stained lid and holoenzyme complexes, a generalized schema was used for image analysis. This schema also minimized user bias during comparison of tagged and deletion constructs with their wild-type counterparts. The contrast transfer function (CTF) of each micrograph was estimated concurrently with data collection using the ACE2 and CTFFind programs<sup>50,51</sup>, providing a quantitative measurement of the imaging quality. Particle selection was also performed automatically concurrent with data collection. Negatively stained lid particles were selected from the micrographs using a difference of Gaussians (DoG) transform-based automated picker<sup>52</sup>, and holoenzyme particles were selected using a template-based particle picker. Micrograph phases were corrected using ACE2, and both lid and holoenzyme particles were extracted using a  $288 \times 288$ -pixel box size. The data were then binned by a factor of two for processing. Each particle was normalized to remove pixels whose values were above or below  $4.5 \sigma$  of the mean pixel value using the XMIPP normalization program<sup>53</sup>.

To remove aggregation, contamination or other non-particle selections, particle stacks were decimated by a factor of 2 and subjected to five rounds of iterative multivariate statistical analysis (MSA) and multi-reference alignment (MRA) using the IMAGIC software package<sup>54</sup>. Two-dimensional class averages depicting properly assembled complexes were manually selected, and the non-decimated particles contributing to these class averages were extracted to create a new stack for further processing. To include a larger range of holoenzyme views, particles contributing to doubly capped proteasome averages were removed. This stack of particles went through five rounds of MSA/MRA in IMAGIC<sup>54</sup>, and a final correspondence analysis and classification based on Eigen images using the SPIDER software package<sup>55</sup> was performed to generate two-dimensional class averages of the complexes.

Initial models for reconstructions of both the holoenzyme and lid were determined using the established “C1 startup” routines in IMAGIC. Two-dimensional class averages were manually inspected to select three images representing orthogonal views of the complex, which were in turn used to assign Eulers in a stepwise fashion to the entire data set of reference-free class averages. The resulting low-resolution models of the lid and holoenzyme were low-pass filtered to 60-Å resolution, and these densities were used as starting points for refinement of the three-dimensional structure.

Three-dimensional reconstructions were all performed using an iterative projection-matching and back-projection approach using libraries from the EMAN2 and SPARX software packages<sup>45,46</sup>. Refinement of the starting models began using an angular increment of  $25^\circ$ , progressing down to  $2^\circ$  for the lid, and  $1^\circ$  for the holoenzyme. The refinement only continued to the subsequent angular increment once greater than 95% of the particles showed a pixel error of less than 1 pixel. The resolution was estimated by splitting the particle stack into two equally sized data sets, calculating the Fourier shell correlation (FSC) between the resulting back-projected volumes. The estimated resolutions for the final endogenous and recombinant lid structures based on their FSC curves at 0.5 were about 15 Å.

**Image processing of cryoelectron microscopy holoenzyme.** Processing of the holoenzyme cryo data set proceeded in a very similar fashion to that of the negatively stained particle data sets. Only ACE2 was used to estimate CTF of the images and measure image quality, and particles were extracted using a box size of 576 pixels. Reference-free two-dimensional classification was performed to remove particles that did not contribute to averages depicting a doubly capped proteasome. Three rounds of reference-free two-dimensional classification, and particles were removed after each round. From an initial data set of 312,483 automatically selected particles, 93,679 were kept for the three-dimensional reconstruction. C2 symmetry was applied to one of the previously determined asymmetric negative-stained reconstructions to serve as a starting model for structure refinement. The reconstruction began using an angular increment of  $25^\circ$ , and iterated down to  $0.6^\circ$ . C2 symmetry was imposed during the reconstruction. Low-resolution Fourier amplitudes of the final map were dampened to match those of an experimental GroEL SAXS curve using the SPIDER software package<sup>55</sup>.

The estimated resolution based on the FSC of the half-volumes at 0.5 was approximately 9 Å, although a local resolution calculation using the “bloccres” function in the Bsoft package<sup>56</sup> indicated a range of resolutions within the density. The majority of the core particle subunits and the AAA + ATPases were resolved to between 7- and 8-Å resolution, whereas the non-ATPase subunits in the regulatory particle ranged from 8- to 12-Å resolution (Supplementary Fig. 7). Notably, Rpn1 and the ubiquitin receptors Rpn10 and Rpn13 were the lowest resolution features of the holoenzyme. To filter the low-resolution portions of the map properly, without destroying the details of the better-ordered features, a resolution-driven adaptive localized low-pass filter was applied to the final volume (G. Cardone, personal communication).

The segmentation analysis was manually performed using the “Volume Tracer” tool in the UCSF Chimera visualization software<sup>47</sup>. This software was additionally used to perform all rigid-body fitting of crystal structures into the holoenzyme cryoelectron microscopy density, as well as to generate all renderings for figure images.

48. Sone, T., Saeki, Y., Toh-e, A. & Yokosawa, H. Sem1p is a novel subunit of the 26 S proteasome from *Saccharomyces cerevisiae*. *J. Biol. Chem.* **279**, 28807–28816 (2004).
49. Kim, H. C. & Huibregtse, J. M. Polyubiquitination by HECT E3s and the determinants of chain type specificity. *Mol. Cell. Biol.* **29**, 3307–3318 (2009).
50. Mallick, S. P., Carragher, B., Potter, C. S. & Kriegman, D. J. ACE: automated CTF estimation. *Ultramicroscopy* **104**, 8–29 (2005).
51. Mindell, J. A. & Grigorieff, N. Accurate determination of local defocus and specimen tilt in electron microscopy. *J. Struct. Biol.* **142**, 334–347 (2003).
52. Voss, N. R., Yoshioka, C. K., Radermacher, M., Potter, C. S. & Carragher, B. DoG Picker and TiltPicker: software tools to facilitate particle selection in single particle electron microscopy. *J. Struct. Biol.* **166**, 205–213 (2009).
53. Sorzano, C. O. et al. XMIPP: a new generation of an open-source image processing package for electron microscopy. *J. Struct. Biol.* **148**, 194–204 (2004).
54. van Heel, M., Harauz, G., Orlova, E. V., Schmidt, R. & Schatz, M. A new generation of the IMAGIC image processing system. *J. Struct. Biol.* **116**, 17–24 (1996).
55. Frank, J. et al. SPIDER and WEB: processing and visualization of images in 3D electron microscopy and related fields. *J. Struct. Biol.* **116**, 190–199 (1996).
56. Heymann, J. B. & Belnap, D. M. Bsoft: image processing and molecular modeling for electron microscopy. *J. Struct. Biol.* **157**, 3–18 (2007).



# A PGC1- $\alpha$ -dependent myokine that drives brown-fat-like development of white fat and thermogenesis

Pontus Boström<sup>1</sup>, Jun Wu<sup>1</sup>, Mark P. Jedrychowski<sup>2</sup>, Anisha Korde<sup>1</sup>, Li Ye<sup>1</sup>, James C. Lo<sup>1</sup>, Kyle A. Rasbach<sup>1</sup>, Elisabeth Almer Boström<sup>3</sup>, Jang Hyun Choi<sup>1</sup>, Jonathan Z. Long<sup>1</sup>, Shingo Kajimura<sup>4</sup>, Maria Cristina Zingaretti<sup>5</sup>, Birgitte F. Vind<sup>6</sup>, Hua Tu<sup>7</sup>, Saverio Cinti<sup>5</sup>, Kurt Højlund<sup>6</sup>, Steven P. Gygi<sup>2</sup> & Bruce M. Spiegelman<sup>1</sup>

Exercise benefits a variety of organ systems in mammals, and some of the best-recognized effects of exercise on muscle are mediated by the transcriptional co-activator PPAR- $\gamma$  co-activator-1  $\alpha$  (PGC1- $\alpha$ ). Here we show in mouse that PGC1- $\alpha$  expression in muscle stimulates an increase in expression of FNDC5, a membrane protein that is cleaved and secreted as a newly identified hormone, irisin. Irisin acts on white adipose cells in culture and *in vivo* to stimulate UCP1 expression and a broad program of brown-fat-like development. Irisin is induced with exercise in mice and humans, and mildly increased irisin levels in the blood cause an increase in energy expenditure in mice with no changes in movement or food intake. This results in improvements in obesity and glucose homeostasis. Irisin could be therapeutic for human metabolic disease and other disorders that are improved with exercise.

PGC1- $\alpha$  is a transcriptional co-activator that mediates many biological programs related to energy metabolism. Originally described as a co-activator of PPAR- $\gamma$  that modulated expression of uncoupling protein 1 (UCP1) and thermogenesis in brown fat<sup>1</sup>, it has also been shown to control mitochondrial biogenesis and oxidative metabolism in many cell types. PGC1- $\alpha$  is induced in muscle by exercise and stimulates many of the best-known beneficial effects of exercise in muscle: mitochondrial biogenesis, angiogenesis and fibre-type switching<sup>2</sup>. It also provides resistance to muscular dystrophy and denervation-linked muscular atrophy<sup>3</sup>. The health benefits of elevated muscle expression of PGC1- $\alpha$  may go beyond the muscle tissue itself. Transgenic mice with mildly elevated muscle PGC1- $\alpha$  are resistant to age-related obesity and diabetes and have a prolonged lifespan<sup>4</sup>. This suggests that PGC1- $\alpha$  stimulates the secretion of factors from skeletal muscle that affect the function of other tissues. Here we show that PGC1- $\alpha$  stimulates the expression of several muscle gene products that are potentially secreted, including FNDC5. The *Fndc5* gene encodes a type I membrane protein that is processed proteolytically to form a newly identified hormone secreted into the blood, termed irisin. Irisin is induced in exercise and activates profound changes in the subcutaneous adipose tissue, stimulating browning and UCP1 expression. Importantly, this causes a significant increase in total body energy expenditure and resistance to obesity-linked insulin resistance. Thus, irisin action recapitulates some of the most important benefits of exercise and muscle activity.

## Muscle PGC1- $\alpha$ transgenics

Mice with transgenically increased PGC1- $\alpha$  in muscle are resistant to age-related obesity and diabetes<sup>4</sup>, suggesting that these animals have a fundamental alteration in systemic energy balance. We therefore analysed the adipose tissue of the PGC1- $\alpha$  transgenic mice for expression of genes related to a thermogenic gene program and genes characteristic

of brown fat development. There were no significant alterations in the expression of brown-fat-selective genes in the interscapular brown adipose tissue or in the visceral (epididymal) white adipose tissue (Fig. 1a). However, the subcutaneous fat layer (inguinal), a white adipose tissue that is particularly prone to 'browning' (that is, formation of multilocular, UCP1-positive adipocytes), had significantly increased levels of *Ucp1* and *Cidea* messenger RNAs (Fig. 1b). We also observed increased UCP1 protein levels and more UCP1-positive stained multilocular cells in transgenic mice compared to controls (Fig. 1c, d). There are recent reports that exercise causes a mild increase in the expression of a thermogenic gene program in the visceral adipose tissue, a depot that has minimal expression of these genes<sup>5</sup>. As it is the subcutaneous white adipose depot that has the greatest tendency to turn on a thermogenic gene program and alter the systemic energy balance of mice<sup>6</sup>, we re-investigated this with regard to browning of the white adipose tissues in two types of exercise. Similar to what has been reported<sup>5</sup>, a twofold increase in *Ucp1* mRNA expression was observed in the visceral, epididymal fat with 3 weeks of wheel running (Supplementary Fig. 1). However, a much larger change (approximately 25 fold) was seen in the same mice in the subcutaneous inguinal fat depot. Similarly, a small increase in *Ucp1* mRNA expression was seen in the epididymal fat with repeated bouts of swimming in warm (32 °C) water (Supplementary Fig. 1); however a very large increase (65 fold) was observed in the inguinal white depot (Supplementary Fig. 1). Thus, muscle-specific expression of PGC1- $\alpha$  drives browning of subcutaneous white adipose tissue, possibly recapitulating part of the exercise program.

## Media from PGC1- $\alpha$ -expressing myocytes

The effect on browning of the adipose tissues from PGC1- $\alpha$ -expressing muscle could be due to direct muscle-fat signalling or to another,

<sup>1</sup>Dana-Farber Cancer Institute and Harvard Medical School, 3 Blackfan Circle, CLS Building, Floor 11, Boston, Massachusetts 02115, USA. <sup>2</sup>Department of Cell Biology, Harvard Medical School, Boston, Massachusetts 02115, USA. <sup>3</sup>Renal Division, Brigham and Women's Hospital, Harvard Medical School, Boston, Massachusetts 02115, USA. <sup>4</sup>UCSF Diabetes Center and Department of Cell and Tissue Biology, University of California, San Francisco, California 94143, USA. <sup>5</sup>Department of Experimental and Clinical Medicine, Università Politecnica delle Marche, Electron Microscopy Unit-Azienda Ospedali Riuniti, Ancona 60020, Italy. <sup>6</sup>Diabetes Research Center, Department of Endocrinology, Odense University Hospital, DK-5000, Odense, Denmark. <sup>7</sup>LakePharma, Inc., 530 Harbor Blvd, Belmont, California 94002, USA.

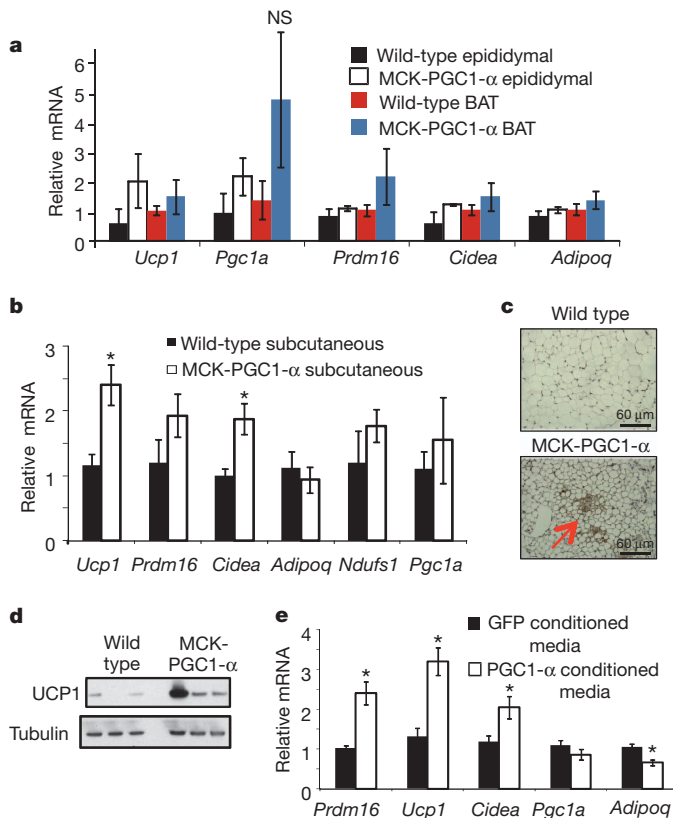


**Figure 1 | Muscle-specific PGC1- $\alpha$  transgenic mice have increased brown/beige fat cells in the subcutaneous depot.** **a**, **b**, Quantitative polymerase chain reaction (qPCR) against brown fat and thermogenic genes in epididymal fat, BAT (**a**) and subcutaneous, inguinal (**b**) fat depots in muscle creatine kinase promoter (MCK)-PGC1- $\alpha$  transgenic mice or littermate controls.  $n = 7$  for each group, repeated in a separate cohort with similar results. **c**, Representative immunohistochemistry against UCP1 in the inguinal depot from indicated mice. **d**, Western blot against UCP1 in the inguinal fat depot ( $n = 3$  and repeated in an independent cohort with similar results). **e**, qPCR against indicated genes in adipocytes differentiated for 6 days from stroma vascular fraction (SVF) cells. This was done in the presence of conditioned media from primary myocytes with forced expression of GFP or PGC1- $\alpha$  (representative for three independent experiments). Data are presented as mean  $\pm$  s.e.m., and  $*P < 0.05$  compared to control group. Student's  $t$ -test was used for single comparisons. NS, not significant.

indirect mechanism. To investigate this, we treated cultured primary subcutaneous adipocytes with serum-free media conditioned by myocytes expressing PGC1- $\alpha$  or cells expressing green fluorescent protein (GFP). As shown in Fig. 1e, the media from cells expressing ectopic PGC1- $\alpha$  increased the mRNA levels of several brown-fat-specific genes (Fig. 1e). This suggested that PGC1- $\alpha$  causes the muscle cells to secrete a molecule(s) that can induce a thermogenic gene program in the cells.

### Candidate, secreted PGC1- $\alpha$ -dependent proteins

We used a combination of Affymetrix-based gene expression arrays and an algorithm that predicts protein secretion to search for proteins that could mediate the browning of adipose tissues under the control of muscle PGC1- $\alpha$  (Methods). Proteins with mitochondrial targeting sequences were excluded, and all candidates were validated in gain-of-function systems for PGC1- $\alpha$  *in vivo* (Methods). Five proteins were identified as PGC1- $\alpha$  target genes in muscle and as likely to be secreted: IL-15, FNDC5, VEGF- $\beta$ , LRG1 and TIMP4 (Fig. 2a). Conversely, expression of these genes was reduced in mice with muscle-specific deletion of PGC1- $\alpha$  (Supplementary Fig. 2). Furthermore, they were also found to be increased at the mRNA level in muscle from exercised mice (Fig. 2b). The expression of this same set of genes was also examined in muscle biopsies from human subjects before and after

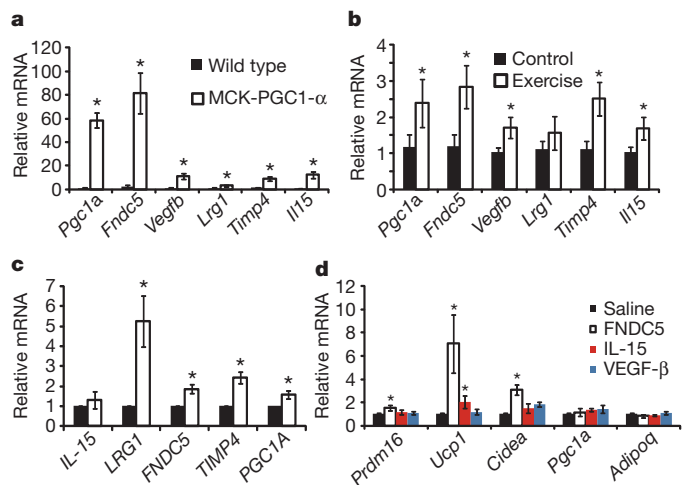


**Figure 2 | FNDC5 is induced with forced PGC1- $\alpha$  expression or exercise, and turns on brown/beige fat gene expression.** **a**, qPCR against indicated genes in skeletal muscle from MCK-PGC1- $\alpha$  transgenic mice or littermate controls ( $n = 7$  from each group). **b**, qPCR against indicated genes in skeletal muscle from sedentary mice or mice given 3 weeks of free wheel running ( $n = 10$  from each group). Mice were rested for 12 h before being killed. **c**, mRNA expression levels from human muscle biopsies before and after 10 weeks of endurance exercise training (8 subjects included). All data points are normalized to baseline levels. **d**, SVF from the inguinal fat depot, differentiated into adipocytes for 6 days in the presence of saline or recombinant FNDC5 (20 nM), IL-15 (10  $\mu$ M) or VEGF- $\beta$  (50  $\mu$ M). The graph shows normalized mRNA levels of indicated genes. This experiment was repeated three times with similar results. For **d**, we performed one-way ANOVA tests where  $*P < 0.05$  for the effect of FNDC5 on *Ucp1* and *Cidea* expression. All other statistics were performed using Student's  $t$ -test, and bar graphs are mean  $\pm$  s.e.m.

a controlled period of endurance exercise<sup>7</sup> (Fig. 2c). *FNDC5*, *VEGFB* and *TIMP4* mRNAs were all significantly induced in humans with exercise. IL-15 has previously been reported as being secreted from muscle under the influence of exercise<sup>8</sup>, while the regulation of *FNDC5*, *VEGF- $\beta$* , *LRG1* and *TIMP4* by exercise has not been described. *FNDC5* mRNA and brown fat markers in subcutaneous fat were not regulated by acute exercise, and *FNDC5* mRNA was not induced by exposure to cold (4 °C) for 6 h (Supplementary Fig. 2).

### Fndc5 induces a browning in vitro

Several of the proteins encoded by these genes were commercially available, so they were applied directly to primary subcutaneous white adipocytes during differentiation. Factors such as IL-15 or VEGF- $\beta$  had minimal effects on the expression of *Ucp1* and other brown fat genes at concentrations of 200 nM or higher. However, FNDC5 promoted a sevenfold induction of *Ucp1* mRNA at a concentration of 20 nM (Fig. 2d). The transcriptional changes induced by FNDC5 were addressed on a global scale using gene expression arrays (Supplementary Fig. 3). Notably, *Ucp1* and three other known brown fat genes, *Elovl3*, *Cox7a1* and *Otop1*, were among the eight most upregulated genes (Supplementary Fig. 4). Conversely, genes characteristic of white fat development were downregulated, such as leptin (Supplementary Fig. 3). These data indicate that the activation of browning and thermogenic genes by FNDC5 is a major part of the action of this polypeptide on these cells.

The effects of FNDC5 treatment were remarkably robust; *Ucp1* mRNA was increased 7–500 fold in more than ten experiments using FNDC5 at a concentration of 20 nM (Fig. 3a and Supplementary Fig. 5). Moreover, we could demonstrate a clear dose-dependence, with an effective range between 20–200 ng ml<sup>-1</sup> (1.5–15 nM) (Fig. 3b). In contrast, BMP7, reported as a potent inducer of browning<sup>9</sup>, had a much smaller effect (maximum of twofold) on the same cells at 3.3  $\mu$ M (Fig. 3a).

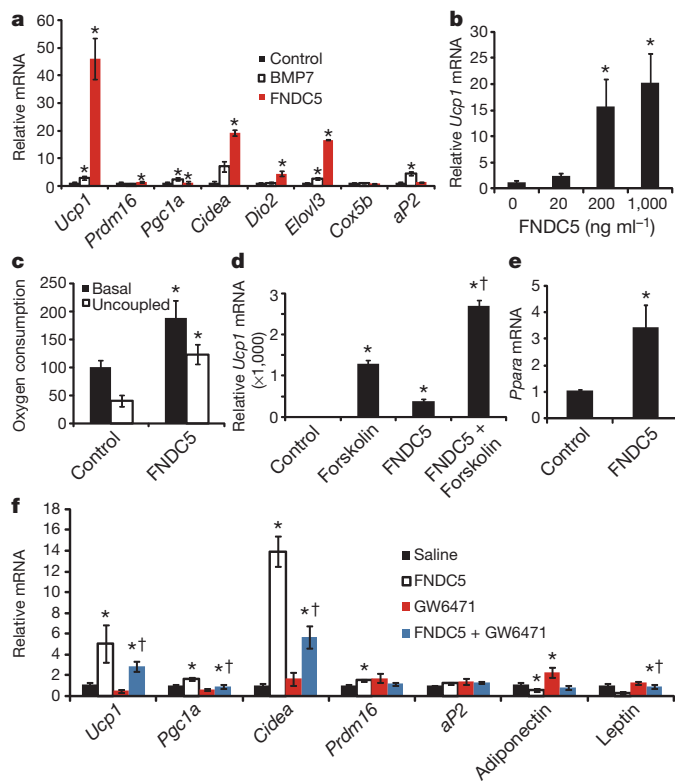


**Figure 3 | FNDC5 is a potent inducer of the brown/beige fat gene program**  
**a**, SVF from the inguinal fat depot was differentiated into adipocytes for 6 days in the presence of saline, recombinant FNDC5 (20 nM) or BMP7 (3.3  $\mu$ M). The graph shows normalized mRNA levels for indicated genes. Similar results were obtained in more than 10 experiments with the fold induction of *Ucp1* between 7–500 fold. **b**, mRNA levels of *Ucp1* from inguinal-derived SVF treated with FNDC5 for 6 days at indicated doses. **c**, Clark electrode measurements of oxygen consumption in SVF from the inguinal fat depot, differentiated into adipocytes for 6 days in the presence of saline or recombinant FNDC5 (20 nM). Data are representative for three independent experiments and normalized to total cellular protein. **d**, qPCR of *Ucp1* mRNA from SVF, differentiated into adipocytes, and treated with FNDC5 or saline for 6 days followed by addition of forskolin for 8 h.  $\dagger P < 0.05$  compared to forskolin treatment. **e**, qPCR of *Ppara* after 6 days of FNDC5 treatment (20 nM) during differentiation of primary SVF. **f**, SVF differentiated into adipocytes and treated with FNDC5 and/or GW6471 for 6 days. The graph shows qPCR of indicated genes.  $\dagger P < 0.05$  compared to FNDC5 treatment. For **d** and **f**, combined one- and two-way ANOVA was used.  $*P < 0.05$ . All other statistics were performed using Student's *t*-test, and bar graphs are mean  $\pm$  s.e.m.

We also used immunohistochemistry to study cells treated with FNDC5 and observed a robust increase in UCP1-positive adipocytes with multilocular lipid droplets (Supplementary Fig. 4). Electron microscopic analysis of FNDC5-treated cells showed a higher density of mitochondria compared to control cells, consistent with a brown-fat-like phenotype and elevated mitochondrial gene expression (Supplementary Fig. 5). The sizes of mitochondria, however, were similar between groups (Supplementary Fig. 4). Lastly, measurements of oxygen consumption provided functional evidence of increased energy expenditure with FNDC5 exposure. Total oxygen consumption was greatly increased (100%) by 20 nM of FNDC5, and the majority of this respiration was uncoupled (Fig. 3c). Thus, FNDC5 potentially induces thermogenesis and a brown-fat-like gene program in cultured adipocytes. In marked contrast, FNDC5 showed little or no effects on the classical brown fat cells isolated from the interscapular depot (Supplementary Fig. 4).

We sought to define the timeframe during the differentiation process when FNDC5 was effective. FNDC5 was applied to cells in 2-day windows from day 0–6, and this was compared to cells to which the protein was added during the entire 6-day differentiation process. As

shown in Supplementary Fig. 5, treatment during days 3–6 was effective at inducing *Ucp1* mRNA, although not as effective as when FNDC5 was present throughout the differentiation process. Furthermore, treatment during the initial 2 days had no effect on *UCP1* levels, suggesting that FNDC5 acts mainly during the differentiation process of cells committed to the adipocyte lineage. Cyclic AMP (cAMP) is an important signalling pathway in thermogenesis, promoting the brown-fat gene program downstream of  $\beta$ -adrenergic stimulation. We therefore asked whether FNDC5 effects were additive or redundant with cAMP signalling. As shown in Fig. 3d, FNDC5-exposed cells increase UCP1 expression in an additive manner when exposed to forskolin, an adenyl cyclase activator. Two-way ANOVA tests demonstrated that there was a significant ( $P < 0.01$ ) interaction between FNDC5 and forskolin treatment, indicating synergistic effects.

### PPAR- $\alpha$ acts downstream of *Fndc5*

A key question is how FNDC5 is able to stimulate a thermogenic gene program. One potentially important transcription factor induced by FNDC5, identified using gene expression arrays, was PPAR- $\alpha$ . This nuclear receptor has been shown to drive *Ucp1* expression and several other genes involved in browning of adipose cells<sup>10</sup>. *Ppara* is increased threefold at the mRNA level by FNDC5 treatment (Fig. 3e). Importantly, the FNDC5-mediated increase in UCP1 was significantly reduced when cells were simultaneously subjected to the selective PPAR- $\alpha$  antagonist GW6471 (Fig. 3f). The functional interaction between the FNDC5 and GW6471 treatments on *UCP1* expression was confirmed using two-way ANOVA ( $P < 0.05$ ). Conversely, the PPAR- $\alpha$  antagonist normalized the reduction seen in white adipose genes leptin and adiponectin after FNDC5 treatment. Together, these data indicate that FNDC5 acts to induce *Ucp1* gene expression, at least in part, via PPAR- $\alpha$ .

### Irisin is a cleaved and secreted fragment of *Fndc5*

FNDC5 (also known as FRCP2 and PeP), was previously shown to have a signal peptide, two fibronectin domains and one hydrophobic domain that is likely to be membrane inserted<sup>11,12</sup> (Fig. 4a). Previous studies did not investigate whether part of this protein might be secreted<sup>11,12</sup>. With this structure in mind, we considered the possibility that FNDC5 might be synthesized as a type I membrane protein, followed by proteolytic cleavage and release of the amino (N)-terminal part of the protein into the extracellular space. Thus, any carboxy (C)-terminal or N-terminal tags would be lost during processing of the mature protein or interfere with localization. Indeed, expression of a C-terminally Flag-tagged FNDC5 (Fig. 4a) did not result in any Flag immunoreactivity in the medium from cells expressing this construct (Fig. 4b). However, when we immunoblotted the same samples with an antibody that recognizes the endogenous FNDC5 protein, we could easily detect substantial amounts of FNDC5 in the media at approximately 32 kilodalton (kDa): this is slightly larger than the cellular FNDC5 (Fig. 4b). These data indicate that FNDC5 is C-terminally cleaved, secreted and possibly further modified.

Western blot of media fractions with antibodies against wild-type FNDC5 showed multiple bands, suggestive of glycosylation, a common feature of secreted proteins. Treatment of supernatants from FNDC5-expressing cells with peptide *N*-glycosidase F (PNGase F) resulted in a significant size decrease as detected by SDS-polyacrylamide gel electrophoresis (SDS-PAGE), from 32 kDa to 20 kDa (Fig. 4c).

Mass spectrometry was used to determine the sequence of the FNDC5-derived polypeptide found in the media (Methods). To do this, we fused the N terminus of FNDC5 (without the signal peptide) to the C terminus of the crystallisable fragment (Fc) domain of immunoglobulin G (IgG). After purification and enzymatic deglycosylation of the secreted material, mass spectrometry analyses indicated that secreted FNDC5 was truncated at glutamic acid 112 (not including the signal sequence), as shown in Fig. 4e. The secreted portion of FNDC5 has remarkable conservation between species, with 100% identity between



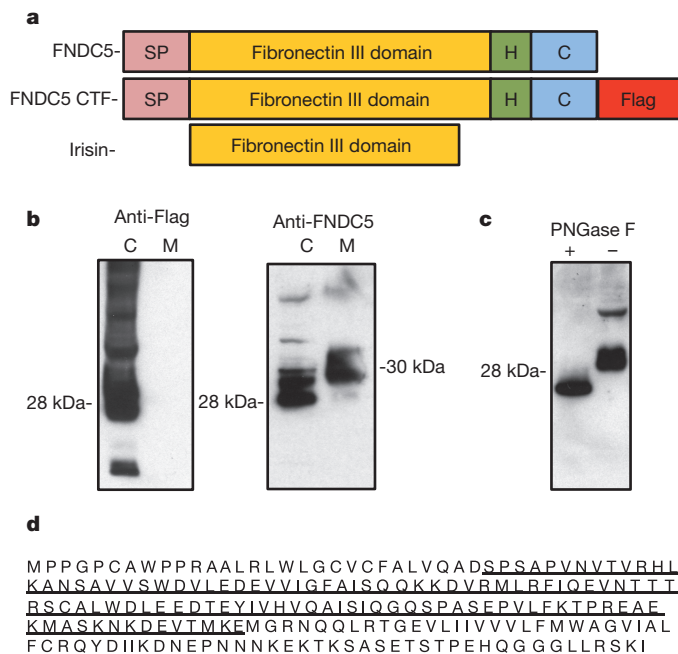


**Figure 4 | FNDC5 is proteolytically cleaved and secreted from cells.**

**a**, Schematic representation of the FNDC5 protein structure (top), Flag-tagged FNDC5 protein (middle) and irisin (bottom). C, C-terminal domain; H, hydrophobic domain; SP, signal peptide. **b**, HEK 293 cells transfected with a vector expressing the C-terminal Flag-tagged FNDC5 (CTF-F5, third panel from **a**), followed by isolation of cell and culture media protein. Samples were adjusted for protein content and western blots were performed against the Flag antigen (left) or FNDC5 (right). This was repeated in several experiments with similar results. Adjusting for volume (instead of protein content) also gave similar results. C, cell fraction; M, media fraction. Arrows indicate molecular weight. **c**, HEK 293 cells transfected with a vector expressing FNDC5-CTF, followed by isolation of cell and media protein. Respective protein fraction was then treated with PNGase F followed by western blot against FNDC5 after SDS-PAGE. **d**, Representation of the full-length FNDC5 and the irisin fragment mapped by mass spectrometry (underlined).

mice and humans (Supplementary Fig. 6). Because this distinct, secreted polypeptide has not been previously described and signals from muscle to other tissues we named it irisin, after Iris, the Greek messenger goddess.

The ability of the anti-FNDC5 antibodies to react with irisin allowed us to investigate the contribution made by irisin to the browning activity caused by muscle cells expressing PGC1- $\alpha$ . Media conditioned by muscle cells that had forced expression of PGC1- $\alpha$  were incubated with control or anti-FNDC5 antibodies before they were applied to the fat cell cultures. As shown in Supplementary Fig. 6, the FNDC5 antibody caused a marked reduction in the ability of the PGC1- $\alpha$  conditioned media to induce *Ucp1* and *Cidea* mRNA in the primary inguinal cells. This suggests that irisin accounts for a significant fraction of this activity found in secreted media from muscle cells with forced PGC1- $\alpha$  expression. We cannot, however, exclude the possibility that other factors might also contribute to this response.

### Irisin is present in mouse and human plasma

We next analysed levels of irisin in plasma from wild-type mice, using intravenous adenoviral delivery of full-length FNDC5 as a positive control. This method results in strong forced expression from the liver and potential secretion to the plasma, where we detected irisin using western blot after albumin/IgG-depletion and deglycosylation. As seen in Fig. 5a, FNDC5-expressing virus resulted in a clear increase in an immunoreactive band at 22 kDa. Importantly, this was the only band altered on these blots. Using western blots of purified FNDC5 protein as a quantitative standard, irisin is present in the plasma of control mice at a concentration of approximately 40 nM. We also

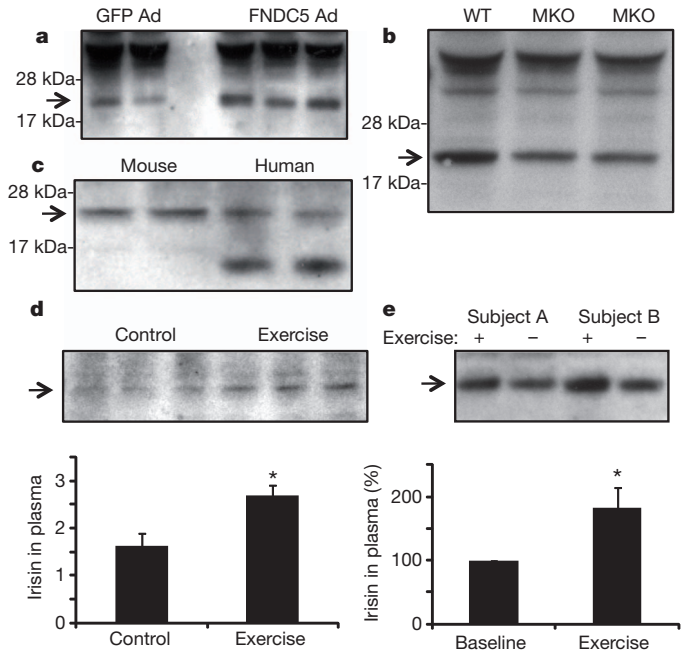


**Figure 5 | Detection of irisin in mouse and human plasma.** **a**, Plasma from mice injected intravenously with adenoviral vectors (Ad) expressing FNDC5 or GFP was subjected to western blot against FNDC5. **b**, Western blot against irisin in plasma from muscle-specific PGC1- $\alpha$  knockout (MKO) mice or control littermates (flox/flox). WT, wild type. **c**, Western blot against irisin in plasma from wild-type mice or two healthy human subjects (representative for 8 subjects analysed identically). **d**, Western blot against irisin in serum from control or 3 weeks exercised mice, followed by 12 h rest. Bottom panel shows quantification of the bands. **e**, Western blot analysis of irisin in plasma from human subjects before and after 10 weeks of endurance exercise. Eight subjects in total were analysed; quantification after internal normalization is displayed in bottom panel. For all plasma analyses, samples were depleted for albumin/IgG, and deglycosylated using PNGase F. Arrow indicated irisin band. Data are presented as mean  $\pm$  s.e.m., and \* $P < 0.05$  compared to control group. Student's *t*-test was used for single comparisons.

analysed plasma of PGC1- $\alpha$  muscle-specific knockout mice as a negative control, and the irisin band at 22 kDa was decreased by 72% in these animals (Fig. 5b). Furthermore, an immunoreactive band of identical electrophoretic mobility was found in plasma from healthy human subjects (Fig. 5c). This band was greatly diminished when the anti-FNDC5 antibody was neutralized with an excess of antigen (Supplementary Fig. 7).

We examined blood levels of irisin after exercise in mice and human subjects. Mice had significantly elevated (65%) plasma concentrations of irisin after they were subjected to 3 weeks of free wheel running (Fig. 5d). Similar analyses in healthy adult humans subjected to supervised endurance exercise training for 10 weeks revealed a twofold increase in the circulating irisin levels compared to the non-exercised state (Fig. 5e). Thus, irisin is present in mouse and human plasma, and is increased with exercise. The increase in circulating protein in both species is roughly proportional to the increases observed at the mRNA level in muscle (Fig. 2c).

### Irisin reduces obesity and insulin resistance

We used adenoviral vectors to express full-length FNDC5 (or a control GFP) and examined its biological and therapeutic effects. This method resulted in a 15-fold increase in liver *Fndc5* mRNA, although the liver expresses very low endogenous levels of this mRNA. Plasma levels of irisin were increased 3–4 fold (Fig. 5a). The mice did not display any adverse reaction, and upon gross pathological examination, there was no apparent toxicity in any major organ system. There was also no increase in plasma AST levels, and inflammatory genes were not significantly altered in the liver when the two groups were compared

(Supplementary Fig. 8). Ten days after injection, *Ucp1* mRNA was increased by 13-fold in the subcutaneous depot relative to the same depot in mice receiving the virus expressing GFP (Fig. 6a,b); *Cidea* was also significantly upregulated (Fig. 6a). There were no changes in expression of UCP1 in the interscapular classical brown fat (BAT), but we did observe a minor elevation in *Prdm16* and *Pgc1a* mRNA (Supplementary Fig. 8). The changes in gene expression in the subcutaneous adipose tissues were accompanied by a clear increase in the number of UCP1-positive, multilocular adipocytes (Fig. 6c). We did not, however, detect any change in body weight in the GFP versus FNDC5 groups of animals. We observed similar results in young C57BL/6 mice (Supplementary Fig. 9). Thus, moderate increases in circulating irisin can induce browning of white adipose tissues *in vivo*, including increased expression of UCP1.

As activation of the classical brown fat or browning of white fat has been shown to improve obesity and glucose homeostasis *in vivo*<sup>6,13</sup>, we delivered FNDC5-expressing adenovirus to mice rendered obese and insulin-resistant by feeding a high fat diet. We chose C57BL/6 mice for these experiments because they are highly prone to diet-induced obesity and diabetes. The expression of irisin increased *Ucp1* gene expression to the same degree as in lean mice (Supplementary Fig. 9).

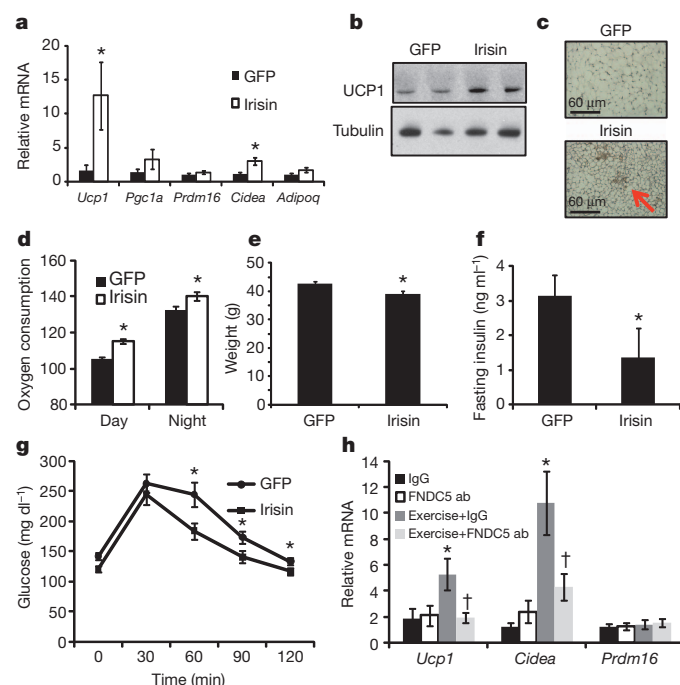


**Figure 6 | Irisin induces browning of white adipose tissues *in vivo* and protects against diet-induced obesity and diabetes.** **a–c**, Wild-type BALB/c mice were injected with  $10^{10}$  GFP- or FNDC5-expressing adenoviral particles intravenously ( $n = 7$  for each group). **a**, **b**, Animals were killed after 10 days and inguinal/subcutaneous fat pads were collected and analysed using qPCR analysis of indicated mRNAs (**a**) and western blot against UCP1 (**b**). **c**, Representative images from immunohistochemistry against UCP1 in these mice. All results in **a–c** were repeated two times with similar results. **d–g**, C57BL/6 mice fed a 60% kcal high-fat diet for 20 weeks were intravenously injected with GFP- or FNDC5-expressing adenovirus and all analyses were done 10 days thereafter ( $n = 7$  for both groups). **d**, Oxygen consumption at day and night. **e**, Body weights of mice 10 days after injection with indicated adenovirus. **f**, Fasting plasma insulin measured using enzyme-linked immunosorbent assay (ELISA). **g**, Intraperitoneal glucose tolerance test. **h**, Mice were injected intraperitoneally with 50  $\mu$ g of rabbit IgG or a rabbit anti-FNDC5 antibody (ab) and were either subjected to swimming for 7 days or kept sedentary ( $n = 10$  for all groups). Data show mRNA expression levels from inguinal white adipose tissue. All data in **d–j** were performed at least twice in a separate mouse cohort with similar results.  $^{\dagger}P < 0.05$  compared to exercise and IgG. One-way ANOVA was used for statistics in **h**. All other statistics were performed using Student's *t*-test, and bar graphs are mean  $\pm$  s.e.m.

There was also an elevation in expression of several mitochondrial genes (Supplementary Fig. 8). Notably, these changes occurred with only moderately increased irisin blood levels, threefold compared to the GFP-expressing mice. This effect was accompanied with a large increase in oxygen consumption (Fig. 6d), consistent with the gene expression data, and body weights of the irisin-expressing mice were slightly reduced after 10 days compared to GFP-expressing controls (Fig. 6e). These effects of irisin on mitochondrial gene expression in the fat were not seen in skeletal muscle *in vivo* or in cultured myocytes (Supplementary Fig. 10). Irisin expression in the mice fed a high fat diet caused a significant improvement in glucose tolerance when compared to the control mice expressing GFP. In addition, fasting insulin was also reduced (Fig. 6f,g). These data illustrate that even moderately increased levels of circulating irisin potentially increase energy expenditure, reduce body weight and improve diet-induced insulin resistance.

Finally, we asked whether irisin is required for the exercise-induced effects on the subcutaneous white fat. Injection of anti-FNDC5 antibodies into mice before 10 days of swim training dramatically reduced the effect of this exercise on *Ucp1* and *Cidea* gene expression, compared to injection of control antibodies (Fig. 6h). In contrast, *Prdm16* mRNA levels were not increased with exercise and were also not affected by the anti-FNDC5 antibodies. Thus, irisin is required for a substantial part of the effect of exercise on these gene expression events in the browning of white fat.

## Discussion

Exercise has the capacity to improve metabolic status in obesity and type 2 diabetes, but the mechanisms are poorly understood. Importantly, exercise increases whole body energy expenditure beyond the calories used in the actual work performed<sup>14</sup>. However, the relative contribution of the adipose tissues to this phenomenon has not been clarified. Because transgenic mice expressing PGC1- $\alpha$  selectively in muscle showed a remarkable resistance to age-related obesity and diabetes<sup>4</sup>, we sought factors secreted from muscle under the control of this co-activator that might increase whole body energy expenditure. We describe a new polypeptide hormone, irisin, which is regulated by PGC1- $\alpha$ , secreted from muscle into blood and activates thermogenic function in adipose tissues. Irisin is remarkable in several respects. First, it has powerful effects on the browning of certain white adipose tissues, both in culture and *in vivo*. Nanomolar levels of this protein increase UCP1 in cultures of primary white fat cells by 50 fold or more, resulting in increased respiration. Perhaps more remarkable, viral delivery of irisin that causes only a moderate increase ( $\sim 3$  fold) in circulating levels stimulates a 10–20 fold increase in UCP1, increased energy expenditure and an improvement in the glucose tolerance of mice fed a high fat diet. As this is in the range of increases seen with exercise in mouse and man, it is likely that irisin is responsible for at least some of the beneficial effects of exercise on the browning of adipose tissues and increases in energy expenditure. It is important to note that the evidence provided here does not exclude a role for other tissues besides muscle in the biological regulation and secretion of irisin.

Second, the cleaved and secreted portion of FNDC5, the hormone irisin, is highly conserved in all mammalian species sequenced. Mouse and human irisin are 100% identical, compared to 85% identity for insulin, 90% for glucagon and 83% identity for leptin. This certainly implies a highly conserved function that is likely to be mediated by a cell surface receptor. The identity of such a receptor is not yet known.

On the basis of the gene structure of *Fndc5*, with a signal peptide that was evidently missed in previous studies<sup>12</sup>, we considered that FNDC5 might be a secreted protein. Indeed, we have observed that the signal peptide is removed, and the mature protein is further proteolytically cleaved and glycosylated, to release the 112-amino-acid polypeptide irisin. The cleavage and secretion of irisin is similar to the release/shedding of other transmembrane polypeptide hormones and hormone-like molecules such as epidermal growth factor (EGF) and transforming growth factor- $\alpha$  (TGF- $\alpha$ ).

As the conservation of calories would probably provide an overall survival advantage for mammals, it seems paradoxical that exercise would stimulate the secretion of a polypeptide hormone that increases thermogenesis and energy expenditure. One explanation for increased irisin expression with exercise in mouse and man may be that it evolved as a consequence of muscle contraction during shivering. Muscle secretion of a hormone that activates adipose thermogenesis during this process might provide a broader, more robust defence against hypothermia.

The therapeutic potential of irisin is obvious. Exogenously administered irisin induces the browning of subcutaneous fat and thermogenesis, and it presumably could be prepared and delivered as an injectable polypeptide. Increased formation of brown or beige/brite fat has been shown to have anti-obesity, antidiabetic effects in multiple murine models<sup>6</sup>, and adult humans have significant deposits of UCP1-positive brown fat<sup>15</sup>. Data presented here show that even relatively short treatments of obese mice with irisin improves glucose homeostasis and causes a small weight loss. Whether longer treatments with irisin and/or higher doses would cause more weight loss remains to be determined. The worldwide, explosive increase in obesity and diabetes renders attractive the therapeutic potential of irisin in these and related disorders.

Another potentially important aspect of this work relates to other beneficial effects of exercise, especially in some diseases for which no effective treatments exist. The clinical data linking exercise with health benefits in many other diseases suggests that irisin could also have significant effects in these disorders.

## METHODS SUMMARY

Primary mouse stromal vascular fractions from adipose tissues were differentiated as described<sup>6</sup>. FNDC5/irisin were purchased from ABNOVA (GST fused), or produced from Syd Laboratories (GST fused) or LakePharma (Fc fusions). Hydrodynamic injections<sup>16</sup>, electron microscopy<sup>17</sup> and treadmill running<sup>18</sup> were performed as previously described. Unless otherwise stated, bar graph data are presented as mean  $\pm$  s.e.m., and  $*P < 0.05$  compared to control group. Student's *t*-test was used for single comparisons and one-way ANOVA for multiple.

**Full Methods** and any associated references are available in the online version of the paper at [www.nature.com/nature](http://www.nature.com/nature).

**Received 14 August; accepted 13 December 2011.**

**Published online 11 January 2012.**

1. Puigserver, P. *et al.* A cold-inducible coactivator of nuclear receptors linked to adaptive thermogenesis. *Cell* **92**, 829–839 (1998).
2. Handschin, C. & Spiegelman, B. M. The role of exercise and PGC1 $\alpha$  in inflammation and chronic disease. *Nature* **454**, 463–469 (2008).
3. Sandri, M. *et al.* PGC-1 $\alpha$  protects skeletal muscle from atrophy by suppressing FoxO3 action and atrophy-specific gene transcription. *Proc. Natl Acad. Sci. USA* **103**, 16260–16265 (2006).
4. Wenz, T., Rossi, S. G., Rotundo, R. L., Spiegelman, B. M. & Moraes, C. T. Increased muscle PGC-1 $\alpha$  expression protects from sarcopenia and metabolic disease during aging. *Proc. Natl Acad. Sci. USA* **106**, 20405–20410 (2009).

5. Xu, X. *et al.* Exercise ameliorates high-fat diet-induced metabolic and vascular dysfunction, and increases adipocyte progenitor cell population in brown adipose tissue. *Am. J. Physiol. Regul. Integr. Comp. Physiol.* **300**, R1115–R1125 (2011).
6. Seale, P. *et al.* Prdm16 determines the thermogenic program of subcutaneous white adipose tissue in mice. *J. Clin. Invest.* **121**, 96–105 (2011).
7. Vind, B. F. *et al.* Impaired insulin-induced site-specific phosphorylation of TBC1 domain family, member 4 (TBC1D4) in skeletal muscle of type 2 diabetes patients is restored by endurance exercise-training. *Diabetologia* **54**, 157–167 (2011).
8. Nielsen, A. R. & Pedersen, B. K. The biological roles of exercise-induced cytokines: IL-6, IL-8, and IL-15. *Appl. Physiol. Nutr. Metab.* **32**, 833–839 (2007).
9. Tseng, Y. H. *et al.* New role of bone morphogenetic protein 7 in brown adipogenesis and energy expenditure. *Nature* **454**, 1000–1004 (2008).
10. Komatsu, M. *et al.* Multiple roles of PPAR $\alpha$  in brown adipose tissue under constitutive and cold conditions. *Genes Cells* **15**, 91–100 (2010).
11. Teufel, A., Malik, N., Mukhopadhyay, M. & Westphal, H. *Frcp1* and *Frcp2*, two novel fibronectin type III repeat containing genes. *Gene* **297**, 79–83 (2002).
12. Ferrer-Martínez, A., Ruiz-Lozano, P. & Chien, K. R. Mouse PEP: a novel peroxisomal protein linked to myoblast differentiation and development. *Dev. Dyn.* **224**, 154–167 (2002).
13. Cederberg, A. *et al.* *FOXO2* is a winged helix gene that counteracts obesity, hypertriglyceridemia, and diet-induced insulin resistance. *Cell* **106**, 563–573 (2001).
14. Speakman, J. R. & Selman, C. Physical activity and resting metabolic rate. *Proc. Nutr. Soc.* **62**, 621–634 (2003).
15. Enerbäck, S. Human brown adipose tissue. *Cell Metab.* **11**, 248–252 (2010).
16. Bell, J. B., Aronovich, E. L., Schreifels, J. M., Beadnell, T. C. & Hackett, P. B. Duration of expression and activity of *Sleeping Beauty* transposase in mouse liver following hydrodynamic DNA delivery. *Mol. Ther.* **18**, 1796–1802 (2010).
17. Cinti, S., Zingaretti, M. C., Cencello, R., Ceresi, E. & Ferrara, P. Morphologic techniques for the study of brown adipose tissue and white adipose tissue. *Methods Mol. Biol.* **155**, 21–51 (2001).
18. Wu, J. *et al.* The unfolded protein response mediates adaptation to exercise in skeletal muscle through a PGC-1 $\alpha$ /ATF6 $\alpha$  complex. *Cell Metab.* **13**, 160–169 (2011).

**Supplementary Information** is linked to the online version of the paper at [www.nature.com/nature](http://www.nature.com/nature).

**Acknowledgements** This study was supported by National Institutes of Health grants DK54477, DK31405, DK61562 to B.M.S. P.B. and E.A.B. were supported by the Wenner-Gren Foundation, Swedish Heart and Lung Foundation and the 'Svenska Sällskapet för Medicinsk Forskning'. J.W. was supported by a postdoctoral fellowship from the American Heart Association (Founders Affiliate #09POST2010078). The animal procedures were in accordance with Institutional Animal Use and Care Committee protocols 110-2008 and 056-2009. The authors thank S. Loffredo and M. Kirschner for discussions and suggestions on the manuscript.

**Author Contributions** P.B. and B.M.S. planned the majority of experiments and wrote the paper, and P.B. executed most of the experiments. J.W. performed a subset of cultured cell experiments and contributed valuable materials. M.P.J. and S.P.G. performed the peptide fingerprinting identification of irisin cleavage. A.K. contributed with technical assistance and L.Y. and S.K. performed the CLARK electrode experiments. E.A.B. assisted with the hydrodynamic injections. J.C.L. assisted with intravenous injections and K.A.R. with bioinformatics. J.Z.L. and J.H.C. performed *in vitro* experiments. P.B. and H.T. and LakePharma designed and provided Fc fusion proteins. K.H. and B.F.V. performed the human cohort study, and M.C.Z. and S.C. performed the electron microscopy studies.

**Author Information** Reprints and permissions information is available at [www.nature.com/reprints](http://www.nature.com/reprints). The authors declare no competing financial interests. Readers are welcome to comment on the online version of this article at [www.nature.com/nature](http://www.nature.com/nature). Correspondence and requests for materials should be addressed to B.M.S. (bruce\_spiegelman@dfci.harvard.edu).



## METHODS

**Materials.** Antibodies against UCP1, tubulin and FNDC5 were from Abcam. Forskolin, insulin, dexamethasone, rosiglitazone, GW6471 and antibody against Flag were from Sigma. Primers for all qPCR experiments are listed in Supplementary Table 1. Recombinant FNDC5, LRG1, IL-15, VEGF- $\beta$  and TIMP4 were from ABNOVA (Taiwan). Coomassie staining kit and Lipofectamine 2000 were from Invitrogen.

**Identification of PGC1- $\alpha$ -dependent secreted proteins.** All PGC1- $\alpha$ -induced genes as judged from gene expression analysis in MCK-PGC1- $\alpha$  muscle with a fold change of at least 2 and  $P < 0.05$  were subjected to the following analysis. The protein sequence of the longest transcript were analysed in the SignalP-software<sup>19</sup> (<http://www.cbs.dtu.dk/services/SignalP/>). Sequences with positive S, C, Y and D scores were considered positive for a signal sequence. All positive proteins were then screened for mitochondrial target sequences (<http://www.cbs.dtu.dk/services/TargetP/>) whereas positive sequences were removed. All remaining hit proteins were then analysed using qPCR in muscle from MCK-PGC1- $\alpha$  mice and myocytes overexpressing PGC1- $\alpha$ .

**Primary cell cultures and recombinant protein treatments.** The SVF from inguinal fat depots of 8–12-week-old BALB/C mice were prepared and differentiated for 6 days as previously described<sup>20</sup>. Rosiglitazone was used for the two first days of differentiation. For all experiments, unless otherwise indicated, recombinant FNDC5 was added to the culture media at a concentration of  $1 \mu\text{g ml}^{-1}$  for the last 4 days of differentiation. Primary myoblasts were cultured and differentiated as described previously<sup>21</sup>.

**Preparation of protein fractions from cells and media.** 293HEK or primary myocytes were transfected by standard methods or transduced with adenovirus at a multiplicity of infection (m.o.i.) of 20 as indicated. Twenty-four hours after transfection, media was removed, and cells were washed in large volumes of PBS five times, followed by incubation in Freestyle serum-free media (GIBCO) for 24 h. The cells and media were then collected separately, and media were centrifuged three times at 2,000g to pellet debris. Thereafter, a quarter volume of ice-cold TCA was added and precipitated protein was pelleted at 6,000g and washed three times in acetone. Pellet was then dried and resuspended in SDS-containing lysis buffer. Protein concentration was measured in both cell and media fraction and adjusted either by protein or volume as indicated.

**RT-PCR.** qPCR was carried out after Trizol-based RNA extraction using RNeasy (Invitrogen) and thereafter SYBR green. All data were normalized to TBP, 18S or indicated in-house genes and quantitative measures were obtained using the  $\Delta\Delta C_T$  method.

**Western blot and quantification.** Protein amounts from all samples were assessed using the BCA-kit (Thermo Scientific) followed by protein concentration normalization before all western blot experiments. Western blot was carried out following standard procedure and final band intensity (QL-BG) was quantified using BioPix iQ<sup>22</sup>. All data were normalized to background and loading controls.

**Additional methods.** CLARK electrode measurements, energy expenditure *in vivo*, interaperitoneal glucose tolerance test (IGTT) and immunohistochemistry against UCP1 were performed as described previously<sup>6</sup>, with the exception that CLARK output was normalized to total cell protein. Fc-fusion construction and protein purification was performed by LakePharma.

**Comprehensive laboratory animal monitoring system.** C57/Bl6J mice were fed a high fat (60% kcal) diet (D12492, Research Diets) for 20 weeks, starting at 6 weeks of age. Mice were then injected with indicated doses of adenovirus expressing GFP or FNDC5, and comprehensive laboratory animal monitoring system (CLAMS; Columbia Instruments)-cage analysis was performed as described previously<sup>6</sup>. Briefly, mice were acclimated in metabolic chambers for 2 days before analysis in order to minimize stress. CO<sub>2</sub> and O<sub>2</sub> levels were then collected every 36 min for a period of 3 days. Data on activity, heat generation and food intake were measured at more frequent intervals. Circadian rhythm was observed for most parameters. Data were not normalized to body weights unless otherwise stated.

**Mass spectrometry and peptide fingerprinting.** Gel bands were digested with sequencing grade trypsin (Promega) or ASP-N (Sigma-Aldrich) as per manufacturer's instructions. Extracted in-gel protein digests were resuspended in 8  $\mu\text{l}$  5% formic acid/5% acetonitrile, and 4  $\mu\text{l}$  were analysed by microcapillary liquid chromatography electrospray ionization tandem mass spectrometry (LC-MS/MS). Analyses were done on a LTQ Orbitrap Velos mass spectrometer (Thermo Fisher Scientific) equipped with a Thermo Fisher Scientific nanospray source, an Agilent 1100 Series binary HPLC pump and a Famos autosampler. Peptides were separated on a 100 m  $\times$  16 cm fused silica microcapillary column with an in-house made needle tip. The column was packed with MagicC18AQ C<sub>18</sub> reversed-phase resin (particle size, 5  $\mu\text{m}$ ; pore size, 200 Å; Michrom Bioresources). Separation was achieved through applying a 30 min gradient from

0–28% acetonitrile in 0.125% formic acid. The mass spectrometer was operated in a data-dependent mode essentially as described previously<sup>23</sup> with a full MS scan acquired with the Orbitrap, followed by up to ten LTQ MS/MS spectra on the most abundant ions detected in the MS scan. Mass spectrometer settings were: full MS (automated gain control,  $1 \times 10^6$ ; resolution,  $6 \times 10^4$ ;  $m/z$  range, 375–1,500; maximum ion time, 1,000 ms); MS/MS (AGC,  $5 \times 10^3$ ; maximum ion time, 120 ms; minimum signal threshold,  $4 \times 10^3$ ; isolation width, 2 Da; dynamic exclusion time setting, 30 s). After MS data acquisition, RAW files were converted into mzXML format and processed using a suite of software tools developed in-house for analysis. All precursors selected for MS/MS fragmentation were confirmed using algorithms to detect and correct errors in monoisotopic peak assignment and refine precursor ion mass measurements. All MS/MS spectra were then exported as individual DTA files and searched with no enzyme using the Sequest algorithm. These spectra were then searched against a database containing sequence of mouse FNDC5 in both forward and reversed orientations. The following parameters were selected to identify FNDC5: 10 p.p.m. precursor mass tolerance, 0.8 Da product ion mass tolerance, fully tryptic or ASP-N digestion, and up to two missed cleavages. Variable modifications were set for methionine (+15.994915). In addition, a fixed modification for the carbamidomethylation for cysteine (+57.021464) was used as well. The C-terminal fragment for FNDC5 was identified (KDEVTMKKE) by trypsin digestion and reconfirmed by a separate ASP-N digestion.

**Preparation of plasma samples for western blot.** Thirty-five microlitres of mouse or human plasma were precleared for albumin/IgG using the ProteoExtract-kit (CalBiochem) as recommended by the manufacturer. Samples were then concentrated to approximately 100  $\mu\text{l}$  and  $>8 \mu\text{g } \mu\text{l}^{-1}$ , followed by deglycosylation of 150  $\mu\text{g}$  using PNGase F (New England Biolabs). Totally, 80  $\mu\text{l}$  were then prepared containing  $1 \times$  sample buffer with reducing agent and  $1.7 \mu\text{g } \mu\text{l}^{-1}$  protein, sonicated, boiled and analysed using western blot against FNDC5 or indicated antibody.

**Construction of adenoviral vectors.** The FNDC5 expression vector was purchased with a C-terminal Flag-tag from OriGene. The QuickChange Multi Site XL Directed Mutagenesis Kit (Aligent Technologies) was used to introduce a Flag tag downstream of the signal sequence and to mutate the C-terminal Flag tag, thus resulting in the N-terminal Flag (NTF)-FNDC5 construct (Fig. 5a). The NTF and CTF FNDC5 constructs were then subcloned into the pENTR1a vector (Invitrogen) and recombined into the pAd-CMV-DEST-V5 vector (Invitrogen) and adenovirus was produced using the virapower system (Invitrogen), including three rounds of amplification. Thereafter, virus was concentrated using the Vivapure adenopack 100 (Sartorius Stedim Biotech) and buffer exchanges to saline reaching a concentration of 9–10 i.f.u.  $\mu\text{l}^{-1}$ . A GFP-containing adenovirus previously used was prepared in parallel.

**Transgenic mice.** The MCK-PGC1- $\alpha$  transgenic and muscle-specific PGC1- $\alpha$  knockout mice have been described previously<sup>24</sup>.

**Exercise protocols.** Twelve-week-old B6 mice were exercised either using swimming<sup>25</sup> or using free wheel running, as described previously<sup>26</sup>.

**Human material and exercise training program.** Blood samples and skeletal muscle biopsies were obtained from eight male non-diabetic individuals before and after 10 weeks of aerobic training as described previously<sup>7</sup>. In brief, the exercise-training program consisted of cycling on stationary bikes with 4–5 sessions of 20–35 min per week at an average intensity of ~65% of maximal oxygen consumption. Informed consent was obtained from all volunteers before participation. The study was approved by the Local Ethics Committee and was performed in accordance with the Helsinki Declaration.

- Emanuelsson, O., Brunak, S., von Heijne, G. & Nielsen, H. Locating proteins in the cell using TargetP, SignalP and related tools. *Nature Protocols* **2**, 953–971 (2007).
- Kajimura, S. *et al.* Initiation of myoblast to brown fat switch by a PRDM16-C/EBP- $\beta$  transcriptional complex. *Nature* **460**, 1154–1158 (2009).
- Rasbach, K. A. *et al.* PGC-1 $\alpha$  regulates a HIF2 $\alpha$ -dependent switch in skeletal muscle fiber types. *Proc. Natl Acad. Sci. USA* **107**, 21866–21871 (2010).
- Bostrom, P. *et al.* The SNARE protein SNAP23 and the SNARE-interacting protein Munc18c in human skeletal muscle are implicated in insulin resistance/type 2 diabetes. *Diabetes* **59**, 1870–1878 (2010).
- Villén, J. & Gygi, S. P. The SCX/IMAC enrichment approach for global phosphorylation analysis by mass spectrometry. *Nature Protocols* **3**, 1630–1638 (2008).
- Handschin, C. *et al.* Skeletal muscle fiber-type switching, exercise intolerance, and myopathy in PGC-1 $\alpha$  muscle-specific knock-out animals. *J. Biol. Chem.* **282**, 30014–30021 (2007).
- Boström, P. *et al.* C/EBP $\beta$  controls exercise-induced cardiac growth and protects against pathological cardiac remodeling. *Cell* **143**, 1072–1083 (2010).
- Chinsomboon, J. *et al.* The transcriptional coactivator PGC-1 $\alpha$  mediates exercise-induced angiogenesis in skeletal muscle. *Proc. Natl Acad. Sci. USA* **106**, 21401–21406 (2009).

## MATERIALS SCIENCE

## A fresh twist for self-assembly

Molecular helicity affects many of the bulk properties of materials. A study finds that helicity also controls the self-assembly of colloidal particles, opening the door to a new generation of functional materials.

VOLKER SCHALLER  
& ANDREAS R. BAUSCH

The next time you go to the supermarket, take a look at the pasta. You'll probably find everything from long, thin spaghetti to butterfly-shaped farfalle and twisted fusilli. On closer inspection, you'll see that the strands of spaghetti readily align and pack closely together, whereas the packing of the fusilli is considerably more complex. This complexity is due to the fusilli's chirality — its helical geometry. In a paper published on *Nature's* website today, Gibaud *et al.*<sup>1</sup> report that such complexity of packing can be exploited to control the self-assembly of nanometre-scale particles, allowing the reversible formation of various architectures.

To closely pack two individual pieces of fusilli, the pasta pieces have to twist with respect to each other so that their long axes are not parallel — this is an effect of their chirality. But when many fusilli are crammed together, this twist hinders the ability of the pasta to align in one direction, as required for efficient packing. The resulting competition between chirality and packing can have astonishing consequences for geometrically constrained chiral objects: if you stack fusilli upright in a beaker, the axes of the fusilli in the centre are perfectly vertical, whereas those at the edges of the beaker twist away from this alignment (Fig. 1).

This balance between geometric constraints and chiral interactions is at the heart of the unique properties of chiral liquid crystals. In 'blue' liquid-crystal phases, for instance, chiral molecules self-assemble into cylinders of twisted molecules that stack in a cubic lattice, giving rise to vividly coloured and reflective materials<sup>2</sup>. And in smectic liquid crystals, chiral interactions lead to a twisted, layered structure that is also manifested in the optical and mechanical properties of the materials<sup>3</sup>.

Gibaud *et al.*<sup>1</sup> examined the balance between chirality and geometric constraints in the self-assembly of colloidal particles. Their model system was an ensemble of rod-like viruses, 7 nanometres in diameter and 880 nm in length, suspended in water. The



**Figure 1 | Pasta packing.** When constrained in a circular container, fusilli pasta pieces mostly pack together so that their long axes are vertically aligned. But at the edges of the container, the pasta twists away from this alignment. This packing arrangement is a consequence of the pasta's helicity (chirality). Gibaud *et al.*<sup>1</sup> report that the chirality of colloidal particles affects the self-assembly of those particles.

chirality of these viruses depends on the ambient temperature: the rods are achiral at high temperatures, but chiral at low temperatures. The authors observed that, as for any other suspension of colloidal particles<sup>4</sup>, the addition of an appropriate polymer that does not adsorb to the rods drove a phase separation of the mixture into a polymer-rich and a colloid-rich phase. At high temperatures, at which the rods are achiral, this led to the self-assembly of a circular colloidal membrane (a monolayer of vertically aligned rods<sup>5</sup>).

The authors observed that the rods at the centre of the membrane readily align parallel to each other, but at the perimeter of the membrane they twist gradually away from the vertical. This twist at the margin minimizes the interface between the polymer-rich and the rod-rich phases, and so reduces the interfacial tension that arises from the imbalance of forces between particles in this region. But twisting rods out of alignment with the other rods in the membrane has its own energetic cost, known as elastic energy. The formation of circular membranes with twisted margins is therefore the result of a trade-off between minimizing the phase interface and minimizing the elastic energy.

But what happens if the rods are chiral, so that twisted packing is preferred — just as it is for closely packed fusilli? Gibaud *et al.* addressed this question by performing experiments at lower temperatures, thereby 'switching on' the chirality of the viruses. They observed that increases in chirality — that is, increases in the contribution of chiral interactions to the energy balance of the system — reduce the elastic energy, thus lowering the energetic cost of creating a twist at the membrane's margin. This destabilizes the edges of the circular membrane and triggers the formation of ribbon-like structures that splay out from the circular membrane (see Fig. 3a of the paper<sup>1</sup>). The effect of increasing the chirality of the viruses in the colloidal membrane is therefore similar to that of adding surfactants to oil–water mixtures: it decreases the interfacial tension and so allows more interfaces to form.

The beauty of the authors' experimental set-up is that it allows all the parameters involved in the self-assembly of chiral colloids to be readily teased out and measured. Another advantage of the system is that the colloidal building blocks are much bigger than the molecules typically used in studies of chiral materials. This allowed Gibaud *et al.* to precisely quantify the colloidal self-assembly process at all scales, from the microscopic movements of individual viruses to the macroscopic properties of the resulting membrane. It also allowed them to exert well-defined local forces on the system, to affect the balance between twist and interfacial energy, and so to induce structural transitions — for example, by pulling on the membrane, they converted it into ribbon structures.

By including chiral interactions in their system, Gibaud *et al.* have added a new degree of freedom to the self-assembly of colloidal particles. Transferring their results to other materials opens the door to the hierarchical assembly of functional materials that could react sensitively to changes in ambient conditions or to mechanical stimuli. One way to extend the functionality of their system could be to make colloidal particles that are not only chiral, but also have surfaces patterned with

V. SCHALLER

microscopic domains that attract or repel each other. Such patterned colloidal particles have recently been shown to self-assemble into useful functional structures such as 'kagome' lattices<sup>6</sup>.

Chiral interactions between particles occur in all kinds of materials, from liquid crystals<sup>2,3</sup> to cytoskeletal filaments in cells (for which the hierarchical assembly of bundle-like structures is dependent on, and sensitive to, the helical twist of the filaments<sup>7,8</sup>). Most of the chiral materials studied so far are passive or in thermal equilibrium. This means that their structural assembly is governed only by diffusion and by local interactions between the constituent particles. But most naturally occurring materials are far from passive. Instead, they constantly consume energy so that their particles self-organize into higher-order structures — the cytoskeletons

of cells are prime examples of this<sup>9,10</sup>.

The next step, therefore, is to apply the principles identified by Gibaud and colleagues<sup>1</sup> to active systems. Imagine replacing the viruses used in this study with self-propelling chiral bacteria — would they still pack together in a two-dimensional membrane, and, if so, would the membrane move, or rotate, across mesoscopic or macroscopic distances? Could actively beating ribbons form, or would the noise stemming from active movement of the bacteria prevent the formation of such structures? All we can say for certain is that chiral interactions will add a new twist not only to the self-assembly of colloids, but also to the self-organization of active materials. ■

**Volker Schaller and Andreas R. Bausch** are at the *Lehrstuhl für Biophysik-E27, Technische*

*Universität München, Garching 85748, Germany.*

*e-mail: abausch@mytum.de*

1. Gibaud, T. *et al. Nature* <http://dx.doi.org/10.1038/nature10769> (2011).
2. Coles, H. J. & Pivnenko, M. N. *Nature* **436**, 997–1000 (2005).
3. Hough, L. E. *et al. Science* **325**, 456–460 (2009).
4. Aarts, D. G. A. L., Schmidt, M. & Lekkerkerker, H. N. W. *Science* **304**, 847–850 (2004).
5. Barry, E. & Dogic, Z. *Proc. Natl Acad. Sci. USA* **107**, 10348–10353 (2010).
6. Chen, Q., Bae, S. C. & Granick, S. *Nature* **469**, 381–384 (2011).
7. Claessens, M. M. A. E., Semmrich, C., Ramos, L. & Bausch, A. R. *Proc. Natl Acad. Sci. USA* **105**, 8819–8822 (2008).
8. Grason, G. M. & Bruinsma, R. F. *Phys. Rev. Lett.* **99**, 098101 (2007).
9. Kasza, K. E. *et al. Curr. Opin. Cell Biol.* **19**, 101–107 (2007).
10. Köhler, S., Schaller, V. & Bausch, A. R. *Nature Mater.* **10**, 462–468 (2011).



## EVOLUTIONARY BIOLOGY

## A ratchet for protein complexity

**Molecular machines containing related protein subunits are common in cells. Reconstruction of ancient proteins suggests that this type of complexity can evolve in the absence of any initial selective advantage.**

W. FORD DOOLITTLE

Organisms and cells are bewilderingly complicated, and the molecular machines that perform many basic cellular functions are often giant, multi-subunit, multifunctional protein complexes with tangled evolutionary histories. It is generally assumed that such complexes arose by the stepwise accretion of individual proteins, each addition representing a selective advantage by adding to or refining the machine's performance. But in a paper published on *Nature's* website today, Thornton and colleagues<sup>1</sup> argue against this standard explanation in one particular instance — that of a ring-shaped protein complex in fungi. The authors show how evolutionary processes entailing loss of function rather than gain might initially drive a system towards complexity, independently of selection.

Many cellular molecular machines contain several proteins that self-assemble into a multi-subunit ring. In simple cases, rings are homo-oligomeric; that is, all the subunits are identical and thus probably the products of a single gene. In more complex (hetero-oligomeric) examples, the protein molecules in the ring are different, but may be related. Often, hetero-oligomeric rings seem to have arisen from homo-oligomeric complexes after a gene encoding a single subunit became duplicated, producing two or more gene copies (called paralogues), with each copy subsequently evolving to encode a slightly different protein.

The question that Thornton and colleagues address is, why does this happen? Do the structurally distinguishable subunits and/or their specific pattern of assembly confer improved or additional functions on the protein complex, with selection for their enhanced performance being the evolutionary driving force? Alternatively, might neutral processes be responsible, at least initially?

To understand how the latter possibility might come about, imagine that a gene encoding, for example, eight subunits of a homo-oligomeric ring undergoes duplication (Fig. 1). The two paralogous gene copies that this duplication produces — and the protein subunits

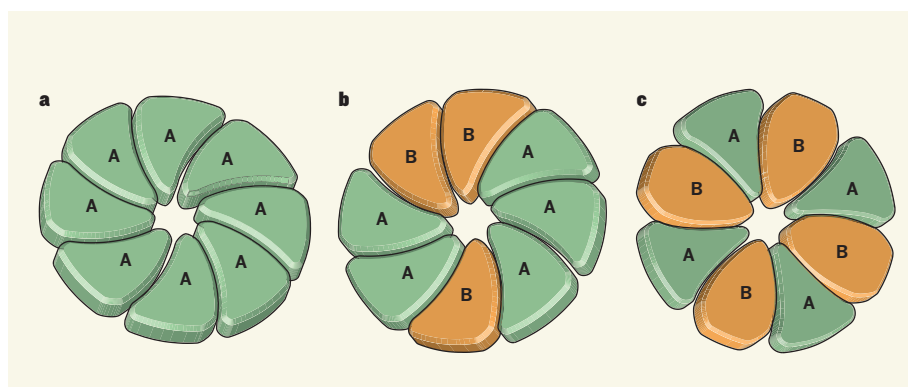


**Figure 1 | Evolution of complexity in a protein ring.** **a**, Homo-oligomeric protein complexes contain identical subunits (A) that are typically encoded by a single gene. **b**, If the gene is duplicated, the two gene copies can diverge through the accumulation of neutral mutations, generating structurally distinguishable but functionally unaltered subunits A and B, which can form functional hetero-oligomeric rings by random mixture. **c**, If additional mutations prevent subunits from binding to others of their own type, functional rings could still be formed by alternating subunit types. As further mutations accumulate, the probability of returning to the initial homo-oligomeric situation becomes very small. Thus, the subunit composition of a protein association may become complex in the absence of initial selective advantages. Thornton and colleagues<sup>1</sup> provide experimental evidence suggesting that this type of process has occurred in the evolution of a six-membered protein ring that forms part of the vacuolar H<sup>+</sup>-ATPase enzymes in fungi.

they encode (call them A and B) — will of necessity begin to diverge through accumulation of neutral mutations. These mutations might not at first affect any of the subunits' functions, so that functional octameric rings could continue to form by a random sampling of A and B subunits. But further mutations might result in each subunit losing the ability to bind others of its own type, A to A or B to B. However, as long as A still binds B and B still binds A, functional rings can form.

As A and B continue to co-evolve through the acquisition of further neutral mutations, the likelihood of reversing back along the mutational path to the initial single-gene homo-oligomeric complex becomes vanishingly small. We can thus see the homo-oligomer to hetero-oligomer transition as an inexorable evolutionary ratchet. And even if there were some slight selective disadvantage to using a hetero-oligomeric complex (for example, complex formation could become slower), this could be overcome in small populations — in which the efficiency of selection is reduced and mildly harmful mutations can be fixed by chance<sup>2</sup>.

Some chaperonins — molecular machines that assist other proteins to fold into functional configurations — have until recently provided the best evidence for such a scenario. Microorganisms known as archaea have one, two or three paralogous genes encoding chaperonin subunits that form rings: homo-oligomeric eight-membered rings when there is a single gene, or hetero-oligomeric eight- or nine-membered rings when there are two or three genes. Such paralogy seems to reoccur frequently in archaea, and a neutral co-evolutionary picture of the sort described above has been suggested<sup>3</sup> to explain it.

Comparative bioinformatic studies<sup>4</sup> support the idea that hetero-oligomeric archaeal chaperonins consisting of two different subunits are not functionally distinct from the homo-oligomers, and thus did arise neutrally. Adaptive changes can follow later, however. Indeed, there is direct evidence for specialized roles for the eight distinct chaperonin subunits of eukaryotes (organisms such as plants, animals and fungi)<sup>5</sup>.

So a more realistic picture might be as follows. Rarely, gene duplication is quickly

followed by functional differentiation (as proposed in early formulations of the hypothesis of evolution by gene duplication<sup>6</sup>). Selection against loss of either duplicate would then be ensured early on. Perhaps more often, though, the paralogous condition might first be locked in by the above-described co-evolutionary ratchet, allowing functional differences (if any) to be acquired later (if ever). That is what Thornton and colleagues<sup>1</sup> argue has happened in the case of a six-membered hetero-oligomeric ring that forms part of the enzymes known as vacuolar H<sup>+</sup>-ATPases (V-ATPases) in fungi. Their argument is especially compelling because it rests not only on bioinformatics, but also on experiments, including the synthesis and testing of proteins that the authors propose are ancestral to the V-ATPase subunits.

In most eukaryotes, the V-ATPase six-membered ring is made up of five copies of the protein Vma3 and one of its paralogue Vma16. In fungi such as budding yeast, by contrast, one of the five Vma3 proteins is replaced by Vma11, which is a fungus-specific paralogue of Vma3. The abilities of these subunits to bind to one another<sup>7</sup> are such that Vma11 must lie between Vma16 and Vma3 in the ring, and Vma3 cannot form the interface with the side of Vma16 that Vma11 can. This represents a sort of functional degeneration, because the last common ancestor of Vma3 and Vma11 must have been able

to interface with either side of Vma16, as Vma3 must still do in organisms other than fungi.

Thornton and colleagues<sup>1</sup> synthesized proteins that matched the phylogenetically inferred ancestor of Vma3 and Vma11, as well as that of Vma16 and other intermediates in the predicted evolutionary pathway. They demonstrate that Anc.3-11, the inferred ancestor of fungal Vma3 and Vma11, does indeed interface with either side of Vma16. The authors tested the functionality of these and other inferred evolutionary ancestors and intermediates by expressing them in yeast mutants that lacked current versions of one or more of the three genes. According to this picture, when Anc.3-11 underwent duplication, one paralogue (which was to become modern fungal Vma3) lost the ability to interact with the 'anticlockwise' side of Vma16. The other paralogue (which became Vma11) lost the ability to interact with the 'clockwise' side of Vma16 and/or the anticlockwise side of Vma3.

A general theory, sometimes called constructive neutral evolution, to explain how neutral processes might drive a system towards complexity is more than a decade old<sup>8–10</sup>. But the study by Thornton and colleagues<sup>1</sup> may provide the most compelling experimental evidence to date. Of course, one can never prove that some subtle, unidentified selective advantage was

not involved in the evolution of the V-ATPase protein ring, but neutrality would seem the most justifiable default hypothesis. Thus, a neutral theory of molecular evolution, normally invoked for nucleotide substitutions, may also apply to certain higher-order structures such as multi-subunit protein rings. How general such neutral mutational drives to complexity might be is one of evolutionary theory's deeper unanswered questions. ■

---

**W. Ford Doolittle** is in the Department of Biochemistry and Molecular Biology, Dalhousie University, Halifax, Nova Scotia B3H 4R2, Canada.  
e-mail: ford@dal.ca

1. Finnigan, G. C., Hanson-Smith, V., Stevens, T. H. & Thornton, J. W. *Nature* <http://dx.doi.org/10.1038/nature10724> (2012).
2. Lynch, M. *Proc. Natl Acad. Sci. USA* **104**, 8597–8604 (2007).
3. Archibald, J. M., Logsdon, J. M. Jr & Doolittle, W. F. *Curr. Biol.* **9**, 1053–1056 (1999).
4. Ruano-Rubio, V. & Fares, M. A. *Mol. Biol. Evol.* **24**, 1384–1396 (2007).
5. Fares, M. A. & Wolfe, K. H. *Mol. Biol. Evol.* **20**, 1588–1597 (2003).
6. Ohno, S. *Evolution by Gene Duplication* (Springer, 1970).
7. Wang, Y., Cipriano, D. J. & Forgac, M. *J. Biol. Chem.* **282**, 34058–34065 (2007).
8. Stoltzfus, A. *J. Mol. Evol.* **49**, 169–181 (1999).
9. Force, A. *et al. Genetics* **151**, 1531–1545 (1999).
10. Gray, M. W., Lukeš, J., Archibald, J. M., Keeling, P. J. & Doolittle, W. F. *Science* **330**, 920–921 (2011).

## ASTRONOMY

## A new class of planet

**Three examples of a new family of planets, which orbit a pair of stars rather than a single one, have been discovered. The Milky Way may contain millions of these circumbinary planets.**

JOHN SOUTHWORTH

Although more than 700 extrasolar planets have been detected, none was known to orbit more than one star until the recent discovery<sup>1</sup> of a circumbinary planet, which orbits a pair of stars. This concept was previously confined to theory — and to science fiction, for example the planet Tatooine in *Star Wars*. In a paper published on *Nature's* website today, Welsh *et al.*<sup>2</sup> describe the discovery of two more such planets and provide insight into their frequency of occurrence. The previously discovered planet<sup>1</sup> and the new ones, each of which orbits its own system of two stars, were found using NASA's Kepler space telescope.

For hundreds of years, scientists assumed that the Solar System is a typical example of a planetary system. That assumption was challenged in 1995 by the discovery<sup>3</sup> of 51 Pegasi b, the first planet to orbit a normal star other than the Sun. Although this planet is probably a gas giant (the lower limit on its mass is 0.47 Jupiter masses), it orbits at only 0.052 astronomical units (AU) from its star (1 AU is the average distance between Earth and the Sun). This means that 51 Pegasi b is 100 times closer to its star than Jupiter is to the Sun.

Planet 51 Pegasi b was discovered through precise measurements of the velocity of its parent star, which revealed the motion induced in the star by the presence of the orbiting planet. This method has proved very successful for spotting planets, and can be credited with the discovery of roughly 400 so far. As observational programmes continue, they become sensitive to planets on wider orbits (longer orbital periods). The dominant population of extrasolar planets currently consists of objects that are more massive than Jupiter and are separated from their host stars by several astronomical units; many of these are in multi-planet systems.

The other very successful method for discovering planets is to look for those that periodically transit (eclipse) their parent star. These transiting planets are a gold mine of information: they are the only ones whose size can be obtained, by measuring the amount of

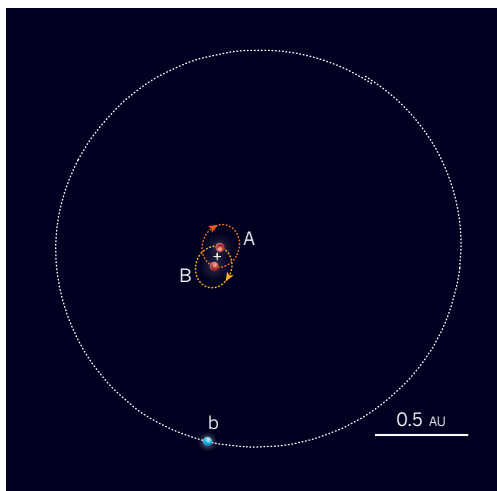


**Figure 1 | Orbital configuration of the Kepler-34 system.** The outer ellipse represents the orbital motion of the circumbinary planet Kepler-34 b, labelled b, around its host binary star system, which is composed of stars A and B in orbit around one another (as indicated by arrows). The plus sign shows the system's centre of mass. Spheres denote the orbital positions of the three bodies. One astronomical unit (AU) is the average distance between Earth and the Sun. Gravitational effects between the three bodies mean that this orbital configuration is gradually changing, so the bodies follow different paths on successive orbits. This is why the orbit of the planet shows a discontinuity in the upper part of the figure. Kepler-34 b is one of two circumbinary planets discovered by Welsh and colleagues<sup>2</sup>. (Modified from ref. 2.)

starlight blocked during transit. This means that their surface gravities and mean densities can be calculated, ultimately allowing the investigation of their internal structure and formation process.

The transit method has led to the discovery of more than 200 planets, predominantly by teams that operate small wide-field robotic survey telescopes at observatories spread around the world, such as HATNet<sup>4</sup> and SuperWASP<sup>5</sup>. These surveys are heavily biased towards large planets with small orbits. As a result, they are unparalleled sources of oddballs such as WASP-17 (ref. 6), the biggest and most rarefied planet known (up to twice the radius of Jupiter and only 6% as dense), and WASP-18 (ref. 7), which is ten times the mass of Jupiter and whirls around its host star every 23 hours (Jupiter's orbital period is 11.9 years).

The overriding aim of planetary research is to find one that might support life. Habitability most probably requires a rocky surface with liquid water, which, in turn, demands a planet no bigger than two Earth radii on an orbit with a period of hundreds of days. The transits of such a body will not only be infrequent but will cause the light from the star to drop by a puny 0.01%. Such a signal is much too meagre to pick up with ground-based telescopes, which suffer from the blurring effect of Earth's atmosphere, as well as inevitable interruptions due to daylight and bad weather.

Finding a habitable planet requires a larger — and much more expensive — telescope outside Earth's atmosphere. Enter the Kepler spacecraft, the primary aim of which is to use the transit method to discover Earth-like planets. It monitors 150,000 stars in the constellations Cygnus and Lyra, and has already found more than 2,000 candidate transiting planets. Three of these have been confirmed to be circumbinary planets: Kepler-34 b (Fig. 1) and Kepler-35 b, which Welsh *et al.* describe in their study<sup>2</sup>, and Kepler-16 b (ref. 1). Not only does each of these three planets transit both of its parent stars, but the stars themselves eclipse each other.

Although the discovery<sup>1</sup> of Kepler-16 b revealed that it was possible for such an object to exist, Welsh and colleagues' identification of two more circumbinary planets not only shows that such a planet is no freak object, but also allows an estimate of their prevalence to be made. The authors<sup>2</sup> find that, for short-period binary star systems, the frequency of occurrence of circumbinary planets is at least 1%. Taking into account the fraction of stars that are short-period binaries, this result implies that there are millions of such planets distributed throughout the Galaxy. This analysis does not account for longer-period binary star systems, which are similarly plentiful in the Galaxy.

Some circumbinary planets may even be habitable, although the three known ones are not. Kepler-16 b is slightly too cold, and Kepler-34 b and Kepler-35 b are too hot. They also have extreme seasons because the light received from their parent stars changes



not only during the stars' orbital periods (tens of days) and the planetary orbital period (hundreds of days), but also on much longer timescales through precession of the orbits due to three-body effects.

What common characteristics do these three planets have? The central binary systems have orbital separations of between 0.18 and 0.22 AU, and the planets orbit their hosts at distances of between 0.6 and 1.1 AU. They are thus all close to the smallest possible stable

orbits, but the fact that such planets were the first to be found is at least partly an effect of the detection method. As Kepler continues to observe, it will become sensitive to planets on longer periods: these three systems may represent only the tip of the iceberg. ■

---

**John Southworth** is in the *Astrophysics Group, Keele University, Newcastle-under-Lyme ST5 5BG, UK.*  
*e-mail: jkt@astro.keele.ac.uk*

1. Doyle, L. R. *et al. Science* **333**, 1602–1606 (2011).
2. Welsh, W. F. *et al. Nature* <http://dx.doi.org/nature.10768> (2012).
3. Mayor, M. & Queloz, D. *Nature* **378**, 355–359 (1995).
4. Bakos, G. Á., Lázár, J., Papp, I., Sári, P. & Green, E. M. *Publ. Astron. Soc. Pacif.* **114**, 974–987 (2002).
5. Pollacco, D. L. *et al. Publ. Astron. Soc. Pacif.* **118**, 1407–1418 (2006).
6. Anderson, D. R. *et al. Astrophys. J.* **709**, 159–167 (2010).
7. Hellier, C. *et al. Nature* **460**, 1098–1100 (2009).

## CELL CYCLE

## A division duet

The orchestration of cell division requires a programme of events choreographed by protein modification. A study shows that the relative activity of a phosphatase enzyme towards its substrates imposes order during the final act of division.

CURT WITTENBERG

Protein phosphorylation plays a central part in the intricate choreography of cell-cycle events<sup>1</sup>. A minimalistic model that holds that simple oscillations in the activity of a kinase enzyme called CDK — which phosphorylates cell-cycle proteins — is sufficient to promote the orderly progression of the cycle has been tested and confirmed<sup>2</sup>. However, protein phosphorylation, like other reversible cellular processes, depends not only on enzymes that catalyse the addition of phosphate groups, but also on those that catalyse dephosphorylation — the protein phosphatases. In a paper published in *Cell*, Bouchoux and Uhlmann<sup>3</sup> show that the intrinsic ability of a protein phosphatase to dephosphorylate specific substrates is crucial for establishing the proper order of events during the final stages of mitotic cell division.

The cell cycle proceeds from the G1 gap phase through the S phase, in which chromosomes are duplicated, and then on to the G2 gap phase and M phase (mitosis). At this point, the duplicated chromosomes are separated, leading to the creation of two daughter cells back at G1 phase. The protein phosphatase Cdc14 is required for the completion of chromosome segregation and subsequent events that lead to the resetting of the 'cell-cycle clock' such that the G1-phase daughter cells can initiate a new cycle<sup>4</sup> (Fig. 1). Those events are prevented before M phase because Cdc14 is sequestered in a region of the nucleus called the nucleolus, and so does not have access to its protein targets. However, it has remained unclear how, after its release, Cdc14 triggers the events that it regulates in a specific order. Indeed, elongation of the mitotic spindle occurs subsequent to spindle attachment to chromosomes, but before cell separation during cytokinesis, the final stage of mitosis.

Potential resolutions of that conundrum were set out in early models that explain the order of events during the cell cycle. In the domino model, order is a consequence of the dependency of later events on completion of those occurring earlier; in the clock model, order is imposed by an intrinsic timer<sup>5</sup>. Bouchoux and Uhlmann's study distinguishes

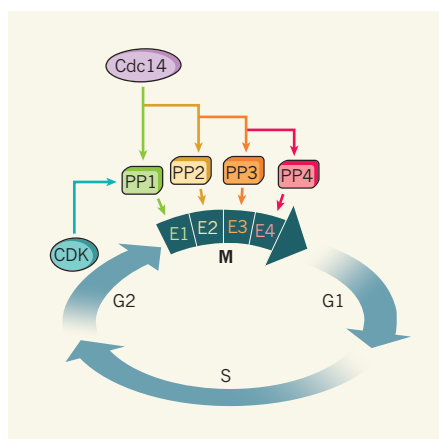


**Figure 1 | Imposing order through protein modification.** The cell cycle proceeds from the G1 phase to the S, G2 and, finally, M phases. At the end of M phase, the cell divides into two daughter cells, which enter the G1 phase. Several events (hypothetical events E1–E4) mediate the passage from M phase into G1 phase, and, for them to occur in an orderly manner, proteins phosphorylated by CDK (hypothetical phosphoproteins PP1–PP4) must be dephosphorylated by Cdc14 in the right order (from PP1 to PP4). Bouchoux and Uhlmann<sup>3</sup> show that the differential activity of Cdc14 towards CDK-phosphorylated proteins determines their orderly dephosphorylation, and so the order of events that depend on them.

between these two models, at least in the context of cell-cycle events that depend on Cdc14.

The authors engineered yeast strains in which the activities of Cdc14 and CDK could be modulated. Using careful *in vivo* analysis, they found that Cdc14 dephosphorylates CDK substrates in a sequence consistent with the order of cell-cycle events. That is, dephosphorylation events that promote spindle elongation occur after those that promote spindle attachment to chromosomes, but before those that promote spindle disassembly.

Cdc14 activity rises upon release from the nucleolus, allowing it to compete with CDK activity<sup>6</sup>. Bouchoux and Uhlmann<sup>3</sup> performed careful analysis using purified proteins *in vitro* and show that the timing of dephosphorylation *in vivo* is a consequence of Cdc14's differential activity towards specific substrates. That is, 'early' Cdc14 substrates — those

dephosphorylated *in vivo* during the initial Cdc14-triggered events — are more efficiently dephosphorylated by this enzyme *in vitro* than are 'late' substrates (Fig. 1). Furthermore, by establishing a competition between CDK and Cdc14 *in vitro* — a situation that exists during anaphase, the penultimate stage of mitosis, when both enzymes are highly active — they showed that dephosphorylation of early substrates is favoured. These findings establish that differences in the intrinsic activity of Cdc14 for specific substrates is sufficient to explain the order of dephosphorylation events observed *in vivo*; they also show that Cdc14 is an important component of a cell-cycle clock.

Could mechanisms besides the intrinsic activity of Cdc14 towards its substrates determine the order of protein dephosphorylation? Bouchoux and Uhlmann go to some lengths to exclude the involvement of Cdc14 localization within the nucleus, the dependence of dephosphorylation on specific events associated with mitotic exit, and the specificity that results from the activation of CDK by its different activating partners (cyclins).

Uhlmann and colleagues<sup>7</sup> have previously suggested that a CDK-based oscillator acting as a counterbalance to protein phosphatases might be responsible for order not just during mitotic exit, but throughout cell division. However, there is substantial biochemical and genetic evidence for interdependent relationships that impose order throughout the cell cycle<sup>6</sup>. For example, a recent study<sup>8</sup> demonstrated that the sequential action of specific cyclin–CDK complexes is required to eliminate Sic1 — a potent CDK inhibitor that restricts passage from G1 into S phase. The researchers<sup>8</sup> report that the order of action of those cyclin–CDK complexes is due not to differences in their intrinsic activity, but to differences in their specificity for particular phosphorylation sites on Sic1. That is, phosphorylation of a set of sites by one cyclin–CDK complex depends on prior phosphorylation of Sic1 by a different cyclin–CDK complex.

It seems, therefore, that multiple mechanisms are involved in imposing order on cell-cycle events. Nevertheless, the finding<sup>2</sup> that a single cyclin–CDK complex can orchestrate an effective cell-division cycle

suggests that, at least in some systems and under certain physiological conditions, the specificity of different cyclin–CDK complexes is dispensable. It remains to be established whether phosphatase-based mechanisms similar to those described by Bouchoux and Uhlmann<sup>3</sup> are essential for ordering cell-cycle events beyond mitotic exit, and whether they are even sufficient to replace cyclin–CDK specificity under particular conditions. It is largely because the other phosphatases

that provide the counterpoint to CDK are poorly understood that the choreography of this intricate dance remains incompletely described. ■

---

**Curt Wittenberg** is in the Department of Molecular Biology, The Scripps Research Institute, La Jolla, California 92024, USA. e-mail: [curtw@scripps.edu](mailto:curtw@scripps.edu)

1. Morgan, D. O. *Annu. Rev. Cell Dev. Biol.* **13**, 261–291 (1997).
2. Coudreuse, D. & Nurse, P. *Nature* **468**, 1074–1079 (2010).
3. Bouchoux, C. & Uhlmann, F. *Cell* **147**, 803–814 (2011).
4. Queralt, E. & Uhlmann, F. *Curr. Opin. Cell Biol.* **20**, 661–668 (2008).
5. Murray, A. W. & Kirschner, M. W. *Science* **246**, 614–621 (1989).
6. Sullivan, M. & Morgan, D. O. *Nature Rev. Mol. Cell Biol.* **8**, 894–903 (2007).
7. Uhlmann, F., Bouchoux, C. & López-Avilés, S. *Phil. Trans. R. Soc. Lond. B* **366**, 3572–3583 (2011).
8. Köivomägi, M. *et al. Nature* **480**, 128–131 (2011).